TECHNISCHE UNIVERSITÄT MÜNCHEN

Lehrstuhl für Aerodynamik und Strömungsmechanik

Weakly Compressible Models for Complex Flows

Felix Sebastian Schranner

Vollständiger Abdruck der von der Fakultät für Maschinenwesen der Technischen Universität München zur Erlangung des akademischen Grades eines

Doktor-Ingenieurs

genehmigten Dissertation.

Vorsitzender:	Prof. Wolfgang Polifke, Ph.D.
Prüfer der Dissertation:	Prof. Dr.-Ing. Nikolaus A. Adams
	Prof. Julian Andrzej Domaradzki, Ph.D.

Die Dissertation wurde am 15.11.2016 bei der Technischen Universität München eingereicht und durch die Fakultät für Maschinenwesen am 13.04.2017 angenommen.

Felix Sebastian Schranner
Graf-Konrad-Straße 2g
85368 Moosburg
Germany

schranne@tum.de

Released May 02, 2016
Typesetting LaTeX

Kurzfassung

In der Verfahrenstechnik werden zur Homogenisierung von flüssigen Medien oftmals Gasblasen eingesetzt. Der Pfad und die Nachlaufströmung der aufsteigenden Gasblasen sind für eine effiziente und effektive Homogenisierung ausschlaggebend. Die gezielte Steuerung ist daher essentiell. Der Vergleich von Ergebnissen aus experimentellen und simulativen phänomenologischen Studien hat gezeigt, dass diese einer Unschärfe unterliegen, beziehungsweise sogar stark divergieren. Anstelle offene Fragen zu klären, brachten numerische Quermethodenvergleiche nur weitere hervor. Parameterabhängigkeiten des Aufstiegspfads und der Nachlaufströmung sind daher weitestgehend unbekannt und eine Steuerung nicht möglich. Eine weitere Erforschung dieser mittels vorhandener numerischer oder experimenteller Methoden ist nicht notwendigerweise erfolgversprechend. Die Hauptintention der vorliegenden Arbeit ist es, numerische Methoden zu entwickeln beziehungsweise weiterzuentwickeln, welche zur Simulation von komplexen, schwach-kompressiblen Ein- und Mehrphasenströmungen mit höchster physikalischer Detailtreue eingesetzt werden können. Der zweite Fokus liegt auf der Entwicklung eines Verfahrens zur Quantifizierung der physikalischen Abbildungsgüte von numerischen Algorithmen und Einschätzung von Simulationsergebnissen entsprechend ihrer Aussagekraft. Die simulative Erforschung der Parameterabhängigkeiten von Pfad und Nachlaufströmung von in Flüssigkeiten aufsteigenden Gasblasen, und somit deren gezielte Steuerung, ist durch diese numerischen Methoden möglich.

Diese kumulative Dissertation gliedert sich folgendermaßen:
Ein Überblick über experimentelle und numerische Untersuchungen zur Erforschung von in Flüssigkeiten aufsteigenden Gasblasen ist in Kapitel 1 gegeben. Eine mathematische Beschreibung von Ein- und Zweiphasenströmungen und des Transports oberflächenspannungsaktiver Stoffe erfolgt in Kapitel 2. Die im Rahmen meiner Arbeit entwickelten beziehungsweise weiterentwickelten numerischen Methoden werden in Kapitel 3 beschrieben. Ein themenbezogener Literaturüberblick der einzelnen Teilgebiete und die wichtigsten Erkenntnisse der Hauptpublikationen wird in Kapitel 4 diskutiert, welche im Anhang B zu finden sind. Eine Aufstellung sämtlicher, im Rahmen dieser Arbeit entstandener, Publikationen befindet sich in Kapitel 5. Schlussfolgerungen dieser Arbeit werden in Kapitel 6 gezogen.

Abstract

In process engineering, gaseous bubbles are commonly used to homogenize fluids. The path and wake flow of gaseous bubbles ascending in liquids are crucial for efficient and effective homogenization. Hence, their controllability is highly desirable. Comparisons of results from experimental and numerical phenomenological investigations respectively have revealed uncertainties or even divergence of these. Numerical cross-method comparisons have not been able to clarify open questions, instead, they have raised further ones. The prevailing uncertainties in the parameter dependencies of the ascent path and wake flow prevent their controllability. Further investigations with existent numerical or experimental methods are not necessarily effective. Thus, the primary intention of this work is to elaborate on numerical methods for high-fidelity numerical simulations of weakly compressible single- and two-phase flows with complex flow structures. The second focus is on developing a method that quantifies the predictive capabilities of a numerical algorithm and distinguish regions of higher from those of lower reliability. The numerical investigation of the parameter dependencies of the path and wake flow of gaseous bubbles ascending in liquids, and thereby their controllability, is made possible with these methods.

This cumulative thesis structures as follows:
An overview of experimental and numerical investigations in the field of gaseous bubbles ascending in a liquids is given in Chapter 1. The governing equations of fluid motion, considering two phases, and surfactant transport are detailed in Chapter 2. The numerical methods that have been developed and further-developed respectively within the scope of this work are described in Chapter 3. A literature review of each topic, followed by key findings of the respective major publications are provided in Chapter 4, copies of these may be found in Appendix B. All publications that have emerged within the scope of this work are listed in Chapter 5. Conclusions of this work are drawn in Chapter 6.

Acknowledgements

Even the busiest bee is lost when on its own,
I am grateful for all the support you have shown.

This work has evolved within 2011 to 2016 during my time as a research assistant at the Institute of Aerodynamics and Fluid Mechanics, Technical University of Munich. At this venue, I express my sincere gratitude to those who have contributed extraordinarily to the success of my work.

I thank my "Doktorvater" Professor Nikolaus A. Adams. You have supported me and my work in countless ways, given guidance and advice, and provided an environment, fortunately tougher than I ever imagined, yet, with many liberties, to develop personally and professionally. Comparing this work to a bonsai, you have provided the seed and the tray.

I also thank Professor Julian A. Domaradzki. I am very proud that you are co-examining my thesis. The project we have pursued has inspired a great interest in me for numerical models as well as quantification of margins and uncertainties. You are one of the most respected people in our field, yet, you have remained a humble genius. I also thank you and your wife Anna for celebrating a wonderful New Year's Eve at your house with Elisa and me. Your contribution to this work is the shaping of the tree.

Professor Mirko Gamba, thank you for providing an invigorating work-environment during my time at Stanford which has turned into a long-term collaboration and thank you for being a true friend. You and all my friends from all over the world, e.g., Andreas, Chrissi, Matthias, Vroni, Jason, Christoph, Jae Hun, are the ones I relax with while pursuing one of the many activity we have hardly any time for. You are the light that a plant needs to survive. Representing my colleagues I thank Stefan, Vladyslav, Jakob, Felix, Christian, Dmitrii, Gustaf, Philipp and Moritz for providing the little extra that a creative work environment needs. You have been sharing your ideas and motivated fascinating new projects and pursuits. You are the water for letting my tree prosper.

My family has been the most important contributor to my work, they are the soil. I thank you, my mother Bärbel and father Gerhard for your continuous support, for parental, unconditional trust and love, for the sparks of hope, when all hope seemed to have faded, for accompanying me during hard and joyful times, as well as for educating me to be open-minded and eager for the unknown. B.J. and John (second set of parents), Birgit and Peter (best parents in-law), I express my deepest gratitude to you for treating me as one of your own children.

I am very grateful to my wife Elisa. You have become my best friend as well as my love of and partner for life. Thank you for many unconditional sacrifices you have given to support me and my work, for your unconditional understanding, patience, love, and traveling this path with me, unconditionally. You are my pillar and the air for my tree.

TABLE OF CONTENTS

NOMENCLATURE

Acronyms:

$2D$, $3D$	Two-dimensional, Three-dimensional
ACA	Artificial compressibility approach
ALDM	Adaptive local deconvolution method
AMR	Adaptive Multi-Resolution
BLG	Bubble rising due to the influence of gravity
CD	Central derivative
CFD	Computational Fluid Dynamics
CFL	Courant-Friedrichs-Lewy
CMP	Conservative mixing procedure
CSD	Computational subdomain
CSF	Continuum surface force
DFG	German Research Foundation (Deutsche Forschungsgemeinschaft)
DO	Design optimization
ENO	Essentially non-oscillatory
EOS	Equation of state
FD	Finite difference
FDM	Finite Difference Method
FV	Finite volume
FVM	Finite Volume Method
GFM	Ghost fluid method
IIM	Interface interaction method, Immersed interface method
ILES	Implicit Large Eddy Simulation/ underresolved DNS
ISGS	Implicit SGS
LES	Large Eddy Simulation
LS	Level-Set
MDEA	Modified differential equation analysis
NSE	Navier-Stokes equations
PDE	Partial differential equation

RANS	Reynolds-averaged-Navier-Stokes
RTI	Rayleigh-Taylor instability
SGS	Subgrid-scale
SIM	Sharp-Interface Method
SPH	Smoothed Particle Hydrodynamics
Surfactant	Surface active agent
TGV	Taylor-Green vortex
TVD	Total-variation diminishing
V&V	Validation & verification
WC	Weakly compressible
WENO	Weighted ENO
WENO-CU6, WENO-CU6-M1	6^{th} order WENO schemes

Greek Letters:

β	Compressibility, Renormalization factor for surfactant concentration [−]
$\boldsymbol{\sigma}_c$	Capillary stress vector [−]
$\boldsymbol{\sigma}_M$	Marangoni stress vector [−]
$\Delta\tau$	Pseudo-time step size [−]
$\Delta\Upsilon$	Interface segment length (2D) / area (3D) [−]
Δt	Time step size [−]
Δ	Difference
$\delta^{(i)}$	Wave strength i [−]
ϵ	Small value, interface thickness [−]
Γ	Domain boundary
γ	Surfactant concentration [−]
γ^*	Dimensional surfactant concentration $\left[\frac{1}{m}\right]$
γ_∞	Surfactant concentration in the maximum packing limit [−]
κ	Interface curvature [−]
κ_M	Mean curvature [−]
Λ	Diagonal eigenvalue matrix [−]
λ	Eigenvalue [−]
β	$(\beta_1, ..., \beta_7)$ Vector of mixing fractions [−]
$\boldsymbol{\Pi}$	Stress tensor [−]
$\mathcal{E}$	Dissipation function [−]
$\mathcal{E}_\nu$, $\mathcal{E}_n$	Viscous, numerical dissipation [−]
μ	Dynamic viscosity [−]
μ^*	Dimensional dynamic viscosity $\left[\frac{kg}{m\ s}\right]$

μ_b	Dynamic bulk viscosity [−]
ν	Kinematic viscosity [−]
ν^*	Dimensional kinematic viscosity $\left[\frac{m^2}{s}\right]$
Ω	Domain
ω	Ratio of specific heats [−]
ϕ	Level-set function [−]
π	Stress $\left[\frac{N}{m^2}\right]$, or ratio of circle circumference to diameter
Ψ	Acoustic work [−]
ρ	Density [−]
ρ^*	Dimensional density $\left[\frac{kg}{m^3}\right]$
σ	Surface tension coefficient [−]
σ^*	Dimensional surface tension coefficient $[\frac{N}{m}]$
θ	Shear-layer thickness [−]
Υ	Two-fluid interface
ξ_1, ξ_2	Fluid phases 1 (bulk), 2 (disperse)
ζ	Surfactant coverage [−]
ζ^{ξ_i}	Volume fraction of fluid $i = 1, 2$ [−]

Subscripts:

0	Initial condition, e.g. $t = 0$
$[\cdot]$	Discrete in space
α, β, γ	Spatial coordinates
$\perp$	Perpendicular
Υ	Interface
υ	Index
i, j, k	Grid indices
n	Numerical
ref	Reference state
s	In interface surface tangential direction
t	Derivative in time
x	Derivative in space

Non-dimensional Groups & Dimensional Parameters:

γ_{ref}	Reference Surfactant concentration $\left[\frac{1}{m}\right]$
μ_{ref}	Reference dynamic viscosity $\left[\frac{kg}{m\ s}\right]$
ν_{ref}	Reference kinematic viscosity $\left[\frac{m^2}{s}\right]$

ρ_{ref}	Reference density $\left[\frac{kg}{m^3}\right]$
σ_{ref}	Reference surface tension coefficient $[\frac{N}{m}]$
D_{ref}	Reference surface diffusivity $\left[\frac{m^2}{s}\right]$
Eo	$= \frac{\Delta\rho g L_{ref}^2}{\sigma_{ref}} \approx \frac{\rho_{ref} g L_{ref}^2}{\sigma_{ref}}$ Eötvös or Bond number $[-]$
Fr^2	$= \frac{We}{Eo} = \frac{U_{ref}^2}{g L_{ref}}$ Froude number $[-]$
L_{ref}	Reference length $[m]$
Mo	$= \frac{Eo\ We^2}{Re^4} = \frac{g\mu_{ref}^4 \Delta\rho}{\rho_{ref}^2 \sigma_{ref}^3}$ Morton number $[-]$
p_{ref}	Reference pressure $\left[\frac{kg}{m\ s^2}\right]$
Pe_s	$= \frac{U_{ref} L_{ref}}{D_s}$ Surface Peclet number $[-]$
Re	$= \frac{U_{ref} L_{ref}}{\nu_{ref}}$ Reynolds number $[-]$
t_{ref}	$= \frac{L_{ref}}{U_{ref}}$ Reference time $[s]$
U_{ref}	Reference velocity $\left[\frac{m}{s}\right]$
We	$= \frac{\rho_{ref} L_{ref} U_{ref}^2}{\sigma_{ref}}$ Weber number $[-]$

Other Symbols:

$\cdot$	Inner product
$:$	Frobenius inner product
Δ	Laplace-operator
δ_{ij}	Kronecker-symbol
$[\![\cdot]\!]$	Jump across material interface
$\mathbb{1}$	Identity operator (matrix, vector)
$\mathcal{O}$	Approximation order
∇	Nabla-operator
∇_n	$= (\mathbf{n}_I \otimes \mathbf{n}_I) \nabla$ Interface-normal gradient operator
∇_s	$= (\mathbb{1} - \mathbf{n}_I \otimes \mathbf{n}_I) \nabla$ Interface-tangential gradient operator
$\otimes$	Outer product, tensor product
$\bar{\cdot}$	Time-averaged
∂	Partial derivative
$\widehat{\cdot}$	Volume-averaged
$\widetilde{\cdot}$	Roe-averaged, volume fraction of variable

Roman Letters:

Δt	Time step $[-]$
$\mathbf{A}$	Local flux Jacobian $[-]$

$\mathbf{c}$	Advection velocity [−]
$\mathbf{D}(\mathbf{u})$	Deformation tensor [−]
$\mathbf{F}_i$	Flux vectors in direction i [−]
$\mathbf{g}$	$= (g_1, g_2, g_3)$ Vector of gravitational acceleration [−]
$\mathbf{K}$	Right eigenvectors corresponding to λ [−]
$\mathbf{L}$	Numerical flux [−]
$\mathbf{M}$	$= (M_1, ..., M_7)$ Mixing flux vector [−]
$\mathbf{m}$	Vector normal to the circumference of an interface element [−]
$\mathbf{n}$	Normal vector [−]
$\mathbf{R}$	$= (r_1, r_2, r_3)$ Vector of surface stresses [−]
$\mathbf{T}$	Viscous stress tensor [−]
$\mathbf{t}^{(1)}, \mathbf{t}^{(2)}$	Tangential vectors [−]
$\mathbf{U}$	$= (\rho, \rho u_1, \rho u_2, \rho u_3, \rho e_t)$ Vector of conservative states [−]
$\mathbf{u}$	$= (u_1, u_2, u_3)$Vector of Cartesian velocities [−]
$\mathbf{V}$	Vector for time iteration and extension [−]
$\mathbf{w}$	Vector of characteristic variables [−]
a	Speed of sound [−]
C_q	Linear weight bias [−]
c_v, c_p	Specific heats at constant velocity and pressure [−]
$D_i^+[\cdot],\ D_i^-[\cdot]$	Forward, backward difference approximation in direction i [−]
$D_i^c[\cdot]$	central difference approximation in direction i [−]
d_0, d_1, d_2, d_3	Ideal WENO weights [−]
D_s	Surface diffusivity [−]
D_s^*	Dimensional surface diffusivity $\left[\frac{m^2}{s}\right]$
E	Surface elasticity, spectral kinetic energy [−]
e_t	Specific total energy [−]
e_{in}	Specific internal energy [−]
E_{kin}	Kinetic energy [−]
e_{kin}	Specific kinetic energy [−]
F_ν	Viscous surface work [−]
F_{ekin}	Kinetic energy flux [−]
G	Surfactant mass [−]
H	Hesse-matrix [−]
h	Enthalpy [−]
k	Wavenumber [−]
$k(r)$	Curvature of osculating circle [−]

k_{max}	Largest resolvable wave number of capillary waves [−]
$l_{\alpha,1}$, $l_{\alpha,2}$	First and last cell of CSD in $\alpha = 1, 2, 3$ direction [−]
L_α	Maximum number of cells in $\alpha = 1, 2, 3$ direction [−]
p	Static pressure [−]
p^*	Dimensional static pressure $\left[\frac{kg}{m\ s^2}\right]$
$P^\perp$	Normal-projection operator [−]
q	Integer power exponent [−]
R	Specific gas constant [−]
r	Radius of osculating circle [−]
S	WENO candidate stencil [−]
s	Perimeter/circumferential area of an interface element [−]
S_g	Work of body forces [−]
t	Time [−]
t^*	Dimensional time $[s]$
u^*_α	Dimensional velocity $\left[\frac{m}{s}\right]$ in direction $\alpha = 1, 2, 3$
w	Characteristic variable [−]
x^*_α	Dimensional space coordinate $[m]$ in direction $\alpha = 1, 2, 3$
Z	$= \rho a$ Acoustic impedance [−]

Superscripts:

$(L), (R)$	Left and right cell-face state
ν	Viscous
$\perp$	Perpendicular
ξ_i	Associated to fluid phase $i = 1, 2$
a	Inviscid, advective
buo	Buoyant
$diff$	Diffusive
$evol$	Due to interface evolution
ext	Extension
n	Instant in time
T	Transpose of a matrix
tot	Total

1 Motivation

1.1 Introduction

This thesis comprises a comprehensible overview of my research in the field of the numerical modeling and evaluation of complex weakly compressible flows. Complex flows are single- and two-phase flows with multiscale flow structures, such as vortical and turbulent structures respectively, as well as interfaces undergoing severe distortions and topology changes respectively. The focus has been on three main topics: the optimal modeling of weakly compressible flows even when underresolving small scales, the evaluation of numerical models by means of extracting the local and global numerical dissipation rate and viscosity, and the modeling of two-phase flows incorporating surface active agents (surfactants).

My research is based on the German Research Foundation (DFG) project AD 186/7-2 "Untersuchung des Aufstiegsverhaltens von Gasblasen in einer Flüssigkeit" (engl. *exploration of the behavior of gaseous bubbles ascending in a liquid*). The focus of AD 186/7-2 is on the phenomenological investigations of single bubbles and bubble clusters during their ascent in liquids for large Reynolds numbers as well as investigations of the parameter-dependencies of bubble ascent paths and bubble wake flows. Moreover, AD 186/7-2 includes analysis of the influence of surfactants.

Flows of bubbles are two-phase flows. These are characterized by the coexistence of two disjunct phases separated by an interface. Two-phase flows may be distinguished either based on the aggregate phases of one fluid, or different chemical properties of two coexisting fluids. Depending on the material combination at the interface, different effects, such as diffusion between the fluids, phase changes, chemical reactions or surface tension effects may arise. Gaseous bubble flows are flows of a disperse gaseous phase within a bulk liquid of much higher density and dynamic viscosity. Within the scope of this work, flows of ascending bubbles are gaseous bubble flows with a dominant direction of motion parallel to the gravitation vector, or a surfactant gradient vector, yet, in opposite direction. During their ascent, the interfacial may evolve complex, multiscale structures.

Ascending bubbles induce vorticity into their wake, improving mixing and homogenization of the bulk phase [1]. The complex, multiscale vortical structures of the wake, at larger Reynolds numbers denoted bubble induced turbulence, strongly effect (turbulent) dispersion of the bubbles, bubble-coalescence, and -breakup [2]. As the individual ascent path and wake flow determine the efficiency of mixing when employing bubbles in process engineering applications, control of these is highly desirable.

1.2 State of the Art

A variety of theoretical and experimental investigations have gathered a multitude of information on ascending single-bubble flows. The first phenomenological investigations on the three-dimensional (3D) bubble dynamics, known to modern society, were conducted by Leonardo da Vinci (1452-1519) [5, 4]. His sketch 1.1 on the spiraling ascent of a gas bubble, is accompanied with the following phenomenological description: "When air together with water is submerged underneath a layer of flowing water, the air returns to the air. Thereby, it passes through the water on a winding path, while changing its shape continuously. And this happens because the lighter (fluid) cannot remain underneath the heavier (fluid). Moreover, it is being compressed continuously by the liquid above.", [6].

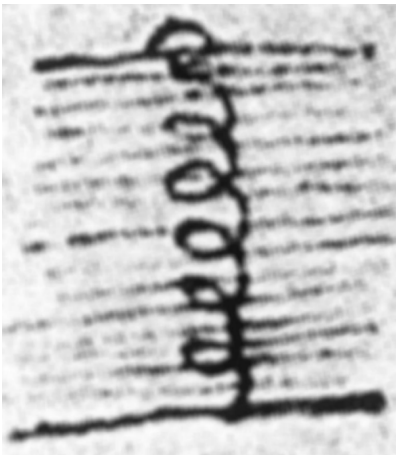

Figure 1.1: Leonardo da Vinci's sketch of a spiraling bubble ascent. Reproduced from [3, 4].

1.2.1 Experimental and Theoretical Studies

Since then, many more have studied the spiral as well as zigzag ascent path instability experimentally and analytically [7, 8, 9, 10, 11]. A series of studies have focused on the terminal ascent velocity, drag and shape of ascending bubbles [12, 13, 14, 15, 16, 17, 18, 19, 20, 21]. Wake flow structures have been investigated experimentally among others by [22, 23, 24]. The interaction of the wake flow with the bubble, potentially causing bubble shape oscillations have been investigated by e.g. [25, 26]. Landel *et al.* [27] find that smaller satellite bubbles which follow a larger one within its wake reduce turbulent dissipation and thereby drag.

Magnaudet and Eames [28] as well as Clift *et al.* [29] provide in depth summaries of the knowledge derived from these early experimental studies. Clift *et al.* have correlated observed bubble shapes, terminal Reynolds (Re), Eötvös (Eo), and Morton (Mo) number, see Fig. 1.2. Moreover, they define three principle shape regimes, spherical at low Reynolds and Eötvös numbers, ellipsoidal at high Reynolds and moderate Eötvös, and spherical-cap or ellipsoidal-cap at high Reynolds and Eötvös numbers. Note that the dimensionless groups $Re = \frac{U_{ref} L_{ref}}{\nu_{ref}}$, $Eo = \frac{\Delta\rho g L_{ref}^2}{\sigma_{ref}} \approx \frac{\rho_{ref} g L_{ref}^2}{\sigma_{ref}}$, $Mo = \frac{Eo\, We^2}{Re^4} = \frac{g\mu_{ref}^4 \Delta\rho}{\rho_{ref}^2 \sigma_{ref}^3}$ relate inertial to viscous forces, buoyant to capillary forces, and viscous to capillary forces, respectively. Herein $We = \frac{\rho_{ref} L_{ref} U_{ref}^2}{\sigma_{ref}}$ is the Weber number, relating inertial to capillary forces, furthermore, U_{ref}, L_{ref}, ρ_{ref}, σ_{ref}, ν_{ref}, and μ_{ref} denote the reference velocity, length-scale, density, surface tension coefficient, kinematic, and dynamic viscosity.

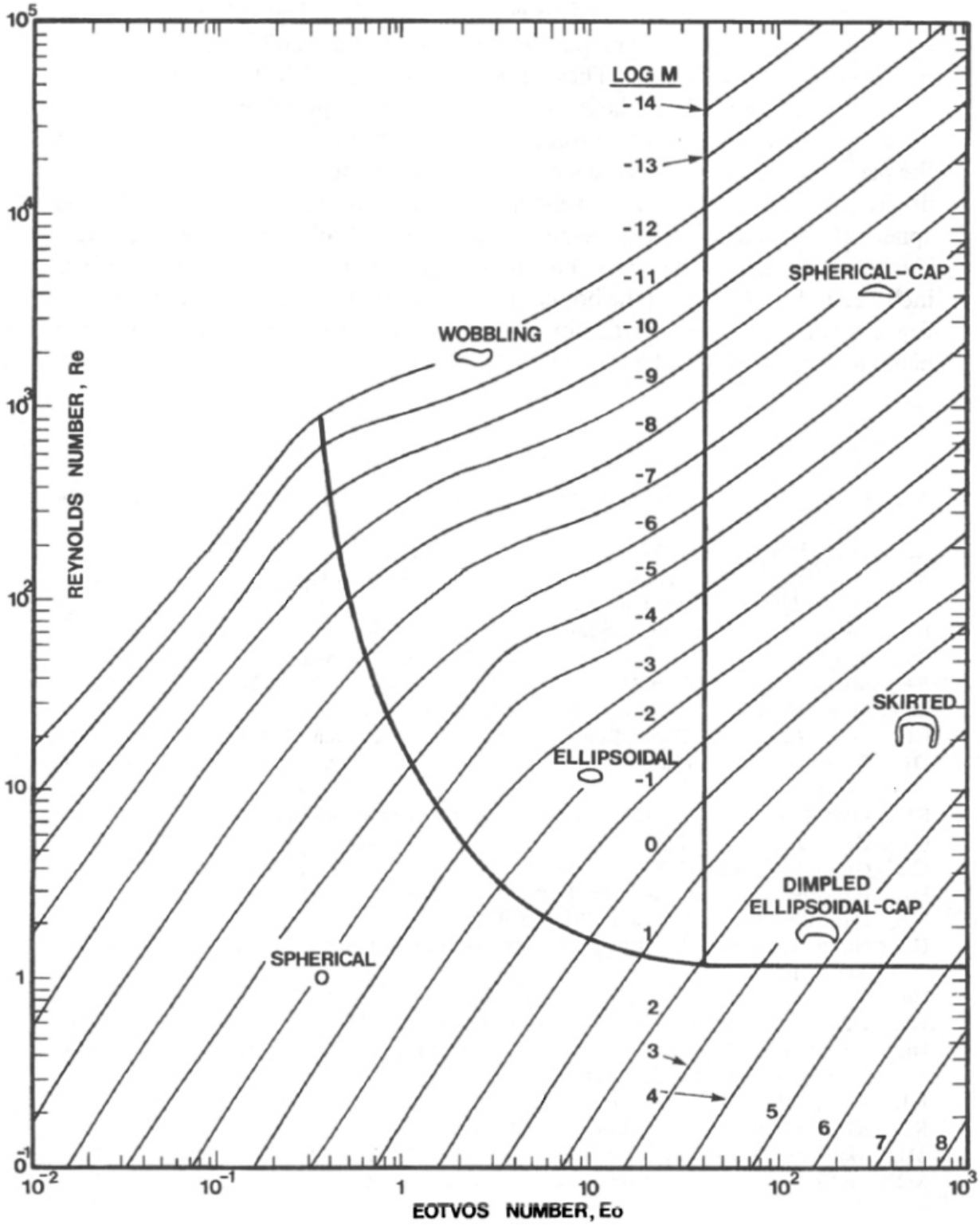

Figure 1.2: Bubble shapes and regimes for free buoyancy driven ascent in liquids. Adopted from [29].

Yet, even when initial and boundary conditions were identical, different bubble shapes and ascent paths have been observed experimentally [30]. The onset of the path instability for bubbles rising in water occurs at a bubble radius of $0.7mm$ in the experiments of Saffman [8], whereas an experiment with 'hyper clean' water [17] indicates a critical radius of $0.91mm$. Moreover, especially for smaller bubbles, the observed ascent velocity is larger than in the experiments of [31]. Comparing the results of [17] to those of Hartunian and Sears [7] shows that the decrease of ascent velocity, which is due to the influence of impurities in distilled water, is less dominant for larger bubbles. The dependence of the influence of surfactants on the kind and concentration has been documented by Bel Fdhila and Duineveld [32]. Aybers and Tapucu [18] record the ascent velocity of bubbles as a function of the distance these have traveled. For small sized bubbles, following a rectilinear path, the ascent velocity reaches its maximum after a short distance, then the bubble decelerates almost at a constant, non-zero rate. They conclude that the decrease is due to surfactant impurities. Their observations are confirmed independently by e.g. [33, 34, 35, 36]. The combined theoretical and experimental investigation of Griffith [37] can be noted as one of the first successful attempts to describe the decrease in ascent velocity due to surfactants for very simple cases. Yber and di Meglio [38] find that because of dilute proteins in water, which accumulate at the interface, ascending bubbles rigidify and decelerate with distance traveled, and in consequence behave hydrodynamically as solid spheres. Apart from an increase of drag, interface contaminations entail higher damping rates of shape oscillations, yet, the oscillation frequencies are unaffected [39]. Any kind of impurities, introduced unintentionally or intentionally, such as tracer particles for particle image velocimetry, act alike surfactants. At large Reynolds numbers interfacial contamination reduces deformation and shape oscillations [28]. Hence, the intrusiveness of experimental methods that rely on tracers intensifies with increasing Re [24]. The experiments of Zhang and Finch [40], however, indicate that below a certain threshold, particularly for dilute solutions, the terminal ascent velocity is independent of the surfactant concentration. The effect of surfactants on confined bubble ascent has been studied experimentally by Almatroushi and Borhan [41]. According to them, surfactants retard the motion of small bubbles due to adverse Marangoni stresses, yet, large bubbles benefit from surfactants as these allow the bubbles to deform away from walls. Besides being intrusive, experimental data acquisition of the shape and wake is challenging. Large, scarcely predictable deflections require real-time tracing and re-positioning of e.g. particle image velocimetry [23] or Schlieren [24] imaging systems. Nonpolar photochromatic dye, as used by Sanada *et al.* [42], is less intrusive, yet, detailed flows structures cannot be observed. In metallurgical applications, with opaque fluids, visual data acquisition is impossible. Alternative techniques such as ultrasound doppler velocimetry [43, 44] or local conductivity probe velocimetry [45, 46, 47] exist. Yet, these are often too costly, and data on flow fields as well as interface-evolution is limited.

1.2.2 Role of Computational Fluid Dynamics

Computational fluid dynamics (CFD) is free of these experimental deficiencies. Accurate prediction of natural and technical ascending bubble flows by means of CFD rely on proper numerical models. Even when resolution is low, these models need to physically consistently [48, 49, 50] reproduce the full range of length scales of vortical structures, which are the key to the technical application of ascending bubble flows. The bubble shape strongly effects its wake and vice versa. Hence, valid models for the interaction at the two-phase interface are essential. On the basis of valid models and their stable implementation, numerical studies can be carried out for a wide range of parameters.

Brabston and Keller [51] have studied the drag coefficients of ascending bubbles for a Reynolds number range between 0.1 to 200. The shape of axisymmetric incompressible bubbles for infinite Reynolds numbers is investigated in [52, 53]. The ascent velocities, drag coefficients and bubble shapes at high Reynolds numbers have been recorded by Miksis *et al.* [54] also assuming axial symmetry.
Toroidal bubbles forming from initially spherical ones and their ascent are the focus of Ref. [55]. Ryskin and Leal [56, 57] have studied numerically the shape, wake (by streamlines) and drag coefficients of axisymmetric buoyancy driven bubbles for $1 < Re < 200$ and for Weber numbers up to 20. Yang *et al.* [58] find that neither the initial bubble shape nor the intermediate relaxation determine the terminal velocity or shape, refuting experimental observations. Mougin *et al.* [59, 60, 61] have studied numerically the ascent of rigid ellipsoidal bubbles. According to them, the path instability is primarily due to a double threaded wake, which itself results from the wake instability. Moreover, the curvature of the bubble is the key parameter. Analysis of the forces acting on spherical bubbles indicate that as soon as the wake becomes 3D, a lateral force in the order of the buoyancy force initiates [61], which conjoined with the corresponding torque, entails horizontal deflections. The rotation of the bubble determines the sign of the trailing vortices and thereby the evolution of the wake during a zigzag ascent. These studies have confirmed the experimentally assumed strong coupling of the wake, shape and path. Yet, the interplay of interface evolution and wake flow were ignored.

Bonometti and Magnaudet [62] have investigated the evolution of shape and ascent velocity of single bubbles within an axisymmetric domain. Direct numerical simulations (DNS) of gaseous bubbles in liquids are challenging due to the large differences in density and viscosity between the phases and the high bubble Reynolds numbers typically encountered [63]. Therefore, fundamental numerical studies such as [64] have been carried out under the assumption of small density and viscosity ratios. Gaudlitz [30] and Gaudlitz and Adams [1] have simulated deforming ascending 3D bubbles with DNS. For bubbles rising steadily along a rectilinear path, their results are in very good agreement with experimental data.

For bubbles ascending along zigzag paths, the periodic shedding of connected hairpin vortices, including the head, as well as shape oscillations have been resolved, see Fig. 1.3.

It is observed that the connected hairpin vortex-legs are the cause of horizontal deflection, which is in agreement with Refs. [59, 60, 61]. Also considering dynamic shape deformations, Refs. [30, 1] show that the turbulent wake leads to symmetric and asymmetric bubble-shape oscillations. The necessity to take realistic bubble shapes into account when investigating path instabilities numerically, in contrast to a frozen shape [65, 66], is confirmed by Cano-Lozano *et al.* [67]. Tripathi *et al.* [68] have studied the shape-evolution and rise patterns of buoyancy driven air bubbles in water for a wide range of Galilei ($Ga = \frac{gL_{ref}^3}{\nu_{ref}^2}$) and Eötvös numbers. Their newly predicted type of bubble breakup, for low Morton numbers, has not yet been confirmed.

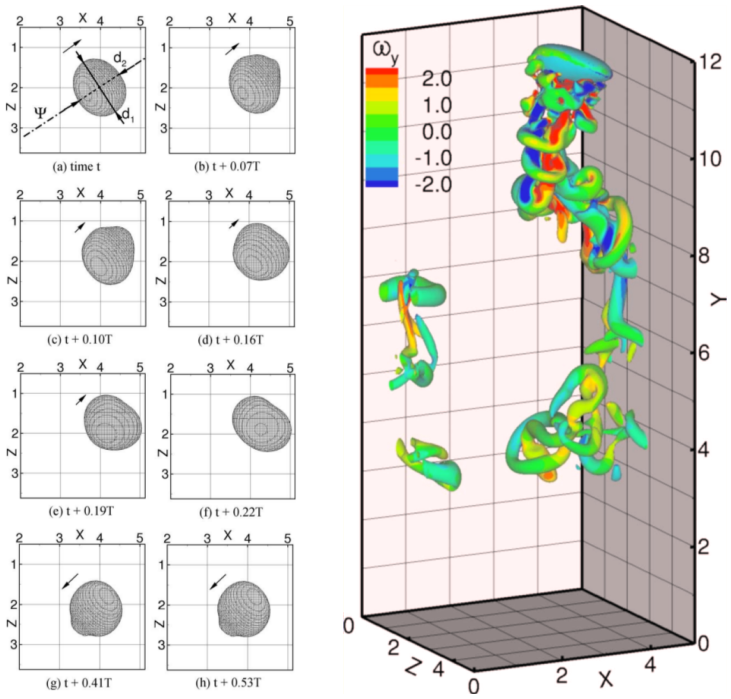

(a) Top views of bubble at different time instants during a half period of the path oscillation.

(b) Bubble with wake at time t, top-left view of Fig. 1.3a. The isosurface $\lambda_2 = -0.2$ viaualizes vortex structures; colored with vertical vorticity ω_y.

Figure 1.3: Simulation of 3D bubble ascending along a zigzag path. Reproduced from [1].

Few numerical investigations have been conducted on the effect of surfactants. In the study of Cuenot *et al.* [69] on spherical, axisymmetric bubbles rising in a liquid contaminated by a weakly soluble surfactant, it is found that when surface diffusion is subordinate to advection, at least parts of the bubble become stagnant. This in turn increases drag significantly up to the level of drag on a rigid sphere. Forking results of numerical and experimental investigations, for a review see e.g. [70], reveal the necessity to intensify research in this field. For instance, Takemura *et al.* [71] have compared experimental to numerical data, which are in good agreement and verify that the stagnant cap model explains the mechanism of the transition from fluid-sphere to solid-particle behavior. From their comparative studies they have even derived equations that estimate the drag coefficient of surfactant contaminated bubbles. Yet, Dijkhuizen *et al.* [72] have studied the drag force on single air bubbles rising in viscous liquids over a wide range of viscosities numerically. Their results are in excellent agreement with analytical theory, whereas their experimental data predict much higher drag forces as expected from existing correlations. These studies highlight the importance of modeling contaminants on the drag force.

1.3 Aim of this Thesis

It is evident that the parameter dependencies for free single-bubble ascent, as well as the influence of surfactants and impurities, have only been elaborated sufficiently enough to gain a basic understanding. Controlling these parameter dependencies effectively is, at this venue, to my knowledge, impossible. Validation of numerical results with experiments and cross-method comparison, see e.g. [73, 74, 75, 76, 77], strongly indicates the necessity for numerical methods that can reproduce the entire range of physical relevant phenomena of these configurations. The interaction of bubble wake and shape determine the ascent, which can only be predicted if local variations of surface tension as well as the propagation of vorticity, generated at the interface, into the wake flow is modeled accurately.

This work includes five contributions to the *exploration of the behavior of gaseous bubbles ascending in a liquid*:

- A physically consistent approach for the underresolved simulation of weakly compressible flows, see Sec. 4.1.
- A method to evaluate numerical fluid flow simulations by extracting the local and global numerical dissipation rate and viscosity, see Sec. 4.2.
- Optimization of the method for the underresolved simulation of weakly compressible flows, see Sec. 4.3.
- Grid-convergent benchmark simulations of classical viscous, incompressible two-phase flows with and without surface tension, see Sec. 4.4.
- A conservative interface-interaction method for the numerical simulation of two-phase flows with insoluble surfactant, see Sec. 4.5.

2 Basic Equations

In this chapter, the theoretical basis of the analytical continuum mechanics background for describing fluids in motion is set forth. Based on the description of the system of Navier-Stokes Equations (NSE) as partial differential equations (PDE), their compact form is developed. Thermodynamic closures for the NSE, applied within the scope of this work, are given. Fundamentals of the Riemann problem, used for solving the Euler equations within this work, are described. The equations describing immiscible two-fluid flows are provided and the chapter is closed with the system of equations describing the evolution of insoluble surfactants. This chapter results from combining Refs. [50, 114, 98, 102, 82].

2.1 Nondimensionalization

Within the scope of this work, all quantities are normalized with a reference state. The nondimensional measures in time and space are $\frac{t^*}{t_{ref}} = t$, $\frac{x^*_\alpha}{L_{ref}} = x_\alpha$. The density, the three Cartesian velocities, the static pressure, and the temperature are $\frac{\rho^*}{\rho_{ref}} = \rho$, $\frac{u^*_\alpha}{U_{ref}} = u_\alpha$, $\frac{p^*}{p_{ref}} = p$, $\frac{T^*}{T_{ref}} = T$. The dynamic, kinematic viscosity, and thermal conductivity are $\frac{\mu^*}{\mu_{ref}} = \mu$, $\frac{\nu^*}{\nu_{ref}} = \nu$, $\frac{\lambda^*}{\lambda_{ref}} = \lambda$. Considering surfactants and capillary effects, the surfactant concentration, surface diffusivity and surface tension coefficient are $\frac{\gamma^*}{\gamma_{ref}} = \gamma$, $\frac{D^*_s}{D_{ref}} = D_s$, $\frac{\sigma^*}{\sigma_{ref}} = \sigma$. $\alpha = 1, 2, 3$ denote the Cartesian directions and $p_{ref} = \frac{1}{2}\rho_{ref} U^2_{ref}$ the reference pressure. In two-fluid configurations, the reference density (ρ_{ref}), dynamic (μ_{ref}), kinematic (ν_{ref}) viscosity, are those of the bulk phase denoted as phase ξ_1. U_{ref}, L_{ref} are problem-dependent.

2.2 Single Phase Equations

2.2.1 The Conservation Equations

The motion of smooth and continuous fluid flows can be described by the conservation of mass, momentum and energy in differential conservation law form:

$$\frac{\partial \rho}{\partial t} + \nabla^T \cdot (\rho \mathbf{u}) = 0 \ , \tag{2.1a}$$

$$\frac{\partial \rho \mathbf{u}}{\partial t} + \nabla^T \cdot [\rho \mathbf{u} \otimes \mathbf{u} - \mathbf{\Pi}] = \frac{1}{Fr^2} \rho \mathbf{g} \ , \tag{2.1b}$$

$$\frac{\partial \rho e_t}{\partial t} + \nabla^T \cdot [(\rho e_t)\mathbf{u} - \mathbf{\Pi} \cdot \mathbf{u} + \mathbf{q}] = \frac{1}{Fr^2} \rho (\mathbf{g}^T \cdot \mathbf{u}) \ . \tag{2.1c}$$

$\mathbf{u} = (u_1, u_2, u_3)^T$, and $\mathbf{g} = (g_1, g_2, g_3)^T$ denote the vectors of Cartesian velocities and body forces respectively. The Froude number ($Fr^2 = \frac{We}{Eo} = \frac{U^2_{ref}}{g L_{ref}}$) relates inertial to buoyant forces. The specific total energy $e_t = e_{kin} + e_{in}$ decomposes into the specific kinetic energy $e_{kin} = \frac{1}{2}\mathbf{u}^2 = \frac{1}{2}u^2_\alpha$ and the specific internal energy e_{in}, for which

$$\frac{\partial \rho e_{kin}}{\partial t} + \nabla^T \cdot [(\rho e_{kin})\,\mathbf{u}] - \mathbf{u}^T \cdot \left(\nabla^T \cdot \mathbf{\Pi}\right) = \frac{1}{Fr^2} \rho (\mathbf{g}^T \cdot \mathbf{u}) \ , \tag{2.2}$$

$$\frac{\partial \rho e_{in}}{\partial t} + \nabla^T \cdot [(\rho e_{in})\,\mathbf{u} + \mathbf{q}] - \mathbf{\Pi} \colon (\nabla \otimes \mathbf{u}) = 0 \tag{2.3}$$

hold. The stress tensor is $\mathbf{\Pi} = -\mathbb{1}p + \mathbf{T}$. Under the assumption of Stokes' hypothesis, the viscous stress tensor is

$$\mathbf{T} = \mathbf{T}(\mathbf{u}) = \frac{1}{Re}\begin{bmatrix}\tau^{11} & \tau^{12} & \tau^{13}\\ \tau^{21} & \tau^{22} & \tau^{23}\\ \tau^{31} & \tau^{32} & \tau^{33}\end{bmatrix} = \frac{1}{Re}\left\{\mu D(\mathbf{u}) + \mathbb{1}\left(\mu_b - \frac{2}{3}\mu\right)(\nabla^T \cdot \mathbf{u})\right\} \tag{2.4}$$

with the deformation tensor $\mathbf{D}(\mathbf{u}) = \left(\frac{\partial u_\alpha}{\partial x_\beta} + \frac{\partial u_\beta}{\partial x_\alpha}\right)$. The dynamic viscosity is $\mu = \nu\rho$. For Newtonian fluids the bulk viscosity $\mu_b = 0$. Within the scope of this work, the dynamic viscosity is constant in each fluid phase, hence

$$\tau^{\alpha\beta} = \frac{\mu}{Re}\left(\frac{\partial u_\alpha}{\partial x_\beta} + \frac{\partial u_\beta}{\partial x_\alpha} - \frac{2}{3}\frac{\partial u_\gamma}{\partial x_\gamma}\delta_{\alpha\beta}\right). \tag{2.5}$$

With α, β, γ representing the three spatial directions. The Kronecker-symbol $\delta_{\alpha\beta}$ is unity for $\alpha = \beta$ and zero for $\alpha \neq \beta$. Within the scope of this work, heat fluxes due to thermal conduction are not considered, hence $\mathbf{q} = 0$. In compact form, the system of conservation laws (2.1) is

$$\frac{\partial \mathbf{U}}{\partial t} + \nabla^T \cdot \mathbb{F} = \mathbf{S}(\mathbf{U}), \tag{2.6}$$

where $\mathbf{U} = (\rho, \rho u_1, \rho u_2, \rho u_3, \rho e_t)^T$ and $\mathbb{F} = \left[\mathbf{F}_1^T, \mathbf{F}_2^T, \mathbf{F}_3^T\right]^T$ denote the vector of conserved variables and the flux tensor. $\mathbf{S}(\mathbf{U})$ are body forces. Within the scope of this work, solely buoyancy contributes,hence

$$\mathbf{S}(\mathbf{U}) = \frac{\rho}{Fr^2}\left[0, \mathbf{g}, \mathbf{g}^T \cdot \mathbf{u}\right]^T \ . \tag{2.7}$$

The flux vectors include advective and viscous components $\mathbf{F}_\beta = \mathbf{F}_\beta^a - \mathbf{F}_\beta^\nu$, $\beta = 1, 2, 3$. The advective (superscript a) and viscous (superscript ν) fluxes are

$$\mathbf{F}_\beta^a(\mathbf{U}) = \begin{pmatrix}\rho u_\beta\\ \rho u_\beta u_1 + p\delta_{\beta 1}\\ \rho u_\beta u_2 + p\delta_{\beta 2}\\ \rho u_\beta u_3 + p\delta_{\beta 3}\\ (\rho e_t + p)\, u_\beta\end{pmatrix}, \ \mathbf{F}_\beta^\nu(\mathbf{u}) = \begin{pmatrix}0\\ \tau^{\beta 1}\\ \tau^{\beta 2}\\ \tau^{\beta 3}\\ \tau^{\beta\alpha}u_\alpha\end{pmatrix}. \tag{2.8}$$

Eq. (2.6) includes partial derivatives. Only smooth solutions are permitted, discontinuities such as shock waves or material interfaces are excluded [78]. Applying Gauss's theorem, the integral of Eq. (2.6) over a domain Ω is

$$\int_\Omega \mathbf{U}_t \ dV + \oint_\Gamma \mathbb{F}^T \cdot \mathbf{n}_\Gamma \ d\Gamma' = \int_\Omega \mathbf{S}(\mathbf{U}) \ dV \ , \tag{2.9}$$

where $\mathbf{n}_\Gamma = (n_1, n_2, n_3)$ is the outward pointing unit normal vector of $\Gamma = \partial\Omega$. Eq. (2.9) admits discontinuous solutions and the smoothness assumption no longer holds [78]. Note that $V = \int_\Omega 1 \ dV = \int_{\Delta x_3}\int_{\Delta x_2}\int_{\Delta x_1} 1 \ dx_1' \ dx_2' \ dx_3'$, with Δx_α , $\alpha = 1, 2, 3$ being the extent in the three spatial directions.

The Kinetic Energy Equation in Integral Form

The integral of Eq. (2.2) over Ω is

$$\frac{\partial\left(E_{kin}\right)}{\partial t}+F_{ekin}+\Psi-F_{\nu}+\mathcal{E}_{\nu}=S_{g}, \tag{2.10}$$

where $E_{kin}=\int_{\Delta x_3}\int_{\Delta x_2}\int_{\Delta x_1}\rho e_{kin}\;dx_1'\;dx_2'\;dx_3'$. The kinetic energy flux, the acoustic work, the viscous surface work, and the work of body forces are

$$F_{ekin}=\int_{\Omega}\nabla^{T}\cdot\left[\left(\rho e_{kin}\right)\mathbf{u}\right]dV=\int_{\Gamma}\mathbf{n}_{\Gamma}^{T}\cdot\left[\left(\rho e_{kin}\right)\mathbf{u}\right]d\Gamma'\;, \tag{2.11}$$

$$\Psi=\int_{\Omega}\mathbf{u}^{T}\cdot\nabla p dV\;, \tag{2.12}$$

$$F_{\nu}=\int_{\Omega}\nabla^{T}\cdot\left(\mathbf{T}\cdot\mathbf{u}\right)dV=\oint_{\Gamma}\mathbf{n}_{\Gamma}^{T}\cdot\left(\mathbf{T}\cdot\mathbf{u}\right)d\Gamma'\;, \tag{2.13}$$

$$S_{g}=\frac{1}{Fr^{2}}\int_{\Omega}\rho(\mathbf{g}^{T}\cdot\mathbf{u})dV\;. \tag{2.14}$$

By denoting

$$\begin{aligned}\mathcal{E} &= \int_{\Omega}\mathcal{E}\;dV=\int_{\Omega}\frac{\tau^{\alpha\beta}}{\rho}\frac{\partial\left(u_{\beta}\right)}{\partial x_{\alpha}}dV= \\ &= \int_{\Delta x_3}\int_{\Delta x_2}\int_{\Delta x_1}\frac{\rho}{Re}\left[2\left(\frac{\partial u_1}{\partial x_1}^{2}+\frac{\partial u_2}{\partial x_2}^{2}+\frac{\partial u_3}{\partial x_3}^{2}\right)-\frac{2}{3}\left(\frac{\partial u_\alpha}{\partial x_\alpha}\right)^{2}+\right. \\ &+ \left.\left(\frac{\partial u_1}{\partial x_2}+\frac{\partial u_2}{\partial x_1}\right)^{2}+\left(\frac{\partial u_1}{\partial x_3}+\frac{\partial u_3}{\partial x_1}\right)^{2}+\left(\frac{\partial u_2}{\partial x_3}+\frac{\partial u_3}{\partial x_2}\right)^{2}\right]\;dx_1'\;dx_2'\;dx_3'\end{aligned} \tag{2.15}$$

as the dissipation function and assuming a constant kinematic viscosity, the viscous dissipation is

$$\mathcal{E}_{\nu}=\nu\mathcal{E}. \tag{2.16}$$

2.2.2 Equations of State

The caloric equation of state (EOS) $p=p(\rho,e_{in})$ closes the equations of fluid motion (2.1), (2.6), or (2.9). Further constitutive equations can be solved successively, e.g. the general relation for the speed of sound which is essential for wave propagation solutions

$$a^{2}=\left.\frac{\partial p}{\partial\rho}\right|_{s}=\left.\frac{\partial p}{\partial\rho}\right|_{e_{in}}+\left.\frac{p}{\rho^{2}}\frac{\partial p}{\partial e}\right|_{\rho}\;. \tag{2.17}$$

A well-defined EOS is thermodynamically stable [79], i.e. the specific internal energy e_{in} is a convex function. Furthermore, a well-posed EOS leads to simple and unique results in the Riemann problem [79].

Artificial Compressibility Approach for Weakly Compressible Fluids

At Mach numbers $Ma = \frac{||\mathbf{u}||}{a} \ll 1$ compressibility is negligible, i.e. $\beta = \frac{1}{\rho}\frac{\partial \rho}{\partial p} \approx 0$. In contrast to classical incompressible approaches, claiming $\beta = 0$, the artificial compressibility approach (ACA) of Chorin and Temam [80, 81] assumes a non-zero, yet constant compressibility. The isentropic compressibility relates to the speed of sound according to $a^2 = \frac{1}{\rho\beta|_s}$, see also Eq. (2.17). For isothermal processes $\beta = \beta|_T = \beta|_s$, and the ratio of specific heats is $\omega = 1$. Pressure and density are linearly related by the caloric EOS

$$p = p(\rho) = a^2\rho \tag{2.18}$$

for such artificially compressible fluids. Density fluctuations are small, if a is large.

Tait's Approach for Weakly Compressible Fluids

Tait's EOS applies to weakly compressible and barotropic fluids. In contrast to the ACA, $\beta|_T \neq \beta|_s$. Hence $\omega = \frac{\beta|_T}{\beta|_s} \neq 1$, and the EOS

$$p = p(\rho) = p_1 \left[\left(\frac{\rho}{\rho_0} \right)^{\omega} - 1 \right] + p_0 \tag{2.19}$$

is highly nonlinear. The speed of sound is

$$a^2 = \frac{p_1}{\rho_0^{\omega}} \omega \rho^{(\omega-1)} = \frac{\omega}{\rho} \left(p - p_0 + p_1 \right) \tag{2.20}$$

Generally, $\omega \in (1; 7.15]$, $p_0 = p(t = 0)$.

Remarks for Fluids Modeled as Weakly Compressible

Remark 1:
For both approaches, the energy equation is decoupled from the continuity and momentum equations, see Eq. (2.6). For the Tait EOS, a formal e_{in} may be obtained from $p = (\omega - 1)\,\rho e_{in}$. The ACA does not permit a valid expression for e_{in}.
Remark 2:
Within the scope of this work, nonlinearity in the EOS is minimized by $\omega = 1 + 10^{-6}$, p_1 is chosen based on a target (artificial) speed of sound $a \approx const.$ and the restriction of constraining Ma below 0.3 according to Eq. (2.20).

2.3 Riemann Problem and Solution to the Euler Equation

A general analytical solution to nonlinear hyperbolic PDEs such as the one-dimensional Euler equations

$$\mathbf{U_t} + \mathbf{F}_x^a(\mathbf{U}) = \mathbf{0}, \tag{2.21}$$

cannot be determined. Yet, their locally linearized approximates permit constructing local solutions that in sum lead to approximate global solutions. Within the following, the concepts for solving transport phenomena described by nonlinear hyperbolic systems are outlined. The basis is the Riemann problem, an initial value problem with piecewise constant, yet discontinuous data,

$$\mathbf{U}(x,0) = \begin{cases} \mathbf{U}^{(L)} & \text{if } \; x \leq 0 \\ \mathbf{U}^{(R)} & \text{if } \; x > 0 \end{cases}, \tag{2.22}$$

in conjunction with a hyperbolic system such as (2.21). $\mathbf{F}_x^a(\mathbf{U})$ of Eq. (2.21) may be rewritten as $\mathbf{F}_x^a(\mathbf{U}) = \frac{\partial \mathbf{F}^a}{\partial \mathbf{U}} \frac{\partial \mathbf{U}}{\partial x} = \mathbf{A}(\mathbf{U})\mathbf{U}_x$, where

$$\mathbf{A}(\mathbf{U}) = \begin{bmatrix} \partial F_1^a/\partial U_1 & \cdots & \partial F_1^a/\partial U_m \\ \partial F_2^a/\partial U_1 & \cdots & \partial F_2^a/\partial U_m \\ \vdots & \ddots & \vdots \\ \partial F_m^a/\partial U_1 & \cdots & \partial F_m^a/\partial U_m \end{bmatrix}$$

denotes the Jacobian matrix of the flux. Replacing $\mathbf{A}(\mathbf{U})$ with a constant Jacobian $\mathbf{A}$, such that $\mathbf{F}^a(\mathbf{U}) = \mathbf{A}\mathbf{U}$, leads to the linear(ized) hyperbolic system

$$\mathbf{U}_t + \mathbf{A}\mathbf{U}_x = \mathbf{0}. \tag{2.23}$$

For a diagonalizable $\mathbf{A}$, i.e. when $\mathbf{A} = \mathbf{K}\Lambda\mathbf{K}^{-1}$, where Λ is the diagonal eigenvalue matrix and $\mathbf{K}$ the matrix of right eigenvectors,

$$\Lambda = \begin{bmatrix} \lambda_1 & \cdots & 0 \\ 0 & \ddots & 0 \\ 0 & \cdots & \lambda_m \end{bmatrix}, \quad \mathbf{K} = \left[\mathbf{K}^{(1)}, \; \cdots, \; \mathbf{K}^{(m)}\right], \quad \mathbf{A}\mathbf{K}^{(i)} = \lambda_i \mathbf{K}^{(i)}, \tag{2.24}$$

with λ_i being the eigenvalues of $\mathbf{A}$ and their corresponding eigenvectors $\mathbf{K}^{(i)}$, a vector $\mathbf{w} = (w_1, \cdots, w_m)^T$ for which

$$\mathbf{w} = \mathbf{K}^{-1}\mathbf{U} \quad \text{and} \quad \mathbf{U} = \mathbf{K}\mathbf{w} \tag{2.25}$$

can be found. $\mathbf{w}$ is the vector of characteristic variables w_i, $i \in [1, m]$ of the system (2.23). Due to $\mathbf{A} = const.$, $\mathbf{K} = const.$, $\mathbf{U}_t = \mathbf{K}\mathbf{w}_t$, and $\mathbf{U}_x = \mathbf{K}\mathbf{w}_x$ follows. Substitution into Eq. (2.23) and left-sided multiplication with $\mathbf{K}^{-1}$ leads to the characteristic form

$$\mathbf{w}_t + \Lambda\mathbf{w}_x = \mathbf{0}\ . \tag{2.26}$$

Let λ_i be a characteristic speed, then for each characteristic variable, w_i, $\frac{\partial w_i}{\partial t} + \lambda_i \frac{\partial w_i}{\partial x} = 0, \quad i = 1, \cdots, m$ holds, i.e. w_i is constant along the characteristic curve λ_i. A system is considered strictly hyperbolic if $\lambda_1 < \lambda_2 < \cdots < \lambda_m$. According to Eq. (2.25),

$$\mathbf{U}(x,t) = \sum_{i=1}^{m} w_i(x,t)\mathbf{K}^{(i)} \ , \tag{2.27}$$

thus a linear combination of the eigenvectors $\mathbf{K}^{(i)}$. Since each $w_i(x,t)$ propagates with constant λ_i, it is

$$\mathbf{U}(x,t) = \sum_{i=1}^{m} w_i^{(0)}(x - \lambda_i t)\mathbf{K}^{(i)} \ , \tag{2.28}$$

where $w_i^{(0)}$ are the initial values of the characteristic variables. $\mathbf{K}^{(i)}$ are linearly independent. Thus, one finds for the constant left $\mathbf{U}^{(L)}$ and right $\mathbf{U}^{(R)}$ states that $\mathbf{U}^{(L)} = \sum_{i=1}^{m} \alpha_i \mathbf{K}^{(i)}$, $\mathbf{U}^{(R)} = \sum_{i=1}^{m} \beta_i \mathbf{K}^{(i)}$, where α_i, β_i are such that the constant propagation of w_i can be stated with velocity λ_i:

$$w_i(x,t) = w_i^{(0)}(x - \lambda_i t) = \begin{cases} \alpha_i \text{ if } x - \lambda_i t \leq 0, \\ \beta_i \text{ if } x - \lambda_i t > 0 \end{cases} \text{ for } i = 1, \cdots, m \tag{2.29}$$

With Eq. (2.28), one finds that

$$\mathbf{U}(x,t) = \sum_{i=I+1}^{m} \alpha^{(i)}\mathbf{K}^{(i)} + \sum_{i=1}^{I} \beta^{(i)}\mathbf{K}^{(i)}, \tag{2.30}$$

where I is the maximal index for which $x - \lambda_i t > 0$. The jump over the wave structure is

$$\Delta\mathbf{U} = \mathbf{U}^{(R)} - \mathbf{U}^{(L)} = \sum_{i=1}^{m} (\beta^{(i)} - \alpha^{(i)})\mathbf{K}^{(i)} = \sum_{i=1}^{m} \delta_i \mathbf{K}^{(i)} \tag{2.31}$$

As $\mathbf{F}^a(\mathbf{U}) = \mathbf{A}\mathbf{U}$,

$$\Delta\mathbf{F}^a(\mathbf{U}) = \mathbf{A}\Delta\mathbf{U} = \mathbf{F}^{a,(R)} - \mathbf{F}^{a,(L)} = \sum_{i=1}^{m} \delta^{(i)}\lambda_i \mathbf{K}^{(i)}, \tag{2.32}$$

with the wave strength $\delta^{(i)}$.

2.4 Two-Phase Problem Formulation

Consider the system of two distinct and immiscible fluid phases ξ_1 and ξ_2 as sketched in Fig. 2.1, where $\Omega^{\xi_i}(t) \subseteq \Omega(t) \mid \Omega^{\xi_1}(t) \cup \Omega^{\xi_2}(t) = \Omega(t)$. The fraction of Ω covered by phase ξ_i is $\zeta^{\xi_i}(t) = \frac{1}{V} \int\limits_{\Omega \cap \Omega^{\xi_i}} dV$. Within Ω $\zeta^{\xi_1} + \zeta^{\xi_2} = 1$. Some part of the boundary of fluid phase ξ_1 is shared with the boundary of phase ξ_2, denoted as $\partial\Omega^{\xi_1}(t)$ and $\partial\Omega^{\xi_2}(t)$. This shared boundary $\Upsilon = \partial\Omega^{\xi_1,\xi_2}(t) = \Omega^{\xi_1}(t) \cap \Omega^{\xi_2}(t)$ of length $\Delta\Upsilon$ is the two-fluid interface, generally $\Upsilon \cap \Gamma = 0$.

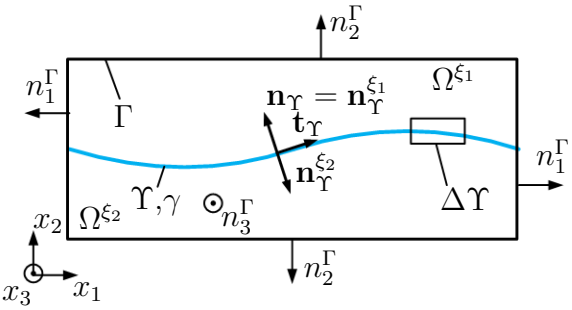

Figure 2.1: Schematic of the two-fluid configuration. Adopted from [82].

In each $\Omega^{\xi_i}(t)$, $i = 1, 2$ the system of conservation equations (2.9) holds [83]. In close proximity to the interface, the conservation equations for mass

$$\frac{d}{d\,t}\int_{\Delta\Upsilon_\varepsilon} \rho dV - \int_{\Delta\Upsilon^{\xi_1}} \rho^{\xi_1} \mathbf{n}_\Upsilon^{T,\xi_1} \cdot \left(\mathbf{u}^{\xi_1} - \mathbf{u}_\Upsilon\right) d\,\Upsilon' - \int_{\Delta\Upsilon^{\xi_2}} \rho^{\xi_2} \mathbf{n}_\Upsilon^{T,\xi_2} \cdot \left(\mathbf{u}^{\xi_2} - \mathbf{u}_\Upsilon\right) d\,\Upsilon' = 0\,, \quad (2.33)$$

and momentum

$$\begin{aligned} &\frac{d}{d\,t}\int_{\Delta\Upsilon_\varepsilon} (\rho\mathbf{u})\, dV - \int_{\Delta\Upsilon^{\xi_1}} \rho\mathbf{u}^{\xi_1}\mathbf{n}_\Upsilon^{T,\xi_1} \cdot \left(\mathbf{u}^{\xi_1} - \mathbf{u}_\Upsilon\right) d\,\Upsilon' - \\ &- \int_{\Delta\Upsilon^{\xi_2}} \rho\mathbf{u}^{\xi_2}\mathbf{n}_\Upsilon^{T,\xi_2} \cdot \left(\mathbf{u}^{\xi_2} - \mathbf{u}_\Upsilon\right) d\,\Upsilon' = \int_{\Delta\Upsilon^{\xi_1}} \mathbf{n}_\Upsilon^{T,\xi_1} \cdot \mathbf{\Pi}(\mathbf{u})^{\xi_1} d\,\Upsilon' + \\ &+ \int_{\Delta\Upsilon^{\xi_2}} \mathbf{n}_\Upsilon^{T,\xi_2} \cdot \mathbf{\Pi}(\mathbf{u})^{\xi_2} d\,\Upsilon' + \frac{1}{Fr^2}\int_{\Delta\Upsilon_\varepsilon} \rho\mathbf{g}\, dV + \frac{1}{We}\oint_s \mathbf{m}\, \sigma ds'\,, \end{aligned} \quad (2.34)$$

hold. $\mathbf{n}_\Upsilon^{\xi_1} = \mathbf{n}_\Upsilon$ and $\mathbf{n}_\Upsilon^{\xi_2} = -\mathbf{n}_\Upsilon$, with $\mathbf{n}_\Upsilon$ denoting the interface-normal vector.

An interface segment of perimeter s, surface area $\Delta\Upsilon^{\xi_1}$ and $\Delta\Upsilon^{\xi_2}$ is sketched in Fig. 2.2. For an infinitesimally thin interface, i.e. $\varepsilon \to 0$, it follows that $\Delta\Upsilon^{\xi_1} = \Delta\Upsilon^{\xi_2} = \Delta\Upsilon$. The interface contains neither mass nor momentum [29], and phase changes do not occur. Continuity at the interface thus implies

$$\mathbf{n}_\Upsilon^T \cdot \mathbf{u}^{\xi_1}\big|_\Upsilon = u_{\Upsilon,\perp}^{\xi_1} = \mathbf{n}_\Upsilon^T \cdot \mathbf{u}^{\xi_2}\big|_\Upsilon = u_{\Upsilon,\perp}^{\xi_2} = u_{\Upsilon,\perp}\,. \quad (2.35)$$

The interface acts as a no-slip boundary [63], hence, the interface-tangential velocity is continuous [84]

$$||\mathbf{u}_{\Upsilon,\parallel}^{\xi_1}|| = ||\mathbf{u}_{\Upsilon,\parallel}^{\xi_2}|| = ||\mathbf{u}_{\Upsilon,\parallel}||. \quad (2.36)$$

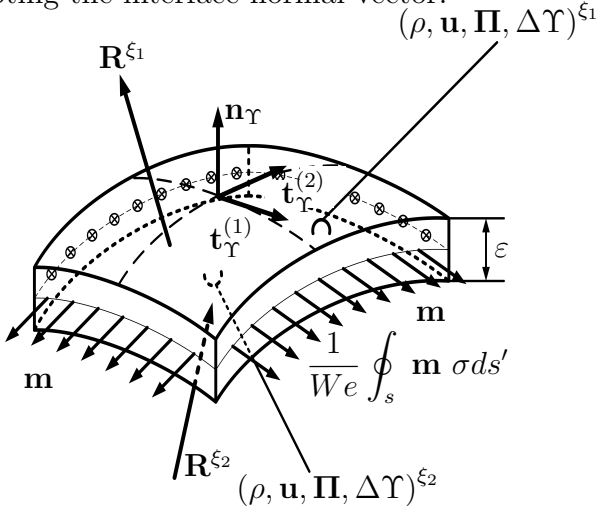

Figure 2.2: $3D$ schematic of an interface element. Adopted from [82].

At the interface, the velocity is $\mathbf{u}_\Upsilon = \mathbf{u}_{\Upsilon,\perp} + \mathbf{u}_{\Upsilon,\parallel}$, with $\mathbf{u}_{\Upsilon,\perp} = u_{\Upsilon,\perp}\mathbf{n}_\Upsilon^T$, and $\mathbf{u}_{\Upsilon,\parallel} = \mathbf{u}_{\Upsilon,\parallel}^{(1)} + \mathbf{u}_{\Upsilon,\parallel}^{(2)} = u_{\Upsilon,\parallel}^{(1)}\mathbf{t}_\Upsilon^{(1)} + u_{\Upsilon,\parallel}^{(2)}\mathbf{t}_\Upsilon^{(2)}$, respectively. Note also that $\mathbf{u}_{\Upsilon,\parallel} \cdot \mathbf{u}_{\Upsilon,\perp} = 0$. The interface-tangentials $\mathbf{t}_\Upsilon^{(1)}$, $\mathbf{t}_\Upsilon^{(2)}$ are computed according to [85]. Together with $\mathbf{n}_\Upsilon$ they build an orthonormal basis on the interface. In 2D, $\mathbf{t}_\Upsilon^{(2)}$ is obsolete. In close proximity to Υ, the two fluids share the interface's characteristic motion, thus, the interface velocity is a property of both phases [86]. Considering Eq. (2.35), the interface momentum equation (2.34) becomes

$$0 = \mathbf{R}^{\xi_1}\Delta\Upsilon - \mathbf{R}^{\xi_2}\Delta\Upsilon + \frac{1}{We}\oint_s \mathbf{m}\,\sigma ds' \,, \tag{2.37}$$

where $\mathbf{R}^{\xi_i}(\mathbf{x}, \mathbf{n}_\Upsilon) = \mathbf{\Pi}(\mathbf{u})^{\xi_i} \cdot \mathbf{n}_\Upsilon$ represents the surface stresses, [84]. The term $\frac{1}{We}\oint_s \mathbf{m}\,\sigma ds'$ denotes the surface tension force exerted in direction of the unit vector tangential to the free surface of area $\Delta\Upsilon$ and normal to the perimeter s. One finds that [87, 88]

$$\begin{aligned}\oint_s \mathbf{m}\,\sigma ds' = \int_{\Delta\Upsilon} \nabla_s\sigma(\mathbf{x},t)d\Upsilon' = \int_{\Delta\Upsilon} \nabla\left(\sigma\left(\mathbb{1} - \mathbf{n}_\Upsilon \otimes \mathbf{n}_\Upsilon\right)\right)d\Upsilon' = \\ = \left[-\sigma\mathbf{n}_\Upsilon\left(\nabla^T \cdot \mathbf{n}_\Upsilon\right) + \left(\nabla_s\sigma\right)\right]\Delta\Upsilon \,.\end{aligned} \tag{2.38}$$

$\nabla_s = \left(\mathbb{1} - \mathbf{n}_\Upsilon \otimes \mathbf{n}_\Upsilon\right)\nabla$ denotes the interface-tangential gradient operator. Consequently, the stress balance at the interface segment is

$$[\![\mathbf{R}]\!]_\Upsilon = -\mathbf{R}^{\xi_1} + \mathbf{R}^{\xi_2} = \frac{1}{We}\left[-\sigma\mathbf{n}_\Upsilon\left(\nabla^T \cdot \mathbf{n}_\Upsilon\right) + \left(\nabla_s\sigma\right)\right] \,. \tag{2.39}$$

The first term on the right of equation (2.39),

$$\boldsymbol{\sigma}_c(\gamma(\mathbf{x},t)) = -\frac{1}{We}\sigma(\gamma(\mathbf{x},t))\mathbf{n}_\Upsilon\left(\nabla^T \cdot \mathbf{n}_\Upsilon\right) = \sigma_c(\gamma(\mathbf{x},t))\mathbf{n}_\Upsilon \tag{2.40}$$

is the capillary stress, balancing the jump in normal stress

$$\begin{aligned}[\![r]\!]_{\Upsilon,\perp} = \mathbf{n}_\Upsilon^T \cdot [\![\mathbf{R}]\!]_\Upsilon = -\mathbf{n}_\Upsilon^T \cdot \mathbf{R}^{\xi_1} + \mathbf{n}_\Upsilon^T \cdot \mathbf{R}^{\xi_2} = \\ = -r_\perp^{\xi_1} + r_\perp^{\xi_2} = \sigma_c(\gamma(\mathbf{x},t)) \,.\end{aligned} \tag{2.41}$$

Note that $r_\perp^{\xi_i} = \mathbf{n}_\Upsilon^T \cdot \mathbf{R}^{\xi_i} = \mathbf{n}_\Upsilon^T \cdot \mathbf{\Pi}^{\xi_i} \cdot \mathbf{n}_\Upsilon = n^\beta \Pi_{\beta\gamma}^{\xi_i} n^\gamma = (\mathbf{n}_\Upsilon \otimes \mathbf{n}_\Upsilon) : \mathbf{\Pi}^{\xi_i} = P^\perp\mathbf{\Pi}^{\xi_i}$, which is the projection of the stress tensor of phase ξ_i normal to the interface by the normal-projection operator $P^\perp$, compare [89]. The surfactant concentration $\gamma(\mathbf{x},t)$ is the amount of surfactant present within an element of interface $\Delta\Upsilon$. Due to (2.35), the shear stresses in interface normal direction diminish ideally, i.e. $\tau_{nn}^{\xi_i} = 0$. The second term,

$$\boldsymbol{\sigma}_M(\gamma) = \frac{1}{We}\nabla_s\sigma(\gamma) \,, \tag{2.42}$$

is the Marangoni stress. It balances the discontinuity of the interface-tangential stresses

$$[\![r]\!]_{\Upsilon,\parallel} = -r_\parallel^{\xi_1} + r_\parallel^{\xi_2} = |\boldsymbol{\sigma}_M(\gamma)| = \sigma_M(\gamma) \,. \tag{2.43}$$

Hereby, $r_{\parallel}^{\xi_i} = \Pi_{\delta\delta}^{\xi_i} - n^{\beta}\Pi_{\beta\gamma}^{\xi_i} n^{\gamma} = (\mathbb{1} - \mathbf{n}_{\Upsilon} \otimes \mathbf{n}_{\Upsilon}) : \mathbf{\Pi}^{\xi_i} = P^{\parallel}\mathbf{\Pi}^{\xi_i}$ is the interface-tangential projection of the shear stress tensor of phase ξ_i. Decomposed into the respective surface-tangential directions (δ),

$$[\![r]\!]_{\Upsilon,\parallel}^{(\delta)} = \mathbf{t}_{\Upsilon}^{(\delta),T} \cdot [\![\mathbf{R}]\!]_{\Upsilon} = -\mathbf{t}_{\Upsilon}^{(\delta),T} \cdot \mathbf{R}^{\xi_1} + \mathbf{t}_{\Upsilon}^{(\delta),T} \cdot \mathbf{R}^{\xi_2} = -r_{\parallel,(\delta)}^{\xi_1} + r_{\parallel,(\delta)}^{\xi_2} = \mathbf{t}_{\Upsilon}^{(\delta),T} \cdot \boldsymbol{\sigma}_M \tag{2.44}$$

is obtained, where $r_{\parallel,(\delta)}^{\xi_i} = t_{\Upsilon,\beta}^{(\delta)} R_{\beta}^{\xi_i} = t_{\Upsilon,\beta}^{(\delta)} \Pi_{\beta\gamma}^{\xi_i} n^{\gamma}$.

2.5 Transport of Surfactant

The surfactant concentration evolves according to

$$\frac{\partial \gamma}{\partial t} + \nabla \cdot (\mathbf{u}_{\Upsilon}\gamma) - \gamma \left((\mathbf{n}_{\Upsilon} \otimes \mathbf{n}_{\Upsilon}) \cdot \nabla\right)^T \cdot \mathbf{u}_{\Upsilon} = \frac{1}{Pe_s} \nabla_s^2 \gamma \ . \tag{2.45}$$

The subscript s indicates transport along the interface-tangential plane. $Pe_s = \frac{U_{ref} L_{ref}}{D_s}$ is the surface Peclet number, that relates interfacial inertial to diffusive forces. The advection term is

$$\nabla^T \cdot (\mathbf{u}_{\Upsilon}\gamma) = \mathbf{u}_{\Upsilon}^T \cdot (\nabla\gamma) + \gamma \nabla^T \cdot \mathbf{u}_{\Upsilon} \ . \tag{2.46}$$

The third term on the left side of Eq. (2.45) accounts for transport due to variations in interface shape. The interface diffusion of γ is

$$\nabla_s^2 \gamma(\mathbf{x}) = \triangle\gamma(\mathbf{x}) - \left(\mathbf{n}_{\Upsilon}^T \cdot \nabla\gamma(\mathbf{x})\right)\left(\nabla^T \cdot \mathbf{n}_{\Upsilon}\right) - \mathbf{n}_{\Upsilon}^T \cdot H_{\gamma} \cdot \mathbf{n}_{\Upsilon} \ , \tag{2.47}$$

with H_{γ} being the Hessian of $\gamma(\mathbf{x}, t)$.

Equation of State for the Surface Tension Coefficient

The dependence of σ on γ follows the nonlinear Langmuir equation [90, 91]

$$\sigma(\gamma) = 1 + E \ \ln(1 - \zeta\gamma) \ . \tag{2.48}$$

For small $\nabla_s\gamma$, $\sigma(\gamma)$ can be approximated as [90, 91]

$$\sigma(\gamma) = 1 - E\zeta\gamma \ . \tag{2.49}$$

$E = \frac{RT\gamma_{\infty}}{\sigma_{ref}}$ and $\zeta = \frac{\gamma_{eq}}{\gamma_{\infty}}$ are the surface elasticity and coverage, σ_{ref} is the surface tension coefficient for a clean interface ($\gamma = 0$). γ_{∞} is the concentration of surfactant in the maximum packing limit, and $\gamma_{eq} = \frac{1}{\Delta\Upsilon} \int_{\Delta\Upsilon} \gamma d\Upsilon' \big|_{t=0}$ is the initial average surfactant concentration.

3 Numerical Methods

Within this chapter, the further-developed and newly-developed numerical methods are presented. The method of finite volumes is explained in the context of solving single-phase configurations. In conjunction with the cell-face reconstruction and Riemann solvers, used within this work, the fundamentals of the implicit large eddy method are set forth. Following that, the numerical treatment of two-phase configurations is described. Thereby, the conservative interface-interaction, surrogate-interface model, and sub-cell space description of the interface are illuminated particularly. Moreover, the algorithms for the propagation of the interface and the extension of fluid states are outlined. The numerical methods for propagating insoluble surfactant conservatively are described. Also, the numerics relevant for advancing the fluids, the interface, and surfactant in time are discussed. The chapter is concluded by describing the method for analysis of the numerical dissipation rate and viscosity. This chapter results from combining Refs. [50, 114, 98, 102, 82].

3.1 The Single-Phase Discretization

The continuous domain Ω is partitioned into a collection of disjunct finite volumes (FV) $\Omega_{[i,j,k]} \leq \Omega \,|\, \Sigma\, \Omega_{[i,j,k]} = \Omega;\ i,j,k \in \mathbb{N}$. For a FV, the conservation equations (2.9) become

$$\frac{\partial \widehat{\mathbf{U}}_{[i,j,k]}}{\partial t} - \left(\frac{\mathbf{F}_{1,[i-\frac{1}{2},j,k]} - \mathbf{F}_{1,[i+\frac{1}{2},j,k]}}{\Delta x_1} + \frac{\mathbf{F}_{2,[i,j-\frac{1}{2},k]} - \mathbf{F}_{2,[i,j+\frac{1}{2},k]}}{\Delta x_2} + \right. \\ \left. + \frac{\mathbf{F}_{3,[i,j,k-\frac{1}{2}]} - \mathbf{F}_{3,[i,j,k+\frac{1}{2}]}}{\Delta x_3} \right) = \widehat{\mathbf{S}}_{[i,j,k]} \ , \tag{3.1}$$

where $\widehat{\mathbf{U}}_{[i,j,k]} = \frac{1}{\Delta V_{[i,j,k]}} \int_{\Omega_{[i,j,k]}} \mathbf{U}_{[i,j,k]}\ dV$, $\widehat{\mathbf{S}}_{[i,j,k]} = \frac{1}{\Delta V_{[i,j,k]}} \int_{\Omega_{[i,j,k]}} \mathbf{S}_{[i,j,k]}\ dV$, are the volume averaged conservative states and sources. Moreover, $\Delta x_1 = x_{1,[i+\frac{1}{2},j,k]} - x_{1,[i-\frac{1}{2},j,k]}$, $\Delta x_2 = x_{2,[i,j+\frac{1}{2},k]} - x_{2,[i,j-\frac{1}{2},k]}$, and $\Delta x_3 = x_{3,[i,j,k+\frac{1}{2}]} - x_{3,[i,j,k-\frac{1}{2}]}$.

Within a short time interval $\Delta t \leq \frac{\Delta x}{u^n_{\max}}$, $\Delta t \to 0$ where $u^n_{\max}$ denotes the maximum wave speed within the domain at time t^n, the solution $\mathbf{U}_{[i\pm\frac{1}{2},j,k]}$ of the Riemann problems at cell faces $[i \pm \frac{1}{2}, j, k]$, with $\mathbf{U}^{(L)} = \widehat{\mathbf{U}}^{n,(L)}_{[i\pm\frac{1}{2},j,k]}$ and $\mathbf{U}^{(R)} = \widehat{\mathbf{U}}^{n,(R)}_{[i\pm\frac{1}{2},j,k]}$, see Fig. 3.1, remains constant with $\lim_{\Delta t \to 0} \mathcal{O}(\Delta t) = 0$, i.e. $\overline{\mathbf{U}}_{[i\pm\frac{1}{2},j,k]} = \lim_{\Delta t \to 0} \frac{1}{\Delta t} \int_{t^n}^{t^{n+1}} \mathbf{U}_{[i\pm\frac{1}{2},j,k]}\ dt$. It follows

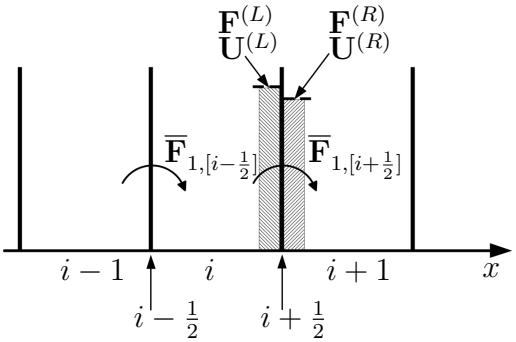

Figure 3.1: Local Riemann problem.

that $\overline{\mathbf{F}}^a_{1,[i\pm\frac{1}{2},j,k]} = \lim_{\Delta t \to 0} \frac{1}{\Delta t} \int_{t^n}^{t^{n+1}} \mathbf{F}(\mathbf{U})^a_{1,[i\pm\frac{1}{2},j,k]}\ dt$, $\overline{\mathbf{F}}^\nu_{1,[i\pm\frac{1}{2},j,k]} = \lim_{\Delta t \to 0} \frac{1}{\Delta t} \int_{t^n}^{t^{n+1}} \mathbf{F}(\widehat{\mathbf{u}})^\nu_{1,[i\pm\frac{1}{2},j,k]}\ dt$, $\overline{\mathbf{S}}^n_{[i,j,k]} = \lim_{\Delta t \to 0} \frac{1}{\Delta t} \int_{t^n}^{t^{n+1}} \widehat{\mathbf{S}}_{[i,j,k]}\ dt$. Same applies for the fluxes $\mathbf{F}_{2,[i,j\pm\frac{1}{2},k]}$ and $\mathbf{F}_{3,[i,j\pm\frac{1}{2},k]}$ at $[i, j \pm \frac{1}{2}, k]$ and $[i, j, k \pm \frac{1}{2}]$. Integration of E.q. (3.1) from t^n to t^{n+1} leads to

$$\widehat{\mathbf{U}}^{n+1}_{[i,j,k]} = \widehat{\mathbf{U}}^n_{[i,j,k]} + \Delta t\ \overline{\mathbf{L}}^n_{[i,j,k]} \tag{3.2}$$

with

$$\overline{\mathbf{L}}^n_{[i,j,k]} = \left[\frac{\overline{\mathbf{F}}_{1,[i-\frac{1}{2},j,k]} - \overline{\mathbf{F}}_{1,[i+\frac{1}{2},j,k]}}{\Delta x_1} + \frac{\overline{\mathbf{F}}_{2,[i,j-\frac{1}{2},k]} - \overline{\mathbf{F}}_{2,[i,j+\frac{1}{2},k]}}{\Delta x_2} + \right. \\ \left. + \frac{\overline{\mathbf{F}}_{3,[i,j,k-\frac{1}{2}]} - \overline{\mathbf{F}}_{3,[i,j,k+\frac{1}{2}]}}{\Delta x_3} + \overline{\mathbf{S}}_{[i,j,k]} \right] \tag{3.3}$$

In the original first order accurate Godunov method [92] $\mathbf{U}^{(L)}$ and $\mathbf{U}^{(R)}$ are extrapolated from the cell average states $\widehat{\mathbf{U}}^n$, e.g. $\mathbf{U}^{(L)}_{[i+\frac{1}{2},j,k]} = \widehat{\mathbf{U}}^n_{[i,j,k]}$ and $\mathbf{U}^{(R)} = \widehat{\mathbf{U}}^{n,(R)}_{[i\pm\frac{1}{2},j,k],R} = \widehat{\mathbf{U}}^n_{[i+1,j,k]}$.

It is not possible for a linear, thus monotone scheme to be both higher than first-order accurate and free of spurious oscillations [92]. Upwind schemes behave dissipatively, while central schemes, although being at least second order accurate, are dispersive. In this work, high-order reconstruction schemes are employed to capture discontinuous solutions as well as steep gradients with high accuracy.

3.1.1 Cell-Face States Reconstruction

To obtain $\mathbf{U}^{(\alpha)}_{[i\pm\frac{1}{2},j,k]}$, $\alpha = L, R$, weighted essentially non-oscillatory (WENO) schemes [93] are used. Thereby, m reconstruction polynomials for non-averaged conservative cell-face vector candidates $\mathbf{u}^{(\alpha,\upsilon)}_{[i+\frac{1}{2},j,k]} = \sum_{l=0}^{m-1} c_{\upsilon,l}\widehat{\mathbf{U}}_{[i-\upsilon+l,j,k]}, \upsilon = 0, ..., m-1$ on m candidate stencils $S_\upsilon[i] \equiv \left\{\widehat{\mathbf{U}}_{[i-\upsilon,j,k]}, ..., \widehat{\mathbf{U}}_{[i,j,k]}, ..., \widehat{\mathbf{U}}_{[i-\upsilon+m-1,j,k]}\right\}$ are combined convexly according to

$$\mathbf{U}^{(\alpha)}_{[i\pm\frac{1}{2},j,k]} = \sum_{\upsilon=0}^{m-1} \omega_\upsilon^{(\alpha)} \widehat{\mathbf{u}}^{(\alpha,\upsilon)}_{[i+\frac{1}{2},j,k]}. \tag{3.4}$$

The set of nonlinear weights $\left\{\omega_\upsilon^{(\alpha)}\right\}$, satisfying $\omega_\upsilon^{(\alpha)} \geq 0$, $\sum_{\upsilon=0}^{m-1} \omega_\upsilon^{(\alpha)} = 1$, ensures stability and consistency. Note that $c_{\upsilon,l}$ are polynomial coefficients. The computationally efficient weights of Jiang *et al.* [94] are C^∞, i.e. smooth functions of the involved cell averages:

$$\omega_\upsilon^{(\alpha)} = \frac{\alpha_\upsilon^{(\alpha)}}{\sum_{s=0}^{m-1} \alpha_s^{(\alpha)}}, \qquad \alpha_\upsilon^{(\alpha)} = f\left(d_\upsilon, \beta_\upsilon^{(\alpha)}\right), \tag{3.5}$$

where d_υ and $\beta_\upsilon^{(\alpha)}$ are the ideal weights and smoothness indicators, respectively. "The smoothness indicators diminish with increasing smoothness of the solution on a stencil" [50]. In defining α_υ, the core idea is to consider each of the $\widehat{\mathbf{u}}^{(\alpha,\upsilon)}_{[i+\frac{1}{2},j,k]}$ according to their smoothness by weighting them appropriately. Thereby, $\omega_\upsilon^{(\alpha)}$ approximates d_υ. Yet, if the solution was to contain a discontinuity in at least one of the stencils $S_\upsilon[i]$, leading to $\beta_\upsilon^{(\alpha)} = \mathcal{O}(1)$, the corresponding weights $\omega_\upsilon^{(\alpha)}$ need to diminish to exclude the approximation $\widehat{\mathbf{u}}^{(\alpha,\upsilon)}_{[i+\frac{1}{2},j,k]}$ and thereby keep the overall non-oscillatory behavior. The weighting factors

$$\alpha_\upsilon^{(\alpha)} = \frac{d_\upsilon}{\left(\epsilon + \beta_\upsilon^{(\alpha)}\right)^q} \tag{3.6}$$

of Jiang *et al.* [94] fulfill these requirements. The WENO-CU6-M1 weights, a further-development of the original WENO weights Eq.(3.6), remedy excessive dissipation of the underlying WENO-CU6 scheme [95], while preserving its shock-capturing properties and

thus allow to recover physical consistency [96]. The weighting factors of the WENO-CU6-M1 scheme are [96]

$$\alpha_{\upsilon}^{(\alpha)} = d_{\upsilon}\left(C_q + \frac{\tau_6^{(\alpha)}}{\epsilon + \beta_{\upsilon}^{(\alpha)}}\right)^q , \qquad \upsilon = 0, ..., 3 , \tag{3.7}$$

where the reference smoothness indicator is $\tau_6^{(\alpha)} = \beta_3^{(\alpha)} - \frac{1}{6}\left(\beta_0^{(\alpha)} + 4\beta_1^{(\alpha)} + \beta_2^{(\alpha)}\right)$ [95, 97]. $\widehat{\mathbf{u}}^{(\alpha,\upsilon)}_{[i+\frac{1}{2},j,k]}$, d_υ, $\beta_\upsilon^{(\alpha)}$, with $\upsilon = 0, 1, 2$ are identical to the ones of the 5^{th} order WENO scheme, which can be found e.g. in App. A.1. $\widehat{\mathbf{u}}^{(\alpha,3)}_{[i+\frac{1}{2},j,k]}$, d_3, $\beta_3^{(\alpha)}$, and the four ideal weights are also provided in App. A.1 as well as in Refs. [98, 99].

3.1.2 The Riemann Solvers of Roe and Roe-Pike

Intercell numerical fluxes are determined at the respective cell faces. The reconstructed non-averaged cell-face left and right conservative states $\mathbf{U}^{(L)}_{[i\pm\frac{1}{2},j,k]}$ and $\mathbf{U}^{(R)}_{[i\pm\frac{1}{2},j,k]}$ generally differ. The solution of the local Riemann problem $\left(\mathbf{U}^{(L)}, \mathbf{U}^{(R)}\right)_{[i\pm\frac{1}{2},j,k]}$ leads to $\overline{\mathbf{F}}^a_{1,[i\pm\frac{1}{2},j,k]}$. Low-dissipation flux approximations are due to Roe [100] as well as Roe and Pike [101]. The key idea of these approximate Riemann-solvers is the linearization of the local flux Jacobian $\widetilde{\mathbf{A}} = \widetilde{\mathbf{A}}\left(\mathbf{U}^{(L)}, \mathbf{U}^{(R)}\right)$, see Sec. 2.3. Thereby, $\widetilde{\mathbf{A}}$ is hyperbolic, i.e. $\widetilde{\lambda}_1 \leq \widetilde{\lambda}_2 \leq \cdots \leq \widetilde{\lambda}_m$, the set of linearly independent right eigenvectors, $\widetilde{\mathbf{K}}^{(1)}, \widetilde{\mathbf{K}}^{(2)}, \cdots, \widetilde{\mathbf{K}}^{(m)}$ is complete, consistency with the exact Jacobian is fulfilled, i.e. $\widetilde{\mathbf{A}}\left(\mathbf{U}^{(L)}, \mathbf{U}^{(R)}\right) = \mathbf{A}(\mathbf{U})$, and conservation across discontinuities holds, i.e. $\mathbf{F}^a(\mathbf{U}^{(R)}) - \mathbf{F}^a(\mathbf{U}^{(L)}) = \widetilde{\mathbf{A}}(\mathbf{U}^{(R)} - \mathbf{U}^{(L)})$. The eigenvalues of $\widetilde{\mathbf{A}}$, $\widetilde{\lambda}_j(\mathbf{U}^{(L)}, \mathbf{U}^{(R)})$ and right eigenvectors $\widetilde{\mathbf{K}}^{(j)}(\mathbf{U}^{(L)}, \mathbf{U}^{(R)})$ are determined, see App. A.2, so that the Roe numerical flux can be computed according to

$$\mathbf{F}^a_{[i+\frac{1}{2},j,k]} = \frac{1}{2}\left(\mathbf{F}^a(\mathbf{U}^{(L)}) + \mathbf{F}^a(\mathbf{U}^{(R)})\right) - \frac{1}{2}\sum_{j=1}^{m} \widetilde{\delta}^{(j)} \left|\widetilde{\lambda}_j\right| \widetilde{\mathbf{K}}^{(j)} , \tag{3.8}$$

where $\widetilde{\delta}^{(j)}$ denote the wave strengths. These are found by evaluating

$$\Delta\mathbf{w} = \mathbf{U}^{(R)} - \mathbf{U}^{(L)} = \sum_{j=1}^{m} \widehat{\delta}^{(j)} \widehat{\mathbf{K}}^{(j)} . \tag{3.9}$$

For the solver of Roe [100] $\Delta\mathbf{w} = \mathbf{U}^{(R)} - \mathbf{U}^{(L)}$, while for the solver of Roe and Pike $\Delta\mathbf{w}$ evaluates a jump of primitive variables. The details for solving $\mathbf{F}^a_{1,[i+\frac{1}{2},j,k]}$, $\mathbf{F}^a_{2,[i,j+\frac{1}{2},k]}$, and $\mathbf{F}^a_{3,[i,j,k+\frac{1}{2}]}$ are in App. A.2.

3.2 The Two-Phase Treatment

In two-phase immiscible flow simulations, only parts of the domain contain either of the fluids. Finite volume cells $\Omega_{[i,j,k]}$ that are not cut by the interface are single fluid cells. For such cells, Eq. (3.2) advances the solution in time. A finite volume $\Omega_{[i,j,k]}$ that contains a portion of the interface Υ is subdivided into two disjunct subdomain $\Omega^{\xi_1}_{[i,j,k]}$ and $\Omega^{\xi_2}_{[i,j,k]}$, see Fig. 3.2. To advance the volume-averaged vector of conservative states $\widehat{\mathbf{U}}^{\xi_i}_{[i,j,k]}$ in time, the conservation of mass, momentum, and energy at the interface, see Sec. 2.4, as well as the partitioning of cut cells needs to be accounted for.

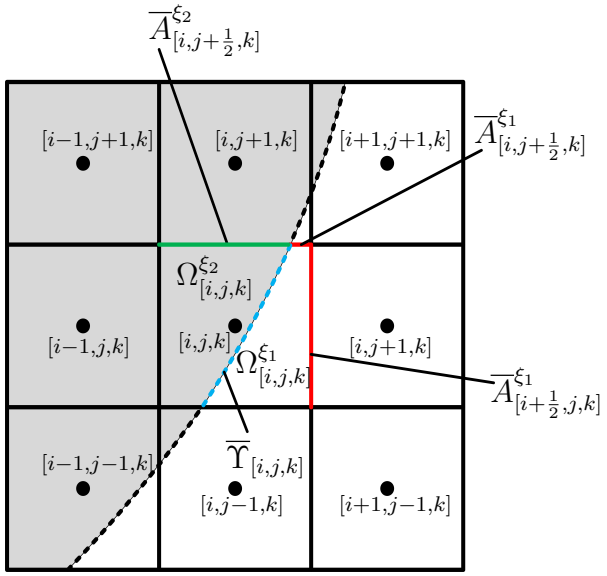

Figure 3.2: $2D$ schematic of conservative discretization of a cut cell. Red and green indicate phase ξ_1, and ξ_2, respectively. Adopted from [102, 82].

3.2.1 Conservation Equations for a Two-Fluid Flow

For each $\widetilde{\mathbf{U}}^{\xi_i}_{[i,j,k]} = \{\zeta^{\xi_i}\widehat{\mathbf{U}}^{\xi_i}\}_{[i,j,k]}$, the discrete, non-dimensional conservation equation

$$\widetilde{\mathbf{U}}^{\xi_i,n+1}_{[i,j,k]} = \widetilde{\mathbf{U}}^{\xi_i,n}_{[i,j,k]} + \Delta t\ \overline{\mathbf{L}}^{\xi_i,n}_{[i,j,k]} \tag{3.10}$$

with

$$\begin{aligned}\overline{\mathbf{L}}^{\xi_i,n}_{[i,j,k]} = \Bigg[&\frac{\overline{\mathbf{X}}^{\xi_i}_{[i,j,k]}}{\Delta V_{[i,j,k]}} + \overline{\mathbf{S}}^{\xi_i}_{[i,j,k]} + \frac{\left[\overline{A}\ \overline{\mathbf{F}}_1\right]^{\xi_i}_{[i-\frac{1}{2},j,k]} - \left[\overline{A}\ \overline{\mathbf{F}}_1\right]^{\xi_i}_{[i+\frac{1}{2},j,k]}}{\Delta x_1} + \\ &+ \frac{\left[\overline{A}\ \overline{\mathbf{F}}_2\right]^{\xi_i}_{[i,j-\frac{1}{2},k]} - \left[\overline{A}\ \overline{\mathbf{F}}_2\right]^{\xi_i}_{[i,j+\frac{1}{2},k]}}{\Delta x_2} + \frac{\left[\overline{A}\ \overline{\mathbf{F}}_3\right]^{\xi_i}_{[i,j,k-\frac{1}{2}]} - \left[\overline{A}\ \overline{\mathbf{F}}_3\right]^{\xi_i}_{[i,j,k+\frac{1}{2}]}}{\Delta x_3}\Bigg]\end{aligned} \tag{3.11}$$

is solved individually. Buoyant forces are modeled such that they diminish within phase ξ_1, i.e. $\overline{\mathbf{S}}^{\xi_i}_{[i,j,k]} = \frac{1}{Fr^2}\left(\overline{\rho}^{\xi_i}_{[i,j,k]} - 1\right)\left[0; \mathbf{g}^T; \mathbf{u}^T \cdot \mathbf{g}\right]^T$. By considering the interface-interaction flux

$$\mathbf{X}^{\xi_i}_{[i,j,k]} = \{\mathbf{X}^{\perp,\xi_i} + \mathbf{X}^{\parallel,\xi_i}\}_{[i,j,k]}\ , \tag{3.12}$$

the two $\Omega^{\xi_i}_{[i,j,k]}$ are coupled and the system is globally conservative. The terms

$$\mathbf{X}^{\perp,\xi_i}_{[i,j,k]} = \{ r^{\xi_i}_{\Upsilon,\perp} \Delta\Upsilon \begin{bmatrix} 0 \\ \mathbf{n}^{\xi_i}_{\Upsilon} \\ u_{\Upsilon,\perp} \end{bmatrix} \}_{[i,j,k]}, \tag{3.13}$$

and

$$\mathbf{X}^{\parallel,\xi_i}_{[i,j,k]} = \left\{ \mathbf{X}^{\parallel,\xi_i,(1)} + \mathbf{X}^{\parallel,\xi_i,(2)} \right\}_{[i,j,k]} , \tag{3.14}$$

account for the flux in interface-normal and tangential direction, respectively. Herein, the tangential flux in direction of $\mathbf{t}^{(\delta)}_{\Upsilon}$ is:

$$\mathbf{X}^{\parallel,\xi_i,(\delta)}_{[i,j,k]} = \{ r^{\xi_i,(\delta)}_{\Upsilon,\parallel} \Delta\Upsilon \begin{bmatrix} 0 \\ \mathbf{t}^{(\delta)}_{\Upsilon} \\ u^{(\delta)}_{\Upsilon,\parallel} \end{bmatrix} \}_{[i,j,k]} . \tag{3.15}$$

The interface stresses $r^{\xi_i}_{\Upsilon,\perp}$, $r^{\xi_i,(\delta)}_{\Upsilon,\parallel}$ and velocities $u_{\Upsilon,\perp}$, $u^{(\delta)}_{\Upsilon,\parallel}$ in Eqs. (3.13), (3.15) are the solution of the two-material Riemann problem arising at the interface Υ, see Sec. 3.2.2. Note that

$$\mathbf{A}^{\xi_i}_n|_{[i,j,k]} = \{ \mathbf{n}^{\xi_i}_{\Upsilon} \Delta\Upsilon \}_{[i,j,k]} = [A_{x_1}, A_{x_2}, A_{x_3}]_{[i,j,k]} = \begin{bmatrix} A^{\xi_i}_{[i-\frac{1}{2},j,k]} - A^{\xi_i}_{[i+\frac{1}{2},j,k]} \\ A^{\xi_i}_{[i,j-\frac{1}{2},k]} - A^{\xi_i}_{[i,j+\frac{1}{2},k]} \\ A^{\xi_i}_{[i,j,k-\frac{1}{2}]} - A^{\xi_i}_{[i,j,k+\frac{1}{2}]} \end{bmatrix} . \tag{3.16}$$

$A^{\xi_i}_{[i\pm\frac{1}{2},j,k]}, A^{\xi_i}_{[i,j\pm\frac{1}{2},k]}, A^{\xi_i}_{[i,j,k\pm\frac{1}{2}]}$ are apertures which are that part of $\Gamma^{\xi_i}_{[i,j,k]}(t)$ not coinciding with $\Upsilon_{[i,j,k]}(t)$ but with the cell face $\Gamma_{[i,j,k]}(t)$, [83]. Within $\Delta t = t^{n+1} - t^n$, they are $\overline{A}^{\xi_i}_{[i+\frac{1}{2},j,k]} = \lim_{\Delta t \to 0} \frac{1}{\Delta t} \int_{t^n}^{t^{n+1}} \int_{\Gamma^{\xi_i}_{[i,j,k]} \cap \Gamma_{[i,j,k]}} 1 dx_2 dx_3 dt$, $\overline{A}^{\xi_i}_{[i,j+\frac{1}{2},k]} = \lim_{\Delta t \to 0} \frac{1}{\Delta t} \int_{t^n}^{t^{n+1}} \int_{\Gamma^{\xi_i}_{[i,j,k]} \cap \Gamma_{[i,j,k]}} 1 dx_1 dx_3 dt$, $\overline{A}^{\xi_i}_{[i,j,k+\frac{1}{2}]} = \lim_{\Delta t \to 0} \frac{1}{\Delta t} \int_{t^n}^{t^{n+1}} \int_{\Gamma^{\xi_i}_{[i,j,k]} \cap \Gamma_{[i,j,k]}} 1 dx_1 dx_2 dt$, see also Fig. 3.2, depicting the right and upper apertures. For single-fluid cells, the apertures of phase ξ_1 are unity within $\Omega^{\xi_1}_{[i,j,k]}$ and zero within $\Omega^{\xi_2}_{[i,j,k]}$, and vice versa for phase ξ_2. Employing the algorithm of [85], without normalization, leads to $\mathbf{A}^{\xi_i,(\delta)}_t|_{[i,j,k]} = \{ \Delta\Upsilon \mathbf{t}^{(\delta)}_{\Upsilon} \}_{[i,j,k]}$. The orthogonal $\left(\mathbf{A}_n, \mathbf{A}^{(1)}_t, \mathbf{A}^{(2)}_t \right)^{\xi_i}_{[i,j,k]}$, which is equivalent to $\left(\mathbf{n}_{\Upsilon}, \mathbf{t}^{(1)}_{\Upsilon}, \mathbf{t}^{(2)}_{\Upsilon} \right)^{\xi_i}_{[i,j,k]} \Delta\Upsilon$, are consistent with the orthonormal basis $\left(\mathbf{n}_{\Upsilon}, \mathbf{t}^{(1)}_{\Upsilon}, \mathbf{t}^{(2)}_{\Upsilon} \right)_{[i,j,k]}$.

Mixing of Small Cells

The intersection of the interface with the Cartesian grid results in two-fluid cells with diminishing $\zeta^{\xi_i}_{[i,j,k]}$, denoted as small cells. Based on the time step constraints of cells with

$\zeta^{\xi_i}_{[i,j,k]} \approx 1$, i.e. full cells, spurious solutions may evolve for small cells [103, 104]. More restrictive constraint on Δt lead to high numerical costs. A conservative mixing procedure (CMP) has been proposed by Hu *et al.* [103] as a remedy. Thereby, the vector of $\Omega_{[i,j,k]}$-averaged conservative states of small cells are mixed with those of neighboring full cells denoted as target cells. The further developed CMP of Lauer *et al.* [104] includes all possible neighbors, i.e. three in two dimensions and seven in three dimensions.
In 2D, cells of $\zeta^{\xi_i}_{[i,j,k]} \leq 0.3$ are small cells, such with $\zeta^{\xi_i}_{[i,j,k]} > 0.3$ are full. In 3D, the threshold is 0.6. For empty cells $\zeta^{\xi_i,n+1}_{[i,j,k]} = 0$. Following cells are mixed with their neighbors [103]:

- small cells at the current time step $n+1$,
- empty cells at $n+1$ which were small or full at time step n,
- empty cells at n which are small or full at $n+1$.

The target cell indices are determined based on $\mathbf{n}^{\xi_i}_{\Upsilon,[i,j,k]}$:

$$
\begin{aligned}
i_{trg} &= \begin{cases} i+1 & \text{if } n^{\xi_i}_{\Upsilon,1,[i,j,k]} > 0 \\ i-1 & \text{if } n^{\xi_i}_{\Upsilon,1,[i,j,k]} < 0 \\ i & \text{else} \end{cases}, \quad
j_{trg} = \begin{cases} j+1 & \text{if } n^{\xi_i}_{\Upsilon,2,[i,j,k]} > 0 \\ j-1 & \text{if } n^{\xi_i}_{\Upsilon,2,[i,j,k]} < 0 \\ j & \text{else} \end{cases}, \\
k_{trg} &= \begin{cases} k+1 & \text{if } n^{\xi_i}_{\Upsilon,3,[i,j,k]} > 0 \\ k-1 & \text{if } n^{\xi_i}_{\Upsilon,3,[i,j,k]} < 0 \\ k & \text{else} \end{cases}.
\end{aligned}
\tag{3.17}
$$

For each mixing target cell, a mixing fraction, indicating the contribution to the mixing, is defined as:

$$
\boldsymbol{\beta}^{\xi_i,n+1}_{[i,j,k]} = \begin{bmatrix} \beta_1 \\ \beta_2 \\ \beta_3 \\ \beta_4 \\ \beta_5 \\ \beta_6 \\ \beta_7 \end{bmatrix}^{\xi_i,n+1}_{[i,j,k]} = \begin{bmatrix} \beta_{[i_{trg},j,k]} \\ \beta_{[i,j_{trg},k]} \\ \beta_{[i_{trg},j_{trg},k]} \\ \beta_{[i,j,k_{trg}]} \\ \beta_{[i_{trg},j,k_{trg}]} \\ \beta_{[i,j_{trg},k_{trg}]} \\ \beta_{[i_{trg},j_{trg},k_{trg}]} \end{bmatrix}^{\xi_i,n+1} = \begin{bmatrix} (n_{\Upsilon,1} n_{\Upsilon,1}) \\ (n_{\Upsilon,2} n_{\Upsilon,2}) \\ (n_{\Upsilon,1} n_{\Upsilon,2}) \\ (n_{\Upsilon,3} n_{\Upsilon,3}) \\ (n_{\Upsilon,1} n_{\Upsilon,3}) \\ (n_{\Upsilon,2} n_{\Upsilon,3}) \\ (n_{\Upsilon,1} n_{\Upsilon,2} n_{\Upsilon,3})^{2/3} \end{bmatrix}^{\xi_i,n+1}_{[i,j,k]} .
\tag{3.18}
$$

Note that for 2D numerical simulations $\beta^{\xi_i,n+1}_4 = \beta^{\xi_i,n+1}_5 = \beta^{\xi_i,n+1}_6 = \beta^{\xi_i,n+1}_7 = 0$. Double mixing between two cells is avoided by enforcing $\beta^{\xi_i,n+1}_{[trg]} = 0$, if $\zeta^{\xi_i,n+1}_{[i,j,k]} > \zeta^{\xi_i,n+1}_{trg}$. $\boldsymbol{\beta}^{\xi_i,n+1}_{[i,j,k]}$ is

normalized, i.e. $\boldsymbol{\beta}^{\xi_i,n+1}_{[i,j,k]} = \frac{\boldsymbol{\beta}^{\xi_i,n+1}_{[i,j,k]}}{\|\boldsymbol{\beta}^{\xi_i,n+1}_{[i,j,k]}\|}$. The mixing flux $\mathbf{M}^{\xi_i,n+1}_{[i,j,k]}$ is computed according to

$$\mathbf{M}^{\xi_i,n+1}_{[i,j,k]} = \begin{bmatrix} M_1 \\ M_2 \\ M_3 \\ M_4 \\ M_5 \\ M_6 \\ M_7 \end{bmatrix}^{\xi_i,n+1}_{[i,j,k]} = \begin{bmatrix} M_{[i_{trg},j,k]} \\ M_{[i,j_{trg},k]} \\ M_{[i_{trg},j_{trg},k]} \\ M_{[i,j,k_{trg}]} \\ M_{[i_{trg},j,k_{trg}]} \\ M_{[i,j_{trg},k_{trg}]} \\ M_{[i_{trg},j_{trg},k_{trg}]} \end{bmatrix}^{\xi_i,n+1} =$$

$$= \begin{bmatrix} \frac{\beta_{[i_{trg},j,k]}}{\zeta_{[i,j,k]}+\zeta_{[i_{trg},j,k]}} \left[\left(\zeta_{[i,j,k]} \widetilde{\mathbf{U}}_{[i_{trg},j,k]} \right) - \left(\zeta_{[i_{trg},j,k]} \widetilde{\mathbf{U}}_{[i,j,k]} \right) \right] \\ \frac{\beta_{[i,j_{trg},k]}}{\zeta_{[i,j,k]}+\zeta_{[i,j_{trg},k]}} \left[\left(\zeta_{[i,j,k]} \widetilde{\mathbf{U}}_{[i,j_{trg},k]} \right) - \left(\zeta_{[i,j_{trg},k]} \widetilde{\mathbf{U}}_{[i,j,k]} \right) \right] \\ \frac{\beta_{[i_{trg},j_{trg},k]}}{\zeta_{[i,j,k]}+\zeta_{[i_{trg},j_{trg},k]}} \left[\left(\zeta_{[i,j,k]} \widetilde{\mathbf{U}}_{[i_{trg},j_{trg},k]} \right) - \left(\zeta_{[i_{trg},j_{trg},k]} \widetilde{\mathbf{U}}_{[i,j,k]} \right) \right] \\ \frac{\beta_{[i,j,k_{trg}]}}{\zeta_{[i,j,k]}+\zeta_{[i,j,k_{trg}]}} \left[\left(\zeta_{[i,j,k]} \widetilde{\mathbf{U}}_{[i,j,k_{trg}]} \right) - \left(\zeta_{[i,j,k_{trg}]} \widetilde{\mathbf{U}}_{[i,j,k]} \right) \right] \\ \frac{\beta_{[i_{trg},j,k_{trg}]}}{\zeta_{[i,j,k]}+\zeta_{[i_{trg},j,k_{trg}]}} \left[\left(\zeta_{[i,j,k]} \widetilde{\mathbf{U}}_{[i_{trg},j,k_{trg}]} \right) - \left(\zeta_{[i_{trg},j,k_{trg}]} \widetilde{\mathbf{U}}_{[i,j,k]} \right) \right] \\ \frac{\beta_{[i,j_{trg},k_{trg}]}}{\zeta_{[i,j,k]}+\zeta_{[i,j_{trg},k_{trg}]}} \left[\left(\zeta_{[i,j,k]} \widetilde{\mathbf{U}}_{[i,j_{trg},k_{trg}]} \right) - \left(\zeta_{[i,j_{trg},k_{trg}]} \widetilde{\mathbf{U}}_{[i,j,k]} \right) \right] \\ \frac{\beta_{[i_{trg},j_{trg},k_{trg}]}}{\zeta_{[i,j,k]}+\zeta_{[i_{trg},j_{trg},k_{trg}]}} \left[\left(\zeta_{[i,j,k]} \widetilde{\mathbf{U}}_{[i_{trg},j_{trg},k_{trg}]} \right) - \left(\zeta_{[i_{trg},j_{trg},k_{trg}]} \widetilde{\mathbf{U}}_{[i,j,k]} \right) \right] \end{bmatrix}^{\xi_i,n+1} . \tag{3.19}$$

Mixing between $\widetilde{\mathbf{U}}^{\xi_i,n+1}_{[i,j,k]}$ and the respective target cells is carried out consecutively [102]. Therefore, the mixing operations associated to the mixing fluxes $M_m, m = 1,..,7$ are ordered in descending magnitude of mixing fractions β_m, i.e. after executing mixing the most "effective" mixing $\widetilde{\mathbf{U}}^{\xi_i,n+1}_{[i,j,k]} = \widetilde{\mathbf{U}}^{\xi_i,n+1}_{[i,j,k]} + M^{\xi_i,n+1}_{1,[i,j,k]}$, $M^{\xi_i,n+1}_{2,[i,j,k]}$ is computed and $\widehat{\mathbf{U}}^{\xi_i,n+1}_{[i,j,k]} = \widetilde{\mathbf{U}}^{\xi_i,n+1}_{[i,j,k]} + M^{\xi_i,n+1}_{2,[i,j,k]}$ executed, followed by $M^{\xi_i,n+1}_{3,[i,j,k]}$ and so forth. Global conservativity is ensured by defining $M^{\xi_i,n+1}_{m,[trg]} = -M^{\xi_i,n+1}_{m,[i,j,k]}$ and executing $\widetilde{\mathbf{U}}^{\xi_i,n+1}_{[trg]} = \widetilde{\mathbf{U}}^{\xi_i,n+1}_{[trg]} + M^{\xi_i,n+1}_{m,[trg]}$. Within all cells, the volume-averaged vector of conservative states is obtained from $\widehat{\mathbf{U}}^{\xi_i,n+1}_{[i,j,k]} = \widetilde{\mathbf{U}}^{\xi_i,n+1}_{[i,j,k]} / \zeta^{\xi_i,n+1}_{[i,j,k]}$.

3.2.2 Surrogate-Interface Conditions and Solution

At the interface, the two-material Riemann problem (2.39), i.e. $\mathcal{R}(\mathbf{U}^{\xi_1}, \mathbf{U}^{\xi_2}) \neq \mathbf{0}$ can be restated as two independent interactions, the one of ξ_1 with the surrogate state $\star_2$ and the one of ξ_2 with the surrogate state $\star_1$, such that

$$\mathcal{R}^{\xi_1,\star_2} = \mathcal{R}(\mathbf{U}^{\xi_1}, \mathbf{U}^{\star_2}) = \mathbf{0} , \tag{3.20a}$$

$$\mathcal{R}^{\xi_2,\star_1} = \mathcal{R}(\mathbf{U}^{\xi_2}, \mathbf{U}^{\star_1}) = \mathbf{0} . \tag{3.20b}$$

In the viewpoint of phase ξ_1, phase ξ_2 has vanished and been replaced by instantaneous, macroscopic interface-surface stresses $\mathbf{R}^{\star_2}$ producing the combined effect of the interface and ξ_2 on Ω^{ξ_1} at Υ^{ξ_1}, see Ref. [84]; the same applies for phase ξ_2. Phase $\star_j$ adopts the density, static pressure, speed of sound and velocity of fluid ξ_j:

$$\rho^{\star_j} = \rho^{\xi_j} \ , \ p^{\star_j} = p^{\xi_j} \ , \ a^{\star_j} = a^{\xi_j} \ , \ \mathbf{u}^{\star_j} = \mathbf{u}^{\xi_j} \tag{3.21}$$

The surrogate-interface Riemann problems (3.20a) and (3.20b) can be solved with the method of characteristics. For a wide range of fluid states and interface stresses the jump over Υ is assumed as an isentropic process [105, 84]. It takes on the characteristics of a contact discontinuity and is solved for the characteristic, continuous interface velocities and interface stresses in the interface normal and tangential directions with an acoustic Riemann solver, see e.g. [106].

$\xi_1 - \star_2$-interface and interface states

Let $\mathbf{R}^{\star_2} = \mathbf{R}^{\xi_2} - (\boldsymbol{\sigma}_c + \boldsymbol{\sigma}_M)$, then the $\xi_1 - \star_2$-interface momentum balance is $-\mathbf{R}^{\xi_1} + \mathbf{R}^{\star_2} = 0$. In direction of the interface-normal and -tangentials, one obtains

$$-r_{\perp}^{\xi_1} + r_{\perp}^{\star_2} = 0 \ , \tag{3.22a}$$

$$-r_{\parallel,(1)}^{\xi_1} + r_{\parallel,(1)}^{\star_2} = 0 \ , \quad -r_{\parallel,(2)}^{\xi_1} + r_{\parallel,(2)}^{\star_2} = 0 \ , \tag{3.22b}$$

where

$$r_{\perp}^{\star_2} = r_{\perp}^{\xi_2} - \sigma_c \ , \tag{3.23a}$$

$$r_{\parallel,(\delta)}^{\star_2} = r_{\parallel,(\delta)}^{\xi_2} - \mathbf{t}_{\Upsilon}^{(\delta),T} \cdot \boldsymbol{\sigma}_M \ . \tag{3.23b}$$

For the interface-normal direction, the solution of the Riemann problem yields

$$u_{\Upsilon,\perp}^{\xi_1} = \frac{Z^{\xi_1} u_{\perp}^{\xi_1} + Z^{\star_2} u_{\perp}^{\star_2}}{Z^{\xi_1} + Z^{\star_2}} + \frac{r_{\perp}^{\xi_1} - r_{\perp}^{\star_2}}{Z^{\xi_1} + Z^{\star_2}} \ , \tag{3.24a}$$

$$r_{\Upsilon,\perp}^{\xi_1} = \frac{Z^{\star_2} r_{\perp}^{\xi_1} + Z^{\xi_1} r_{\perp}^{\star_2}}{Z^{\xi_1} + Z^{\star_2}} + \frac{Z^{\xi_1} Z^{\star_2}}{Z^{\xi_1} + Z^{\star_2}} \left(u_{\perp}^{\xi_1} - u_{\perp}^{\star_2} \right) \ . \tag{3.24b}$$

The interface tangential velocity $u_{\Upsilon,\parallel}^{\xi_1,(\delta)}$, and stress $r_{\Upsilon,\parallel}^{\xi_1,(\delta)}$ are

$$u_{\Upsilon,\parallel}^{\xi_1,(\delta)} = \frac{Z^{\xi_1} u_{\parallel}^{\xi_1,(\delta)} + Z^{\star_2} u_{\parallel}^{\star_2,(\delta)}}{Z^{\xi_1} + Z^{\star_2}} + \frac{r_{\parallel}^{\xi_1,(\delta)} - r_{\parallel}^{\star_2,(\delta)}}{Z^{\xi_1} + Z^{\star_2}} \ , \tag{3.25a}$$

$$r_{\Upsilon,\parallel}^{\xi_1,(\delta)} = \frac{Z^{\star_2} r_{\parallel}^{\xi_1,(\delta)} + Z^{\xi_1} r_{\parallel}^{\star_2,(\delta)}}{Z^{\xi_1} + Z^{\star_2}} + \frac{Z^{\xi_1} Z^{\star_2}}{Z^{\xi_1} + Z^{\star_2}} \left(u_{\parallel}^{\xi_1,(\delta)} - u_{\parallel}^{\star_2,(\delta)} \right) \ . \tag{3.25b}$$

$Z^{\xi_i} = \rho^{\xi_i} a^{\xi_i}$ is the acoustic impedance of the respective fluid.

$\xi_2 - \star_1$-interface

Assuming $\mathbf{R}^{\star_1} = \mathbf{R}^{\xi_1} + (\boldsymbol{\sigma}_c + \boldsymbol{\sigma}_M)$, the $\xi_2 - \star_2$-interface the momentum balance is $-\mathbf{R}^{\star_1} + \mathbf{R}^{\xi_2} = 0$. For the interface-normal and -tangential directions, one obtains:

$$-r_{\perp}^{\star_1} + r_{\perp}^{\xi_2} = 0 \ , \tag{3.26a}$$

$$-r_{\parallel,(1)}^{\star_1} + r_{\parallel,(1)}^{\xi_2} = 0 \ , \quad -r_{\parallel,(2)}^{\star_1} + r_{\parallel,(2)}^{\xi_2} = 0 \ , \tag{3.26b}$$

where

$$r_{\perp}^{\star_1} = r_{\perp}^{\xi_1} + \sigma_c \ , \tag{3.27a}$$

$$r_{\parallel,(\delta)}^{\star_1} = r_{\parallel,(\delta)}^{\xi_1} + \mathbf{t}_{\Upsilon}^{(\delta),T} \cdot \boldsymbol{\sigma}_M \tag{3.27b}$$

The solution of the Riemann problem, in the interface-normal direction, yields the interface normal velocity and stress

$$u_{\Upsilon,\perp}^{\xi_2} = \frac{Z^{\star_1} u_{\perp}^{\star_1} + Z^{\xi_2} u_{\perp}^{\xi_2}}{Z^{\star_1} + Z^{\xi_2}} + \frac{r_{\perp}^{\star_1} - r_{\perp}^{\xi_2}}{Z^{\star_1} + Z^{\xi_2}} \ , \tag{3.28a}$$

$$r_{\Upsilon,\perp}^{\xi_2} = \frac{Z^{\xi_2} r_{\perp}^{\star_1} + Z^{\star_1} r_{\perp}^{\xi_2}}{Z^{\star_1} + Z^{\xi_2}} + \frac{Z^{\star_1} Z^{\xi_2}}{Z^{\star_1} + Z^{\xi_2}} \left(u_{\perp}^{\star_1} - u_{\perp}^{\xi_2} \right) \ . \tag{3.28b}$$

The interface tangential velocity $u_{\Upsilon,\parallel}^{\xi_2,(\delta)}$, and stress $r_{\Upsilon,\parallel}^{\xi_2,(\delta)}$ are

$$u_{\Upsilon,\parallel}^{\xi_2,(\delta)} = \frac{Z^{\star_1} u_{\parallel}^{\star_1,(\delta)} + Z^{\xi_2} u_{\parallel}^{\xi_2,(\delta)}}{Z^{\star_1} + Z^{\xi_2}} + \frac{r_{\parallel}^{\star_1,(\delta)} - r_{\parallel}^{\xi_2,(\delta)}}{Z^{\star_1} + Z^{\xi_2}} \ , \tag{3.29a}$$

$$r_{\Upsilon,\parallel}^{\xi_2,(\delta)} = \frac{Z^{\xi_2} r_{\parallel}^{\star_1,(\delta)} + Z^{\star_1} r_{\parallel}^{\xi_2,(\delta)}}{Z^{\star_1} + Z^{\xi_2}} + \frac{Z^{\star_1} Z^{\xi_2}}{Z^{\star_1} + Z^{\xi_2}} \left(u_{\parallel}^{\star_1,(\delta)} - u_{\parallel}^{\xi_2,(\delta)} \right) \ . \tag{3.29b}$$

Summary of the Model

Equations (3.24) to (3.25) and (3.28) to (3.29) can be summarized. The interface-normal velocity $u_{\Upsilon,\perp}^{\xi_i}$, and stress $r_{\Upsilon,\perp}^{\xi_i}$ are:

$$u_{\Upsilon,\perp} = \frac{Z^{\xi_1} u_{\perp}^{\xi_1} + Z^{\xi_2} u_{\perp}^{\xi_2}}{Z^{\xi_1} + Z^{\xi_2}} + \frac{r_{\perp}^{\xi_1} - r_{\perp}^{\xi_2} + \sigma_c}{Z^{\xi_1} + Z^{\xi_2}} \ , \tag{3.30a}$$

$$r_{\Upsilon,\perp}^{\xi_i} = \frac{Z^{\xi_2} \left(r_{\perp}^{\xi_1} + \sigma_c \delta_{i2} \right) + Z^{\xi_1} \left(r_{\perp}^{\xi_2} - \sigma_c \delta_{i1} \right)}{Z^{\xi_1} + Z^{\xi_2}} + \frac{Z^{\xi_1} Z^{\xi_2}}{Z^{\xi_1} + Z^{\xi_2}} \left(u_{\perp}^{\xi_1} - u_{\perp}^{\xi_2} \right) \ . \tag{3.30b}$$

For the interface tangential velocity and stress, one finds:

$$u_{\Upsilon,\parallel}^{(\delta)} = \frac{Z^{\xi_1} u_\parallel^{\xi_1,(\delta)} + Z^{\xi_2} u_\parallel^{\xi_2,(\delta)}}{Z^{\xi_1} + Z^{\xi_2}} + \frac{\left(r_\parallel^{\xi_1,(\delta)} - r_\parallel^{\xi_2,(\delta)} + \mathbf{t}_\Upsilon^{(\delta),T} \cdot \boldsymbol{\sigma}_M \right)}{Z^{\xi_1} + Z^{\xi_2}} \ , \tag{3.31a}$$

$$r_{\Upsilon,\parallel}^{\xi_i,(\delta)} = \frac{Z^{\xi_2} \left(r_\parallel^{\xi_1,(\delta)} + \mathbf{t}_\Upsilon^{(\delta),T} \cdot \boldsymbol{\sigma}_M \delta_{i2} \right) + Z^{\xi_1} \left(r_\parallel^{\xi_2,(\delta)} - \mathbf{t}_\Upsilon^{(\delta),T} \cdot \boldsymbol{\sigma}_M \delta_{i1} \right)}{Z^{\xi_1} + Z^{\xi_2}} + \tag{3.31b}$$
$$+ \frac{Z^{\xi_1} Z^{\xi_2}}{Z^{\xi_1} + Z^{\xi_2}} \left(u_\parallel^{\xi_1,(\delta)} - u_\parallel^{\xi_2,(\delta)} \right) \ .$$

3.2.3 Description of the Interface

Defining a scalar function $\phi(\mathbf{x},t)$ with $|\nabla\phi| = 1$ such that $\phi(\mathbf{x},t) \equiv 0$ on $\Upsilon(\mathbf{x},t)$ captures the interface implicitly within an Eulerian framework [107, 108, 109]. Furthermore, $\phi(\mathbf{x},t) < 0$ in $\Omega^{\xi_2}(\mathbf{x},t)$ and $\phi(\mathbf{x},t) > 0$ in $\Omega^{\xi_1}(\mathbf{x},t)$. Based on $\phi(\mathbf{x},t)$, defined within a narrow band in the vicinity of $\Upsilon(\mathbf{x},t)$ [110], geometrical quantities of Υ, such as the normalized outward pointing normal vector $\mathbf{n}_\Upsilon(\mathbf{x}) = \frac{\nabla\phi(\mathbf{x})}{\|\nabla\phi(\mathbf{x})\|}$, and the mean curvature, which correlates to the divergence of the interface normal vector according to $\kappa_M = \left(\nabla^T \cdot \mathbf{n}_\Upsilon\right)$ in 2D, and $2\kappa_M = \left(\nabla^T \cdot \mathbf{n}_\Upsilon\right)$ in 3D, can be obtained. Numerically, the 1^{st} and 2^{nd} spatial derivatives are approximated with 2^{nd}-order central differences. The curvature is evaluated at the cell center, where not necessarily $\phi_{[i,j,k]} = 0$. The sub-cell corrected κ_Υ is obtained directly at the interface by

$$\kappa_\Upsilon = \left(|\kappa_{[i,j,k]}| + \kappa_{[i,j,k]}^2 \phi_{[i,j,k]} \right) \mathrm{sgn}\left(\kappa_{[i,j,k]} \right) \ , \tag{3.32}$$

Details on the derivation are provided e.g. in App. A.3.2.

3.2.4 Propagation of the Interface

The interface is advected with the interface-normal velocity:

$$\frac{\partial\phi(\mathbf{x},t)}{\partial t}\Big|_{\phi=0} + \left(\mathbf{u}_{\Upsilon,\perp}(\mathbf{x},t) \cdot \nabla\phi(\mathbf{x},t) \right)\Big|_{\phi=0} = 0 \ . \tag{3.33}$$

Numerically, not only $\phi = 0$ is advanced from time-instant n to $n+1$. Instead, within a band of three cells around Υ, the discrete level-set $\phi_{[i,j,k]}^n$ propagates according to

$$\phi_{[i,j,k]}^{n+1} = \phi_{[i,j,k]}^n + \Delta t \sum_{\alpha=1}^{3} \overline{F}_\alpha^a [\phi]_{[i,j,k]} \ . \tag{3.34}$$

Herein, $\overline{F}^{a}_{\alpha}[\phi]_{[i,j,k]} = -\{u_{\Upsilon,\perp,\alpha} D_\alpha[\phi]\}_{[i,j,k]}$, $\alpha = 1,2,3$. The differential operator $D_\alpha[\phi]$ represents a directed difference operator such that

$$D_\alpha[\phi] = \begin{cases} D^-_\alpha[\phi] & \text{if } u_{\Upsilon,\perp,\alpha} > 0 \\ D^+_\alpha[\phi] & \text{if } u_{\Upsilon,\perp,\alpha} < 0 \\ 0 & \text{if } u_{\Upsilon,\perp,\alpha} = 0 \end{cases} .$$

A 5^{th}-order upwind WENO scheme with $\epsilon = 10^{-6}$ is used to approximate it, [82, 102].

Advection is only valid for $\phi = 0$. Solving Eq. (3.34) perturbs any $\phi \neq 0$ and leads to an irregular $\phi(\mathbf{x}, t)$ [111]. To ensure $|\nabla\phi| = 1$, $\phi(\mathbf{x}, t)$ is reinitialized according to [111]

$$\frac{\partial \phi}{\partial \tau} = \operatorname{sgn}(\phi_0)\,(1 - |\nabla\phi|) \ , \tag{3.35}$$

with $\phi_0 = \phi(\mathbf{x}, t = 0)$. Thereby, ϕ_0 remains unchanged as $\operatorname{sgn}(\phi_0) = 0$. Within the original reinitialization algorithm of Sussman *et al.* [111], a smoothed sign function serves to suppress reinitialization in cells containing the interface. The algorithm developed within the scope of this work excludes such cells explicitly [82, 102], see A.3.1.

3.2.5 Extension of Fluid States

To solve for the numerical intercell fluxes $\overline{\mathbf{F}}_{\alpha,[i,j,k]}$, $\alpha = 1,2,3$, interface stresses $r^{\zeta_i,(\delta)}_{\Upsilon,\parallel}$, $r^{\zeta_i}_{\Upsilon,\perp}$ and velocities $u^{(\delta)}_{\Upsilon,\parallel}$, $u_{\Upsilon,\perp}$ in close proximity to the interface, extension of $\mathbf{V} = (u_1, u_2, u_3, p, \rho)^T$ from one partial domain into the cells of the ghost domain, collocated to the cells of the partial domain of the other fluid, is required. Following [105], the extension equation $\frac{\partial \mathbf{V}(\mathbf{x})}{\partial \tau} - \mathbf{n}_\Upsilon(\mathbf{x})^{\zeta_i,T} \cdot \nabla \mathbf{V}(\mathbf{x}) = 0$ in space-time-discrete form, i.e.

$$\mathbf{V}^{m+1}_{[i,j,k]} = \mathbf{V}^{m}_{[i,j,k]} + \Delta\tau \sum_{\alpha=1}^{3} \overline{F}^{ext}_{\alpha}[\mathbf{V}_{[i,j,k]}], \tag{3.36}$$

is solved for 20 pseudo-time steps, $\Delta\tau = 0.5\Delta x$, to populate a narrow band of ghost cells. Thereby, $\overline{F}^{ext}_{\alpha}[\mathbf{V}_{\alpha,[i,j,k]}] = \{\overline{n}^{\xi_i}_{\Upsilon,\alpha} \overline{D}_\alpha[\mathbf{V}]\}\big|_{[i,j,k]}$, $\alpha = 1,2,3$. The difference operator is

$$D_\alpha[\mathbf{V}]_{[i,j,k]} = \begin{cases} D^-_\alpha[\mathbf{V}_{[i,j,k]}] & \text{if } -n^{\xi_i}_{\Upsilon,\alpha,[i,j,k]} > 0 \\ D^+_\alpha[\mathbf{V}_{[i,j,k]}] & \text{if } -n^{\xi_i}_{\Upsilon,\alpha,[i,j,k]} < 0 \\ 0 & \text{if } -n^{\xi_i}_{\Upsilon,\alpha,[i,j,k]} = 0 \end{cases} .$$

In [102, 82], D^- and D^+ are approximated with 1^{st}-order biased differences.

3.3 Discrete Evolution of the Surfactant

The transport of insoluble surfactant along the interface is due to advection, diffusion, and interface-evolution.

3.3.1 Extension of the Surfactant Concentration

To confine surfactant to the interface, so that $\nabla_n \gamma(\mathbf{x},t)) = (\mathbf{n}_\Upsilon \otimes \mathbf{n}_\Upsilon)\,\nabla\gamma(\mathbf{x},t))$ vanishes, γ is extended off Υ according to $\frac{\partial \gamma}{\partial \tau} + \mathbf{n}_\Upsilon^{\zeta_i,T} \cdot \nabla\gamma = 0$, $\gamma(\mathbf{x}, t=0) = \gamma_0(\mathbf{x})$ prior to solving Eq. (2.45). Within the scope of this work, in space-time discrete form

$$\gamma_{[i,j,k]}^{m+1} = \gamma_{[i,j,k]}^{m} - \Delta\tau \left[\sum_{\alpha=1}^{3} \overline{F}_\alpha^{ext}[\gamma]_{[i,j,k]}^{m} \right], \tag{3.37}$$

is solved for 20 pseudo-time iterations to populate non-interfacial cells. The fluxes are $\overline{F}_\alpha^{ext}[\gamma]_{[i,j,k]}^{m} = \{n_{\Upsilon,\alpha}^{i} D_\alpha[\gamma]\}_{[i,j,k]}$, $\alpha = 1,2,3$, and $\Delta\tau = 0.5\Delta x$. Note that

$$D_\alpha[\gamma] = \begin{cases} D_\alpha^-[\gamma]_{[i,j,k]} & \text{if } n_{\Upsilon,\alpha,[i,j,k]}^{\zeta_i} > 0 \\ D_\alpha^+[\gamma]_{[i,j,k]} & \text{if } n_{\Upsilon,\alpha,[i,j,k]}^{\zeta_i} < 0 \\ 0 & \text{if } n_{\Upsilon,\alpha,[i,j,k]}^{\zeta_i} = 0 \end{cases} .$$

D^- and D^+ are approximated with 1^{st}-order biased differences [82].

3.3.2 Discrete Surfactant Transport

Within a narrow band around the interface, $\gamma_{[i,j,k]}$ is advanced in time by

$$\gamma_{[i,j,k]}^{n+1} = \gamma_{[i,j,k]}^{n} + \Delta t\ \overline{\mathbf{L}}[\gamma]_{[i,j,k]} \ . \tag{3.38}$$

where $\overline{\mathbf{L}}[\gamma]_{[i,j,k]} = \overline{\mathbf{L}}[\gamma]_{[i,j,k]}^{a} + \overline{\mathbf{L}}[\gamma]_{[i,j,k]}^{diff} + \overline{\mathbf{L}}[\gamma]_{[i,j,k]}^{evol}$ denotes the numerical flux. The evolution of surfactant due to advection with $\mathbf{u}_\Upsilon$ is accounted for by

$$\overline{\mathbf{L}}[\gamma]_{[i,j,k]}^{a} = -\left(\sum_{\beta=1}^{3} F_\beta^a[\gamma]_{[i,j,k]} + \gamma\,[D^c[u_{\Upsilon\alpha}]_\beta]_{[i,j,k]} \right) \ , \tag{3.39}$$

where $F^a_\beta[\gamma]_{[i,j,k]} = \{u_{\Upsilon,\beta} D_\beta[\gamma]\}_{[i,j,k]}$, $\beta = 1,2,3$, with $D_\beta[\gamma] = \begin{cases} D^-_\beta[\gamma] & \text{if } u_{\Upsilon,\beta} > 0 \\ D^+_\beta[\gamma] & \text{if } u_{\Upsilon,\beta} < 0 \\ 0 & \text{if } u_{\Upsilon,\beta} = 0 \end{cases}$.
A 5^{th}-order upwind WENO scheme [94] is used for $D_\beta[\gamma]$. The surface diffusion flux is

$$\begin{aligned} \overline{\mathbf{L}}[\gamma]^{diff}_{[i,j,k]} &= \frac{1}{Pe_s}\{\nabla_s^2 \gamma\}_{[i,j,k]} = \\ &= \frac{1}{Pe_s}\{\Delta\gamma(\mathbf{x}) - \left(\mathbf{n}_\Upsilon^T \cdot \nabla\gamma(\mathbf{x})\right)\left(\nabla^T \cdot \mathbf{n}_\Upsilon\right) - \mathbf{n}_\Upsilon^T \cdot H_\gamma \cdot \mathbf{n}_\Upsilon\}_{[i,j,k]} = \\ &= \frac{1}{Pe_s}\left[\frac{\partial^2\gamma}{\partial x_\alpha^2} - \left(n_{\Upsilon,\alpha}\,\frac{\partial\gamma}{\partial x_\alpha}\right)\,\kappa - \left(n_{\Upsilon,\alpha}\frac{\partial^2\gamma}{\partial x_\alpha\,\partial x_\beta} n_{\Upsilon,\beta}\right)\right]_{[i,j,k]} \approx \\ &\approx \frac{1}{Pe_s}\left[D^{2,c}[\gamma]_\alpha - \left(n_{\Upsilon,\alpha} D^c[\gamma]_\alpha\right)\kappa - \left(n_{\Upsilon,\alpha}\; D^c[D^c[\gamma]_\alpha]_\beta\; n_{\Upsilon,\beta}\right)\right]_{[i,j,k]} . \end{aligned} \tag{3.40}$$

Herein, $\kappa = \frac{|\nabla\phi|^2 tr\left(H_\phi\right) - (\nabla\phi)^T \cdot H_\phi \cdot (\nabla\phi)}{|\nabla\phi|^3}$. Interface deformation entails transport of $\gamma_{[i,j,k]}$:

$$\begin{aligned} \overline{\mathbf{L}}[\gamma]^{evol}_{[i,j,k]} &= \{\gamma\left((\mathbf{n}_\Upsilon \otimes \mathbf{n}_\Upsilon)\cdot\nabla\right)\cdot\mathbf{u}\}_{[i,j,k]} = \left\{\gamma\left(\mathbf{n}_\Upsilon^T\cdot(\nabla\mathbf{u})\cdot\mathbf{n}_\Upsilon\right)\right\}_{[i,j,k]} = \\ &= \left\{\gamma\; n_{\Upsilon,\alpha}\frac{\partial u_\alpha}{\partial x_\beta} n_{\Upsilon,\beta}\right\}_{[i,j,k]} \approx \{\gamma\; n_{\Upsilon,\alpha} D^c[u_\alpha]_\beta n_{\Upsilon,\beta}\}_{[i,j,k]} \;, \end{aligned} \tag{3.41}$$

where $D^c[u_\alpha]_\beta$ denotes the central approximation to the derivative of u_α in direction β, it is approximated with a 2^{nd}-order central scheme [82].

3.3.3 Conservation of Surfactant

The evolution equation of surfactant concentration is not conservative. Conservation of surfactant mass, i.e. $G(t) = \int_{\Delta\Upsilon}\gamma(\mathbf{x},t)d\Upsilon' = \int_{\Delta\Upsilon}\gamma(\mathbf{x},0)d\Upsilon' = G_0$, can be ensured. Therefore, the surfactant concentration is renormalized after each time step according to $\gamma(\mathbf{x},t) = \beta\widetilde{\gamma}$, where $\beta = \frac{\int_{\Delta\Upsilon}\widetilde{\gamma}d\Upsilon'\Big|^0}{\int_{\Delta\Upsilon}\gamma d\Upsilon'\Big|^{n+1}}$. $\widetilde{\gamma}$ the result of Eq. (3.38) [112]. In the sharp-interface framework the interface segment length/area $\Delta\Upsilon_{[i,j,k]}$ is computed geometrically in each cell containing a portion of the interface [82]. Such cells are considered exclusively within the algorithm.

3.4 Time Integration

The conservation equations (3.2), (3.10), (3.34), (3.38) for advancing the conservative states $\mathbf{U}$, level-set ϕ, and surfactant-concentration γ in time numerically, are formally discretized with the first-order Euler scheme. The order of accuracy is $\mathcal{O}(\Delta t)$. Runge-Kutta schemes

maintain strong stability in any semi-norm (total variation norm, maximum norm, entropy condition, etc.) of the forward Euler step [113] and are of higher order.

3.4.1 Discretization in Time

Within the scope of this work [50, 114, 115, 99, 98, 82], a 3^{rd}-order total-variation diminishing (TVD) Runge-Kutta scheme is employed [116]:

$$\begin{aligned}
\mathbf{V}^{(1)}_{[i,j,k]} &= \mathbf{V}^{n}_{[i,j,k]} + \Delta t \overline{\mathbf{L}}^{n}_{[i,j,k]}, \\
\mathbf{V}^{(2)}_{[i,j,k]} &= \frac{3}{4}\mathbf{V}^{n}_{[i,j,k]} + \frac{1}{4}\mathbf{V}^{(1)}_{[i,j,k]} + \frac{1}{4}\Delta t \overline{\mathbf{L}}^{(1)}_{[i,j,k]}, \\
\mathbf{V}^{n+1}_{[i,j,k]} &= \frac{1}{3}\mathbf{V}^{n}_{[i,j,k]} + \frac{2}{3}\mathbf{V}^{(2)}_{[i,j,k]} + \frac{2}{3}\Delta t \overline{\mathbf{L}}^{(2)}_{[i,j,k]}.
\end{aligned} \tag{3.42}$$

In high-resolution two-phase flow simulations [102, 82], interface-distant regions may be resolved low, without deteriorating the accuracy near the interface and within the bubble wake. A wavelet-based adaptive multi-resolution algorithm [117] is used to obtain a high spatial resolution near the interface and a low resolution in interface-distant regions. To further improve computational efficiency, the two-step TVD Runge-Kutta scheme [116]

$$\begin{aligned}
\mathbf{V}^{(1)}_{[i,j,k]} &= \mathbf{V}^{n}_{[i,j,k]} + \Delta t \overline{\mathbf{L}}^{n}_{[i,j,k]}, \\
\mathbf{V}^{n+1}_{[i,j,k]} &= \frac{1}{2}\mathbf{V}^{n}_{[i,j,k]} + \frac{1}{2}\mathbf{V}^{(1)}_{[i,j,k]} + \frac{1}{2}\Delta t \overline{\mathbf{L}}^{(1)}_{[i,j,k]}.
\end{aligned} \tag{3.43}$$

is used. Note that $\mathbf{V}_{[i,j,k]}$ may be $\phi_{[i,j,k]}$, $\gamma_{[i,j,k]}$, $\widehat{\mathbf{U}}_{[i,j,k]}$, or $\widetilde{\mathbf{U}}_{[i,j,k]}$.

3.4.2 Control of the Time Step Size

The advective terms of the transport equations limit the time step size Δt according to the Courant-Friedrichs-Lewy (CFL) condition

$$\Delta t^{a} = \frac{\min\left(\Delta x_{\alpha}\right)}{\max|u^{\xi_i}_{\alpha} + a^{\xi_i}|}\ , \tag{3.44}$$

where α represents one of the spatial directions $1, 2, 3$. Furthermore, Δt may be limited due to buoyancy [118],

$$\Delta t^{buo} = \frac{2\min\left(\Delta x_{\alpha}\right)}{\max|u^{\xi_i}_{\alpha} + a^{\xi_i}| + \sqrt{\left(\max|u^{\xi_i}_{\alpha} + a^{\xi_i}|\right)^2 + \frac{4\ \min(\Delta x_{\alpha})}{Fr^2}}} \tag{3.45}$$

as well as viscous effects [118]

$$\Delta t^{\nu} = \frac{3}{14} \min\left(\frac{\rho^{\xi_1}}{\mu^{\xi_1}}; \frac{\rho^{\xi_2}}{\mu^{\xi_2}}\right) Re \ \left(\min\left(\Delta x_{\alpha}\right)\right)^2 \tag{3.46}$$

The diffusion of γ limits Δt according to

$$\Delta t^{D} = \frac{1}{6} Pe_s \left(\min\left(\Delta x_{\alpha}\right)\right)^2 \ . \tag{3.47}$$

The explicit treatment of surface tension forces is stable under the condition that the time step allows to represent capillary wave motion on the computational grid [119]. The largest resolvable advection speed of capillary waves is $u^{cap} = \sqrt{\frac{We \ k_{\max}}{\rho^{\xi_1}+\rho^{\xi_2}}}$, where $k_{\max} = \frac{2\pi}{2 \ \min(\Delta x_{\alpha})} = \frac{\pi}{\min(\Delta x_{\alpha})}$ denotes the largest resolvable wave number. Considering that two capillary waves with opposite direction of advection may concurrently enter the same cell one obtains

$$\Delta t^{cap} = \frac{1}{2} \frac{\min\left(\Delta x_{\alpha}\right)}{u^{cap}} = \sqrt{\frac{\min\left(\Delta x_{\alpha}\right)^3 We \ \left(\rho^{\xi_1} + \rho^{\xi_2}\right)}{4\pi}} \tag{3.48}$$

Assuming a CFL = 0.3, the time step size is determined per iteration according to

$$\Delta t = \mathrm{CFL} \cdot \min\left(\Delta t^{a}; \Delta t^{buo}; \Delta t^{\nu}; \Delta t^{D}; \Delta t^{cap}\right) . \tag{3.49}$$

3.5 Analysis of the Numerical Dissipation Rate and Viscosity

For numerical simulations performed with an arbitrary finite-difference (FD) Navier-Stokes solver, the derivatives in Eq. (2.2) are replaced with difference approximations, introducing numerical discretization errors. Generally, these do not vanish, and the local residual

$$\begin{aligned} -\mathcal{E}_{n,[i,j,k]} = \quad & \{D^c[(\rho e_{kin})]_t + D^c[(\rho e_{kin} u_{\alpha})]_{\alpha} + u_{\alpha} D^c[p]_{\alpha} - \\ & - D^c[\left(u_{\beta}\tau^{\alpha\beta}\right)]_{\alpha} + \tau^{\alpha\beta} D^c[u_{\beta}]_{\alpha} - \tfrac{\rho g_{\alpha} u_{\alpha}}{Fr^2}\}_{[i,j,k]} \end{aligned} \tag{3.50}$$

at the grid point $[i, j, k]$ defines the numerical dissipation, due to discretization errors of the FD Navier-Stokes solver [120]. Similarly, a FV approximation is contaminated with numerical truncation errors that affect the kinetic-energy decay rate in each finite volume $\Omega_{[i,j,k]}$ and for which the local residual is [114]

$$-\mathcal{E}_{n,[i,j,k]} = \{D^c[\Delta E_{kin}]_t + F_{ekin} - F_{\nu} - \Psi + \mathcal{E}_{\nu} - S_g\}_{[i,j,k]} . \tag{3.51}$$

The individual terms in the energy equation (2.10) are computed numerically as [114]

$$E_{kin} = (\rho e_{kin})_{[i,j,k]} \ \Delta x_1 \Delta x_2 \Delta x_3 \ , \tag{3.52}$$

$$\begin{aligned} F_{ekin} &\approx (\rho e_{kin} u_1)_{[i+\frac{1}{2},j,k]} - (\rho e_{kin} u_1)_{[i-\frac{1}{2},j,k]}]\Delta x_2 \Delta x_3 + \\ &+ [(\rho e_{kin} u_2)_{[i,j+\frac{1}{2},k]} - (\rho e_{kin} u_2)_{[i,j-\frac{1}{2},k]}]\Delta x_1 \Delta x_3 + \\ &+ [(\rho e_{kin} u_3)_{[i,j,k+\frac{1}{2}]} - (\rho e_{kin} u_3)_{[i,j,k-\frac{1}{2}]}]\Delta x_1 \Delta x_2 \ , \end{aligned} \tag{3.53}$$

$$\begin{aligned} F_{\nu} &\approx [\left(\tau^{1\beta} u_\beta\right)_{[i+\frac{1}{2},j,k]} - \left(\tau^{1\beta} u_\beta\right)_{i-\frac{1}{2},j,k}]\Delta x_2 \Delta x_3 + \\ &+ [\left(\tau^{2\beta} u_\beta\right)_{[i,j+\frac{1}{2},k]} - \left(\tau^{2\beta} u_\beta\right)_{[i,j-\frac{1}{2},k]}]\Delta x_1 \Delta x_3 + \\ &+ [\left(\tau^{3\beta} u_\beta\right)_{[i,j,k+\frac{1}{2}]} - \left(\tau^{3\beta} u_\beta\right)_{[i,j,k-\frac{1}{2}]}]\Delta x_1 \Delta x_2 \ , \end{aligned} \tag{3.54}$$

$$S_g \approx \frac{1}{Fr^2} \left\{\rho g_\alpha u_\alpha\right\}_{[i,j,k]} \Delta x_1 \Delta x_2 \Delta x_3 \ , \tag{3.55}$$

$$\Psi \approx \left\{p D^c[u_\alpha]_\alpha\right\}_{[i,j,k]} \Delta x_1 \Delta x_2 \Delta x_3 \ , \tag{3.56}$$

$$\begin{aligned} \mathcal{E}_{\nu,[i,j,k]} &= \nu \mathcal{E}_{[i,j,k]} \approx \frac{\nu}{Re} \left\{\rho \left[2 \left((D^c[u_1]_1)^2 + (D^c[u_2]_2)^2 + (D^c[u_3]_3)^2\right) - \right.\right. \\ &- \frac{2}{3} \left(D^c[u_\alpha]_\alpha\right)^2 + \left(D^c[u_1]_2 + D^c[u_2]_1\right)^2 \\ &+ \left.\left. \left(D^c[u_1]_3 + D^c[u_3]_1\right)^2 + \left(D^c[u_2]_3 + D^c[u_3]_2\right)^2 \right] \right\}_{[i,j,k]} \Delta x_1 \Delta x_2 \Delta x_3 \ . \end{aligned} \tag{3.57}$$

For the flux terms, Eqs. (3.53) and (3.54), $v = (p, \mathbf{u}, \rho)$ are reconstructed at respective cell faces, e.g. $[i \pm \frac{1}{2}, j, k]$, from nearby data with a 6^{th}-order central scheme, e.g. $v_{[i\pm\frac{1}{2},j,k]} \approx \frac{1}{60}\left\{v_{[i\pm3,j,k]} - 8\left(v_{[i\pm2,j,k]} + v_{[i\mp1,j,k]}\right) + 37\left(v_{[i\pm1,j,k]} + v_{[i,j,k]}\right) + v_{[i\mp2,j,k]}\right\}$. The dissipation $\mathcal{E}$, Eq. (3.57) is approximated with at least 2^{nd}-order accuracy [114]. Integrating Eq. (3.51) over a set of FVs, comprising a closed computational subdomain (CSD), $i \in [l_{1,1}; l_{1,2}]$, $j \in [l_{2,1}; l_{2,2}]$, $k \in [l_{3,1}; l_{3,2}]$ with $0 \le l_{\alpha,1} \le l_{\alpha,2} \le L_\alpha$, where L_α is the extent of the domain Ω in x_α-direction, and its bounding surface, results in its numerical dissipation rate

$$\mathcal{E}_n^{CSD} = \sum_{i=l_{1,1}}^{l_{1,2}} \sum_{j=l_{2,1}}^{l_{2,2}} \sum_{k=l_{3,1}}^{l_{3,2}} \mathcal{E}_{n,[i,j,k]} \ . \tag{3.58}$$

For the entire computational domain, $l_{\alpha,1} = 0$, and $l_{\alpha,2} = L_\alpha$, one obtains the total numerical dissipation rate $\mathcal{E}_n^{tot}$. Similarly, one may find the numerical viscosity either locally $\nu_{n,[i,j,k]} = \frac{\mathcal{E}_{n,[i,j,k]}}{\mathcal{E}_{[i,j,k]}}$, in a CSD $\nu_n^{CSD} = \frac{\mathcal{E}_n^{CSD}}{\mathcal{E}^{CSD}}$, or within Ω $\nu_n^{tot} = \frac{\mathcal{E}_n^{tot}}{\mathcal{E}^{tot}}$. For FD corresponding definitions may be defined.

4 Accomplishments

In this chapter, the accomplished further-developments and developments are presented. For each topic, a brief literature review summarizes the state of the art. Limitations as well as open questions, which are the motivation for the individual research that have been overcome by the respective research, are discussed. Thereby this chapter results from combining Refs. [50, 114, 98, 102, 82].

4.1 A PHYSICALLY CONSISTENT WEAKLY COMPRESSIBLE HIGH-RESOLUTION APPROACH FOR UNDERRESOLVED DNS OF INCOMPRESSIBLE FLOWS

The hyperbolic nature of the (weakly) compressible NSE, in contrast to the elliptic(-parabolic) incompressible NSE, permits the use of high-order conservative finite volume methods with higher spatial accuracy and better inherent numerical stability [78]. Adequate solution strategies for systems of hyperbolic PDEs allow to simulate unsteady turbulent and non-turbulent flows, such as bubble wake flows, with a wide range of scales even when underresolved. Spectral methods are most accurate for well-resolved flows, yet, they do not account for subgrid-scale (SGS) energy transfer without explicit SGS models [121, 122].

Mathematical consistency of numerical discrete functions is necessary for convergence of numerical results. It is, however, hardly relevant when the available resolution of the flow is far from resolving the asymptotic range of the local truncation error. Modified differential equation analysis (MDEA) [123] has revealed that the truncation error of nonlinear discretization schemes can be constructed such to recover the theoretical spectral eddy viscosity, in other words, to represent an implicit SGS (ISGS) model [124, 125] for implicit large eddy simulations (ILES) of underresolved turbulent flows. The nonlinear regularization mechanism of high order, finite volume schemes with shock-capturing capabilities has made this approach applicable to ILES [126]. The correct physical SGS behavior modeling by means of the non-negligible local truncation error of a numerical scheme is called *physically consistent* behavior [48, 49]. In [122], it has been demonstrated that standard finite-difference and spectral methods do not provide the basis for physically consistent SGS modeling capability.

WENO weighting implies measuring the local resolution of the flow. It potentially allows to state a physically consistent scheme with a truncation error shaped to exhibit implicit subgrid-scale modeling capabilities for turbulent as well as non-turbulent flows [124, 125]. A low-dissipative WENO-scheme, combining the advantages of an upwind scheme, e.g. the 5^{th}-order WENO scheme [94], and a 6^{th}-order central scheme, denoted as WENO-CU6, has been proposed by Hu *et al.* [95]. Hu and Adams [96] have investigated the physical consistency of the underresolved contribution of WENO-CU6. A proper modification of WENO-weights has resulted in a separation of contributions from the resolved and non-resolved scales to the locally reconstructed solution [50]. Thus, non-resolved scales are subject to dissipation, while the shock-capturing capabilities and the order of accuracy are maintained in smooth flow regions. The scheme is denoted WENO-CU6-M1. Evidence strongly suggests that a scheme suitable for the underrsolved simulation of high-Reynolds number flows cannot exclusively be based on the local truncation error of the underlying high-order reconstruction scheme. It is, however, a well-balanced interaction of the thermodynamic fluid-modeling, the reconstruction scheme and the intercell-numerical flux, i.e.

the nonlinear regularization mechanism of high-order finite-volume schemes with shock-capturing capabilities.

The three-dimensional Taylor-Green vortex (TGV) [127] is the most simple generic flow to study the generation and evolution of small scale turbulent structures by vortex stretching and the evolution of isotropic turbulence in time. Shu *et al.* [122] have found that the fifth-order WENO scheme shows unphysical dissipation, yet allows for stable underresolved simulations of the inviscid, nearly incompressible TGV.

In **Felix S. Schranner, Xiangyu Y. Hu, Nikolaus A. Adams**: *A physically consistent weakly compressible high-resolution approach to underresolved simulations of incompressible flows*; Computers & Fluids, Volume 86, pp. 109-114, November 2013 [50]

it is demonstrated that a physically consistent high-resolution model for ILES of incompressible flows can be constructed by matching the WENO-CU6-M1 weighting to the weakly compressible flow modeling of Chorin and Temam [128, 129, 81] and a low-dissipative Roe-Pike [100, 130, 131] solver. A 6^{th}-order central reconstruction for density is employed. The separated reconstruction for the density and the velocities emphasizes the ISGS model on the pure nature of incompressible turbulence.

The correct transition of the TGV to self-similar isotropic turbulence, even at large Reynolds numbers and for the inviscid case, is reproduced. General validity of the weakly compressible WENO-CU6-M1 based scheme for underresolved DNS is confirmed by considering also moderate Reynolds number decaying grid generated turbulence.

Moreover, the underresolution prediction capability for non-turbulent flows of the physically consistent weakly compressible numerical high-resolution model is demonstrated. The instability of the inviscid, yet, finite-thickness double shear layer [132, 133] is studied even in the highly nonlinear stages. With an equivalent resolution as in a pseudospectral and a centered vorticity-stream function method, a similar quality of predictions is achieved. Yet, in the underresolved setup, the alternative methods need stabilization with artificial, numerical viscosity that exceeds physical viscosity. The exploration of the infinitely thin double shear layer at zero viscosity with the newly developed weakly compressible WENO-CU6-M1-based method with an implicit SGS model confirms the speculation of Brown and Minion [132] that the final stage of shear layer evolution is a single vortex. This final stage is independent of shear layer thickness and Reynolds number.

Furthermore, a viscous-inviscid interaction of a vortex dipole colliding with a no-slip wall is considered. The simulation results are in excellent agreement with reference data of [134, 135] at much lower resolution.

For the lid driven cavity, the model predictions agree with reference solutions that are based on high-resolution schemes, see [136, 137, 138] and on strictly incompressible formulations. For $Re \leq 7500$, steady state solutions comparable to reference DNS are obtained with underresolved DNS. At $Re = 10000$, a flow with low-frequency periodic unsteadiness is found. Since this result is grid independent, the periodic behavior is likely to be physically correct, whereas the steady state behavior observed in Refs. [137, 138], is due to numerical damping.

My contribution to this work lies in developing the method and its implementation in an in-house code. Moreover, I have verified the implementation and validated the method, hence, performed the numerical simulations. The algorithm for postprocessing and analyzing the results is due to me. The manuscript for the publication has been written predominantly by me.

4.2 Assessing the numerical dissipation rate and viscosity in numerical simulations of fluid flows

The discretization of the governing differential equations for fluid flows entails contamination of the simulation results by the local truncation errors, which diminishes if all physical relevant scales are resolved adequately. For a lower resolution, the effects of truncation errors may be of similar magnitude as physical effects. The simulation results are thereby influenced. This situation is most frequently encountered in numerical simulations of turbulent flows at high Reynolds numbers. Such flows require modeling contributions of unresolved scales according to common turbulence modeling procedures. For Reynolds-averaged Navier-Stokes (RANS) simulations, a large number of turbulence models exists, ranging from mathematically simple and numerically cheap algebraic models to complex and expensive Reynolds stress models, for an overview see e.g. [139, 140, 141]. For Large Eddy Simulation (LES), a variety of explicit as well as implicit subgrid-scale models have been proposed, for an overview refer to e.g. [142, 143, 144, 145].

ISGS models of ILES schemes rely on the nonlinear contributions of the truncation error, which is necessarily far from an asymptotic behavior. Classical tools for truncation error analysis fail [145, 120]. The modified differential equation cannot be written down in closed form, and Taylor series expansions are of no use as the truncation error is not asymptotically small. The current rather vague definition of SGS modeling capabilities of the wide range of the existing ILES schemes demands a more systematic approach to determine the effective dissipation aposteriori. The first aposteriori method for computing integral numerical dissipation has been proposed by Domaradzki *et al.* [146]. Flow evolutions from identical initialization, yet, solved with a scheme of finite numerical dissipation and a spectral reference code with negligible numerical dissipation, are compared. Based on results of this analytical method, Hickel *et al.* [49] have developed the Adaptive Local Deconvolution Method (ALDM), that recovers the physical energy transfer in turbulence. The method of analysis [146] is in spectral space to allow one-to-one comparisons with spectral eddy viscosities obtained from analytical theories of turbulence, and it measures the global (spectral) dissipation rate.

In **Felix S. Schranner, J.Andrzej Domaradzki, Stefan Hickel, Nikolaus A. Adams**: *Assessing the numerical dissipation rate and viscosity in numerical simulations of fluid flows*; Computers & Fluids, Volume 114, pp. 84-97, July 2015 [114],

a method for analyzing grid-based fluid flow simulations for the numerical dissipation rate and numerical viscosity is developed. It is free of the deficiencies of the spectral space method of Domaradzki *et al.* [146]. Which means that it does not require the use of an additional spectral code for analysis, which is practically unfeasible. Furthermore, it is not restricted to fully periodic computational domains. Consequently, it seeks its application in non-periodic flows of practical interest.

The novel physical space method of analysis is validated by comparing results for the effective numerical dissipation rate with exact reference data. These have been obtained with an accurate spectral-space approach. As the optimal test case for the validation study, the Taylor-Green vortex is selected. Excellent agreement of both methods is achieved on arbitrary, non-periodic domains. This holds even true for temporal and spatial derivative approximations of only second-order accuracy.

The predictive capabilities of the novel physical space method depend neither on the size nor shape of the computational domain under consideration. Yet, generally, the larger the numerical dissipation rate, the smaller is the uncertainty in predicting it. This particularly true for high Reynolds numbers. Since the method is designed to analyze simulations for their non-diminishing numerical errors, this constraint is rather natural.

In contrast to the reference method, the newly developed method is applicable to arbitrary flows and non-uniform unstructured grids in a straightforward manner. The studies performed within the scope of this work clearly indicate that considering a diminishing time-step size for the analysis is not necessary. Hence, the aposteriori application is straightforward to results of simulations fulfilling the CFL-stability criterion.

The methods capabilities are demonstrated for underresolved TGV flows. A Reynolds number range of $Re = 100$ to $Re = 3000$ has been considered.

Besides evaluating the global numerical dissipation rate and viscosity within the simulation domain, even local estimates can be obtained. Thereby it is even possible to analyze the computational cell-wise numerical dissipation rate and viscosity.

Our studies show that the larger the numerical dissipation rate and viscosity, the smaller the uncertainty in predicting these. In consequence, critical flow regions may thus be identified and evaluated easily.

My contribution to this work lies in the development of the method. This physical space method and the reference spectral space method have been implemented by me. Moreover, I verified the implementation and validated the method, hence, performed the numerical analysis. The algorithm for postprocessing and analyzing the results is due to me. Major parts of the manuscript for the publication have been written by me.

4.3 Optimization of an Implicit Large-Eddy Simulation Method for Underresolved Incompressible Flow Simulations

In underresolved regions, the truncation error of the underlying numerical schemes strongly affects the solution. If the local truncation error of the underlying numerical scheme functions as an ISGS model, i.e. it models the evolution of otherwise resolved scales, resolution may remain low. Thereby, computational efficiency is improved. The range of applications of WENO-CU6-M1 [96] has been extended from compressible to incompressible flows by Schranner *et al.* [50]. In combination with the material modeling and appropriate Riemann-solver, an adjusted scheme has recovered self-similar isotropic turbulence when physical viscosity diminishes. Mere by adapting the scheme's free parameters, $(C_q; q)$, the ISGS modeling capability has been ported. As in e.g. Refs. [94, 147], in Schranner *et al.* [50] an adequate set for free parameters has been determined through "extensive numerical experiments". This approach is neither efficient nor does it guarantee an optimal model performance.

Finding an optimal weakly compressible WENO-CU6-M1 model for underresolved simulations is considered within a deterministic design optimization framework in

Felix S. Schranner, Vladyslav Rozov, Nikolaus Adams: *Optimization of an Implicit Large-Eddy Simulation Method for Underresolved Incompressible Flow Simulations*; AIAA Journal, Volume 54 Number 5, pp. 1567-1577, February 2016 [98].

Therefore, the potential of weakly compressible WENO-CU6-M1 Roe Riemann-solver formulations to reproduce Kolmogorov scaling in the quasi-isotropic state of an infinite Reynolds number TGV flow is evaluated. The previous works [50, 115] are extended on this subject to a more general scope.

Evaluating potential surrogate modeling and sampling strategies for their applicability shows that the approximation quality of polynomial regression surrogate models of a certain order depends predominantly on sampling resolution. These demonstrate as inadequate for design optimization of WENO-CU6-M1. A thin plate spline interpolation model determines an optimal set of WENO-CU6-M1 parameters, which closely approximates the fittest sample. The relative difference in fitness between these is below 1%. At already 30% of the highest level resolution, the response surface approximation has been sufficient to localize the optimal $(C_q; q)$ approximately.

The design of an ISGS model according to "best recovery of the inertial subrange $E(k)$ according to Kolmogorov theory" leads to a stronger correlation of SGS dissipation and small scales. The correlation of kinetic energy dissipation, quantified with the method of Schranner *et al.* [114], and existence of small scales is more apparent in the optimized scheme than in the reference. Insights into areas of physical and numerical kinetic energy dissipation are gained by visualizing the local, dissipation structures. In the TGV flow, these exist independent of the underlying ILES scheme in each octant of the domain and are point-reflectional symmetric with respect to the center of the domain [114]. Yet, when a WENO-CU6-M1 based SGS model is physically consistent, that is, when scale-separation is optimally controlled, small-scale structures are of a longer life span.

The effective dissipation rates of low to high Re TGV flows, simulated with the optimal scheme, are compared to reference DNS data. For very low Re it is found that even when no subgrid-scales are present, the model adds a minimum amount of dissipation. For medium to high Re, the surrogate weakly compressible WENO-CU6-M1 model predictions agree well with DNS. A comparison of optimized weakly compressible WENO-CU6-M1-based model results to those of alternative ILES and LES simulations at medium to infinite Re TGV flows show its superior performance.

The concept of this study is due to me. I implemented the thin plate spline interpolation model, analyzed and evaluated the results. Furthermore, I performed the two comparative studies, namely the one involving the optimal, surrogate, original scheme and the one also incorporating reference data. Major parts of the manuscript for the publication have been written by me.

4.4 On the convergence of the weakly compressible sharp-interface method for two-phase flows

The numerical simulation of incompressible, immiscible, two-phase flows is challenging due to large density and viscosity ratios of gas-liquid systems, which may deteriorate numerical stability, especially when numerical dissipation is sought to be low. Furthermore, the numerical method needs to accurately reproduce the dynamic interface evolution even for complex interface topology evolution at affordable numerical cost. Interface singularities, such as capillary stresses, may entail discontinuities in field quantities. For flow configurations, ranging from small scale micro fluidics to larger scale microgravity sloshing surface tension effects dominate areas of the flow. These requirements have lead to a variety of Lagrangian and Eulerian approaches. Independent of the approach, method and code development typically passes through two stages. Firstly, a single-phase flow solver with increasing spatial dimensionality, incorporating viscous and boundary-treatment is implemented, validated and verified (V&V). Validation is "the process of determining the degree to which a model is an accurate representation of the real world from the perspective of the intended uses of the model" [148]. Verification is "the process of determining that a model implementation accurately represents the developer's conceptual description of the model and the solution to the model" [148]. In the second stage, the solver is extended to model the interaction and evolution of multiple immiscible fluids, V&V concludes this stage. For the verification of single-fluid algorithms, analytical solutions and reference DNS-results of a variety of generic test flows are available. Such data may be found in Refs. [149, 50] for the *Taylor-Green vortex*, Refs. [150, 151] for the *turbulent channel flow*, Refs. [133, 132] for the $2D$ *double shear layer*, Refs. [135, 152, 50] for a *vortex pair-wall interaction*, and [136, 138, 50] for a *lid-driven cavity*. A list of references for validation experiments may e.g. be found in Oberkampf and Trucano [153].

Verification of two-phase algorithms, especially in 2D, is accomplished best by cross-method comparison as suitable analytical solutions are scarce. Validation basis on visual inspection and comparison with experimental data. One frequently used test case for verification of two-phase flow solvers is the dam break experiment by Martin and Moyce [154]. The 2D, or axisymmetric, dam break is helpful only during early stages of code development. The lack in small-scale interface evolution restricts its subsequent use.

The *Rayleigh-Taylor instability* (RTI) suits to evaluate the capability of a two-phase solver to resolve fine-scaled density stratifications, while maintaining a sharp interface, in the absence of surface tension. According to Cummings and Rudman [155]: a "numerical simulation of the Rayleigh-Taylor instability keeps on producing finer scales of density stratification until the resolution of the method is reached". Simulations of 2D submerged air bubbles rising due to the influence of gravity (BLG) can assess capillary and viscous effects, as they combine all relevant phenomena of two-phase, immiscible flows. While the benchmark results of Cummins and Rudman [155] resolve a sharp interface, charac-

teristic for Lagrangian approaches, they are underresolved. The data of Sussman *et al.* [111], used for comparison in e.g. [77, 156, 74], are based on the Eulerian diffuse-interface, level-set continuum method. The lack of conservativity is the main drawback of diffuse-interface methods, such as volume-of-fluid [157], level-set continuum [109] or phase-field [158] methods. Smoothed particle hydrodynamics (SPH) methods can be mass and momentum conservative, see e.g. Adami *et al.* [159]. Szewc *et al.* [76, 160] have simulated the RTI and a BLG with several SPH formulations and found forking solutions. Neither for the RTI nor for the BLG, resolution-independent, mass- and momentum conservative, sharp-interface-maintaining solutions were available for proper cross-method comparisons.

Providing these data has been the goal of

Felix S. Schranner, Xiangyu Hu, Nikolaus A. Adams: *On the convergence of the weakly compressible sharp-interface method for two-phase flows*; Journal of Computational Physics, Volume 324, pp. 94-114, July 2016 [102].

The algorithm of [102] relies on a mass and momentum conservative, weakly compressible, fully Eulerian, sharp-interface method [103] for immiscible, viscous, weakly compressible two-phase flows. For computing the finite volume fluxes, a fifth-order WENO reconstruction [161] is coupled to a weakly compressible Roe-Riemann solver [50, 115, 98]. Sub-cell corrections for interfacial viscous [162] and capillary stresses improve the spatial accuracy. Due to resolving only near-interface regions at highest accuracy and permitting underresolution otherwise, numerical cost remain low.

With this algorithm, the RTI is studied until late stages. Local resolution is increased until grid independence of the interface and integral quantities is observed. Thereby, fine-scale structures appear to evolve grid-independently.

For the BLG different physically dominant phenomena are identified at sufficient spatial resolution. Firstly, a low-Reynolds/ supercritical (for cusp formation) capillary number configuration of the BLG is studied. Unsteady cusp formation and shedding of bubbles are observed when the bubble is subject to large shear rates. Moreover, tertiary bubbles result from the viscous interaction of the bulk fluid flow with the secondary bubbles, from which they detach. Secondly, a high Reynolds number (low Ca) BLG is considered. Viscous effects are subordinate, the interface development is complex. The interface shape and the location of secondary bubbles can be resolved adequately at moderate grid resolution. At higher resolution capillary waves are captured and the secondary-bubble sizes are grid-independent.

For both Re, the disperse-phase integral quantities centroid and degree of circularity are monitored. The x_2-centroid, monitored for both Re, indicates the convergence of primary and secondary bubbles. When secondary bubbles detach, the primary bubble regains a stable cap and ascent. The x_1-centroid and circularity mark the occurrence of bubble shedding. DNS of a freely ascending high-Re bubble are performed. It is observed that the wake flow of the primary, cap-shaped, bubble is the driving motor for the evolution of the secondary bubbles.

In summary, the results of these two flow configuration [102] ought to serve as a reference for cross-method comparison of two-phase models incorporating interfacial capillary and viscous effects and verification of their implementation.

My contribution to this work lies in the development of the concept of this study and the method to obtain the sub-cell corrected interface curvature. Moreover, I implemented most of the algorithm, validated the models and verified the implementations. I performed the numerical simulations and evaluated the results. The algorithm for postprocessing is due to me. The manuscript for the publication has been written predominantly by me.

4.5 A CONSERVATIVE INTERFACE-INTERACTION MODEL WITH INSOLUBLE SURFACTANT

Numerical methods for solving interfacial flows with surfactants may be categorized into *interface tracking* and *interface capturing*. Interface tracking methods either use an interface-adapted grid or marker particles to represent the interface. A surface mesh is used instead in boundary integral methods. A boundary integral method for studying the effect of insoluble surfactants on drop deformation has been developed in [163, 164]. In the front-tracking method [165], a fixed grid is used for the flow, and a set of connected marker particles tracks the interface and surfactant. A front-tracking method for insoluble surfactants is due to Jan [166]. The immersed boundary method [167] was used to simulate interfacial flows with insoluble surfactant A ghost-cell immersed boundary method [168] was employed in Ref. [169] to study the effects of diffusion-controlled surfactant on a viscous drop injected into a viscous medium. The dynamics of capillary waves with insoluble surfactant were investigated using a hybrid level-set/front-tracking approach [170]. Another front-tracking method, combining a finite element methodology with adaptive body-fitted meshes, served to simulate the deformation and breakup of axisymmetric liquid bridges [171] and thin filaments [172], considering insoluble surfactants.

In general, interface tracking methods are very accurate, yet, especially in 3D and for evolving interfaces, the implementation is complicated. Possible drawbacks of marker Lagrangian approaches include difficulties in evaluating topology changes, the need to remove parts of the evolving front (delooping) to correctly characterize the viscosity solution, the need to adaptively add and remove points, and complexities in three dimensions [110].
Interface capturing methods define the interface implicitly with an auxiliary function, e.g. a level-set, phase-field or color function. Gridding, discretization and handling of topological changes is straightforward. In [173], Teigen *et al.* develop and apply the diffuse interface approach [158] to simulate flows with soluble and insoluble surfactants.
A level-set method [107, 109] for solving the surfactant transport is due to Adalsteinsson *et al.* [174] and Xu *et al.* [175]. It is coupled with the immersed interface method (IIM) [176] in [112]. With the IIM, the interface jump conditions are handled explicitly by modifying the discretization stencils near the interface. As a simple and robust alternative to IIM Xu *et al.* have modeled interface forces within the level-set framework by a continuous surface force (CSF). A common property of these incompressible level-set and phase-field methods is the smoothing of material properties such as density and viscosity at the interface. This implies their drawbacks: The lack of discrete conservation and ineffectiveness at large density and viscosity ratios.

The fully conservative level-set based Sharp-Interface Method (SIM) for compressible flows [103], is robust even for large interface topology changes [117], and large density and viscosity ratios [177, 102]. It has been further developed to model viscous, weakly compressible two-phase flows [162]. The key idea of the SIM framework, where the Navier-Stokes equations are solved on a Cartesian grid, is the modification of FVs that are cut by the interface

to allow explicit application of the interface-jump conditions, see Sec. 3.2. Interaction terms considering capillary forces for a constant surface-tension coefficient and viscous forces have been proposed in Ref. [162]. Yet, the formulation cannot account for a jump condition in interface-tangential direction, occurring in the general case of non-vanishing Marangoni stresses [84, 178].

In **Felix S. Schranner, Nikolaus A. Adams**: *A conservative interface-interaction model with insoluble surfactant*; Journal of Computational Physics, Volume 327, pp. 653-677, September 2016 [82],

a robust and consistent interface-interaction model is developed that accounts for the fluid-fluid interaction, as well as capillary and Marangoni stresses explicitly at the sharp interface. The interface-exchange is a direct solution of the interface jump conditions as discussed in Sec. 2.4. The novel model is simpler than the CSF-approach and the IIM-based approach of [112, 173].

The temporal evolution of surfactant concentration, level-set, and fluid phases follow an identical Runge-Kutta algorithm. Level-set and surfactant evolution are evaluated only within a narrow band near the interface, thus being highly efficient. Within the SIM framework, local interface-segment lengths/areas are computed, avoiding the need for a smoothed delta-function, for approximation of the interface length.

The algorithm of Xu et al. [112] is further-developed to employ these interface-segment lengths/areas. A significant improvement in efficiency, compared to the alternative smoothed delta-function formulation of [112], is achieved. Furthermore, due to the algorithm it is unnecessary to propagate the interface area as another variable as proposed in [91].

The expected Marangoni and viscous stresses are predicted for a thermocapillary flow configuration [179], validating the method. Physically expected behavior for the general case of non-zero interface curvature is demonstrated on basis of drops propelled by a surfactant gradient.

As an application demonstration the dynamic evolution of a single, two-dimensional drop in a shear flow is analyzed with respect to the capillary ($Ca = \frac{\mu_{ref} U_{ref}}{\sigma_{ref}}$), Weber, and Reynolds number, surfactant coverage, and surface Peclet number. The observations are in agreement with previous numerical and experimental studies. Parameter analysis indicate that decreasing Re increases initial drop stretching, and larger We entail more distinct interface dynamics. Yet, very small We stiffen the drop, so that it remains more circular even at low Re. The presence of surfactant lowers the interface stabilizing surface tension, and thus leads to larger elongation at steady-state. Recovery of an ellipsoidal drop shape is delayed with increasing surfactant coverage and elasticity. In case of a harmonically oscillating drop, increasing surfactant coverage shows only minor effects. Moreover, the critical We appears to be independent of surfactant coverage.

My contribution to this work lies in developing the concept of this study, as well as the methods. I implemented the methods and algorithm. Moreover, I have verified the implementations and validated the methods, hence, performed the numerical simulations. The algorithm for postprocessing and analyzing the results is due to me. I have written major parts of the manuscript for the publication.

5 List of Publications

5.1 Peer-Reviewed Journal Publications

- **Felix S. Schranner, Xiangyu Y. Hu, Nikolaus A. Adams**: *A physically consistent weakly compressible high-resolution approach to underresolved simulations of incompressible flows*; Computers & Fluids, Volume 86, pp. 109-114, November 2013
- **Felix S. Schranner, J.Andrzej Domaradzki, Stefan Hickel, Nikolaus A. Adams**: *Assessing the numerical dissipation rate and viscosity in numerical simulations of fluid flows*; Computers & Fluids, Volume 114, pp. 84-97, July 2015
- **Felix S. Schranner, Vladyslav Rozov, Nikolaus Adams**: *Optimization of an Implicit Large-Eddy Simulation Method for Underresolved Incompressible Flow Simulations*; AIAA Journal, Volume 54, Number 5, pp. 1567-1577, February 2016
- **Felix S. Schranner, Xiangyu Hu, Nikolaus A. Adams**: *On the convergence of the weakly compressible sharp-interface method for two-phase flows*; Journal of Computational Physics, Volume 324, pp. 94-114, July 2016
- **Felix S. Schranner, Nikolaus A. Adams**: *A conservative interface-interaction model with insoluble surfactant*; Journal of Computational Physics, Volume 327, pp. 653-677, September 2016

5.2 Book Sections

- **Castiglioni, Domaradzki, Krais, Beck, Munz & Schranner**: *Characterization of Numerical Dissipation Rates in Numerical Simulations Performed Using Discontinuous Galerkin Methods*; in Proceedings of the 2015 summer program within the SFBTRR40, Munich, Germany, 2015

5.3 Conference Proceedings Contributions

- **Felix S. Schranner, Xiangyu Y. Hu, Nikolaus A. Adams**: *Long-Time Evolution of the Incompressible Three-Dimensional Taylor-Green Vortex at Very High Reynolds Number*; Proceedings of the Eighth International Symposium on Turbulence and Shear Flow Phenomena (TSFP-8), Poitiers, France, August 2013
- **Felix S. Schranner, J. Andrzej Domaradzki, Stefan Hickel, Nikolaus A. Adams**: *Assessing the numerical dissipation rate and viscosity in CFD simulations of fluid flows*; Proceedings of the 67th Annual Meeting of the APS Division of Fluid Dynamics, San Francisco, California, USA, November 2014

- **Felix S. Schranner, Vladyslav Rozov, Nikolaus Adams**: *Optimization of an Implicit LES Method for Underresolved Simulations of Incompressible Flows*; Proceedings of the 54th AIAA Aerospace Sciences Meeting, AIAA Science and Technology Forum and Exposition; San-Diego, California, USA January 2016

6 Conclusion

Replacing a strictly incompressible with a weakly compressible approach reduces data communication of the single-fluid algorithm significantly. Moreover, validation simulations indicate that the weakly compressible WENO-CU6-M1 model, incorporating an implicit subgrid-scale model, is a reliable method for the simulation of a wide range of 2D and 3D turbulent and non-turbulent flows with underresolved, complex multiscale structures. A self-contained method for quantifying the effective numerical dissipation rate and viscosity in CFD simulations has been developed. It relies exclusively on simulated flow-field data. Hence, it suits as a stand-alone post-processing tool to alleviate estimation of the reliability of the acquired data. Deterministic design optimization of the weakly compressible WENO-CU6-M1 scheme has allowed to recover Kolmogorov inertial subrange scaling for an infinite Reynolds number Taylor-Green vortex in its quasi-isotropic turbulent state. For finite, yet, high Re TGV flows, the optimized model performs superior to alternative explicit and implicit SGS models, allowing for two-phase flow simulations in these regimes. The design optimization framework is general, hence application to alternative gradient-capturing schemes for underresolved DNS is straightforward. Three distinct, two-dimensional, complex interface evolutions from initially simple setups, characteristic for a wide range of academic and industrial two-phase flow applications have been realized at unprecedented accuracy. The high-resolution data define a benchmark suite for cross-method comparison and method verification of interface-capturing or tracking methods. A sharp-interface momentum exchange consistently accounting for the interface-interaction of two immiscible, weakly compressible fluids, as well as capillary and Marangoni stresses has been developed and integrated into the sharp-interface framework. Conservative insoluble surfactant transport along the sharp interface is consistent to the fluid, and level-set transport on a Cartesian grid and explicit in time. The sharp-interface surfactant conservation algorithm is at least as accurate as its original diffusive interface formulation, yet, computationally more efficient. Sub-cell space interface reconstruction and curvature computation enables very accurate computations of capillary stresses and surfactant diffusion.

In conclusion, computationally efficient and physically valid simulations of complex, incompressible single- and two-phase flows with potentially underresolved multiscale structures are straightforward with the methods developed within the scope of this work. In particular, studying ascending gaseous bubbles in liquids has been made possible for a wide range of Reynolds, Eötvös and Morton numbers. Thereby, physical conditions such as at least weakly compressible effects, large density and viscosity ratios, sharp-interfaces, and small-scale turbulent structures can be accounted for. Moreover, even the dynamics of insoluble surfactants and their effect on bubble evolution can be considered. Additionally, evaluation of numerical simulation results for their local and global reliability is henceforth similarly straightforward as in experimental studies. Alike the numerical methods for single- and two-phase flow simulations, this method of analysis is directly applicable to a wide range of scientific and industrial computational fluid dynamics configurations.

A Mathematical Appendix

A.1 Interpolation of Cell Face States

Parameters of the 5^{th}-order WENO Scheme

The ideal weights are [93]:

$$d_0 = \frac{1}{10}, d_1 = \frac{3}{5}, d_2 = \frac{3}{10}. \tag{A.1}$$

Upwind Interpolation

Three different 3^{rd}-order approximations of the non-averaged upwind cell-face value $\mathbf{u}_{i+\frac{1}{2}}^{(L,\upsilon)}$ are formulated on the three-point candidate stencils S_0, S_1, S_2:

$$\begin{aligned}
\mathbf{u}_{i+\frac{1}{2}}^{(L,0)} &= \frac{1}{6}\left(2\widehat{\mathbf{U}}_{[i-2]} - 7\widehat{\mathbf{U}}_{[i-1]} + 11\widehat{\mathbf{U}}_{[i]}\right) \ , \\
\mathbf{u}_{i+\frac{1}{2}}^{(L,1)} &= \frac{1}{6}\left(-\widehat{\mathbf{U}}_{[i-1]} + 5\widehat{\mathbf{U}}_{[i]} + 2\widehat{\mathbf{U}}_{[i+1]}\right) \ , \\
\mathbf{u}_{i+\frac{1}{2}}^{(L,2)} &= \frac{1}{6}\left(2\widehat{\mathbf{U}}_{[i]} + 5\widehat{\mathbf{U}}_{[i+1]} - \widehat{\mathbf{U}}_{[i+2]}\right) \ .
\end{aligned} \tag{A.2}$$

From these three upwind candidate stencils, a 5^{th}-order accurate WENO cell-face $\overline{\mathbf{U}}_{[i+\frac{1}{2}]}^{(L)}$ is calculated by equation (3.4). Via

$$\beta_{\upsilon}^{(\alpha)} = \sum_{l=1}^{m-1} \int_{x_{i-\frac{1}{2}}}^{x_{i+\frac{1}{2}}} \Delta x^{2l-1} \left(\frac{\partial^l \mathbf{u}^{(\alpha,\upsilon)}(x)}{\partial x^l}\right)^2 dx, \tag{A.3}$$

the smoothness indicators are calculated as:

$$\begin{aligned}
\beta_0^{(L)} &= \frac{1}{4}\left(\widehat{\mathbf{U}}_{[i-2]} - 4\widehat{\mathbf{U}}_{[i-1]} + 3\widehat{\mathbf{U}}_{[i]}\right)^2 + \frac{13}{12}\left(\widehat{\mathbf{U}}_{[i-2]} - 2\widehat{\mathbf{U}}_{[i-1]} + \widehat{\mathbf{U}}_{[i]}\right)^2 \ , \\
\beta_1^{(L)} &= \frac{1}{4}\left(\widehat{\mathbf{U}}_{[i-1]} - \widehat{\mathbf{U}}_{[i+1]}\right)^2 + \frac{13}{12}\left(\widehat{\mathbf{U}}_{[i-1]} - 2\widehat{\mathbf{U}}_{[i]} + \widehat{\mathbf{U}}_{[i+1]}\right)^2 \ , \\
\beta_2^{(L)} &= \frac{1}{4}\left(3\widehat{\mathbf{U}}_{[i]} - 4\widehat{\mathbf{U}}_{[i+1]} + \widehat{\mathbf{U}}_{[i+2]}\right)^2 + \frac{13}{12}\left(\widehat{\mathbf{U}}_{[i]} - 2\widehat{\mathbf{U}}_{[i+1]} + \widehat{\mathbf{U}}_{[i+2]}\right)^2 \ .
\end{aligned} \tag{A.4}$$

Downwind Interpolation

Three different 3^{rd}-order approximations of the non-averaged downwind cell-face value $\mathbf{u}_{i+\frac{1}{2}}^{(R,v)}$ are formulated on the three-point candidate stencils S_0, S_1, S_2:

$$\begin{aligned}
\mathbf{u}_{i+\frac{1}{2}}^{(R,0)} &= \frac{1}{6}\left(2\widehat{\mathbf{U}}_{[i+3]} - 7\widehat{\mathbf{U}}_{[i+2]} + 11\widehat{\mathbf{U}}_{[i+1]}\right) , \\
\mathbf{u}_{i+\frac{1}{2}}^{(R,1)} &= \frac{1}{6}\left(-\widehat{\mathbf{U}}_{[i+2]} + 5\widehat{\mathbf{U}}_{[i+1]} + 2\widehat{\mathbf{U}}_{[i]}\right) , \\
\mathbf{u}_{i+\frac{1}{2}}^{(R,2)} &= \frac{1}{6}\left(2\widehat{\mathbf{U}}_{[i+1]} + 5\widehat{\mathbf{U}}_{[i]} - \widehat{\mathbf{U}}_{[i-1]}\right) .
\end{aligned} \tag{A.5}$$

From these three upwind candidate stencils, a 5^{th}-order accurate WENO cell-face $\overline{\mathbf{U}}_{[i+\frac{1}{2}]}^{(R)}$ is calculated by equation (3.4). The smoothness indicators are:

$$\begin{aligned}
\beta_0^{(R)} &= \frac{1}{4}\left(\widehat{\mathbf{U}}_{[i+3]} - 4\widehat{\mathbf{U}}_{[i+2]} + 3\widehat{\mathbf{U}}_{[i+1]}\right)^2 + \frac{13}{12}\left(\widehat{\mathbf{U}}_{[i+3]} - 2\widehat{\mathbf{U}}_{[i+2]} + \widehat{\mathbf{U}}_{[i+1]}\right)^2 , \\
\beta_1^{(R)} &= \frac{1}{4}\left(\widehat{\mathbf{U}}_{[i+2]} - \widehat{\mathbf{U}}_{[i]}\right)^2 + \frac{13}{12}\left(\widehat{\mathbf{U}}_{[i+2]} - 2\widehat{\mathbf{U}}_{[i+1]} + \widehat{\mathbf{U}}_{[i]}\right)^2 , \\
\beta_2^{(R)} &= \frac{1}{4}\left(3\widehat{\mathbf{U}}_{[i+1]} - 4\widehat{\mathbf{U}}_{[i]} + \widehat{\mathbf{U}}_{[i-1]}\right)^2 + \frac{13}{12}\left(\widehat{\mathbf{U}}_{[i+1]} - 2\widehat{\mathbf{U}}_{[i]} + \widehat{\mathbf{U}}_{[i-1]}\right)^2 .
\end{aligned} \tag{A.6}$$

Extension of the Parameter Set to Allow for 6^{th}-order CU-WENO-M1 Reconstruction

The ideal weights adapt to account for four stencils:

$$d_0 = d_3 = \frac{1}{20}, d_1 = d_2 = \frac{9}{20}. \tag{A.7}$$

Upwind Interpolation

The fourth 3^{rd}-order approximation to $\overline{\mathbf{U}}_{[i+\frac{1}{2}]}^{(L)}$, based on the three-point candidate stencil S_4, is:

$$\mathbf{u}_{i+\frac{1}{2}}^{(L,3)} = \frac{1}{6}\left(11\widehat{\mathbf{U}}_{[i+1]} - 7\widehat{\mathbf{U}}_{[i+2]} + 2\widehat{\mathbf{U}}_{[i+3]}\right) . \tag{A.8}$$

The fourth smoothness indicator evaluates as:

$$\begin{aligned}\beta_3^{(L)} = \frac{1}{10080}\Big|&271779\widehat{\mathbf{U}}_{[i-2]}^2 + \widehat{\mathbf{U}}_{[i-2]}(-2380800\widehat{\mathbf{U}}_{[i-1]} + 4086352\widehat{\mathbf{U}}_{[i]} - 3462252\widehat{\mathbf{U}}_{[i+1]} \\ &+ 1458762\widehat{\mathbf{U}}_{[i+2]} - 245620\widehat{\mathbf{U}}_{[i+3]}) \\ &+ \widehat{\mathbf{U}}_{[i-1]}(5653317\widehat{\mathbf{U}}_{[i-1]} - 20427884\widehat{\mathbf{U}}_{[i]} + 17905032\widehat{\mathbf{U}}_{[i+1]} \\ &- 7727988\widehat{\mathbf{U}}_{[i+2]} + 1325006\widehat{\mathbf{U}}_{[i+3]}) \\ &+ \widehat{\mathbf{U}}_{[i]}\left(19510972\widehat{\mathbf{U}}_{[i]} - 35817664\widehat{\mathbf{U}}_{[i+1]} + 15929912\widehat{\mathbf{U}}_{[i+2]} - 2792660\widehat{\mathbf{U}}_{[i+3]}\right) \\ &+ \widehat{\mathbf{U}}_{[i+1]}\left(17195652\widehat{\mathbf{U}}_{[i+1]} - 15880404\widehat{\mathbf{U}}_{[i+2]} + 2863984\widehat{\mathbf{U}}_{[i+3]}\right) \\ &+ \widehat{\mathbf{U}}_{[i+2]}\left(3824847\widehat{\mathbf{U}}_{[i+2]} - 1429976\widehat{\mathbf{U}}_{[i+3]}\right) + 139633\widehat{\mathbf{U}}_{[i+3]}^2\Big| \,.\end{aligned} \tag{A.9}$$

Downwind Interpolation

The fourth 3^{rd}-order approximation to $\overline{\mathbf{U}}^{(R)}_{[i+\frac{1}{2}]}$, based on the three-point candidate stencil S_4, is:

$$\mathbf{u}^{(R,3)}_{i+\frac{1}{2}} = \frac{1}{6}\left(11\widehat{\mathbf{U}}_{[i]} - 7\widehat{\mathbf{U}}_{[i-1]} + 2\widehat{\mathbf{U}}_{[i-2]}\right) \,. \tag{A.10}$$

The fourth smoothness indicator for the downwind reconstruction evaluates as:

$$\begin{aligned}\beta_3^{(R)} = \frac{1}{10080}\Big|&271779\widehat{\mathbf{U}}_{[i+3]}^2 + \widehat{\mathbf{U}}_{[i+3]}(-2380800\widehat{\mathbf{U}}_{[i+2]} + 4086352\widehat{\mathbf{U}}_{[i+1]} - 3462252\widehat{\mathbf{U}}_{[i]} \\ &+ 1458762\widehat{\mathbf{U}}_{[i-1]} - 245620\widehat{\mathbf{U}}_{[i-2]}) \\ &+ \widehat{\mathbf{U}}_{[i+2]}(5653317\widehat{\mathbf{U}}_{[i+2]} - 20427884\widehat{\mathbf{U}}_{[i+1]} + 17905032\widehat{\mathbf{U}}_{[i]} \\ &- 7727988\widehat{\mathbf{U}}_{[i-1]} + 1325006\widehat{\mathbf{U}}_{[i-2]}) \\ &+ \widehat{\mathbf{U}}_{[i+1]}\left(19510972\widehat{\mathbf{U}}_{[i+1]} - 35817664\widehat{\mathbf{U}}_{[i]} + 15929912\widehat{\mathbf{U}}_{[i-1]} - 2792660\widehat{\mathbf{U}}_{[i-2]}\right) \\ &+ \widehat{\mathbf{U}}_{[i]}\left(17195652\widehat{\mathbf{U}}_{[i]} - 15880404\widehat{\mathbf{U}}_{[i-1]} + 2863984\widehat{\mathbf{U}}_{[i-2]}\right) \\ &+ \widehat{\mathbf{U}}_{[i-1]}\left(3824847\widehat{\mathbf{U}}_{[i-1]} - 1429976\widehat{\mathbf{U}}_{[i-2]}\right) + 139633\widehat{\mathbf{U}}_{[i-2]}^2\Big| \,.\end{aligned} \tag{A.11}$$

A.2 Equation of State Dependent Roe and Roe-Pike Riemann Solver

Given the cell-face normal vector $\mathbf{n} = (n_1, n_2, n_3)$, which is $\mathbf{n} = (1, 0, 0)$ for computing $\mathbf{F}_1$, $\mathbf{n} = (0, 1, 0)$ for computing $\mathbf{F}_2$, and $\mathbf{n} = (0, 0, 1)$ for computing $\mathbf{F}_3$, the cell-face tangent vectors are $\mathbf{t}^{(1)} = (-n_2, n_1, 0)$, $\mathbf{t}^{(2)} = \mathbf{n} \times \mathbf{t}^{(1)} = (-n_3 n_1, -n_2 n_3, n_1 n_1 + n_2 n_2)$.

A.2.1 Common Roe Averaged States

$$\begin{aligned} \widetilde{\rho} &= \sqrt{\rho^{(L)}\rho^{(R)}}, \\ \widetilde{u}_1 &= \frac{\sqrt{\rho^{(L)}}u_1^{(L)} + \sqrt{\rho^{(R)}}u_1^{(R)}}{\sqrt{\rho^{(L)}} + \sqrt{\rho^{(R)}}}, \\ \widetilde{u}_2 &= \frac{\sqrt{\rho^{(L)}}u_2^{(L)} + \sqrt{\rho^{(R)}}u_2^{(R)}}{\sqrt{\rho^{(L)}} + \sqrt{\rho^{(R)}}}, \\ \widetilde{u}_3 &= \frac{\sqrt{\rho^{(L)}}u_3^{(L)} + \sqrt{\rho^{(R)}}u_3^{(R)}}{\sqrt{\rho^{(L)}} + \sqrt{\rho^{(R)}}}, \end{aligned} \tag{A.12}$$

and $\widetilde{\mathbf{u}}^2 = \widetilde{u}_1^2 + \widetilde{u}_2^2 + \widetilde{u}_3^2$

A.2.2 $\Delta\mathbf{w}$ for the Evaluation of Roe Wave Strengths

According to Roe [100]$\Delta\mathbf{w}$ evaluates as

$$\Delta\mathbf{w} = \begin{bmatrix} \Delta w_0 \\ \Delta w_1 \\ \Delta w_2 \\ \Delta w_3 \end{bmatrix} = \mathbf{U}^{(R)} - \mathbf{U}^{(L)} = \begin{bmatrix} \Delta\rho \\ \Delta\left(\rho u_1\right) \\ \Delta\left(\rho u_2\right) \\ \Delta\left(\rho u_3\right) \\ \Delta\left(\rho e_t\right) \end{bmatrix} = \begin{bmatrix} \rho^{(L)} - \rho^{(R)} \\ \left(\rho u_1\right)^{(L)} - \left(\rho u_1\right)^{(R)} \\ \left(\rho u_2\right)^{(L)} - \left(\rho u_2\right)^{(R)} \\ \left(\rho u_3\right)^{(L)} - \left(\rho u_3\right)^{(R)} \end{bmatrix}. \tag{A.13}$$

A.2.3 $\Delta\mathbf{w}$ for the Evaluation of Roe-Pike Wave Strengths

Roe and Pike [101] simplify $\Delta\mathbf{w}$ by evaluating:

$$\Delta\mathbf{w} = \begin{bmatrix} \Delta w_0 \\ \Delta w_1 \\ \Delta w_2 \\ \Delta w_3 \end{bmatrix} = \begin{bmatrix} \Delta\rho \\ \Delta\rho\widetilde{u}_1 + \Delta u_1\widetilde{\rho} \\ \Delta\rho\widetilde{u}_2 + \Delta u_2\widetilde{\rho} \\ \Delta\rho\widetilde{u}_3 + \Delta u_3\widetilde{\rho} \end{bmatrix}. \tag{A.14}$$

A.2.4 Common Roe Wave Strengths:

$$\begin{aligned}
\widetilde{\delta}^{(1)} &= \tfrac{1}{2\widetilde{a}}\left[\Delta w_0\left(\widetilde{a}+\mathbf{n}\cdot\widetilde{\mathbf{u}}\right)-\Delta\mathbf{u}\cdot\mathbf{n}-\widetilde{a}\delta^{(2)}\right],\\
\widetilde{\delta}^{(3)} &= \left(\Delta\mathbf{u}-\widetilde{\mathbf{u}}\Delta w_0\right)\cdot\mathbf{t}_1,\\
\widetilde{\delta}^{(4)} &= \left(\Delta\mathbf{u}-\widetilde{\mathbf{u}}\Delta w_0\right)\cdot\mathbf{t}_2,\\
\widetilde{\delta}^{(5)} &= \tfrac{1}{\widetilde{a}}\left[\Delta\mathbf{u}-\widetilde{\mathbf{u}}\Delta w_0\right]\cdot\mathbf{n}+\widetilde{\delta}^{(1)}\ .
\end{aligned} \tag{A.15}$$

A.2.5 Common Roe-Pike Wave Strengths:

$$\begin{aligned}
\widetilde{\delta}^{(1)} &= \tfrac{1}{2\widetilde{a}^2}\left[\left(p^{(R)}-p^{(L)}\right)-\widetilde{\rho}\widetilde{a}\left(\mathbf{u}^{(R)}-\mathbf{u}^{(L)}\right)\cdot\mathbf{n}\right],\\
\widetilde{\delta}^{(3)} &= \widetilde{\rho}\left(\mathbf{u}^{(R)}-\mathbf{u}^{(L)}\right)\cdot\mathbf{t}_1,\\
\widetilde{\delta}^{(4)} &= \widetilde{\rho}\left(\mathbf{u}^{(R)}-\mathbf{u}^{(L)}\right)\cdot\mathbf{t}_2,\\
\widetilde{\delta}^{(5)} &= \tfrac{1}{2\widetilde{a}^2}\left[\left(p^{(R)}-p^{(L)}\right)+\widetilde{\rho}\widetilde{a}\left(\mathbf{u}^{(R)}-\mathbf{u}^{(L)}\right)\cdot\mathbf{n}\right]\ .
\end{aligned} \tag{A.16}$$

A.2.6 Artificially Compressible EOS

EOS specific Roe Averages:

$$\widetilde{a} = a\ . \tag{A.17}$$

EOS specific Roe Wave Strength $\delta^{(2)}$:

$$\widetilde{\delta}^{(2)} = 0\ . \tag{A.18}$$

EOS specific Roe-Pike Wave Strength $\delta^{(2)}$:

$$\widetilde{\delta}^{(2)} = 0\ . \tag{A.19}$$

Right Eigenvectors:

$$\begin{aligned}
\mathbf{K}^{(1)} &= \begin{bmatrix} 1 \\ \widetilde{u}_1-\widetilde{a}\cdot n_1 \\ \widetilde{u}_2-\widetilde{a}\cdot n_2 \\ \widetilde{u}_3-\widetilde{a}\cdot n_3 \end{bmatrix}, \quad \mathbf{K}^{(3)} = \begin{bmatrix} 0 \\ \mathbf{t}^{(1)} \end{bmatrix},\\
\mathbf{K}^{(4)} &= \begin{bmatrix} 0 \\ \mathbf{t}^{(2)} \end{bmatrix}, \quad \mathbf{K}^{(5)} = \begin{bmatrix} 1 \\ \widetilde{u}_1+\widetilde{a}\cdot n_1 \\ u_2+\widetilde{a}\cdot n_2 \\ \widetilde{u}_3+\widetilde{a}\cdot n_3 \end{bmatrix}\ .
\end{aligned} \tag{A.20}$$

A.2.7 TAIT EOS

EOS specific Roe averages:

$$\begin{gathered}\widetilde{h} = \widetilde{e}_{kin} + \omega \widetilde{e}_{in}, \\ \text{with} \quad \widetilde{e}_{in} = \tfrac{\widetilde{p}}{\widetilde{\rho}(\omega-1)} \quad \text{where} \quad \widetilde{p} = p_1 \left[\left(\tfrac{\widetilde{\rho}}{\rho_0} \right)^{\kappa} - 1 \right] + p_0, \\ \widetilde{a} = \sqrt{\tfrac{p_1}{\rho_0^{\omega}} \omega \widetilde{\rho}^{(\omega-1)}} \; .\end{gathered} \tag{A.21}$$

EOS specific Roe Wave Strength $\delta^{(2)}$:

$$\widetilde{\delta}^{(2)} = \left[\widetilde{u}_1 \Delta w_1 + \widetilde{u}_2 \Delta w_2 + \widetilde{u}_3 \Delta w_3 + \Delta w_0 \left(\widetilde{h} - 2\widetilde{e}_{kin} \right) - \Delta w_4 \right] \; . \tag{A.22}$$

EOS specific Roe-Pike Wave Strength $\delta^{(2)}$:

$$\widetilde{\delta}^{(2)} = \frac{\omega}{\widetilde{\rho}(\omega-1)} \left(p_0 - p_1 \right) \left(\rho^{(R)} - \rho^{(L)} \right) \; . \tag{A.23}$$

Right Eigenvectors:

$$\begin{gathered}\mathbf{K}^{(1)} = \begin{bmatrix} 1 \\ \widetilde{u}_1 - \widetilde{a} \cdot n_1 \\ \widetilde{u}_2 - \widetilde{a} \cdot n_2 \\ \widetilde{u}_3 - \widetilde{a} \cdot n_3 \\ \widetilde{h} - \widetilde{a} \; \mathbf{u} \cdot \mathbf{n} \end{bmatrix}, \quad \mathbf{K}^{(2)} = \begin{bmatrix} 0 \\ 0 \\ 0 \\ 0 \\ -1 \end{bmatrix}, \quad \mathbf{K}^{(3)} = \begin{bmatrix} 0 \\ \mathbf{t}^{(1)} \\ \widetilde{\mathbf{u}} \cdot \mathbf{t}^{(1)} \end{bmatrix}, \\ \mathbf{K}^{(4)} = \begin{bmatrix} 0 \\ \mathbf{t}^{(2)} \\ \widetilde{\mathbf{u}} \cdot \mathbf{t}^{(2)} \end{bmatrix}, \quad \mathbf{K}^{(5)} = \begin{bmatrix} 1 \\ \widetilde{u}_1 + \widetilde{a} \cdot n_1 \\ u_2 + \widetilde{a} \cdot n_2 \\ \widetilde{u}_3 + \widetilde{a} \cdot n_3 \\ \widetilde{h} + \widetilde{a} \; \mathbf{u} \cdot \mathbf{n} \end{bmatrix} \; .\end{gathered} \tag{A.24}$$

A.3 Interface Transport and Representation

A.3.1 Details of the Level-set Reinitialization

Eq. (3.35) can be rewritten as

$$\frac{\partial \phi}{\partial t} + \mathbf{c} \cdot \nabla \phi = \operatorname{sgn}(\phi_0) \ , \tag{A.25}$$

where the advection velocity is

$$\mathbf{c} = \operatorname{sgn}(\phi_0) \left(\frac{\Delta \phi}{|\Delta \phi|} \right) \ . \tag{A.26}$$

The characteristics of the nonlinear hyperbolic equation (A.25), emanating from $\phi(\mathbf{x}) = 0$, lead to reinitialization of $\phi(\mathbf{x})$ in sequence with the distance to the interface.
To obtain the level set field ϕ^{n+1} at the pseudo time step $n+1$, the discretized Eq. (A.25),

$$\phi^{n+1}_{[i,j,k]} = \phi^{n}_{[i,j,k]} + \Delta\tau \overline{\mathbf{L}}_{[i,j,k]} \ , \tag{A.27}$$

is solved for $\phi_0 \neq 0$. This is realized by explicitly marking and omitting cells that contain the interface. $\overline{\mathbf{L}}_{[i,j,k]} = \operatorname{sgn}\left(\phi_{[i,j,k],n=0}\right) \overline{G}(\phi_{[i,j,k]})$ denotes the difference operator and

$$\overline{G}(\phi|_{[i,j,k]}) = \begin{cases} 1 - \sqrt{\max\left((a^+)^2 ; (b^-)^2\right) + \max\left((c^+)^2 ; (d^-)^2\right) + \max\left((e^+)^2 ; (f^-)^2\right)} & \text{if } \phi_{[i,j,k]} > 0 \\ 1 - \sqrt{\max\left((a^-)^2 ; (b^+)^2\right) + \max\left((c^-)^2 ; (d^+)^2\right) + \max\left((e^-)^2 ; (f^+)^2\right)} & \text{if } \phi_{[i,j,k]} > 0 \\ 0 & \text{otherwise} \end{cases} \ , \tag{A.28}$$

where

$$\begin{aligned} a^+ &= \max\left(D_1^-[\phi_{[i,j,k]}]; 0\right), & a^- &= \min\left(D_1^-[\phi_{[i,j,k]}]; 0\right) \ , \\ b^+ &= \max\left(D_1^+[\phi_{[i,j,k]}]; 0\right), & b^- &= \min\left(D_1^+[\phi_{[i,j,k]}]; 0\right) \ , \\ c^+ &= \max\left(D_2^-[\phi_{[i,j,k]}]; 0\right), & c^- &= \min\left(D_2^-[\phi_{[i,j,k]}]; 0\right) \ , \\ d^+ &= \max\left(D_2^+[\phi_{[i,j,k]}]; 0\right), & d^- &= \min\left(D_2^+[\phi_{[i,j,k]}]; 0\right) \ , \\ e^+ &= \max\left(D_3^-[\phi_{[i,j,k]}]; 0\right), & e^- &= \min\left(D_3^-[\phi_{[i,j,k]}]; 0\right) \ , \\ f^+ &= \max\left(D_3^+[\phi_{[i,j,k]}]; 0\right), & f^- &= \min\left(D_3^+[\phi_{[i,j,k]}]; 0\right) \ . \end{aligned} \tag{A.29}$$

The upwind differences are approximated with a 1^{st}-order scheme, i.e. e.g. $D_1^-[\phi_{[i,j,k]}] = \frac{\phi_{[i,j,k]} - \phi_{[i-1,j,k]}}{\Delta x_1}$, and $D_1^+[\phi_{[i,j,k]}] = \frac{\phi_{[i+1,j,k]} - \phi_{[i,j,k]}}{\Delta x_1}$, in the appropriate direction. The pseudo-time step size is $\Delta\tau = \frac{1}{4}\sqrt{(\Delta x_1)^2 + (\Delta x_2)^2 + (\Delta x_3)^2}$. Ten iterations are performed to reach steady state.

A.3.2 Sub-cell Corrected Interface Curvature

Let the radius of the osculating circle at a point on the interface be r, then its curvature, which is the reciprocal of its radius,

$$k(r) = \frac{1}{r} \ , \tag{A.30}$$

equals the principal curvature of the local interface segment. In two-dimensional space, the mean curvature is

$$\kappa_M(r) = k(r) \ . \tag{A.31}$$

By Taylor-series expansion of (A.31), one obtains a 1^{st}-order accurate approximation to the interface curvature

$$\kappa_\Upsilon = \kappa_M(r) + \frac{d\kappa_M(r)}{dr}\Delta r + \mathcal{O}^2 = \kappa_M(r) - \frac{1}{r^2}\Delta r + \mathcal{O}^2 = \kappa_M(r) - \kappa_M(r)^2\Delta r + \mathcal{O}^2 \ . \tag{A.32}$$

Considering that $\kappa_M(r)$ may also be negative, Eq. (A.32) is modified as

$$\kappa_{\Upsilon,2\mathrm{D}} = \kappa_M(r + \Delta r) \approx \left(|\kappa_M(r)| - \kappa_M(r)^2\Delta r\right)\mathrm{sgn}(\kappa_M(r)) \ . \tag{A.33}$$

In 3D, the local mean curvature relates to the radii of the maximal and minimal osculating circles as

$$\kappa_M = \frac{1}{2}(k_1 + k_2) = \frac{1}{2}\left(\frac{1}{r_1} + \frac{1}{r_2}\right) \ . \tag{A.34}$$

Assuming an osculating sphere of $k_1 = k_2 = k$, Eq. (A.34) becomes

$$\kappa_M(r) = k = \frac{1}{r} \ , \tag{A.35}$$

from which it can readily be seen that

$$\kappa_{\Upsilon,3\mathrm{D}} = \kappa_{\Upsilon,2\mathrm{D}} \ . \tag{A.36}$$

Note that $\phi_{[i,j,k]} < 0$ corresponds to $\Delta r > 0$ and vice versa. Generally, the local mean curvature $\kappa(\mathbf{x}, t)$ of the interface is obtained from the local level-set according to

$$\begin{aligned} \kappa_{M,2D}(\phi) &= \frac{|\nabla\phi|^2\, tr\left(H_\phi\right) - (\nabla\phi)^T \cdot H_\phi \cdot (\nabla\phi)}{|\nabla\phi|^3} = \\ &= \frac{\frac{\partial\phi}{\partial x_1}^2\frac{\partial^2\phi}{\partial x_2^2} + \frac{\partial\phi}{\partial x_2}^2\frac{\partial^2\phi}{\partial x_1^2} - 2\frac{\partial\phi}{\partial x_1}\frac{\partial\phi}{\partial x_2}\frac{\partial^2\phi}{\partial x_1\partial x_2}}{\left(\frac{\partial\phi}{\partial x_1}^2 + \frac{\partial\phi}{\partial x_2}^2\right)^{3/2}} \end{aligned} \tag{A.37}$$

in 2D, and with

$$\begin{aligned}\kappa_{M,3D}(\phi) &= \frac{|\nabla\phi|^2\, tr\,(H_\phi) - (\nabla\phi)^T \cdot H_\phi \cdot (\nabla\phi)}{2\,|\nabla\phi|^3} = \\ &= \frac{\frac{\partial\phi}{\partial x_1}^2\left(\frac{\partial^2\phi}{\partial x_2^2}+\frac{\partial^2\phi}{\partial x_3^2}\right)+\frac{\partial\phi}{\partial x_2}^2\left(\frac{\partial^2\phi}{\partial x_1^2}+\frac{\partial^2\phi}{\partial x_3^2}\right)+\frac{\partial\phi}{\partial x_3}^2\left(\frac{\partial^2\phi}{\partial x_1^2}+\frac{\partial^2\phi}{\partial x_2^2}\right)}{2\left(\frac{\partial\phi}{\partial x_1}^2+\frac{\partial\phi}{\partial x_2}^2+\frac{\partial\phi}{\partial x_3}^2\right)^{3/2}} - \\ &- \frac{2\left(\frac{\partial\phi}{\partial x_1}\frac{\partial\phi}{\partial x_2}\frac{\partial^2\phi}{\partial x_1\partial x_2}+\frac{\partial\phi}{\partial x_1}\frac{\partial\phi}{\partial x_3}\frac{\partial^2\phi}{\partial x_1\partial x_3}+\frac{\partial\phi}{\partial x_2}\frac{\partial\phi}{\partial x_3}\frac{\partial^2\phi}{\partial x_1\partial x_2}\right)}{2\left(\frac{\partial\phi}{\partial x_1}^2+\frac{\partial\phi}{\partial x_2}^2+\frac{\partial\phi}{\partial x_3}^2\right)^{3/2}}\end{aligned} \tag{A.38}$$

in 3D, where $\mathrm{tr}\,(H_\phi)$ denotes the trace of the Hessian of ϕ.

B Major Peer-Reviewed Journal Publications

B.1 A PHYSICALLY CONSISTENT WEAKLY COMPRESSIBLE HIGH-RESOLUTION APPROACH TO UNDERRESOLVED SIMULATIONS OF INCOMPRESSIBLE FLOWS

ELSEVIER LICENSE TERMS AND CONDITIONS

Oct 12, 2016

This Agreement between Felix S Schranner ("You") and Elsevier ("Elsevier") consists of your license details and the terms and conditions provided by Elsevier and Copyright Clearance Center.

License Number	3897820775110
License date	Jun 28, 2016
Licensed Content Publisher	Elsevier
Licensed Content Publication	Computers & Fluids
Licensed Content Title	A physically consistent weakly compressible high-resolution approach to underresolved simulations of incompressible flows
Licensed Content Author	Felix S. Schranner,Xiangyu Y. Hu,Nikolaus A. Adams
Licensed Content Date	5 November 2013
Licensed Content Volume Number	86
Licensed Content Issue Number	n/a
Licensed Content Pages	16
Start Page	109
End Page	124
Type of Use	reuse in a thesis/dissertation
Intended publisher of new work	other
Portion	full article
Format	both print and electronic
Are you the author of this Elsevier article?	Yes
Will you be translating?	No
Order reference number	
Title of your thesis/dissertation	Weakly Compressible Models for Complex Flows
Expected completion date	Nov 2016
Estimated size (number of pages)	212
Elsevier VAT number	GB 494 6272 12
Requestor Location	Felix S Schranner Boltzmannstrasse 15 Garching, 85748 Germany Attn: Felix S Schranner

Total **0.00 EUR**

Terms and Conditions

INTRODUCTION

1. The publisher for this copyrighted material is Elsevier. By clicking "accept" in connection with completing this licensing transaction, you agree that the following terms and conditions apply to this transaction (along with the Billing and Payment terms and conditions established by Copyright Clearance Center, Inc. ("CCC"), at the time that you opened your Rightslink account and that are available at any time at http://myaccount.copyright.com).

GENERAL TERMS

2. Elsevier hereby grants you permission to reproduce the aforementioned material subject to the terms and conditions indicated.
3. Acknowledgement: If any part of the material to be used (for example, figures) has appeared in our publication with credit or acknowledgement to another source, permission must also be sought from that source. If such permission is not obtained then that material may not be included in your publication/copies. Suitable acknowledgement to the source must be made, either as a footnote or in a reference list at the end of your publication, as follows:
"Reprinted from Publication title, Vol /edition number, Author(s), Title of article / title of chapter, Pages No., Copyright (Year), with permission from Elsevier [OR APPLICABLE SOCIETY COPYRIGHT OWNER]." Also Lancet special credit - "Reprinted from The Lancet, Vol. number, Author(s), Title of article, Pages No., Copyright (Year), with permission from Elsevier."
4. Reproduction of this material is confined to the purpose and/or media for which permission is hereby given.
5. Altering/Modifying Material: Not Permitted. However figures and illustrations may be altered/adapted minimally to serve your work. Any other abbreviations, additions, deletions and/or any other alterations shall be made only with prior written authorization of Elsevier Ltd. (Please contact Elsevier at permissions@elsevier.com)
6. If the permission fee for the requested use of our material is waived in this instance, please be advised that your future requests for Elsevier materials may attract a fee.
7. Reservation of Rights: Publisher reserves all rights not specifically granted in the combination of (i) the license details provided by you and accepted in the course of this licensing transaction, (ii) these terms and conditions and (iii) CCC's Billing and Payment terms and conditions.
8. License Contingent Upon Payment: While you may exercise the rights licensed immediately upon issuance of the license at the end of the licensing process for the transaction, provided that you have disclosed complete and accurate details of your proposed use, no license is finally effective unless and until full payment is received from you (either by publisher or by CCC) as provided in CCC's Billing and Payment terms and conditions. If full payment is not received on a timely basis, then any license preliminarily granted shall be deemed automatically revoked and shall be void as if never granted. Further, in the event that you breach any of these terms and conditions or any of CCC's Billing and Payment terms and conditions, the license is automatically revoked and shall be void as if never granted. Use of materials as described in a revoked license, as well as any use of the materials beyond the scope of an unrevoked license, may constitute copyright infringement and publisher reserves the right to take any and all action to protect its copyright in the materials.
9. Warranties: Publisher makes no representations or warranties with respect to the licensed material.
10. Indemnity: You hereby indemnify and agree to hold harmless publisher and CCC, and their respective officers, directors, employees and agents, from and against any and all claims arising out of your use of the licensed material other than as specifically authorized pursuant to this license.
11. No Transfer of License: This license is personal to you and may not be sublicensed, assigned, or transferred by you to any other person without publisher's written permission.
12. No Amendment Except in Writing: This license may not be amended except in a writing signed by both parties (or, in the case of publisher, by CCC on publisher's behalf).
13. Objection to Contrary Terms: Publisher hereby objects to any terms contained in any purchase order, acknowledgment, check endorsement or other writing prepared by you, which terms are inconsistent with these terms and conditions or CCC's Billing and Payment terms and conditions. These terms and conditions, together with CCC's Billing and Payment terms and conditions (which are incorporated herein), comprise the entire agreement between you and publisher (and CCC) concerning this licensing transaction. In the event of any conflict between your obligations established by these terms and conditions and those established by CCC's Billing and Payment terms and conditions, these terms and conditions shall control.
14. Revocation: Elsevier or Copyright Clearance Center may deny the permissions described in this License at their sole discretion, for any reason or no reason, with a full refund payable to you. Notice of such denial will be made using the contact information provided by you. Failure to receive such notice will not alter or invalidate the denial. In no event will Elsevier or Copyright Clearance Center be responsible or liable for any costs, expenses or damage incurred by you as a result of a denial of your permission request, other than a refund of the amount(s) paid by you

to Elsevier and/or Copyright Clearance Center for denied permissions.

LIMITED LICENSE

The following terms and conditions apply only to specific license types:

15. **Translation**: This permission is granted for non-exclusive world **English** rights only unless your license was granted for translation rights. If you licensed translation rights you may only translate this content into the languages you requested. A professional translator must perform all translations and reproduce the content word for word preserving the integrity of the article.

16. **Posting licensed content on any Website**: The following terms and conditions apply as follows: Licensing material from an Elsevier journal: All content posted to the web site must maintain the copyright information line on the bottom of each image; A hyper-text must be included to the Homepage of the journal from which you are licensing at http://www.sciencedirect.com/science/journal/xxxxx or the Elsevier homepage for books at http://www.elsevier.com; Central Storage: This license does not include permission for a scanned version of the material to be stored in a central repository such as that provided by Heron/XanEdu.

Licensing material from an Elsevier book: A hyper-text link must be included to the Elsevier homepage at http://www.elsevier.com . All content posted to the web site must maintain the copyright information line on the bottom of each image.

Posting licensed content on Electronic reserve: In addition to the above the following clauses are applicable: The web site must be password-protected and made available only to bona fide students registered on a relevant course. This permission is granted for 1 year only. You may obtain a new license for future website posting.

17. **For journal authors:** the following clauses are applicable in addition to the above:

Preprints:

A preprint is an author's own write-up of research results and analysis, it has not been peer-reviewed, nor has it had any other value added to it by a publisher (such as formatting, copyright, technical enhancement etc.).

Authors can share their preprints anywhere at any time. Preprints should not be added to or enhanced in any way in order to appear more like, or to substitute for, the final versions of articles however authors can update their preprints on arXiv or RePEc with their Accepted Author Manuscript (see below).

If accepted for publication, we encourage authors to link from the preprint to their formal publication via its DOI. Millions of researchers have access to the formal publications on ScienceDirect, and so links will help users to find, access, cite and use the best available version. Please note that Cell Press, The Lancet and some society-owned have different preprint policies. Information on these policies is available on the journal homepage.

Accepted Author Manuscripts: An accepted author manuscript is the manuscript of an article that has been accepted for publication and which typically includes author-incorporated changes suggested during submission, peer review and editor-author communications.

Authors can share their accepted author manuscript:

- immediately
  - via their non-commercial person homepage or blog
  - by updating a preprint in arXiv or RePEc with the accepted manuscript
  - via their research institute or institutional repository for internal institutional uses or as part of an invitation-only research collaboration work-group
  - directly by providing copies to their students or to research collaborators for their personal use
  - for private scholarly sharing as part of an invitation-only work group on commercial sites with which Elsevier has an agreement
- after the embargo period
  - via non-commercial hosting platforms such as their institutional repository
  - via commercial sites with which Elsevier has an agreement

In all cases accepted manuscripts should:

- link to the formal publication via its DOI
- bear a CC-BY-NC-ND license - this is easy to do
- if aggregated with other manuscripts, for example in a repository or other site, be shared in alignment with our hosting policy not be added to or enhanced in any way to appear more like, or to substitute for, the published journal article.

Published journal article (JPA): A published journal article (PJA) is the definitive final record of published research that appears or will appear in the journal and embodies all value-adding publishing activities including peer review co-ordination, copy-editing, formatting, (if relevant) pagination and online enrichment.

Policies for sharing publishing journal articles differ for subscription and gold open access articles:
Subscription Articles: If you are an author, please share a link to your article rather than the full-text. Millions of researchers have access to the formal publications on ScienceDirect, and so links will help your users to find, access, cite, and use the best available version.
Theses and dissertations which contain embedded PJAs as part of the formal submission can be posted publicly by the awarding institution with DOI links back to the formal publications on ScienceDirect.
If you are affiliated with a library that subscribes to ScienceDirect you have additional private sharing rights for others' research accessed under that agreement. This includes use for classroom teaching and internal training at the institution (including use in course packs and courseware programs), and inclusion of the article for grant funding purposes.
Gold Open Access Articles: May be shared according to the author-selected end-user license and should contain a CrossMark logo, the end user license, and a DOI link to the formal publication on ScienceDirect.
Please refer to Elsevier's posting policy for further information.
18. **For book authors** the following clauses are applicable in addition to the above: Authors are permitted to place a brief summary of their work online only. You are not allowed to download and post the published electronic version of your chapter, nor may you scan the printed edition to create an electronic version. **Posting to a repository:** Authors are permitted to post a summary of their chapter only in their institution's repository.
19. **Thesis/Dissertation**: If your license is for use in a thesis/dissertation your thesis may be submitted to your institution in either print or electronic form. Should your thesis be published commercially, please reapply for permission. These requirements include permission for the Library and Archives of Canada to supply single copies, on demand, of the complete thesis and include permission for Proquest/UMI to supply single copies, on demand, of the complete thesis. Should your thesis be published commercially, please reapply for permission. Theses and dissertations which contain embedded PJAs as part of the formal submission can be posted publicly by the awarding institution with DOI links back to the formal publications on ScienceDirect.

Elsevier Open Access Terms and Conditions
You can publish open access with Elsevier in hundreds of open access journals or in nearly 2000 established subscription journals that support open access publishing. Permitted third party re-use of these open access articles is defined by the author's choice of Creative Commons user license. See our open access license policy for more information.
Terms & Conditions applicable to all Open Access articles published with Elsevier:
Any reuse of the article must not represent the author as endorsing the adaptation of the article nor should the article be modified in such a way as to damage the author's honour or reputation. If any changes have been made, such changes must be clearly indicated.
The author(s) must be appropriately credited and we ask that you include the end user license and a DOI link to the formal publication on ScienceDirect.
If any part of the material to be used (for example, figures) has appeared in our publication with credit or acknowledgement to another source it is the responsibility of the user to ensure their reuse complies with the terms and conditions determined by the rights holder.
Additional Terms & Conditions applicable to each Creative Commons user license:
CC BY: The CC-BY license allows users to copy, to create extracts, abstracts and new works from the Article, to alter and revise the Article and to make commercial use of the Article (including reuse and/or resale of the Article by commercial entities), provided the user gives appropriate credit (with a link to the formal publication through the relevant DOI), provides a link to the license, indicates if changes were made and the licensor is not represented as endorsing the use made of the work. The full details of the license are available at http://creativecommons.org/licenses/by/4.0.
CC BY NC SA: The CC BY-NC-SA license allows users to copy, to create extracts, abstracts and new works from the Article, to alter and revise the Article, provided this is not done for commercial purposes, and that the user gives appropriate credit (with a link to the formal publication through the relevant DOI), provides a link to the license, indicates if changes were made and the licensor is not represented as endorsing the use made of the work. Further, any new works must be made available on the same conditions. The full details of the license are available at http://creativecommons.org/licenses/by-nc-sa/4.0.
CC BY NC ND: The CC BY-NC-ND license allows users to copy and distribute the Article, provided this is not done for commercial purposes and further does not permit distribution of the Article if it is changed or edited in any way, and provided the user gives appropriate credit (with a link to the formal publication through the relevant DOI), provides a link to the license, and that the licensor is not represented as endorsing the use made of the work. The full details of the license are available at http://creativecommons.org/licenses/by-nc-nd/4.0. Any commercial reuse of Open Access articles published with a CC BY NC SA or CC BY NC ND license requires permission from Elsevier

and will be subject to a fee.
Commercial reuse includes:

- Associating advertising with the full text of the Article
- Charging fees for document delivery or access
- Article aggregation
- Systematic distribution via e-mail lists or share buttons

Posting or linking by commercial companies for use by customers of those companies.

20. **Other Conditions**:

v1.8

Questions? customercare@copyright.com or +1-855-239-3415 (toll free in the US) or +1-978-646-2777.

Computers & Fluids 86 (2013) 109–124

Contents lists available at ScienceDirect

Computers & Fluids

journal homepage: www.elsevier.com/locate/compfluid

A physically consistent weakly compressible high-resolution approach to underresolved simulations of incompressible flows

Felix S. Schranner *, Xiangyu Y. Hu, Nikolaus A. Adams

Technische Universität München, Institute of Aerodynamics, 85747 Garching, Germany

ARTICLE INFO

Article history:
Received 25 February 2013
Received in revised form 24 June 2013
Accepted 28 June 2013
Available online 15 July 2013

Keywords:
Weakly compressible model
High resolution scheme
Implicit large-eddy simulation
Physically consistent
Underresolved computation

ABSTRACT

In engineering applications critical complex unsteady flows often are, at least in certain flow areas, only marginally resolved. Within these areas, the truncation error of the underlying difference schemes strongly affects the solution. Therefore, a significant gain in computational efficiency is possible if the truncation error functions as physically consistent, i.e. reproducing the correct evolution of resolved scales, subgrid-scale (SGS) model. The truncation error of high-order WENO-based schemes can be exploited to function as an implicit subgrid-scale (SGS) model. A recently developed sixth-order adaptive central-upwind weighted essentially non-oscillatory scheme with implicit scale-separation has been demonstrated to incorporate a physically consistent implicit SGS model for compressible turbulent flows. We consider the implicit SGS modeling capabilities of an improved version of this scheme simultaneously for underresolved turbulent and non-turbulent incompressible flows, thus extending previous works on this subject to a more general scope. With this model we are able to reach very long integration times for the incompressible Taylor–Green vortex at infinite Reynolds number, and recover in particular a low-mode transition to isotropy. Inviscid shear-layer instabilities are resolved to highly nonlinear stages, which is shown by considering the doubly periodic two-dimensional shear layer as test configuration. Proper resolved-scale prediction is also obtained for viscous–inviscid interactions and fully confined viscous flows. These properties are demonstrated by applying the model to a vortex–wall interaction problem and lid-driven cavity flow.

1. Introduction

Truncation error asymptotic analysis (sufficiently small grid spacing) is hardly relevant for practical applications, when the available grid resolution in certain parts of the computational domain is far from resolving all physically relevant flow structures. Thus, in most practical computations, the effect of the truncation error is not small and it contributes to the solution as an effective subgrid-scale model. The idea arises to adjust the local truncation error in order to function as a physically consistent subgrid-scale (SGS) model, i.e. delivering an accurate solution for resolved slow structures without determinating its asymptotic behavior at the fine-resolution limit. Modified differential equation analysis (MDEA) [1] has enabled us to show that the truncation error of nonlinear discretization schemes can be constructed such as to represent an implicit SGS model for turbulent flows [2]. It is known that the nonlinear regularization mechanism of high-order finite-volume schemes with shock-capturing capabilities can be used for implicit large eddy simulations (LES), for a review refer to [3]. A spectral extension of MDEA has allowed for designing the truncation error of a nonlinear scheme such that it recovers the theoretical spectral eddy viscosity when the flow is turbulent and underresolved. Such a situation, where the non-negligible local truncation error of a numerical scheme recovers correct physical SGS behavior is called in the following "physically consistent" behavior [4,5] in order to distinguish the analysis from that for asymptotically small truncation errors. Successful applications for physically consistent implicit LES models have been shown for a wide range of compressible and incompressible turbulent flows, e.g. [6–8]. Hu and Adams [9] have investigated the physical consistency of the underresolved contribution of an existing low-dissipation scheme (WENO-CU6) [10]. A proper modification of WENO-weights has resulted in a scale separation between contributions from the resolved and non-resolved scales to the locally reconstructed solution so that non-resolved scales are subject to dissipation, while the shock-capturing capabilities and the sixth order of accuracy in smooth flow regions of the underlying scheme are maintained.

Shu et al. have studied the evolution of the nearly incompressible, inviscid three-dimensional Taylor–Green vortex (TGV) [11]. They have found that the fifth-order WENO scheme shows unphysical dissipation effects but allows for stable underresolved

* Corresponding author. Tel.: +49 89 289 16396; fax: +49 89 289 16139.
E-mail addresses: felix.schranner@aer.mw.tum.de (F.S. Schranner), xiangyu.hu@tum.de (X.Y. Hu), Nikolaus.Adams@tum.de (N.A. Adams).

0045-7930/$ - see front matter © 2013 Elsevier Ltd. All rights reserved.
http://dx.doi.org/10.1016/j.compfluid.2013.06.034

simulations. It is well established that spectral methods are most efficient in well-resolved cases but cannot provide SGS energy transfer without explicit SGS models, e.g. [12,11]. In [11] it has been demonstrated that standard finite-difference and spectral methods do not provide the basis for physically consistent implicit SGS modeling capability. Furthermore, it has been found that integral flow quantities, such as enstrophy and kinetic energy, do not allow for a clear assessment of underresolved flow simulations. On the other hand, a discretization scheme that reproduces self-similar Kolmogorov spectra of a decaying isotropic turbulent flow at infinite Reynolds numbers is more likely to be robust to under-resolution. As WENO weighting involves measuring of flow resolution, it offers the potential to derive a physically consistent high-resolution scheme with a truncation error adjusted such that it exhibits implicit subgrid-scale modeling capabilities for both, turbulent and non-turbulent flows. We emphasize that for extremely large-scale simulations on massively parallel computers the weakly compressible flow model faces renewed significance as an alternative to strictly incompressible approaches. This is due to the fact that the weakly compressible flow model inherently requires less memory communication, as all operations are local unlike the strictly incompressible model, where the elliptic pressure-projection leads to global communication needs.

The objective of the current paper is to develop and to investigate physical consistency of a weakly compressible non-linear high-resolution approach for the under-resolved simulation of turbulent and non-turbulent incompressible flows. Due to the lack of analytic accessibility of the case dependent large truncation errors that occur in these cases, such an analysis mostly needs to rely on empirical investigation for a range of carefully selected test flow configurations that capture the essential properties of later target applications. A conservative approximate Roe–Pike solver is adapted to a weakly compressible flow model and combined with a low-dissipation WENO scheme. A modification of the underlying WENO scheme is proposed in order to obtain physical consistency of the resulting implicit SGS model.

As reference flow for implicit SGS model development we consider the three-dimensional Taylor–Green vortex (TGV) at infinite Reynolds number, in particular also extending previous considerations to very late times. The implicit LES capability for moderate Reynolds number ranges is assessed by the Comte–Bellot Corrsin decaying grid generated isotropic turbulence. The evolution of shear layer instabilities into and throughout highly nonlinear stages can be studied by considering the two-dimensional doubly-periodic shear layer with finite thickness, further extended to infinitely thin shear-layers at infinite Reynolds numbers. The interaction between large scale vortical structures with the very-small-scale structures of viscous boundary layers walls is studied by considering an isolated vortex dipole colliding with a no-slip wall, following Refs. [13–16]. The lid-driven cavity is discussed as an example for a fully confined wall-bounded non-turbulent, but with respect to proper numerical resolution highly demanding two-dimensional flow.

2. Model formulation

2.1. Artificial compressibility approach

At Mach numbers $M \ll 1$ compressibility is negligible, i.e. $\beta = \frac{1}{\rho}\frac{\partial \rho}{\partial p} \approx 0$. The *artificial compressibility* approach of Chorin and Temam [17,18] assumes a nonzero but constant compressiblity for weakly compressible flows. The isentropic compressibility relates to the sound speed by $a^2 = \frac{1}{\rho\beta|_s}$. For flows with $M = 0.1$, as considered within this work, the isentropic compressibility is on the order of $\beta|_s = 0.01$. For isothermal processes $\beta = \beta|_s$, and the ratio of specific heats is $\gamma = 1$. Pressure and density are directly related by

$$p = a^2\rho. \tag{1}$$

It is evident that density fluctuations can be considered as small, if a is a sufficiently large constant.

2.2. Numerical-flux computation adapted to weakly compressible fluid treatment

Within the weakly compressible approach total energy is determined by the evolution of mechanical energy. Thus, the flow is governed by equations for the conservation of mass and momentum. In one dimension (for simplicity) $\mathbf{u} = (\rho, \rho u)$ is the solution of

$$\frac{\partial \mathbf{u}}{\partial t} + \frac{\partial}{\partial x}\mathbf{f}(\mathbf{u}) = 0. \tag{2}$$

In a discrete space–time-domain, the discrete conservation equation

$$\frac{d\mathbf{U}_i}{dt} = -\frac{1}{\Delta x_i}\left(\mathbf{F}\left(\mathbf{u}\left(x_{i+\frac{1}{2}}, t\right)\right) - \mathbf{F}\left(\mathbf{u}\left(x_{i-\frac{1}{2}}, t\right)\right)\right), \tag{3}$$

for the cell-averaged solution $\mathbf{U}_i$ requires approximations of the cell-face fluxes $\mathbf{F}_{i+\frac{1}{2}}$. A straightforward low-dissipation flux approximation is due to the Roe [19] approximate Riemann solver. Successful applications of Roe schemes to the solution of weakly compressible flows have been demonstrated by Marx [20] and Elsworth and Toro [21].

Roe's linearization of the local flux Jacobian $\tilde{\mathbf{A}}_j = \tilde{\mathbf{A}}(\hat{u}_L, \hat{u}_R)$ is essential. The eigenvalues of $\tilde{\mathbf{A}}_j$ are $\tilde{\lambda}_j(\hat{u}_L, \hat{u}_R)$ and its right eigenvectors $\tilde{\mathbf{K}}^{(j)}(\hat{u}_L, \hat{u}_R)$ are determined so that the Roe numerical flux function can be computed as

$$\hat{\mathbf{F}}_{i+\frac{1}{2}} = \frac{1}{2}(\hat{f}_L + \hat{f}_R) - \frac{1}{2}\sum_{j=1}^{m}\tilde{\alpha}_j|\tilde{\lambda}_j|\tilde{\mathbf{K}}^{(j)}. \tag{4}$$

Using the left and right reconstructed states $\hat{\mathbf{u}}_L$ and $\hat{\mathbf{u}}_R$ at the interface $i = \frac{1}{2}$, the procedure to compute the eigenvalues $\tilde{\lambda}_j$, right eigenvectors $\tilde{\mathbf{K}}^{(j)}$ and wave speeds $\tilde{\alpha}_j$ is straightforward. The Roe averaged density $\tilde{\rho}$ and velocity $\tilde{u}$ are obtained from the left and right states as

$$\begin{aligned}\tilde{\rho} &= \sqrt{\rho_L\rho_R},\\ \tilde{u} &= \frac{\sqrt{\rho_L}u_L + \sqrt{\rho_R}u_R}{\sqrt{\rho_L} + \sqrt{\rho_R}}.\end{aligned} \tag{5}$$

Within the weakly compressible approach the local Roe-averaged speed of sound $\tilde{a}$ is replaced by the constant speed of sound a. Thus, $\tilde{\lambda}_j, \tilde{\mathbf{K}}^{(j)}$ and $\tilde{\alpha}_j$ are:

$$\tilde{\lambda}_1 = \tilde{u} - a, \quad \tilde{\lambda}_2 = \tilde{u} + a, \tag{6}$$

$$\tilde{\mathbf{K}}^{(1)} = \begin{bmatrix}1\\ \tilde{u} - a\end{bmatrix}, \quad \tilde{\mathbf{K}}^{(2)} = \begin{bmatrix}1\\ \tilde{u} + a\end{bmatrix}, \tag{7}$$

$$\begin{aligned}\tilde{\alpha}_1 &= \frac{1}{2a^2}[(p_R - p_L) - \tilde{\rho}a(\hat{u}_R - \hat{u}_L)],\\ \tilde{\alpha}_2 &= \frac{1}{2a^2}[(p_R - p_L) + \tilde{\rho}a(\hat{u}_R - \hat{u}_L)].\end{aligned} \tag{8}$$

The resulting semi-discrete evolution equation

$$\frac{d\mathbf{U}_i}{dt} = -\frac{1}{\Delta x_i}\left(\hat{\mathbf{F}}\left(x_{i+\frac{1}{2}}, t\right) - \hat{\mathbf{F}}\left(x_{i-\frac{1}{2}}, t\right)\right), \tag{9}$$

can be advanced in time with a three-step TVD Runge–Kutta scheme [22].

2.3. Revisiting the WENO-CU6-M1 weighting

Based on the sixth order adaptive central-upwind scheme WENO-CU6 [10], a central-upwind WENO scheme with implicit SGS modeling capabilities has been developed (WENO-CU6-M1) [9]. The modified weighting of the WENO-CU6-M1 formulation remedies excessive dissipation of the underlying WENO-CU6 scheme while preserving its shock-capturing properties and thus recovers physical consistency for both, the solenoidal and the dilatational components of the velocity field, without the need to explicitely distinguish these, see. e.g. [9].

The modified weights of the WENO-CU6-M1 scheme are

$$\omega_r = \frac{\alpha_r}{\sum_{s=0}^{3}\alpha_s}, \quad \alpha_r = d_r\left(C_q + \frac{\tau_6}{\epsilon+\beta_r}\right)^q, \quad r = 0,\ldots,3 \tag{10}$$

with the reference smoothness indicator $\tau_6 = \beta_3 - \frac{1}{6}(\beta_0 + 4\beta_1 + \beta_2)$. ϵ is a small number. Following Jiang and Shu [23], smoothness indicators are computed as

$$\beta_r = \sum_{l=1}^{m-1}\int_{x_{i-\frac{1}{2}}}^{x_{i+\frac{1}{2}}} \Delta x^{2l-1}\left(\frac{\partial^l \hat{u}_r(x)}{\partial x^l}\right)^2 dx, \tag{11}$$

where

$$\begin{aligned}
\beta_0 &= \tfrac{1}{4}(u_{i-2} - 4u_{i-1} + 3u_i)^2 + \tfrac{13}{12}(u_{i-2} - 2u_{i-1} + u_i)^2,\\
\beta_1 &= \tfrac{1}{4}(u_{i-1} - u_{i+1})^2 + \tfrac{13}{12}(u_{i-1} - 2u_i + u_{i+1})^2,\\
\beta_2 &= \tfrac{1}{4}(3u_i - 4u_{i+1} + u_{i+2})^2 + \tfrac{13}{12}(u_i - 2u_{i+1} + u_{i+2})^2.\\
\beta_3 &= \tfrac{1}{10{,}080}\big|271{,}779u_{i-2}^2 + u_{i-2}(-2{,}380{,}800u_{i-1} + 4{,}086{,}352u_i\\
&\quad -3{,}462{,}252u_{i+1} + 1{,}458{,}762u_{i+2} - 245{,}620u_{i+3})\\
&\quad +u_{i-1}(5{,}653{,}317u_{i-1} - 20{,}427{,}884u_i + 17{,}905{,}032u_{i+1}\\
&\quad -7{,}727{,}988u_{i+2} + 1{,}325{,}006u_{i+3}) + u_i(19{,}510{,}972u_i\\
&\quad -35{,}817{,}664u_{i+1} + 15{,}929{,}912u_{i+2} - 2{,}792{,}660u_{i+3})\\
&\quad +u_{i+1}(17{,}195{,}652u_{i+1} - 15{,}880{,}404u_{i+2} + 2{,}863{,}984u_{i+3})\\
&\quad +u_{i+2}(3{,}824{,}847u_{i+2} - 1{,}429{,}976u_{i+3}) + 139{,}633u_{i+3}^2\big|.
\end{aligned} \tag{12}$$

Taylor series expansion of β_r, $r = 0, 1, 2, 3$ about u_i gives

$$\begin{aligned}
\beta_0 &= u_i'^2\Delta x^2 + \left(\frac{13}{12}u_i''^2 - \frac{2}{3}u_i'u_i'''\right)\Delta x^4 - \left(\frac{13}{6}u_i''u_i''' - \frac{1}{2}u_i'u_i''''\right)\Delta x^5\\
&\quad + \mathcal{O}(\Delta x^6),\\
\beta_1 &= u_i'^2\Delta x^2 + \left(\frac{13}{12}u_i''^2 + \frac{1}{3}u_i'u_i'''\right)\Delta x^4 + \mathcal{O}(\Delta x^6),\\
\beta_2 &= u_i'^2\Delta x^2 + \left(\frac{13}{12}u_i''^2 - \frac{2}{3}u_i'u_i'''\right)\Delta x^4 - \left(\frac{13}{6}u_i''u_i''' - \frac{1}{2}u_i'u_i''''\right)\Delta x^5\\
&\quad + \mathcal{O}(\Delta x^6),\\
\beta_3 &= u_i'^2\Delta x^2 + \frac{13}{12}u_i''^2\Delta x^4 + \mathcal{O}(\Delta x^6).
\end{aligned} \tag{13}$$

The smoothness indicators diminish with increasing smoothness of the solution on a stencil. If ϵ is a small constant number, both α_r and the solution are dominated by the choice of ϵ instead of the linear-weight bias C_q. An example of a function with a non-smooth stencil is

$$u(x) = x^3 + \cos(x). \tag{14}$$

When it is evaluated at $x_0 = 0$ the first and third derivatives are zero and the second and fourth -1 and 1, respectively. Thus, the smoothness indicators become

$$\beta_0 = \beta_1 = \beta_2 = \beta_3 = -\frac{13}{12}\Delta x^4 + \mathcal{O}(\Delta x^6). \tag{15}$$

For a computational grid with $\Delta x \to 0$, β_r approaches zero with an error order of $\mathcal{O}(\Delta x^6)$ for smooth stencils and at most $\mathcal{O}(\Delta x^4)$ for non-smooth stencils. Thus, to ensure α_r to be bounded in the case when β_r vanishes, ϵ should be of $\mathcal{O}(\Delta x^6)$ so that it does not affect the overall order of the scheme.

3. Analysis of the implicit subgrid scale model – isotropic turbulence

Physical consistency of an implicit SGS model can be investigated by means of time evolution of the three-dimensional kinetic energy spectrum of an underresolved, isotropic turbulent flow. At very high Reynolds numbers a Kolmogorov scaling inertial subrange should be recovered by a SGS model. The three-dimensional Taylor–Green vortex (TGV) [24] evolving from the initial two-dimensional condition

$$\begin{aligned}
u(x,y,z,0) &= \sin(x)\cos(y)\cos(z),\\
v(x,y,z,0) &= -\cos(x)\sin(y)\cos(z),\\
w(x,y,z,0) &= 0,\\
\rho(x,y,z,0) &= 1.0,\\
p(x,y,z,0) &= 100 + \frac{1}{16}[(\cos(2x) + \cos(2y))(2 + \cos(2z)) - 2],
\end{aligned} \tag{16}$$

within a periodic domain is a commonly used model flow therefore. After $t \approx 9$ and at very high Reynolds numbers the incompressible TGV has developed three-dimensional, statistically isotropic turbulence [25]. The flow field exhibits self-similar scaling of $E(k) \propto k^{-5/3}$ within the inertial subrange. In agreement with high resolution LES of Grinstein and Fureby [26], Hu and Adams [9] have obtained a Kolmogorov inertial range. In their simulations, the flow is described by the compressible Navier–Stokes equation and the ideal-gas equation of state. With the original WENO-CU6-M1 formulation [9] transition of the TGV at infinite high Reynolds number is observed, however, Kolmogorov scaling of the resolved inertial subrange is not obtained, see Fig. 1. In the following section we propose a modification of the scheme that recovers the inertial-range scaling.

3.1. Parameter identification

Through modification of the weighting of the WENO-CU6-M1 scheme, transition to isotropic turbulence and a self-similar

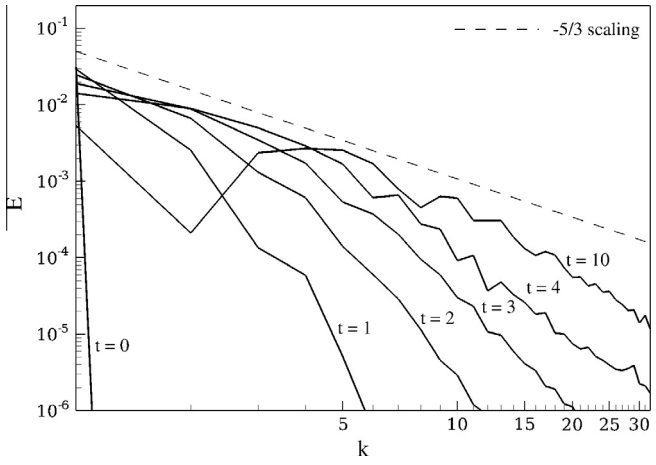

Fig. 1. Evolution of the three-dimensional kinetic energy spectrum for the early stages ($t \leqslant 10$) of the inviscid, incompressible Taylor–Green vortex. WENO-CU6-M1 formulation as in Ref. [9] with weakly compressible model.

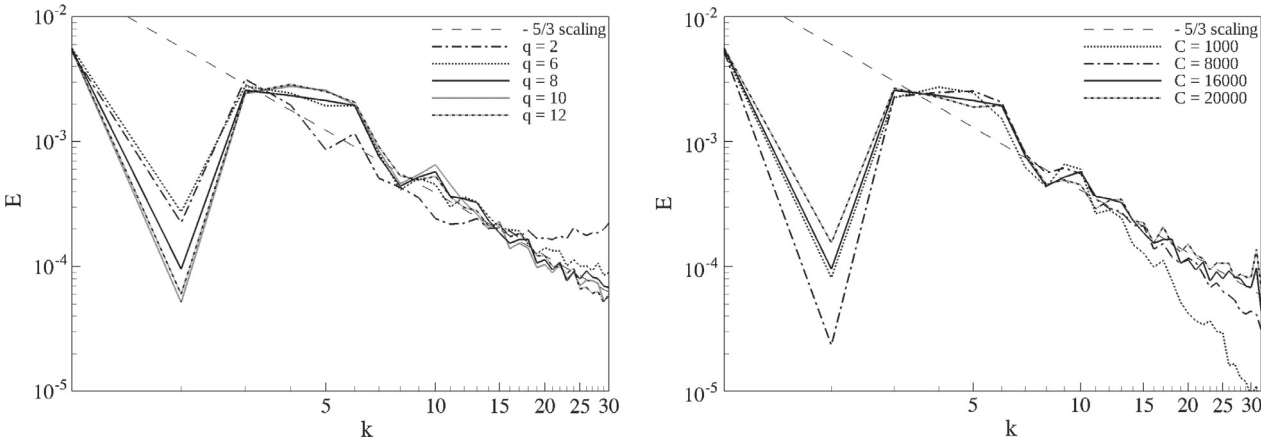

(a) C_q is 16,000. The integer power exponent q is varied from 2 to 12.

(b) q is 8. The linear-weight bias is varied between $C_q = 1{,}000$ and $C_q = 20{,}000$.

Fig. 2. 3-D energy spectra of ILES (64^3 cells) when varying a) q and b) C_q of inviscid 3-D TGV at $t = 10$. Results are compared to the theoretical $E(k) \propto k^{-5/3}$ scaling.

physically consistent inertial subrange with Kolmogorov scaling can be obtained for inviscid, weakly compressible flows, see Section 3.2. Based on the following considerations, a suitable set of WENO-CU6-M1 model parameters (C_q,q) is derived as the proposed modification. For stencils with smooth solutions variations of $\frac{\tau_6}{\epsilon+\beta_r}$ over the respective stencil support are small. Thus, the linear-weight bias C_q emphasizes a non-dissipative symmetric reconstruction of $u_{i\pm\frac{1}{2}}$. Increasing C_q effectively decreases the numerical dissipation for resolved scales, excessive values for C_q, however, result in spurious oscillations near discontinuities [27,28]. This can be relevant for the inverse kinetic-energy cascade (backscatter). Outscatter and backscatter of an energy cascade can be controlled by q in Eq. (10). Larger values of q result in stronger separation of resolved and unresolved scales.

3.1.1. Effect of the integer power exponent q

In the original formulations [10,23], the integer power exponent q is a free parameter, that does not affect the order of the numerical truncation error. It does, however, control the amount of nonlinear dissipation [29], which increases with q, see Ref. [30]. According to [23] an integer $q \geqslant 1$ is chosen in order to push the weight of the non-smooth stencil to zero as $\Delta x \to 0$. In [31] it has been suggested to use $q = m$, with $2m - 1$ being the order of accuracy. However, Jiang and Shu [23] found that $q = 2$ is sufficient for $m \leqslant 3$. Gerolymos et al. [30] have experimented with varying q for $m \leqslant 9$. They find that q has to increase with increasing m to obtain ENO behavior. A sensitivity analysis of q for incompressible very high Reynolds number TGV flows with weakly compressible flow model is performed for $2 \leqslant q \leqslant 12$. From Fig. 2a we observe that when $q \leqslant m = 6$ inertial range scaling is lost for wavenumbers exceeding $k \approx 18$, thus indicating non-physical behavior. Effective dissipation increases with q. Physically consistent inertial range scaling, characteristic for isotropic turbulence, is found for $q \approx 8$. For larger q, the effect of the non-resolved dissipation range is over-emphasized, resulting in an excessively dissipative scheme for the chosen linear-weight bias of $C_q = 16{,}000$.

3.1.2. The linear-weight bias C_q

$C_q \gg 1$ emphasizes the contribution of optimal weights when the smoothness indicators are of similar magnitude [28,10]. Higher values for C_q reduce numerical dissipation [9]. For compressible, isotropic turbulence it has been observed that proper inertial range scaling is obtained for $C_q = 1000$ [9]. Fig. 2b shows 3-D kinetic energy spectra at $t = 10$ for $1000 \leqslant C_q \leqslant 20000$. For $C_q = 1000$, the resulting scheme predicts a too steep inertial subrange indicating excessive overall dissipation. Proper Kolmogorov scaling is achieved with $C_q \approx 16{,}000$. Further increase of C_q, e.q. $C_q = 20{,}000$, leads to unphysical energy pile-up at higher wavenumbers.

3.2. Evolution of the incompressible three-dimensional Taylor–Green vortex at infinite Reynolds number over longer times

As we have found a physically consistent implicit SGS model for simulating TGV evolution to its quasi-isotropic state at $t \approx 9$ [25], it is now possible to explore the long-term evolution of the under-resolved, incompressible TGV at infinite Reynolds number in detail.

The evolution of the resolved energy spectrum for $t \in [0,10]$ is shown in Fig. 3a. The energy spectrum evolves from a single Fourier mode of $E(k = 1) = 0.125$ to span the entire range of resolvable scales ($k \in [1,32]$), whereas at $t \approx 3.4$ subgrid-scales are produced and kinetic energy decays due to SGS dissipation. For $t \in [9,11]$ $E(t) \propto t^{-1.3}$ is identified, Fig. 3b. For $t \in [11,30]$ $E(t) \propto t^{-1.6}$ and for $t \geqslant 30$,$E(t) \propto t^{-2.6}$ is observed, see Fig. 4. For very late stages, $t \geqslant 100$, $E(t) \propto t^{-2}$ is found, however, the magnitude of E is very small. The decay of kinetic energy is also well observable in the 3-D energy spectrum of the resolved inertial subrange, Fig. 5, which scales to $E(k) \propto k^{-5/3}$ at least until $t \approx 70$. After $t \approx 100$ the bandwidth of the inertial subgrange narrows noticeably. At $t = 200$ only the band $2 \lesssim k \lesssim 9$ shows Kolmogorov scaling, whereas higher modes scale according to $E(k) \propto k^{-7/3}$ For the temporal evolution of 3-D TGV isotropic turbulent decay we identify two scaling ranges.

1. $E_1(k,t) \propto k^{-5/3} 1.6^{(-t/10)}$ for $10 \leqslant t \leqslant 80$.
2. $E_2(k,t) \propto k^{-5/3} 1.3^{-(t-60)/20}$ is observed for later times ($t \geqslant 80$).

For $10 \leqslant t \leqslant 30$ redistribution of kinetic energy among the large scale structures is a characteristic indicator of high-Re TGV transition to isotropy, see Fig. 6. Our implicit SGS captures this low-mode transition for $Re = \infty$ and $Re = 3000$. During the redistribution of kinetic energy, scaling within the inertial subrange is lost momentarily, compare E–k-plot for $t = 20$. At $t \approx 10$ as well as at $t \approx 18$ temporal minima of the kinetic energy of the second mode are identified. Coinciding with the initiation of this low-mode transition at $t \approx 10$, an overall inter-modal kinetic energy redistribution process initiates, equalizing the kinetic energy distribution. Later, $E(k)$ follows an isotropic Kolmogorov-spectra.

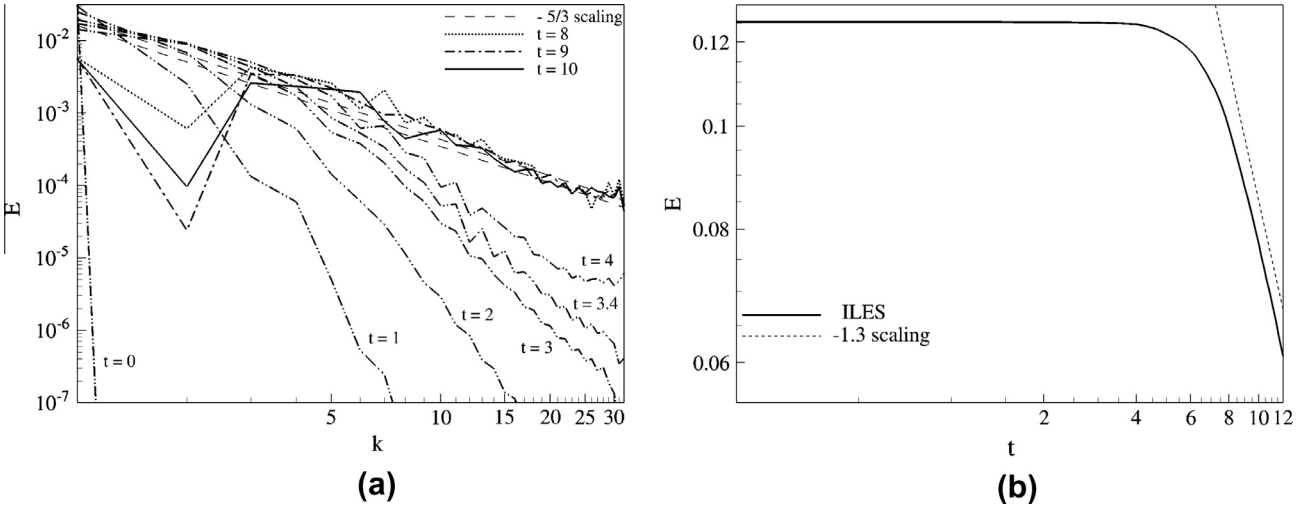

Fig. 3. Evolution of the kinetic energy during early stages ($t \leqslant 10$) of the inviscid, incompressible TGV. (a) Spectral decomposition of kinetic energy and (b) total kinetic energy.

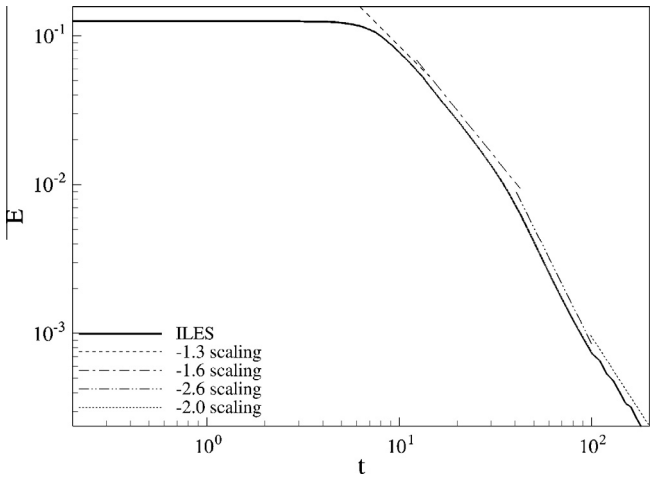

Fig. 4. Time evolution of the kinetic energy of the 3D TGV for $0 \leqslant t \leqslant 200$ as compared to idealized scaling of $t^{-1.3}$ for $t \in [9,11]$, $t^{-1.6}$ for $t \in (11,30]$, $t^{-2.6}$ for $t \in [30,100]$, $t^{-2.0}$ for $t \geqslant 100$

These results confirm, that the proposed scheme modification indeed recovers physically consistent SGS model behavior for this challenging test case, that includes instability development and nonlinear flow evolution to the isotropic-turbulent state.

3.3. Underresolved numerical simulations of the incompressible three-dimensional Taylor–Green vortex at finite Reynolds numbers

Now we extend the scope towards including viscous effects and conduct simulations of TGV flows with $Re = 100$ to $Re = 3000$ within a domain of $(2\pi)^3$. We use a coarse grid of 64^3 cells. Periodic boundary conditions are applied. For assessing resolution effects for $Re \geqslant 800$, a refined grid of 128^3 cells has been used. The DNS of Brachet et al. [32,33] provide reference data.

The time evolution of the total dissipation rate $\varepsilon = \frac{dE}{dt}$ is an essential quantity to be reproduced by LES. Fig. 7 shows the dissipation rates for LES with a conventional ($C_s = 0.18$) and a dynamic Smagorinsky model as well as for WENO-CU6-M1-based implicit LES with parameters as determined in Section 3.1 ($C_q = 16{,}000; q = 8$).

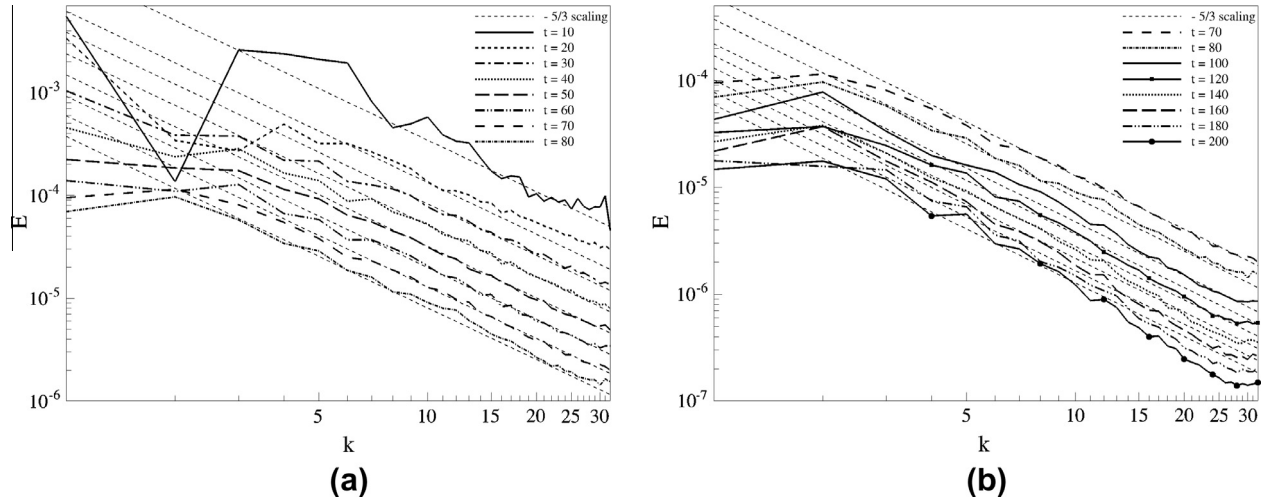

Fig. 5. 3-D energy spectrum within resolved inertial subrange at different times compared to the Kolmogorov scaling $E(k) \propto k^{-5/3}$.

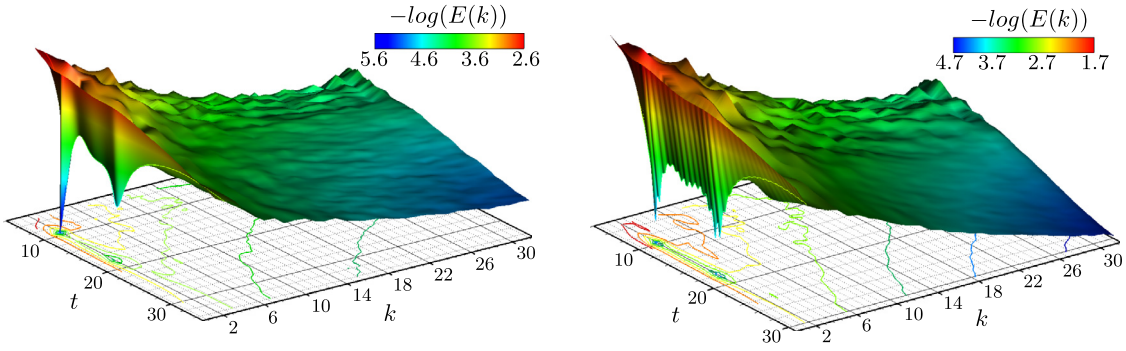

(a) $Re = \infty$ (b) $Re = 3000$

Fig. 6. Spectral decomposition of energy (logarithmic scale) for the 3-D TGV ILES. Projected contours on $t - k$-plane are in increments of $10^{0.5}$ for 10^{-6} to 10^{-2}.

The Smagorinsky model with constant C_s overpredicts dissipation even for the smallest considered $Re = 100$. For larger Reynolds numbers it returns an unphysical flow evolution, missing laminar-turbulent transition. A dynamic Smagorinsky parameter improves predictions significantly. For Reynolds numbers 100 and 200 the agreement with DNS is good. For Reynolds numbers of $Re \geqslant 400$, however, the dynamic Smagorinsky model overestimates dissipation rates.

With advancing laminar-turbulent transition, the dissipation rate increases due to non-linear vortex stretching. The decrease in $\varepsilon(t)$ at later times is due to viscous damping. For $Re \leqslant 800$, the dissipation rates obtained with the implicit LES based on the WENO-CU6-M1 scheme with the coarse grid are in good agreement with DNS, Fig. 7c. For 128^3 resolution equally good agreement is observed with DNS for $Re \geqslant 800$. Comparable results are obtained with the adaptive local deconvolution model (ALDM) [5] for $Re \leqslant 1600$. At higher Reynolds numbers ALDM overpredicts small scale structures and thus the dissipation rate, whereas the WENO-CU6-M1 scheme underpredicts these, see Fig. 7e.

The decomposition of the total dissipation rate ε for Reynolds numbers of 1600 and 3000 into the resolved ε_r and the SGS modeled dissipation rate $\varepsilon_{sgs} = \varepsilon - \varepsilon_r$ is used for analysis of the subgrid-scale (SGS) model behavior, Fig. 8. The subgrid-scale dissipation rate increases with a delay compared to the resolved dissipation rate, in combination leading to a physically consistent total dissipation rate, see Fig. 8b and c. We can conclude that our implicit SGS model performs slightly better than the dynamic Smagorinsky model, but not quite as good as ALDM. Note, however, that the current model is computationally much cheaper than ALDM.

3.4. Analysis of the implicit subgrid scale capabilities for turbulent decay

As final test for unbounded turbulent flow, we consider the decay of isotropic turbulence at moderate Reynolds number. Comte–Bellot and Corrsin (CBC) experimentally investigated decaying grid generated isotropic turbulence. At selected locations downstream

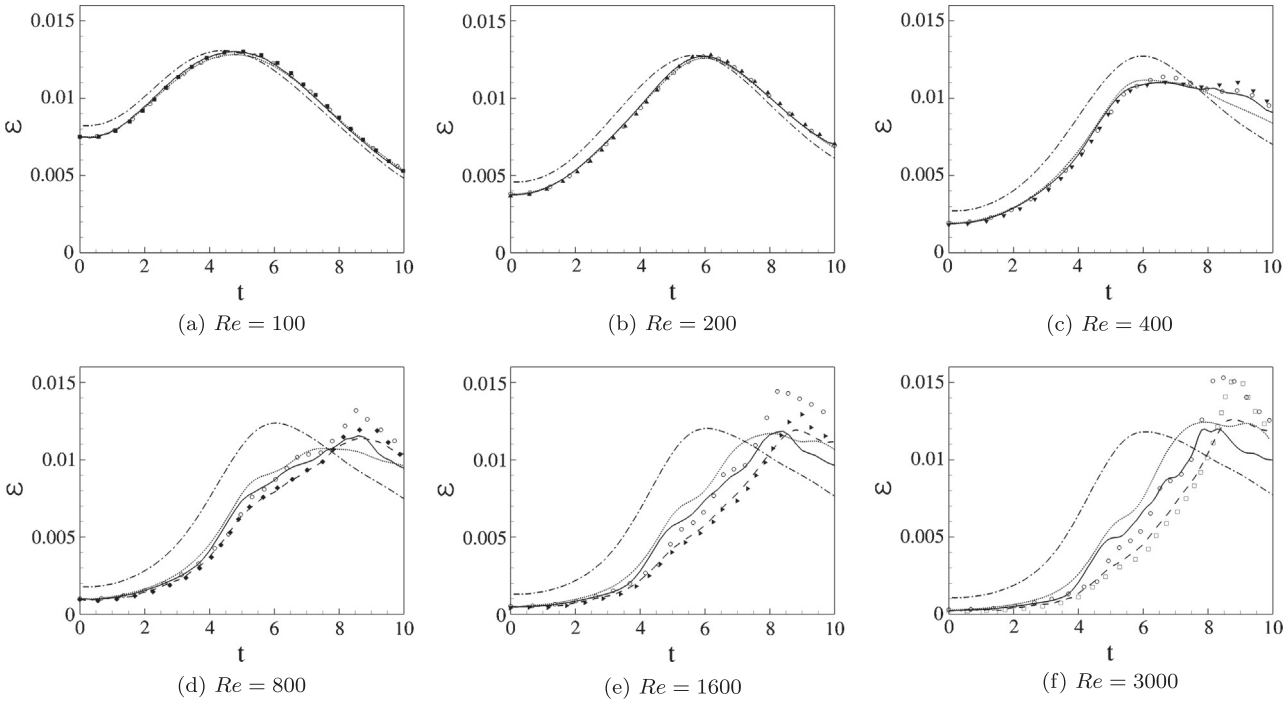

(a) $Re = 100$ (b) $Re = 200$ (c) $Re = 400$

(d) $Re = 800$ (e) $Re = 1600$ (f) $Re = 3000$

Fig. 7. Reynolds number specific dissipation rate $\varepsilon(t)$ for the 3-D TGV. On 64^3 finite volumes (FV): _____ WENO-CU6-M1 implicit LES, – · – · – · – constant-C_s Smagorinsky LES, ····· dynamic Smagorinsky LES. On 128^3 FV for $Re \geqslant 800$: – – – – WENO-CU6-M1 ILES. Implicit LES with ALDM [5] on 64^3 cells: ◦. Following symbols indicate DNS data by Brachet et al.: ■: $Re = 100$, ▲: $Re = 200$, ▼: $Re = 400$, ♦: $Re = 800$, ►: $Re = 1600$, □: $Re = 3000$.

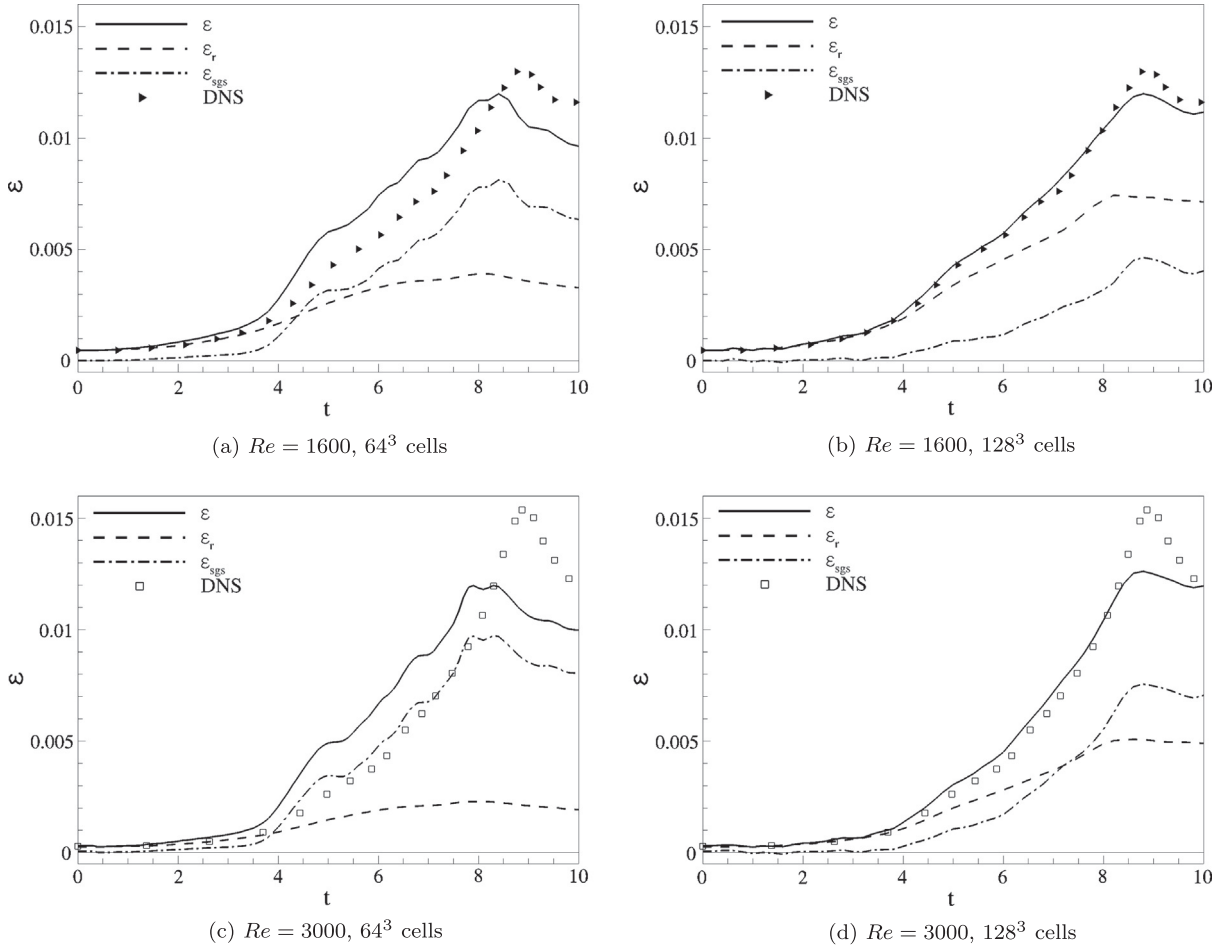

Fig. 8. Decomposition of total dissipation rate (ε) _____ into resolved (ε_r) – – – – – – and subgrid-scale modeled (ε_{sgs}) – · – · – · – dissipation rate as computed on grids of 64^3 and 128^3 cells. DNS results by Brachet et al. [32] is provided alongside.

of a mesh with a width of $M = 5.08$ cm they have recorded streamwise turbulent energy spectra. Under the assumption of local isotropy the corresponding three-dimensional turbulent energy spectra are calculated and listed in [34] for three locations. The Taylor microscale Reynolds numbers $Re_\lambda = u'\lambda/\nu$ are $Re_{\lambda,1} = 71.6$, $Re_{\lambda,2} = 65.1$, and $Re_{\lambda,3} = 60.7$. Under the assumption of approximately constant mean convection invoking Taylor hypothesis, the spatial evolution of the experimental data relates to temporal evolution of simulated decaying turbulence in a periodic domain of $(2\pi)^3$ discretized with a collocated grid of 64^3 cells. Given the 3-D energy spectrum for $Re_{\lambda,1}$, velocity components are generated by three sets of random numbers, $(\theta_1, \theta_2, \phi)$, uniformly distributed on $[0, 2\pi]$. Complex velocities that satisfy the requirement of a solenoidal velocity field in wavenumber space, $k_i u_i = 0$, are [35]

$$(\tilde{u}_1; \tilde{u}_2; \tilde{u}_3) = \frac{1}{|k| k_h}, \left(\alpha |k| k_2 + \beta k_1 k_3; -\alpha |k| k_2 + \beta k_3 k_2; \beta k_h^2\right). \quad (17)$$

Furthermore,

$$(\alpha; \beta) = \frac{E(k, t=0)}{4\pi k^2} (\exp(i\theta_1). \cos(\phi); \exp(i\theta_2) \sin(\phi)). \quad (18)$$

The decaying turbulent flow is evolved and the computational 3-D energy spectra are compared to experimental spectra at $Re_{\lambda,2}$ and $Re_{\lambda,3}$, see Fig. 9a. The WENO-CU6-M1 implicit LES predicted energy spectra at later times, i.e. lower Re_λ, agree well with the experimentally observed ones. At the second measurement station, where $Re_{\lambda,2} = 65.7$, the ALDM implicit LES and LES with Chollet's eddy viscosity model [5] compare well in terms of $E(k)$. At later times and especially at higher wavenumbers, the shape of $E(k)$ predicted with the WENO-CU6-M1 implicit LES resemble those of the LES with a dynamic Smagorinsky model. The overall kinetic energy of the WENO-CU6-M1 implicit LES is similar to the ALDM predictions, which recovers the experimentally observed ones [5]. For the observed time interval the kinetic energy is found to develop approximately as $E(t) \propto t^{-1.0}$, see Fig. 9b, where a trend to rather following $E(t) \propto t^{-1.3}$ at later times also can be seen. Similar conclusions made for the implicit SGS capability of the current model as observed in the previous sections transfer to the current case.

4. Analysis of implicit SGS model capabilities for non-turbulent flows

For a unified study of implicit SGS capabilities of our model for turbulent and non-turbulent flows it is necessary to investigate a range of carefully selected non-turbulent flow cases to complement the studies for turbulent flow provided in the previous sections.

Key phenomena in two-dimensional wall-bounded flows are shear-layer instabilities and the interaction between vorticity structures and the viscous boundary layers at no-slip walls.

For the prediction of the interaction of large scale vortices with small-scale near-wall structures it is essential to resolve all contributing scales adequately. The underresolution issue of these

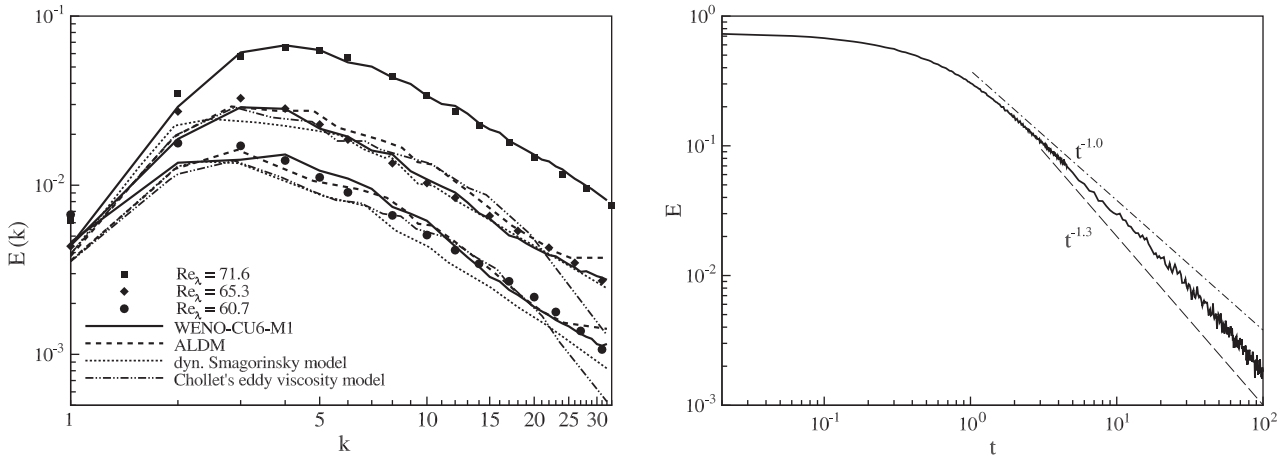

(a) 3−D energy spectra. Symbols: experimental data of [34]. Energy spectra as with ALDM iLES, LES with dynamic Smagorinsky and Chollet's eddy viscosity SGS model, see Ref. [5].

(b) Total kinetic energy over time.

Fig. 9. WENO-CU6-M1 implicit LES on 64^3 cells for Comte–Bellot–Corrsin 'isotropic' decaying turbulence.

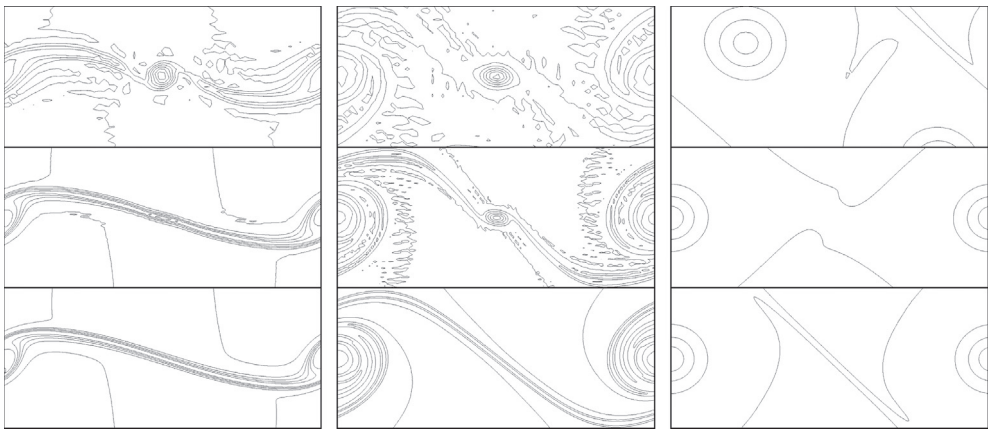

(a) $t = 0.6$ s (b) $t = 1$ s (c) $t = 10$ s

Fig. 10. Vorticity contour −70 to 70 by 10 on grids of 64^2 cells (top row), 128^2 cells (middle row), 256^2 cells (bottom row). $\theta = 80$.

wall-bounded configurations is addressed in the following test case.

Among others, Kramer et al. [36], Clercx and Bruneau [37] and Keetels et al. [38] have studied the vortex–wall interaction in detail and investigated the collision of a single vortex dipole with a no-slip wall. As viscous effects are relatively confined to a near-wall region for an integral Reynolds number of $Re = 1250$ [36] we assess our method for this particular setup [36,37]. We supplement tabulated benchmark data with vortex-trajectories [36], and a sequence of vortex contour plots alike [5] of Ref. [38].

The lid-driven cavity with reference DNS data of Ghia et al. [39,40] and Erturk [41] for $1000 \leqslant Re \leqslant 7500$ serves to benchmark our WENO-CU6-M1-based weakly compressible ILES approach for fully-confined wall-bounded flows. As a peculiarity of this configuration the cavity flow reaches steady state for low to mid Reynolds numbers. For high-Re cavity flows it is yet unclear whether the flow reaches steady state or becomes time-periodic.

4.1. 2-D free-shear flow – the double shear layer

Kelvin–Helmholtz instabilities are prone to evolve spurious vortices when underresolved. Numerical methods that suppress spurious vortices are more likely to lead to incorrect predictions of the long-time behavior. For this reason, we first investigate the long-term behavior of free-shear Kelvin–Helmholtz instabilities for diminishing shear-layer thickness and infinite Reynolds number.

Brown and Minion [42], Minion and Brown [43], and Bell et al. [44] have analyzed the under-resolution issue of a very simple flow configuration, the two-dimensional doubly-periodic shear layer, with respect to robustness of their spatial discretization schemes to underresolution. We follow and extend their analysis with our WENO-CU6-M1 scheme. A domain of 1×1 with periodic boundary conditions is initialized with a two-dimensional periodic shear layer

$$u(y) = \begin{cases} \tanh((y - 1/4)/\theta), & \text{if } y \leqslant 0.5 \\ \tanh((3/4 - y)/\theta), & \text{if } y > 0.5 \end{cases}$$

of thickness $1/\theta$. It is disturbed by a cross flow of

$$v(x) = \delta \sin(2\pi x), \tag{19}$$

with $\delta = 0.05$.

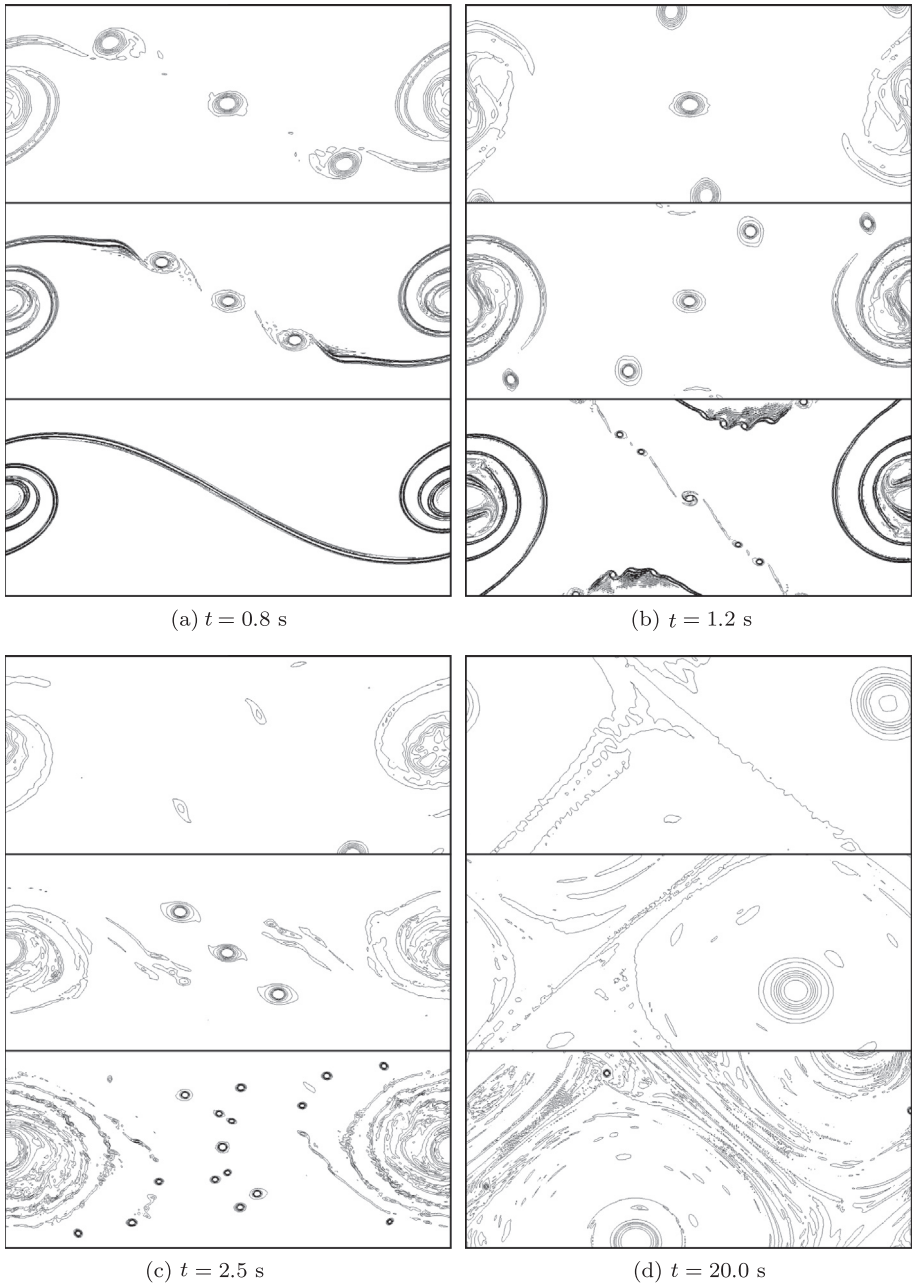

Fig. 11. Vorticity contour −70 to 70 by 10 on grids of 128^2 cells (top row), 256^2 cells (middle row), 512^2 cells (bottom row). 0 vorticity contour only shown for $t = 20.0$. $\theta = 100$.

Minion and Brown mentioned the development of spurious vortices [43]. They found that spurious vortices evolve when the grid is too coarse to resolve the smallest scales, as the truncation error of the discretization scheme initiates a vortical instability. Their tendendcy to occur depends on the respective spatial discretization method. In particular, grids can be coarser for central discretizations than for upwind discretizations in order to prevent these artifacts. However, without artificial viscosity, central discretizations become unstable. It is a challenge to devise a scheme that on one hand provides high wavenumber resolution and on the other hand sufficient dissipation to prevent instability.

The under-resolved simulations of the thin, $\theta = 80$, double shear layer and $Re = 10{,}000$ show oscillations as under-resolution artifacts of the central reconstruction [43] in smooth stencils at $t = 0.6$ and $t = 1.0$ on grids of 64^2 and 128^2 cells, Fig. 10. Between the two counter-rotating vortices a spurious vortex is found. At later times, oscillations are damped. While the spurious vortices pair with the largest vortices, only on the grids with a resolution of 128^2 and 256^2 the primary vortices are stationary, whereas on the coarse grid the primary vortices revolve around each other. Later, the large vortices become stationary. At this final stage, the flow field is similar to the final stage of a two-dimensional random-noise initialized field. In the case of the under-resolved thick, $\theta = 30$, double shear layer the primary vortices are stationary, independently of the grid resolution. Although smaller structures develop for finer grids, on all grids the vortices pair to two counter-rotating vortices as with the $\theta = 100$ shear layer for $t \to \infty$, Fig. 11. For $Re \to \infty$ and $\theta \to \infty$ very small structures develop which

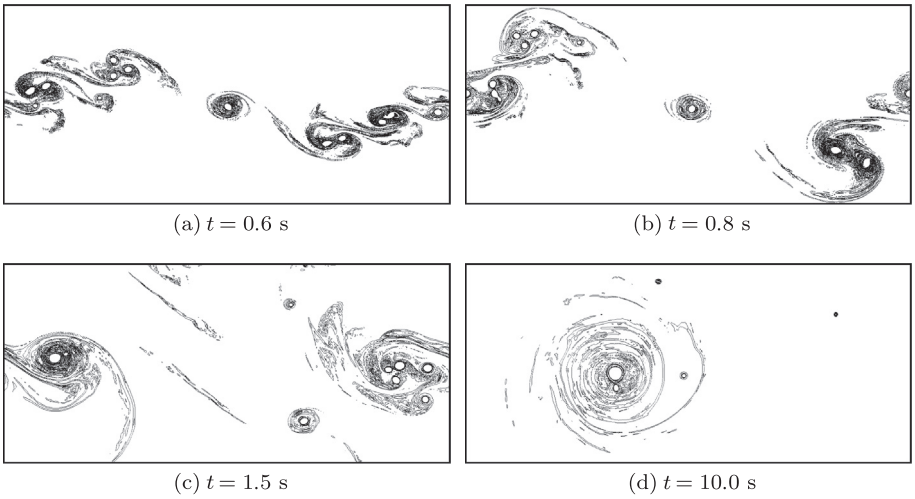

Fig. 12. Vorticity contour −100 to 100 by 10 on grids of 1024^2 cells. 0 vorticity contour not shown. $\theta = 10^6$.

Table 1
The maximum vorticity in the positive dipole half ω_d at its location along x_d and normal y_d to the wall at $y = 0$. Dipole is symmetric to $x = 0$. x_d measures distance along the wall and y_d is distance normal to wall. Results are compared to benchmark results of Kramer et al. [36].

	512×512		1024×1024		KCH	
t	(x_d, y_d)	ω_d	(x_d, y_d)	ω_d	(x_d, y_d)	ω_d
0.6	(0.1231, 0.1464)	218.14	(0.1416, 0.1298)	218.783	(0.1506, 0.1260)	219.29
0.625	(0.1348, 0.1270)	215.05	(0.1670, 0.1181)	215.025	(0.1725, 0.1157)	216.15
1.0	(0.2285, 0.1699)	169.10	(0.2490, 0.1533)	169.935	(0.2568, 0.1515)	170.30
1.4	(0.2832, 0.2207)	131.67	(0.2959, 0.1943)	132.522	(0.2914, 0.1908)	132.73

are only resolvable with extremely fine grids. The evolution of such an infinitely thin shear layer is, however, similar as that of shear layers of finite θ, see Fig. 12.

Artificial viscosity for central methods or a hyperviscosity model for the pseudospectral method are suggested in [42] to stabilize these under-resolved very thin shear-layer, high-*Re* flows. This thickens the shear layer and consequentially prevents the evolution of spurious vortices. As demonstrated, our model may not fully prevent the formation of spurious vortices in the case of diminishing physical viscosity and shear layer thickness. However, even in the underresolved setup marginally resolved vortex structures remain unaffected by numerical dissipation indicating physical consistency.

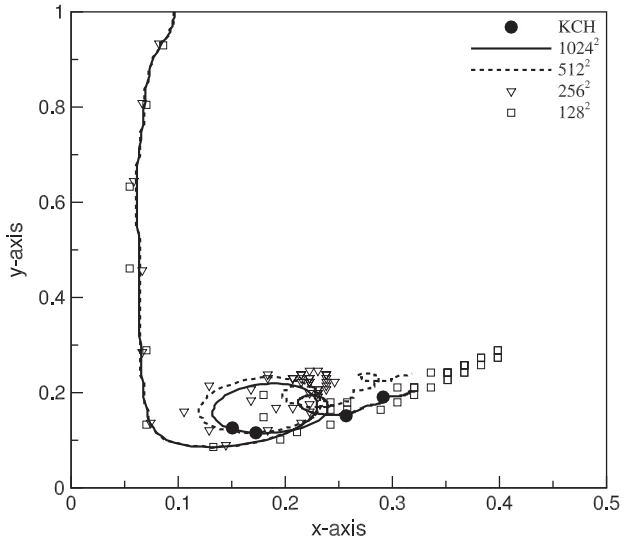

Fig. 13. Resolution dependent trajectories of the positive half of a dipole when colliding with a no-slip boundary for *Re* = 1250.

4.2. Convergence of a dipole–wall collision

For applications, the predictive capability of an implicit SGS model for under-resolved viscous–inviscid-interaction problems is very important. For this purpose we investigate the interaction of a vortex dipole (as primarily inviscid element) and the viscous wall layer (as viscosity dominated element). As reference we follow the setup of Kramer et al. [36] and Clercx and Bruneau [37], who have studied the normal dipole–wall collision experiment with an integral-scale Reynolds number $Re = UW/\nu = 1250$. U denotes the average velocity derived from the total kinetic energy $E(t) = \frac{1}{2}\int_{-1}^{1}\int_{-1}^{1}\mathbf{u}^2(\mathbf{x}, t)dxdy$ of the flow and W the half-width of the square domain $\Omega = \mathbf{x} \in \mathscr{R}^2 | -1 \leqslant x \leqslant 1, -1 \leqslant y \leqslant 1$. In the references it was shown that this flow case poses extreme demands on numerical resolution. Grid convergence was obtained at $t \leqslant 1$ for an equidistant finite-difference scheme with 1536^2 cells, and for a Fourier–Cheybeshev pseudospectral scheme with 512×512 collocation points.

At $t = 0$ the vorticity field ω_0 is given by

$$\omega_0 = \omega_e\left(1 - (r/r_0)^2\right)\exp\left(-(r/r_0)^2\right), \tag{20}$$

with $r = (x^2 + y^2)^{1/2}$ being the distance from the center of the monopole, $r_0 = 0.1$ its length scale and $\omega_e \approx 299.5283$ its maximum

vorticity. For further details on the choice of parameters, refer to Ref. [38]. The initial velocity field $\mathbf{u}_0 = (u_0, v_0)$ follows as

$$u_0 = \frac{1}{2}|\omega_e|\left(-(y-y_1)\exp\left(-(r_1/r_0)^2\right) + (y-y_2)\exp\left(-(r_2/r_0)^2\right)\right),$$
$$v_0 = \frac{1}{2}|\omega_e|\left((x-x_1)\exp\left(-(r_1/r_0)^2\right) - (x-x_2)\exp\left(-(r_2/r_0)^2\right)\right), \tag{21}$$

with $r_i^2 = (x-x_i)^2 + (y-y_i)^2$. For our convergence studies, square equidistant grids with resolutions of 128^2 (A), 256^2 (B), 512^2 (C) and 1024^2 (D) are used. The time-step is fixed at $\Delta t = 10^{-5}$ to make sure that the spatial truncation error is dominant.

The trajectory of the positive dipole contribution along and normal to the wall and its vorticity are reported in Table 1 and compared to the data of [36], denoted as KCH. It is evident that already with 512^2 cells we achieve essentially grid independence for the maximum vorticity. The relative difference to KCH of vortex core positions for grid (C) is on the order of up to 22%, whereas for grid (D) it is below 6% in the x-direction and 3% in y-direction, both for $t = 0.6$. The vortex trajectory of the positive dipole half as predicted on grids (A) to (D) are shown in Fig. 13. It can be seen that already with grid (C) we recover the reference until after the second wall collision. Fig. 14 illustrates the vorticity contour evolution within the positive quadrant of the coordinate system. We can conclude that even for this very challenging test case our model gives reliable results already at an equidistant grid resolution of the same magnitude as for a Fourier–Chebyshev scheme. Note that collocation points condense with a cosine-function towards the wall for Chebyshev collocation.

4.3. 2-D wall-bounded flow – the lid-driven cavity

As final test configuration we consider the well-established lid-driven cavity as an example for a fully confined shear flow that

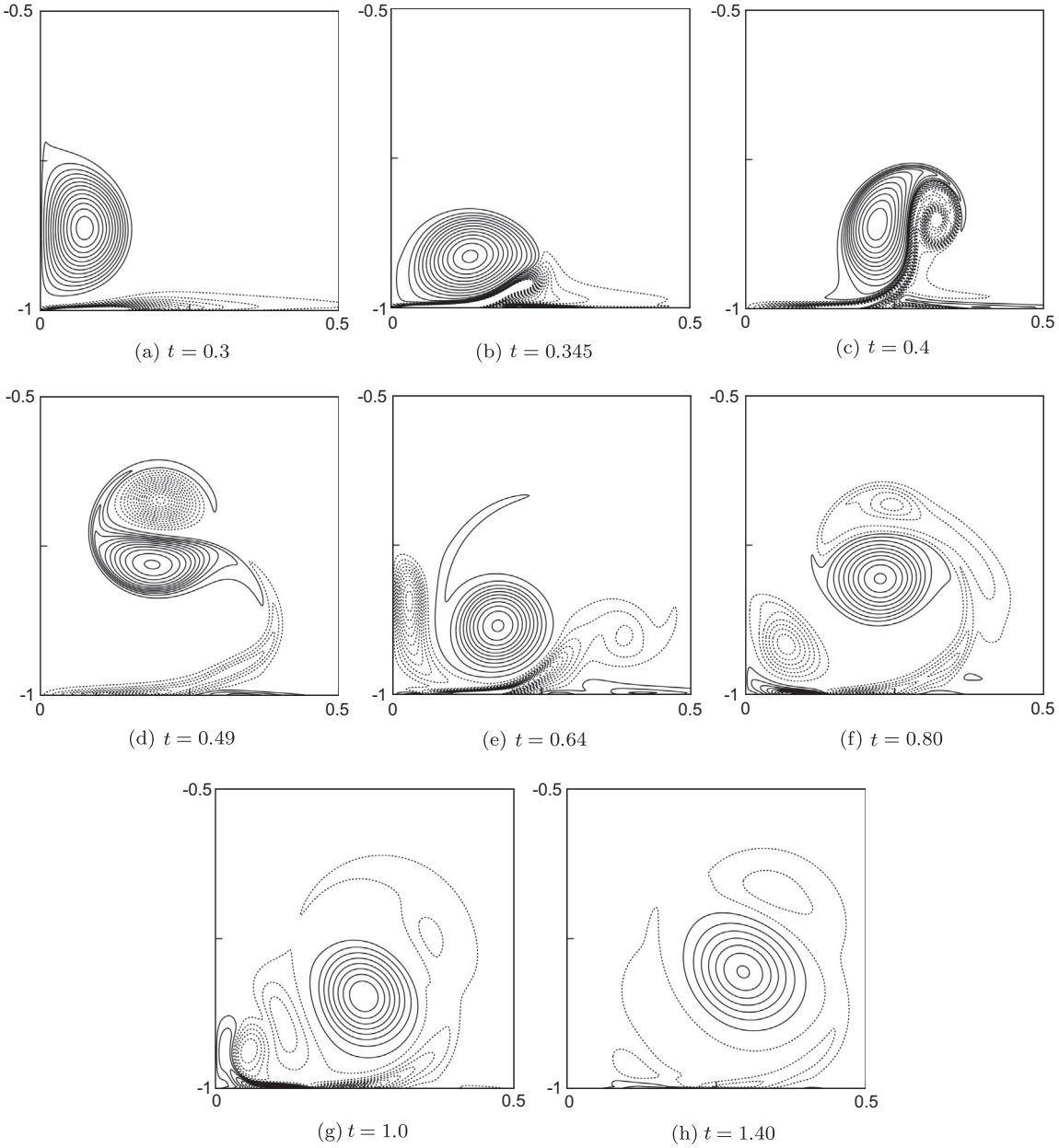

Fig. 14. Vorticity contour plots showing the evolution of a dipole half colliding with a no-slip wall for integral scale Reynolds number $Re = 1250$. Contour levels are -310, -290, …, -10, 10, …, 290, 310. Solid/dotted lines indicate positive/negative vorticity.

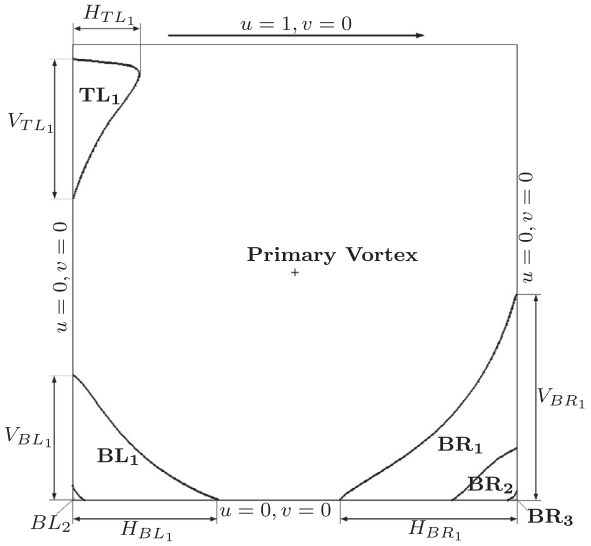

Fig. 15. Schematic of lid-driven cavity flow configuration.

poses particular demands on resolving secondary flows and thin viscous wall layers. Normal and tangential velocity boundary conditions are imposed at the domain boundary of a 2-D square cavity with initial flow at rest, see Fig. 15. We compare our under-resolved simulations with well-resolved reference data of Ghia et al. [39,40] and Erturk [41] for $1000 \leqslant Re \leqslant 7500$.

Predicted vortex core locations, vorticity and vortex extents are recorded in Tables 2–4 for $Re = 1000$, $Re = 5000$, and $Re = 7500$, respectively. Computed u and v velocity profiles along a vertical and horizontal line through the geometric center of the cavity

Table 2
Vortex core locations (x_{vc}, y_{vc}), vorticity ω_{vc} of primary and induced vortices as well as horicontal and vertical extent of induced vortices (H, V) of underresolved lid-driven cavity flows at Reynolds numbers $Re = 1000$.

Ghia et al. [40]			
Grid size:	129×129		
Property:	(x_{vc}, y_{vc})	ω_{vc}	(H, V)
Vortex:			
Primary	(0.5313, 0.5625)	2.04968	–
BL_1	(0.0859, 0.0781)	−0.36175	(0.2188, 0.1680)
BR_1	(0.8594, 0.1094)	−1.15465	(0.3034, 0.3536)
BR_2	(0.9922, 0.0078)	8.52782×10^{-3}	(0.0078, 0.0078)
ILES 1			
Grid size:	128×128		
Property:	(x_{vc}, y_{vc})	ω_{vc}	(H, V)
Vortex:			
Primary	(0.5308, 0.5657)	2.05614	–
BL_1	(0.08297, 0.07773)	−0.34410	(0.2254, 0.1702)
BR_1	(0.8627, 0.1124)	−1.11013	(0.3061, 0.3676)
BR_2	(0.9922, 0.0065)	0.011575	(0.0151, 0.0146)
ILES 2			
Grid size:	64×64		
Property:	(x_{vc}, y_{vc})	ω_{vc}	(H, V)
Vortex:			
Primary	(0.5307, 0.5669)	2.02648	–
BL_1	(0.08225, 0.07664)	−0.32429	(0.2205, 0.1671)
BR_1	(0.8590, 0.1135)	−1.11236	(0.3132, 0.3722)
BR_2	*N/A*	*N/A*	(0.0093, 0.0111)
ILES 3			
Grid size:	32×32		
Property:	(x_{vc}, y_{vc})	ω_{vc}	(H, V)
Vortex:			
Primary	(0.5291, 0.5738)	1.94975	–
BL_1	(0.0811522, 0.0710211)	−0.254183	(0.200667, 0.152209)
BR_1	(0.838987, 0.121804)	−1.18967	(0.356496, 0.408139)
BR_2	*N/A*	*N/A*	*N/A*

Table 3
Vortex core locations (x_{vc}, y_{vc}), vorticity ω_{vc} of primary and induced vortices as well as horicontal and vertical extent of induced vortices (H, V) of underresolved lid-driven cavity flows at Reynolds numbers $Re = 5000$.

Ghia et al. [40]			
Grid size:	257×257		
Property:	(x_{vc}, y_{vc})	ω_{vc}	(H, V)
Vortex:			
Primary	(0.5117, 0.5352)	1.86016	–
TL_1	(0.0625, 0.9102)	−2.08843	(0.1211, 0.2693)
BL_1	(0.0703, 0.1367)	−1.53055	(0.3184, 0.2643)
BR_1	(0.8086, 0.0742)	−2.66354	(0.3565, 0.4180)
BL_2	(0.0117, 0.0078)	1.88395×10^{-2}	(0.0156, 0.0163)
BR_2	(0.9805, 0.0195)	3.19311×10^{-2}	(0.0528, 0.0417)
ILES 1			
Grid size:	256×256		
Property:	(x_{vc}, y_{vc})	ω_{vc}	(H, V)
Vortex:			
Primary	(0.514796, 0.535558)	1.91205	–
TL_1	(0.0640276, 0.909221)	−2.06326	(0.121723, 0.272916)
BL_1	(0.0727773, 0.13644)	−1.49726	(0.326987, 0.267884)
BR_1	(0.802286, 0.0729475)	−2.74792	(0.367117, 0.431899)
BL_2	(0.00752025, 0.00801852)	0.00957388	(0.018039, 0.018674)
BR_2	(0.977799, 0.0194042)	0.0344873	(0.058756, 0.044715)
ILES 2			
Grid size:	128×128		
Property:	(x_{vc}, y_{vc})	ω_{vc}	(H, V)
Vortex:			
Primary	(0.5137, 0.5363)	1.89086	–
TL_1	(0.0654, 0.9070)	−2.05207	(0.1245, 0.2707)
BL_1	(0.0724, 0.1347)	−1.44506	(0.3207, 0.2640)
BR_1	(0.7942, 0.0732)	−2.78520	(0.3774, 0.4398)
BL_2	(0.0062, 0.0072)	1.20161×10^{-2}	(0.014373, 0.0154)
BR_2	(0.9731, 0.0209)	3.98882×10^{-2}	(0.062783, 0.0498)
ILES 3			
Grid size:	64×64		
Property:	(x_{vc}, y_{vc})	ω_{vc}	(H, V)
Vortex:			
Primary	(0.5082, 0.5415)	1.82477	–
TL_1	(0.0699, 0.8976)	−1.73942	(0.1331, 0.2696)
BL_1	(0.0699, 0.1237)	−1.22613	(0.2883, 0.2412)
BR_1	(0.7525, 0.0747)	−3.21003	(0.4293, 0.5222)
BL_2	*N/A*	*N/A*	(0.0913, 0.0161)
BR_2	(0.9433, 0.0348)	0.07116	(0.1238, 0.0873)

$(x, y) = (0.5, 0.5)$ are compared to the reference data, see Figs. 16–19.

Steady state solutions are obtained for grids with at least 16^2 cells at $Re \leqslant 1000$, with 32^2 cells at $Re \leqslant 5000$, and with 128^2 cells at $Re = 7500$. At $Re = 10{,}000$ our simulations predict a periodic flow with distinct harmonic frequencies independent of the grid, i.e. for resolutions of 128^2 and 256^2 cells, see Fig. 20. A periodic vortex movement is observed at a dominant frequency of $t \approx 0.421$ Hz. Large-scale structures such as the primary and secondary vortex core locations and sizes are accurately resolved, independent of the considered grid resolutions. The relative deviation from the reference data is less than approximately 1%. Reference velocity profiles through the geometric center of the cavity are accurately reproduced with significantly coarser resolution than used in the reference.

5. Discussion and conclusion

Nonlinear high resolution schemes have the potential of providing physically consistent under-resolved predictions, i.e. predictions that produce the correct resolved-scale evolution, of turbulent flows. Connecting to earlier work [42–44] we have demonstrated in this paper that this notion can be extended to non-turbulent flows. Moreover, by replacing a strictly incompressible flow model by a weakly compressible approach one can obtain a significant reduction of communication loads of the resulting computer

Table 4
Vortex core locations (x_{vc}, y_{vc}), vorticity ω_{vc} of primary and induced vortices as well as horicontal and vertical extent of induced vortices (H, V) of underresolved lid-driven cavity flows at Reynolds numbers $Re = 7500$.

Ghia et al. [40]			
Grid size:	257×257		
Property:	(x_{vc}, y_{vc})	ω_{vc}	(H, V)
Vortex:			
Primary	(0.5117, 0.5322)	1.87987	–
TL_1	(0.0664, 0.9141)	−2.15507	(0.1445, 0.2993)
BL_1	(0.0645, 0.1504)	−1.78511	(0.3339, 0.2793)
BR_1	(0.7813, 0.0625)	−3.49312	(0.3779, 0.4375)
BL_2	(0.0117, 0.0117)	1.72980×10^{-2}	(0.0234, 0.0254)
BR_2	(0.9492, 0.0430)	1.41058×10^{-1}	(0.1270, 0.0938)
BR_3	(0.9961, 0.0039)	–	(0.0039, 0.0039)
ILES 1			
Grid size:	256×256		
Property:	(x_{vc}, y_{vc})	ω_{vc}	(H, V)
Vortex:			
Primary	(0.512565, 0.53231)	1.90658	–
TL_1	(0.067591, 0.911266)	−2.19939	(0.147129, 0.309638)
BL_1	(0.0642259, 0.151967)	−1.85996	(0.342326, 0.283213)
BR_1	(0.787636, 0.0654213)	−3.21949	(0.380513, 0.448191)
BL_2	(0.0106178, 0.0112304)	0.013239	(0.0252095, 0.0283785)
BR_2	(0.950083, 0.0435404)	0.163971	(0.126247, 0.0992314)
BR_3	(0.998002, 0.00210992)	0.00216711	(0.00255, 0.00255)
ILES 2			
Grid size:	128×128		
Property:	(x_{vc}, y_{vc})	ω_{vc}	(H, V)
Vortex:			
Primary	(0.5107, 0.5334)	1.86490	–
TL_1	(0.0691, 0.9087)	−2.11330	(0.1522, 0.3077)
BL_1	(0.0637, 0.1490)	−1.77755	(0.33232, 0.276788)
BR_1	(0.7692, 0.0644)	−3.43703	(0.399768, 0.461295)
BL_2	(0.0098, 0.0093)	0.972509×10^{-2}	(0.0222, 0.0241)
BR_2	(0.9399, 0.0514)	1.88414×10^{-1}	(0.149005, 0.11703)
BR_3	*N/A*	*N/A*	*N/A*

code, at the expense of a certain level of density fluctuations. If these density errors do not adversely affect the resolved scales, the weakly compressible model is valid in terms of an overall coarse-grained flow prediction and not by principle inferior to the strictly incompressible model. For obtaining a weakly compressible implicit SGS model for turbulent and non-turbulent flows we have modified a low-dissipation sixth-order adaptive central-upwind WENO scheme, denoted as WENO-CU6-M1, in combination with a weakly compressible Roe-Pike approximate Riemann solver.

The implicit SGS capability of WENO-CU6-M1 is due to the incorporated scale-separation [9] which is controlled by the linear-weight bias C_q and an integer power exponent q. Implicit SGS models rely on the nonlinear contributions of the truncation error, which is necessarily far from an asymptotic behavior so that classical tools for truncation error analysis fail. The modified differential equation cannot even be written down in closed form, and Taylor expansions are at odds with the fact that the truncation error is not asymptotically small. Therefore, analysis of the implicit SGS modeling capability needs to rely on empirical investigations of a set of carefully selected reference configurations.

With a WENO-CU6-M1 parameter set of $(C_q = 16{,}000; q = 8)$ we reproduce the correct transition to self-similar isotropic turbulence of the Taylor–Green vortex even at large Reynolds numbers and for the inviscid case. For the $Re = 3000$ and $Re = \infty$ cases we have recovered a low-mode transition, i.e. a transient re-arrangement of energy within the low-wavenumber range before isotropic turbulence sets in, which can also be seen from the results of Ref. [45]. We find that the weakly compressible WENO-CU6-M1 based implicit LES is superior to the dynamic Smagorinsky model and performs almost as well as ADLM. At same resolution, however, the more complex ALDM is computationally more expensive than WENO-CU6-M1.

We have confirmed the general validity of the parameter set of WENO-CU6-M1 that was identified for TGV flow by considering also moderate Reynolds number decaying grid generated turbulence. For a time interval before the final decay we observe a total energy decay $E(t) \propto t^{-1}$. This scaling had been discussed by Speziale [46] and Davidson [47] as the theoretical minimum energy decay rate in quasi-isotropic grid turbulence at high turbulent Reynolds numbers. We note however, that the scaling exponent depends on how the time interval for curve fitting is chosen and that the difference to the more commonly reported decay $E(t) \propto t^{-1.3}$ is weak. For an extended time-frame exceeding the time difference between the first and the third experimental measuring stations, i.e. $Re_{\lambda,1} = 71.6$ and $Re_{\lambda,3} = 60.7$, we rather observe $E(t) \propto t^{-1.1}$ followed by $E(t) \propto t^{-1.2}$.

A main objective of the paper is to address whether the proposed implicit SGS model transfers its coarse-resolution prediction capability also to non-turbulent flows without further adjustments to its parameters. First, we follow up on [42,43] and consider the instability of the inviscid but finite-thickness double shear layer in the highly nonlinear stages. With equivalent resolution we obtain a similar quality of prediction as reported for a pseudospectral and a centered vorticity–streamfunction method. However, to stabilize these methods in the underresolved setup artificial viscosity, exceeding physicial viscosity, is required. The exploration of the $\theta \to \infty$, $Re \to \infty$ with our WENO-CU6-M1 based method with an implicit SGS model has confirmed the speculation of Brown and

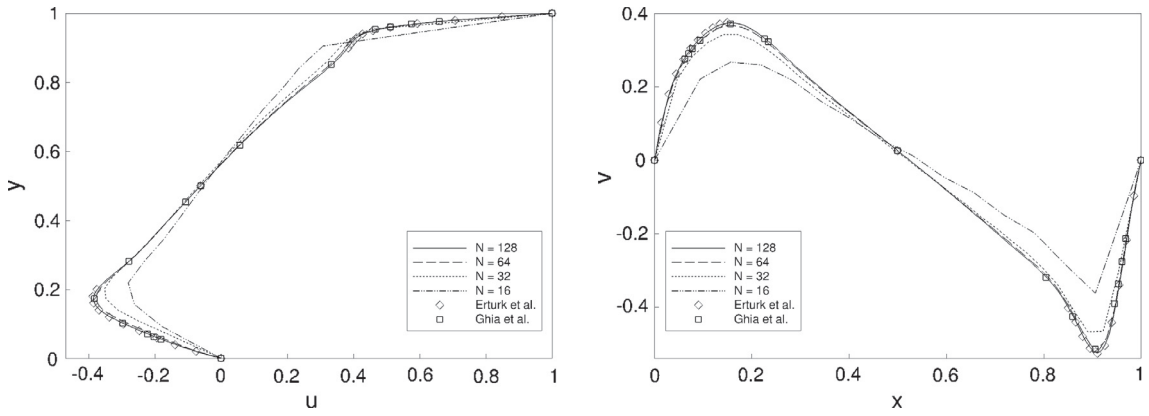

(a) $u-$ velocity as a function of y at $(x = 0.5)$. (b) $v-$ velocity as a function of x at $(y = 0.5)$.

Fig. 16. Velocities along the geometric center lines as found for a lid-driven cavity flow of $Re = 1000$.

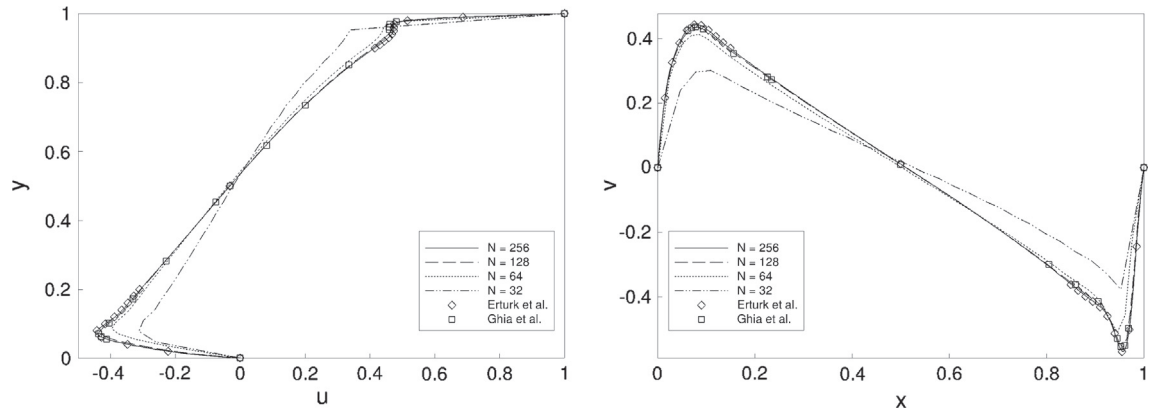

(a) $u-$ velocity as a function of y at $(x = 0.5)$. (b) $v-$ velocity as a function of x at $(y = 0.5)$.

Fig. 17. Velocities along the geometric center lines as found for a lid-driven cavity flow of *Re* = 5000.

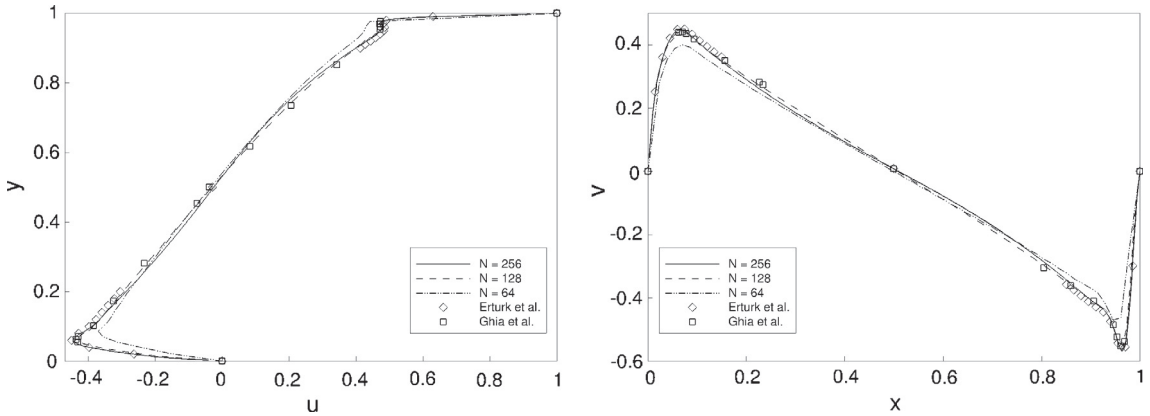

(a) $u-$ velocity as a function of y at $(x = 0.5)$. (b) $v-$ velocity as a function of x at $(y = 0.5)$.

Fig. 18. Velocities along the geometric center lines as found for a lid-driven cavity flow of *Re* = 7500.

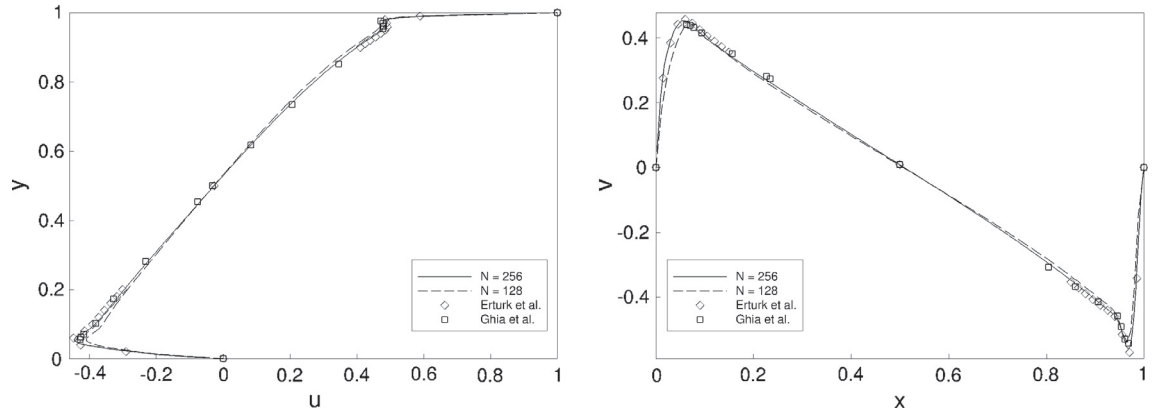

(a) $u-$ velocity as a function of y at $(x = 0.5)$. (b) $v-$ velocity as a function of x at $(y = 0.5)$.

Fig. 19. Velocities along the geometric center lines as found for a lid-driven cavity flow of *Re* = 10,000.

Minion [42] that the final stage of shear-layer evolution is just a single vortex which is independent of θ and *Re*.

The resolution of viscous wall-layers is crucial for practical applications. We have considered a case of viscous-inviscid interaction where a vortex dipole collides with a no-slip wall. We find that our model produces results in excellent agreement with reference data of Ref. [36,37] at much lower resolution. A fully confined case is the classical lid driven cavity. Our predictions agree with reference solutions that are based on high-resolution schemes, see Ref. [41,39,40] and on strictly incompressible formulations. For Reynolds numbers smaller than 7500 steady state solutions comparable to reference DNS have been obtained with much

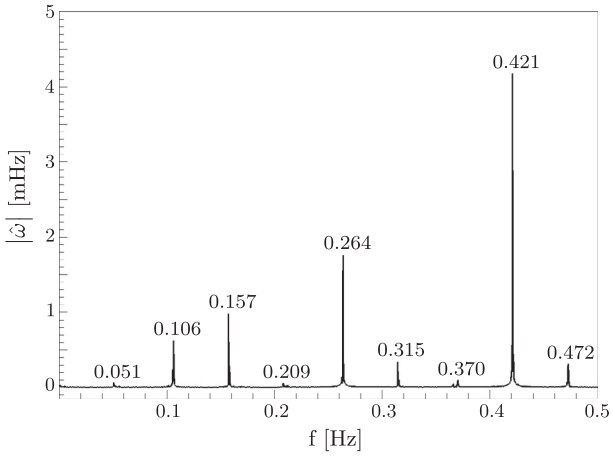

Fig. 20. Spectogram of vorticity for a lid-driven cavity flow of $Re = 10{,}000$. Timeframe: $800 < t < 5000$.

lower spatial resolution. At $Re = 10{,}000$ we obtain a flow with low-frequency periodic unsteadiness. Since this result is grid independent, we believe that the periodic behavior is most likely physically correct, and the steady state behavior observed by Ghia et al. at same parameters may be caused by numerical damping.

It can be concluded, that the weakly compressible WENO-CU6-M1 with the identified parameter set, ($C_q = 16{,}000; q = 8$), can serve as a reliable method for simulations of a wide range of underresolved turbulent and non-turbulent flow simulations. The results for all considered cases agree with reference data at lower resolution than used for obtaining these reference data, albeit not always being more accurate than other state-of-the-art methods for certain configurations.

Acknowledgements

The authors thank the Deutsche Forschungsgemeinschaft (DFG) for funding. F.S.S. expresses his gratitude to the Hanns-Seidel-Foundation (HSS). We also thank Dr. S. Hickel for the contribution of reference data as well as F. Örley and E. Fischer for continuous proofreading and invigorating discussions.

References

[1] Margolin LG, Rider WJ. A rationale for implicit turbulence modelling. Int J Numer Methods Fluids 2002;39:821–41. http://dx.doi.org/10.1002/fld.331.
[2] Adams N, Hickel S, Franz S. Implicit subgrid-scale modeling by adaptive deconvolution. J Comput Phys 2004;200:412–31.
[3] Grinstein F, Margolin L, Rider W. Implicit large eddy simulation: computing turbulent fluid dynamics. Cambridge Univ Press; 2007.
[4] Balsara DS, Shu C-W. Monotonicity preserving weighted essentially non-oscillatory schemes with increasingly high order of accuracy. J Comput Phys 2000;160:405–52. http://dx.doi.org/10.1006/jcph.2000.6443.
[5] Hickel S, Adams N, Domaradzki J. An adaptive local deconvolution method for implicit les. J Comput Phys 2006;213:413–36.
[6] Meyer M, Hickel S, Adams N. Assessment of implicit large-eddy simulation with a conservative immersed interface method for turbulent cylinder flow. Int J Heat Fluid Flow 2010;31:368–77. doi: 10.1016/j.ijheatfluidflow.2010.02.026.
[7] Hickel S, Adams NA. On implicit subgrid-scale modeling in wall-bounded flows. Phys Fluids 2007;19:105106. http://dx.doi.org/10.1063/1.2773765.
[8] Remmler S, Hickel S. Spectral structure of stratified turbulence: direct numerical simulations and predictions by large eddy simulation. Theor Comput Fluid Dyn 2012:1–18. doi: 10.1007/s00162-012-0259-9.
[9] Hu X, Adams N. Scale separation for implicit large eddy simulation. J Comput Phys 2011;230:7240–9. doi: 10.1016/j.jcp.2011.05.023.
[10] Hu XY, Wang Q, Adams NA. An adaptive central-upwind weighted essentially non-osciallatory scheme. J Comput Phys 2010;229:8952–65. http://dx.doi.org/10.1016/j.jcp.2010.08.019.
[11] Shu C-W, Don W-S, Gottlieb D, Schilling O, Jameson L. Numerical convergence study of nearly incompressible inviscid Taylor–Green vortex flow. J Sci Comput 2005;24:1–27. http://dx.doi.org/10.1007/s10915-004-5407-y.
[12] Tadmor E. Convergence of spectral methods for nonlinear conservation laws. SIAM J Numer Anal 1989;26:30–44. http://dx.doi.org/10.1137/0726003.
[13] Wells MG, Clercx HJH, van Heijst GJF. Vortices in oscillating spin-up. J Fluid Mech 2007;573:339–69. http://dx.doi.org/10.1017/S0022112006003909.
[14] Clercx HJH, Heijst GJF. Energy spectra for decaying 2D turbulence in a bounded domain. Phys Rev Lett 2000;85:306–9. http://dx.doi.org/10.1103/PhysRevLett.85.306.
[15] Bruneau CH, Greffier O, Kellay H. Numerical study of grid turbulence in two dimensions and comparison with experiments on turbulent soap films. Phys Rev E 1999;60:R1162–5. http://dx.doi.org/10.1103/PhysRevE.60.R1162.
[16] Wells J, Afanasyev Y. Decaying quasi-two-dimensional turbulence in a rectangular container: laboratory experiments. Geophys Astrophys Fluid Dyn 2004;98:1–20. http://dx.doi.org/10.1080/03091920410001648390.
[17] Chorin AJ. A numerical method for solving incompressible viscous flow problems. J Comput Phys 1997;135:118–25.
[18] Temam R. Une méthode d'approximation des solutions des équations Navier–Stokes. Bull Soc Math 1968;98:115–52.
[19] Roe PL. Approximate riemann solvers parameter vectors and difference schemes. J Comput Phys 1981;43:357–72.
[20] Marx Y. Evaluation of the artificial compressibility method for the solution of the incompressible Navier–Stokes equations. In: 9th GAMM conference of numerical methods in fluid mechanics, Lausanne; 1991.
[21] Elsworth D, Toro E. Riemann solvers for solving the incompressible Navier–Stokes equations using the artificial compressibility method. Technical report, Cranfield, College of Aeronautics Report No 9208, June 1992.
[22] Shu C-W. High-order finite difference and finite volume WENO schemes and discontinuous Galerkin methods for CFD. Int J Comput Fluid Dyn 2003;17:107–18. http://dx.doi.org/10.1080/1061856031000104851.
[23] Jiang G-S, Shu C-W. Efficient implementation of weighted ENO schemes. J Comput Phys 1996;126:202–28.
[24] Taylor GI, Green A. Mechanism of the production of small eddies from larger ones. Proc R Soc Lond A 1937;158:499–521.
[25] Fauconnier D, Langhe CD, Dick E. Construction of explicit and implicit dynamic finite difference schemes and application to the large-eddy simulation of the Taylor–Green vortex. J Comput Phys 2009;228:8053–84. doi: 10.1016/j.jcp.2009.07.028.
[26] Grinstein FF, Fureby C. Recent progress on flux-limiting based implicit large eddy simulation. In: European conference on computational fluid dynamics. ECCOMAS CFD; 2006.
[27] Martin M, Taylor E, Wu M, Weirs V. A bandwidth-optimized WENO scheme for the effective direct numerical simulation of compressible turbulence. J Comput Phys 2006;220:270–89. doi: 10.1016/j.jcp.2006.05.009.
[28] Taylor EM, Wu M, Martin M. Optimization of nonlinear error sources for weighted essentially non-oscillatory methods in direct numerical simulations of compressible turbulence. AIAA Paper; 2006. p. 44.
[29] Henrick AK, Aslam TD, Powers JM. Mapped weighted essentially non-oscillatory schemes: achieving optimal order near critical points. J Comput Phys 2005;207:542–67. doi: 10.1016/j.jcp.2005.01.023.
[30] Gerolymos G, Sénéchal D, Vallet I. Very-high-order weno schemes. J Comput Phys 2009;228:8481–524. doi: 10.1016/j.jcp.2009.07.039.
[31] Liu X-D, Osher S, Chan T. Weighted essentially non-oscillatory schemes. J Comput Phys 1994;115:200–12. doi: 10.1006/jcph.1994.1187.
[32] Brachet ME, Meiron D, Orszag S, Nickel B, Morf R, Frisch U. The Taylor–Green vortex and fully developed turbulence. J Statist Phys 1984;34:1049–63.
[33] Brachet M, Meneguzzi M, Vincent A, Politano H, Sulem P-L. Numerical evidence of smooth self-similar dynamics and possibility of subsequent collapse for three-dimensional ideal flow. Phys Fluids 1992;4:2845–54.
[34] Comte-Bellot G, Corrsin S. Simple Eulerian time correlation of full-and narrow-band velocity signals in grid-generated, turbulence. J Fluid Mech 1971;48:273–337. http://dx.doi.org/10.1017/S0022112071001599.
[35] Rogallo RS. Numerical experiments in homogeneous turbulence. NASA TM-81315 1981:1–91.
[36] Kramer W, Clercx HJ, van Heijst GJ. Vorticity dynamics of a dipole colliding with a no-slip wall. Phys Fluids 2007;19:1–13. http://dx.doi.org/10.1063/1.2814345.
[37] Clercx H, Bruneau C-H. The normal and oblique collision of a dipole with a no-slip boundary. Comput Fluids 2006;35:245–79. http://dx.doi.org/10.1016/j.compfluid.2004.11.009.
[38] Keetels G, D'Ortona U, Kramer W, Clercx H, Schneider K, van Heijst G. Fourier spectral and wavelet solvers for the incompressible Navier–Stokes equations with volume-penalization: aonvergence of a dipole–wall collision. J Comput Phys 2007;227:919–45. http://dx.doi.org/10.1016/j.jcp.2007.07.036.
[39] Ghia K, Hankey Jr. W, Hodge J. Study of incompressible Navier–Stokes equations in primitive variables using implicit numerical technique. In: 3rd Computational fluid dynamics conference; 1977. p. 156–67.
[40] Ghia U, Ghia KN, Shin CT. High-Re solutions for incompressible flow using the Navier–Stokes equations and a multigrid method. J Comput Phys 1982;48:387–411. http://dx.doi.org/10.1016/0021-9991(82)90058-4.
[41] Erturk E. Discussions on driven cavity flow. Int J Numer Methods Fluids 2009;60:275–94.
[42] Brown DL, Minion ML. Performance of under-resolved two-dimensional incompressible flow simulations. J Comput Phys 1995;122:165–83.

[43] Minion ML, Brown DL. Performance of under-resolved two-dimensional incompressible flow simulations, II. J Comput Phys 1997;138:734–65. http://dx.doi.org/10.1006/jcph.1997.5843.
[44] Bell J, Colella P, Glaz H. A second order projection method for the incompressible Navier–Stokes equations. J Comput Phys 1989;85:257–83.
[45] Fauconnier D, Bogey C, Dick E. On the performance of relaxation filtering for large-eddy simulation. J Turbul 2013;14:22–49. doi: 10.1080/14685248.2012.740567.
[46] Speziale CG. The energy decay in self-preserving isotropic turbulence revisited. J Fluid Mech 1992;241:645–67.
[47] Davidson PA. The minimum energy decay rate in quasi-isotropic grid turbulence. Phys Fluids 2011;23:085108. http://dx.doi.org/10.1063/1.3614479.

B.2 ASSESSING THE NUMERICAL DISSIPATION RATE AND VISCOSITY IN NUMERICAL SIMULATIONS OF FLUID FLOWS

ELSEVIER LICENSE TERMS AND CONDITIONS

Oct 12, 2016

This Agreement between Felix S Schranner ("You") and Elsevier ("Elsevier") consists of your license details and the terms and conditions provided by Elsevier and Copyright Clearance Center.

License Number	3897810157671
License date	Jun 28, 2016
Licensed Content Publisher	Elsevier
Licensed Content Publication	Computers & Fluids
Licensed Content Title	Assessing the numerical dissipation rate and viscosity in numerical simulations of fluid flows
Licensed Content Author	Felix S. Schranner,J. Andrzej Domaradzki,Stefan Hickel,Nikolaus A. Adams
Licensed Content Date	2 July 2015
Licensed Content Volume Number	114
Licensed Content Issue Number	n/a
Licensed Content Pages	14
Start Page	84
End Page	97
Type of Use	reuse in a thesis/dissertation
Portion	full article
Format	both print and electronic
Are you the author of this Elsevier article?	Yes
Will you be translating?	No
Order reference number	
Title of your thesis/dissertation	Weakly Compressible Models for Complex Flows
Expected completion date	Nov 2016
Estimated size (number of pages)	212
Elsevier VAT number	GB 494 6272 12
Requestor Location	Felix S Schranner Boltzmannstrasse 15 Garching, 85748 Germany Attn: Felix S Schranner
Total	**0.00 EUR**
Terms and Conditions	

INTRODUCTION

1. The publisher for this copyrighted material is Elsevier. By clicking "accept" in connection with completing this licensing transaction, you agree that the following terms and conditions apply to this transaction (along with the Billing and Payment terms and conditions established by Copyright Clearance Center, Inc. ("CCC"), at the time that you opened your Rightslink account and that are available at any time at http://myaccount.copyright.com).

GENERAL TERMS

2. Elsevier hereby grants you permission to reproduce the aforementioned material subject to the terms and conditions indicated.

3. Acknowledgement: If any part of the material to be used (for example, figures) has appeared in our publication with credit or acknowledgement to another source, permission must also be sought from that source. If such permission is not obtained then that material may not be included in your publication/copies. Suitable acknowledgement to the source must be made, either as a footnote or in a reference list at the end of your publication, as follows:

"Reprinted from Publication title, Vol /edition number, Author(s), Title of article / title of chapter, Pages No., Copyright (Year), with permission from Elsevier [OR APPLICABLE SOCIETY COPYRIGHT OWNER]." Also Lancet special credit - "Reprinted from The Lancet, Vol. number, Author(s), Title of article, Pages No., Copyright (Year), with permission from Elsevier."

4. Reproduction of this material is confined to the purpose and/or media for which permission is hereby given.

5. Altering/Modifying Material: Not Permitted. However figures and illustrations may be altered/adapted minimally to serve your work. Any other abbreviations, additions, deletions and/or any other alterations shall be made only with prior written authorization of Elsevier Ltd. (Please contact Elsevier at permissions@elsevier.com)

6. If the permission fee for the requested use of our material is waived in this instance, please be advised that your future requests for Elsevier materials may attract a fee.

7. Reservation of Rights: Publisher reserves all rights not specifically granted in the combination of (i) the license details provided by you and accepted in the course of this licensing transaction, (ii) these terms and conditions and (iii) CCC's Billing and Payment terms and conditions.

8. License Contingent Upon Payment: While you may exercise the rights licensed immediately upon issuance of the license at the end of the licensing process for the transaction, provided that you have disclosed complete and accurate details of your proposed use, no license is finally effective unless and until full payment is received from you (either by publisher or by CCC) as provided in CCC's Billing and Payment terms and conditions. If full payment is not received on a timely basis, then any license preliminarily granted shall be deemed automatically revoked and shall be void as if never granted. Further, in the event that you breach any of these terms and conditions or any of CCC's Billing and Payment terms and conditions, the license is automatically revoked and shall be void as if never granted. Use of materials as described in a revoked license, as well as any use of the materials beyond the scope of an unrevoked license, may constitute copyright infringement and publisher reserves the right to take any and all action to protect its copyright in the materials.

9. Warranties: Publisher makes no representations or warranties with respect to the licensed material.

10. Indemnity: You hereby indemnify and agree to hold harmless publisher and CCC, and their respective officers, directors, employees and agents, from and against any and all claims arising out of your use of the licensed material other than as specifically authorized pursuant to this license.

11. No Transfer of License: This license is personal to you and may not be sublicensed, assigned, or transferred by you to any other person without publisher's written permission.

12. No Amendment Except in Writing: This license may not be amended except in a writing signed by both parties (or, in the case of publisher, by CCC on publisher's behalf).

13. Objection to Contrary Terms: Publisher hereby objects to any terms contained in any purchase order, acknowledgment, check endorsement or other writing prepared by you, which terms are inconsistent with these terms and conditions or CCC's Billing and Payment terms and conditions. These terms and conditions, together with CCC's Billing and Payment terms and conditions (which are incorporated herein), comprise the entire agreement between you and publisher (and CCC) concerning this licensing transaction. In the event of any conflict between your obligations established by these terms and conditions and those established by CCC's Billing and Payment terms and conditions, these terms and conditions shall control.

14. Revocation: Elsevier or Copyright Clearance Center may deny the permissions described in this License at their sole discretion, for any reason or no reason, with a full refund payable to you. Notice of such denial will be made using the contact information provided by you. Failure to receive such notice will not alter or invalidate the denial. In no event will Elsevier or Copyright Clearance Center be responsible or liable for any costs, expenses or damage incurred by you as a result of a denial of your permission request, other than a refund of the amount(s) paid by you to Elsevier and/or Copyright Clearance Center for denied permissions.

LIMITED LICENSE

The following terms and conditions apply only to specific license types:
15. **Translation**: This permission is granted for non-exclusive world **English** rights only unless your license was granted for translation rights. If you licensed translation rights you may only translate this content into the languages you requested. A professional translator must perform all translations and reproduce the content word for word preserving the integrity of the article.
16. **Posting licensed content on any Website**: The following terms and conditions apply as follows: Licensing material from an Elsevier journal: All content posted to the web site must maintain the copyright information line on the bottom of each image; A hyper-text must be included to the Homepage of the journal from which you are licensing at http://www.sciencedirect.com/science/journal/xxxxx or the Elsevier homepage for books at http://www.elsevier.com; Central Storage: This license does not include permission for a scanned version of the material to be stored in a central repository such as that provided by Heron/XanEdu.
Licensing material from an Elsevier book: A hyper-text link must be included to the Elsevier homepage at http://www.elsevier.com . All content posted to the web site must maintain the copyright information line on the bottom of each image.

Posting licensed content on Electronic reserve: In addition to the above the following clauses are applicable: The web site must be password-protected and made available only to bona fide students registered on a relevant course. This permission is granted for 1 year only. You may obtain a new license for future website posting.
17. **For journal authors:** the following clauses are applicable in addition to the above:
Preprints:
A preprint is an author's own write-up of research results and analysis, it has not been peer-reviewed, nor has it had any other value added to it by a publisher (such as formatting, copyright, technical enhancement etc.).
Authors can share their preprints anywhere at any time. Preprints should not be added to or enhanced in any way in order to appear more like, or to substitute for, the final versions of articles however authors can update their preprints on arXiv or RePEc with their Accepted Author Manuscript (see below).
If accepted for publication, we encourage authors to link from the preprint to their formal publication via its DOI. Millions of researchers have access to the formal publications on ScienceDirect, and so links will help users to find, access, cite and use the best available version. Please note that Cell Press, The Lancet and some society-owned have different preprint policies. Information on these policies is available on the journal homepage.
Accepted Author Manuscripts: An accepted author manuscript is the manuscript of an article that has been accepted for publication and which typically includes author-incorporated changes suggested during submission, peer review and editor-author communications.
Authors can share their accepted author manuscript:

- immediately
  - via their non-commercial person homepage or blog
  - by updating a preprint in arXiv or RePEc with the accepted manuscript
  - via their research institute or institutional repository for internal institutional uses or as part of an invitation-only research collaboration work-group
  - directly by providing copies to their students or to research collaborators for their personal use
  - for private scholarly sharing as part of an invitation-only work group on commercial sites with which Elsevier has an agreement
- after the embargo period
  - via non-commercial hosting platforms such as their institutional repository
  - via commercial sites with which Elsevier has an agreement

In all cases accepted manuscripts should:

- link to the formal publication via its DOI
- bear a CC-BY-NC-ND license - this is easy to do
- if aggregated with other manuscripts, for example in a repository or other site, be shared in alignment with our hosting policy not be added to or enhanced in any way to appear more like, or to substitute for, the published journal article.

Published journal article (JPA): A published journal article (PJA) is the definitive final record of published research that appears or will appear in the journal and embodies all value-adding publishing activities including peer review co-ordination, copy-editing, formatting, (if relevant) pagination and online enrichment.
Policies for sharing publishing journal articles differ for subscription and gold open access articles:
Subscription Articles: If you are an author, please share a link to your article rather than the full-text. Millions of

researchers have access to the formal publications on ScienceDirect, and so links will help your users to find, access, cite, and use the best available version.
Theses and dissertations which contain embedded PJAs as part of the formal submission can be posted publicly by the awarding institution with DOI links back to the formal publications on ScienceDirect.
If you are affiliated with a library that subscribes to ScienceDirect you have additional private sharing rights for others' research accessed under that agreement. This includes use for classroom teaching and internal training at the institution (including use in course packs and courseware programs), and inclusion of the article for grant funding purposes.
Gold Open Access Articles: May be shared according to the author-selected end-user license and should contain a CrossMark logo, the end user license, and a DOI link to the formal publication on ScienceDirect.
Please refer to Elsevier's posting policy for further information.
18. **For book authors** the following clauses are applicable in addition to the above: Authors are permitted to place a brief summary of their work online only. You are not allowed to download and post the published electronic version of your chapter, nor may you scan the printed edition to create an electronic version. **Posting to a repository:** Authors are permitted to post a summary of their chapter only in their institution's repository.
19. **Thesis/Dissertation**: If your license is for use in a thesis/dissertation your thesis may be submitted to your institution in either print or electronic form. Should your thesis be published commercially, please reapply for permission. These requirements include permission for the Library and Archives of Canada to supply single copies, on demand, of the complete thesis and include permission for Proquest/UMI to supply single copies, on demand, of the complete thesis. Should your thesis be published commercially, please reapply for permission. Theses and dissertations which contain embedded PJAs as part of the formal submission can be posted publicly by the awarding institution with DOI links back to the formal publications on ScienceDirect.

Elsevier Open Access Terms and Conditions
You can publish open access with Elsevier in hundreds of open access journals or in nearly 2000 established subscription journals that support open access publishing. Permitted third party re-use of these open access articles is defined by the author's choice of Creative Commons user license. See our open access license policy for more information.
Terms & Conditions applicable to all Open Access articles published with Elsevier:
Any reuse of the article must not represent the author as endorsing the adaptation of the article nor should the article be modified in such a way as to damage the author's honour or reputation. If any changes have been made, such changes must be clearly indicated.
The author(s) must be appropriately credited and we ask that you include the end user license and a DOI link to the formal publication on ScienceDirect.
If any part of the material to be used (for example, figures) has appeared in our publication with credit or acknowledgement to another source it is the responsibility of the user to ensure their reuse complies with the terms and conditions determined by the rights holder.
Additional Terms & Conditions applicable to each Creative Commons user license:
CC BY: The CC-BY license allows users to copy, to create extracts, abstracts and new works from the Article, to alter and revise the Article and to make commercial use of the Article (including reuse and/or resale of the Article by commercial entities), provided the user gives appropriate credit (with a link to the formal publication through the relevant DOI), provides a link to the license, indicates if changes were made and the licensor is not represented as endorsing the use made of the work. The full details of the license are available at http://creativecommons.org/licenses/by/4.0.
CC BY NC SA: The CC BY-NC-SA license allows users to copy, to create extracts, abstracts and new works from the Article, to alter and revise the Article, provided this is not done for commercial purposes, and that the user gives appropriate credit (with a link to the formal publication through the relevant DOI), provides a link to the license, indicates if changes were made and the licensor is not represented as endorsing the use made of the work. Further, any new works must be made available on the same conditions. The full details of the license are available at http://creativecommons.org/licenses/by-nc-sa/4.0.
CC BY NC ND: The CC BY-NC-ND license allows users to copy and distribute the Article, provided this is not done for commercial purposes and further does not permit distribution of the Article if it is changed or edited in any way, and provided the user gives appropriate credit (with a link to the formal publication through the relevant DOI), provides a link to the license, and that the licensor is not represented as endorsing the use made of the work. The full details of the license are available at http://creativecommons.org/licenses/by-nc-nd/4.0. Any commercial reuse of Open Access articles published with a CC BY NC SA or CC BY NC ND license requires permission from Elsevier and will be subject to a fee.
Commercial reuse includes:

- Associating advertising with the full text of the Article
- Charging fees for document delivery or access
- Article aggregation
- Systematic distribution via e-mail lists or share buttons

Posting or linking by commercial companies for use by customers of those companies.

20. **Other Conditions**:

v1.8

Questions? customercare@copyright.com or +1-855-239-3415 (toll free in the US) or +1-978-646-2777.

Computers & Fluids 114 (2015) 84–97

Contents lists available at ScienceDirect

Computers & Fluids

journal homepage: www.elsevier.com/locate/compfluid

Assessing the numerical dissipation rate and viscosity in numerical simulations of fluid flows

Felix S. Schranner [a,*], J. Andrzej Domaradzki [b], Stefan Hickel [a], Nikolaus A. Adams [a]

[a] Technische Universität München, Institute of Aerodynamics, 85748 Garching, Germany
[b] University of Southern California, Department of Aerospace and Mechanical Engineering, Los Angeles, CA 90089, USA

ARTICLE INFO

Article history:
Received 22 June 2014
Received in revised form 14 January 2015
Accepted 23 February 2015
Available online 3 March 2015

Keywords:
Numerical dissipation
Numerical viscosity
Physical space
Local numerical dissipation
Pseudo-spectral space

ABSTRACT

We propose a method for quantifying the *effective numerical dissipation rate* and *effective numerical viscosity* in Computational Fluid Dynamics (CFD) simulations. Different from previous approaches that were formulated in spectral space, the proposed method is developed in a physical-space representation and allows for determining numerical dissipation rates and viscosities locally, that is, at the individual cell level, or for arbitrary subdomains of the computational domain. The method is self-contained and uses only the results produced by the Navier–Stokes solver being investigated. As no further information is required, it is suitable for a straightforward quantification of numerical dissipation as a post-processing step. We demonstrate the method's capabilities on the example of implicit large-eddy simulations of a three-dimensional Taylor–Green vortex flow, serving as a test flow going through laminar, transitional, and turbulent stages of time evolution. For validation, we compare results for the effective numerical dissipation rate with exact reference data we obtained with an accurate, spectral-space approach.

1. Introduction

Results of numerical simulations of fluid flows are always contaminated by truncation errors introduced by the discretization of governing differential equations. Truncation errors are only negligible if all physical scales are well resolved by the given mesh and time-step size. For lower temporal or spatial resolution, however, truncation errors affect the simulation results and can be of similar magnitude as physical effects. This situation is most frequently encountered in numerical simulations of turbulent flows at high Reynolds numbers. Simulating such flows usually requires modeling contributions of unresolved scales by various turbulence modeling procedures, leading to Reynolds-averaged Navier–Stokes (RANS) simulations or large-eddy simulations (LES).

In recent years, it has been recognized that the truncation errors may even act as a substitute for modelling of non-resolved scales. In turbulence, this approach is known as monotonically integrated LES (MILES) or implicit LES (ILES), and was originally proposed by Boris et al. [1] and reviewed more recently in a monograph edited by Grinstein et al. [2]. With ILES, the Navier–Stokes equations are solved numerically on a coarse LES mesh without explicit SGS models. Often one relies on nonlinearly stable methods, such as total variation diminishing (TVD), flux-corrected-transport (FCT) and flux-limited and sign-preserving schemes [3–5], originally developed to control numerical oscillations in configurations involving steep gradients or discontinuities. In the stabilized spectral LES [6] the numerical stability is not provided by the truncation error of the numerical discretization (which is exponentially small for a spectral method [7]) but by the spectral filter that strongly attenuates the small resolved scales if applied at each time step. In the same spirit, Bogey and Bailly [8] use an explicit filter applied every few time steps as a substitute for a SGS model in LES of a turbulent jet flow. Such methodologies are justified on a basis of the practical observation that truncation errors in non-oscillatory methods, as well as explicit filtering, introduce numerical dissipation, and that they effectively act as SGS models. For instance, [9] report the development of the $k^{-5/3}$ inertial subrange in numerical simulations of isotropic turbulence performed using the piecewise parabolic method (PPM) implemented in an Euler solver. This is a nominally inviscid case where the kinetic energy should be conserved but in the simulations it decays in agreement with Navier–Stokes dynamics because of numerical dissipation. Despite a wealth of positive results it should be recognized that the presence of numerical dissipation or explicit filtering does not guarantee physically correct dynamics of the resolved scales. For example, Garnier et al. [10] analyzed several different

* Corresponding author. Tel.: +49 89 289 16396; fax: +49 89 289 16139.
E-mail addresses: felix.schranner@aer.mw.tum.de (F.S. Schranner), jad@usc.edu (J.A. Domaradzki), sh@tum.de (S. Hickel), Nikolaus.Adams@tum.de (N.A. Adams).

http://dx.doi.org/10.1016/j.compfluid.2015.02.011
0045-7930/

shock-capturing Euler schemes applied to decaying isotropic turbulence and the conclusions were less favorable for ILES. While it was possible to obtain the inertial subrange, other results, such as probability densities of velocity derivatives and pressure, showed characteristics of low Reynolds number flows rather than what would have been expected from high Reynolds number LES. This behavior was attributed to the fact that the numerical dissipation often overwhelms the SGS dissipation computed for the same field using an explicit SGS model. Similar conclusions were drawn by Domaradzki and Radhakrishnan [11], who showed that the results obtained with the MPDATA method [12] for rotating and non-rotating turbulence were sensitive to the time-step size, and the method failed to produce theoretically expected results for certain initial conditions, and for rotating turbulence. The current rather vague definition of SGS modeling capabilities of the wide range of ILES schemes proposed in literature demands a more systematic approach to determine the effective dissipation aposteriori. Such a tool would allow comparisons of the effective numerical dissipation with the physical dissipation provided by resolved viscous stresses, and by explicit SGS models. Analytical information about the truncation errors can be obtained from the modified equation analysis but this approach is not feasible for multidimensional, nonlinear transport equations. The first aposteriori method for computing integral numerical dissipation has been proposed by Domaradzki et al. [13]. It is based on comparing flow evolutions from the same initial condition using two different discretization schemes, a scheme with finite numerical dissipation and a spectral code with negligible numerical dissipation. The method was used to analyze ILES simulations performed with the MPDATA approach for freely decaying high Reynolds number homogeneous turbulence with and without Coriolis forces Domaradzki and Radhakrishnan [11] and for a spectral multidomain simulations stabilized by spectral filtering and penalty methods Diamessis et al. [14]. The procedure computes the effective, wavenumber-dependent, numerical dissipation rate $\widehat{\mathcal{E}}_{n,sp}(\kappa,t)$ and the corresponding numerical viscosity $\hat{\nu}_{n,sp}(\kappa,t)$ for comparison with the analytical theories of turbulence. This procedure was employed by Hickel et al. [15] to develop a specific ILES method that is consistent with the physical energy transfer in turbulence, the so-called adaptive local deconvolution method (ALDM). It is based on a nonlinear discretization scheme which contains several free deconvolution parameters that allow to control its truncation error. The free parameters are constrained so that the numerical viscosity optimally matches the theoretical eddy viscosity predicted by the analytical theories of turbulence. While the optimization was performed for isotropic turbulence, the parameters of the scheme, once determined, proved to be valid also for simulations of other turbulent flows. Another method for estimating the numerical dissipation in LES was proposed recently by Zhou et al. [16] and is based on using the energy flux from the large, resolved scales as the numerical dissipation estimate.

The analysis of Domaradzki et al. [13] was developed in spectral space (to allow one-to-one comparisons with spectral eddy viscosities obtained from analytical theories of turbulence) and measures the global (spectral) dissipation rate. Despite being very accurate, Fourier-space based analysis of the numerical dissipation has some limitations. Since the computational domain must be periodic, the method cannot be easily generalized to non-periodic flows for which a local estimate of physical-space numerical dissipation is of particular practical interest. Also, using an additional spectral code for analysis is not always feasible.

The objective of this work is to develop and validate a more general procedure, free of the limitations listed above, for assessing the numerical dissipation rate for any given grid-based Navier–Stokes solver and a wide range of flows. The proposed method is equally applicable to periodic and non-periodic flows, provides a numerical-dissipation field, and can be employed as a post-processing tool for computational data.

2. Basic equations

The evolution of smooth and continuous fluid flows can be described by the conservation of mass, momentum and total energy. For a fluid with constant dynamic viscosity $\mu = \nu\rho$ as assumed for this study this set of equations, denoted as the Navier–Stokes equations (NSE), is

$$\frac{\partial \rho}{\partial t} + \frac{\partial(\rho u_\alpha)}{\partial x_\alpha} = 0, \tag{1a}$$

$$\frac{\partial(\rho u_\alpha)}{\partial t} + \frac{\partial(\rho u_\alpha u_\beta)}{\partial x_\beta} = -\frac{\partial p}{\partial x_\alpha} + \mu \frac{\partial(\tau^{\alpha\beta})}{\partial x_\beta}, \tag{1b}$$

$$\frac{\partial(\rho e_t)}{\partial t} + \frac{\partial(\rho e_t u_\alpha)}{\partial x_\alpha} = -\frac{\partial(p u_\alpha)}{\partial x_\alpha} + \mu \frac{\partial(u_\beta \tau^{\alpha\beta})}{\partial x_\alpha} - \frac{\partial}{\partial x_\alpha}\left(k \frac{\partial T}{\partial x_\alpha}\right) \tag{1c}$$

The stress tensor is

$$\tau^{\alpha\beta} = \frac{\partial u_\alpha}{\partial x_\beta} + \frac{\partial u_\beta}{\partial x_\alpha} - \frac{2}{3}\frac{\partial u_\gamma}{\partial x_\gamma}\delta_{\alpha\beta}, \tag{2}$$

u_α are the components of the velocity vector, p denotes the pressure, T is the temperature and k is the thermal conductivity. For when $\nu = 0$ the second term on the right-hand side of the momentum and total-energy transport equations, Eqs. (1b) and (1c), vanish and the system of conservation equations is denoted Euler equations. The transport of e_t can be separated into the transport equation for internal energy e_{in}

$$\frac{\partial(\rho e_{in})}{\partial t} + \frac{\partial(\rho e_{in} u_\alpha)}{\partial x_\alpha} = -p\frac{\partial(u_\alpha)}{\partial x_\alpha} + \mu\tau^{\alpha\beta}\frac{\partial(u_\beta)}{\partial x_\alpha} - \frac{\partial}{\partial x_\alpha}\left(k\frac{\partial T}{\partial x_\alpha}\right) \tag{3}$$

and kinetic energy $e_{kin} = \frac{1}{2}u_\alpha u_\alpha$

$$\frac{\partial(\rho e_{kin})}{\partial t} + \frac{\partial(\rho e_{kin} u_\alpha)}{\partial x_\alpha} = -u_\alpha\frac{\partial(p)}{\partial x_\alpha} + \mu u_\beta \frac{\partial(\tau^{\alpha\beta})}{\partial x_\alpha}. \tag{4}$$

The second term on the right hand side of Eq. (4) is the viscous contribution to the kinetic energy equation. To express the transfer of kinetic energy by viscous dissipation to the internal energy more clearly, the viscous contribution may be rewritten as

$$\mu u_\beta \frac{\partial(\tau^{\alpha\beta})}{\partial x_\alpha} = \mu\frac{\partial(u_\beta\tau^{\alpha\beta})}{\partial x_\alpha} - \mu\tau^{\alpha\beta}\frac{\partial(u_\beta)}{\partial x_\alpha}. \tag{5}$$

The first term on the right hand side of Eq. (5) is the the viscous work. Thus, the kinetic energy transport equation (for compressible flows) is:

$$\frac{\partial(\rho e_{kin})}{\partial t} + \frac{\partial(\rho e_{kin} u_\alpha)}{\partial x_\alpha} + u_\alpha\frac{\partial(p)}{\partial x_\alpha} - \mu\frac{\partial(u_\beta\tau^{\alpha\beta})}{\partial x_\alpha} + \mu\tau^{\alpha\beta}\frac{\partial(u_\beta)}{\partial x_\alpha} = 0. \tag{6}$$

Integration of the kinetic-energy transport Eq. (6) over the control volume $V = L_1 \times L_2 \times L_3$ leads to its integral form

$$\frac{\partial(E_{kin})}{\partial t} + F_{ekin} + F_{ac} - F_v - \Pi + \mathcal{E}_v = 0, \tag{7}$$

where

$$E_{kin} = \int_0^{L_1}\int_0^{L_2}\int_0^{L_3} \rho e_{kin} dx_1 dx_2 dx_3 \tag{8}$$

and the kinetic and acoustic energy fluxes as well as the viscous surface work are

$$F_{ekin} = \iiint_V \frac{\partial(\rho e_{kin} u_\alpha)}{\partial x_\alpha} dV = \iint_A n_\alpha(\rho e_{kin} u_\alpha) dA \tag{9}$$

$$F_{ac} = \iiint_V \frac{\partial(pu_\alpha)}{\partial x_\alpha} dV = \iint_A n_\alpha (pu_\alpha) dA \tag{10}$$

$$F_\nu = \nu \iiint_V \rho \frac{\partial(u_\beta \tau^{\alpha\beta})}{\partial x_\alpha} dV = \nu \iint_A \rho n_\alpha (u_\beta \tau^{\alpha\beta}) dA \tag{11}$$

where n_α with $\alpha \in [1,2,3]$ are the components of the outward pointing unit vector normal to the surface A bounding the volume V. The compression work

$$\Pi = \iiint_V p \frac{\partial u_\alpha}{\partial x_\alpha} dV \tag{12}$$

vanishes for incompressible flows. In this work, we express the viscous dissipation $\mathcal{E}_\nu$ as

$$\mathcal{E}_\nu = \nu \mathcal{E}, \tag{13}$$

with $\mathcal{E}$ denoting the dissipation function for the general case of compressible flows

$$\begin{aligned}\mathcal{E} &= \iiint_V \mathcal{E} dV = \iiint_V \rho \tau^{\alpha\beta} \frac{\partial(u_\beta)}{\partial x_\alpha} dV \\ &= \int_0^{L_1}\int_0^{L_2}\int_0^{L_3} \rho \left[2\left(\frac{\partial u_1}{\partial x_1}^2 + \frac{\partial u_2}{\partial x_2}^2 + \frac{\partial u_3}{\partial x_3}^2 \right) - \frac{2}{3}\left(\frac{\partial u_\alpha}{\partial x_\alpha} \right)^2 \right. \\ &\quad \left. + \left(\frac{\partial u_1}{\partial x_2} + \frac{\partial u_2}{\partial x_1} \right)^2 + \left(\frac{\partial u_1}{\partial x_3} + \frac{\partial u_3}{\partial x_1} \right)^2 + \left(\frac{\partial u_2}{\partial x_3} + \frac{\partial u_3}{\partial x_2} \right)^2 \right] dx_1 dx_2 dx_3\end{aligned} \tag{14}$$

The simplification of Eq. (14) for incompressible flows with constant density is straightforward.

3. The effect of discretization errors on the kinetic-energy transport equation

3.1. Basic concept

To explain the concept behind the proposed method let us consider the incompressible Navier–Stokes equations for a constant density fluid (say, $\rho = 1.0$) obtained by assuming an incompressible flow, for which the incompressible continuity equation $\partial u_\alpha / \partial x_\alpha = 0$ holds and consequently allows to reformulate (1b) such that

$$\frac{\partial u_\alpha}{\partial t} + u_\beta \frac{\partial u_\alpha}{\partial x_\beta} = -\frac{\partial p}{\partial x_\alpha} + \nu \frac{\partial^2 u_\alpha}{\partial x_\beta^2}. \tag{15}$$

Written symbolically Eq. (15) is

$$\frac{\partial \bar{\mathbf{u}}}{\partial t} + (NS)\bar{\mathbf{u}} = 0, \tag{16}$$

where the operator NS encompasses all spatial derivative terms and $\bar{\mathbf{u}}$ denotes the analytical, and generally unknown, solution for some particular fluid flow problem. A numerical Navier–Stokes solver is obtained by discretizing Eq. (16) symbolically,

$$\left(\frac{\partial \mathbf{u}}{\partial t} \right)_d + (NS)_d \mathbf{u} = 0, \tag{17}$$

and provides the numerical velocity field $\mathbf{u}_{i,j,k}(t_n)$ at all mesh points $0 \leqslant i < N_1, 0 \leqslant j < N_2, 0 \leqslant k < N_3$and time steps t_n. Note that the numerical solution $\mathbf{u}$ is not identical to the analytical solution $\bar{\mathbf{u}}$. In analyzing numerical schemes the discretized Eq. (17) sometimes can be rewritten as the partial differential equation in a form of the so called modified equation

$$\left(\frac{\partial \mathbf{u}}{\partial t} \right)_d + (NS)_d \mathbf{u} = \frac{\partial \mathbf{u}}{\partial t} + (NS)\mathbf{u} + \mathbf{E} = 0, \tag{18}$$

where $\mathbf{E}$ is the truncation error of the scheme. Hence, one obtains an expression for the truncation error:

$$-\mathbf{E} = \frac{\partial \mathbf{u}}{\partial t} + (NS)\mathbf{u}, \tag{19}$$

which, so far, is only formal because it requires the knowledge of the numerical solution $\mathbf{u}$ as an analytical function for which the time derivative and spatial derivatives in the operator (NS) can be calculated. Nevertheless, Eq. (19) is an useful starting point for elucidating how the truncation error can be estimated. Assuming that the velocity field $\mathbf{u}_{i,j,k}(t)$ has been determined with an arbitrary Navier–Stokes solver at several consecutive time steps, e.g., $t_{n-1} = t_n - \triangle t, t_n, t_{n+1} = t_n + \triangle t$, the time derivative in Eq. (19) can be approximated at time t_n using central differences

$$\frac{\partial \mathbf{u}_{i,j,k}}{\partial t}|_{CD} \approx \frac{\mathbf{u}_{i,j,k}(t_n + \triangle t) - \mathbf{u}_{i,j,k}(t_n - \triangle t)}{2\triangle t}. \tag{20}$$

Note that this time derivative is affected by the discretization errors of the original Navier–Stokes solver. Subsequently, to use Eq. (19) the differential Navier–Stokes operator should be applied to the velocity field $\mathbf{u}_{i,j,k}(t_n)$ at time t_n. If no analytical expression for $\mathbf{u}$ as a function of x, y, z exists the spatial derivatives must be computed numerically, and to minimize the numerical errors the highest order numerical formulas should be employed, leading to the approximate numerical formula for the truncation error

$$-\mathbf{E}_{i,j,k}(t_n) \approx \frac{\partial \mathbf{u}_{i,j,k}}{\partial t}|_{CD} + (NS)_{ho}\mathbf{u}_{i,j,k}(t_n), \tag{21}$$

where $(NS)_{ho}$ is the discretized Navier–Stokes operator using arbitrary high order numerical differentiation formulas. In practice, whenever possible, spectral methods are used (see [11,13]. From Eq. (17) we see that the second term on the r.h.s. of (21) is the rate of change of the velocity field computed using a high order scheme, allowing to rewrite Eq. (21) as

$$-\mathbf{E}_{i,j,k} \approx \frac{\partial \mathbf{u}_{i,j,k}}{\partial t}|_{CD} - \frac{\partial \mathbf{u}_{i,j,k}}{\partial t}|_{ho}. \tag{22}$$

The above formula involves computation of time derivatives for the same velocity field $\mathbf{u}_{i,j,k}$ but computed with two different discretizations of the same Navier–Stokes operator. Multiplying each time derivative by the velocity $\mathbf{u}_{i,j,k}$ and using a product rule will formally lead to time derivatives for the energy $e_{i,j,k} = \mathbf{u}_{i,j,k}\mathbf{u}_{i,j,k}/2$. While the same velocity is used in the computations, the resulting derivatives will be different because of different discretizations of the momentum equation. One can think of the given velocity field as an initial condition which is advanced forward in time with two differently discretized Navier–Stokes operators, leading to different rates of change of the energy. This results in the error estimate for the kinetic energy equation

$$-\mathcal{E}^{i,j,k}_{n,ho} = \left.\frac{\partial e_{i,j,k}}{\partial t}\right|_{CD} - \left.\frac{\partial e_{i,j,k}}{\partial t}\right|_{ho}, \tag{23}$$

i.e., we define the error as the difference between how the energy did evolved using a given FD/FV code and how it would have evolved if the discretization errors could be neglected.

The Eq. (23) can thus be viewed as the residual of computing the energy decay rate in two different ways. In applying this concept in practice the first term on the r.h.s. of Eq. (23) is computed directly as a discretized time derivative of the energy data obtained in the numerical simulation, i.e., the energy $e_{i,j,k} = \mathbf{u}_{i,j,k}\mathbf{u}_{i,j,k}/2$ is obtained from the velocity field at several time steps and the time derivative at time t_n is approximated, e.g., using central differences involving time levels t_{n+1} and t_{n-1}. The second term on the r.h.s. of Eq. (23) is computed indirectly, using terms in the energy equation originating from the spatial terms of the Navier–Stokes equation, i.e., from the representation symbolically given by the second term on the r.h.s. of Eq. (21). In this representation only the velocity field at time t_n and its spatial derivatives are used. While the indirect

computation assumes that high order numerical formulas are used, in what follows we generalize this concept to the analysis of the energy equation without a reference to spectral schemes.

We will consider the residual

$$-\mathcal{E}_n^{i,j,k} = \left.\frac{\partial e_{i,j,k}}{\partial t}\right|_{CD} - \left.\frac{\partial e_{i,j,k}}{\partial t}\right|_{FD/FV}, \tag{24}$$

where the first term on the r.h.s. is computed directly from the energy data and the second term is computed using Finite Difference or finite volume discretized spatial terms in the energy balance equation. The estimate may depend on the discretization order and possibly on the form of the fluxes used. Yet, with the availability of the energy error results obtained using spectral methods for the high order discretization in Eq. (23) the accuracy of the approximations made in (24) can be assessed easily. We demonstrate in the following sections that the accuracy of the estimate is robust, and largely independent of the FD/FV discretizations used, and very accurate when compared with the spectral results. We attribute this to the fact that the kinetic energy is a derived quantity, obtained from the primitive variables, and the discretized kinetic energy balance Eq. (24) is not subject directly to the constrains for the momentum Eq. (21) that requires the application of a high order discretization.

3.2. Finite volume formulation

For numerical simulations performed with an arbitrary, grid-based, compressible Navier–Stokes solver the symbolic Eq. (24) is replaced by the discretization of Eq. (6)

$$-\mathcal{E}_n^{i,j,k} = \frac{\triangle(\rho e_{kin})}{\triangle t} + \frac{\triangle(\rho e_{kin} u_\alpha)}{\triangle x_\alpha} + u_\alpha \frac{\triangle(p)}{\triangle x_\alpha} - \mu u_\beta \frac{\triangle(\tau^{\alpha\beta})}{\triangle x_\alpha}, \tag{25}$$

where the time derivative on the r.h.s is approximated using the kinetic energy data from the simulations at time steps t_{n-1} and t_{n+1}. The remaining terms are discretized spatial terms in the energy equation at time step t_n. The residual $\mathcal{E}_n^{i,j,k}$ may be designated as the numerical dissipation due to discretization errors of the Navier–Stokes solver. In general, the residual contains effects of all terms in the truncation error of a numerical scheme, including dissipative as well as dispersive errors. Yet, as shown later in Section 6.2, for sufficiently large subdomains the dissipative contributions dominate in a sense that the subdomain-integrated $\mathcal{E}_n^{i,j,k}$ is positive.

In a finite volume framework Eq. (25) is formally equivalent to

$$-\mathcal{E}_n^{i,j,k} = \frac{\triangle E_{kin}}{\triangle t} + F_{ekin} + F_{ac} - F_v - \Pi + \mathcal{E}_v^{i,j,k}, \tag{26}$$

where the kinetic energy is approximated as

$$E_{kin} = (\rho e_{kin})_{i,j,k} \triangle x_1 \triangle x_2 \triangle x_3, \tag{27}$$

and the remaining terms in (26) are computed numerically as (see also formulas (9)–(14) for the energy Eq. (7))

$$\begin{aligned} F_{ekin} \approx\ & [(\rho e_{kin} u_1)_{i+\frac{1}{2},j,k} - (\rho e_{kin} u_1)_{i-\frac{1}{2},j,k}] \triangle x_2 \triangle x_3 \\ & + [(\rho e_{kin} u_2)_{i,j+\frac{1}{2},k} - (\rho e_{kin} u_2)_{i,j-\frac{1}{2},k}] \triangle x_1 \triangle x_3 \\ & + [(\rho e_{kin} u_3)_{i,j,k+\frac{1}{2}} - (\rho e_{kin} u_3)_{i,j,k-\frac{1}{2}}] \triangle x_1 \triangle x_2 \end{aligned} \tag{28}$$

$$\begin{aligned} F_{ac} \approx\ & [(p u_1)_{i+\frac{1}{2},j,k} - (p u_1)_{i-\frac{1}{2},j,k}] \triangle x_2 \triangle x_3 + [(p u_2)_{i,j+\frac{1}{2},k} \\ & - (p u_2)_{i,j-\frac{1}{2},k}] \triangle x_1 \triangle x_3 + [(p u_3)_{i,j,k+\frac{1}{2}} - (p u_3)_{i,j,k-\frac{1}{2}}] \triangle x_1 \triangle x_2 \end{aligned} \tag{29}$$

$$\begin{aligned} F_v \approx\ & \nu[(\rho \tau^{1\beta} u_\beta)_{i+\frac{1}{2},j,k} - (\rho \tau^{1\beta} u_\beta)_{i-\frac{1}{2},j,k}] \triangle x_2 \triangle x_3 \\ & + \nu[(\rho \tau^{2\beta} u_\beta)_{i,j+\frac{1}{2},k} - (\rho \tau^{2\beta} u_\beta)_{i,j-\frac{1}{2},k}] \triangle x_1 \triangle x_3 \\ & + \nu[(\rho \tau^{3\beta} u_\beta)_{i,j,k+\frac{1}{2}} - (\rho \tau^{3\beta} u_\beta)_{i,j,k-\frac{1}{2}}] \triangle x_1 \triangle x_2 \end{aligned} \tag{30}$$

$$\Pi \approx \left\{ p \frac{\triangle u_\alpha}{\triangle x_\alpha} \right\}_{i,j,k} \triangle x_1 \triangle x_2 \triangle x_3 \tag{31}$$

$$\begin{aligned} \mathcal{E}_v^{i,j,k} &= \nu \mathcal{E}^{i,j,k} \\ &\approx \nu \left\{ \rho \left[2 \left(\frac{\triangle u_1}{\triangle x_1}^2 + \frac{\triangle u_2}{\triangle x_2}^2 + \frac{\triangle u_3}{\triangle x_3}^2 \right) - \frac{2}{3} \left(\frac{\triangle u_\alpha}{\triangle x_\alpha} \right)^2 + \left(\frac{\triangle u_1}{\triangle x_2} + \frac{\triangle u_2}{\triangle x_1} \right)^2 \right. \right. \\ &\quad \left. \left. + \left(\frac{\triangle u_1}{\triangle x_3} + \frac{\triangle u_3}{\triangle x_1} \right)^2 + \left(\frac{\triangle u_2}{\triangle x_3} + \frac{\triangle u_3}{\triangle x_2} \right)^2 \right] \right\}_{i,j,k} \triangle x_1 \triangle x_2 \triangle x_3 \end{aligned} \tag{32}$$

To denote the FV faces terms $\pm\frac{1}{2}$ are added to the corresponding cell indices. The edge-length in the relevant direction α is denoted as $\triangle x_\alpha$.

Alternatively, the FV formulation of Eq. (25) can be written as

$$-\mathcal{E}_n^{i,j,k} = \frac{\triangle E_{kin}}{\triangle t} + F_{ekin,V} + F_{\nabla p} - \mathcal{S}_v. \tag{33}$$

In Eq. (33) the cell face flux terms of Eq. (26) are replaced by volumetric fluxes. To itemize, the kinetic energy flux $F_{ekin,V}$ is approximated as

$$\begin{aligned} F_{ekin,V} &= \iiint_V \frac{\partial(\rho e_{kin} u_\alpha)}{\partial x_\alpha} dV \approx \left(\frac{\triangle(\rho e_{kin} u_\alpha)}{\triangle x_\alpha} \right)_{i,j,k} \triangle x_1 \triangle x_2 \triangle x_3 \\ &= \left(\frac{\triangle(\rho e_{kin} u_1)}{\triangle x_1} + \frac{\triangle(\rho e_{kin} u_2)}{\triangle x_2} + \frac{\triangle(\rho e_{kin} u_3)}{\triangle x_3} \right)_{i,j,k} \triangle x_1 \triangle x_2 \triangle x_3, \end{aligned} \tag{34}$$

the pressure gradient advection becomes

$$\begin{aligned} F_{\nabla p} &= \iiint_V u_\alpha \frac{\partial(p)}{\partial x_\alpha} dV \approx \left(u_\alpha \frac{\triangle p}{\triangle x_\alpha} \right)_{i,j,k} \triangle x_1 \triangle x_2 \triangle x_3 \\ &= \left(u_1 \frac{\triangle p}{\triangle x_1} + u_2 \frac{\triangle p}{\triangle x_2} + u_3 \frac{\triangle p}{\triangle x_3} \right)_{i,j,k} \triangle x_1 \triangle x_2 \triangle x_3 \end{aligned} \tag{35}$$

and the viscous contribution to the kinetic energy equation may be expressed as

$$\begin{aligned} \mathcal{S}_v &= \iiint_V \mu u_\beta \frac{\partial(\tau^{\alpha\beta})}{\partial x_\alpha} dV \\ &\approx \mu \left\{ \left[u_1 \left(\frac{\triangle^2 u_1}{\triangle x_1^2} + \frac{\triangle^2 u_1}{\triangle x_2^2} + \frac{\triangle^2 u_1}{\triangle x_3^2} \right) + u_2 \left(\frac{\triangle^2 u_2}{\triangle x_1^2} + \frac{\triangle^2 u_2}{\triangle x_2^2} + \frac{\triangle^2 u_2}{\triangle x_3^2} \right) \right. \right. \\ &\quad \left. + u_3 \left(\frac{\triangle^2 u_3}{\triangle x_1^2} + \frac{\triangle^2 u_3}{\triangle x_2^2} + \frac{\triangle^2 u_3}{\triangle x_3^2} \right) \right] - \frac{2}{3} \left[u_1 \left(\frac{\triangle^2 u_1}{\triangle x_1^2} + \frac{\triangle^2 u_2}{\triangle x_1 \triangle x_2} + \frac{\triangle^2 u_3}{\triangle x_1 \triangle x_3} \right) \right. \\ &\quad + u_2 \left(\frac{\triangle^2 u_2}{\triangle x_1 \triangle x_2} + \frac{\triangle^2 u_2}{\triangle x_2^2} + \frac{\triangle^2 u_3}{\triangle x_2 \triangle x_3} \right) + u_3 \left(\frac{\triangle^2 u_1}{\triangle x_1 \triangle x_3} + \frac{\triangle^2 u_2}{\triangle x_2 \triangle x_3} + \frac{\triangle^2 u_3}{\triangle x_3^2} \right) \left. \left. \right] \right\}_{i,j,k} \\ &\quad \times \triangle x_1 \triangle x_2 \triangle x_3. \end{aligned} \tag{36}$$

Integrating Eq. (26) or (33) over an arbitrary set of FVs, corresponding to a closed computational subdomain (CSD), $i \in [l_1; l_2]$, $j \in [m_1; m_2]$, $k \in [n_1; n_2]$ with $0 \leqslant l_\alpha,\ m_\alpha,\ n_\alpha \leqslant N_\alpha$, and its bounding surface, gives the numerical dissipation rate within the subdomain

$$\mathcal{E}_n^{CSD} = \sum_{i=l_1}^{l_2} \sum_{j=m_1}^{m_2} \sum_{k=n_1}^{n_2} \mathcal{E}_n^{i,j,k}. \tag{37}$$

For the entire computational domain, $l_1 = m_1 = n_1 = 0$, and $l_2 = N_1,\ m_2 = N_2,\ n_2 = N_3$, one obtains the total numerical dissipation rate $\mathcal{E}_n^{tot}$. Similarly, one may find the numerical viscosity either locally

$$\nu_n^{i,j,k} = \frac{\mathcal{E}_n^{i,j,k}}{\mathcal{E}^{i,j,k}}, \tag{38}$$

in an arbitrary computational subdomain

$$\nu_n^{CSD} = \frac{\mathcal{E}_n^{CSD}}{\mathcal{E}^{CSD}}, \tag{39}$$

or within the total volume

$$v_n^{tot} = \frac{\mathcal{E}_n^{tot}}{\mathcal{E}^{tot}}. \tag{40}$$

Denominators in the above expressions are obtained from Eq. (32) either for a single FV (i,j,k) or a summation over a subdomain (*CSD*) or the total domain (*tot*).

4. Fourier-space analysis of numerical dissipation

4.1. The spectral kinetic energy equation for incompressible flows

We assume a periodic domain with $V = (2\pi)^3$ and an ideal low-pass filter with a Nyquist wavenumber $\kappa_{N,1d}$ identical in each spatial direction. The Nyquist wavenumber in three-dimensional spectral space is $\kappa_{N,3d} = \sqrt{3}\,\kappa_{N,1d}$. The Fourier-transformed low-pass filtered velocity vectors $\hat{u}_\alpha(\boldsymbol{\kappa},t) = \mathcal{F}\{u_\alpha(\mathbf{x},t)\}$ $\alpha = 1,\ 2,\ 3$ are

$$\hat{u}_\alpha(\kappa_\beta,t) = \begin{cases} \hat{u}_\alpha(\kappa_\beta,t), & \forall\ \kappa_\beta \leqslant \kappa_{N,1d}, \\ 0, & else \end{cases} \tag{41}$$

with $\beta = 1,\ 2,\ 3$. The complex conjugate of $\hat{\mathbf{u}}$ is denoted as $\hat{\mathbf{u}}^{\star}$. The kinetic-energy and the dissipation spectra in three-dimensional spectral space are

$$\hat{e}(\boldsymbol{\kappa},t) = \frac{1}{2}\hat{\mathbf{u}}(\boldsymbol{\kappa},t)^2 = \frac{1}{2}\hat{u}_\alpha(\boldsymbol{\kappa},t)\hat{u}_\alpha^{\star}(\boldsymbol{\kappa},t), \tag{42}$$

$$\widehat{\mathcal{E}}(\boldsymbol{\kappa},t) = 2\kappa^2\hat{e}(\boldsymbol{\kappa},t), \tag{43}$$

with the wavenumber $\kappa = \sqrt{\kappa_\beta^2}$. As in physical space, the viscous dissipation rate is defined as the product

$$\widehat{\mathcal{E}}_v(\boldsymbol{\kappa},t) = \nu\widehat{\mathcal{E}}(\boldsymbol{\kappa},t). \tag{44}$$

The kinetic-energy transport equation in Fourier space is

$$\frac{\partial\hat{e}(\boldsymbol{\kappa},t)}{\partial t} = \hat{t}(\boldsymbol{\kappa},t) - \widehat{\mathcal{E}}_v(\boldsymbol{\kappa},t), \tag{45}$$

where the *nonlinear energy transfer* term $\hat{t}(\boldsymbol{\kappa},t)$ accounts for pressure and nonlinear effects. Its exact form is

$$\hat{t}(\boldsymbol{\kappa},t) = \frac{1}{2}Im\left\{\hat{u}_\alpha^{\star}(\boldsymbol{\kappa})P_{\alpha\gamma\beta}(\boldsymbol{\kappa})\int_{|\boldsymbol{\kappa}'|\leqslant\kappa_{N,3d}}\left[\hat{u}_\gamma(\boldsymbol{\kappa})\hat{u}_\beta(\boldsymbol{\kappa}-\boldsymbol{\kappa}')d\boldsymbol{\kappa}'\right]\right\} \tag{46}$$

where

$$P_{\alpha\gamma\beta}(\boldsymbol{\kappa}) = \kappa_\beta\left(\delta_{\alpha\gamma} - \kappa_\alpha\kappa_\gamma/\kappa^2\right) + \kappa_\gamma\left(\delta_{\alpha\beta} - \kappa_\alpha\kappa_\beta/\kappa^2\right). \tag{47}$$

The integral of the nonlinear transfer term over the entire domain vanishes.

4.2. Spectral numerical dissipation

Consider a velocity field $\mathbf{u}$ in a periodic domain obtained in a dissipative code. The discretization of the domain of volume $V = (2\pi)^3$ with N^3 FVs, implicitly defines the Nyquist wavenumber as $\kappa_{N,1d} = \frac{N}{2}$. Expressions $\hat{e}(\boldsymbol{\kappa},t)$, $\widehat{\mathcal{E}}_v(\boldsymbol{\kappa},t)$ and $\hat{t}(\boldsymbol{\kappa},t)$ defined in Section 4.1 can be computed numerically with negligible errors in Fourier-space with discrete wave numbers $\boldsymbol{\kappa} = (\kappa_1,\kappa_2,\kappa_3)$ with $\kappa_\alpha \in [0,\kappa_{N,1d}]$, $\alpha = 1,2,3$ and the rate of change of the kinetic energy at time t_n can be computed from Eq. (45) with the spectral accuracy:

$$\left.\frac{\partial\hat{e}(\boldsymbol{\kappa},t)}{\partial t}\right|_{sp}^{t=t_n} = \hat{t}(\boldsymbol{\kappa},t_n) - \widehat{\mathcal{E}}_v(\boldsymbol{\kappa},t_n). \tag{48}$$

On the other hand, the rate of change of the kinetic energy provided by the dissipative code is obtained by approximating the rate using a second-order central differences in time

$$\left.\frac{\partial\hat{e}(\boldsymbol{\kappa},t)}{\partial t}\right|_{CD}^{t=t_n} \approx \frac{\hat{e}(\boldsymbol{\kappa},t+\triangle t) - \hat{e}(\boldsymbol{\kappa},t-\triangle t)}{2\triangle t}. \tag{49}$$

The residual of these expressions is the three-dimensional spectral numerical dissipation rate (see [13,11,14])

$$-\widehat{\mathcal{E}}_{n,sp}(\boldsymbol{\kappa},t) = \frac{\hat{e}(\boldsymbol{\kappa},t+\triangle t) - \hat{e}(\boldsymbol{\kappa},t-\triangle t)}{2\triangle t} - \hat{t}(\boldsymbol{\kappa},t) + \widehat{\mathcal{E}}_v(\boldsymbol{\kappa},t). \tag{50}$$

Summation over shells with the radius κ

$$\hat{e}(\kappa,t) \approx \sum_{\kappa_1=-\kappa_{N,1d}}^{\kappa_{N,1d}}\sum_{\kappa_2=-\kappa_{N,1d}}^{\kappa_{N,1d}}\sum_{\kappa_3=-\kappa_{N,1d}}^{\kappa_{N,1d}}\hat{e}(\boldsymbol{\kappa}',t)\delta(|\boldsymbol{\kappa}'|-\kappa) \tag{51}$$

$$\widehat{\mathcal{E}}(\kappa,t) = \sum_{\kappa_1=-\kappa_{N,1d}}^{\kappa_{N,1d}}\sum_{\kappa_2=-\kappa_{N,1d}}^{\kappa_{N,1d}}\sum_{\kappa_3=-\kappa_{N,1d}}^{\kappa_{N,1d}}\widehat{\mathcal{E}}(\boldsymbol{\kappa}',t)\delta(|\boldsymbol{\kappa}'|-\kappa) \tag{52}$$

$$\hat{t}(\kappa,t) = \sum_{\kappa_1=-\kappa_{N,1d}}^{\kappa_{N,1d}}\sum_{\kappa_2=-\kappa_{N,1d}}^{\kappa_{N,1d}}\sum_{\kappa_3=-\kappa_{N,1d}}^{\kappa_{N,1d}}\hat{t}(\boldsymbol{\kappa}',t)\delta(|\boldsymbol{\kappa}'|-\kappa) \tag{53}$$

results in the κ-dependent effective spectral numerical dissipation rate

$$-\widehat{\mathcal{E}}_{n,sp}(\kappa,t) = \frac{\hat{e}(\kappa,t+\triangle t) - \hat{e}(\kappa,t-\triangle t)}{2\triangle t} - \hat{t}(\kappa,t) + \widehat{\mathcal{E}}_v(\kappa,t), \tag{54}$$

see also [13,11,15]. The *effective total numerical dissipation rate* in spectral space

$$-\widehat{\mathcal{E}}_{n,sp}(t) = \frac{\widehat{E}(t+\triangle t) - \widehat{E}(t-\triangle t)}{2\triangle t} + \widehat{\mathcal{E}}_v(t) \tag{55}$$

is obtained by summation of Eq. (54) over $\kappa \in [0;\kappa_{N,3d}]$, where the individual terms are:

$$\widehat{E}(t) = \sum_{\kappa=0}^{\kappa_{N,3d}}\hat{e}(\kappa,t), \tag{56}$$

$$\widehat{\mathcal{E}}_v(t) = \sum_{\kappa=0}^{\kappa_{N,3d}}\widehat{\mathcal{E}}_v(\kappa,t). \tag{57}$$

It is obvious that in total the non-linear transfer vanishes:

$$\widehat{T}(t) = \sum_{\kappa=0}^{\kappa_{N,3d}}\hat{t}(\kappa,t) = 0. \tag{58}$$

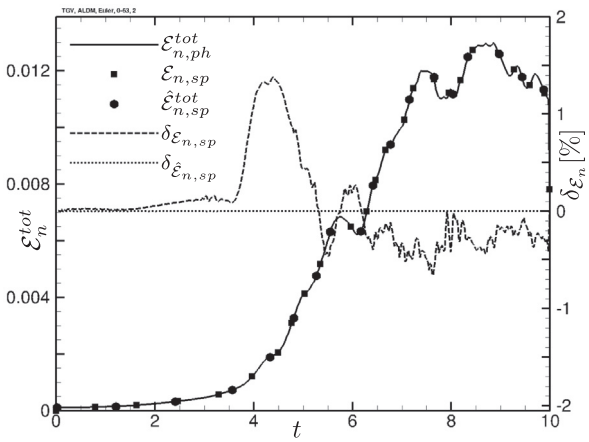

Fig. 1. $\mathcal{E}_{n,ph}^{tot}(t)$, $\widehat{\mathcal{E}}_{n,sp}^{tot}(t)$, $\mathcal{E}_{n,sp}^{tot}(t)$, $\delta_{\mathcal{E}_{n,sp}}$, $\delta_{\widehat{\mathcal{E}}_{n,sp}}$ for $Re = \infty$.

5. Physical-space analysis of numerical dissipation

5.1. Implementation of the method

To compute the effective numerical dissipation rate and viscosity within a computational subdomain (CSD) Eq. (26) is employed if not noted otherwise, and two different approaches can be used. In the first approach Eq. (26) is evaluated locally in each computational cell, providing local $\mathcal{E}^{loc}_{n,ph}$ values, where subscript *ph* indicates physical space computation as opposed to spectral space computation. Integrating $\mathcal{E}^{loc}_{n,ph}$ over the domain of interest, the computational sub-domain denoted as CSD, results in $\mathcal{E}^{CSD}_{n,ph}$.

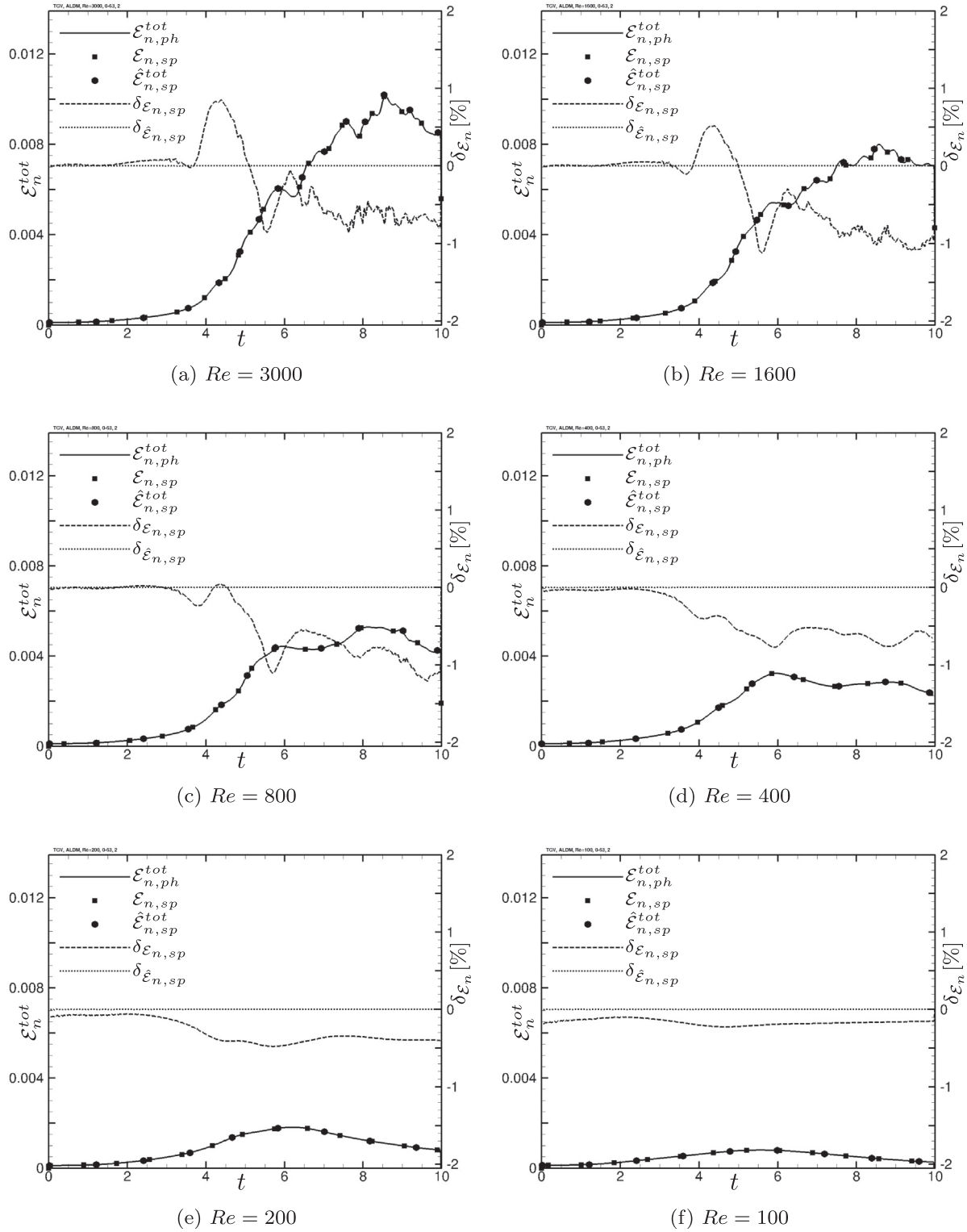

(a) $Re = 3000$ (b) $Re = 1600$

(c) $Re = 800$ (d) $Re = 400$

(e) $Re = 200$ (f) $Re = 100$

Fig. 2. $\mathcal{E}^{tot}_{n,ph}(t)$, $\widehat{\mathcal{E}}^{tot}_{n,sp}(t)$, $\mathcal{E}^{tot}_{n,sp}(t)$, $\delta_{\mathcal{E}_{n,sp}}$, $\delta_{\widehat{\mathcal{E}}_{n,sp}}$.

In the second approach Eq. (26) can be directly evaluated on the domain of interest. Hereby the flux terms are only evaluated over the bounding surface of the CSD. Although mathematically as well as numerically identical to the first procedure, the latter procedure is computationally less demanding since it does not involve local evaluation of all individual terms contributing to $\mathcal{E}_{n,ph}$.

We note that instead of using Eq. (26) one may also employ its volumetric equivalent, Eq. (33), to evaluate $\mathcal{E}^{loc}_{n,ph}$ or $\mathcal{E}^{CSD}_{n,ph}$.

The rate of change of kinetic energy is approximated using a second-order central derivative [11]

$$\frac{\triangle E_{kin}(t)}{\triangle t} = \left.\frac{\triangle E_{kin}(t)}{\triangle t}\right|_{CD} \approx \frac{E_{kin}(t+\triangle t) - E_{kin}(t-\triangle t)}{2\triangle t}. \tag{59}$$

For the flux terms, Eqs. (29), (28) and (30), necessary data (e.g., p, u, ρ) need to be reconstructed at the bounding surface from nearby data. The data at the bounding surface located at $i \pm \frac{1}{2}$, with i being the index of the cell that shares the relevant face with the domain surface, is reconstructed with a sixth-order central scheme to minimize the approximation errors:

$$f_{i\pm\frac{1}{2}} = \frac{1}{60}\left(f_{i\pm3} - 8f_{i\pm2} + 37f_{i\pm1} + 37f_i - 8f_{i\mp1} + f_{i\mp2}\right) + \mathcal{O}(\triangle x^6). \tag{60}$$

Spatial derivatives in viscous terms are often approximated with second-order accuracy. In general, the order of approximation for the spatial derivatives should be consistent with the order used in the Navier–Stokes solver. Numerical viscosities, $\nu^{CSD}_{n,ph}$ or $\nu^{tot}_{n,ph}$, are determined directly from Eqs. (39) and (40), respectively.

A particular case of interest is the numerical dissipation for the entire computational domain with periodic boundary conditions. The flux terms in Eq. (26) should cancel exactly if integrated over a full periodic domain. Thus, the total numerical dissipation rate $\mathcal{E}^{tot}_{n,ph}$ and consequently $\nu^{tot}_{n,ph}$ depend only on the rate of change of the total kinetic energy (59) and total viscous dissipation (13) if the physical viscosity is non-zero:

$$-\mathcal{E}_n = \frac{E_{kin}(t+\triangle t) - E_{kin}(t-\triangle t)}{2\triangle t} + \mathcal{E}_\nu. \tag{61}$$

According to the Parseval theorem [17] it is $\hat{e}(t) = E_{kin}(t)$ and $\widehat{\mathcal{E}}(t) = \mathcal{E}(t)$. Consequently, Eqs. (55) and (61) and in particular their left hand sides are identical: $\widehat{\mathcal{E}}_{n,sp}(t) = \mathcal{E}_{n,ph}(t)$. Note that the exact correspondence between spectral and physical space analysis holds only for the full periodic domain.

5.2. Physical-space reference solution for the local numerical dissipation

Assume that the velocity field $\mathbf{u}_{i,j,k}(t)$ has been determined with an arbitrary physical space solver at several consecutive time steps, e.g., $t_{n-1} = t_n - \triangle t, t_n, t_{n+1} = t_n + \triangle t$. In the Navier–Stokes equation, the time derivative of the velocity can be approximated at time t_n as

$$\frac{\partial \mathbf{u}_{i,j,k}}{\partial t} \approx \frac{\mathbf{u}_{i,j,k}(t_n+\triangle t) - \mathbf{u}_{i,j,k}(t_n-\triangle t)}{2\triangle t}. \tag{62}$$

Multiplying Eq. (62) by $\mathbf{u}_{i,j,k}(t_n)$ yields the numerical kinetic-energy decay rate at each point

$$\left.\frac{\partial e_{i,j,k}}{\partial t}\right|_{CD} \approx \mathbf{u}_{i,j,k}(t_n)\frac{\mathbf{u}_{i,j,k}(t_n+\triangle t) - \mathbf{u}_{i,j,k}(t_n-\triangle t)}{2\triangle t}. \tag{63}$$

Since the time-evolving velocity $\mathbf{u}_{i,j,k}(t)$ is approximated by a Navier–Stokes solver, the energy decay rate is affected by its approximation errors. For a triply-periodic domain the time derivative of the velocity (62) and consequently the r.h.s. of Eq. (63) can be computed without dispersive and dissipative artefacts by evaluating all spatial derivative terms in Fourier space and then transforming back to the physical space, i.e., using a pseudo-spectral method (see also Section 4.2). We have used a skew-symmetric pseudo-spectral scheme, hence dissipation-free. We refrain from applying de-aliasing as these rules, e.g. 2/3- or 1/2-rule, imply spectral cutoff filters of the nonlinear convective terms.

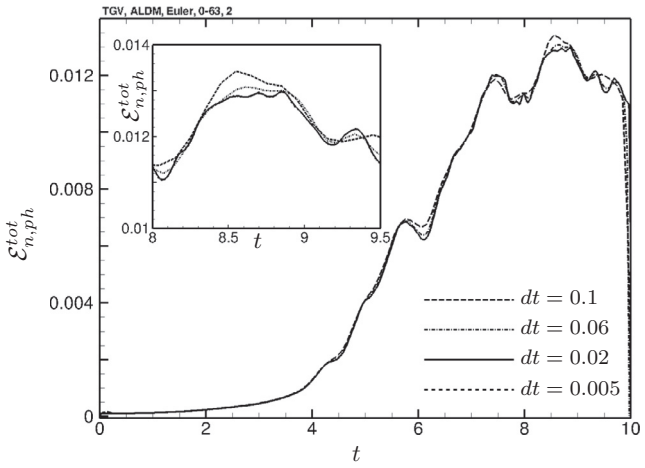

Fig. 3. $\mathcal{E}^{tot}_{n,ph}(t)$ for varying $\triangle t$, $Re = \infty$.

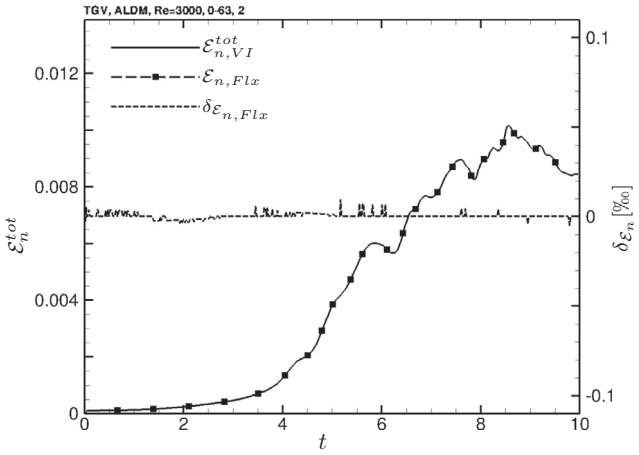

Fig. 4. $\mathcal{E}^{tot}_{n,VI}(t)$, $\mathcal{E}^{tot}_{n,Flx}(t)$ and $\delta_{\mathcal{E}_{n,Flx}}$ for $Re = 3000$.

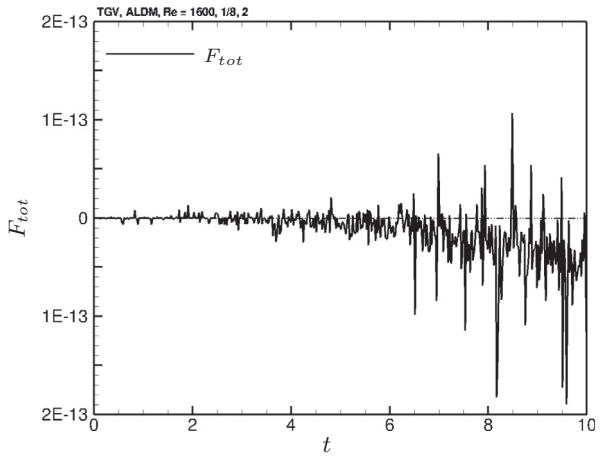

Fig. 5. F_{tot} in first octant of the TGV for $Re = 1600$.

The difference between kinetic-energy decay rates computed in these two ways provides an estimate of the numerical error introduced by the FD/FV discretization

$$-\mathcal{E}_{n,sp}^{i,j,k} = \left.\frac{\partial e_{i,j,k}}{\partial t}\right|_{CD} - \left.\frac{\partial e_{i,j,k}}{\partial t}\right|_{sp}, \tag{64}$$

where the subscript *sp* indicates the energy rate computed with the help of the pseudo-spectral scheme. Unlike the spectral method of the previous section, implemented solely in spectral space and determining the spectral numerical dissipation (or viscosity), Eq. (64) yields the physical-space numerical dissipation distribution, i.e., the numerical dissipation on each individual mesh point i, j, k.

5.3. Computation of the viscous dissipation term

It must be recognized that the derivatives in the viscous dissipation term are normally contaminated by the truncation errors of the discretization used by a numerical solver. In contrast, a spectral code uses exact Fourier-space derivatives, represented by $\frac{d\hat{f}(x)}{dx} \propto -i\kappa\hat{f}$. Therefore, one may expect that the value of the viscous dissipation will be different depending on which method is used. The comparison between results for these different ways of computing the viscous dissipation is provided in Appendix A. However, when validating the physical space approach with the help of an external spectral code, we constrain the spectral computation of the viscous dissipation to be consistent with the way it is computed in the actual, dissipative code. This is accomplished by using the Fourier differentiation formulas with modified wavenumbers. Specifically, the exact wavenumbers in Eqs. (43) are replaced with the modified wavenumbers appropriate for a given numerical discretization, e.g., for the second-order central derivatives $\kappa_{\alpha,mod} = \frac{sin(\kappa_\alpha\ \triangle x_\alpha)}{\triangle x_\alpha}$ and for the fourth-order central derivatives $\kappa_{\alpha,mod} = \frac{sin(\kappa_\alpha\ \triangle x_\alpha)}{3\ \triangle x_\alpha}[4 - cos(\kappa_\alpha\ \triangle x_\alpha)]$. This is done as we are interested in the numerical dissipation provided by the code in excess of the explicit viscous dissipation, even if the latter is not exact because of the approximation errors in computing spatial derivatives.

6. Feasibility study

Fourier-space analyzes permit to determine total numerical dissipation rates exactly (and mode-dependent), however, they are limited to fully periodic flows. We will show that the three methods at hand, Fourier-space, pseudo-spectral, and physical-space, result in the same predictions of numerical dissipation rates for such flows. For non-periodic flows Fourier-space analysis is no possible. However, the pseudo-spectral reference method permits to determine numerical energy dissipation rates locally for arbitrary, non-periodic, subdomains of periodic domains. Note that the existence of an underlying periodic domain is not required in the context of the direct physical-space analysis. In contrast to the pseudo-spectral method, the physical-space method is also applicable to non-uniform or unstructured grids. Hence, it is sufficient, and essential, to base a feasibility study on one well-defined flow, with the prerequisite that it shows, independent of the resolution, all characteristics of laminar, transitional and turbulent flows within arbitrary subdomains.

All these requirements are fulfilled for a three-dimensional Taylor–Green vortex (TGV) flow [18], which evolves from the original two-dimensional laminar state

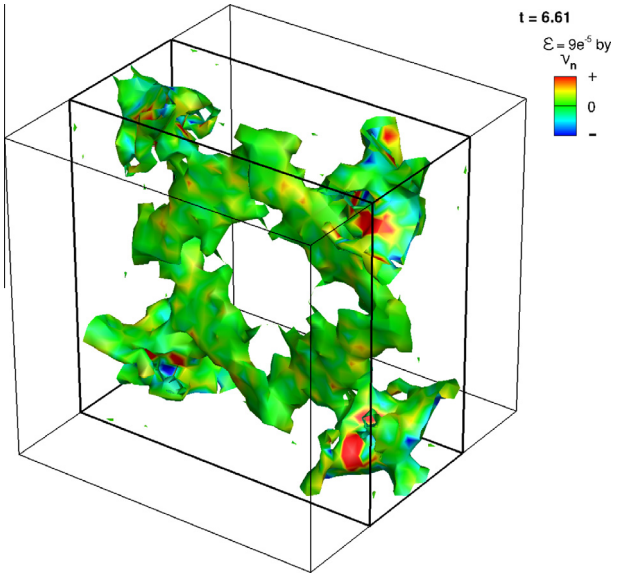

Fig. 6. $\mathcal{E} = 9e^{-5}$ colored by $sgn(\nu_{n,ph})$ for $Re = 1600$.

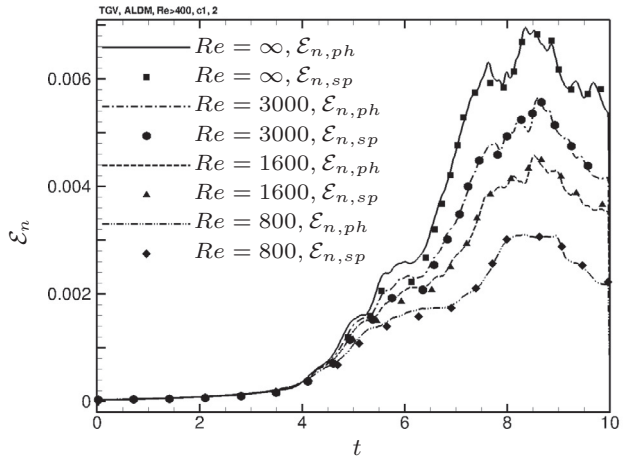

(a) $Re \geq 800$

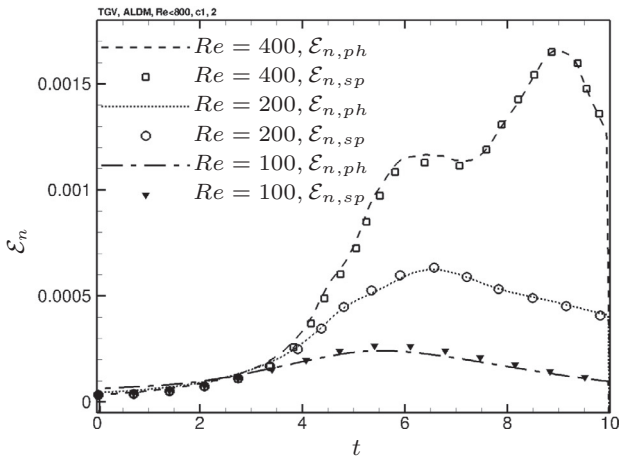

(b) $Re \leq 400$

Fig. 7. $\mathcal{E}_{n,ph}(t)$ (Lines), $\mathcal{E}_{n,sp}(t)$ (Symbols) for CSD1.

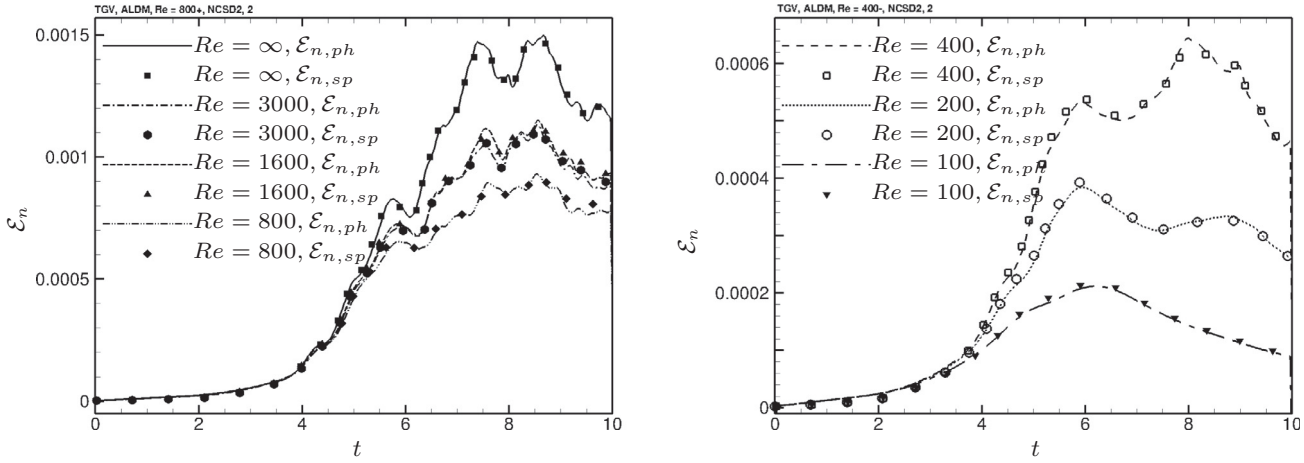

(a) $Re \geq 800$ (b) $Re \leq 400$

Fig. 8. $\mathcal{E}_{n,ph}(t)$ (Lines), $\mathcal{E}_{n,sp}(t)$ (Symbols) for NCSD2.

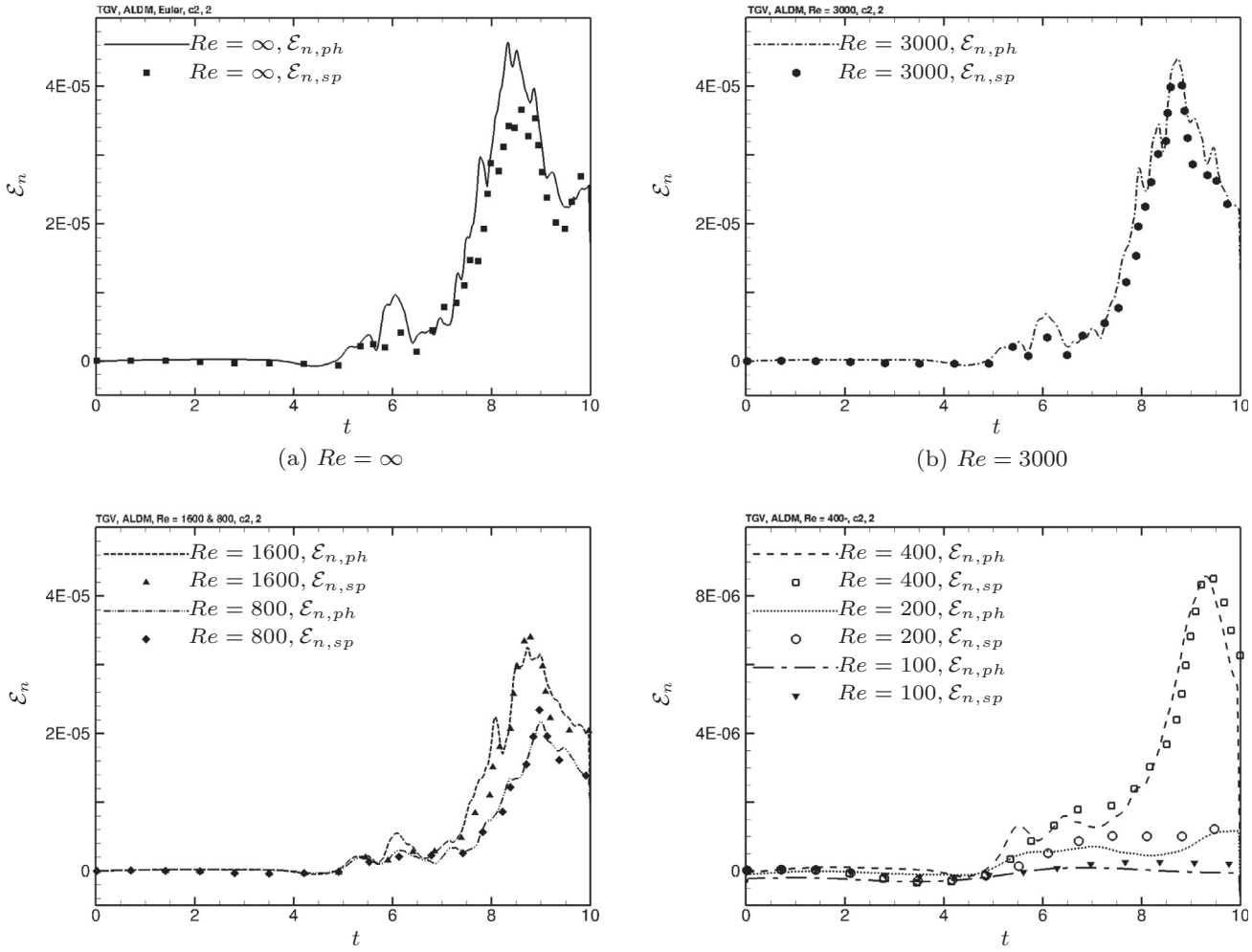

(a) $Re = \infty$ (b) $Re = 3000$

(c) $Re = 800$ and $Re = 1600$ (d) $Re \leq 400$

Fig. 9. $\mathcal{E}_{n,ph}(t)$ (Lines), $\mathcal{E}_{n,sp}(t)$ (Symbols) for CSD2.

$$
\begin{aligned}
u(x,y,z,0) &= \sin(x)\cos(y)\cos(z),\\
v(x,y,z,0) &= -\cos(x)\sin(y)\cos(z),\\
w(x,y,z,0) &= 0,\\
\rho(x,y,z,0) &= 1.0,\\
p(x,y,z,0) &= 100 + \frac{1}{16}[(\cos(2x)+\cos(2y))(2+\cos(2z)) - 2]
\end{aligned}
\tag{65}
$$

to a turbulent flow with a self-similar $\widehat{E}(\kappa) \propto k^{-5/3}$ scaling at late times, $t > 9$. Furthermore, the vast amount of reported data allows to neglect discussion of the flow itself but instead focus on the feasibility study of estimating the numerical dissipation.

The data for this study are obtained using incompressible TGV flows simulated with the ALDM model of Hickel et al. [15]. All simulations are carried out in a periodic domain of $V = (2\pi)^3$ discretized with 64^3 finite volumes. The time step is constant, $\triangle t = \frac{T}{500} = 0.02$ if not noted otherwise. An explicit three-step TVD Runge–Kutta method [19] is used to integrate the equations in time.

In the first step, the physical-space method of Section 5.1 and the pseudo-spectral method of Section 5.2 are compared to the effective total numerical dissipation rate computed according to Eq. (55) in Fourier-space. Both, the spectral and pseudo-spectral method rely on fully periodic flows, hence the comparison is based on such. In contrast to the Fourier-space method, with which only $\widehat{\varepsilon}^{tot}_{n,sp}$ is computable, the pseudo-spectral method permits to determine $\varepsilon^{i,j,k}_{n,sp}$ at individual mesh points. An intermediate step serves to demonstrate that the total flux, $F_{tot}(t) = F_{ekin}(t) + F_{ac}(t) - F_v(t)$ is determined correctly for arbitrary subdomains. In the second and final step the physical-space analysis is extended to random, arbitrary, non-periodic subdomains. Embedding these in larger, fully periodic domains allows for pseudo-spectral reference $\varepsilon^{CSD}_{n,sp}$ to be available for comparisons.

6.1. Analysis for the fully periodic domain

We note that for all tested Reynolds numbers, and independently of compressible or incompressible data, analysis of $\varepsilon_{n,ph}$ via Eq. (61) instead of (26) numerically is exact. Furthermore, results are identical for both approaches described in Section 5.1. The physical space results, discussed in the following subsection, are obtained by evaluation of Eq. (26) for each individual finite volume and summing over all finite volumes (approach one, see Section 5.1).

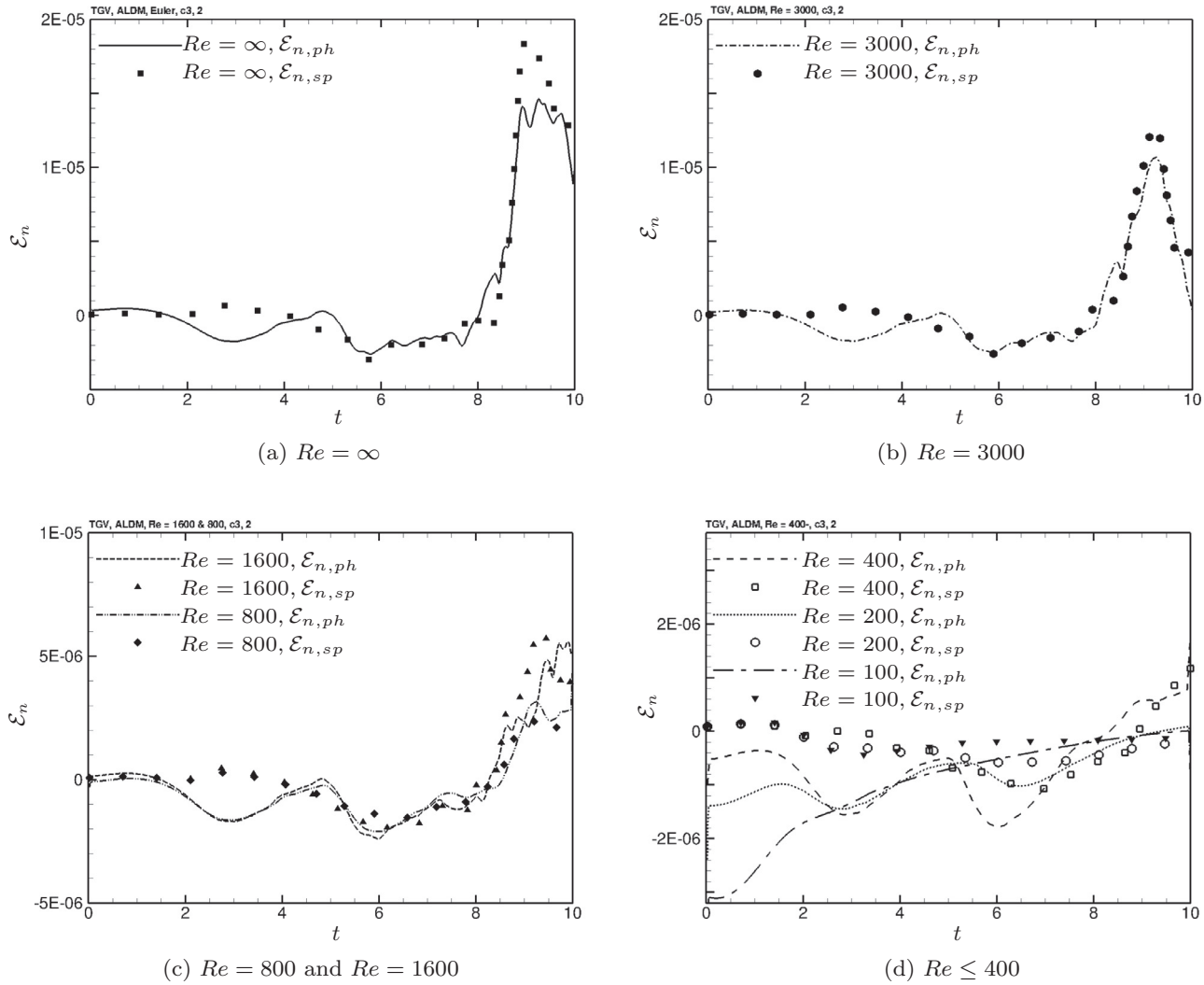

(a) $Re = \infty$ (b) $Re = 3000$

(c) $Re = 800$ and $Re = 1600$ (d) $Re \leq 400$

Fig. 10. $\varepsilon_{n,ph}(t)$ (Lines), $\varepsilon_{n,sp}(t)$ (Symbols) for CSD3.

6.1.1. Comparison of spectral and physical total effective numerical dissipation rates

The Fourier-space approach as well as the physical space approach employ the identical formulation of the rate of change of total kinetic energy and viscous dissipation rate, except that the relevant quantities, the total energy and the total viscous dissipation, are computed either in the Fourier space or the physical space representation. For the inviscid case, Eqs. (61) and (55) reduce to $-\mathcal{E}^{tot}_{n,ph} = \frac{E_{kin}(t+\triangle t)-E_{kin}(t-\triangle t)}{2\triangle t} = \frac{\triangle E_{kin}(t)}{\triangle t}|_{CD}$ and $-\widehat{\mathcal{E}}^{tot}_{n,sp}(t) = \frac{\widehat{E}(t+\triangle t)-\widehat{E}(t-\triangle t)}{2\triangle t} = \frac{\triangle \widehat{E}}{\triangle t}|_{CD}$, respectively. For this inviscid case the total dissipation rate computed in three different ways is shown in Fig. 1. Quantities $\mathcal{E}^{tot}_{n,ph}$ and $\widehat{\mathcal{E}}^{tot}_{n,sp}$ are described above. Quantity $\mathcal{E}^{tot}_{n,sp}$ is based on the rate of change of the total kinetic energy computed by the pseudo-spectral code in the physical space, i.e., Eq. (64). All three approaches are in an excellent agreement with the relative error

$$\delta_{\mathcal{E}_{n,sp}} = \frac{\mathcal{E}^{tot}_{n,ph} - \mathcal{E}^{tot}_{n,sp}}{\mathcal{E}^{tot}_{n,sp}} \tag{66}$$

between the pseudo-spectral and the physical-space approaches on the order of $\pm 0.5\%$ – hence negligible – for most of the evolution time. The error increases slightly only for a short time period around $t \approx 4$, which is the time of a rapid generation of small scales in the TGV flow. The difference between the physical space and fully spectral computations, also shown in Fig. 1, is exactly zero, as expected.

Fig. 2a–f shows comparisons among all three different methods for several finite Reynolds numbers, i.e., accounting for the explicit viscous dissipation terms in (55) and (61). All three methods produce basically the same results. The error $\delta_{\mathcal{E}_{n,sp}}$ becomes noticeable at times $t \geqslant 4$ for $Re > 400$, but is generally less than 1%. For smaller Re the evolution of small scales is inhibited and the error is uniformly small. Overall, $\delta_{\mathcal{E}_{n,sp}}$ decreases with increase of the molecular viscosity.

6.1.2. Effect of the time-step size

For determining the influence of the time-step size, we consider $\mathcal{E}^{tot}_{n,ph}(t)$ for $Re = \infty$ for which the total numerical kinetic-energy dissipation rate depends solely on the rate of change of the total kinetic energy. We compute the TGV flow with four different $\triangle t : \triangle t_1 = 0.1,\ \triangle t_2 = 0.06,\ \triangle t_3 = 0.02$ and $\triangle t_4 = 0.005$, keeping the mesh size constant, $\triangle x \approx 0.1$. While $\triangle t_1$and $\triangle t_2$ are on the order of $\triangle x$, $\triangle t_3$ and $\triangle t_4$ are much smaller than $\triangle x$. As seen in Fig. 3 $\mathcal{E}^{tot}_{n,ph}(t)$ exhibits only weak dependence on $\triangle t$ and a time-step size on the order of $\triangle t_3$ is sufficient for obtaining $\triangle t$-independent results.

6.1.3. Form of the kinetic energy transport equation

As discussed in Section 3 the numerical dissipation rate may be obtained according to two different approaches either using Eq.

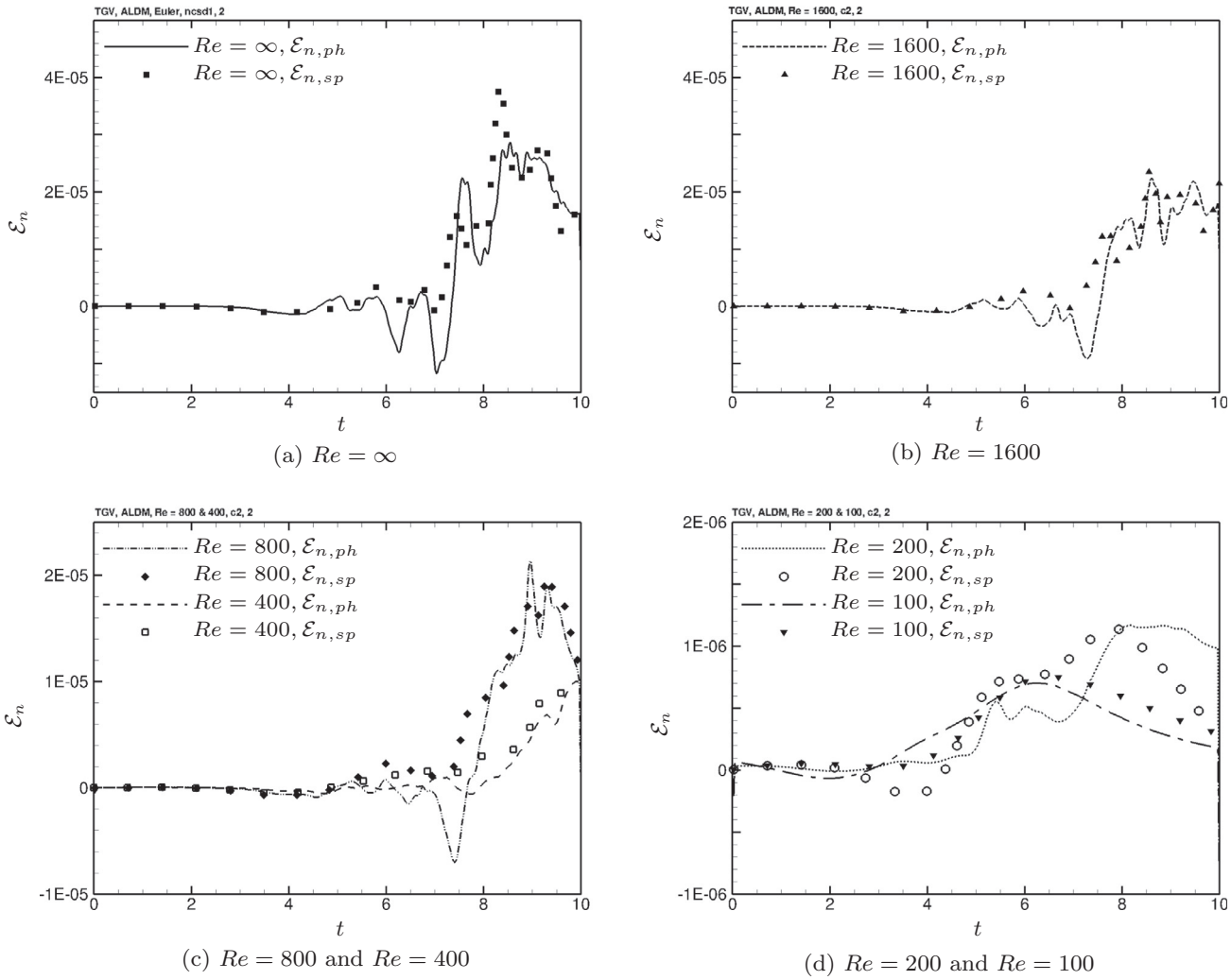

(a) $Re = \infty$ (b) $Re = 1600$

(c) $Re = 800$ and $Re = 400$ (d) $Re = 200$ and $Re = 100$

Fig. 11. $\mathcal{E}_{n,ph}(t)$ (Lines), $\mathcal{E}_{n,sp}(t)$ (Symbols) for NCSD1.

(33) or Eq. (26). For comparing $\mathcal{E}_n^{tot}(t)$ data of Eq. (33) to those of Eq. (26), we employ the second approach. We denote the respective results as $\mathcal{E}_{n,Vl}^{tot}(t)$ (the volumetric integral) and $\mathcal{E}_{n,Flx}^{tot}(t)$ (the flux form) and the relative difference as $\delta_{\mathcal{E}_{n,Flx}}$. For the evaluation of Eq. (33) cell face state reconstruction is not required, local differences, however, are approximated with the same order as in Eq. (26). We chose a finite *Re* of 3000 to account for differences in the formulation of viscous terms. As seen in Fig. 4 both evaluations lead to essentially identical results.

6.2. Analysis within subdomains

6.2.1. Self-contained flow within an octant

The symmetries of the TGV flow allow to reconstruct the whole solution from one octant. Although the octants are not periodic, the fluxes over each octant's boundary should cancel. The total flux, $F_{tot}(t) = F_{ekin}(t) + F_{ac}(t) - F_v(t)$, over the boundary of the first octant, $0 \leqslant i,j,k < 32$, for $Re = 1600$ is shown in Fig. 5 as an example. We note that $F_{ac}(t) = 0$ because $\mathbf{u}$ vanishes. It is seen that the total flux computed as described in Sections 3 and 5.1 is zero within machine precision.

Within each octant $\mathcal{E}(\mathbf{x},t), \mathcal{E}_n(\mathbf{x},t)$ as well as their derived quantities such as $v_n(\mathbf{x},t)$, reflect point-reflexion symmetry with respect to the center of the domain (see Fig. 6). The major contribution to $\mathcal{E}_{eff}(\mathbf{x},t)$ originates in subdomain $L_1 \approx \frac{1}{2}\pi,\ L_2 = L_3 = \pi$, see outlined box.

6.2.2. Arbitrary non-periodic subdomains

In Figs. 7–11 we compare results for the physical space method $\mathcal{E}_{n,ph}(t)$ and the reference solution $\mathcal{E}_{n,ps}(t)$ obtained as described in Section 5.2 on three cubic (CSD) and two non-cubic (NCSD) subdomains. Subdomains CSD1–CSD3 and NCSD1 are picked randomly. The subdomain CSD1 consists of cells from $i,j,k = 10$ to 56, CSD2 from $i,j,k = 10$ to 15, and CSD3 includes cells from 57 to 62. NCSD1 is composed of cells with $i \in [12;14]$, $j \in [14;19]$, $k \in [19;27]$. The region within octant one with non-negligible numerical dissipation is denoted NCSD2, and consists of cells $i \in [8;23], j,k \in [0;31]$.

The match between $\mathcal{E}_{n,ph}(t)$ and $\mathcal{E}_{n,sp}(t)$ within CSD1 and NCSD2 is almost perfect for the entire *Re* range and simulations times. For the three smaller subdomains $\mathcal{E}_{n,ph}(t)$ and $\mathcal{E}_{n,sp}(t)$ agree very well for medium to high Reynolds numbers, i.e. $800 \leqslant Re \leqslant 3000$. However, discrepancies become noticeable for smaller *Re*. Even though CSD2 and CSD3 have the same volume, 6^3 cells, $\mathcal{E}_{n,ph}(t)$ and $\mathcal{E}_{n,sp}(t)$ agree better in CSD2 than in CSD3 for a wide range of *Re*. However, $\mathcal{E}_n^{CSD2}(t) \gg \mathcal{E}_n^{CSD3}(t)$.

Overall, the comparison is very encouraging, clearly indicating the robustness of the analysis for moderately sized subdomains.

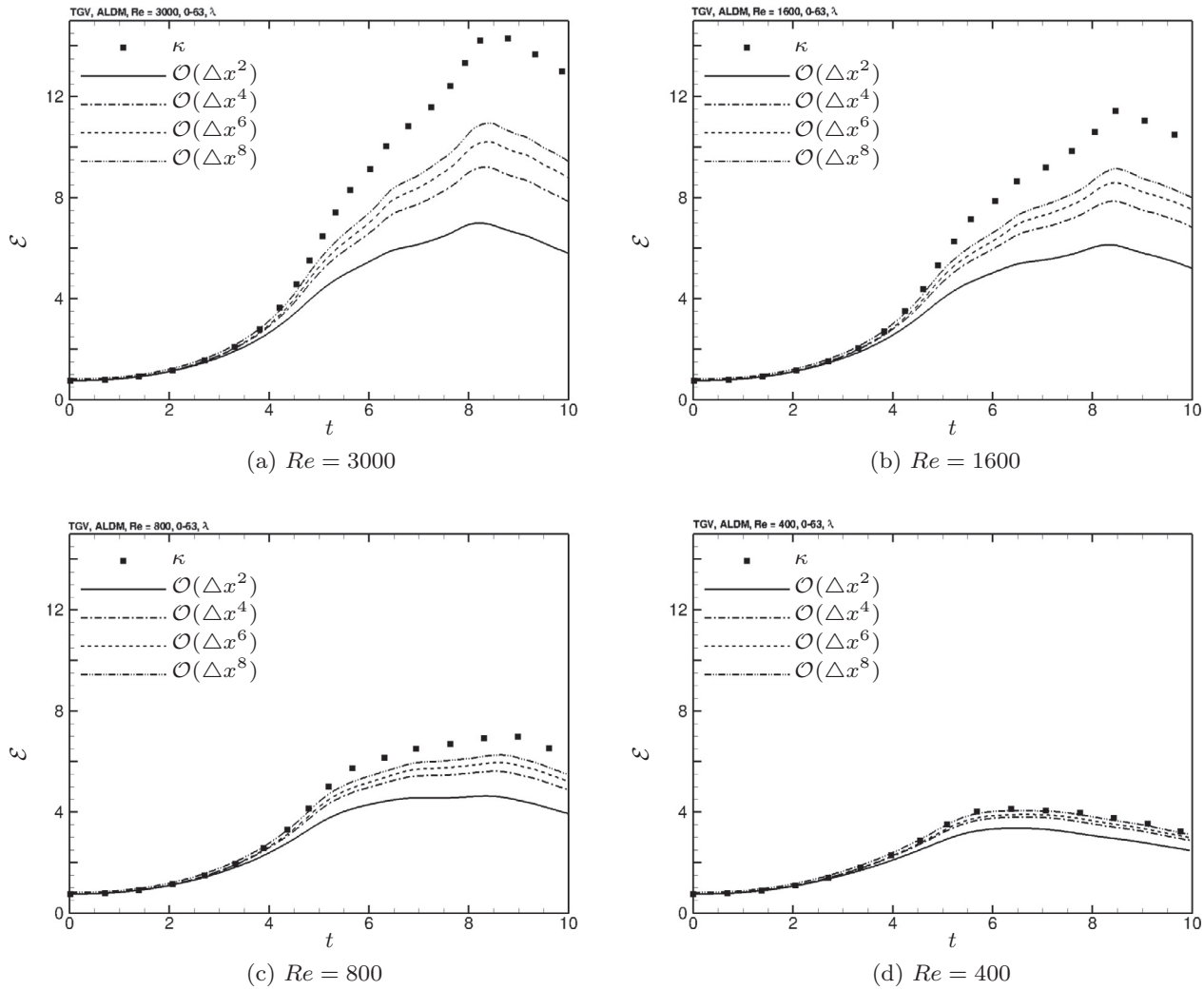

(a) $Re = 3000$ (b) $Re = 1600$

(c) $Re = 800$ (d) $Re = 400$

Fig. 12. $\mathcal{E}(t)$ (Lines), $\widehat{\mathcal{E}}_{sp}(t)$ (Symbols).

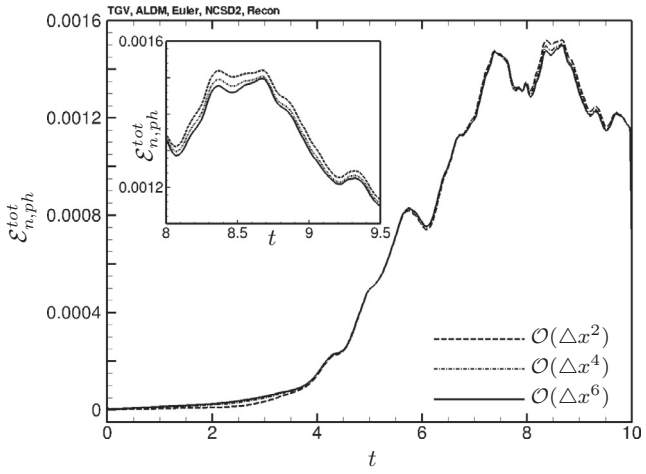

Fig. 13. $\mathcal{E}^{tot}_{n,ph}(t)$ for varying order of cell-face state reconstructions, $Re = \infty$.

7. Summary and conclusion

We have proposed a method for analyzing grid-based flow simulations for the effective numerical dissipation and local numerical viscosity of the underlying CFD solver. The method is based on computing a residual of the kinetic-energy evolution equation locally in the physical space. It generalizes previous approaches that were formulated for periodic domains in spectral-space and have required an extraneous spectral solver. The current method can serve as a post-processing tool for the quantification of numerical errors in CFD simulations in a self-contained framework.

Its capabilities have been demonstrated for three-dimensional Taylor–Green vortex flows for a large range of Reynolds numbers. Determining the total *numerical* dissipation via spectral-space analysis is more accurate than in physical-space, though limited to periodic domains. The physical-space analysis, on the other hand, estimates numerical kinetic-energy dissipation rates in very good agreement with spectral-space findings. This holds even for temporal and spatial derivative approximations of second-order accuracy, and high to infinite Reynolds number fully turbulent flows.

An excellent agreement between spectral-space and physical-space methods has also been observed for arbitrary, non-periodic domains for which the physical-space method is sought to be applied. In contrast to the spectral-space reference method, this novel physical-space method is applicable to arbitrary flows and non-uniform unstructured grids in a straightforward manner.

Moreover, we find that the choice of a time step size has negligible influence as long as the time-integration error is below or on the order of the spatial discretization error. This is generally the case for explicit time marching schemes and when a CFL condition $\mathrm{CFL} \approx 1$ is satisfied. Even for larger time-steps numerical dissipation rates are still estimated fairly accurately. Considering an especially low time-step size for the analysis is therefore not necessary. Since the method itself is conservative, the way intercell fluxes are evaluated is of no concern.

Acknowledgments

We acknowledge the Deutsche Forschungsgemeinschaft (DFG) for funding. JAD wishes to thank the Alexander von Humboldt Foundation for supporting his visit to Technical University of Munich, where this research has been initiated. Additional support was provided by the NSF Grant No. 1233160. FSS is member of the Technische Universität München (TUM) Graduate School.

Appendix A

A.1. The influence of the order of spatial differentiation

In addition to numerical errors introduced by the flux terms in the energy balance Eq. (26), the viscous dissipation term $\mathcal{E}_v = \nu\mathcal{E}$ is also affected by truncation errors when using discrete FD/FV operators. However, since $\mathcal{E}$ is positive-definite and one is usually interested in the numerical dissipation in excess of the viscous dissipation produced already by a given code, the error in computing $\mathcal{E}$ is of less interest than errors introduced by the remaining terms in the energy balance equation. For the comparison of FD/FV results with spectral reference data, the exact wavenumbers in Eq. (43) were replaced with the appropriate modified wavenumbers to account for the approximation of spatial derivatives in physical space. This forces the viscous dissipation computed with spectral formulas (using modified wavenumbers) to be equal to the viscous dissipation computed using difference formulas. Effectively, in our tests, the total dissipation is the sum of the resolved viscous dissipation and the numerical dissipation caused by discrete approximations of the terms in the energy balance Eq. (26) other than $\mathcal{E}_v$. Furthermore, while the explicit calculation of the viscous dissipation contribution for a given code is straightforward, computing the viscous dissipation with spectral accuracy would always require an external spectral code, which is to be avoided. Nevertheless, in this work we can compute the numerical dissipation with spectral accuracy $\widehat{\mathcal{E}}_{v,sp}(t)$ using spectral expressions defined in Section 4.1 (using the actual, un-modified wavenumber κ). Such results are presented below for completeness.

The difference between $\widehat{\mathcal{E}}_{sp}(t)$ and the approximate $\mathcal{E}(t)$ increases with the presence of small-scale structures, see Figs. 12a–d. $\widehat{\mathcal{E}}_{sp}$ is always larger than $\mathcal{E}$ because κ is always equal or larger than the modified wave number. Higher-order approximations to spatial differences predict $\mathcal{E}(t)$ more accurately. Finally, the approximation also improves for well resolved flows, either at the initial times when primarily large scale modes are active, or for decreasing Reynolds numbers when the flow remains laminar.

A.2. On the order of reconstruction of the cell-face states

In certain cases a flow configuration under investigation may not permit computing the flux terms described in Section 3 based on high-order reconstructed cell-face states. We are thus evaluating the influence of the order of the reconstruction when choosing more local stencils based on considering $\mathcal{E}^{tot}_{n,ph}(t)$ for $Re = \infty$ in NCSD2.

Besides the sixth-order reconstruction (60) we have employed a second-order central, i.e., $f_{i\pm\frac{1}{2}} = \frac{1}{2}(f_i + f_{i\mp1})$, and a fourth-order central, i.e., $f_{i\pm\frac{1}{2}} = \frac{1}{16}(-f_{i\pm1} + 9f_i + 9f_{i\mp1} - f_{i\mp2})$, scheme to obtain cell face states.

The resulting $\mathcal{E}^{tot}_{n,ph}(t)$ are depicted in Fig. 13. For most of the time, especially within the transitional period, identical numerical dissipation rates are predicted with all three schemes. Only for short periods of time marginal differences among different methods can be observed, e.g., for $t \in [8; 9.5]$ the relative difference of $\mathcal{E}^{tot}_{n,ph}$ computed with second-order reconstructions to the one based on sixth-order reconstructions is within 2.8%.

Appendix B. Supplementary material

Supplementary data associated with this article can be found, in the online version, at http://dx.doi.org/10.1016/j.compfluid.2015.02.011.

References

[1] Boris J, Grinstein F, Oran E, Kolbe R. New insights into large eddy simulation. Fluid Dyn Res 1992;10:199–228.
[2] Grinstein F, Margolin L, Rider W. Implicit large eddy simulation. Cambridge University Press; 2007.
[3] Sweby P. High resolution schemes using flux limiters for hyperbolic conservation laws. SIAM J Numer Anal 1984;21:995.
[4] Zalesak S. Fully multidimensional flux-corrected transport algorithms for fluids. J Comput Phys 1979;31:335.
[5] Harten A, Engquist B, Osher S, Chakravarthy SR. Uniformly high-order accurate essentially non-oscillatory schemes III. J Comput Phys 1987;71:231.
[6] Minguez M, Pasquetti R, Serre E. Spectral vanishing viscosity stabilized LES of the Ahmed body turbulent wake. J Comput Phys 2009;5:635–48.
[7] Boyd JP. Chebyshev and Fourier spectral methods. Mineola (New York): Dover; 2001.
[8] Bogey C, Bailly C. Large eddy simulations of transitional round jets: influence of the Reynolds number on the flow development and energy dissipation. Phys Fluids 2006;18:065101.
[9] Porter D, Woodward P. High resolution simulations of compressible convection using the piecewise-parabolic method. Astrophys J 1994;93:309–49.
[10] Garnier E, Mossi M, Sagaut P, Comte P, Deville M. On the use of shock-capturing schemes for large-eddy simulation. J Comput Phys 1999;153:273–311.
[11] Domaradzki J, Radhakrishnan S. Effective eddy viscosities in implicit modeling of decaying high Reynolds number turbulence with and without rotation. Fluid Dyn Res 2005;36:385–406.
[12] Smolarkiewicz P, Margolin L. MPDATA: a finite-difference solver for geophysical flows. J Comput Phys 1998;140:459–80.
[13] Domaradzki JA, Xiao Z, Smolarkiewicz P. Effective eddy viscosities in implicit large eddy simulations of turbulent flows. Phys Fluids 2003;15:3890–3.
[14] Diamessis P, Lin Y, Domaradzki J. Effective numerical viscosity in spectral multidomain penalty method-based simulations of localized turbulence. J Comput Phys 2008;227:8145–64.
[15] Hickel S, Adams NA, Domaradzki JA. An adaptive local deconvolution method for implicit LES. J Comput Phys 2006;213:413–36.
[16] Zhou Y, Grinstein FF, Wachtor AJ, Haines BM. Estimating the effective Reynolds number in implicit large-eddy simulation. Phys Rev E 2014;89:013303. <http://link.aps.org/doi/10.1103/PhysRevE.89.013303>.
[17] Plancherel M. Contribution a l'etude de la representation d'une fonction arbitraire par les integrales dfinies. Rendi Circ Mate Palermo 1910;30:298–335.
[18] Taylor AGGI. Mechanism of the production of small eddies from larger ones. Proc R Soc Lond A 1937;158:499–521.
[19] Gottlieb S, Shu C-W. Total variation diminishing Runge–Kutta schemes. Math Comput 1998;67(221):73–85. ISSN 0025-5718(98)00913-2.

B.3 Optimization of an Implicit Large-Eddy Simulation Method for Underresolved Incompressible Flow Simulations

AIAA JOURNAL
Vol. 54, No. 5, May 2016

Optimization of an Implicit Large-Eddy Simulation Method for Underresolved Incompressible Flow Simulations

Felix S. Schranner,* Vladyslav Rozov,† and Nikolaus A. Adams‡
Technische Universität München, 85748 Garching, Germany

DOI: 10.2514/1.J054741

In engineering applications, resolution is often low. In these underresolved regions, the truncation error of the underlying numerical schemes strongly affects the solution. If the truncation error functions as a physically consistent subgrid-scale model (that is, it models the evolution of otherwise resolved scales), resolution may remain low. Thereby, computational efficiency is improved. The sixth-order adaptive central-upwind weighted essentially nonoscillatory scheme with implicit scale separation, denoted as WENO-CU6-M1, potentially allows for physically consistent implicit subgrid-scale modeling, when shaped accordingly. In this work, finding an optimal formulation of WENO-CU6-M1 is considered within a deterministic design optimization framework. Possible surrogate modeling and sampling strategies are considered. Design optimization is based on evaluating the potential of a WENO-CU6-M1 scheme formulation to reproduce Kolmogorov scaling for a Taylor–Green vortex in its quasi-isotropic state. As in the absence of physical viscosity, kinetic energy dissipates exclusively due to the subgrid-scales, the Reynolds number is infinite, and the evolution of the flow is determined by proper subgrid-scale modeling. To complete the work, the effective numerical dissipation rate of the WENO-CU6-M1 model optimized for artificially compressible fluid flows is quantified, and it is compared to the original one. Not only is the zero viscosity limit considered, but the model behavior is benchmarked offdesign, for low to high Reynolds numbers. A comparison to an alternative explicit and implicit subgrid-scale model demonstrates its superior behavior for the chosen test flow.

I. Introduction

MODIFIED differential equation analysis (MDEA) [1] has shown that the truncation error of nonlinear discretization schemes can be constructed to represent an implicit subgrid-scale (SGS) model for turbulent flows [2]. The nonlinear regularization mechanism of high-order finite volume schemes with shock-capturing capabilities can be employed for implicit large-eddy simulations (ILES). For a review refer to [3]. On the basis of a spectral extension of the MDEA, the truncation error of a nonlinear scheme has been designed to recover the theoretical spectral eddy viscosity when the flow is turbulent and underresolved. Such a situation, where the nonnegligible local truncation error of a numerical scheme recovers correct physical SGS behavior, is called physically consistent behavior [4,5].

Hu et al. [6] proposed a weighted, essentially nonoscillatory (WENO) scheme combining the advantages of an upwind scheme, e.g., the fifth-order WENO scheme [7], and a sixth-order central scheme. It adaptively alters its biasing between central and upwind by evaluation of the smoothness indicators of the optimal higher-order stencil and lower-order upwind stencils. Thereby, it decreases numerical dissipation in smooth flow regions and permits a numerically stable solution in nonsmooth flow regions while preserving shock-capturing capabilities. It is denoted as WENO-CU6. Hu and Adams [8] investigated the physical consistency of the underresolved contribution of WENO-CU6. Based thereupon, a central-upwind WENO scheme with implicit SGS modeling capabilities has been developed [8]; it is denoted as WENO-CU6-M1.

Schranner et al. [9] identified that WENO-CU6-M1 offers a set of free parameters, enabling implicit subgrid-scale modeling by controlling scale separation of resolved and nonresolved scales for compressible as well as incompressible flows. In combination with the material modeling, i.e., equation of state (EOS), and an appropriate Riemann solver, an adjustment of the model permits recovery of self-similar isotropic turbulence when physical viscosity diminishes.

A method that quantifies the effective numerical dissipation rate $\mathscr{E}^n$ and effective numerical viscosity ν^n in computational fluid dynamics was proposed in [10]. It permits a straightforward quantitative evaluation of SGS modeling capabilities of a numerical algorithm.

The objective of this work is to determine an optimal combination of the WENO-CU6-M1 modeling parameters by means of design optimization (DO). The notion of being optimal implies that the transition is predicted physically consistently and inertial subrange scaling, which is characteristic of isotropic turbulence, is recovered as most optimal when dissipating energy only within the SGS. On the basis of an optimal WENO-CU6-M1 weighting, we are stating a physically consistent implicit large-eddy simulation (LES) model for incompressible, underresolved flows. Proceeding forward, the effective numerical dissipation rates of the optimal and original WENO-CU6-M1 scheme are compared. We thereby demonstrate that optimization of a quantifiable spectral-space norm entails improvements in a physical-space norm. Subsequently, we evaluate the offdesign behavior of the optimized WENO-CU6-M1 model by comparing simulation results of low to high, yet finite, Reynolds number Re Taylor–Green vortex (TGV) [11] flows to direct numerical simulation (DNS) data [12,13]. Furthermore, benchmarking to established explicit and implicit SGS models at these Reynolds numbers is included.

II. Model Formulation

A. Artificial Compressibility Approach

At Mach numbers of $Ma \ll 1$, compressibility is negligible. This means that the compressibility β, relating the relative change of density to the change of pressure, is almost zero:

$$\beta = \frac{1}{\rho}\frac{\partial \rho}{\partial p} \approx 0$$

Presented as Paper 2016-3205 at the 54th AIAA Aerospace Sciences Meeting, AIAA Science and Technology Forum and Exposition 2016, San Diego, CA, 4–8 January 2016; received 8 September 2015; revision received 10 December 2015; accepted for publication 14 December 2015; published online 25 February 2016.

*Research Associate, Institute of Aerodynamics and Fluid Mechanics. Student Member AIAA.
†Research Associate, Institute of Aerodynamics and Fluid Mechanics.
‡Professor Ordinarius, Institute of Aerodynamics and Fluid Mechanics. Member AIAA.

In contrast to classical incompressible approaches, claiming $\beta = 0$, the artificial compressibility approach (ACA) of Chorin [14] and Temam [15] assumes a nonzero yet constant compressibility. Such flows may be considered weakly compressible. The isentropic compressibility relates to the sound speed by

$$a^2 = \frac{1}{\rho\beta|_s}$$

For isothermal processes. $\beta = \beta|_T = \beta|_s$; and the ratio of specific heats κ is one. The pressure and density are linearly related by the caloric EOS $p = p(\rho) = a^2\rho$ for these artificially compressible fluids. It is evident that density fluctuations are small if a is sufficiently large.

B. Numerical-Flux Computation Adapted to Weakly Compressible Fluid Treatment

Within the ACA, the energy equation is decoupled from the continuity and momentum equations. Thus, the flow is governed by equations for the conservation of mass and momentum only. In one dimension (for simplicity), $\boldsymbol{U} = (\rho, \rho u)$ is the solution of

$$\frac{\partial \boldsymbol{U}}{\partial t} + \frac{\partial}{\partial x}\boldsymbol{F}(\boldsymbol{U}) = 0 \tag{1}$$

In a discrete space-time domain, the discrete conservation equation

$$\hat{\boldsymbol{U}}_{[i]}^{n+1} = \hat{\boldsymbol{U}}_{[i]}^{n} + \frac{\Delta t}{\Delta x_{[i]}}\left(\bar{\boldsymbol{F}}_{[i-(1/2)]} - \bar{\boldsymbol{F}}_{[i+(1/2)]}\right) \tag{2}$$

for the cell-averaged solution

$$\hat{\boldsymbol{U}}_{[i]} = \frac{1}{\Delta x_{[i]}}\int_{\Delta x_{[i]}} \boldsymbol{U}_{[i]}^{n}\,\mathrm{d}x$$

requires approximations of the cell-face fluxes

$$\bar{\boldsymbol{F}}_{[i\pm(1/2)]} = \frac{1}{\Delta t}\int_{t^n}^{t^{n+1}} \boldsymbol{F}_{[i\pm(1/2)]}\,\mathrm{d}t = \frac{1}{\Delta t}\int_{t^n}^{t^{n+1}} \boldsymbol{F}\left(\boldsymbol{U}_{[i\pm(1/2)]}\right)\mathrm{d}t \tag{3}$$

where Δt is sufficiently small. Note that, generally, the flux vectors include advective and viscous components: $\bar{\boldsymbol{F}} = \bar{\boldsymbol{F}}^a - \bar{\boldsymbol{F}}^\nu$. Computation of $\bar{\boldsymbol{F}}^\nu$ is straightforward within the scope of this work and at fourth-order accuracy.

A low-dissipation advective flux approximation is due to the Roe [16] approximate Riemann solver, which is used within the scope of this work. The key idea of this class of solvers is using the linearized local flux Jacobian $\tilde{\boldsymbol{A}} = \tilde{\boldsymbol{A}}(\bar{U}^{(l)}, \bar{U}^{(r)})$. The high-order reconstructed conservative states at the left and right sides of the cell face are denoted by $[i \pm (1/2)](l)$ and (r). The eigenvalues of $\tilde{\boldsymbol{A}}$, $\tilde{\lambda}^{(j)}(\bar{U}^{(l)}, \bar{U}^{(r)})$, and right eigenvectors $\tilde{\boldsymbol{K}}^{(j)}(\bar{U}^{(l)}, \bar{U}^{(r)})$ are determined (see Appendix A), so that the Roe numerical flux can be computed as

$$\bar{\boldsymbol{F}}_{[i+(1/2)]} = \frac{1}{2}\left(\bar{\boldsymbol{F}}(\bar{\boldsymbol{U}}^{(l)}) + \bar{\boldsymbol{F}}(\bar{\boldsymbol{U}}^{(r)})\right) - \frac{1}{2}\sum_{j=1}^{m}\tilde{\delta}^{(j)}|\tilde{\lambda}^{(j)}|\tilde{\boldsymbol{K}}^{(j)} \tag{4}$$

where $\tilde{\delta}^{(j)}$ denotes the wave strengths.

C. Time Integration and Time-Step Constraints

The conservation equations [Eq. (2)] are integrated explicitly in time with a third-order total variation diminishing Runge–Kutta scheme [17]. The time step is chosen adaptively as

$$\Delta t = \mathrm{CFL} \cdot \min(\Delta t^a; \Delta t^\nu) \tag{5}$$

with a Courant–Friedrichs–Lewy (CFL) of 0.3:

$$\Delta t^a = \frac{\min(\Delta x_\alpha)}{\max|u_\alpha + a|}$$

and $\Delta t^\nu = \frac{3}{14}Re(\min(\Delta x_\alpha))^2$ where α represents one of the spatial directions.

D. Reconstructing Cell-Face States and WENO-CU6-M1 Weighting

To obtain $\bar{\boldsymbol{U}}_{[i\pm(1/2)]}^{(\alpha)}$, where α is either l or r, weighted essentially nonoscillatory schemes [18] define m reconstruction polynomials for nonaveraged conservative cell-face vector candidates

$$\boldsymbol{u}_{[i+(1/2)]}^{(\alpha,\gamma)} = \sum_{j=0}^{m-1} c_{\gamma,j}\hat{\boldsymbol{U}}_{i-\gamma+j}, \qquad \gamma = 0, ..., m-1 \tag{6}$$

on m candidate stencils $S_\gamma[i] \equiv \{\hat{\boldsymbol{U}}_{[i-\gamma]}, \ldots, \hat{\boldsymbol{U}}_{[i]}, \ldots, \hat{\boldsymbol{U}}_{[i-\gamma+m-1]}\}$ in the vicinity of the cell face and combine these convexly according to

$$\bar{\boldsymbol{U}}_{[i\pm(1/2)]}^{(\alpha)} = \sum_{\gamma=0}^{m-1}\omega_\gamma^{(\alpha)}\boldsymbol{u}_{i+(1/2)}^{(\alpha,\gamma)} \tag{7}$$

Hereby, the set of nonlinear weights $\{\omega_\gamma^{(\alpha)}\}$ satisfying

$$\omega_\gamma^{(\alpha)} \geq 0, \qquad \sum_{\gamma=0}^{m-1}\omega_\gamma^{(\alpha)} = 1$$

ensures stability and consistency. Jiang and Shu [7] have formulated computationally efficient weights such that these are C^∞, i.e., smooth functions of the involved cell averages:

$$\omega_\gamma^{(\alpha)} = \frac{\alpha_\gamma^{(\alpha)}}{\sum_{s=0}^{m-1}\alpha_s^{(\alpha)}}, \alpha_\gamma^{(\alpha)} = f(d_\gamma, \beta_\gamma^{(\alpha)}) \tag{8}$$

where d_β and $\beta_\gamma^{(\alpha)}$ are the ideal weights and smoothness indicators, respectively.

"The smoothness indicators diminish with increasing smoothness of the solution on a stencil" [9]. In defining α_γ, the core idea is to consider each of the $\boldsymbol{u}_{i+(1/2)}^{(\gamma)}$ according to their smoothness by weighting them appropriately. Thereby, $\omega_\gamma^{(\alpha)}$ approximates d_β. Yet, if $\boldsymbol{u}(x)$ was to contain a discontinuity in at least one of the stencils $S_\gamma[i]$, leading to $\beta_\gamma^{(\alpha)} = \mathcal{O}(1)$, the corresponding weights $\omega_\gamma^{(\alpha)}$ need to diminish to exclude the approximation $\boldsymbol{u}_{i+(1/2)}^{(\gamma)}$, and thereby keep the overall nonoscillatory behavior. The WENO weighting factors $\alpha_\gamma^{(\alpha)}$ of Jiang and Shu [7] fulfill these requirements:

$$\alpha_\gamma^{(\alpha)} = \frac{d_\gamma}{(\epsilon + \beta_\gamma^{(\alpha)})^q} \tag{9}$$

The WENO-CU6-M1 weights, a further development of the original WENO weights (9), remedy excessive dissipation of the underlying WENO-CU6 scheme while preserving its shock-capturing properties, and thus allow recovery of physical consistency for both the solenoidal and the dilatational components of the velocity field, without the need to explicitly distinguish these; see, e.g., [8]. The WENO weighting factors of the WENO-CU6-M1 scheme are

$$\alpha_\gamma^{(\alpha)} = d_\gamma\left(C_q + \frac{\tau_6^{(\alpha)}}{\epsilon + \beta_\gamma^{(\alpha)}}\right)^q, \qquad \gamma = 0, \ldots, 3, \tag{10}$$

where the reference smoothness indicator is

$$\tau_6^{(\alpha)} = \beta_3^{(\alpha)} - \frac{1}{6}(\beta_0^{(\alpha)} + 4\beta_1^{(\alpha)} + \beta_2^{(\alpha)})$$

see, therefore, [6,19]. Also, $\boldsymbol{u}_{i+(1/2)}^{(\alpha,\gamma)}$, d_γ, and $\beta_\gamma^{(\alpha)}$ with $\gamma = 0, 1, 2$ are identical to the ones of the fifth-order WENO scheme, which can be found in Appendix B; $\boldsymbol{u}_{i+(1/2)}^{(\alpha,3)}$, d_3, $\beta_3^{(\alpha)}$, as well as the four ideal weights, may be found in Appendix C.

To allow for weights in nonsmooth stencils to approach zero at an accelerated rate as $\Delta x \to 0$, the integer power exponent q has to be chosen accordingly. In the original formulations [6,7], the integer

power exponent q is a free parameter that does not affect the order of the numerical truncation error. It does, however, control the amount of nonlinear dissipation [20], which increases with q; see [21]. According to [7], an integer of $q \geq 1$ is chosen in order to push the weight of the nonsmooth stencil to zero as $\Delta x \to 0$. In [22], it has been suggested to use $q = m$, with $2m - 1$ being the order of accuracy. However, Jiang and Shu [7] find by "extensive numerical experiments" [7] that $q = 2$ is adequate to obtain essentially nonoscillatory approximation for $m \leq 3$. Gerolymos et al. [21] have experimented with varying q for $m \leq 9$. They found that q had to increase with increasing m to obtain essentially nonoscillatory behavior.

$C_q \gg 1$ emphasizes the contribution of optimal weights when the smoothness indicators are of similar magnitude [6,23]. Higher values for C_q reduce numerical dissipation [8]. For compressible, isotropic turbulence, inertial range scaling is obtained for $C_q = 1{,}000$ [8]. Schranner et al. [9] identified that a proper choice of $(C_q; q)$ potentially enabled implicit subgrid-scale modeling, not only for compressible flows but for a wide range of material fluid models. Note that $\epsilon > 0$ has the purpose of ensuring a nonzero denominator.

III. Optimization

A. Statement of the Problem

For a given material modeling and Riemann solver, an optimal combination of $(C_q; q)$ is sought so that the thereby stated implicit LES model is fulfilling the following two design requirements best: First, transitioning of the incompressible, physically inviscid, originally two-dimensional Taylor–Green vortex [11],

$$\begin{aligned} u_1(x,y,z,0) &= \sin(x)\cos(y)\cos(z),\\ u_2(x,y,z,0) &= -\cos(x)\sin(y)\cos(z),\\ u_3(x,y,z,0) &= 0,\\ \rho(x,y,z,0) &= 1.0,\\ p(x,y,z,0) &= 100 + \frac{1}{16}[(\cos(2x)+\cos(2y))(2+\cos((2z)) - 2] \end{aligned} \tag{11}$$

defined within a periodic domain, to three-dimensional statistically isotropic turbulence [24] must occur. Completion of transition is expected at $t \approx 9$ s. Second, and as a consequence of proper transition, a Kolmogorov scaling inertial subrange, i.e.,

$$E(k) = C\epsilon^{2/3}k^{-5/3} \tag{12}$$

ought to be recovered most optimally.

The linear weight bias C_q and the power exponent q define the parameter set $\boldsymbol{x} = (C_q; q)$. Based on [8,9], we expect the global optimum within the parameter domain $\boldsymbol{X} = 1{,}000 \leq C_q \leq 20{,}000\times$ $1 \leq q \leq 20$.

The quality of a sample (model) is evaluated on the basis of the total least-squares difference [25,26] between the numerically simulated $E[k_i]$ and the theoretical $E(k_i)$ as

$$z(\boldsymbol{x}) = \sum_{i=n}^{m} (E[k_i] - E(k_i))^2 \tag{13}$$

where n and m mark the first and last wave number of the inertial subrange. Within the scope of this work, $n = 2$ and $m = 32$, where the latter is equivalent to the Nyquist wave number. The $\boldsymbol{x}$ with the global $\min(z(\boldsymbol{x}))$ (i.e., showing best fitness) is sought. The fitness function [Eq. (13)] is evaluated at $t = 10$.

B. Optimization Strategy

Simulating a TGV evolution up to $t = 10$ for a possible sample requires approximately 63 min on a dual-socket Intel SandyBridge-EP Xeon E5–2670 node. Furthermore, up to this venue, the characteristics of the response surface (RS) corresponding to Eq. (13) within $\boldsymbol{X}$ are unknown.

1. Surrogate Modeling

A variety of optimization approaches, deterministic and stochastic, exist. The choice of method primarily depends on the optimization task [27]. Stochastic approaches, such as evolutionary algorithms, have the advantage of coping with discontinuous fitness functions or when noise is severe [28]; yet, potentially, a large number of samples needs to be evaluated. Deterministic approaches are commonly gradient based. The common properties of these are that an optimum is generally found and the number of iterations therefore is comparably low when the response surface is shaped appropriately. Yet, when the optimization task is not confined enough (that is, when the response surface contains several local optima apart from the global optimum), gradient-based approaches are likely to find a local one [29].

The response surface approach, considered within the scope of this work, leads to continuous surrogate models. Within the deterministic surrogate model framework, the response surface is approximated with a simplified model. For such a surrogate model, a system response [i.e., $z(\boldsymbol{x})$, for any $\boldsymbol{x} \in \boldsymbol{X}$] is at hand instantly and at a low numerical cost. To differentiate the ILES system response from the surrogate model response, the latter will be denoted as $\hat{z}(\boldsymbol{x})$. Within the scope of this work, two approaches have been selected for further testing regarding their applicability to the optimization task formulated in Sec. III.A. Both the response surface approximation by polynomial regression (PR) and the radial basis function interpolation (RBFI) models qualify, as they are both robust, simple, and easy to code. This does not hold for artificial neural networks.

2. Response Surface Approximation by Polynomial Regression

Response surface approximation by polynomials is a regression approach, which implies that, generally, $\hat{y}(\boldsymbol{x}) \neq y(\boldsymbol{x})$, $\forall \boldsymbol{x} \in \boldsymbol{X}$. Moreover, the degrees of freedom are fewer, leading to an overdetermined system of equations. Let

$$\begin{aligned} \hat{y}(\boldsymbol{x}) &= b_0 + b_1x_1 + b_2x_2 + b_3x_1x_2 + b_4x_1^2 + b_5x_2^2 + \ldots\\ &= \sum_{k=0}^{n} b_k p_k(\boldsymbol{x}) \end{aligned} \tag{14}$$

be the polynomial that approximates the response surface with a desired order. To derive the model, the unknown polynomial coefficients b_k are determined by minimizing the least-squares difference of $\hat{y}(\boldsymbol{x})$ and $y(\boldsymbol{x})$:

$$\begin{aligned} z(\boldsymbol{x}) &= \sum_{j=0}^{m} e_j^2 = \sum_{j=0}^{m} (y(\boldsymbol{x}_j) - \hat{y}(\boldsymbol{x}_j))^2\\ &= \sum_{j=0}^{m} \left(y(\boldsymbol{x}_j)^2 - \sum_{k=0}^{n} b_k p_k(\boldsymbol{x}_j) \right)^2 \end{aligned} \tag{15a}$$

which in vector notation reads

$$z(\boldsymbol{x}) = \boldsymbol{e}^T \cdot \boldsymbol{e} = (\boldsymbol{y} - \boldsymbol{P}\boldsymbol{b})^T \cdot (\boldsymbol{y} - \boldsymbol{P}\boldsymbol{b}) \tag{15b}$$

Herein,

$$\boldsymbol{e} = \begin{pmatrix} e_0 \\ e_1 \\ \vdots \\ e_m \end{pmatrix}, \quad \boldsymbol{y} = \begin{pmatrix} y_0 \\ y_1 \\ \vdots \\ y_m \end{pmatrix}, \quad \boldsymbol{b} = \begin{pmatrix} b_0 \\ b_1 \\ \vdots \\ b_n \end{pmatrix},$$

$$\boldsymbol{P} = \begin{pmatrix} 1 & p_{0,1} & \cdots & p_{0,n} \\ 1 & p_{1,1} & \cdots & p_{1,n} \\ \vdots & \ddots & \vdots & \\ 1 & p_{m,n} & \cdots & p_{m,n} \end{pmatrix} \tag{16}$$

Note that $m \geq n$. Minimizing of the objective function [Eq. (15)] is achieved by solving

$$\frac{\partial z(\boldsymbol{x})}{\partial \boldsymbol{b}} = \frac{\partial(\boldsymbol{e}^T\boldsymbol{e})}{\partial \boldsymbol{b}} = \frac{\partial\left(\sum_{j=0}^{m} e_j^2\right)}{\partial b_k} = 0 \tag{17}$$

from which the coefficients are determined. Therefore, one evaluates

$$\boldsymbol{b} = (\boldsymbol{P}^T\boldsymbol{P})^{-1}\boldsymbol{P}^T\boldsymbol{y} \tag{18}$$

3. Interpolation of the Response Surface via Radial Basis Functions

When interpolating a higher-order response surface from samples of an nth-order RS via radial basis functions (RBFs), it is

$$\hat{y}(\boldsymbol{x}) = y(\boldsymbol{x}), \quad \forall\, \boldsymbol{x} \in \boldsymbol{X} \tag{19}$$

RBFs are local, such that their value at $\boldsymbol{x}_j$ is only a function of the distance to its origin $\boldsymbol{x}_i$:

$$\phi(\boldsymbol{x}_i, \boldsymbol{x}_j) = \phi(\|\boldsymbol{x}_i - \boldsymbol{x}_j\|) = \phi(r_{ij}) \tag{20}$$

A simple RBF, which allows for easy coding of a straightforward solution algorithm, results in a C^∞ response surface, and has been demonstrated to deliver sufficiently accurate results is the thin-plate spline, [30]

$$\phi(r_{ij}) = \begin{cases} r_{ij}^2 \log(r_{ij}) & r_{ij} \neq 0, \\ 0 & r_{ij} = 0 \end{cases} \tag{21}$$

At each contributing sample point $\boldsymbol{x}_i$, an ω_i-weighted RBF is stated. The sum of all weighted RBFs constitutes the two-dimensional RS approximation according to [31]

$$\begin{aligned} \hat{y}(\boldsymbol{x}_j) &= b_0 + b_1 x_{1,j} + b_2 x_{2,j} + \sum_{i=0}^{m} \omega_i \phi(\boldsymbol{x}_i, \boldsymbol{x}_j) \\ &= \sum_{i=0}^{2} b_i p_i(\boldsymbol{x}_j) + \sum_{i=0}^{m} \omega_i \phi_{ij} = \hat{y}_j \end{aligned} \tag{22}$$

where the weights ω_i as well as polynomial coefficients b_0, b_1, and b_2 are to be determined such that Eq. (19) is fulfilled. Note that m is the number of sample or support points. Furthermore,

$$\sum_{i=0}^{m} p_{ji}\omega_i = 0 \tag{23}$$

Equation (22) and condition (23) constitute a linear system of equations

$$\begin{pmatrix} \boldsymbol{\Phi} & \boldsymbol{P} \\ \boldsymbol{P}^T & \boldsymbol{O} \end{pmatrix} \cdot \begin{pmatrix} \boldsymbol{w} \\ \boldsymbol{b} \end{pmatrix} = \boldsymbol{L} \cdot \begin{pmatrix} \boldsymbol{w} \\ \boldsymbol{b} \end{pmatrix} = \begin{pmatrix} \boldsymbol{y} \\ \boldsymbol{o} \end{pmatrix} \tag{24}$$

where

$$\boldsymbol{\Phi} = \begin{pmatrix} \phi_{00} & \cdots & \phi_{0\,m} \\ \phi_{10} & \cdots & \phi_{1\,m} \\ \vdots & \ddots & \vdots \\ \phi_{m0} & \cdots & \phi_{mm} \end{pmatrix}, \qquad \boldsymbol{P} = \begin{pmatrix} 1 & x_{1,0} & x_{2,0} \\ \vdots & \vdots & \vdots \\ 1 & x_{1,m} & x_{2,m} \end{pmatrix},$$

$$\boldsymbol{w} = \begin{pmatrix} \omega_0 \\ \vdots \\ \omega_m \end{pmatrix}, \qquad \boldsymbol{b} = \begin{pmatrix} b_0 \\ b_1 \\ b_2 \end{pmatrix}, \qquad \hat{\boldsymbol{y}} = \begin{pmatrix} \hat{y}(\boldsymbol{x}_j) \\ \vdots \\ \hat{y}(\boldsymbol{x}_m) \end{pmatrix} \tag{25}$$

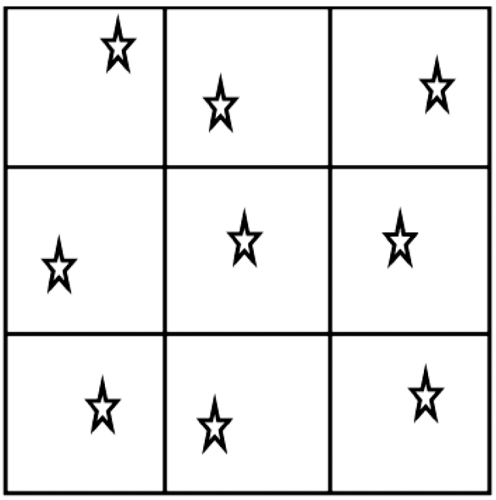

Fig. 1 Full factorial design within a two-dimensional parameter space X and three levels.

$\boldsymbol{O}$ and $\boldsymbol{o}$ are a 3×3 matrix and a 3×1 vector of zeros. Note that the polynomial terms are necessary to ensure that $\boldsymbol{L}$ is nonsingular [32]. For a small number of sampling points, as within the scope of this work, one may directly evaluate the polynomial coefficients and weights as

$$\boldsymbol{b} = (\boldsymbol{P}^T\boldsymbol{\Phi}^{-1}\boldsymbol{P})^{-1}\boldsymbol{P}^T\boldsymbol{\Phi}^{-1}\boldsymbol{y}, \qquad \boldsymbol{w} = \boldsymbol{\Phi}^{-1}(\boldsymbol{y} - \boldsymbol{P}\boldsymbol{b}) \tag{26}$$

4. Sampling

A proper surrogate model approximates the response surface adequately. Therefore, a sufficient number of samples needs to be evaluated for their fitness. The parameter dependence can be considered as unknown and the number of parameters is only two; hence, we pursue a full factorial sampling strategy of $\boldsymbol{X}$. The parameter space $\boldsymbol{X}$ is subdivided into l disjoint levels with level spacing Δx_i. At each level, one sample is evaluated. As shown in Fig. 1, the distribution of samples is not necessarily equispaced. An m-dimensional parameter space with l levels implies $|N| = l^m$ samples, where N is the set of samples.

IV. Results

A. Best Choice for a Reference $E(k)$

We restate the reference inertial subrange spectrum [Eq. (12)] as

$$E(k) = Ak^{-5/3} \tag{27}$$

where $A = C\epsilon^{2/3}$ summarizes the dependence of $E(k)$ on the Kolmogorov constant C and dissipation rate $\epsilon(k)$, which are both irrelevant to this DO task.

Evaluation of the fitness function [Eq. (13)] requires a priori knowledge of A, which is different for each sample. Regression analysis, as described in Sec. III.B.2, is used to determine A. The RS approximating polynomial, coefficient vector, matrix, and RS function are

$$\hat{y}_i = Ak_i^{-5/3} \tag{28}$$

$$\boldsymbol{b} = A, \qquad \boldsymbol{P} = \begin{pmatrix} k_n^{-5/3} \\ \vdots \\ k_m^{-5/3} \end{pmatrix} \tag{29}$$

$$y[k]_i = E[k_i] \tag{30}$$

Table 1 Comparison of possible regression models

Order	$\Delta(C_q;q)$	$\hat{z}_{\min}$	$z(\boldsymbol{x}_{\min})$	$\varepsilon[\%]$	$\bar{\varepsilon}[\%]$	$(C_q;q)_{\min}$
3	(4,000;4)	1.3028	1.5785	82.5	11.12	(20,000;9)
4	(4,000;4)	1.2457	1.607	77.5	9.33	(20,000;7)
5	(4,000;4)	1.3028	1.5785	82.5	7.82	(15,702;6)
3	(3,000;3)	1.5824	11.523	95.9	10.96	(14,961;5)
4	(3,000;3)	1.2936	1.607	80.5	9.73	(20,000;7)
5	(3,000;3)	1.2939	1.4994	86.3	9.04	(12,892;5)
3	(2,000;2)	1.5021	1.4400	95.7	10.58	(20,000;9)
4	(2,000;2)	1.6326	1.8933	86.2	9.41	(84,57;1)
5	(2,000;2)	1.4886	2.1415	69.5	7.48	(66,65;1)
3	(1,000;1)	1.5060	1.5874	94.9	10.33	(16,610;6)
4	(1,000;1)	1.2603	1.6065	78.4	8.80	(20,000;7)
5	(1,000;1)	1.3754	1.4737	93.3	7.13	(14,561;5)

B. Evaluation and Comparison of Surrogate Models

By ILES, $|N| = 400$ samples are evaluated with a level resolution of $\Delta(C_q;q) = (1{,}000;1)$. To train the PR and RBFI models, training sets $T \subset N$ are used. The training sets T contain one sample of each level, e.g., for $l = 5$, $|T| = 25$. We increase l from 5 to 20 iteratively. In each iteration, we reevaluate potential surrogate models on basis of increasing training sets T. The capability of the derived model to approximate the RS and whether it converges to an optimal sample are of interest.

1. *Polynomial Regression Models*

PR models of third, fourth, and fifth order are constructed. For each PR surrogate model, the global minimum in $\hat{z}(\boldsymbol{X})$, denoted as $\hat{z}_{\min} = \hat{z}(\boldsymbol{x}_{\min})$, and the corresponding coordinates $\boldsymbol{x}_{\min} = (C_q;q)_{\min}$ are sought and listed in Table 1. We also determine $z(\boldsymbol{x}_{\min})$ according to Eq. (13). ΔC_q and Δq denote the level resolution. To assess the quality of $\hat{z}(\boldsymbol{x})$ locally, the approximation certainty

$$\varepsilon = 1 - \left| \frac{z_{\min} - \hat{z}_{\min}}{z_{\min}} \right| \tag{31}$$

at $(C_q;q)_{\min}$ is evaluated. The capability of a PR model to approximate the RS is validated on basis of the holdout error

$$\bar{\varepsilon} = \frac{1}{|V|} \sum_{n \in V} \left| \frac{z_n - \hat{z}_n}{z_n} \right| \tag{32}$$

Except for $\Delta(C_q;q) = (1{,}000;1)$, where $V = N$ and the holdout error becomes the mean approximation error, the set of samples $V \subset N$ with $V \cap T = \varnothing$ is used as the validation set. Neither varying the polynomial order nor increasing l entails convergence to an optimal $\boldsymbol{x}$. Yet, for polynomials of fourth and fifth order, $\bar{\varepsilon}$ remains below 10%, even for $l = 5$. Even when the order is three, $\bar{\varepsilon}$ is not larger than 11% for $l = 5$. Note that $\bar{\varepsilon}$ decreases with the polynomial order and l.

Table 2 Comparison of interpolation models

$\lvert T\rvert$	$\Delta(C_q;q)$	$\hat{z}_{\min}$	$z(\boldsymbol{x}_{\min})$	$\varepsilon\%$	$\bar{\varepsilon}\%$	$(C_q;q)_{\min}$
25	(4,000;4)	1.2934	1.6259	79.6	6.64	(19,500;7)
49	(3,000;3)	1.2078	1.2820	94.2	6.21	(9,700;4)
100	(2,000;2)	1.1819	1.1679	98.8	5.47	(5,800;2)
400	(1,000;1)	1.1204	1.1602	99.9	— —	(5,200;2)

Figure 2 visualizes $\hat{z}$ of the fifth-order polynomial regression model, which is based on $\Delta(C_q;q) = (1{,}000;1)$. The fitnesses corresponding to the respective samples are visualized as dots. These data indicate that the polynomial regression $\hat{z}(\boldsymbol{x})$ provides an estimate of $z(\boldsymbol{x})$ and where to expect subspaces of high fitness. Yet, small local subspaces potentially containing local optima are not predictable.

2. *Interpolation Model*

Consecutively increased training sets are used to construct the interpolation models. Each RBFI model is evaluated for its global minimum $\hat{z}_{\min}$. Together with the corresponding $\boldsymbol{x}_{\min}$, as well as $z(\boldsymbol{x}_{\min})$ and ε, they are listed in Table 2. On bases of V, the holdout error is computed according to Eq. (32).

When increasing the number of levels, the interpolation models converge to $(C_q;q) = (5{,}200;2)$, with a certainty of 99.9% at $\Delta(C_q;q) = (1{,}000;1)$. The holdout error is below 7% for $|T| = 25$ and decreases with decreasing $\Delta(C_q;q)$. At least $|T| = 100$ samples are necessary to resolve the subspace containing the absolute minimum, such that an optimum, which is close to the actual optimal sample, is located there. Yet, already, $|T| = 49$ permits us to find a local optimum with 94.2% accuracy and a fitness that is 8% lower than the one found with $|T| = 400$.

Figure 3 shows the interpolation model based on $\Delta(C_q;q) = (1{,}000;1)$. Dominant structures in the RS are apparent: 1) a region in the response surface with low fitness, i.e., large $z(\boldsymbol{x})$. It is found for $C_q(q) < 1{,}000q$; and 2) for $C_q(q) > 1{,}000q$, a region of high fitness, i.e., small $z(\boldsymbol{x})$, is identified. Local minima are expected for

$$C_q \approx 2{,}600q, \qquad 2 \le q \le 5 \tag{33}$$

3. *Comparison of the Models*

Independent of the resolution and polynomial order of the polynomial regression models, the thin-plate RBF models approximate the response surface at much smaller $\bar{\varepsilon}$. To complete our study of optimizing WENO-CU6-M1 with surrogate models, several samples

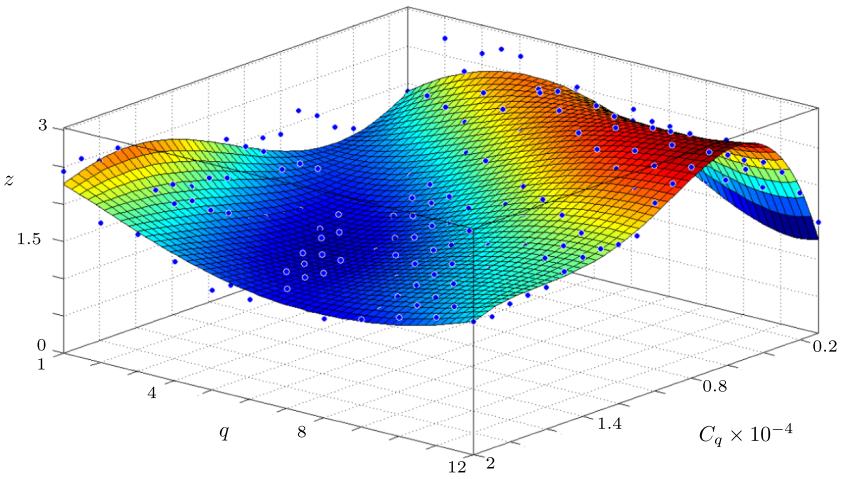

Fig. 2 Surrogate model: fifth-order polynomial, full factorial design. Parameter space reduced to $q \in [1;12] \times C_q \in [2{,}000;20{,}000]$ for better visualization.

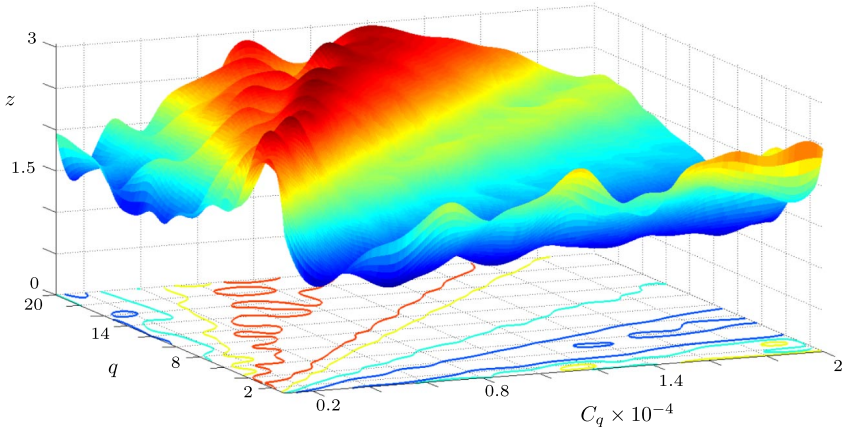

Fig. 3 Surrogate model: interpolation model, full factorial design, $\Delta(C_q; q) = (1{,}000; 1)$.

in the vicinity of the potential absolute minima $(C_q; q)_{\text{pol}} = (14{,}561; 5)$ and $(C_q; q)_{\text{int}} = (5{,}200; 2)$ are evaluated. Thereby, the globally optimal sample $(C_q; q)_{\text{opt}} = (5{,}300; 2)$, with $z(\boldsymbol{x}_{\text{opt}}) = 1.1405$, is determined. One finds that $(z(\boldsymbol{x}_{\text{opt}}) - \hat{z}(\boldsymbol{x}_{\text{int}}))/z(\boldsymbol{x}_{\text{opt}}) = 0.04\%$.

C. Evaluation of the Optimized WENO-CU6-M1 ILES Model for Infinite Reynolds Numbers

In Fig. 4, the kinetic energy spectra at $t = 10$ for the WENO-CU6-M1 scheme based on $\boldsymbol{x}_{\text{int}}$, $\boldsymbol{x}_{\text{opt}}$, and $\boldsymbol{x}_{\text{orig}}$ [8] are depicted. For comparison, the theoretically expected $E(k) \propto k^{-5/3}$ is shown alongside. The spectrum corresponding to $\boldsymbol{x}_{\text{opt}}$ is almost identical to the surrogate model sample $\boldsymbol{x}_{\text{sgt}} = \boldsymbol{x}_{\text{int}}$ in the relevant wave-number range. Moreover, these spectra coincide with the Kolmogorov spectrum.

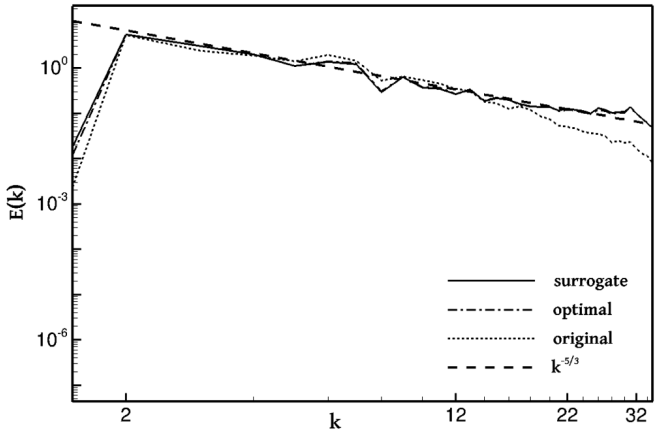

Fig. 4 Comparison of $E[k]$ for the original $x_{\text{orig}} = (1{,}000; 4)$, surrogate $x_{\text{int}} = (5{,}200; 2)$, and optimal $x_{\text{opt}} = (5{,}300; 2)$ model to the theoretical $E(k) \propto k^{-5/3}$ inertial subrange spectrum.

The temporal evolution of the effective numerical viscosity ν^n for the WENO-CU6-M1 schemes with $\boldsymbol{x}_{\text{orig}}$ and $\boldsymbol{x}_{\text{sgt}}$, evaluated according to [10], are depicted in Fig. 5a. In [9], $t_{\text{SGS}} \approx 3.4$ is the time noted for the onset of SGS dissipation. For $t < t_{\text{SGS}}$, the TGV develops its full range of scales, and a ν^n analysis is hardly applicable due to the lack of SGS. For $t \geq t_{\text{SGS}}$, ν^n is lower for $\boldsymbol{x}_{\text{sgt}}$ as for $\boldsymbol{x}_{\text{orig}}$. The relative difference in ν^n

$$\delta_\nu = \frac{\nu^n_{\text{orig}} - \nu^n_{\text{sgt}}}{\nu^n_{\text{sgt}}}$$

evaluated for $t \geq 4$, is found to be in the order of 20 to 77%. Especially within early times, yet past t_{SGS} (which are most relevant for correct transition), the improvement in prediction of numerical dissipation is significant. Kinetic energy dissipation onset is later for $\boldsymbol{x}_{\text{sgt}}$; see Fig. 5b. For $\boldsymbol{x}_{\text{sgt}}$ the full range of scales has evolved further, before SGS dissipation initiates, see also [9]. Hence, the correlation of SGS dissipation to smaller scales is stronger, as for $\boldsymbol{x}_{\text{orig}}$. Time series 6 visualizes the local dissipation function $\mathscr{E}(t)_{[i,j,k]}$ colored by the local numerical dissipation rate $\mathscr{E}^n_{[i,j,k]}$ within one octant of the TGV. We rotate the view about the z axis, and α indicates the angle of rotation corresponding to the current time. In the bottom half of Figs. 6a and 6b, a view with $\alpha + 90$ deg is shown. For $\boldsymbol{x}_{\text{sgt}}$, $\mathscr{E}^n$ is, for the most part, less diffuse and locally of larger magnitude, as for $\boldsymbol{x}_{\text{orig}}$.

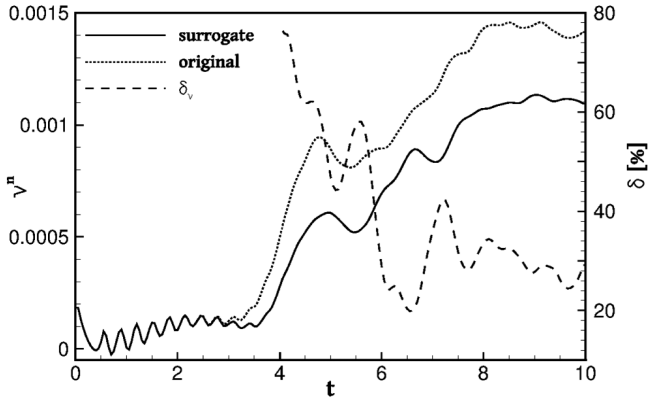

a) $\nu^n(t)$ and $\delta_\nu(t)$

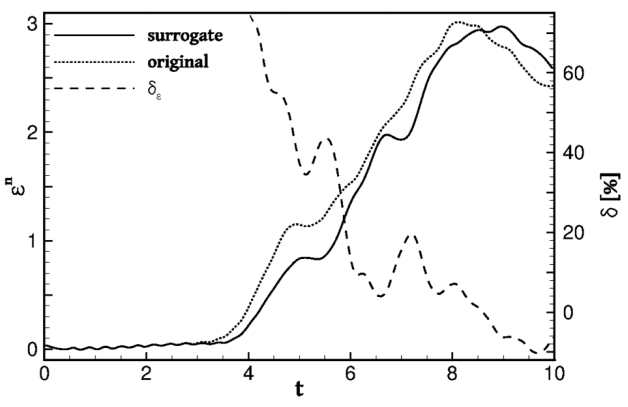

b) $\varepsilon^n(t)$ and $\delta_\varepsilon(t)$

Fig. 5 Comparison of temporal dissipation behavior for ILES schemes based on x_{orig} and x_{sgt}.

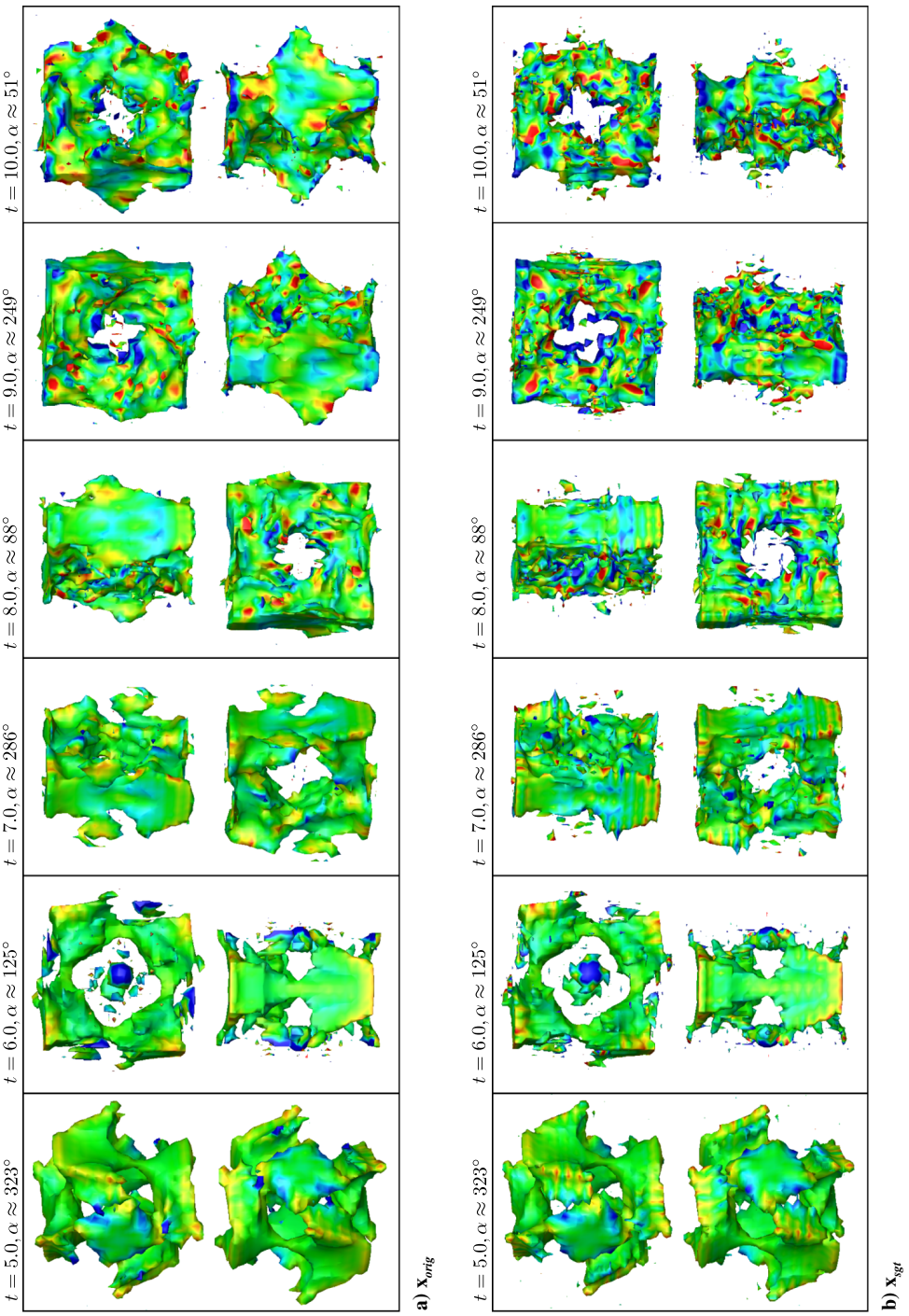

Fig. 6 Dissipation function $\mathscr{E} = 0.52$ with local numerical dissipation $\mathscr{E}^n$.

D. Model Behavior for Finite Reynolds Number

In a final set of simulations, we consider TGV flows for $Re = 100$ to $Re = 3{,}000$. The DNS of Brachet et al. [12,13] provide primary reference data. Furthermore, Fig. 7 depicts data obtained with the dynamic Smagorinsky model and the adaptive local deconvolution approach (ALDM) [5]. Note that DNS data and dynamic Smagorinsky $\mathscr{E}^{\text{eff}} = \mathscr{E}^n + \mathscr{E}^\nu$ are normalized by $(2\pi)^3$. The original ALDM simulations [5] were repeated in [10].

With advancing laminar-turbulent transition, the dissipation rate increases due to nonlinear vortex stretching. The decrease in $\mathscr{E}^{\text{eff}}$ at later times is due to viscous damping. For $Re \leq 200$, both the dynamic Smagorinsky model and ALDM slightly underpredict $\mathscr{E}^{\text{eff}}$, whereas the $\boldsymbol{x}_{\text{sgt}}$-based WENO-CU6-M1 model overpredicts $\mathscr{E}^{\text{eff}}$. Yet, the relative difference to the DNS data, evaluated at $Re = 100$ and $t \approx 4.6$, remains below 5%. For $400 \leq Re \leq 800$, the dissipation rates of the $\boldsymbol{x}_{\text{sgt}}$-based simulations are in good agreement with DNS. Especially for $Re \geq 1{,}600$, the $\boldsymbol{x}_{\text{sgt}}$-based WENO-CU6-M1 model predicts the onset and increase of $\mathscr{E}^{\text{eff}}$ as more strongly correlated to the existence of SGS (i.e., later) than the two alternative models. Moreover, $\mathscr{E}^{\text{eff}}_{\text{DNS}}(t)$ for $0 \leq t \leq 10$ is best represented with the $\boldsymbol{x}_{\text{sgt}}$-based WENO-CU6-M1 model. The peak effective dissipation rate is higher, and thereby closer, to the DNS results with the ALDM and dynamic Smagorinsky model. The dissipated kinetic energy

$$\Delta E_{\text{kin}} = \int_{t=0}^{10} \mathscr{E}^{\text{eff}}(t')\,\mathrm{d}t'$$

for the DNS and the three underresolved simulations are $\Delta E_{\text{kin,DNS}} \approx 11.59$, $\Delta E_{\text{kin,dynSmago}} \approx 14.83$, $\Delta E_{\text{kin,ALDM}} \approx 13.70$, and $\Delta E_{\text{kin,sgt}} \approx 12.52$ for $Re = 3{,}000$.

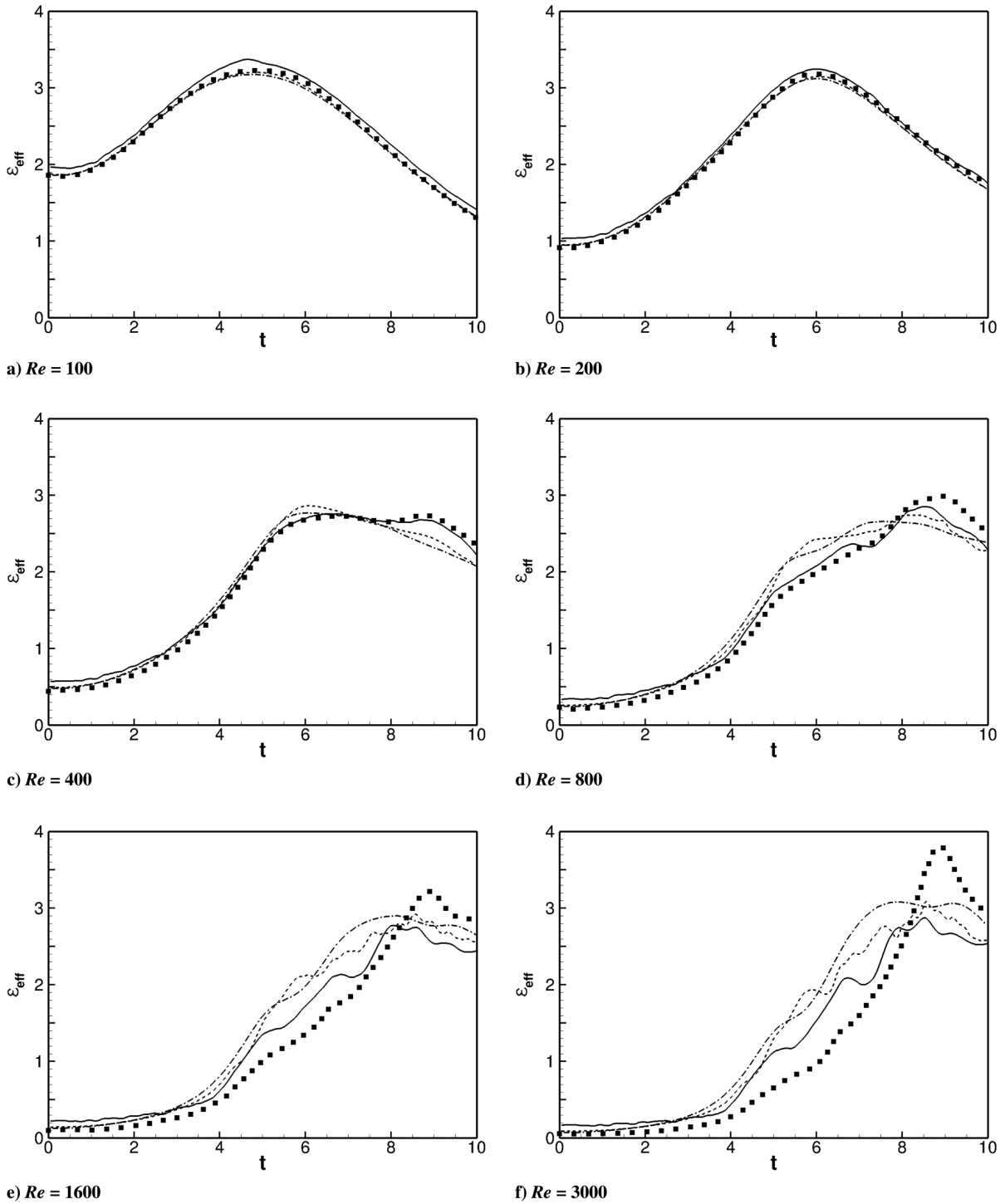

Fig. 7 $\mathscr{E}_{\text{eff}}$ **(*Re*) for the viscous TGV: x_{sgt} based ILES (solid lines), dynamic Smagorinsky LES [5] (dashed–dotted lines), and ALDM ILES [10] (dotted lines) on 64^3 finite volumes as compared to DNS data by Brachet et al. [12,13] (filled squares).**

V. Conclusions

The approximation quality of considered polynomial regression surrogate models primarily depends on the order and number of levels. Still, even the fifth-order polynomial model does not represent fine structures of the highly nonlinear response surface. The response surface approximation may be better when the number of samples is large, yet we find that, especially at higher polynomial orders, overfitting deteriorates the surrogate model. It has not been possible to constitute PR models in subspaces with large local gradients and at $\Delta(C_q; q) = (1{,}000; 1)$ or $\Delta(C_q; q) = (2{,}000; 2)$. Furthermore, due to overfitting for the number of training samples provided at $\Delta(C_q; q) = (1{,}000; 1)$, polynomials of an even higher order have shown to not be applicable. Based on the polynomial surrogate models, a comparably large subspace of high fitness has been considered as potentially containing the optimal sample; however, it does not.

The thin-plate RBF model approximation quality has proven to be superior to the polynomial models, independent of the resolution and polynomial order. The RS has been approximated sufficiently well with the RBF model at $\Delta(C_q; q) = (3{,}000; 3)$. Besides indicating a holdout error of only 6.21%, a local minimum fulfilling Eq. (33) and of certainty greater than 94% are found. At higher resolution, the RBF interpolation model indeed determines an optimal set of $(C_q; q)$, which closely approximates the fittest sample. The relative difference in fitnesses between these is below 1%. Already with 25% of the maximum number of samples, the response surface approximation fidelity has been sufficient to correctly localize the subspace containing the optimal $(C_q; q)$.

Although not discussed explicitly, within the scope of this work, Latin hypercube sampling has been tested for a potential sampling strategy. Due to the distinct nonlinearity of the fitness function response surface, it has proven to be inadequate.

In future attempts, to optimize WENO-CU6-M1's SGS modeling capabilities, an iterative search optimization should be included. Yet, effective iterative approaches, deterministic or stochastic, require an estimated model behavior. In this work, it has been shown that it can and should be gained with response surface interpolation surrogate models. Optimal WENO-CU6-M1-based ILES models for different Riemann solver/material modeling combinations could, in the future, be derived by an advanced procedure. In a first step, surrogate modeling, based on a coarse-level full factorial sampling, provides an estimate of the response surface $z(\boldsymbol{x})$, $\boldsymbol{x} \in \boldsymbol{X}$. A second step may consist of a local iterative search for the global minimum.

Before this work, various attempts to determine the power exponent q and linear weight bias C_q have been pursued, such as numerical testing (see, e.g., [7,9]), linking q to the order of accuracy [21,22]. The linear weight bias C_q in WENO-CU6 has been determined by increasing its value from unity as in [19] until the numerical dissipation for the resolved scales reduces [6]. In [8] $C_q^{\mathrm{WENO}-CU6M1} \gg C_q^{\mathrm{WENO}-CU6}$. Future numerical WENO-based schemes potentially introduce other free parameters. Determining these by extensive numerical testing or relating these to other quantities may instead be considered within the outlined deterministic design optimization framework. Besides gaining higher certainty in the value of the parameters, one can expect that fewer numerical tests are necessary, reducing costs, and finding parameter dependencies is facilitated.

Proof has been provided that optimization of a WENO-CU6-M1 ILES scheme in the spectral-space norm "optimal recovery of Kolmogorov inertial subrange scaling" improves the physical-space norm ν^n. Moreover, proper design of an implicit SGS model has resulted in a better correlation of SGS dissipation and small scales. Evaluating $\mathscr{E}^n(t)$ has shown that, as a consequence, kinetic energy dissipation occurs at times, when smaller scales dominate the flow. Local three-dimensional dissipation structures have been visualized by computing the local dissipation function. Thereby, macroscopic structures have been identified in which kinetic energy is dissipated. Such structures occur principally independent of the underlying ILES scheme in each octant of the domain. Yet, when a WENO-CU6-M1-based SGS model is physically consistent, these take the fine-scaled structures into account better.

Low- to high-Reynolds-number TGV flows have been simulated, and the effective dissipation rates (i.e., the sum of numerical and viscous dissipation rates) have been compared to reference data. At limited Reynolds numbers, the model's offdesign performance has thereby been characterized. Only, for very low Reynolds numbers, kinetic energy dissipation rates are overpredicted slightly. This implies that, even when no subgrid-scales are present, the model adds a minimum amount of dissipation. For medium to high Reynolds numbers, the surrogate, weakly compressible WENO-CU6-M1 implicit LES model predictions agree well with DNS. The current simulations have been compared to those obtained with the dynamic Smagorinsky model, which is an explicit SGS model, and the ALDM, which is an implicit LES model. It was found that the surrogate, weakly compressible WENO-CU6-M1 implicit LES model performed in a superior manner to the dynamic Smagorinsky model and the ALDM for medium- to infinite-Reynolds-number TGV flows. Only, for low Reynolds number, the two alternative models outperform the current model by a maximum of 5% relative difference to DNS predictions.

Appendix A: Details of the Artificially Compressible Roe Solver

The details of Roe's solver adapted to the artificial compressibility approach in the general case of a three-dimensional intercell numerical-flux vector are provided within the following:

Roe averaged states:

$$\tilde{\rho} = \sqrt{\rho^{(l)}\rho^{(r)}}, \qquad \tilde{u}_\beta = \frac{\sqrt{\rho^{(l)}}u_\beta^{(l)} + \sqrt{\rho^{(r)}}u_\beta^{(r)}}{\sqrt{\rho^{(l)}} + \sqrt{\rho^{(r)}}},$$
$$\text{and} \quad \tilde{\boldsymbol{u}}^2 = \tilde{u}_1^2 + \tilde{u}_2^2 + \tilde{u}_3^2 \tag{A1}$$

Given the cell-face normal vector $\boldsymbol{n} = (n_1, n_2, n_3)$, which is $\boldsymbol{n} = (1,0,0)$ for computing $\bar{\boldsymbol{F}}_1$, $\boldsymbol{n} = (0,1,0)$ for computing $\bar{\boldsymbol{F}}_2$, and $\boldsymbol{n} = (0,0,1)$ for computing $\bar{\boldsymbol{F}}_3$, the cell-face tangent vectors $\boldsymbol{t}^{(1)}$ and $\boldsymbol{t}^{(2)}$ are

$$\begin{aligned} \boldsymbol{t}^{(1)} &= (-n_2, n_1, 0), \\ \boldsymbol{t}^{(2)} &= \boldsymbol{n} \times \boldsymbol{t}^{(1)} = (-n_3 n_1, -n_2 n_3, n_1 n_1 + n_2 n_2) \end{aligned} \tag{A2}$$

The wave strengths are found by evaluating

$$\Delta \boldsymbol{U} = \boldsymbol{U}^{(r)} - \boldsymbol{U}^{(l)} = \sum_{j=1}^{m} \tilde{\delta}^{(j)} \tilde{\boldsymbol{K}}^{(j)}$$

$$\Delta \boldsymbol{U} = \begin{bmatrix} \Delta w_0 \\ \Delta w_1 \\ \Delta w_2 \\ \Delta w_3 \end{bmatrix} = \boldsymbol{U}^{(r)} - \boldsymbol{U}^{(l)} = \begin{bmatrix} \Delta\rho \\ \Delta(\rho u_1) \\ \Delta(\rho u_2) \\ \Delta(\rho u_3) \end{bmatrix} = \begin{bmatrix} \rho^{(l)} - \rho^{(r)} \\ (\rho u_1)^{(l)} - (\rho u_1)^{(r)} \\ (\rho u_2)^{(l)} - (\rho u_2)^{(r)} \\ (\rho u_3)^{(l)} - (\rho u_3)^{(r)} \end{bmatrix} \tag{A3}$$

and

$$\begin{aligned} \tilde{\delta}^{(1)} &= \frac{1}{2\tilde{a}}[\Delta w_0(\tilde{a} + \boldsymbol{n} \cdot \tilde{\boldsymbol{u}}) - \Delta \boldsymbol{u} \cdot \boldsymbol{n}], \\ \tilde{\delta}^{(2)} &= (\Delta \boldsymbol{u} - \tilde{\boldsymbol{u}}\Delta w_0) \cdot \boldsymbol{t}_1, \\ \tilde{\delta}^{(3)} &= (\Delta \boldsymbol{u} - \tilde{\boldsymbol{u}}\Delta w_0) \cdot \boldsymbol{t}_2, \\ \tilde{\delta}^{(4)} &= \frac{1}{\tilde{a}}[\Delta \boldsymbol{u} - \tilde{\boldsymbol{u}}\Delta w_0] \cdot \boldsymbol{n} + \tilde{\delta}^{(1)} \end{aligned} \tag{A4}$$

The right eigenvectors corresponding to the eigenvalues $\tilde{\lambda}^{(1)} = \tilde{u} - \tilde{a}$, $\tilde{\lambda}^{(2)} = \tilde{\lambda}^{(3)} = \tilde{u}$, and $\tilde{\lambda}^{(4)} = \tilde{u} + \tilde{a}$ are

$$\tilde{\boldsymbol{K}}^{(1)} = \begin{bmatrix} 1 \\ \tilde{u}_1 - \tilde{a} \cdot n_1 \\ \tilde{u}_2 - \tilde{a} \cdot n_2 \\ \tilde{u}_3 - \tilde{a} \cdot n_3 \end{bmatrix}, \qquad \tilde{\boldsymbol{K}}^{(2)} = \begin{bmatrix} 0 \\ \boldsymbol{t}^{(1)} \end{bmatrix}, \qquad \tilde{\boldsymbol{K}}^{(3)} = \begin{bmatrix} 0 \\ \boldsymbol{t}^{(2)} \end{bmatrix},$$
$$\tilde{\boldsymbol{K}}^{(4)} = \begin{bmatrix} 1 \\ \tilde{u}_1 + \tilde{a} \cdot n_1 \\ u_2 + \tilde{a} \cdot n_2 \\ \tilde{u}_3 + \tilde{a} \cdot n_3 \end{bmatrix} \tag{A5}$$

Note that $\tilde{a} = a = \text{const}$.

Appendix B: Parameters of the Fifth-Order WENO Scheme

The ideal weights are [18]

$$d_0 = \frac{1}{10}, \qquad d_1 = \frac{3}{5}, \qquad d_2 = \frac{3}{10} \tag{B1}$$

For upwind interpolation, three different third-order approximations of the nonaveraged upwind cell-face value $\boldsymbol{u}_{i+(1/2)}^{(l,\gamma)}$ are formulated on the three-point candidate stencils S_0, S_1, and S_2:

$$\begin{aligned}
\boldsymbol{u}_{i+(1/2)}^{(l,0)} &= \frac{1}{6}(2\hat{\boldsymbol{U}}_{i-2} - 7\hat{\boldsymbol{U}}_{i-1} + 11\hat{\boldsymbol{U}}_i),\\
\boldsymbol{u}_{i+(1/2)}^{(l,1)} &= \frac{1}{6}(-\hat{\boldsymbol{U}}_{i-1} + 5\hat{\boldsymbol{U}}_i + 2\hat{\boldsymbol{U}}_{i+1}),\\
\boldsymbol{u}_{i+(1/2)}^{(l,2)} &= \frac{1}{6}(2\hat{\boldsymbol{U}}_i + 5\hat{\boldsymbol{U}}_{i+1} - \hat{\boldsymbol{U}}_{i+2})
\end{aligned} \tag{B2}$$

From these three upwind candidate stencils, a fifth-order-accurate WENO cell face $\bar{\boldsymbol{U}}_{[i+1/2]}^{(l)}$ is calculated by Eq. (7). Via

$$\beta_\gamma^{(\alpha)} = \sum_{l=1}^{m-1} \int_{x_{i-1/2}}^{x_{i+1/2}} \Delta x^{2l-1} \left(\frac{\partial^l \boldsymbol{u}^{(\alpha,\gamma)}(x)}{\partial x^l} \right)^2 \mathrm{d}x \tag{B3}$$

the smoothness indicators are calculated as

$$\begin{aligned}
\beta_0^{(l)} &= \frac{1}{4}(\hat{\boldsymbol{U}}_{i-2} - 4\hat{\boldsymbol{U}}_{i-1} + 3\hat{\boldsymbol{U}}_i)^2 + \frac{13}{12}(\hat{\boldsymbol{U}}_{i-2} - 2\hat{\boldsymbol{U}}_{i-1} + \hat{\boldsymbol{U}}_i)^2,\\
\beta_1^{(l)} &= \frac{1}{4}(\hat{\boldsymbol{U}}_{i-1} - \hat{\boldsymbol{U}}_{i+1})^2 + \frac{13}{12}(\hat{\boldsymbol{U}}_{i-1} - 2\hat{\boldsymbol{U}}_i + \hat{\boldsymbol{U}}_{i+1})^2,\\
\beta_2^{(l)} &= \frac{1}{4}(3\hat{\boldsymbol{U}}_i - 4\hat{\boldsymbol{U}}_{i+1} + \hat{\boldsymbol{U}}_{i+2})^2 + \frac{13}{12}(\hat{\boldsymbol{U}}_i - 2\hat{\boldsymbol{U}}_{i+1} + \hat{\boldsymbol{U}}_{i+2})^2
\end{aligned} \tag{B4}$$

For downwind interpolation, three different third-order approximations of the nonaveraged downwind cell-face value $\boldsymbol{u}_{i+(1/2)}^{(r,\gamma)}$ are formulated on the three-point candidate stencils S_0, S_1, and S_2:

$$\begin{aligned}
\boldsymbol{u}_{i+(1/2)}^{(r,0)} &= \frac{1}{6}(2\hat{\boldsymbol{U}}_{i+3} - 7\hat{\boldsymbol{U}}_{i+2} + 11\hat{\boldsymbol{U}}_{i+1}),\\
\boldsymbol{u}_{i+(1/2)}^{(r,1)} &= \frac{1}{6}(-\hat{\boldsymbol{U}}_{i+2} + 5\hat{\boldsymbol{U}}_{i+1} + 2\hat{\boldsymbol{U}}_i),\\
\boldsymbol{u}_{i+(1/2)}^{(r,2)} &= \frac{1}{6}(2\hat{\boldsymbol{U}}_{i-1} + 5\hat{\boldsymbol{U}}_i - \hat{\boldsymbol{U}}_{i-2})
\end{aligned} \tag{B5}$$

From these three upwind candidate stencils, a fifth-order-accurate WENO cell face $\bar{\boldsymbol{U}}_{[i+(1/2)]}^{(r)}$ is calculated by Eq. (7). The smoothness indicators are

$$\begin{aligned}
\beta_0^{(r)} &= \frac{1}{4}(\hat{\boldsymbol{U}}_{i+3} - 4\hat{\boldsymbol{U}}_{i+2} + 3\hat{\boldsymbol{U}}_{i+1})^2 + \frac{13}{12}(\hat{\boldsymbol{U}}_{i+3} - 2\hat{\boldsymbol{U}}_{i+2} + \hat{\boldsymbol{U}}_{i+1})^2,\\
\beta_1^{(r)} &= \frac{1}{4}(\hat{\boldsymbol{U}}_{i+2} - \hat{\boldsymbol{U}}_i)^2 + \frac{13}{12}(\hat{\boldsymbol{U}}_{i+2} - 2\hat{\boldsymbol{U}}_{i+1} + \hat{\boldsymbol{U}}_i)^2,\\
\beta_2^{(r)} &= \frac{1}{4}(3\hat{\boldsymbol{U}}_{i+1} - 4\hat{\boldsymbol{U}}_i + \hat{\boldsymbol{U}}_{i-1})^2 + \frac{13}{12}(\hat{\boldsymbol{U}}_{i+1} - 2\hat{\boldsymbol{U}}_i + \hat{\boldsymbol{U}}_{i-1})^2
\end{aligned} \tag{B6}$$

Appendix C: Extension for the Parameter Set to Allow for WENO-CU6-M1 Reconstruction

The ideal weights adapt to account for four stencils:

$$d_0 = d_3 = \frac{1}{20}, \qquad d_1 = d_2 = \frac{9}{20} \tag{C1}$$

For upwind interpolation, the fourth third-order approximation to $\bar{\boldsymbol{U}}_{[i+(1/2)]}^{(l)}$, based on the three-point candidate stencil S_4, is

$$\boldsymbol{u}_{i+(1/2)}^{(l,3)} = \frac{1}{6}(11\hat{\boldsymbol{U}}_{i+1} - 7\hat{\boldsymbol{U}}_{i+2} + 2\hat{\boldsymbol{U}}_{i+3}) \tag{C2}$$

The fourth smoothness indicator evaluates as

$$\begin{aligned}
\beta_3^{(l)} = \frac{1}{10,080}|&271,779\hat{\boldsymbol{U}}_{i-2}^2 + \hat{\boldsymbol{U}}_{i-2}(-2,380,800\hat{\boldsymbol{U}}_{i-1}\\
&+ 4,086,352\hat{\boldsymbol{U}}_i - 3,462,252\hat{\boldsymbol{U}}_{i+1}\\
&+ 1,458,762\hat{\boldsymbol{U}}_{i+2} - 245,620\hat{\boldsymbol{U}}_{i+3})\\
&+ \hat{\boldsymbol{U}}_{i-1}(5,653,317\hat{\boldsymbol{U}}_{i-1} - 20,427,884\hat{\boldsymbol{U}}_i + 17,905,032\hat{\boldsymbol{U}}_{i+1}\\
&- 7,727,988\hat{\boldsymbol{U}}_{i+2} + 1,325,006\hat{\boldsymbol{U}}_{i+3})\\
&+ \hat{\boldsymbol{U}}_i(19,510,972\hat{\boldsymbol{U}}_i - 35,817,664\hat{\boldsymbol{U}}_{i+1} + 15,929,912\hat{\boldsymbol{U}}_{i+2}\\
&- 2,792,660\hat{\boldsymbol{U}}_{i+3})\\
&+ \hat{\boldsymbol{U}}_{i+1}(17,195,652\hat{\boldsymbol{U}}_{i+1} - 15,880,404\hat{\boldsymbol{U}}_{i+2} + 2,863,984\hat{\boldsymbol{U}}_{i+3})\\
&+ \hat{\boldsymbol{U}}_{i+2}(3,824,847\hat{\boldsymbol{U}}_{i+2} - 1,429,976\hat{\boldsymbol{U}}_{i+3}) + 139,633\hat{\boldsymbol{U}}_{i+3}^2|
\end{aligned} \tag{C3}$$

For downwind interpolation, the fourth third-order approximation to $\bar{\boldsymbol{U}}_{[i+(1/2)]}^{(r)}$, based on the three-point candidate stencil S_4, is

$$\boldsymbol{u}_{i+(1/2)}^{(r,3)} = \frac{1}{6}(11\hat{\boldsymbol{U}}_i - 7\hat{\boldsymbol{U}}_{i-1} + 2\hat{\boldsymbol{U}}_{i-2}). \tag{C4}$$

The fourth smoothness indicator for the downwind reconstruction evaluates as

$$\begin{aligned}
\beta_3^{(r)} = \frac{1}{10,080}|&271,779\hat{\boldsymbol{U}}_{i+3}^2 + \hat{\boldsymbol{U}}_{i+3}(-2,380,800\hat{\boldsymbol{U}}_{i+2}\\
&+ 4,086,352\hat{\boldsymbol{U}}_{i+1} - 3,462,252\hat{\boldsymbol{U}}_i + 1,458,762\hat{\boldsymbol{U}}_{i-1} - 245,620\hat{\boldsymbol{U}}_{i-2})\\
&+ \hat{\boldsymbol{U}}_{i+2}(5,653,317\hat{\boldsymbol{U}}_{i+2} - 20,427,884\hat{\boldsymbol{U}}_{i+1} + 17,905,032\hat{\boldsymbol{U}}_i\\
&- 7,727,988\hat{\boldsymbol{U}}_{i-1} + 1,325,006\hat{\boldsymbol{U}}_{i-2})\\
&+ \hat{\boldsymbol{U}}_{i+1}(19,510,972\hat{\boldsymbol{U}}_{i+1} - 35,817,664\hat{\boldsymbol{U}}_i + 15,929,912\hat{\boldsymbol{U}}_{i-1}\\
&- 2,792,660\hat{\boldsymbol{U}}_{i-2})\\
&+ \hat{\boldsymbol{U}}_i(17,195,652\hat{\boldsymbol{U}}_i - 15,880,404\hat{\boldsymbol{U}}_{i-1} + 2,863,984\hat{\boldsymbol{U}}_{i-2})\\
&+ \hat{\boldsymbol{U}}_{i-1}(3,824,847\hat{\boldsymbol{U}}_{i-1} - 1,429,976\hat{\boldsymbol{U}}_{i-2}) + 139,633\hat{\boldsymbol{U}}_{i-2}^2|
\end{aligned} \tag{C5}$$

Acknowledgments

We acknowledge the Deutsche Forschungsgemeinschaft for funding. We thank the Munich Centre of Advanced Computing for providing computational resources. F. S. Schranner and V. Rozov are members of the Technische Universität München Graduate School. We thank E. Schranner for proofreading.

References

[1] Margolin, L. G., and Rider, W. J., "A Rationale for Implicit Turbulence Modelling," *International Journal for Numerical Methods in Fluids*, Vol. 39, No. 9, 2002, pp. 821–841. doi:10.1002/(ISSN)1097-0363

[2] Adams, N., Hickel, S., and Franz, S., "Implicit Subgrid-Scale Modeling by Adaptive Deconvolution," *Journal of Computational Physics*, Vol. 200, No. 2, 2004, pp. 412–431. doi:10.1016/j.jcp.2004.04.010

[3] Grinstein, F., Margolin, L., and Rider, W., *Implicit Large Eddy Simulation: Computing Turbulent Fluid Dynamics*, Cambridge Univ Press, Cambridge, England, U.K., 2007.

[4] Balsara, D. S., and Shu, C.-W., "Monotonicity Preserving Weighted Essentially Non-Oscillatory Schemes with Increasingly High Order of Accuracy," *Journal of Computational Physics*, Vol. 160, No. 2, 2000, pp. 405–452. doi:10.1006/jcph.2000.6443

[5] Hickel, S., Adams, N., and Domaradzki, J., "An Adaptive Local Deconvolution Method for Implicit LES," *Journal of Computational Physics*, Vol. 213, No. 1, 2006, pp. 413–436. doi:10.1016/j.jcp.2005.08.017

[6] Hu, X. Y., Wang, Q., and Adams, N. A., "An Adaptive Central-Upwind Weighted Essentially Non-Oscillatory Scheme," *Journal of Computational Physics*, Vol. 229, No. 23, 2010, pp. 8952–8965. doi:10.1016/j.jcp.2010.08.019

[7] Jiang, G., and Shu, C.-W., "Efficient Implementation of Weighted ENO Schemes," *Journal of Computational Physics*, Vol. 126, No. 1, 1996, pp. 202–228. doi:10.1006/jcph.1996.0130

[8] Hu, X. Y., and Adams, N. A., "Scale Separation for Implicit Large Eddy Simulation," *Journal of Computational Physics*, Vol. 230, No. 19, 2011, pp. 7240–7249. doi:10.1016/j.jcp.2011.05.023

[9] Schranner, F. S., Hu, X., and Adams, N. A., "A Physically Consistent Weakly Compressible High-Resolution Approach to Underresolved Simulations of Incompressible Flows," *Computers and Fluids*, Vol. 86, Nov. 2013, pp. 109–124. doi:10.1016/j.compfluid.2013.06.034

[10] Schranner, F. S., Domaradzki, J. A., Hickel, S., and Adams, N. A., "Assessing the Numerical Dissipation Rate and Viscosity in Numerical Simulations of Fluid Flows," *Computers and Fluids*, Vol. 114, July 2015, pp. 84–97. doi:10.1016/j.compfluid.2015.02.011

[11] Taylor, G. I., and Green, A., "Mechanism of the Production of Small Eddies from Larger Ones," *Proceedings of the Royal Society of London, Series A: Mathematical and Physical Sciences*, Vol. 158, No. 895, 1937, pp. 499–521.

[12] Brachet, M., Meiron, D., Orszag, S., Nickel, B., Morf, R., and Frisch, U., "The Taylor–Green Vortex and Fully Developed Turbulence," *Journal of Statistical Physics*, Vol. 34, Nos. 5–6, 1984, pp. 1049–1063. doi:10.1007/BF01009458

[13] Brachet, M., Meneguzzi, M., Vincent, A., Politano, H., and Sulem, P.-L., "Numerical Evidence of Smooth Self-Similar Dynamics and Possibility of Subsequent Collapse for Three-Dimensional Ideal Flow," *Physics of Fluids*, Vol. 4, No. 12, 1992, pp. 2845–2854. doi:10.1063/1.858513

[14] Chorin, A. J., "A Numerical Method for Solving Incompressible Viscous Flow Problems," *Journal of Computational Physics*, Vol. 135, No. 2, 1997, pp. 118–125. doi:10.1006/jcph.1997.5716

[15] Temam, R., "Une Méthode d'Approximation des Solutions des Équations Navier-Stokes," *Bulletin de la Société Mathématique de France*, Vol. 96, 1968, pp. 115–152.

[16] Roe, P. L., "Approximate Riemann Solvers, Parameter Vectors, and Difference Schemes," *Journal of Computational Physics*, Vol. 43, No. 2, 1981, pp. 357–372. doi:10.1016/0021-9991(81)90128-5

[17] Shu, C.-W., and Osher, S., "Efficient Implementation of Essentially Non-Oscillatory Shock-Capturing Schemes," *Journal of Computational Physics*, Vol. 77, No. 2, 1988, pp. 439–471. doi:10.1016/0021-9991(88)90177-5

[18] Shu, C.-W., "Essentially Non-Oscillatory and Weighted Essentially Non-Oscillatory Schemes for Hyperbolic Conservation Laws," *Advanced Numerical Approximation of Nonlinear Hyperbolic Equations*, Vol. 1697, edited by Quarteroni, A., Lecture Notes in Mathematics, Springer, Berlin, 1998, pp. 325–432.

[19] Borges, R., Carmona, M., Costa, B., and Don, W., "An Improved Weighted Essentially Non-Oscillatory Scheme for Hyperbolic Conservation Laws," *Journal of Computational Physics*, Vol. 227, No. 6, 2008, pp. 3191–3211. doi:10.1016/j.jcp.2007.11.038

[20] Henrick, A., Aslam, T., and Powers, J., "Mapped Weighted Essentially Non-Oscillatory Schemes: Achieving Optimal Order Near Critical Points," *Journal of Computational Physics*, Vol. 207, No. 2, 2005, pp. 542–567. doi:10.1016/j.jcp.2005.01.023

[21] Gerolymos, G., Sénéchal, D., and Vallet, I., "Very-High-Order Weno Schemes," *Journal of Computational Physics*, Vol. 228, No. 23, 2009, pp. 8481–8524. doi:10.1016/j.jcp.2009.07.039

[22] Xu-Dong, L., and Stanley Osher, T. C., "Weighted Essentially Non-Oscillatory Schemes," *Journal of Computational Physics*, Vol. 115, No. 1, 1994, pp. 200–212. doi:10.1006/jcph.1994.1187

[23] Taylor, E., Wu, M., and Martin, M., "Optimization of Nonlinear Error for Weighted Essentially Non-Oscillatory Methods in Direct Numerical Simulations of Compressible Turbulence," *Journal of Computational Physics*, Vol. 223, No. 1, 2007, pp. 384–397. doi:10.1016/j.jcp.2006.09.010

[24] Fauconnier, D., Langhe, C. D., and Dick, E., "Construction of Explicit and Implicit Dynamic Finite Difference Schemes and Application to the Large-Eddy Simulation of the Taylor–Green Vortex," *Journal of Computational Physics*, Vol. 228, No. 21, 2009, pp. 8053–8084. doi:10.1016/j.jcp.2009.07.028

[25] Gram, J., "Über die Entwicklung Reeler Funktionen in Reihen Mittels der Methode der Kleinsten Quadrate," *Journal für die Reine und Angewandte Mathematik*, Vol. 94, 1883, pp. 41–73.

[26] Legendre, A. M., *Nouvelles Methodes pour la Determination des Orbites des Comtes*, F. Didot, Paris, 1805, pp. 72–75.

[27] Venter, G., *Review of Optimization Techniques*, Wiley, Hoboken, NJ, 2010, pp. 7–8.

[28] Beasley, D., Martin, R., and Bull, D., "An Overview of Genetic Algorithms: Part 1. Fundamentals," *University Computing*, Vol. 15, No. 2, 1993, pp. 58–69.

[29] Zingg, D. W., Nemec, M., and Pulliam, T. H., "A Comparative Evaluation of Genetic and Gradient-Based Algorithms Applied to Aerodynamic Optimization," *European Journal of Computational Mechanics*, Vol. 17, Nos. 1–2, May 2008, pp. 103–126. doi:10.3166/remn.17.103-126

[30] Harder, R. L., and Desmarais, R., "Interpolation Using Surface Splines," *Journal of Aircraft*, Vol. 9, No. 2, 1972, pp. 189–191. doi:10.2514/3.44330

[31] Wilson, D. C., and Mair, B. A., *Applied and Numerical Harmonic Analysis*, Springer Science+Business Media, New York, 2003, pp. 311–341, Chap. 12.

[32] Powell, M. J. D., "A Thin Plate Spline Method for Mapping Curves into Curves in Two Dimensions," *Computational Techniques and Applications (CTAC95)*, edited by May, R. L., and Easton, A. K., World Scientific, Singapore, 1995, pp. 43–57.

C. Bailly
Associate Editor

B.4 On the convergence of the weakly compressible sharp-interface method for two-phase flows

ELSEVIER LICENSE TERMS AND CONDITIONS

Oct 12, 2016

This Agreement between Felix S Schranner ("You") and Elsevier ("Elsevier") consists of your license details and the terms and conditions provided by Elsevier and Copyright Clearance Center.

License Number	3930370328313
License date	Aug 15, 2016
Licensed Content Publisher	Elsevier
Licensed Content Publication	Journal of Computational Physics
Licensed Content Title	On the convergence of the weakly compressible sharp-interface method for two-phase flows
Licensed Content Author	Felix S. Schranner,Xiangyu Hu,Nikolaus A. Adams
Licensed Content Date	1 November 2016
Licensed Content Volume Number	324
Licensed Content Issue Number	n/a
Licensed Content Pages	21
Start Page	94
End Page	114
Type of Use	reuse in a thesis/dissertation
Portion	full article
Format	both print and electronic
Are you the author of this Elsevier article?	Yes
Will you be translating?	No
Order reference number	
Title of your thesis/dissertation	Weakly Compressible Models for Complex Flows
Expected completion date	Nov 2016
Estimated size (number of pages)	212
Elsevier VAT number	GB 494 6272 12
Requestor Location	Felix S Schranner Boltzmannstrasse 15 Garching, 85748 Germany Attn: Felix S Schranner
Total	**0.00 EUR**
Terms and Conditions	

The following terms and conditions apply only to specific license types:
15. **Translation**: This permission is granted for non-exclusive world **English** rights only unless your license was granted for translation rights. If you licensed translation rights you may only translate this content into the languages you requested. A professional translator must perform all translations and reproduce the content word for word preserving the integrity of the article.
16. **Posting licensed content on any Website**: The following terms and conditions apply as follows: Licensing material from an Elsevier journal: All content posted to the web site must maintain the copyright information line on the bottom of each image; A hyper-text must be included to the Homepage of the journal from which you are licensing at http://www.sciencedirect.com/science/journal/xxxxx or the Elsevier homepage for books at http://www.elsevier.com; Central Storage: This license does not include permission for a scanned version of the material to be stored in a central repository such as that provided by Heron/XanEdu.
Licensing material from an Elsevier book: A hyper-text link must be included to the Elsevier homepage at http://www.elsevier.com . All content posted to the web site must maintain the copyright information line on the bottom of each image.

Posting licensed content on Electronic reserve: In addition to the above the following clauses are applicable: The web site must be password-protected and made available only to bona fide students registered on a relevant course. This permission is granted for 1 year only. You may obtain a new license for future website posting.
17. **For journal authors:** the following clauses are applicable in addition to the above:
Preprints:
A preprint is an author's own write-up of research results and analysis, it has not been peer-reviewed, nor has it had any other value added to it by a publisher (such as formatting, copyright, technical enhancement etc.).
Authors can share their preprints anywhere at any time. Preprints should not be added to or enhanced in any way in order to appear more like, or to substitute for, the final versions of articles however authors can update their preprints on arXiv or RePEc with their Accepted Author Manuscript (see below).
If accepted for publication, we encourage authors to link from the preprint to their formal publication via its DOI. Millions of researchers have access to the formal publications on ScienceDirect, and so links will help users to find, access, cite and use the best available version. Please note that Cell Press, The Lancet and some society-owned have different preprint policies. Information on these policies is available on the journal homepage.
Accepted Author Manuscripts: An accepted author manuscript is the manuscript of an article that has been accepted for publication and which typically includes author-incorporated changes suggested during submission, peer review and editor-author communications.
Authors can share their accepted author manuscript:

- immediately
  - via their non-commercial person homepage or blog
  - by updating a preprint in arXiv or RePEc with the accepted manuscript
  - via their research institute or institutional repository for internal institutional uses or as part of an invitation-only research collaboration work-group
  - directly by providing copies to their students or to research collaborators for their personal use
  - for private scholarly sharing as part of an invitation-only work group on commercial sites with which Elsevier has an agreement
- after the embargo period
  - via non-commercial hosting platforms such as their institutional repository
  - via commercial sites with which Elsevier has an agreement

In all cases accepted manuscripts should:

- link to the formal publication via its DOI
- bear a CC-BY-NC-ND license - this is easy to do
- if aggregated with other manuscripts, for example in a repository or other site, be shared in alignment with our hosting policy not be added to or enhanced in any way to appear more like, or to substitute for, the published journal article.

Published journal article (JPA): A published journal article (PJA) is the definitive final record of published research that appears or will appear in the journal and embodies all value-adding publishing activities including peer review co-ordination, copy-editing, formatting, (if relevant) pagination and online enrichment.
Policies for sharing publishing journal articles differ for subscription and gold open access articles:
Subscription Articles: If you are an author, please share a link to your article rather than the full-text. Millions of

researchers have access to the formal publications on ScienceDirect, and so links will help your users to find, access, cite, and use the best available version.
Theses and dissertations which contain embedded PJAs as part of the formal submission can be posted publicly by the awarding institution with DOI links back to the formal publications on ScienceDirect.
If you are affiliated with a library that subscribes to ScienceDirect you have additional private sharing rights for others' research accessed under that agreement. This includes use for classroom teaching and internal training at the institution (including use in course packs and courseware programs), and inclusion of the article for grant funding purposes.
Gold Open Access Articles: May be shared according to the author-selected end-user license and should contain a CrossMark logo, the end user license, and a DOI link to the formal publication on ScienceDirect.
Please refer to Elsevier's posting policy for further information.
18. **For book authors** the following clauses are applicable in addition to the above: Authors are permitted to place a brief summary of their work online only. You are not allowed to download and post the published electronic version of your chapter, nor may you scan the printed edition to create an electronic version. **Posting to a repository:** Authors are permitted to post a summary of their chapter only in their institution's repository.
19. **Thesis/Dissertation**: If your license is for use in a thesis/dissertation your thesis may be submitted to your institution in either print or electronic form. Should your thesis be published commercially, please reapply for permission. These requirements include permission for the Library and Archives of Canada to supply single copies, on demand, of the complete thesis and include permission for Proquest/UMI to supply single copies, on demand, of the complete thesis. Should your thesis be published commercially, please reapply for permission. Theses and dissertations which contain embedded PJAs as part of the formal submission can be posted publicly by the awarding institution with DOI links back to the formal publications on ScienceDirect.

Elsevier Open Access Terms and Conditions
You can publish open access with Elsevier in hundreds of open access journals or in nearly 2000 established subscription journals that support open access publishing. Permitted third party re-use of these open access articles is defined by the author's choice of Creative Commons user license. See our open access license policy for more information.
Terms & Conditions applicable to all Open Access articles published with Elsevier:
Any reuse of the article must not represent the author as endorsing the adaptation of the article nor should the article be modified in such a way as to damage the author's honour or reputation. If any changes have been made, such changes must be clearly indicated.
The author(s) must be appropriately credited and we ask that you include the end user license and a DOI link to the formal publication on ScienceDirect.
If any part of the material to be used (for example, figures) has appeared in our publication with credit or acknowledgement to another source it is the responsibility of the user to ensure their reuse complies with the terms and conditions determined by the rights holder.
Additional Terms & Conditions applicable to each Creative Commons user license:
CC BY: The CC-BY license allows users to copy, to create extracts, abstracts and new works from the Article, to alter and revise the Article and to make commercial use of the Article (including reuse and/or resale of the Article by commercial entities), provided the user gives appropriate credit (with a link to the formal publication through the relevant DOI), provides a link to the license, indicates if changes were made and the licensor is not represented as endorsing the use made of the work. The full details of the license are available at http://creativecommons.org/licenses/by/4.0.
CC BY NC SA: The CC BY-NC-SA license allows users to copy, to create extracts, abstracts and new works from the Article, to alter and revise the Article, provided this is not done for commercial purposes, and that the user gives appropriate credit (with a link to the formal publication through the relevant DOI), provides a link to the license, indicates if changes were made and the licensor is not represented as endorsing the use made of the work. Further, any new works must be made available on the same conditions. The full details of the license are available at http://creativecommons.org/licenses/by-nc-sa/4.0.
CC BY NC ND: The CC BY-NC-ND license allows users to copy and distribute the Article, provided this is not done for commercial purposes and further does not permit distribution of the Article if it is changed or edited in any way, and provided the user gives appropriate credit (with a link to the formal publication through the relevant DOI), provides a link to the license, and that the licensor is not represented as endorsing the use made of the work. The full details of the license are available at http://creativecommons.org/licenses/by-nc-nd/4.0. Any commercial reuse of Open Access articles published with a CC BY NC SA or CC BY NC ND license requires permission from Elsevier and will be subject to a fee.
Commercial reuse includes:

- Associating advertising with the full text of the Article
- Charging fees for document delivery or access
- Article aggregation
- Systematic distribution via e-mail lists or share buttons

Posting or linking by commercial companies for use by customers of those companies.

20. **Other Conditions**:

v1.8

Questions? customercare@copyright.com or +1-855-239-3415 (toll free in the US) or +1-978-646-2777.

Journal of Computational Physics 324 (2016) 94–114

Contents lists available at ScienceDirect

Journal of Computational Physics

www.elsevier.com/locate/jcp

On the convergence of the weakly compressible sharp-interface method for two-phase flows

Felix S. Schranner *, Xiangyu Hu, Nikolaus A. Adams

Technische Universität München, Institute of Aerodynamics, 85748 Garching, Germany

ARTICLE INFO

Article history:
Received 24 September 2015
Received in revised form 13 March 2016
Accepted 27 July 2016
Available online 1 August 2016

Keywords:
Weakly compressible
Sharp-interface method
Benchmark suite
Surface tension
Rayleigh–Taylor instability
Rising bubble

ABSTRACT

A weakly compressible sharp-interface framework for two-phase flows is presented. Special emphasis is on investigating its convergence properties. For this purpose a well-defined set of benchmark configurations is introduced. These may serve as future references for the verification of sharp-interface methods. Global mass and momentum conservation is ensured by the conservative sharp-interface method. Viscous and capillary stresses are considered directly at the interface. A low-dissipation weakly compressible Roe Riemann solver, in combination with a 5th-order WENO scheme, leads to high spatial accuracy. A wavelet-based adaptive multi-resolution approach permits to combine computational efficiency with physical consistency. The first test configuration is a Rayleigh–Taylor instability at moderate Reynolds number and infinite Eötvös number. A second group of benchmark cases are isolated air bubbles rising in water at high Eötvös numbers, and low to high Reynolds numbers. With these test cases, three distinct types of complex interface evolution, which are typical for a wide range of industrial applications, are realized.

1. Introduction

Numerical methods for the simulation of two-phase flows may be categorized into *interface tracking* and *interface capturing* methods. Interface tracking methods either use an interface-adapted grid or marker particles to represent the interface. In general, interface tracking methods are very accurate, yet, they lack efficiency in three dimensions, and, with varying interface topology, the implementation effort can be overwhelming. Interface capturing methods define the interface implicitly by means of an auxiliary function, such as a level-set function. This simplifies grid generation, discretization and handling of topological variations. Simulations of immiscible, incompressible two-phase flows are commonly based on the Eulerian, diffuse-interface, level-set continuum approaches [1]. Major drawbacks of diffuse-interface methods, such as volume-of-fluid [2], level-set continuum [3], phase-field [4] methods, are their lack of conservativity as well as difficulties in maintaining large gradients of viscosity and density.

A fully conservative, Eulerian, level-set sharp-interface method (SIM) for compressible flows has been introduced by Hu et al. [5]. It accurately predicts two-phase flows, with each phase obeying different equations of state, and large density and viscosity ratios [6]. Further-development of the SIM to model viscous, incompressible two-phase flows is described in [7]. Schranner et al. [8] have derived a low-dissipative, physically consistent WENO-based implicit subgrid-scale model for weakly compressible flows.

* Corresponding author. Fax: +49 89 289 16139.
E-mail addresses: felix.schranner@aer.mw.tum.de (F.S. Schranner), xiangyu.hu@tum.de (X. Hu), Nikolaus.Adams@tum.de (N.A. Adams).

http://dx.doi.org/10.1016/j.jcp.2016.07.037
0021-9991/

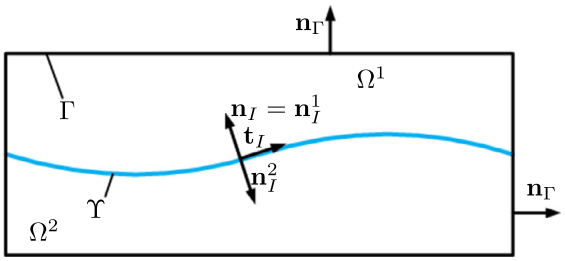

Fig. 1. Two-dimensional schematic of the multi-fluid configuration.

Verification of two-phase numerical algorithms, especially in 2D, is best accomplished by cross comparison of different methods as suitable analytical solutions are scarce. Apart from comparing integral quantities of the interface and disperse phase, see e.g. [9], validation is often based on visual inspection and comparison with experimental or numerical references. For evaluating the capabilities of a two-phase solver to reproduce increasingly fine-scaled density stratifications, while maintaining a sharp interface, in the absence of surface tension, the *Rayleigh–Taylor instability* (RTI) is a suitable configuration. Simulations of two-dimensional submerged air bubbles rising due to the influence of gravity (BLG) serve to assess capillary and viscous effects, and thus comprise a variety of phenomena relevant to a wide range of two-phase, immiscible flows. Neither for the RTI nor for the BLG, both undergoing severe interface topology changes, spatial-resolution-independent, mass- and momentum conservative, sharp-interface-maintaining references are available that would permit method cross comparison.

The objective of this work is twofold: (i) we propose and describe in detail, a weakly compressible sharp-interface method (WCSIM) to numerically simulate two-phase flows of immiscible, incompressible fluids and (ii) we establish high fidelity solutions with the WCSIM that can serve as a reference for future model developments by concurrently assessing the WCSIM's convergence properties. In section 2, we state the governing equations of motion, the weakly compressible method is outlined and the section concludes with providing further details on the numerical model, such as time integration, and time-step constraints. Section 3 is devoted to explaining the specifics of the sharp-interface momentum exchange as well as the modeling of the propagating interface. Resolved numerical results are presented in section 4, concluding remarks are given in section 5.

2. Basic two-fluid flow equations

Consider two immiscible fluid phases in two dimensions, as sketched in Fig. 1. The fluid phases occupy two non-overlapping subdomains $\Omega^1(t)$ and $\Omega^2(t)$. Ω is bounded by $\Gamma = \partial\Omega$, corresponding boundaries exist for the subdomains. For each phase, $\Omega^i(t),\ i = 1, 2$ the system of conservation equations for weakly compressible fluids in differential, non-dimensional form

$$\frac{\partial \rho}{\partial t} + \nabla^T \cdot (\rho \mathbf{u}) = 0\,, \tag{1a}$$

$$\frac{\partial \rho \mathbf{u}}{\partial t} + \nabla^T \cdot [\rho \mathbf{u} \otimes \mathbf{u} - \mathbf{\Pi}] = \frac{1}{Fr^2}\rho \mathbf{g} \tag{1b}$$

holds [10], where ρ denotes the density, $\mathbf{u} = (u_1, u_2)^T$ the vector of Cartesian velocities, and $\mathbf{g} = (g_1, g_2)^T$ the vector of body forces. Furthermore, the stress tensor is defined as

$$\mathbf{\Pi} = -\mathbb{I}p + \mathbf{T}\,, \tag{2}$$

p is the static pressure. With the Stokes hypothesis for a Newtonian fluid the viscous stress tensor is

$$\mathbf{T} = \mathbf{T}(\mathbf{u}) = \begin{bmatrix} \tau^{11} & \tau^{12} \\ \tau^{21} & \tau^{22} \end{bmatrix}, \tag{3}$$

where $\mu = \nu\rho$ is the dynamic viscosity, and the components of $\mathbf{T}(\mathbf{u})$ are

$$\tau^{\alpha\beta} = \frac{\mu}{Re}\left(\frac{\partial u_\alpha}{\partial x_\beta} + \frac{\partial u_\beta}{\partial x_\alpha} - \frac{2}{3}\frac{\partial u_\gamma}{\partial x_\gamma}\delta_{\alpha\beta}\right). \tag{4}$$

Herein, $\alpha, \beta, \gamma = 1, 2$. Moreover, $Fr^2 = \frac{U_{ref}^2}{g_{ref} L_{ref}}$, $Re = \frac{U_{ref} L_{ref}}{\nu_{ref}}$, $Eo = \frac{\rho_{ref} g_{ref} L_{ref}^2}{\sigma_{ref}}$, and $Ca = \frac{\mu_{ref} U_{ref}}{\sigma_{ref}}$ denote the Froude, Reynolds, Eötvös, and capillary number. $U_{ref} = \sqrt{g_{ref} L_{ref}}$, $T_{ref} = \frac{L_{ref}}{U_{ref}} = \sqrt{\frac{L_{ref}}{g_{ref}}}$. When considering a bubble, $L_{ref} = d_0$, i.e. the bubble diameter at $t = 0$. For the case of Rayleigh–Taylor instability $L_{ref} = L_{x_1}$, where L_{x_1} is the extent of the domain in x_1-direction.

2.1. Conservation equations

The integral form of Eq. (1) is

$$\int_{\Omega} \mathbf{U}_t \, dV + \oint_{\Gamma} (\mathbf{F}_1, \mathbf{F}_2) \cdot \mathbf{n}_{\Gamma} \, d\Gamma' = \int_{\Omega} \mathbf{S}(\mathbf{U}) \, dV \tag{5}$$

where

$$\mathbf{U} = (\rho, \rho u_1, \rho u_2)^T \, , \tag{6}$$

$\mathbf{n}_{\Gamma}$ is the normal on Γ, see Fig. 1. The flux vectors include advective and viscous components $\mathbf{F}_i = \mathbf{F}_i^a - \mathbf{F}_i^{\nu}$ with $i = 1, 2$.

The advective fluxes (superscript a) are

$$\mathbf{F}_1^a(\mathbf{U}) = \begin{pmatrix} \rho u_1 \\ \rho u_1^2 + p \\ \rho u_1 u_2 \end{pmatrix}, \mathbf{F}_2^a(\mathbf{U}) = \begin{pmatrix} \rho u_2 \\ \rho u_1 u_2 \\ \rho u_2^2 + p \end{pmatrix}. \tag{7}$$

The viscous fluxes (superscript ν) are

$$\mathbf{F}_1^{\nu}(\mathbf{u}) = \frac{1}{Re} \begin{pmatrix} 0 \\ \tau^{11} \\ \tau^{12} \end{pmatrix}, \mathbf{F}_2^{\nu}(\mathbf{u}) = \frac{1}{Re} \begin{pmatrix} 0 \\ \tau^{21} \\ \tau^{22} \end{pmatrix}. \tag{8}$$

The fraction of the finite volume (FV) V covered by fluid phase i is $\zeta^i(t) = \frac{1}{V} \int\limits_{\Omega \cap \Omega^i} dV$. Within Ω, $\zeta^1 + \zeta^2 = 1$ must be satisfied.

According to [5,11] the conservation equations (5) are integrated in time for each fluid phase and coupled by the interface interaction $\mathbf{X}^i = \int_{\Delta\Upsilon} \mathbf{F} \cdot \mathbf{n}_I^i \, d\Upsilon'$, which ensures global conservation. It accounts for transfer of mass and momentum across the interface $\Upsilon = \partial\Omega^{1,2}(t) = \Omega^1(t) \cap \Omega^2(t)$. Note that $\mathbf{n}_I^1 = \mathbf{n}_I$ and $\mathbf{n}_I^2 = -\mathbf{n}_I$, with $\mathbf{n}_I$ denoting the interface-normal vector, Fig. 1. Considering the interaction of the two immiscible fluids at the interface, for each

$$\widetilde{\mathbf{U}}^i = \zeta^i \mathbf{U}^i \tag{9}$$

the system of conservation equations

$$\int_{t^n}^{t^{n+1}} dt \int_{\Omega \cap \Omega^i} \frac{\partial \widetilde{\mathbf{U}}^i}{\partial t} \, dV + \int_{t^n}^{t^{n+1}} dt \int_{\Gamma} \left(\mathbf{F}_1^i, \mathbf{F}_2^i \right) \cdot \mathbf{n}_{\Gamma} \, d\Gamma' = \int_{t^n}^{t^{n+1}} dt \int_{\Omega \cap \Omega^i} \mathbf{S}^i \, dV + \int_{t^n}^{t^{n+1}} dt \, \mathbf{X}^i \tag{10}$$

holds, where $\mathbf{F}_{\beta}^i = \mathbf{F}_{\beta}(\mathbf{U}^i)$, and $\mathbf{S}^i = \mathbf{S}(\mathbf{U}^i)$. For a time interval $\Delta t \leq \frac{\Delta x}{s_{\max}^n}$, where $s_{\max}^n$ denotes the maximum wave speed within the domain at time t^n, we define:

$$\overline{\mathbf{F}}_{\beta} = \lim_{\Delta t \to 0} \frac{1}{\Delta t} \int_{t^n}^{t^{n+1}} \mathbf{F}_{\beta} \, dt \, , \; \overline{\mathbf{X}} = \lim_{\Delta t \to 0} \frac{1}{\Delta t} \int_{t^n}^{t^{n+1}} \mathbf{X} \, dt \, , \; \overline{\mathbf{S}} = \lim_{\Delta t \to 0} \frac{1}{\Delta t} \int_{t^n}^{t^{n+1}} \mathbf{S} \, dt \, . \tag{11}$$

2.2. Discrete solution of the conservation equations

In discrete, Cartesian space, for each FV of $\Delta V_{[i,j]}$ we define a cell-averaged vector of conservative states at time t^n as $\widetilde{\mathbf{U}}_{[i,j]}^{i,n} = \frac{1}{\Delta V_{[i,j]}} \int\limits_{\Delta V_{[i,j]} \cap \Omega_{[i,j]}^i} \mathbf{U}_{[i,j]}^{i,n} dV = \widehat{\mathbf{U}}_{[i,j]}^{i,n} \zeta_{[i,j]}^{i,n}$ with $\widehat{\mathbf{U}}_{[i,j]}^{i,n} = \frac{1}{\Delta V_{[i,j]}^{i,n}} \int\limits_{\Delta V_{[i,j]}^{i,n}} \mathbf{U}_{[i,j]}^{i,n} dV$. In order to calculate the fluxes for the respective phase across the cell-faces, cell-face apertures are defined. The time-dependent aperture is the part of $\Gamma_{[i,j]}^i(t)$ that does not coincide with $\Upsilon_{[i,j]}(t)$ but with the cell face $\Gamma_{[i,j]}(t)$, [10].

At the right and upper cell face these are defined as depicted in Fig. 2.

For single-fluid cells, which are those not intersected by the interface, the apertures of phase 1 are unity within $\Omega_{[i,j]}^1$ and zero within $\Omega_{[i,j]}^2$, and vice versa for phase 2. Within the scope of this work, the cell-face apertures are calculated as in Hu et al. [5].

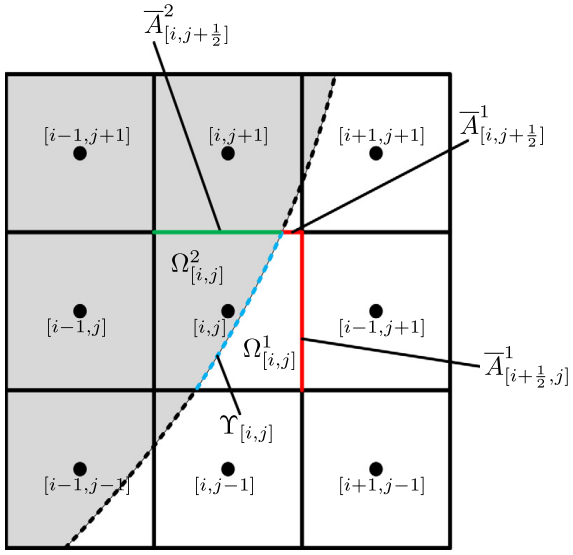

Fig. 2. Two-dimensional schematic of conservative discretization of a cut cell.

Calculating $\zeta^i_{[i,j]}$, and $\Delta\Upsilon_{[i,j]}$ according to Lauer et al. [11] allows to evaluate

$$\widetilde{\mathbf{U}}^{i,n+1}_{[i,j]} = \widetilde{\mathbf{U}}^{i,n}_{[i,j]} + \Delta t \left(\frac{\overline{A}^i_{[i-\frac{1}{2},j]}\overline{\mathbf{F}}^i_{[i-\frac{1}{2},j]} - \overline{A}^i_{[i+\frac{1}{2},j]}\overline{\mathbf{F}}^i_{[i+\frac{1}{2},j]}}{\Delta x_1} + \right. \\ \left. + \frac{\overline{A}^i_{[i,j-\frac{1}{2}]}\overline{\mathbf{G}}^i_{[i,j-\frac{1}{2}]} - \overline{A}^i_{[i,j+\frac{1}{2}]}\overline{\mathbf{G}}^i_{[i,j+\frac{1}{2}]}}{\Delta x_2} + \frac{\overline{\mathbf{X}}^i_{[i,j]}}{\Delta x_1 \Delta x_2} + \overline{\mathbf{S}}^i_{[i,j]} \right) , \tag{12}$$

where $\overline{\mathbf{X}}^i_{[i,j]}$ summarizes the exchange terms which are based on the solution of the interface interaction equations. The contributions to the interfacial exchange, relevant within the scope of this work, are discussed in section 3.2. Buoyant forces are accounted for by

$$\overline{\mathbf{S}}^i_{[i,j]} = \frac{1}{Fr^2}\left(\overline{\rho}^i_{[i,j]} - 1\right)\begin{bmatrix}0\\ \mathbf{g}\end{bmatrix} \tag{13}$$

2.2.1. Discrete solution of the intercell fluxes

The governing equations of the individual fluids are discretized by a 5th-order WENO scheme [12] in combination with a Roe Riemann solver [13] adapted to weakly compressible fluids. Successful applications of Roe schemes to the solution of weakly compressible flows have been demonstrated by e.g. Marx [14], Elsworth et al. [15] and Schranner et al. [8] in combination with the artificial-compressibility approach (ACA) of Chorin and Temam [16,17] for closure of the systems of conservation equations.

Tait's approach for weakly compressible fluids

A drawback of the ACA [8,16] is that for large density ratios the speed of sound of the less dense fluid is huge as $\left(\rho a^2\right)^1 = \left(\rho a^2\right)^2$, entailing an unphysically stiff gaseous phase and diminishing Δt. Independent artificial sound speeds can be obtained with the Tait equation of state (EoS)

$$p = p(\rho) = p_1\left[\left(\frac{\rho}{\rho_0}\right)^{\omega} - 1\right] + p_0 \,, \tag{14a}$$

$$a^2 = \frac{p_1}{\rho_0^{\omega}}\omega\rho^{(\omega-1)} = \frac{\omega}{\rho}\left(p - p_0 + p_1\right) \tag{14b}$$

with $\omega = 1 + 10^{-7}$. $p_0 = p\ (t = 0)$ is a free parameter and p_1 is based on a targeted (artificial) speed of sound, chosen to constrain the Mach number well below 0.3, globally. Note that as long as $M < 0.3$ is maintained by proper choice of $a^{\alpha}, \alpha = 1, 2$, the solutions are insensitive to variations of a.

Weakly compressible Roe Riemann solver

Tait's EoS requires adaption of the compressible Roe [13] numerical intercell-flux function

$$\overline{\mathbf{F}}_{[i+\frac{1}{2}]} = \frac{1}{2}\left(\overline{\mathbf{F}}(\overline{\mathbf{U}}^{(l)}) + \overline{\mathbf{F}}(\overline{\mathbf{U}}^{(r)})\right) - \frac{1}{2}\sum_{i=1}^{m} \widetilde{\delta}_i \left|\widetilde{\lambda}_i\right| \widetilde{\mathbf{K}}^{(i)}. \tag{15}$$

In Roe's approach the linearization of the local flux Jacobian $\widetilde{\mathbf{A}} = \widetilde{\mathbf{A}}\left(\overline{\mathbf{U}}^{(l)}, \overline{\mathbf{U}}^{(r)}\right)$ is essential. (l) and (r) denote the high-order reconstructed conservative states at the left and right side of cell face $[i+\frac{1}{2}]$. For reconstruction a 5th-order WENO scheme [12] with $\epsilon = 10^{-15}$ is employed. The Roe matrix $\widetilde{\mathbf{A}}$ with the eigenvalues $\widetilde{\lambda}_i$, right eigenvectors $\widetilde{\mathbf{K}}^{(i)}$, and wave strengths $\widetilde{\delta}_i$ is given in App. A.1.

2.2.2. Time integration and time-step constraints

The conservation equations (12) are integrated in time explicitly with a 2nd-order TVD Runge–Kutta scheme [18]. The time-step is determined according to the following considerations:

- The advective terms of the transport equations limit $\triangle t$ according to

$$\triangle t_{adv} = \frac{min\left(\triangle x_\alpha\right)}{max|u_\alpha + a|} \tag{16}$$

  where α represents one of the spatial directions.
- Furthermore, $\triangle t$ may be limited due to buoyancy [19],

$$\triangle t_{grav} = \frac{2min\left(\triangle x_\alpha\right)}{max|u_\alpha + a| + \sqrt{\left(max|u_\alpha + a|\right)^2 + \frac{4min(\triangle x_\alpha)}{Fr_{ref}^2}}} \tag{17}$$

- as well as viscous stresses [19],

$$\triangle t_{visc} = \frac{3}{14} min\left(\frac{\rho_1}{\mu_1}; \frac{\rho_2}{\mu_2}\right) Re_{ref} \left(min\left(\triangle x_\alpha\right)\right)^2 . \tag{18}$$

- The explicit treatment of capillary stresses is stable when the chosen time step size allows to represent capillary wave motion on the computational grid, [20]. The maximum resolvable wave number is

$$k_{max} = \frac{2\pi}{\lambda_{min}} = \frac{2\pi}{2min\left(\triangle x_\alpha\right)} = \frac{\pi}{min\left(\triangle x_\alpha\right)}. \tag{19}$$

  The maximum advection speed of capillary waves is

$$c_{kap} = \sqrt{\frac{We_{ref} k_{max}}{\rho_1 + \rho_2}} . \tag{20}$$

  Considering that two capillary waves with opposite direction of advection may concurrently enter the same cell, one obtains

$$\triangle t_{cap} = \frac{1}{2}\frac{min\left(\triangle x_\alpha\right)}{c_{kap}} = \sqrt{\frac{min\left(\triangle x_\alpha\right)^3 We_{ref}\left(\rho_1 + \rho_2\right)}{4\pi}} . \tag{21}$$

Consequently, the time step size is determined per iteration according to

$$\triangle t = CFL \cdot min\left(\triangle t_{adv}; \triangle t_{grav}; \triangle t_{visc}; \triangle t_{cap}\right) , \tag{22}$$

where $CFL = 0.3$ is chosen.

The intersection of the interface with the Cartesian grid may result in cells of diminishing volume fraction $\zeta^i_{[i,j]}$, denoted as "small cells". Based on the time step constraints of cells with $\zeta^i_{[i,j]} \approx 1$, denoted as "full cells", spurious solutions may evolve for "small cells". A more restrictive constraint on Δt would be numerically too expensive. A conservative mixing procedure has been proposed by Hu et al. [5] as a remedy. In contrast to [5], where all mixing operations are gathered once to update $\widetilde{\mathbf{U}}^{i,n+1}_{[i,j]}$, mixing between $\widetilde{\mathbf{U}}^{i,n+1}_{[i,j]}$ and the respective target cells is carried out consecutively. For this purpose, the mixing operations are ordered in descending magnitude of mixing fractions β_m, $m = 1, 2, 3$. The sequential execution takes into account that $\widetilde{\mathbf{U}}^{i,n+1}_{[i,j]}$ has been altered by preceding mixing operations with target cells and larger β_m. Only cells of $\zeta^{i,n+1}_{[i,j]} \leq 0.3$ need to be considered as small cells to obtain stable solutions, whereas in [5] cells of $\zeta^{i,n+1}_{[i,j]} \leq 0.5$ are defined as small cells. In addition, a wavelet-based adaptive multi-resolution algorithm [21] is employed for improving computational efficiency. The adaptive grid-refinement follows a two-step procedure. Firstly, a multi-resolution representation of the

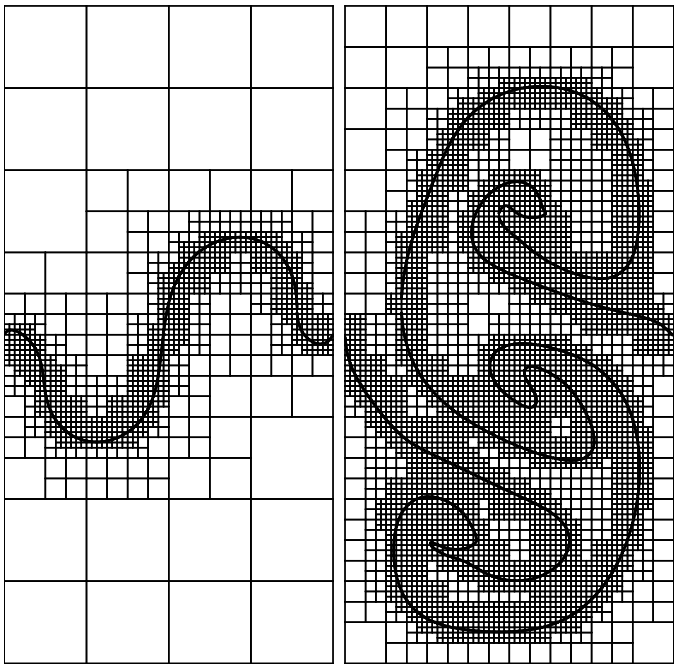

(a) $t = 1.5$ (b) $t = 4.5$

Fig. 3. Adaptive block structure due to wavelet-based adaptive multi-resolution algorithm [21]. Six refinement levels, each block contains 16×16 FVs. Test case: RTI.

interface and flow field at the interface is generated. Secondly, multi-resolution analysis within Ω^1 and Ω^2, starting at the coarsest level leads to successive grid adaption. Data are structured pyramidal, and block-based storage of data packages is disconnected from data operation. The algorithm is employed as described in [21]. Fig. 3 visualizes the resulting dynamically adapted block structure for the simulation of a RTI, see Sec. 4.1.

3. Modeling of the interface

3.1. Description and propagation of the interface

The interface is captured implicitly by a level-set function $\phi(\mathbf{x}, t)$ [3,22] with $|\nabla\phi| = 1$ such that $\phi(\mathbf{x}, t) \equiv 0$ at $\Upsilon(\mathbf{x}, t)$. In $\Omega^2(\mathbf{x}, t)$ $\phi(\mathbf{x}, t) < 0$, and $\phi(\mathbf{x}, t) > 0$ in $\Omega^1(\mathbf{x}, t)$. Based on $\phi(\mathbf{x}, t)$, defined in a narrow band around $\Upsilon(\mathbf{x}, t)$ [23], a normalized interface normal vector, directed from Ω^2 to Ω^1,

$$\mathbf{n}_I(\mathbf{x}) = \frac{\nabla\phi(\mathbf{x})}{|\nabla\phi(\mathbf{x})|} \tag{23}$$

can be constructed everywhere on $\Upsilon(\mathbf{x}, t)$. Second-order central approximations to $\frac{\partial\phi(\mathbf{x})}{\partial x_\alpha}$ are used within this work. For $\phi(\mathbf{x}, t) = 0$ the transport equation with the interface velocity $\mathbf{u}_I = \mathbf{u}_{I,\perp}(\mathbf{x}, t)$ [24] holds

$$\frac{\partial\phi(\mathbf{x}, t)}{\partial t}\Big|_{\phi=0} + \mathbf{u}_I^T(\mathbf{x}, t) \cdot (\nabla\phi(\mathbf{x}, t))\Big|_{\phi=0} = 0\,. \tag{24}$$

To propagate ϕ in time by Eq. (24) while maintaining its signed distance property, the integration of the transport equation for $\phi(\mathbf{x}, t)$ has two substeps, *advection* and *reinitialization*, see e.g. [1,25]. Within the original reinitialization algorithm of Sussman et al. [1], a smoothed sign function serves to suppress reinitialization in cells containing the interface. In this work, we explicitly exclude such cells. Details on the algorithm are provided in App. A.2.

3.2. Interface exchange terms

We assume neither mass nor energy exchange across the interface, and a constant surface tension coefficient. According to Luo et al. [7] the interfacial momentum flux due to surface tension is naturally incorporated into the inviscid flux such that $\overline{\mathbf{X}}^i_{[i,j]} = \left(\overline{\mathbf{X}}^+ + \overline{\mathbf{X}}^\nu\right)^i_{[i,j]}$, where $\overline{\mathbf{X}}^{+,i}$ and $\overline{\mathbf{X}}^{\nu,i}$ denote the inviscid and viscous interface exchange of momentum, respectively, for fluid phase i.

Inviscid interface exchange

At mechanical equilibrium, the interfacial stress balance in interface-normal direction leads to

$$[\![p]\!]_\Upsilon = p^1 - p^2 = -\frac{1}{We}\sigma\kappa_\Upsilon \ = \sigma_c, \tag{25}$$

where σ is the surface tension coefficient and $\kappa_\Upsilon = \nabla\cdot\mathbf{n}_I$ denotes the interface mean curvature. Eq. (23) is evaluated at the cell center, where not necessarily $\phi_{[i,j]} = 0$. The 2D sub-cell corrected κ_Υ at the interface is

$$\kappa_{\Upsilon,2d} = \left(|\kappa_{[i,j]}| + \kappa^2_{[i,j]}\phi_{[i,j]}\right) S\left(\kappa_{[i,j]}\right) \ , \tag{26}$$

where (ϕ) is the sign function. $\kappa_{[i,j]}$ is the local mean curvature and approximated with 2nd-order central differences according to

$$\kappa(\phi)_{[i,j]} = \left[\frac{D^c_{x_1}[\phi]^2 D^c_{x_2}[D^c_{x_2}[\phi]] + D^c_{x_2}[\phi]^2 D^c_{x_1}[D^c_{x_1}[\phi]] - 2D^c_{x_1}[\phi]D^c_{x_2}[\phi]D^c_{x_1}[D^c_{x_2}[\phi]]}{\left(D^c_{x_1}[\phi]^2 + D^c_{x_2}[\phi]^2\right)^{3/2}}\right]_{[i,j]} . \tag{27}$$

Details on the derivation of Eq. (26) are provided in A.3. To impose the interface normal momentum exchange due to Eq. (25) a constrained Riemann problem [26] is solved with an acoustic Riemann solver [27] for

$$u_{I,\perp} = \frac{Z^1 u^1_\perp + Z^2 u^2_\perp}{Z^1 + Z^2} - \frac{\left(p^1 - p^2 - \sigma_c\right)}{Z^1 + Z^2} \ , \text{ and} \tag{28a}$$

$$p^i_I = \frac{Z^2\left(p^1 - \sigma_c\delta_{i2}\right) + Z^1\left(p^2 + \sigma_c\delta_{i1}\right)}{Z^1 + Z^2} - \frac{Z^1 Z^2}{Z^1 + Z^2}\left(u^1_\perp - u^2_\perp\right), \tag{28b}$$

where $Z^i = \rho^i a^i$ are the acoustic impedances of the respective fluid i, δ_{ij} is the Kronecker-symbol. Note that the approximated interface values of Eq. (28) result from linearization of the primitive-variable Euler equations [28].

The inviscid exchange term is

$$\overline{\mathbf{X}}^{+,i}_{[i,j]} = \int_{\Delta\Upsilon} \overline{\mathbf{F}}_{[i,j]}\cdot\overline{\mathbf{n}}^i_{I,[i,j]}\, d\Upsilon' = -\overline{p}^i_{I,[i,j]}\,\overline{\Delta\Upsilon}_{[i,j]}\begin{bmatrix}0\\ \overline{n}^i_{I,1}\\ \overline{n}^i_{I,2}\end{bmatrix}_{[i,j]} \ , \tag{29}$$

with the interface segment length

$$\overline{\Delta\Upsilon}_{[i,j]} = \left|\overline{\mathbf{\Delta\Upsilon}}_{[i,j]}\right| , \tag{30}$$

and

$$\overline{\mathbf{\Delta\Upsilon}}_{[i,j]} = \overline{\Delta\Upsilon}_{[i,j]}\overline{\mathbf{n}}^i_I = \begin{bmatrix}\left(A^i_{[i-\frac{1}{2},j]} - A^i_{[i+\frac{1}{2},j]}\right)\Delta x_2\\ \left(A^i_{[i,j-\frac{1}{2}]} - A^i_{[i,j+\frac{1}{2}]}\right)\Delta x_1\end{bmatrix} . \tag{31}$$

Viscous interface exchange

To account for the exchange of viscous momentum, Luo et al. [7] have constructed a viscous interface exchange term,

$$\overline{\mathbf{X}}^{\nu,i}_{[i,j]} = \int_{\Delta\Upsilon}\left(\overline{\mathbf{F}}^{\nu,\Upsilon} + \overline{\mathbf{G}}^{\nu,\Upsilon}\right)_{[i,j]}\cdot\overline{\mathbf{n}}^i_{I,[i,j]}\, d\Upsilon' = \overline{\Delta\Upsilon}_{[i,j]}\begin{bmatrix}0\\ \overline{\mathbf{T}}^\Upsilon\end{bmatrix}_{[i,j]}\cdot\begin{bmatrix}0\\ \overline{\mathbf{n}}^i_I\end{bmatrix}_{[i,j]} \ , \tag{32}$$

that is continuous across the interface. The effective viscosity μ^Υ is defined as the harmonic mean of μ^1 and μ^2 with respect to the volume fractions of the two fluids,

$$\mu^\Upsilon = \frac{\mu^1\mu^2}{\mu^1\zeta^1 + \mu^2\zeta^2} \ . \tag{33}$$

The spatial derivatives of the velocities necessary to formulate the components of the shear-stress tensor are constructed from the fluid velocities on the respective side of the interface.

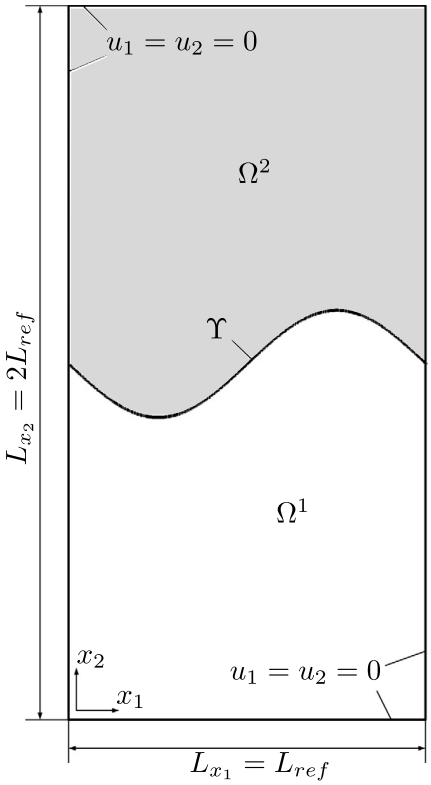

Fig. 4. Initial setup and boundary conditions for the RTI, adopted from [29].

4. Numerical results

As benchmark configurations, a 2D Rayleigh–Taylor instability and several cases of single gas bubbles rising in a liquid due to the influence of gravity at different Reynolds numbers are considered. For all configurations we employ the non-dimensional conservation equations (12) with the two-step algorithm for the interface propagation, see Sec. 3.1. In order to facilitate cross-method comparison and verification, we display and analyse results in non-dimensional form. E.g., RTI simulations have been performed with $L_{ref} = 1.0$ m. With Eq. (14) we optain $p_1 \approx 100\ \mathrm{kg\,m^{-1}\,s^{-2}}$ and $p_1 \approx 180\ \mathrm{kg\,m^{-1}\,s^{-2}}$ for phase 1 and 2, respectively. We have chosen $L_{ref} = 0.5$ m for the BLG and obtain $p_1 \approx 144\ \mathrm{kg\,m^{-1}\,s^{-2}}$ and $p_1 \approx 2.5\ \mathrm{kg\,m^{-1}\,s^{-2}}$ for phase 1 and 2, respectively. Moreover, for the RTI and BLG case it is $\rho_{ref} = 1.0\ \mathrm{kg\,m^{-3}}$, $U_{ref} = 1.0\ \mathrm{m\,s^{-1}}$, $p_0 = 1000\ \mathrm{kg\,m^{-1}\,s^{-2}}$, and $g_{ref} = 1\ \mathrm{m\,s^{-2}}$.

4.1. Rayleigh–Taylor instability

We investigate the evolution of a 2D Rayleigh–Taylor instability at a Reynolds number $Re = 420$. Two immiscible fluids are enclosed in a rectangular domain, Fig. 4. The interface is located at $x_2 = L_{ref}\ [1 - 0.15sin\left(\frac{2\pi x_1}{L_{ref}}\right)]$. Fluid 2, with $\rho^2 = 1.8\ \rho_{ref}$, is in the upper half of the domain while fluid 1, with $\rho^1 = \rho_{ref}$, is within the lower half. The kinematic viscosities are equal, $\nu^1 = \nu^2$. The system is under the influence of gravity with $\mathbf{g} = g\,(0, -1)$, $\sigma\,(\mathbf{x}, t) = 0$. Furthermore, $a = a^1 = a^2 = 10\ U_{ref}$. Data is normalized with T_{ref}.

Fig. 5 depicts the vorticity and interface for four consecutive times. The initial distortion entails vorticity generation at the interface. At the solid walls, a second shear layer evolves. Due to buoyancy and initiated by the distortion, fluid of phase 2 is directed downward penetrating fluid of phase 1 and vice versa. Fluid of the other phase is displaced. At the interface, momentum conservation holds and momentum is transfered from the fluid of higher momentum to the one of lower momentum. The acceleration of the less dense fluid 1 is larger than the deceleration of phase 2. In close proximity to the interface, phase 1 has a larger velocity gradient in interface normal direction and due to incompressibility, the velocity gradient in interface tangential direction is larger as well. This leads to broader plumes of phase 1.

In the interface-tangential direction, the no-slip boundary condition holds. The gradient of the interface-tangential velocity component in phase 1 in interface-normal direction is stronger, and vorticity magnitudes are higher. Due to the central vortex, the plumes are deflected counterclockwise. The formation of the roll-up in the lower left corner is primarily due to deflection of the plume of phase 2 at the solid walls. The roll-up in the upper right corner is due to viscous interaction of the two phases.

For a convergence study, we increase the refinement level until Υ of two consecutive levels of refinement are identical. For at least $t \leq 5.0$, the interface is adequately resolved with $\Delta x = \frac{1}{2048}$, as data with $\Delta x = \frac{1}{2048}$ and $\Delta x = \frac{1}{4096}$ are

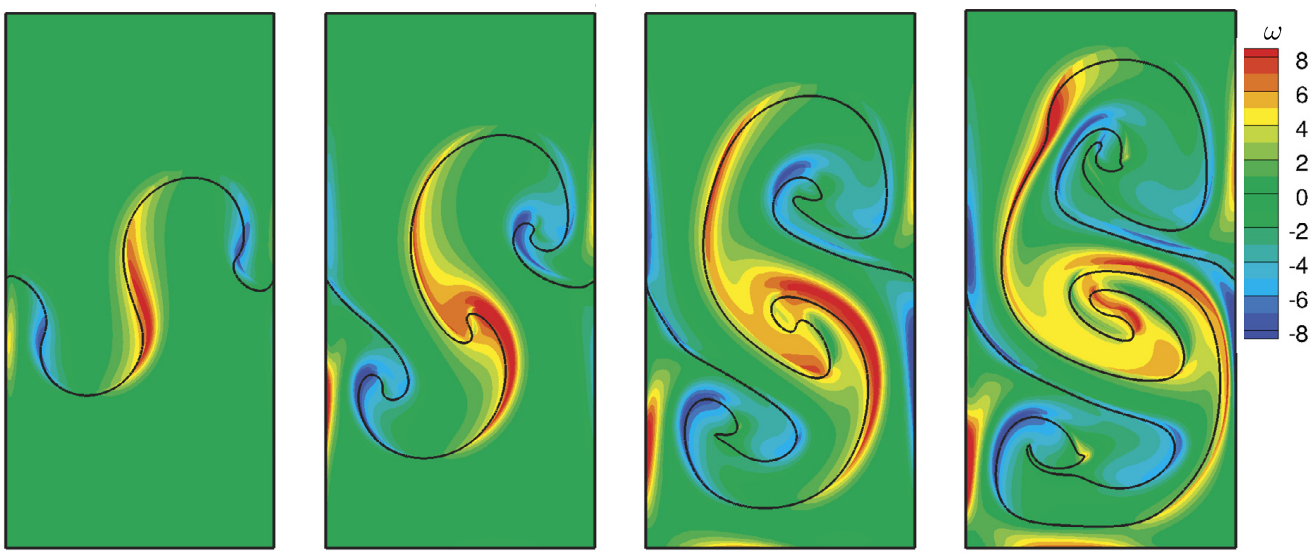

(a) $t = 2.0$ (b) $t = 3.0$ (c) $t = 4.0$ (d) $t = 5.0$

Fig. 5. Interface representation at maximum local resolution of $\Delta x = 1.0/2048$ (————) and vorticity contours.

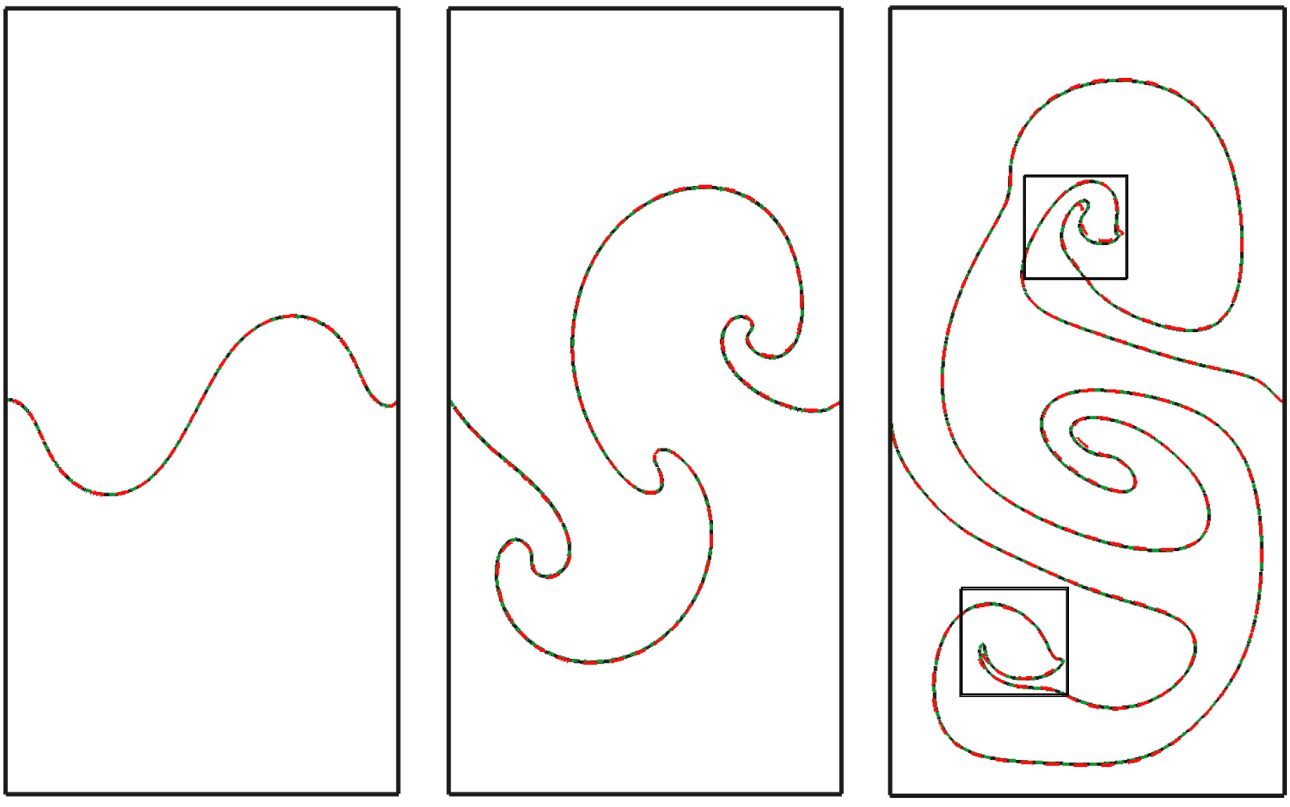

(a) $t = 1.0$ (b) $t = 3.0$ (c) $t = 5.0$

Fig. 6. Interface representation at maximum local resolution of $\Delta x = 1.0/4096$ (————), $\Delta x = 1.0/2048$ (----------), $\Delta x = 1.0/1024$ (– – – – –).

indistinguishable, see Figs. 6 and 7. Intersections of the interface with $x_2 = L_{ref}$ and $x_1 = L_{ref}/2$ for $0.5 \leq t \leq 7.0$ and at a resolution of $\Delta x = \frac{1}{2048}$ are listed in Tables 1 and 2, respectively.

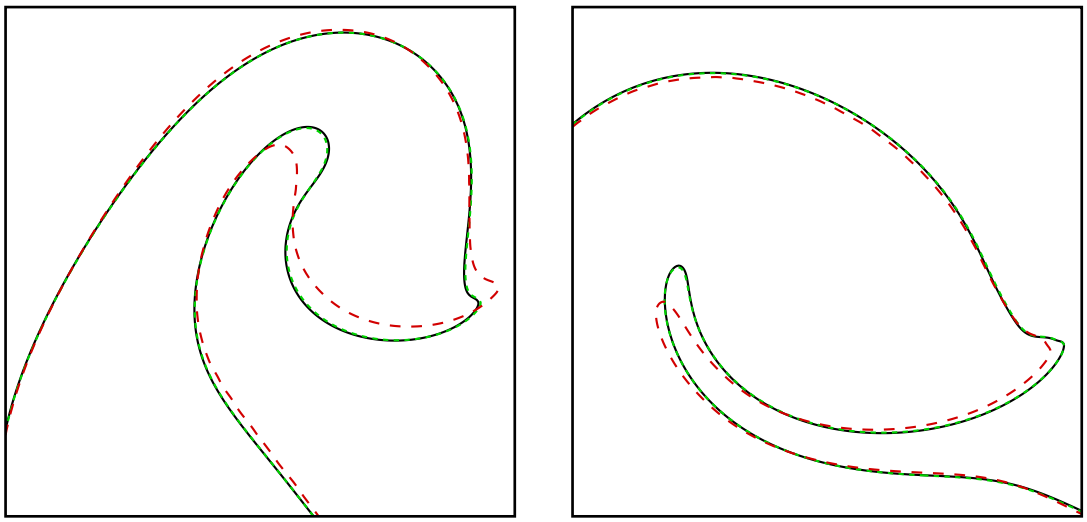

(a) Upper section. (b) Lower section.

Fig. 7. Details of the interface, at $t = 5.0$. $\Delta x = 1.0/4096$ (——), $\Delta x = 1.0/2048$ (- - - -), $\Delta x = 1.0/1024$ (– – – –).

Table 1
Intersections of the interface (x_1) with $x_2 = L_{ref}$, $\Delta x = 1.0/2048$.

	$t = 0.5$	$t = 1.0$	$t = 1.5$	$t = 2.0$	$t = 2.5$	$t = 3.0$	$t = 3.5$
x_1	0.503672	0.023899	0.058131	0.062492	0.019726	0.105964	0.000122
	0.992432	0.500253	0.483937	0.452159	0.394785	0.388668	0.285265
	0.000258	0.945981	0.910802	0.873745	0.836397	–	0.996961
	0.999722	0.999877	0.999866	–	–	–	–
	$t = 4.0$	$t = 4.5$	$t = 5.0$	$t = 5.5$	$t = 6.0$	$t = 6.5$	$t = 7.0$
x_1	0.232108	0.180109	0.137103	0.106934	0.089343	0.082465	0.083193
	0.998339	0.996767	0.414494	0.314355	0.24333	0.205198	0.18961
	–	–	0.704767	0.448609	0.355729	0.333713	0.289151
	–	–	0.994631	0.499606	0.697146	0.763754	0.795402
	–	–	–	0.854808	0.910221	0.935924	0.951385
	–	–	–	0.995551	0.99749	0.999553	0.999756

Table 2
Intersections of the interface (x_2) with $x_1 = L_{ref}/2$, $\Delta x = 1.0/2048$.

	$t = 0.5$	$t = 1.0$	$t = 1.5$	$t = 2.0$	$t = 2.5$	$t = 3.0$	$t = 3.5$
x_2	0.981001	0.999164	1.09427	0.705403	0.516944	0.368138	0.244674
	–	–	–	0.854852	0.850503	0.767477	0.713227
	–	–	–	1.28075	1.39891	1.49877	0.865207
	–	–	–	–	–	–	0.891191
	–	–	–	–	–	–	1.59009

	$t = 4.0$	$t = 4.5$	$t = 5.0$	$t = 5.5$	$t = 6.0$	$t = 6.5$	$t = 7.0$	$t = 7.0$
x_2	0.151672	0.992232	0.078166	0.067884	0.055377	0.057976	0.044096	1.68286
	0.333385	0.254584	0.232559	0.232921	0.242811	0.0634833	0.084999	1.7494
	0.519346	0.521001	0.524987	0.554973	0.574103	0.172037	0.229264	1.7704
	0.692652	0.670757	0.655282	0.653748	0.651787	0.28534	0.408715	1.81614
	0.829705	0.808479	0.799878	0.800913	0.788599	0.580936	0.429772	1.82349
	0.934364	0.971003	0.87513	0.863213	0.850494	0.642853	0.438751	1.87578
	1.20807	1.18642	0.95689	0.999741	1.0262	0.746517	0.576227	1.89181
	1.34565	1.30998	1.02671	1.08382	1.1258	0.817401	0.62762	1.94955
	1.66868	1.4017	1.18062	1.18224	1.1905	1.0684	0.703288	
	–	1.46238	1.3067	1.29747	1.30818	1.1564	0.767833	
	–	1.73707	1.41169	1.48887	1.60779	1.20272	1.10399	
	–	–	1.48369	1.54951	1.78855	1.5554	1.18155	
	–	–	1.50752	1.61011	1.91721	1.70557	1.21844	
	–	–	1.55593	1.66376	–	1.87531	1.52033	
	–	–	1.80365	1.86803	–	1.94224	1.58119	

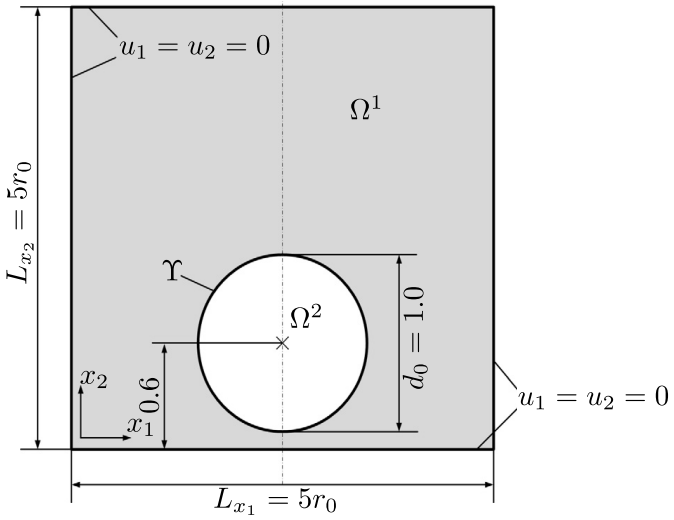

Fig. 8. Initial setup and boundary conditions for the BLG.

4.2. Air bubble submerged in a denser liquid and rising due to the influence of gravity

The evolution of a single bubble rising under the influence of gravity is studied, i.e. $\mathbf{g} = g\,(0, -1)$. The setup is depicted in Fig. 8. Following Sussman et al. [1], the density and viscosity ratios are $\frac{\rho^1}{\rho^2} = 1000$, $\frac{\mu^1}{\mu^2} = 100$ with $\rho^1 = \rho_{ref}$ and $Eo = 200$. Two Reynolds numbers are considered, namely $Re_l = 100$ and $Re_h = 1000$. For Re_l the corresponding capillary number is $Ca_l = 2$; $Ca_h = 0.2$ corresponds to Re_h. Furthermore, $a^1 = 12\ U_{ref}$ and $a^2 = 50\ U_{ref}$.

Low Reynolds number

Grid resolution is increased until $\Upsilon(\mathbf{x}, t)$ converges. Results for three consecutive grid resolutions are shown. Fig. 9 depicts the interface, the velocity magnitude and vorticity are shown in Fig. 10. Fig. 11 depicts the centroid,

$$\mathbf{y}_c = (y_1, y_2) = \frac{\int_{dV} \zeta^\alpha \mathbf{x}\, dV'}{\int_{dV} \zeta^\alpha\, dV'} \approx \frac{\sum_{[i,j]}\{\zeta^\alpha \mathbf{x} \Delta V\}}{\sum_{[i,j]}\{\zeta^\alpha \Delta V\}}\,, \tag{34}$$

and the degree of circularity,

$$C = \frac{P_a}{P_b} = \frac{\pi d_a}{\int_{\Delta\Upsilon} 1 d\Upsilon'} \approx \frac{\pi d_a}{\sum_{[i,j]}\{\overline{\Delta\Upsilon}\}} \tag{35}$$

over time for $\Delta x = 2.5/2048$ and $\Delta x = 2.5/1024$. In Eqs. (34), (35) α, $\mathbf{x}$, P_a denote the disperse phase, the Cartesian coordinate vector, and the perimeter of an area-equivalent circle, with diameter $d_a \approx 2\sqrt{\sum_{[i,j]}\{\zeta^\alpha \Delta V\}/\pi}$. Note that for a perfectly circular drop C is unity. The x_1-component of the centroid, y_1 considers half of the bubble. The degree of circularity, centroid, as well as the lower and upper axial position of the interface for $0.5 \leq t \leq 6$ with $\Delta t = 0.5$, $\Delta x = 2.5/2048$ are tabulated in Table 3.

Primary bubble evolution from circular to cap shape occurs dominantly within $0 \leq t \leq 3$, while for $t \approx 4$ the bubble is ascending freely. From the beginning of bubble evolution, two counter-rotating vortices can be observed at the bubble flanks, one clock-wise (negative ω) and one counter clock-wise. With increasing time, their magnitude increases and the bubble flanks become thinner. At $t \approx 3.2$ small, at first elongated, secondary bubbles shear off the flanks. The strong correlation of this incident to the discontinuity in $y_1(t)$, and $C(t)$ is apparent. The bubble diameter of the secondary bubbles is $d \approx 0.01$, implying $Eo \approx 0.02$, and $Re \approx 0.1$. Shortly after $t \approx 4$ the primary bubble ascent is interrupted. As a consequence of high local shear rates and comparably low local surface tension, unstable bubble cusps form for $t \geq 4.5$. In consequence a series of small bubbles sheads off, see Fig. 12.

Grid-independence of the results is observed for $\Delta x \leq 2.5/1024$. At lower resolutions sheading of small bubbles is not captured. The positions and shape of the primary and secondary bubbles are grid-independent for $\Delta x \leq 2.5/512$. For both resolutions C agrees perfectly for $t \leq 5$. A relative error of $\delta = \frac{C|_{2.5/2048} - C|_{2.5/1024}}{C|_{2.5/2048}} \leq 3\%$ is noted for the remaining time.

High Reynolds number

Results for three consecutive levels of grid refinement are reported. The evolving interface is depicted in Fig. 13, and the velocity magnitude and vorticity in Fig. 15. Fig. 14 illustrates the temporal evolutions of disperse-phase centroid and the degree of circularity for $\Delta x = 2.5/4096$ and $\Delta x = 2.5/2048$. Table 4 lists values for the degree of circularity, centroid, as well as the lower and upper axial position of the interface for $0.5 \leq t \leq 6$ with $\Delta t = 0.5$, $\Delta x = 2.5/4096$.

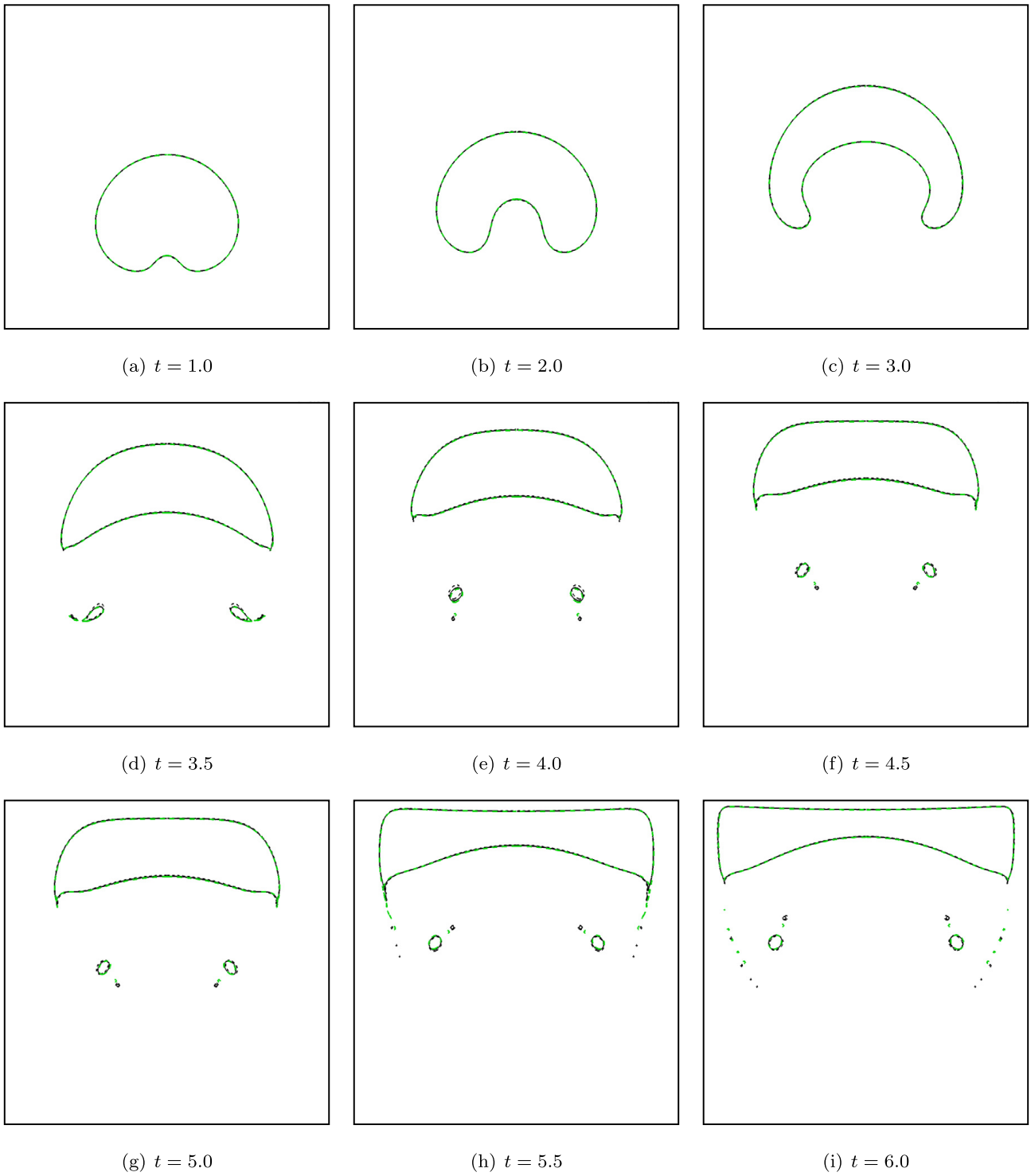

Fig. 9. Interface representation at maximum local resolution of $\Delta x = 2.5/2048$ (- - - - - - - - - - -), $\Delta x = 2.5/1024$ (———————), $\Delta x = 2.5/512$ (- - - - - - - - - - -), $Re = 100$, $Ca = 2$.

Viscous forces are subordinate to capillary forces in this low Ca bubble evolution. The initial bulk flow velocity is approximately 35% larger than in the low-Re case. The bubble evolves its temporary horse-shoe shape faster and more pronounced. The small-scale interface evolution leads to a decrease of the degree of circularity. The final cap shape is rapidly obtained.

In contrast to the low-Re case the secondary bubbles, detaching from the flanks of the primary bubble, are much larger. Their rise velocity (u_2) is negligible, indicated by a slower increase of $y_2(t)$. When resolution suffices, capillary waves of diminishing amplitude and high frequency revolve along the interface of the secondary bubbles. Time series 13 and 15 indicate grid-independence of the interface and dominant flow structures for $\Delta x \geq 2.5/2048$. For most of the time $C(t)$ is identical at the two highest resolutions. For the remaining, intermediate time frame $\delta = \frac{C|_{2.5/2048} - C|_{2.5/4096}}{C|_{2.5/2048}} \leq 6\%$; yet, y_2 is

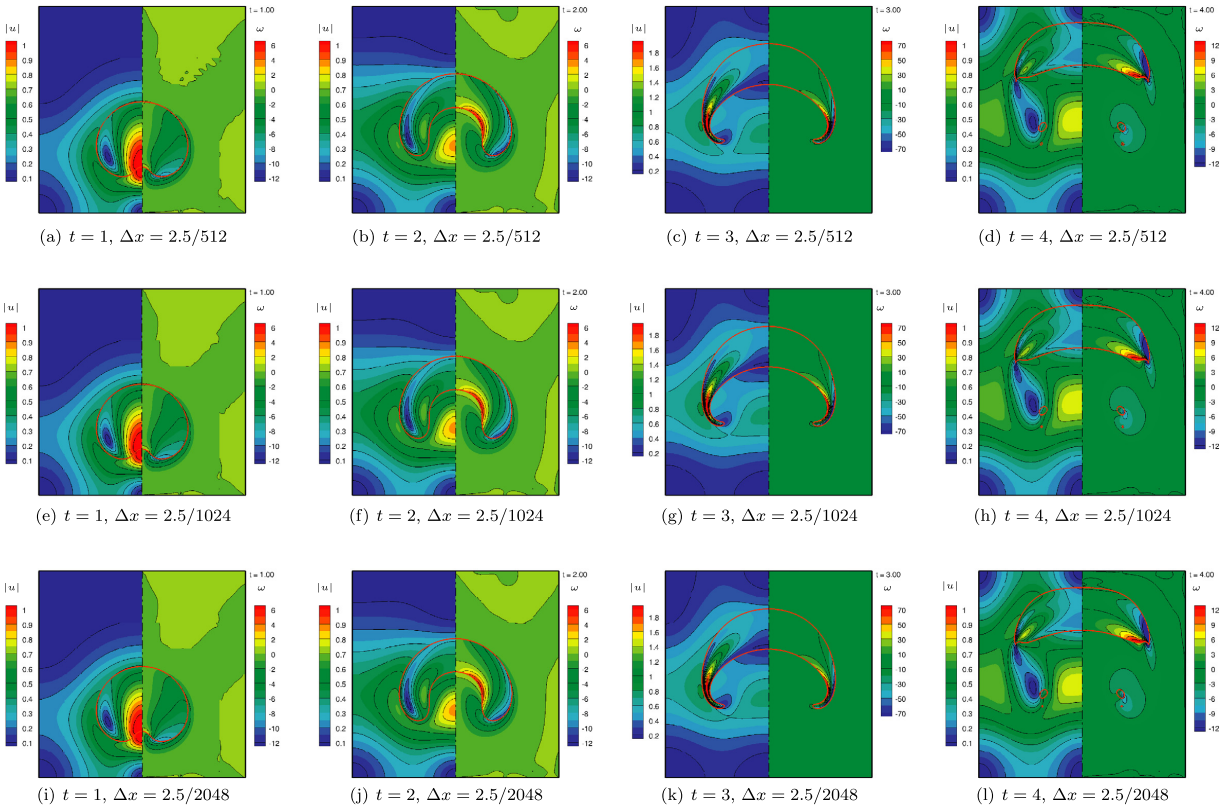

(a) $t = 1$, $\Delta x = 2.5/512$ (b) $t = 2$, $\Delta x = 2.5/512$ (c) $t = 3$, $\Delta x = 2.5/512$ (d) $t = 4$, $\Delta x = 2.5/512$

(e) $t = 1$, $\Delta x = 2.5/1024$ (f) $t = 2$, $\Delta x = 2.5/1024$ (g) $t = 3$, $\Delta x = 2.5/1024$ (h) $t = 4$, $\Delta x = 2.5/1024$

(i) $t = 1$, $\Delta x = 2.5/2048$ (j) $t = 2$, $\Delta x = 2.5/2048$ (k) $t = 3$, $\Delta x = 2.5/2048$ (l) $t = 4$, $\Delta x = 2.5/2048$

Fig. 10. Interface Υ (orange line), velocity magnitude $|\mathbf{u}|$ (left half), and vorticity ω (right half) at four time instances, resolutions of $\Delta x = 2.5/512$, $\Delta x = 2.5/1024$, $\Delta x = 2.5/2048$ are shown. (For interpretation of the references to color in this figure legend, the reader is referred to the web version of this article.)

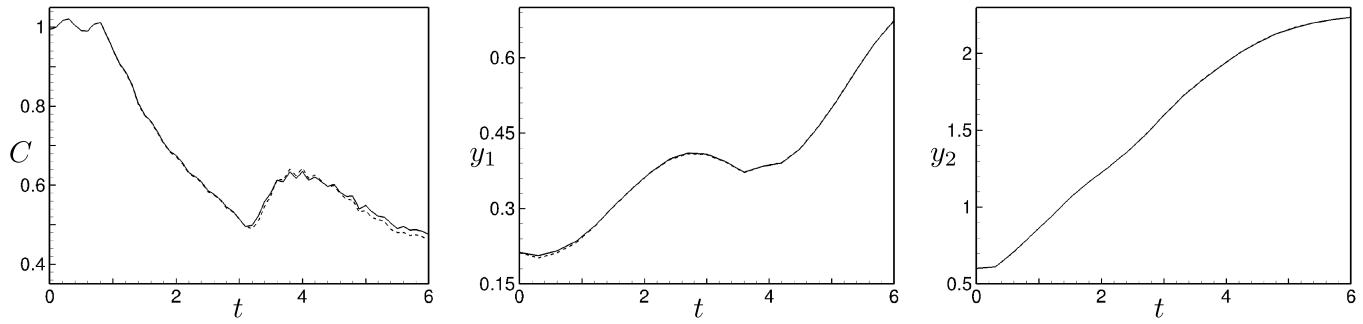

Fig. 11. Centroid and degree of circularity over time for a resolution of $\Delta x = 2.5/2048$ (——————), $\Delta x = 2.5/1024$ (- - - - - - - - - - -). $Re = 100$, $Ca = 2$.

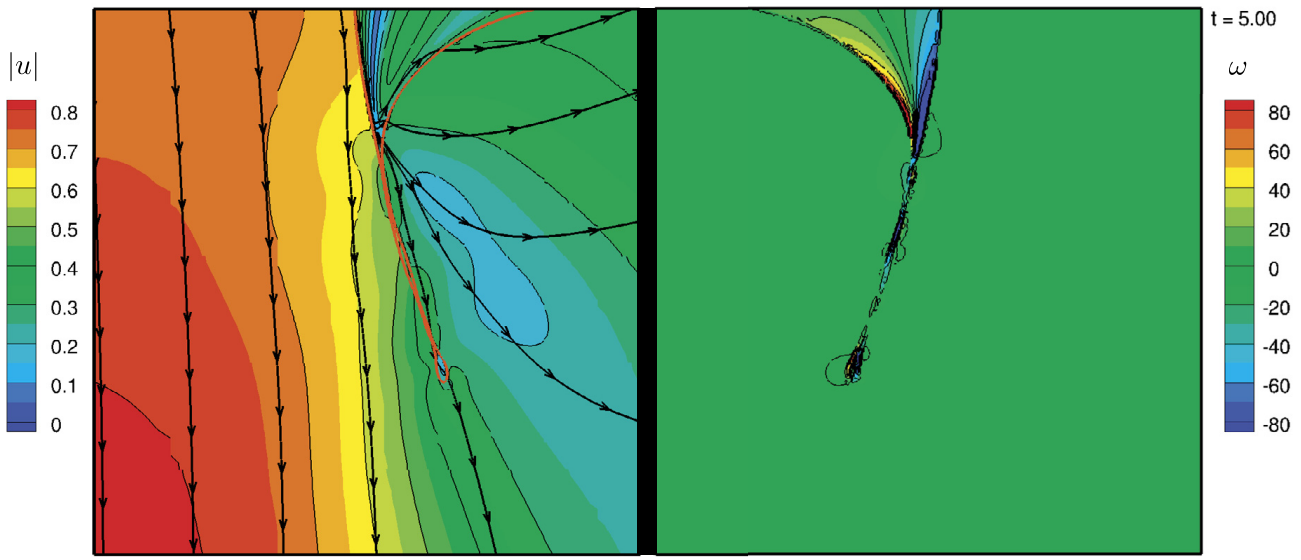

Fig. 12. Closeup of the cusp region at $t = 5$. Left side shows velocity magnitude, streamlines and Υ. Right side shows vorticity; note that the vorticity is clipped from $\omega_{min} \approx -220$ and $\omega_{max} \approx 130$ to $\omega_{min/max} = \pm 80$, $\Delta x = 2.5/4096$.

Table 3
Circularity (C), centroid (y_1, y_2), lower and upper axial position of the interface (z_1, z_2) at selected times for BLG, Re_l, Ca_l, $\Delta x = 2.5/2048$.

t	0.5	1.0	1.5	2.0	2.5	3.0
C	0.96484	0.90594	0.73158	0.59405	0.50696	0.42901
y_1	0.21239	0.24458	0.30381	0.36157	0.40194	0.40816
y_2	0.67636	0.86401	1.06169	1.22438	1.39200	1.59781
z_1	0.15302	0.56222	1.00058	1.28040	1.44658	1.55324
z_2	1.18091	1.34463	1.52181	1.68068	1.87805	2.04024
t	3.5	4.0	4.5	5.0	5.5	6.0
C	0.4424	0.49915	0.48933	0.41254	0.36491	0.37145
y_1	0.37935	0.38630	0.41932	0.49972	0.59390	0.66042
y_2	1.78878	1.94309	2.07029	2.15381	2.20701	2.23577
z_1	1.65767	1.78225	1.91655	2.04572	2.15483	2.22450
z_2	2.18876	2.29845	2.36693	2.40350	2.42423	2.43710

identical and y_1 differs with less than 1%. Moreover, the shape of the upper and lower side of the cap is resolved adequately at a resolution of $\Delta x = 2.5/512$.

Free ascent at high Reynolds number

The domain height is increased to $L_{x_2} = 7.5r_0$, permitting free ascent of the cap-shaped primary bubble at stationary rise velocity after pinch-off of the secondary bubbles. The data are plotted alongside the underresolved results of Sussman et al. [1] for rough comparison whenever applicable. The resolution is chosen as the one necessary for a converged ascent-trajectory and interface-shape at this Re, i.e. $\Delta x = 2.5/2048$. Interface representations agree until $t \approx 3.2$. For later stages the shape and ascent-velocity of the primary cap-bubble as well as the centre of mass of the secondary bubbles

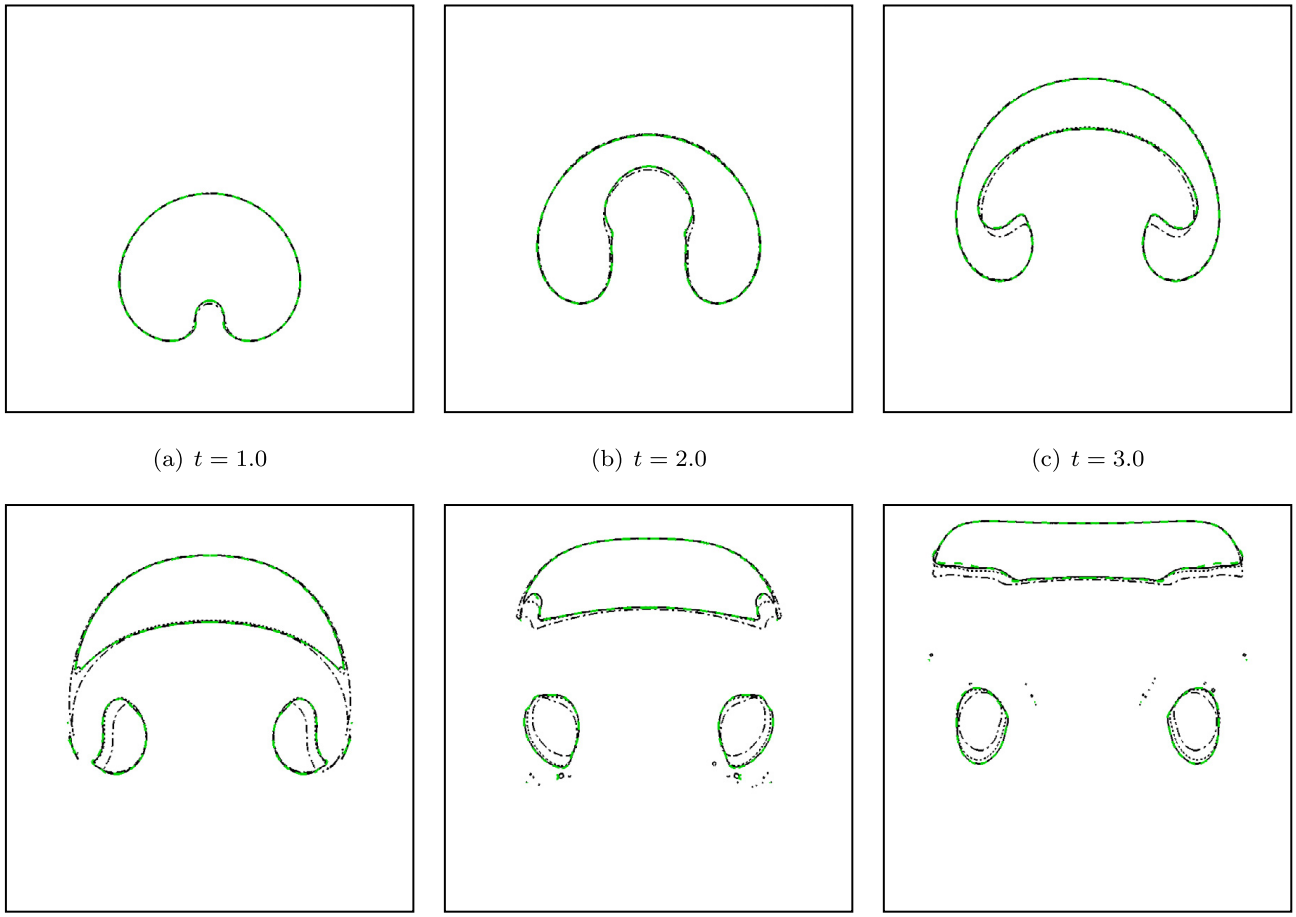

(a) $t = 1.0$ (b) $t = 2.0$ (c) $t = 3.0$

(d) $t = 3.5$ (e) $t = 4.0$ (f) $t = 5.0$

Fig. 13. Interface representation at maximum local resolution of 2.5/4096 (- - - - - - - - - - -), 2.5/2048 (———————), 2.5/1024 (- - - - - - - - - - -) , 2.5/512 (— - — - — - —), $Re = 1000$, $Ca = 0.2$.

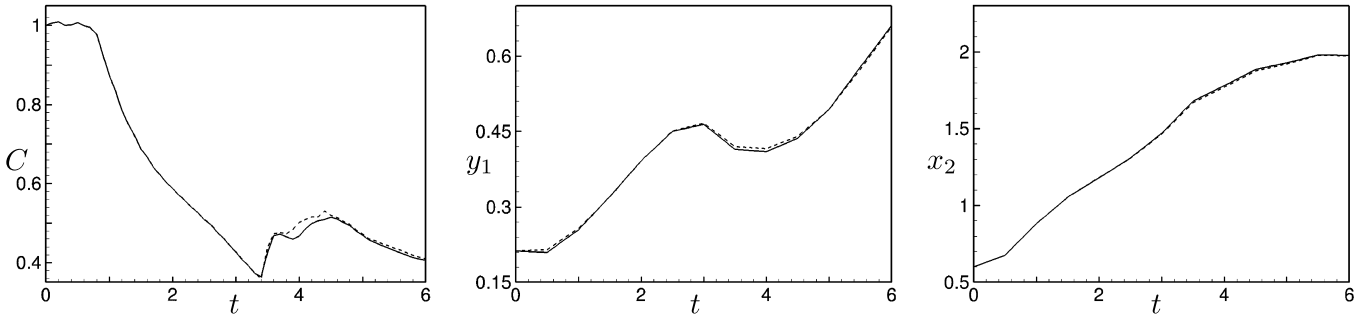

(a) $C(t)$ (b) $y_1(t)$ (c) $y_2(t)$

Fig. 14. Centroid and degree of circularity over time for a resolution of 2.5/4096 (———————), 2.5/2048 (- - - - - - - - - - -). $Re = 1000$, $Ca = 0.2$.

agree well with reference data, compare Fig. 16. In Ref. [1] another pair of bubbles is shown to form at pinch-off of the secondary bubbles. These are much smaller, which is in agreement with the observations of Grenier et al. [30]. The tertiary bubbles revolve around the rotating secondary ones until these are elongated and washed upwards in the wake flow of the cap. Furthermore, capillary waves of significant amplitude propagate from the rim to the symmetry axis of the cap. These waves, originating at the small bubble pinch-off, diminish over time. The shape of the top of the cap depends only on the stationary bulk fluid, at later stages on the upper domain boundary.

5. Summary and conclusion

In this work, a mass and momentum conservative, weakly compressible, fully Eulerian, sharp-interface method for the simulation of immiscible, viscous, incompressible two-phase flows has been presented. Coupled with a fifth-order WENO

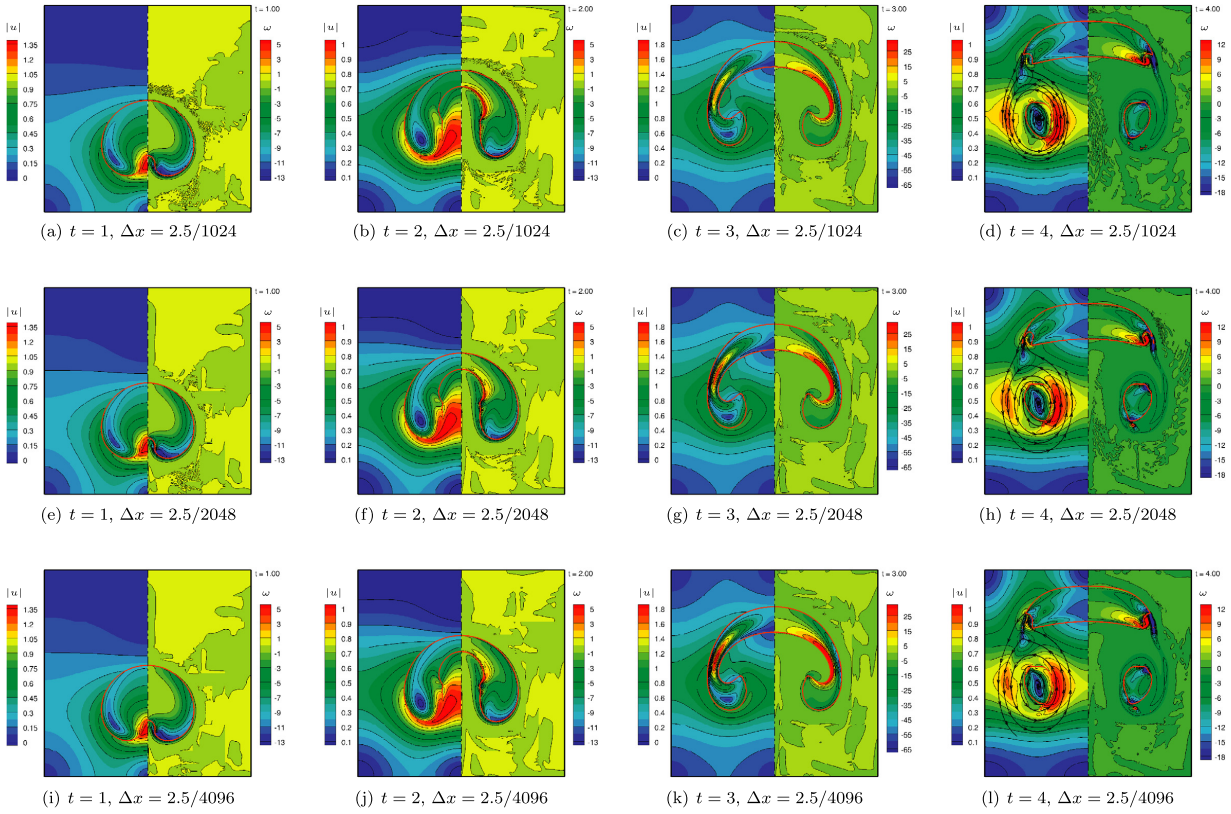

(a) $t = 1$, $\Delta x = 2.5/1024$ (b) $t = 2$, $\Delta x = 2.5/1024$ (c) $t = 3$, $\Delta x = 2.5/1024$ (d) $t = 4$, $\Delta x = 2.5/1024$

(e) $t = 1$, $\Delta x = 2.5/2048$ (f) $t = 2$, $\Delta x = 2.5/2048$ (g) $t = 3$, $\Delta x = 2.5/2048$ (h) $t = 4$, $\Delta x = 2.5/2048$

(i) $t = 1$, $\Delta x = 2.5/4096$ (j) $t = 2$, $\Delta x = 2.5/4096$ (k) $t = 3$, $\Delta x = 2.5/4096$ (l) $t = 4$, $\Delta x = 2.5/4096$

Fig. 15. Interface Υ (orange line), velocity magnitude $|\mathbf{u}|$ (left half), and vorticity ω (right half) at four time instances, resolutions of $\Delta x = 2.5/512$, $\Delta x = 2.5/1024$, $\Delta x = 2.5/2048$ are shown, Re_h, Ca_h. Note that the vorticity is clipped to allow better visualization. (For interpretation of the references to color in this figure legend, the reader is referred to the web version of this article.)

Table 4
Circularity (C), centroid (y_1, y_2), lower and upper axial position of the interface (z_1, z_2) at selected times for BLG, Re_h, Ca_h, $\Delta x = 2.5/4096$.

t	0.5	1.0	1.5	2.0	2.5	3.0
C	1.00590	0.86603	0.67626	0.55569	0.47028	0.38298
y_1	0.20957	0.254647	0.32057	0.39158	0.45008	0.46473
y_2	0.67768	0.88282	1.05422	1.18032	1.30818	1.46945
z_1	0.15592	0.68508	1.19529	1.51325	1.67713	1.74718
z_2	1.17103	1.34681	1.53050	1.70633	1.88737	2.05435
t	3.5	4.0	4.5	5.0	5.5	6.0
C	0.37962	0.43251	0.44821	0.42045	0.38834	0.35624
y_1	0.41410	0.40977	0.43658	0.49392	0.57798	0.67336
y_2	1.67867	1.78190	1.88685	1.92863	1.98145	1.97809
z_1	1.78529	1.87601	1.96079	2.06080	2.13882	2.22732
z_2	2.19664	2.30306	2.36565	2.39881	2.41757	2.42944

reconstruction, a low-dissipative, weakly compressible Roe Riemann solver has been utilized for computing the finite volume fluxes within each phase. Sub-cell correction for interfacial viscous and capillary stresses improves spatial accuracy as these are applied exactly at the interface. In combination with an adaptive multi-resolution algorithm numerical cost are low, while near interfaces sufficient resolution has been guaranteed and accuracy is maintained.

We have investigated complex, two-dimensional two-fluid configurations that comprise numerically challenging flow features of immiscible two-fluid flows. Local resolution has been increased until grid independence of the interface and integral quantities has been observed. In the first test case, a two-dimensional Rayleigh–Taylor instability, viscous shearing at the interface controls the interface evolution. Simulating the RTI to late stages has shown grid-independent evolution of very fine scale structures.

The second example is an isolated air bubble submerged in water and evolving under the influence of buoyancy. Different physically dominant phenomena have been observed at sufficient spatial resolution. Firstly, a low-Reynolds/supercritical (for cusp formation) capillary number configuration has been studied. Unsteady cusp formation and sheading of bubbles has been observed thereby, when the bubble is subjected to large shear rates as viscous forces dominate over capillary forces. Secondly, a high Reynolds/low capillary number setup has been considered. Viscous effects are subordinate and the interface develops complex structures. The interface shape and the location of secondary bubbles can be resolved adequately at moderate grid resolution. However, further refinement is necessary to capture capillary waves and to achieve grid-independent secondary-bubble sizes. For freely ascending high-Re bubbles high-resolution illustrations of the interface are provided. These may serve as a reference for cross-method comparison of two-phase models incorporating interfacial capillary and viscous effects.

Acknowledgements

We acknowledge the Deutsche Forschungsgemeinschaft (DFG) for funding this work under Grant No. AD 186/7-2. Felix S. Schranner is a member of the Technische Universität München (TUM) Graduate School.

Appendix A

A.1. Details of the Tait weakly compressible Roe solver

Details of the Roe solver adapted to Tait's EoS are provided in this appendix.

Roe averaged states

$$\begin{aligned}
&\widetilde{\rho} = \sqrt{\rho^{(l)}\rho^{(r)}}\ ,\ \widetilde{u}_1 = \frac{\sqrt{\rho^{(l)}}u_1^{(l)} + \sqrt{\rho^{(r)}}u_1^{(r)}}{\sqrt{\rho^{(l)}} + \sqrt{\rho^{(r)}}}\ ,\\
&\widetilde{u}_2 = \frac{\sqrt{\rho^{(l)}}u_2^{(l)} + \sqrt{\rho^{(r)}}u_2^{(r)}}{\sqrt{\rho^{(l)}} + \sqrt{\rho^{(r)}}}\\
&\text{and } \widetilde{\mathbf{u}}^2 = \widetilde{u}_1^2 + \widetilde{u}_2^2
\end{aligned} \tag{36}$$

Furthermore,

$$\begin{aligned}
&\widetilde{p} = p_1\left[\left(\frac{\widetilde{\rho}}{\rho_0}\right)^{\omega} - 1\right] + p_0,\\
&\widetilde{a} = \sqrt{\frac{p_1}{\rho_0^{\omega}}\omega\widetilde{\rho}^{(\omega-1)}}.
\end{aligned} \tag{37}$$

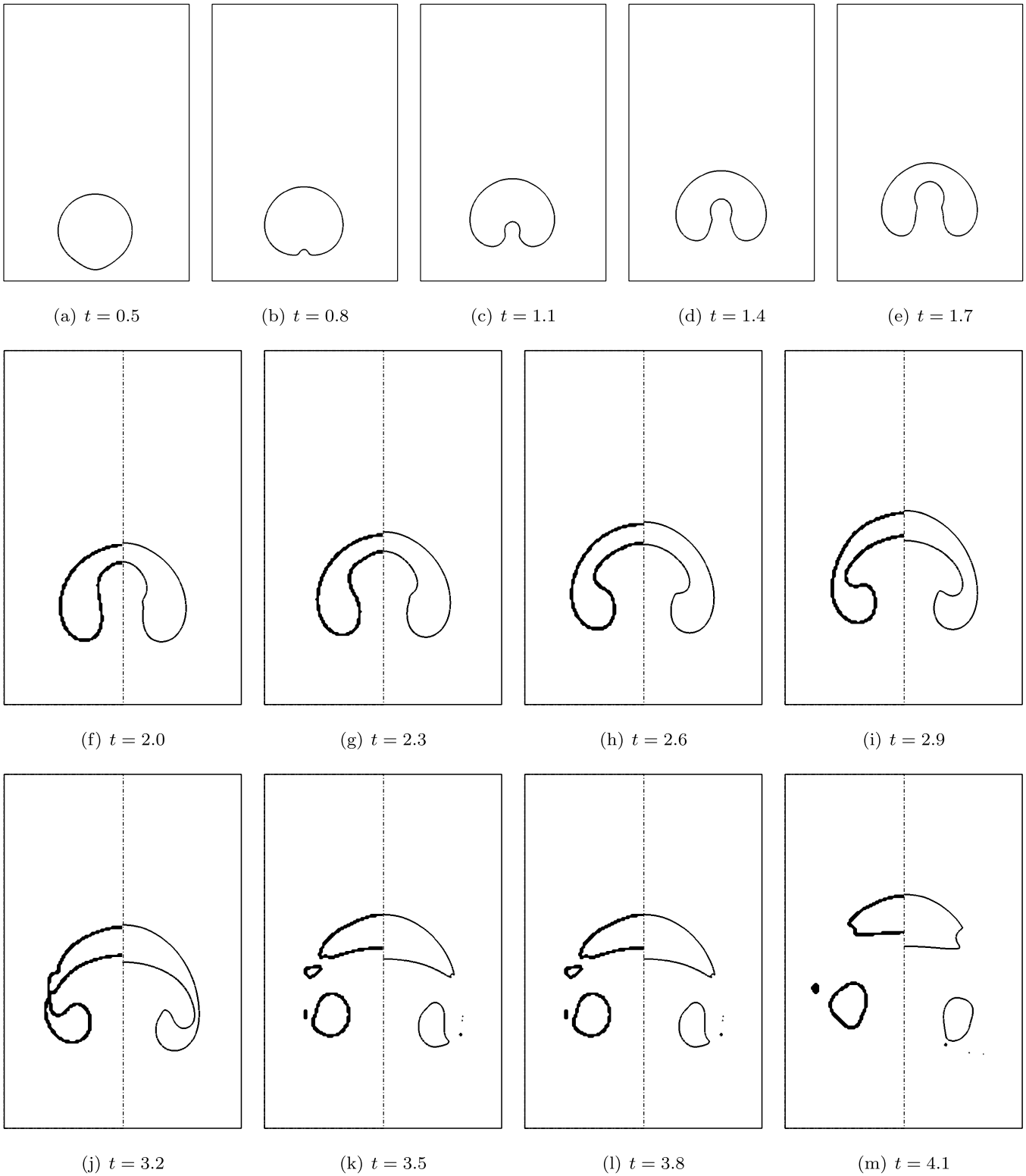

Fig. 16. Interface representation at maximum local resolution of 2.5/2048 FV. If available, the data is compared to those of Ref. [1], $Re = 1000$, $Eo = 200$.

Given the cell normal vector $\mathbf{n} = (n_1, n_2)$ which is $\mathbf{n} = (1, 0)$ for computing $\overline{\mathbf{F}}_1$, and $\mathbf{n} = (0, 1)$ for $\overline{\mathbf{F}}_2$ the cell-face tangent vector $\mathbf{t}^{(1)}$ is:

$$\mathbf{t}^{(1)} = (-n_2, n_1)\,. \tag{38}$$

The wave strengths are found by evaluating $\Delta\mathbf{U} = \mathbf{U}^{(r)} - \mathbf{U}^{(l)} = \sum_{i=1}^{m} \widehat{\delta}_i \widehat{\mathbf{K}}^{(i)}$:

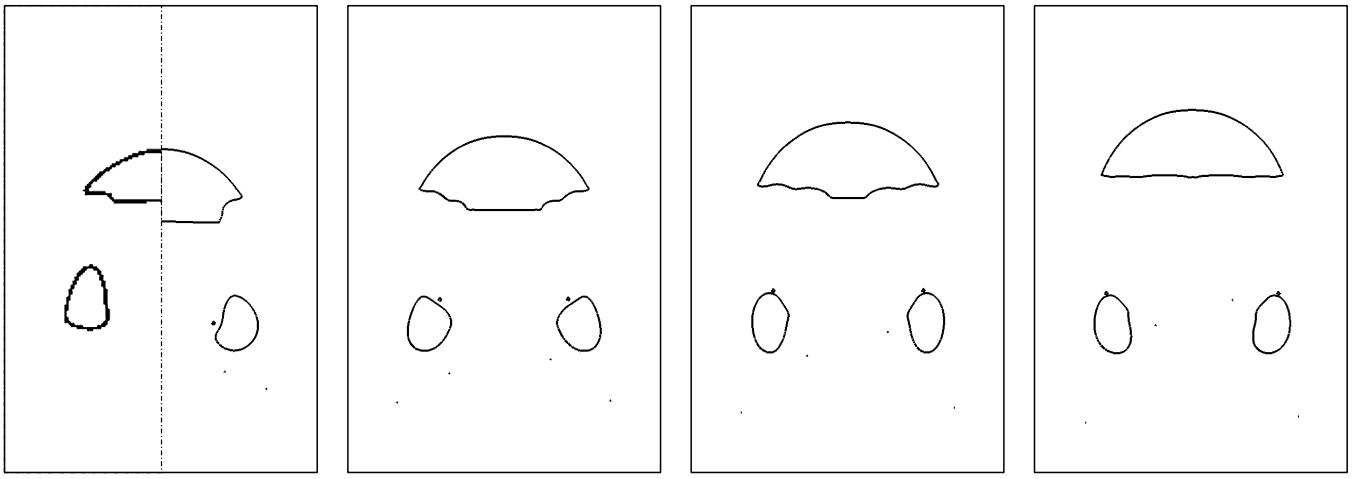

(n) $t = 4.4$ (o) $t = 4.7$ (p) $t = 5.0$ (q) $t = 5.3$

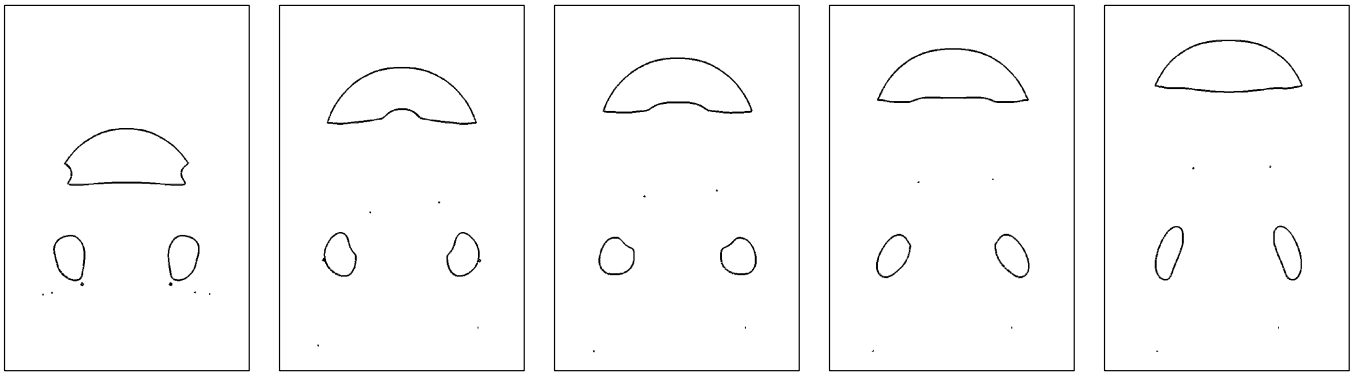

(r) $t = 5.6$ (s) $t = 5.9$ (t) $t = 6.2$ (u) $t = 6.5$ (v) $t = 6.8$

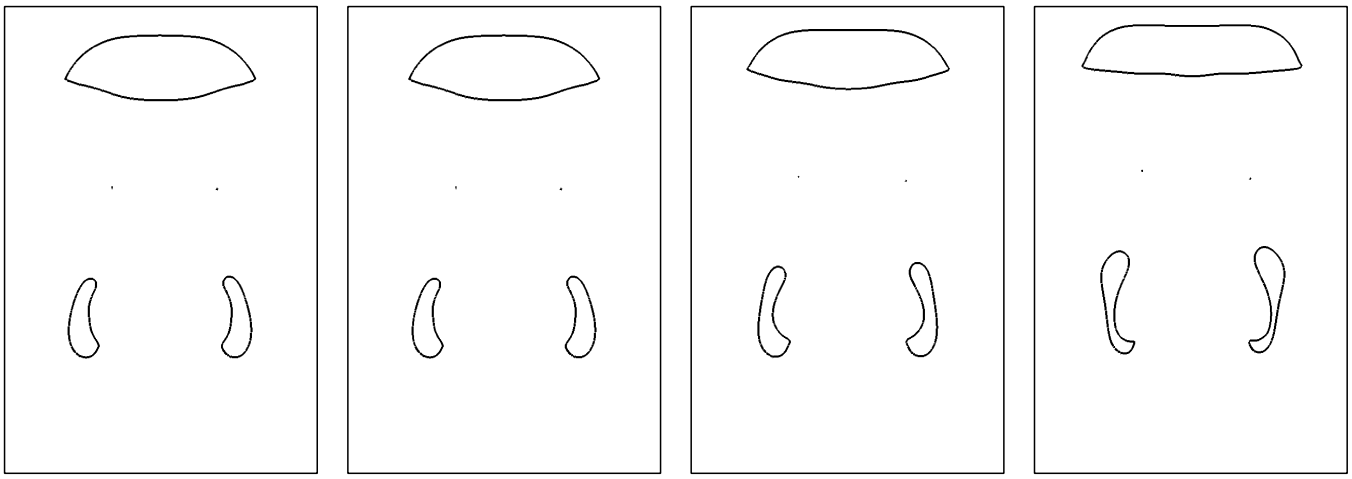

(w) $t = 7.1$ (x) $t = 7.4$ (y) $t = 7.7$ (z) $t = 8.0$

Fig. 16. (*continued*)

$$\Delta\mathbf{U} = \begin{bmatrix} \triangle w_0 \\ \triangle w_1 \\ \triangle w_2 \end{bmatrix} = \begin{bmatrix} \triangle \rho \\ \triangle (\rho u_1) \\ \triangle (\rho u_2) \end{bmatrix} = \begin{bmatrix} \rho^{(r)} - \rho^{(l)} \\ (\rho u_1)^{(r)} - (\rho u_1)^{(l)} \\ (\rho u_2)^{(r)} - (\rho u_2)^{(l)} \end{bmatrix} \tag{39}$$

$$\begin{aligned} \widetilde{\delta}_1 &= \tfrac{1}{2\widetilde{a}} \left[\triangle w_0 \left(\widetilde{a} + \mathbf{n} \cdot \widetilde{\mathbf{u}} \right) - \triangle \mathbf{u} \cdot \mathbf{n} - \widetilde{a} \delta_2 \right], \\ \widetilde{\delta}_2 &= \left(\triangle \mathbf{u} - \widetilde{\mathbf{u}} \triangle w_0 \right) \cdot \mathbf{t}_1, \\ \widetilde{\delta}_3 &= \tfrac{1}{\widetilde{a}} \left[\triangle \mathbf{u} - \widetilde{\mathbf{u}} \triangle w_0 \right] \cdot \mathbf{n} + \widetilde{\delta}_1 \end{aligned} \tag{40}$$

The right eigenvectors corresponding to the eigenvalues $\widetilde{\lambda}_1 = \widetilde{u} - \widetilde{a}$, $\widetilde{\lambda}_2 = \widetilde{u}$, and $\widetilde{\lambda}_3 = \widetilde{u} + \widetilde{a}$ are

$$\mathbf{K}^{(1)} = \begin{bmatrix} 1 \\ \widetilde{u}_1 - \widetilde{a} \cdot n_1 \\ \widetilde{u}_2 - \widetilde{a} \cdot n_2 \end{bmatrix}, \quad \mathbf{K}^{(2)} = \begin{bmatrix} 0 \\ \mathbf{t}^{(1)} \end{bmatrix}, \quad \mathbf{K}^{(3)} = \begin{bmatrix} 1 \\ \widetilde{u}_1 + \widetilde{a} \cdot n_1 \\ u_2 + \widetilde{a} \cdot n_2 \end{bmatrix}. \tag{41}$$

A.2. Description of the procedure for advancing the level-set field

A.2.1. Advection of the zero level-set

For advection, the level-set transport equation (24) is solved numerically not only for $\phi(\mathbf{x}, t) = 0$, but within a narrow band of 3 cells around the interface. The discrete $\phi^n_{[i,j]}$ is advanced in time from time-step n to $n+1$ according to

$$\phi^{n+1}_{[i,j]} = \phi^n_{[i,j]} - \Delta t \left[\overline{F}_1[\phi]_{[i,j]} + \overline{F}_2[\phi]_{[i,j]} \right] , \tag{42}$$

where

$$\overline{F}_\alpha[\phi]_{[i,j]} = \{ u_\alpha D_\alpha[\phi] \}_{[i,j]} , \alpha = 1, 2 \tag{43}$$

The differential operator $D_\alpha[\phi]$ represents a directed difference operator such that

$$D_\alpha[\phi] = \begin{cases} D^-_\alpha[\phi] & \text{if } u_\alpha > 0 \\ D^+_\alpha[\phi] & \text{if } u_\alpha < 0 \\ 0 & \text{if } u_\alpha = 0 \end{cases} \tag{44}$$

We follow the line of [25,26] and employ a 5th-order upwind WENO scheme with $\epsilon = 10^{-6}$ for evaluating the finite difference fluxes (44) numerically. For consistency Eq. (42) is integrated in time with a 2nd-order TVD Runge–Kutta scheme [18].

A.2.2. Reinitialization

The transport equation (24) is only valid for $\phi = 0$. Solving (42) may perturb any $\phi \neq 0$ and, in the course of time, lead to an irregular $\phi(\mathbf{x}, t)$, [1]. In order to ensure that within Ω the exact distance to the interface is maintained, $\phi(\mathbf{x}, t)$ is reinitialized regularly by the following equation [1]:

$$\frac{\partial \phi}{\partial t} = S(\phi_0)(1 - |\nabla \phi|) \tag{45}$$

with $\phi_0 = \phi$ $(\mathbf{x}, t = 0)$. Thereby, $\phi = \phi_0$ remains unchanged as the sign of $S(\phi_0)$ is zero for $\phi_0 = 0$. In contrast to Sussman et al. [1] we do not require the use of a smoothed sign function as within the framework [5] the exact interface position is at hand. For further implementational details refer to Ref. [5].

A.3. Constructing the sub-cell corrected interface curvature

In a two-dimensional plane, the radius of a circle that approximates a line segment locally is r, hence, the curvature of this circle is defined as the reciprocal of its radius,

$$\kappa(r) = \frac{1}{r} . \tag{46}$$

By Taylor-series expansion of (46), one obtains a first-order accurate approximation to the interface curvature

$$\kappa_\Upsilon = \kappa(r) + \frac{d\kappa(r)}{dr} \triangle r + \mathcal{O}^2 = \kappa(r) - \frac{1}{r^2} \triangle r + \mathcal{O}^2 = \kappa(r) - \kappa(r)^2 \triangle r + \mathcal{O}^2 . \tag{47}$$

Considering that $\kappa(r)$ may also be negative, Eq. (47) is modified as

$$\kappa_{\Upsilon,2d} = \kappa(r + \triangle r) \approx \Big(|\kappa(r)| - \kappa(r)^2 \triangle r \Big) S(\kappa(r)) . \tag{48}$$

Appendix B. Supplementary material

Supplementary material related to this article can be found online at http://dx.doi.org/10.1016/j.jcp.2016.07.037.

References

[1] M. Sussman, P. Smereka, S. Osher, A level set approach for computing solutions to incompressible two-phase flow, J. Comput. Phys. 114 (1) (1994) 146–159.
[2] R. Scardovelli, S. Zaleski, Direct numerical simulation of free-surface and interfacial flow, Annu. Rev. Fluid Mech. 31 (1999) 567–603.
[3] J. Sethian, P. Smereka, Level set methods for fluid interfaces, Annu. Rev. Fluid Mech. 35 (2003) 341–372.
[4] D. Anderson, G.B. McFadden, A. Wheeler, Diffuse-interface methods in fluid mechanics, Annu. Rev. Fluid Mech. 30 (1) (1998) 139–165.
[5] X. Hu, B. Khoo, N.A. Adams, F. Huang, A conservative interface method for compressible flows, J. Comput. Phys. 219 (2) (2006) 553–578.
[6] E. Lauer, X.Y. Hu, S. Hickel, N.A. Adams, Numerical investigation of collapsing cavity arrays, Phys. Fluids 24 (2012) 052104.
[7] J. Luo, X. Hu, N. Adams, A conservative sharp interface method for incompressible multiphase flows, J. Comput. Phys. 284 (2015) 547–565.
[8] F.S. Schranner, X. Hu, N.A. Adams, A physically consistent weakly compressible high-resolution approach to underresolved simulations of incompressible flows, Comput. Fluids 86 (2013) 109–124.
[9] S. Hysing, S. Turek, D. Kuzmin, N. Parolini, E. Burman, S. Ganesan, L. Tobiska, Quantitative benchmark computations of two-dimensional bubble dynamics, Int. J. Numer. Methods Fluids 60 (11) (2009) 1259–1288.
[10] G. Miller, P. Colella, A conservative three-dimensional Eulerian method for coupled solid–fluid shock capturing, J. Comput. Phys. 183 (1) (2002) 26–82.
[11] E. Lauer, X.Y. Hu, S. Hickel, N.A. Adams, Numerical modelling and investigation of symmetric and asymmetric cavitation bubble dynamics, Comput. Fluids 69 (2012) 1–19.
[12] G. Jiang, C.-W. Shu, Efficient implementation of weighted eno schemes, J. Comput. Phys. 126 (1996) 202–228.
[13] P.L. Roe, Approximate Riemann solvers, parameter vectors, and difference schemes, J. Comput. Phys. 43 (1981) 357–372.
[14] Y. Marx, Evaluation of the artificial compressibility method for the solution of the incompressible Navier–Stokes equations, in: 9th GAMM Conference of Numerical Methods in Fluid Mechanics, Lausanne, 1991.
[15] D. Elsworth, E. Toro, Riemann solvers for solving the incompressible Navier–Stokes equations using the artificial compressibility method, Tech. rep., Cranfield, College of Aeronautics Report No 9208, June 1992.
[16] A.J. Chorin, A numerical method for solving incompressible viscous flow problems, J. Comput. Phys. 135 (1997) 118–125.
[17] R. Temam, Une méthode d'approximation des solutions des équations Navier–Stokes, Bull. Soc. Math. 98 (1968) 115–152.
[18] C.-W. Shu, S. Osher, Efficient implementation of essentially non-oscillatory shock-capturing schemes, J. Comput. Phys. 77 (2) (1988) 439–471.
[19] M. Sussman, E.G. Puckett, A coupled level set and volume-of-fluid method for computing 3d and axisymmetric incompressible two-phase flows, J. Comput. Phys. 162 (2) (2000) 301–337.
[20] J. Brackbill, D. Kothe, C. Zemach, A continuum method for modeling surface tension, J. Comput. Phys. 100 (2) (1992) 335–354.
[21] L. Han, X. Hu, N. Adams, Adaptive multi-resolution method for compressible multi-phase flows with sharp interface model and pyramid data structure, J. Comput. Phys. 262 (2014) 131–152.
[22] S. Osher, R.P. Fedkiw, Level set methods: an overview and some recent results, J. Comput. Phys. 169 (2) (2001) 463–502.
[23] D. Adalsteinsson, J.A. Sethian, A fast level set method for propagating interfaces, J. Comput. Phys. 118 (2) (1995) 269–277.
[24] R.L. Panton, Incrompressible Flows, 3rd edition, John Wiley & Sons, Inc., 2005.
[25] R.P. Fedkiw, T. Aslam, B. Merriman, S. Osher, A non-oscillatory Eulerian approach to interfaces in multimaterial flows (the ghost fluid method), J. Comput. Phys. 152 (2) (1999) 457–492.
[26] X.Y. Hu, B.C. Khoo, An interface interaction method for compressible multifluids, J. Comput. Phys. 198 (1) (2004) 35–64.
[27] R. Saurel, S. Gavrilyuk, F. Renaud, A multiphase model with internal degrees of freedom: application to shock–bubble interaction, J. Fluid Mech. 495 (2003) 283–321.
[28] E.F. Toro, Riemann Solvers and Numerical Methods for Fluid Dynamics, 2nd edition, Springer-Verlag, 1999.
[29] S.J. Cummins, M. Rudman, An sph projection method, J. Comput. Phys. 152 (2) (1999) 584–607.
[30] N. Grenier, M. Antuono, A. Colagrossi, D.L. Touzé, B. Alessandrini, An hamiltonian interface sph formulation for multi-fluid and free surface flows, J. Comput. Phys. 228 (22) (2009) 8380–8393.

B.5 A CONSERVATIVE INTERFACE-INTERACTION MODEL WITH INSOLUBLE SURFACTANT

ELSEVIER LICENSE TERMS AND CONDITIONS

Oct 17, 2016

This Agreement between Felix S Schranner ("You") and Elsevier ("Elsevier") consists of your license details and the terms and conditions provided by Elsevier and Copyright Clearance Center.

License Number	3971300990739
License date	Oct 12, 2016
Licensed Content Publisher	Elsevier
Licensed Content Publication	Journal of Computational Physics
Licensed Content Title	A conservative interface-interaction model with insoluble surfactant
Licensed Content Author	Felix S. Schranner,Nikolaus A. Adams
Licensed Content Date	15 December 2016
Licensed Content Volume Number	327
Licensed Content Issue Number	n/a
Licensed Content Pages	25
Start Page	653
End Page	677
Type of Use	reuse in a thesis/dissertation
Portion	full article
Format	both print and electronic
Are you the author of this Elsevier article?	Yes
Will you be translating?	No
Order reference number	
Title of your thesis/dissertation	Weakly Compressible Models for Complex Flows
Expected completion date	Nov 2016
Estimated size (number of pages)	212
Elsevier VAT number	GB 494 6272 12
Requestor Location	Felix S Schranner Boltzmannstrasse 15 Garching, 85748 Germany Attn: Felix S Schranner
Billing Type	Invoice

Billing Address	Felix S Schranner Boltzmannstrasse 15 Garching, Germany 85748 Attn: Felix S Schranner
Total	**0.00 EUR**

Terms and Conditions

INTRODUCTION

1. The publisher for this copyrighted material is Elsevier. By clicking "accept" in connection with completing this licensing transaction, you agree that the following terms and conditions apply to this transaction (along with the Billing and Payment terms and conditions established by Copyright Clearance Center, Inc. ("CCC"), at the time that you opened your Rightslink account and that are available at any time at http://myaccount.copyright.com).

GENERAL TERMS

2. Elsevier hereby grants you permission to reproduce the aforementioned material subject to the terms and conditions indicated.
3. Acknowledgement: If any part of the material to be used (for example, figures) has appeared in our publication with credit or acknowledgement to another source, permission must also be sought from that source. If such permission is not obtained then that material may not be included in your publication/copies. Suitable acknowledgement to the source must be made, either as a footnote or in a reference list at the end of your publication, as follows:
"Reprinted from Publication title, Vol /edition number, Author(s), Title of article / title of chapter, Pages No., Copyright (Year), with permission from Elsevier [OR APPLICABLE SOCIETY COPYRIGHT OWNER]." Also Lancet special credit - "Reprinted from The Lancet, Vol. number, Author(s), Title of article, Pages No., Copyright (Year), with permission from Elsevier."
4. Reproduction of this material is confined to the purpose and/or media for which permission is hereby given.
5. Altering/Modifying Material: Not Permitted. However figures and illustrations may be altered/adapted minimally to serve your work. Any other abbreviations, additions, deletions and/or any other alterations shall be made only with prior written authorization of Elsevier Ltd. (Please contact Elsevier at permissions@elsevier.com)
6. If the permission fee for the requested use of our material is waived in this instance, please be advised that your future requests for Elsevier materials may attract a fee.
7. Reservation of Rights: Publisher reserves all rights not specifically granted in the combination of (i) the license details provided by you and accepted in the course of this licensing transaction, (ii) these terms and conditions and (iii) CCC's Billing and Payment terms and conditions.
8. License Contingent Upon Payment: While you may exercise the rights licensed immediately upon issuance of the license at the end of the licensing process for the transaction, provided that you have disclosed complete and accurate details of your proposed use, no license is finally effective unless and until full payment is received from you (either by publisher or by CCC) as provided in CCC's Billing and Payment terms and conditions. If full payment is not received on a timely basis, then any license preliminarily granted shall be deemed automatically revoked and shall be void as if never granted. Further, in the event that you breach any of these terms and conditions or any of CCC's Billing and Payment terms and conditions, the license is automatically revoked and shall be void as if never granted. Use of materials as described in a revoked license, as well as any use of the materials beyond the scope of an unrevoked license, may constitute copyright infringement and publisher reserves the right to take any and all action to protect its copyright in the materials.
9. Warranties: Publisher makes no representations or warranties with respect to the licensed material.
10. Indemnity: You hereby indemnify and agree to hold harmless publisher and CCC, and their respective officers, directors, employees and agents, from and against any and all claims arising out of your use of the licensed material other than as specifically authorized pursuant to this license.
11. No Transfer of License: This license is personal to you and may not be sublicensed, assigned, or transferred by you to any other person without publisher's written permission.
12. No Amendment Except in Writing: This license may not be amended except in a writing signed by both parties (or, in the case of publisher, by CCC on publisher's behalf).
13. Objection to Contrary Terms: Publisher hereby objects to any terms contained in any purchase order, acknowledgment, check endorsement or other writing prepared by you, which terms are inconsistent with these terms and conditions or CCC's Billing and Payment terms and conditions. These terms and conditions, together with CCC's Billing and Payment terms and conditions (which are incorporated herein), comprise the entire agreement between you and publisher (and CCC) concerning this licensing transaction. In the event of any conflict between your obligations established by these terms and conditions and those established by CCC's Billing and

Payment terms and conditions, these terms and conditions shall control.
14. Revocation: Elsevier or Copyright Clearance Center may deny the permissions described in this License at their sole discretion, for any reason or no reason, with a full refund payable to you. Notice of such denial will be made using the contact information provided by you. Failure to receive such notice will not alter or invalidate the denial. In no event will Elsevier or Copyright Clearance Center be responsible or liable for any costs, expenses or damage incurred by you as a result of a denial of your permission request, other than a refund of the amount(s) paid by you to Elsevier and/or Copyright Clearance Center for denied permissions.

LIMITED LICENSE

The following terms and conditions apply only to specific license types:
15. **Translation**: This permission is granted for non-exclusive world **English** rights only unless your license was granted for translation rights. If you licensed translation rights you may only translate this content into the languages you requested. A professional translator must perform all translations and reproduce the content word for word preserving the integrity of the article.
16. **Posting licensed content on any Website**: The following terms and conditions apply as follows: Licensing material from an Elsevier journal: All content posted to the web site must maintain the copyright information line on the bottom of each image; A hyper-text must be included to the Homepage of the journal from which you are licensing at http://www.sciencedirect.com/science/journal/xxxxx or the Elsevier homepage for books at http://www.elsevier.com; Central Storage: This license does not include permission for a scanned version of the material to be stored in a central repository such as that provided by Heron/XanEdu.
Licensing material from an Elsevier book: A hyper-text link must be included to the Elsevier homepage at http://www.elsevier.com . All content posted to the web site must maintain the copyright information line on the bottom of each image.

Posting licensed content on Electronic reserve: In addition to the above the following clauses are applicable: The web site must be password-protected and made available only to bona fide students registered on a relevant course. This permission is granted for 1 year only. You may obtain a new license for future website posting.
17. **For journal authors:** the following clauses are applicable in addition to the above:
Preprints:
A preprint is an author's own write-up of research results and analysis, it has not been peer-reviewed, nor has it had any other value added to it by a publisher (such as formatting, copyright, technical enhancement etc.).
Authors can share their preprints anywhere at any time. Preprints should not be added to or enhanced in any way in order to appear more like, or to substitute for, the final versions of articles however authors can update their preprints on arXiv or RePEc with their Accepted Author Manuscript (see below).
If accepted for publication, we encourage authors to link from the preprint to their formal publication via its DOI. Millions of researchers have access to the formal publications on ScienceDirect, and so links will help users to find, access, cite and use the best available version. Please note that Cell Press, The Lancet and some society-owned have different preprint policies. Information on these policies is available on the journal homepage.
Accepted Author Manuscripts: An accepted author manuscript is the manuscript of an article that has been accepted for publication and which typically includes author-incorporated changes suggested during submission, peer review and editor-author communications.
Authors can share their accepted author manuscript:

- immediately
  - via their non-commercial person homepage or blog
  - by updating a preprint in arXiv or RePEc with the accepted manuscript
  - via their research institute or institutional repository for internal institutional uses or as part of an invitation-only research collaboration work-group
  - directly by providing copies to their students or to research collaborators for their personal use
  - for private scholarly sharing as part of an invitation-only work group on commercial sites with which Elsevier has an agreement
- after the embargo period
  - via non-commercial hosting platforms such as their institutional repository
  - via commercial sites with which Elsevier has an agreement

In all cases accepted manuscripts should:

- link to the formal publication via its DOI
- bear a CC-BY-NC-ND license - this is easy to do
- if aggregated with other manuscripts, for example in a repository or other site, be shared in alignment with

our hosting policy not be added to or enhanced in any way to appear more like, or to substitute for, the published journal article.

Published journal article (JPA): A published journal article (PJA) is the definitive final record of published research that appears or will appear in the journal and embodies all value-adding publishing activities including peer review co-ordination, copy-editing, formatting, (if relevant) pagination and online enrichment.
Policies for sharing publishing journal articles differ for subscription and gold open access articles:
Subscription Articles: If you are an author, please share a link to your article rather than the full-text. Millions of researchers have access to the formal publications on ScienceDirect, and so links will help your users to find, access, cite, and use the best available version.
Theses and dissertations which contain embedded PJAs as part of the formal submission can be posted publicly by the awarding institution with DOI links back to the formal publications on ScienceDirect.
If you are affiliated with a library that subscribes to ScienceDirect you have additional private sharing rights for others' research accessed under that agreement. This includes use for classroom teaching and internal training at the institution (including use in course packs and courseware programs), and inclusion of the article for grant funding purposes.
Gold Open Access Articles: May be shared according to the author-selected end-user license and should contain a CrossMark logo, the end user license, and a DOI link to the formal publication on ScienceDirect.
Please refer to Elsevier's posting policy for further information.
18. **For book authors** the following clauses are applicable in addition to the above: Authors are permitted to place a brief summary of their work online only. You are not allowed to download and post the published electronic version of your chapter, nor may you scan the printed edition to create an electronic version. **Posting to a repository:** Authors are permitted to post a summary of their chapter only in their institution's repository.
19. **Thesis/Dissertation**: If your license is for use in a thesis/dissertation your thesis may be submitted to your institution in either print or electronic form. Should your thesis be published commercially, please reapply for permission. These requirements include permission for the Library and Archives of Canada to supply single copies, on demand, of the complete thesis and include permission for Proquest/UMI to supply single copies, on demand, of the complete thesis. Should your thesis be published commercially, please reapply for permission. Theses and dissertations which contain embedded PJAs as part of the formal submission can be posted publicly by the awarding institution with DOI links back to the formal publications on ScienceDirect.

Elsevier Open Access Terms and Conditions
You can publish open access with Elsevier in hundreds of open access journals or in nearly 2000 established subscription journals that support open access publishing. Permitted third party re-use of these open access articles is defined by the author's choice of Creative Commons user license. See our open access license policy for more information.
Terms & Conditions applicable to all Open Access articles published with Elsevier:
Any reuse of the article must not represent the author as endorsing the adaptation of the article nor should the article be modified in such a way as to damage the author's honour or reputation. If any changes have been made, such changes must be clearly indicated.
The author(s) must be appropriately credited and we ask that you include the end user license and a DOI link to the formal publication on ScienceDirect.
If any part of the material to be used (for example, figures) has appeared in our publication with credit or acknowledgement to another source it is the responsibility of the user to ensure their reuse complies with the terms and conditions determined by the rights holder.
Additional Terms & Conditions applicable to each Creative Commons user license:
CC BY: The CC-BY license allows users to copy, to create extracts, abstracts and new works from the Article, to alter and revise the Article and to make commercial use of the Article (including reuse and/or resale of the Article by commercial entities), provided the user gives appropriate credit (with a link to the formal publication through the relevant DOI), provides a link to the license, indicates if changes were made and the licensor is not represented as endorsing the use made of the work. The full details of the license are available at http://creativecommons.org/licenses/by/4.0.
CC BY NC SA: The CC BY-NC-SA license allows users to copy, to create extracts, abstracts and new works from the Article, to alter and revise the Article, provided this is not done for commercial purposes, and that the user gives appropriate credit (with a link to the formal publication through the relevant DOI), provides a link to the license, indicates if changes were made and the licensor is not represented as endorsing the use made of the work. Further, any new works must be made available on the same conditions. The full details of the license are available at http://creativecommons.org/licenses/by-nc-sa/4.0.

Journal of Computational Physics 327 (2016) 653–677

Contents lists available at ScienceDirect

Journal of Computational Physics

www.elsevier.com/locate/jcp

A conservative interface-interaction model with insoluble surfactant

Felix S. Schranner *, Nikolaus A. Adams

Technical University of Munich, Institute of Aerodynamics, 85748 Garching, Germany

ARTICLE INFO

Article history:
Received 25 April 2016
Received in revised form 20 September 2016
Accepted 25 September 2016
Available online 30 September 2016

Keywords:
Weakly compressible model
Sharp-interface model
Marangoni stress
Multiphase flow
Level-set

ABSTRACT

In this paper we extend the conservative interface-interaction method of Hu et al. (2006) [34], adapted for weakly-compressible flows by Luo et al. (2015) [37], to include the effects of viscous, capillary, and Marangoni stresses consistently as momentum-exchange terms at the sharp interface. The interface-interaction method is coupled with insoluble surfactant transport which employs the underlying sharp-interface representation. Unlike previous methods, we thus achieve discrete global conservation in terms of interface interactions and a consistently sharp interface representation. The interface is reconstructed locally, and a sub-cell correction of the interface curvature improves the evaluation of capillary stresses and surfactant diffusion in particular for marginal mesh resolutions. For a range of numerical test cases we demonstrate accuracy and robustness of the method. In particular, we show that the method is at least as accurate as previous diffuse-interface models while exhibiting throughout the considered test cases improved computational efficiency. We believe that the method is attractive for high-resolution level-set interface-tracking simulations as it straightforwardly incorporates the effects of variable surface tension into the underlying conservative interface-interaction approach.

1. Introduction

Flows of two incompressible, immiscible, viscous fluids with surface tension frequently are encountered in industry and nature [1–5]. At their interface the fluids exchange mass, momentum, and energy. The presence of *surface active agents* (surfactants) effects capillary phenomena and needs to be taken into account [3,6,7]. In many classical two-phase flows, such as viscous fingering [8], drop break-up and coalescence [9], tip-streaming [10], and buoyancy-driven bubble-motion [11], surfactant related effects are significant.

Surfactants accumulate at fluid interfaces [12]. They are transported along, adsorbed to or desorbed from the interface. Their distribution along the interface modulates surface tension: higher concentration of surfactant implies lower surface tension. Inhomogeneous surface tension entails interfacial stresses in interface-normal and tangential directions, denoted as *capillary* and *Marangoni* stresses, respectively.

Numerical methods for solving interfacial flows with surfactants may be categorized into *interface tracking* and *interface capturing* methods. Interface tracking methods either use an interface-adapted grid or marker particles to represent the interface. Boundary integral methods employ a surface mesh to track the interface. In the context of surfactants, a boundary integral method for studying the effect of insoluble surfactants on drop deformation was developed in [13,14]. Another

* Corresponding author. Fax: +49 89 289 16139.
E-mail addresses: felix.schranner@aer.mw.tum.de (F.S. Schranner), Nikolaus.Adams@tum.de (N.A. Adams).

http://dx.doi.org/10.1016/j.jcp.2016.09.058
0021-9991/

interface-tracking method is the front-tracking method [15], where a fixed grid is used to compute the flow, while a set of connected marker particles tracks the interface and surfactant on the interface. A front-tracking method for insoluble surfactant was developed in [16]. A related front tracking method is the immersed boundary method [17], which was used to simulate interfacial flows with insoluble surfactants by the surfactant-conserving marker- and cell (MAC) algorithm [18]. A ghost-cell immersed boundary method was introduced in [19], and employed to study the effects of diffusion-controlled surfactant on a viscous drop injected into a viscous medium [20].

A hybrid level-set/front-tracking approach was used to study the dynamics of capillary waves with insoluble surfactant [21]. Another front-tracking method which combines a finite element methodology with adaptive body-fitted meshes served to simulate the deformation and breakup of axisymmetric liquid bridges [22] and thin filaments [23] with insoluble surfactants. Interface tracking methods are very accurate, yet, especially for topological changes and in three dimensions, the implementation-effort can be overwhelming. Possible drawbacks of marker Lagrangian approaches include difficulties with evaluating topological changes, the need to remove parts of the evolving front (delooping) to characterize the viscosity solution correctly, the need to adaptively add and remove points, and complexities in three dimensions [24].

With interface capturing methods the interface is implicitly defined by an auxiliary function, such as a level-set, color or phase-field function. This simplifies gridding, discretization and handling of topological changes. For example, a volume-of-fluid (VOF) method [4], for insoluble surfactants was developed in [25]. Hameed et al. [26] have used the Arbitrary Lagrangian–Eulerian (ALE) method combined with a coupled level-set and volume of fluid method to simulate flows containing fluid interfaces with insoluble surfactant.

With the diffuse-interface, or phase-field method the interface of a multi-fluid domain is represented by a phase-field function, which is an approximation of the characteristic function of the bulk fluid domain [27]. In [28] Teigen et al. develop and apply the diffuse interface approach to simulate flows in the presence of soluble and insoluble surfactants.

A level-set method [5,29] for solving the surfactant transport equation has been presented by Adalsteinsson et al. [30] and Xu et al. [31], and coupled with the immersed-interface method (IIM) [32] in [33]. With the IIM, the interface jump conditions are handled explicitly by modifying the discretization stencils near the interface. As a simple and robust alternative to IIM Xu et al. have modeled interface forces within the level-set framework by a continuous surface force (CSF). A common property of these incompressible level-set methods, which they share with phase-field methods, is the smoothing of material properties, such as density and viscosity, at the interface across several grid points. This implies their main drawbacks, the lack of discrete conservation and ineffectiveness at large density and viscosity ratios.

A fully conservative level-set based sharp-interface method (SIM) for compressible flows [34], robust even for large topological interface changes [35], has been applied to two-phase flows where each phase may obey different equations of state, and large density and viscosity ratios [36]. It has been further developed to model viscous, incompressible two-phase flows [37] by incorporating a weakly compressible fluid model [37,38]. High accuracy has been demonstrated for the buoyancy driven motion of viscous, immiscible flows [39].

Key idea of the SIM framework employed in our model, where the Navier–Stokes equations are solved on a Cartesian grid, is the modification of finite volumes that are cut by the interface in order to allow explicit application of interface-jump conditions, including interactions due to capillary and Marangoni stresses. In Ref. [37] Luo et al. propose interaction terms that consider capillary forces for a constant surface-tension coefficient and viscous interactions. This formulation of the viscous momentum exchange, however, does not allow for a jump condition in interface-tangential direction, occurring in the general case of non-vanishing Marangoni stresses [40,41].

In this paper we develop a robust and consistent interface interaction model, incorporating inviscid, viscous, capillary, and Marangoni stresses into the SIM framework. The resulting interface flux is derived from an interface Riemann problem. The model is simpler than the CSF approach and the IIM-based approach of [28,33]. Explicit time integration is applied for the evolution of surfactant concentration, level-set, and fluid phases. Efficiency is enhanced by a multi-resolution (MR) algorithm [35]. Level-set transport and surfactant-concentration transport are evaluated only within a narrow band near the interface. Within the SIM framework, local interface-segment lengths/areas are computed, avoiding the need for a smoothed delta-function, for approximation of the interface length. We show that surfactant mass and interface fluxes are generally predicted more accuratly than in previous works [28,31]. Costly propagation of the interface area as an additional variable, as proposed in [25], also is avoided.

In Section 2, the governing equations are given. Section 3 describes the numerical discretization. In Section 4 we present simulation results demonstrating the capability of the method. Validation simulations for passive transport of surfactant are presented in section 4.1. A thermocapillary flow is considered for demonstrating the correct prediction of Marangoni and viscous stresses at the interface, Sec. 4.2. For demonstrating robustness and performance of the method when also inviscid and capillary stresses are present at the interface, a two-dimensional and a three-dimensional test configuration is selected, Sec. 4.3. A drop in a shear-flow serves to demonstrate the performance of the model for interfaces evolving under external shear forces, Sec. 5.

2. Basic equations

Consider the system of two immiscible fluid phases, as sketched in Fig. 1. The fluid phases occupy two non-overlapping subdomains $\Omega^{\xi_1}(t)$ and $\Omega^{\xi_2}(t)$. Ω is bounded by $\Gamma = \partial\Omega$, corresponding boundaries exist for the subdomains. For each

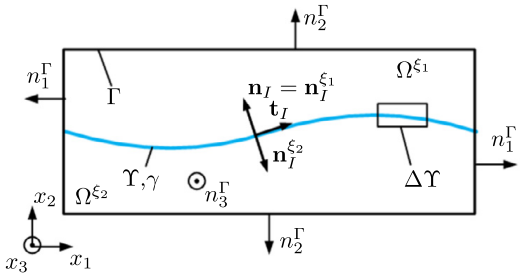

Fig. 1. Two-dimensional schematic of the multi-fluid configuration.

phase, $\Omega^{\xi_i}(t)$, $i = 1, 2$ the system of conservation equations for weakly compressible fluids in differential, non-dimensional form

$$\begin{aligned} \frac{\partial \rho}{\partial t} + \nabla^T \cdot (\rho \mathbf{u}) &= 0 \,, \\ \frac{\partial \rho \mathbf{u}}{\partial t} + \nabla^T \cdot [\rho \mathbf{u} \otimes \mathbf{u} - \mathbf{\Pi}] &= 0 \end{aligned} \tag{1}$$

holds [42], where ρ denotes the non-dimensional density, and $\mathbf{u} = (u_1, u_2, u_3)^T$ the vector of non-dimensional Cartesian velocities. The non-dimensional states are the dimensional states divided by a reference density and velocity, respectively, such that $\rho = \frac{\rho^\star}{\rho_{ref}}$, $u_\alpha = \frac{u_\alpha^\star}{U_{ref}}$. Furthermore, the stress tensor is defined as

$$\mathbf{\Pi} = -\mathbb{1} p + \mathbf{T} \,, \tag{2}$$

p is the static, non-dimensional pressure, which relates to the dimensional pressure according to $p = \frac{p^\star}{U_{ref}^2 \rho_{ref}}$. With Stokes' hypothesis for a Newtonian fluid the viscous stress tensor is

$$\mathbf{T} = \mathbf{T}(\mathbf{u}) = \begin{bmatrix} \tau^{11} & \tau^{12} & \tau^{13} \\ \tau^{21} & \tau^{22} & \tau^{23} \\ \tau^{31} & \tau^{32} & \tau^{33} \end{bmatrix} . \tag{3}$$

$\mu = \nu\rho$ is the non-dimensional dynamic viscosity, which relates to the dimensional dynamic viscosity according to $\mu = \frac{\mu^\star}{\mu_{ref}}$. The components of $\mathbf{T}(\mathbf{u})$ are

$$\tau^{\alpha\beta} = \frac{\mu}{Re} \left(\frac{\partial u_\alpha}{\partial x_\beta} + \frac{\partial u_\beta}{\partial x_\alpha} - \frac{2}{3} \frac{\partial u_\gamma}{\partial x_\gamma} \delta_{\alpha\beta} \right) . \tag{4}$$

Herein, $\alpha, \beta, \gamma = 1, 2, 3$. Note that $\mu_{ref} = \mu^{\star,\xi_1}$, $\nu_{ref} = \nu^{\star,\xi_1}$, $\rho_{ref} = \rho^{\star,\xi_1}$. Moreover, $Re = \frac{U_{ref} L_{ref}}{\nu_{ref}}$, $Ca = \frac{\mu_{ref} U_{ref}}{\sigma_0}$, and $We = \frac{\rho_{ref} L_{ref} U_{ref}^2}{\sigma_0}$ denote the Reynolds, capillary, and Weber number. If not noted otherwise, $U_{ref} = L_{ref} u'$, where $u' = \frac{\partial u_1}{\partial x_2}$, $L_{ref} = r_0$.

2.1. Tait's equation for weakly compressible fluids

For low Mach number flows, Tait's equation of state (EoS),

$$p = p(\rho) = p_1 \left[\left(\frac{\rho}{\rho_0} \right)^\omega - 1 \right] + p_0 \,, \tag{5}$$

can be used to model fluids as weakly compressible, i.e. $\frac{1}{\rho} \frac{\partial \rho}{\partial p} \ll 1$, and close Eq. (1). The (artificial) speed of sound is

$$a^2 = \frac{p_1}{\rho_0^\omega} \omega \rho^{(\omega-1)} = \frac{\omega}{\rho} (p - p_0 + p_1) \,, \tag{6}$$

where $\omega = 1 + 10^{-6}$, $p_0 = p(t = 0)$. p_1 is found from Eq. (6) by constraining $Ma = ||\mathbf{u}||/a < 0.1$.

2.2. Transport of surfactant concentration

The amount of surfactant within an interface segment $\Delta\Upsilon$, see Fig. 1, is the interfacial surfactant concentration $\gamma(\mathbf{x}, t)$. It evolves according to the non-dimensional surfactant advection–diffusion equation

$$\frac{\partial \gamma}{\partial t} + \nabla^T \cdot (\mathbf{u}_I \gamma) - \gamma \left((\mathbf{n}_I \otimes \mathbf{n}_I) \cdot \nabla \right) \cdot \mathbf{u}_I = \frac{1}{Pe_s} \nabla_s^2 \gamma \ . \tag{7}$$

The subscript s indicates transport along the interface-tangential plane. $Pe_s = \frac{U_{ref} L_{ref}}{D_s}$ denotes the interface diffusion Peclet number, D_s is the diffusivity of γ along Υ. The advection term is

$$\nabla^T \cdot (\mathbf{u}_I \gamma) = \mathbf{u}_I^T \cdot (\nabla \gamma) + \gamma \nabla^T \cdot \mathbf{u}_I \ . \tag{8}$$

The third term on the left side of Eq. (7), accounts for transport due to variations in interface shape. The interface diffusion of γ can be decomposed as

$$\nabla_s^2 \gamma(\mathbf{x}) = \Delta \gamma(\mathbf{x}) - \left(\mathbf{n}_I^T \cdot \nabla \gamma(\mathbf{x}) \right) \left(\nabla^T \cdot \mathbf{n}_I \right) - \mathbf{n}_I^T \cdot H_\gamma \cdot \mathbf{n}_I \ , \tag{9}$$

with H_γ being the Hessian of $\gamma(\mathbf{x}, t)$.

2.3. Constitutive equation for the surface tension coefficient

The dependence of σ on γ follows the non-linear Langmuir equation [25,43]

$$\sigma(\gamma) = 1 + E \ln(1 - \zeta \gamma) \ . \tag{10}$$

To avoid negative values of $\sigma(\gamma)$, Eq. (10) has been implemented in a modified form

$$\sigma(\gamma) = \max\{0.01, 1 + E \ln(\max\{0.01, 1 - \zeta \gamma\})\} \ . \tag{11}$$

For small $\nabla_s \gamma$, $\sigma(\gamma)$ can be approximated as [25,43]

$$\sigma(\gamma) = 1 - E \zeta \gamma \ . \tag{12}$$

$E = \frac{RT\gamma_\infty}{\sigma_0}$ and $\zeta = \frac{\gamma_{eq}}{\gamma_\infty}$ are the surfactant elasticity and coverage. R, T, and σ_0 denote the ideal gas constant, the temperature, and the surface tension coefficient for a clean interface ($\gamma = 0$). γ_∞ is the concentration of surfactant in the maximum packing limit, and $\gamma_{eq} = \frac{1}{\Delta\Upsilon} \int_{\Delta\Upsilon} \gamma d\Upsilon' \big|_{t=0}$ is the initial average surfactant concentration.

3. Numerical method

3.1. Discretization of conservation equations for fluid transport

Applying Gauss' theorem, the integral form of Eq. (1) becomes

$$\int_\Omega \mathbf{U}_t \, dV + \oint_\Gamma \left(\mathbf{F}_1^T, \mathbf{F}_2^T, \mathbf{F}_3^T \right) \cdot \mathbf{n}_\Gamma d\Gamma' = 0 \tag{13}$$

where

$$\mathbf{U} = (\rho, \rho u_1, \rho u_2, \rho u_3)^T \ , \tag{14}$$

$\mathbf{n}_\Gamma$ is the normal on Γ, see Fig. 1. The flux vectors include advective and viscous components $\mathbf{F}_\beta = \mathbf{F}_\beta^a - \mathbf{F}_\beta^\nu$, $\beta = 1, 2, 3$. The advective (superscript a) and viscous (superscript ν) fluxes are

$$\mathbf{F}_\beta^a(\mathbf{U}) = \begin{pmatrix} \rho u_\beta \\ \rho u_\beta u_1 + p\delta_{\beta 1} \\ \rho u_\beta u_2 + p\delta_{\beta 2} \\ \rho u_\beta u_3 + p\delta_{\beta 3} \end{pmatrix}, \ \mathbf{F}_\beta^\nu(\mathbf{u}) = \begin{pmatrix} 0 \\ \tau^{\beta 1} \\ \tau^{\beta 2} \\ \tau^{\beta 3} \end{pmatrix}. \tag{15}$$

In a neighborhood of the interface the conservation equations for mass

$$\frac{d}{dt} \int_{\Delta\Upsilon\varepsilon} \rho dV - \int_{\Delta\Upsilon^{\xi_1}} \rho^{\xi_1} \mathbf{n}_I^{T,\xi_1} \cdot \left(\mathbf{u}^{\xi_1} - \mathbf{u}_I \right) d\Upsilon' - \int_{\Delta\Upsilon^{\xi_2}} \rho^{\xi_2} \mathbf{n}_I^{T,\xi_2} \cdot \left(\mathbf{u}^{\xi_2} - \mathbf{u}_I \right) d\Upsilon' = 0 \ , \tag{16}$$

and momentum

$$\begin{aligned} &\frac{d}{dt} \int_{\Delta\Upsilon\varepsilon} (\rho \mathbf{u}) dV - \int_{\Delta\Upsilon^{\xi_1}} \rho \mathbf{n}_I^{T,\xi_1} \cdot \left(\mathbf{u}^{\xi_1} - \mathbf{u}_I \right) d\Upsilon' - \int_{\Delta\Upsilon^{\xi_2}} \rho \mathbf{n}_I^{T,\xi_2} \cdot \left(\mathbf{u}^{\xi_2} - \mathbf{u}_I \right) d\Upsilon' = \\ &= \int_{\Delta\Upsilon^{\xi_1}} \mathbf{n}_I^{T,\xi_1} \cdot \mathbf{\Pi}(\mathbf{u})^{\xi_1} d\Upsilon' + \int_{\Delta\Upsilon^{\xi_2}} \mathbf{n}_I^{T,\xi_2} \cdot \mathbf{\Pi}(\mathbf{u})^{\xi_2} d\Upsilon' + \frac{1}{We} \oint_s \mathbf{m} \, \sigma ds' \ , \end{aligned} \tag{17}$$

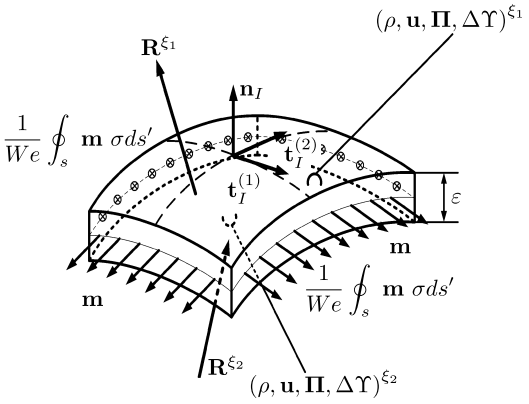

Fig. 2. Three-dimensional schematic of a small interface element.

hold. Note that $\mathbf{n}_I^{\xi_1} = \mathbf{n}_I$ and $\mathbf{n}_I^{\xi_2} = -\mathbf{n}_I$ with $\mathbf{n}_I$ being the interface-normal vector. An interface segment of perimeter s, surface area $\Delta\Upsilon^{\xi_1}$ and $\Delta\Upsilon^{\xi_2}$ is sketched in Fig. 2. For an infinitesimally thin interface, i.e. $\varepsilon \to 0$, it follows that $\Delta\Upsilon^{\xi_1} = \Delta\Upsilon^{\xi_2} = \Delta\Upsilon$. The interface itself has no mass nor momentum [2], and phase changes do not occur. Continuity at the interface thus implies

$$\mathbf{n}_I^T \cdot \mathbf{u}^{\xi_1}\big|_\Upsilon = u_{I,\perp}^{\xi_1} = \mathbf{n}_I^T \cdot \mathbf{u}^{\xi_2}\big|_\Upsilon = u_{I,\perp}^{\xi_2} = u_{I,\perp} \,. \tag{18}$$

The interface acts as a no-slip boundary [44], hence, the interface-tangential velocity is continuous [40]

$$\left|\mathbf{u}_{I,\parallel}^{\xi_1}\right| = \left|\mathbf{u}_{I,\parallel}^{\xi_2}\right| = \left|\mathbf{u}_{I,\parallel}\right| \,, \text{ and } \mathbf{u}_{I,\parallel} \cdot \mathbf{u}_{I,\perp} = 0 \,. \tag{19}$$

At the interface, the velocity is $\mathbf{u}_I = \mathbf{u}_{I,\perp} + \mathbf{u}_{I,\parallel}$, with $\mathbf{u}_{I,\perp} = u_{I,\perp}\mathbf{n}_I^T$, and $\mathbf{u}_{I,\parallel} = \mathbf{u}_{I,\parallel}^{(1)} + \mathbf{u}_{I,\parallel}^{(2)} = u_{I,\parallel}^{(1)}\mathbf{t}_I^{(1)} + u_{I,\parallel}^{(2)}\mathbf{t}_I^{(2)}$, respectively. The two interface-tangentials $\mathbf{t}_I^{(1)}$ and $\mathbf{t}_I^{(2)}$ are computed according to [45]. Together with $\mathbf{n}_I$ they build an orthonormal basis on the interface. Note that in 2D $\mathbf{t}_I^{(2)}$ is obsolete. In close proximity to Υ both fluids take on the interface velocity [46]. Considering Eq. (18) the interface momentum equation (17) becomes

$$0 = \mathbf{R}^{\xi_1}\Delta\Upsilon - \mathbf{R}^{\xi_2}\Delta\Upsilon + \frac{1}{We}\oint_s \mathbf{m}\,\sigma ds' \,, \tag{20}$$

where $\mathbf{R}^{\xi_i}(\mathbf{x}, \mathbf{n}_I) = \mathbf{\Pi}(\mathbf{u})^{\xi_i} \cdot \mathbf{n}_I$ represents the surface stresses, [40]. The term $\frac{1}{We}\oint_s \mathbf{m}\,\sigma ds'$ denotes the surface tension force exerted in direction of the unit vector tangential to the free surface of area $\Delta\Upsilon$ and normal to the perimeter s. One finds that [47,48]

$$\oint_s \mathbf{m}\,\sigma ds' = \int_{\Delta\Upsilon} \nabla_s\sigma(\mathbf{x}, t) d\Upsilon' = \int_{\Delta\Upsilon} \nabla\left(\sigma\left(\mathbb{1} - \mathbf{n}_I \otimes \mathbf{n}_I\right)\right) d\Upsilon' = \left[-\sigma\mathbf{n}_I\left(\nabla^T \cdot \mathbf{n}_I\right) + \left(\nabla_s\sigma\right)\right]\Delta\Upsilon \,. \tag{21}$$

$\nabla_s = (\mathbb{1} - \mathbf{n}_I \otimes \mathbf{n}_I)\nabla$ denotes the interface-tangential gradient operator.

Consequently, the stress balance at the interface segment is

$$[\![\mathbf{R}]\!]_\Upsilon = -\mathbf{R}^{\xi_1} + \mathbf{R}^{\xi_2} = \frac{1}{We}\left[-\sigma\mathbf{n}_I\left(\nabla^T \cdot \mathbf{n}_I\right) + \left(\nabla_s\sigma\right)\right] \,. \tag{22}$$

The first term on the right of equation (22),

$$\boldsymbol{\sigma}_c(\gamma(\mathbf{x}, t)) = -\frac{1}{We}\sigma(\gamma(\mathbf{x}, t))\mathbf{n}_I\left(\nabla^T \cdot \mathbf{n}_I\right) = \sigma_c(\gamma(\mathbf{x}, t))\mathbf{n}_I \tag{23}$$

is the capillary stress, balancing the jump in normal stress

$$\begin{aligned}[\![r]\!]_{\Upsilon,\perp} &= \mathbf{n}_I^T \cdot [\![\mathbf{R}]\!]_\Upsilon = -\mathbf{n}_I^T \cdot \mathbf{R}^{\xi_1} + \mathbf{n}_I^T \cdot \mathbf{R}^{\xi_2} = \\ &= -r_\perp^{\xi_1} + r_\perp^{\xi_2} = \sigma_c(\gamma(\mathbf{x}, t)) \,.\end{aligned} \tag{24}$$

Note that $r_\perp^{\xi_i} = \mathbf{n}_I^T \cdot \mathbf{R}^{\xi_i} = \mathbf{n}_I^T \cdot \mathbf{\Pi}^{\xi_i} \cdot \mathbf{n}_I = n^\beta \Pi_{\beta\gamma}^{\xi_i} n^\gamma = (\mathbf{n}_I \otimes \mathbf{n}_I) : \mathbf{\Pi}^{\xi_i} = P^\perp \mathbf{\Pi}^{\xi_i}$, which is the projection of the stress tensor of phase ξ_i normal to the interface by the normal-projection operator $P^\perp$, compare [49]. The second term,

$$\boldsymbol{\sigma}_M(\gamma) = \frac{1}{We}\nabla_s\sigma(\gamma) \,, \tag{25}$$

is the Marangoni stress. It balances the discontinuity of the interface-tangential stresses

$$[\![r]\!]_{\Upsilon,\parallel} = -r_{\parallel}^{\xi_1} + r_{\parallel}^{\xi_2} = |\boldsymbol{\sigma}_M(\gamma)| = \sigma_M(\gamma)\,, \tag{26}$$

where $r_{\parallel}^{\xi_i} = \Pi_{\delta\delta}^{\xi_i} - n^{\beta}\Pi_{\beta\gamma}^{\xi_i} n^{\gamma} = (\mathbb{1} - \mathbf{n}_I \otimes \mathbf{n}_I) : \boldsymbol{\Pi}^{\xi_i} = P^{\parallel}\boldsymbol{\Pi}^{\xi_i}$ is the interface-tangential projection of the shear stress tensor of phase ξ_i. Decomposed into the respective surface-tangential directions (δ), one obtains

$$[\![r]\!]_{\Upsilon,\parallel}^{(\delta)} = \mathbf{t}_I^{(\delta),T} \cdot [\![\mathbf{R}]\!]_{\Upsilon} = -\mathbf{t}_I^{(\delta),T} \cdot \mathbf{R}^{\xi_1} + \mathbf{t}_I^{(\delta),T} \cdot \mathbf{R}^{\xi_2} = -r_{\parallel,(\delta)}^{\xi_1} + r_{\parallel,(\delta)}^{\xi_2} = \mathbf{t}_I^{(\delta),T} \cdot \boldsymbol{\sigma}_M \tag{27}$$

where $r_{\parallel,(\delta)}^{\xi_i} = t_{I,\beta}^{(\delta)} R_{\beta}^{\xi_i} = t_{I,\beta}^{(\delta)} \Pi_{\beta\gamma}^{\xi_i} n^{\gamma}$.

To impose the interface-normal and tangential momentum exchange due to Eqs. (24) and (27) a constrained Riemann problem is solved with an acoustic Riemann solver [50] for

$$u_{I,\perp} = \frac{Z^{\xi_1} u_{\perp}^{\xi_1} + Z^{\xi_2} u_{\perp}^{\xi_2}}{Z^{\xi_1} + Z^{\xi_2}} + \frac{r_{\perp}^{\xi_1} - r_{\perp}^{\xi_2} + \sigma_c}{Z^{\xi_1} + Z^{\xi_2}} \tag{28a}$$

$$r_{I,\perp}^{\xi_i} = \frac{Z^{\xi_2}\left(r_{\perp}^{\xi_1} + \sigma_c\delta_{i2}\right) + Z^{\xi_1}\left(r_{\perp}^{\xi_2} - \sigma_c\delta_{i1}\right)}{Z^{\xi_1} + Z^{\xi_2}} + \frac{Z^{\xi_1} Z^{\xi_2}}{Z^{\xi_1} + Z^{\xi_2}}\left(u_{\perp}^{\xi_1} - u_{\perp}^{\xi_2}\right) \tag{28b}$$

and

$$u_{I,\parallel}^{(\delta)} = \frac{Z^{\xi_1} u_{\parallel}^{\xi_1,(\delta)} + Z^{\xi_2} u_{\parallel}^{\xi_2,(\delta)}}{Z^{\xi_1} + Z^{\xi_2}} + \frac{\left(r_{\parallel}^{\xi_1,(\delta)} - r_{\parallel}^{\xi_2,(\delta)} + \mathbf{t}_I^{(\delta),T} \cdot \boldsymbol{\sigma}_M\right)}{Z^{\xi_1} + Z^{\xi_2}} \tag{29a}$$

$$r_{I,\parallel}^{\xi_i,(\delta)} = \frac{Z^{\xi_2}\left(r_{\parallel}^{\xi_1,(\delta)} + \mathbf{t}_I^{(\delta),T} \cdot \boldsymbol{\sigma}_M\delta_{i2}\right) + Z^{\xi_1}\left(r_{\parallel}^{\xi_2,(\delta)} - \mathbf{t}_I^{(\delta),T} \cdot \boldsymbol{\sigma}_M\delta_{i1}\right)}{Z^{\xi_1} + Z^{\xi_2}} + \frac{Z^{\xi_1} Z^{\xi_2}}{Z^{\xi_1} + Z^{\xi_2}}\left(u_{\parallel}^{\xi_1,(\delta)} - u_{\parallel}^{\xi_2,(\delta)}\right) \tag{29b}$$

where $Z^{\xi_i} = \rho^{\xi_i} a^{\xi_i}$ are the acoustic impedances of the respective fluid and δ_{ij} is the Kronecker-symbol.

Global momentum conservation is ensured by considering the numerical interface-momentum flux in normal and tangential direction

$$\mathbf{X}^{\perp,\xi_i} = r_{I,\perp}^{\xi_i} \Delta\Upsilon \begin{bmatrix} 0 \\ \mathbf{n}_I^{\xi_i} \end{bmatrix}, \tag{30}$$

and

$$\mathbf{X}^{\parallel,\xi_i} = \mathbf{X}^{\parallel,\xi_i,(1)} + \mathbf{X}^{\parallel,\xi_i,(2)}\,. \tag{31}$$

The tangential fluxes in direction of $\mathbf{t}_I^{(\delta)}$ are

$$\mathbf{X}^{\parallel,\xi_i,(\delta)} = r_{I,\parallel}^{\xi_i,(\delta)} \Delta\Upsilon \begin{bmatrix} 0 \\ \mathbf{t}_I^{(\delta)} \end{bmatrix}. \tag{32}$$

Note that $\mathbf{A}_n^{\xi_i} = \mathbf{n}_I^{\xi_i}\Delta\Upsilon = \left[A_{x_1}, A_{x_2}, A_{x_3}\right]^T$. Employing the algorithm of [51] without normalization, leads to $\mathbf{A}_t^{\xi_i,(\delta)} = \Delta\Upsilon\mathbf{t}_I^{(\delta)}$.

Within finite volume (FV) cells containing only a fraction $\zeta^{\xi_i}(t) = \frac{1}{V}\int\limits_{\Omega\cap\Omega^{\xi_i}} dV$ of fluid phase ξ_i, the system of conservation equations

$$\int_{t^n}^{t^{n+1}} dt \int_{\Omega\cap\Omega^{\xi_i}} \frac{\partial\widetilde{\mathbf{U}}^{\xi_i}}{\partial t}\, dV + \int_{t^n}^{t^{n+1}} dt \int_{\Gamma} \left(\mathbf{F}_1^{T,\xi_i}, \mathbf{F}_2^{T,\xi_i}, \mathbf{F}_3^{T,\xi_i}\right) \cdot \mathbf{n}_{\Gamma} d\Gamma' = \int_{t^n}^{t^{n+1}} dt\, \mathbf{X}^{\xi_i} \tag{33}$$

holds for $\widetilde{\mathbf{U}}^{\xi_i} = \zeta^{\xi_i}\mathbf{U}^{\xi_i}$, where $\mathbf{F}_{\alpha}^{\xi_i} = \mathbf{F}_{\alpha}(\mathbf{U}^{\xi_i})$ and $\mathbf{X}^{\xi_i} = \mathbf{X}^{\perp,\xi_i} + \mathbf{X}^{\parallel,\xi_i}$. Within Ω, $\zeta^{\xi_1} + \zeta^{\xi_2} = 1$ must be satisfied. For a time interval $\Delta t \leq \frac{\Delta x}{s_{max}^n}$, where s_{max}^n denotes the maximum wave speed within the domain at time t^n, the cell-face and interface fluxes are

$$\overline{\mathbf{F}}_{\alpha} = \lim_{\Delta t\to 0} \frac{1}{\Delta t} \int_{t^n}^{t^{n+1}} \mathbf{F}_{\alpha}\, dt\,,\ \overline{\mathbf{X}} = \lim_{\Delta t\to 0} \frac{1}{\Delta t} \int_{t^n}^{t^{n+1}} \mathbf{X}\, dt\,. \tag{34}$$

In discrete Cartesian space, for each FV of $\Delta V_{[i,j,k]} = [\Delta x_1 \Delta x_2 \Delta x_3]_{[i,j,k]}$ the cell-averaged vector of conservative states at time t^n is $\widetilde{\mathbf{U}}_{[i,j,k]}^{\xi_i,n} = \frac{1}{\Delta V_{[i,j,k]}} \int\limits_{\Delta V_{[i,j,k]}\cap\Omega_{[i,j,k]}^{\xi_i}} \mathbf{U}_{[i,j,k]}^{\xi_i,n} dV = \widehat{\mathbf{U}}_{[i,j,k]}^{\xi_i,n} \zeta_{[i,j,k]}^{\xi_i,n}$ with $\widehat{\mathbf{U}}_{[i,j,k]}^{\xi_i,n} = \frac{1}{\Delta V_{[i,j,k]}^{\xi_i,n}} \int\limits_{\Delta V_{[i,j,k]}^{\xi_i,n}} \mathbf{U}_{[i,j,k]}^{\xi_i,n} dV$. To consider the

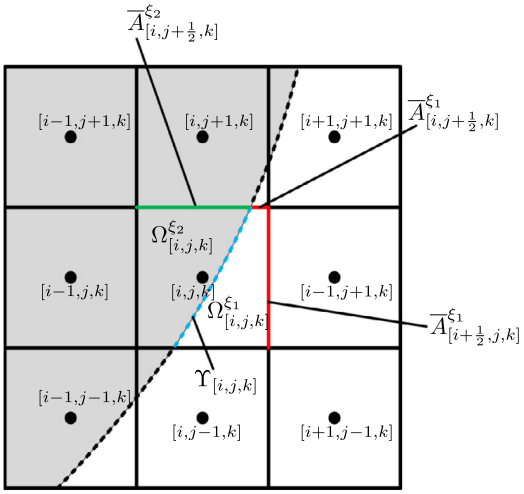

Fig. 3. Two-dimensional schematic of conservative discretization of a cut cell. Red, green indicate phase ξ_1, ξ_2, respectively. (For interpretation of the references to color in this figure legend, the reader is referred to the web version of this article.)

fluxes for the respective phase across the cell-faces, cell-face apertures are computed. Apertures are that part of $\Gamma^{\xi_i}_{[i,j,k]}(t)$ not coinciding with $\Upsilon_{[i,j,k]}(t)$, yet with the cell face $\Gamma_{[i,j,k]}(t)$, [42]. At the right and upper cell face these are defined as depicted in Fig. 3. For single-fluid cells, which are those not cut by the interface, the apertures of phase ξ_1 are unity within $\Omega^{\xi_1}_{[i,j,k]}$ and zero within $\Omega^{\xi_2}_{[i,j,k]}$, and vice versa for phase ξ_2. $\overline{\Delta\Upsilon}_{[i,j,k]}$, $\overline{A}^{\xi_i}_{[i+\frac{1}{2},j,k]}$, $\overline{A}^{\xi_i}_{[i,j+\frac{1}{2},k]}$, $\overline{A}^{\xi_i}_{[i,j,k+\frac{1}{2}]}$, and $\overline{\zeta}^{\xi_i}_{[i,j,k]}$ are reconstructed geometrically.

To advance each phase in time, the discrete conservation equations

$$\widetilde{\mathbf{U}}^{\xi_i,n+1}_{[i,j,k]} = \widetilde{\mathbf{U}}^{\xi_i,n}_{[i,j,k]} + \Delta t \left[\frac{\overline{\mathbf{X}}^{\xi_i}_{[i,j,k]}}{\Delta V_{[i,j,k]}} + \frac{\left[\overline{A\mathbf{F}}_1\right]^{\xi_i}_{[i-\frac{1}{2},j,k]} - \left[\overline{A\mathbf{F}}_1\right]^{\xi_i}_{[i+\frac{1}{2},j,k]}}{\Delta x_1} + \right. \\ \left. + \frac{\left[\overline{A\mathbf{F}}_2\right]^{\xi_i}_{[i,j-\frac{1}{2},k]} - \left[\overline{A\mathbf{F}}_2\right]^{\xi_i}_{[i,j+\frac{1}{2},k]}}{\Delta x_2} + \frac{\left[\overline{A\mathbf{F}}_3\right]^{\xi_i}_{[i,j,k-\frac{1}{2}]} - \left[\overline{A\mathbf{F}}_3\right]^{\xi_i}_{[i,j,k+\frac{1}{2}]}}{\Delta x_3} \right] \tag{35}$$

are solved within each Ω^{ξ_i} for each fluid phase ξ_i individually. The advective fluxes for fluid transport are solved with the weakly compressible high resolution approach of Schranner et al. [38,52]. The viscous fluxes for fluid transport are discretized with 4th-order accuracy.

3.2. Description and propagation of the interface

The interface is captured implicitly by a level-set function $\phi(\mathbf{x},t)$ [5,29,53] with $|\nabla\phi| = 1$ such that $\phi(\mathbf{x},t) \equiv 0$ at $\Upsilon(\mathbf{x},t)$. In $\Omega^{\xi_2}(\mathbf{x},t)$ $\phi(\mathbf{x},t) < 0$, and $\phi(\mathbf{x},t) > 0$ in $\Omega^{\xi_1}(\mathbf{x},t)$.

Based on $\phi(\mathbf{x},t)$, defined in a narrow band in the vicinity of $\Upsilon(\mathbf{x},t)$ [24], geometrical quantities of Υ, such as the normalized outward pointing normal vector and the mean curvature, which corresponds to the divergence of the interface normal vector according to

$$\begin{aligned} \kappa_M &= \left(\nabla^T \cdot \mathbf{n}_I\right) \text{ in 2D and} \\ 2\kappa_M &= \left(\nabla^T \cdot \mathbf{n}_I\right) \text{ in 3D,} \end{aligned} \tag{36}$$

can be obtained. Numerically, the 1st and 2nd spatial derivatives are approximated with 2nd-order central differences. The curvature is evaluated at the cell center, where not necessarily $\phi_{[i,j,k]} = 0$. The sub-cell corrected κ_Υ is obtained directly at the interface by

$$\kappa_\Upsilon = \left(|\kappa_{[i,j,k]}| + \kappa^2_{[i,j,k]}\phi_{[i,j,k]}\right) \operatorname{sgn}\left(\kappa_{[i,j,k]}\right) . \tag{37}$$

Details on the derivation are provided in App. 7.1. For $\phi(\mathbf{x},t) = 0$, the transport equation with the interface velocity $\mathbf{u}_I(\mathbf{x},t)$ [40] holds

$$\frac{\partial\phi(\mathbf{x},t)}{\partial t}\Big|_{\phi=0} + \mathbf{u}_I^T(\mathbf{x},t) \cdot (\nabla\phi(\mathbf{x},t))\Big|_{\phi=0} = 0 . \tag{38}$$

To propagate ϕ in time by Eq. (38) while maintaining its signed distance property, the integration of the transport equation for $\phi(\mathbf{x},t)$ has two sub-steps, *advection* and *reinitialization*, see e.g. [54,55]. Within the original reinitialization algorithm of Sussman et al. [54], a smoothed sign function serves to suppress reinitialization in cells containing the interface. In this work, such cells are excluded explicitly [39].

3.3. Discrete evolution of the surfactant concentration

Insoluble γ evolution is confined to the interface so that $\nabla_n \gamma(\mathbf{x},t) = (\mathbf{n}_I \otimes \mathbf{n}_I)\nabla\gamma(\mathbf{x},t)$ vanishes, which is ensured by extending γ off the interface prior to solving Eq. (7). Note that τ is a pseudo-time. Details of the algorithm for γ-extension and transport are provided in Apps. 7.2 and 7.3 respectively.

3.4. Time integration and time-step constraints

Time integration of the fluid, level-set, and surfactant transport equations is conducted with a 3rd-order Runge–Kutta scheme [56]. The time-step is set by the following constraints:

- Advection limits Δt according to

$$\Delta t_{adv} = \frac{\min(\Delta x_\alpha)}{\max|u_\alpha + a|} \tag{39}$$

  where α represents one of the spatial directions.
- Viscous stresses entail Δt to be [57],

$$\Delta t_{visc} = \frac{3}{14}\min\left(\frac{\rho^{\xi_1}}{\mu^{\xi_1}};\frac{\rho^{\xi_2}}{\mu^{\xi_2}}\right) Re\,(\min(\Delta x_\alpha))^2 \ . \tag{40}$$

- The explicit treatment of capillary stresses is stable when the chosen time step size allows to represent capillary wave motion on the computational grid, [58]. The maximum resolvable wave number is

$$k_{max} = \frac{2\pi}{\lambda_{min}} = \frac{2\pi}{2\min(\Delta x_\alpha)} = \frac{\pi}{\min(\Delta x_\alpha)}. \tag{41}$$

  The maximum advection speed of capillary waves is

$$c_{kap} = \sqrt{\frac{We\,k_{max}}{\rho^{\xi_1}+\rho^{\xi_2}}} \ . \tag{42}$$

  Considering that two capillary waves with opposite direction of advection may concurrently enter the same cell, one obtains

$$\Delta t_{cap} = \frac{1}{2}\frac{\min(\Delta x_\alpha)}{c_{kap}} = \sqrt{\frac{\min(\Delta x_\alpha)^3\,We\left(\rho^{\xi_1}+\rho^{\xi_2}\right)}{4\pi}} \ . \tag{43}$$

- The diffusion of surfactant concentration γ restricts Δt by

$$\Delta t_D = \frac{1}{6} Pe_s\,(\min(\Delta x_\alpha))^2 \ . \tag{44}$$

Consequently, the time-step size is determined according to

$$\Delta t = \mathrm{CFL}\cdot\min\left(\Delta t_{adv}, \Delta t_{visc}, \Delta t_D, \Delta t_{cap}\right) \ , \tag{45}$$

$\mathrm{CFL} = 0.3$ is chosen for all validation and application examples in this paper.

The intersection of the interface with the Cartesian grid may result in cells with small $\zeta^{\xi_i}_{[i,j,k]}$, denoted as "small cells", for which the time step constraints of cells with $\zeta^{\xi_i}_{[i,j,k]} \approx 1$ may generate spurious solutions. Application of a CFL condition for small cells may result in very small Δt. As remedy, a conservative mixing procedure similar to the one in Ref. [59] is employed. In contrast to [59], where all mixing operations are summed up to update $\widetilde{\mathbf{U}}^{\xi_i,n+1}_{[i,j,k]}$ and respective target cells at once, mixing between $\widetilde{\mathbf{U}}^{\xi_i,n+1}_{[i,j,k]}$ and the respective target cells is carried out consecutively, i.e. the mixing operations are ordered by descending magnitude of the mixing factors β_m. Such a sequential execution takes into account that $\widetilde{\mathbf{U}}_{[i,j,k]}$ has been altered by preceding mixing operations. Furthermore, cells of $\zeta^{\xi_i}_{[i,j,k]} \le 0.3$ are considered as small, in [59] cells of $\zeta^{\xi_i}_{[i,j,k]} \le 0.6$ are small. To improve computational efficiency, a wavelet-based multi-resolution algorithm [35] is employed.

4. Numerical validation and application examples

4.1. Transport mechanisms of surfactant concentration

In this section, the accuracy of our scheme for $\gamma(\mathbf{x},t)$-transport by advection, diffusion and interface evolution is investigated. A test case proposed by Xu and Zhao [31] is considered. An analytical solution exists in the case of pure advection or diffusion.

4.1.1. Example 1 – Diffusion along a stationary interface with uniform curvature

We assess the spatial convergence behavior of the surfactant concentration diffusion discretization by simulating diffusion of γ along a stationary, circular interface with radius $r_0 = 1.0$ located at the center, $(x_{1,0}, x_{2,0}) = (2;2)$ of a periodic domain of length and height $L = 4$. The surface diffusion operator (9) becomes $\nabla_s^2\gamma(\mathbf{x}) = \frac{1}{r_0^2}\frac{\partial^2\gamma(\mathbf{x})}{\partial\theta^2}$, where $\theta = \arcsin\left(\frac{x_2}{\sqrt{x_1^2+x_2^2}}\right)$ denotes the angle with the x_1-axis. The initial γ distribution is given by

$$\gamma_0(\theta) = \sin(n\theta) + c\,. \tag{46}$$

The surface diffusion equation reduces to the standard diffusion equation in cylindrical coordinates

$$\begin{cases} \frac{\partial\gamma(\theta,t)}{\partial t} = \frac{1}{Pe_s}\frac{1}{r_0^2}\frac{\partial^2\gamma(\theta,t)}{\partial\theta^2} & ,0 \le \theta \le 2\pi\,, \\ \gamma(\theta,0) = \gamma_0(\theta) & , \\ \gamma(0,t) = \gamma_0(2\pi,t) & , \end{cases}$$

and the solution is

$$\gamma(\theta,t) = \gamma(\mathbf{x},t) = e^{-\frac{1}{Pe_s}\frac{n^2 t}{r^2}}\sin(n\theta) + c\,, \tag{47}$$

with $r = \sqrt{(\Delta x_1)^2 + (\Delta x_2)^2} - r_0$. Since we employ the level-set function $\phi(\mathbf{x}) = r$ to represent the interface, Eq. (47) is the solution to the surfactant concentration diffusion equation

$$\frac{\partial\gamma(\mathbf{x},t)}{\partial t} = \frac{1}{Pe_s}\nabla_s^2\gamma(\mathbf{x},t). \tag{48}$$

$n = 1$, $c = 2$ and $Pe_s = 1$. Reinitialization of γ is omitted. Extension of the surfactant concentration is not applied, instead the diffusion equation is solved within a band around the interface. The time step is $\Delta t = 7\cdot 10^{-6}$, satisfying the stability criterion (45) at a resolution of $\Delta x_1 = \Delta x_2 = 1/80$. According to Tornberg et al. [60,61] one may assess the quality of interfacial $\gamma(\mathbf{x},t)$ transport when a Cartesian grid is used and the interface curvature is generally nonzero on basis of

$$||\epsilon||_1 = \sum_M \{\epsilon\}_{[i,j]}\,, \tag{49a}$$

$$||\epsilon||_2 = \left(\sum_M \{\epsilon^2\}_{[i,j]}\right)^{1/2}\,, \tag{49b}$$

$$||\epsilon||_\infty = \max_{i\in M}\{|\epsilon_i|\}\,. \tag{49c}$$

M are cells for which $|\phi| \le 4\sqrt{\Delta x_1^2 + \Delta x_2^2}$, and

$$\epsilon = |\gamma(\mathbf{x},t) - \gamma_{analy.}(\mathbf{x},t)|\delta_{\epsilon_1}\delta_{\epsilon_2}\,, \tag{50}$$

$$\delta_{\epsilon_i} = \delta(\phi_i/\Delta x_i) = \delta(y) = \Delta x_i \begin{cases} 1 - \frac{1}{2}|y| - |y|^2 + \frac{1}{2}|y|^3 & \text{if } 0 \le |y| \le 1, \\ 1 - \frac{11}{6}|y| + |y|^2 - \frac{1}{6}|y|^3 & \text{if } 1 < |y| \le 2, \\ 0 \quad \text{else}\,, \end{cases} \tag{51}$$

where $(\phi_1, \phi_2) = \phi\ \mathbf{n}_I$. Fig. 4 shows the errors and convergence rates for $||\epsilon||_1$, $||\epsilon||_2$, and $||\epsilon||_\infty$. With increasing resolution $||\epsilon||_1$, $||\epsilon||_2$, and $||\epsilon||_\infty$ diminish with convergence rates within 1.5 and 2.5.

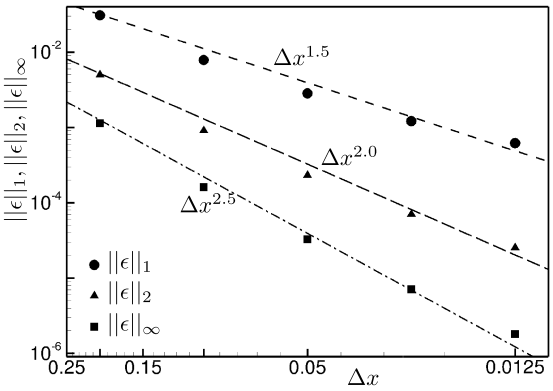

Fig. 4. Grid dependent errors for surfactant concentration at times $t_2 = 2.0$ with $\Delta t = 7 \cdot 10^{-6}$.

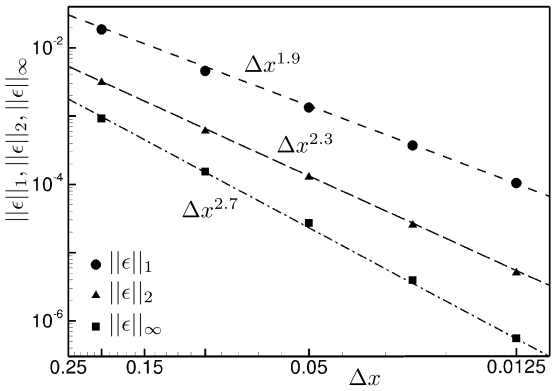

Fig. 5. Grid dependent errors for surfactant concentration at times $t_2 = 2.0$ with $\Delta t = 7 \cdot 10^{-6}$.

4.1.2. Example 2 – Advection with a circular interface in an uniform flow field

A circular interface represented by the zero level-set of the level-set field $\phi(\mathbf{x}) = r = \sqrt{(x_1 - x_{1,0})^2 + (x_2 - x_{2,0})^2} - r_0$ with $r_0 = 1.0$, $(x_{1,0}, x_{2,0}) = (2; 2)$ within a domain of $[0; 6] \times [0; 4]$ is considered. As in Example 1, the initial surfactant concentration distribution follows Eq. (46). Furthermore, $n = 1$ and $c = 2$. The interface and $\gamma(\mathbf{x}, t)$ are subjected to an uniform velocity field $\mathbf{u} = (1; 0)$.

Within a narrow band of three cells around the interface, the surfactant transport equation (7), with $D_s = 0$ is solved, where $\mathbf{u}_\gamma = \mathbf{u}_\phi = \mathbf{u}^{\xi_1} = \mathbf{u}^{\xi_2}$ is set. Advection is the only transport mechanism, hence, $\gamma(\mathbf{x}, t) = \gamma(\mathbf{x}, 0)$. The time-step size is $\Delta t = 7 \cdot 10^{-6} = const.$ for consistency with Example 1. $||\epsilon||_1$, $||\epsilon||_2$, and $||\epsilon||_\infty$ are evaluated at different levels of uniform grid refinement, the results are shown in Fig. 5. While the errors are of the same magnitude as for pure diffusion, the rates of convergence are higher.

4.1.3. Example 3 – Advection and diffusion with and along a circular interface in an uniform flow field

With $D_s = 1$, $\gamma(\mathbf{x}, t)$ evolves now by advection and diffusion. The setup and Δt are as in Sec. 4.1.2. Fig. 6 shows the error evolution with grid refinement. For $||\epsilon||_1$, $||\epsilon||_2$, and $||\epsilon||_\infty$ the convergence rates remain within an order of approximately 1.4 to 2.3.

4.1.4. Example 4 – Transport of surfactant concentration along a deforming interface

In this example, γ, initialized according to Eq. (46), $n = 1$ and $c = 2$, evolves on a deforming interface given by $\phi(\mathbf{x}) = r = \sqrt{(x - x_{1,0})^2 + (x - x_{2,0})^2} - r_0$, $r_0 = 1$ and $(x_{1,0}; x_{2,0}) = (3; 2)$. The interface is subjected to a shear flow with

$$\mathbf{u}(\mathbf{x}, 0) = \begin{cases} \left((x_2 - x_{2,0})^2, 0\right) & \text{if } x_2 \geq x_{2,0} \\ \left(-(x_2 - x_{2,0})^2, 0\right) & \text{if } x_2 < x_{2,0}. \end{cases} \tag{52}$$

At the lower and upper boundaries of the domain, with $[0; 6] \times [0; 4]$, symmetry conditions are applied and in flow direction the domain is periodic, Δt is according to Eq. (45). Due to the large interface deformation, this test case serves to assess the effect of grid resolution on area- and surfactant-conservation.

The improvement of disperse phase area conservation and surfactant mass conservation due to grid refinement is significant, see Figs. 7 and 8. The observed relative change of area and surfactant mass is 0.4% and 3% respectively, for $\Delta x = 4/256$ at $t = 4$. The convergence rates are 1.5 and 1.3 respectively.

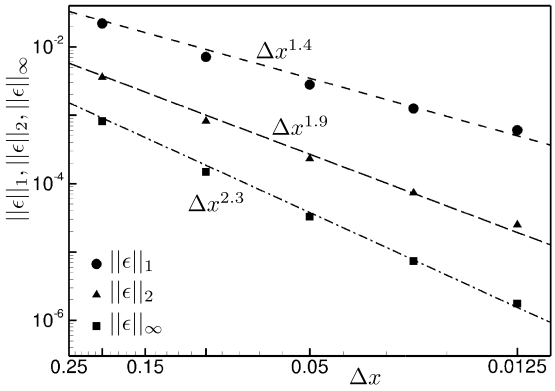

Fig. 6. Error evolution with grid refinement for surfactant concentration at times $t_2 = 2.0$ with $\Delta t = 7 \cdot 10^{-6}$.

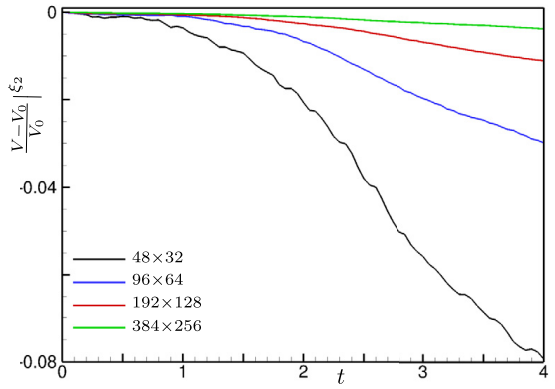

Fig. 7. Grid dependent relative change of area.

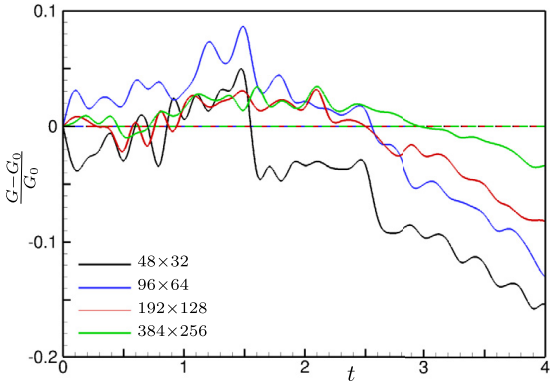

Fig. 8. Grid dependent relative change of surfactant mass with (dashed lines) and without (solid lines) surfactant-conservation correction.

Improving surfactant-conservation

To improve surfactant mass conservation, i.e. ensuring $G(t) = \int_{\Delta\Upsilon} \gamma(\mathbf{x}, t) d\Upsilon' = \int_{\Delta\Upsilon} \gamma(\mathbf{x}, 0) d\Upsilon' = G_0$, the procedure of Xu et al. [33] is employed. Therefore the surfactant concentration is renormalized after each time step according to $\gamma(\mathbf{x}, t) = \beta\widetilde{\gamma}$ where $\beta = \frac{\int_{\Delta\Upsilon} \widetilde{\gamma} d\Upsilon'\big|^0}{\int_{\Delta\Upsilon} \gamma d\Upsilon'\big|^{n+1}}$. In our framework, the interface segment length $\Delta\Upsilon_{[i,j,k]}$ is computed in each cell containing a portion of the interface.

The surfactant-conservation correction suppresses variations of $G(t)$ as intended, which can arise due to interface deformation, see Fig. 8. Fig. 9 visualizes $\beta(t) - 1$ within $0 \le t \le 4$. Grid refinement leads to a significant decrease in $|\beta(t) - 1|$, hence, improvement in surfactant mass conservation. Nevertheless, $|\beta(t) - 1|$ is less than 0.002 for $\Delta x = 4/48$. On the finest grid, $\frac{1}{T}\int_{t=0}^{4}(\beta(t) - 1)dt$ is approximately $1.0 \cdot 10^{-6}$. Fig. 10 depicts $\gamma(t)$ at $t = 0.5$ and $t = 2.5$ for Example 4 without (left column) and with (right column) surfactant-conservation correction. The evolution of $\gamma(\Upsilon, t)$ as predicted within $0 \le t \le 3.0$ as well as a grid of MR blocks are visualized in Fig. 11.

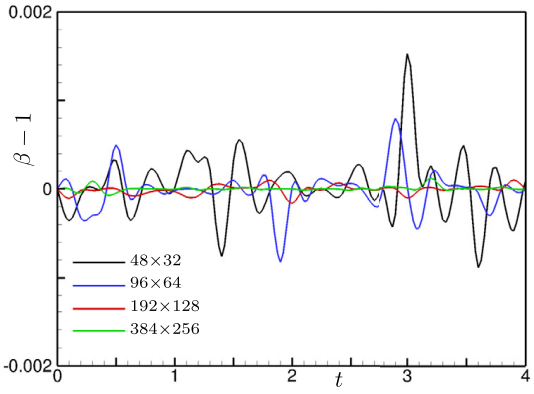

Fig. 9. $\beta(t) - 1$ at different grid resolutions.

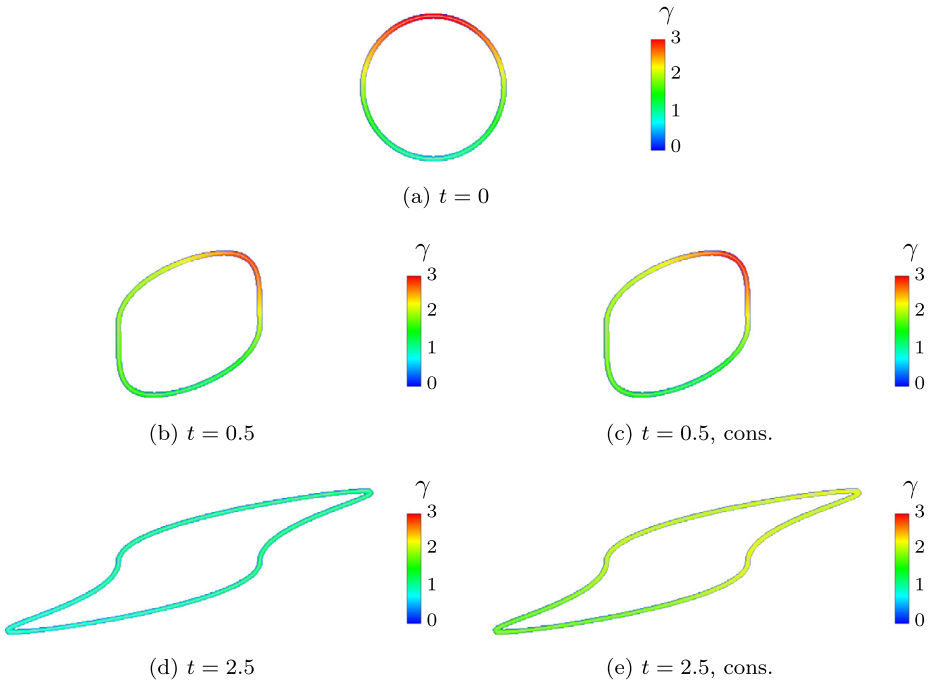

(a) $t = 0$

(b) $t = 0.5$

(c) $t = 0.5$, cons.

(d) $t = 2.5$

(e) $t = 2.5$, cons.

Fig. 10. Comparison of $\gamma(\Upsilon(\mathbf{x}), t)$ for surfactant evolution without (left column) and with (right column) surfactant-conservation correction, $\Delta x = 4/512$.

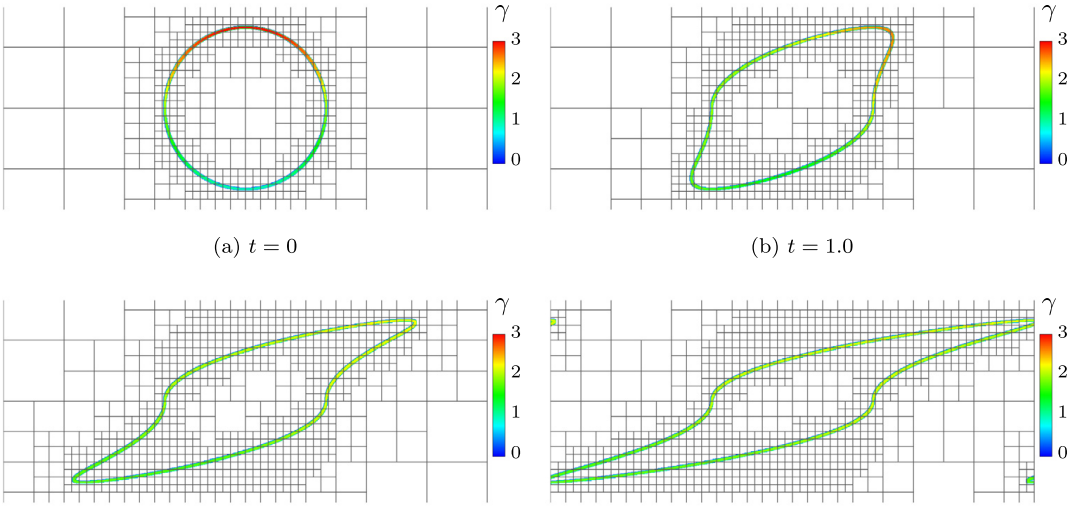

(a) $t = 0$

(b) $t = 1.0$

(c) $t = 2.0$

(d) $t = 3.0$

Fig. 11. Evolution of $\gamma(\Gamma(\mathbf{x}), t)$ on a deforming interface with AMR of maximum resolution $\Delta x = 6/1024$ and surfactant-conservation correction.

Table 1
CPU time required for 1000 time steps of the sharp interface (SI) and diffuse interface (DI) algorithms at $t_0 = 0$, $t_1 = 1$, $t_2 = 2$, $t_3 = 3$, and ratio of execution times.

Time	Grid size	$\Delta t_{DI}[ms]$	$\Delta t_{SI}[ms]$	$\Delta t_{DI}/\Delta t_{SI}$
0	48×32	47.473	17.392	2.73
	96×64	137.547	67.572	2.04
	192×128	445.701	256.307	1.74
	384×256	1550.36	1000.57	1.55
1.0	48×32	50.052	18.092	2.77
	96×64	146.589	69.717	2.10
	192×128	466.455	259.931	1.79
	384×256	1595.52	1002.81	1.59
2.0	48×32	56.793	19.899	2.85
	96×64	169.625	73.711	2.30
	192×128	517.664	272.107	1.90
	384×256	1707.25	1018.57	1.68
3.0	48×32	64.758	20.502	3.16
	96×64	192.397	76.943	2.50
	192×128	570.996	284.686	2.06
	384×256	1835.19	1059.53	1.73

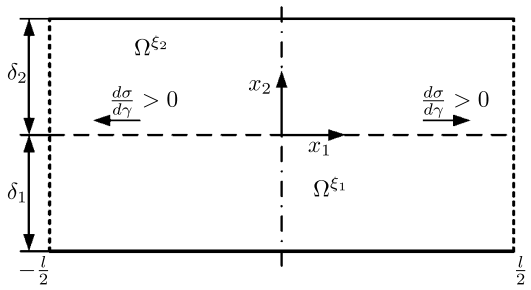

Fig. 12. Geometric setup of two immiscible fluids in a micro channel. The temperature of the lower and upper walls are $T(x_1, -\delta_1) = T_h + \Delta T \cos(\widetilde{x_1})$ and $T(x_1, \delta_2) = T_c$, respectively, $T_h > T_c > \Delta T > 0$, and $\omega = \frac{2\pi}{l}$ is a wave number. The gravity is zero.

Increase of efficiency due to sharp-interface formulation

The surfactant-conservation correction method of [33] employs the diffuse interface (DI) framework [31]. Our sharp-interface (SI) framework reduces the execution time by a factor of up to about 3 for coarse grids or large interface deformation, and by about 2 for very fine grids or small interface deformation, see Table 1, using Example 4 and uniform grids. For the timings, the interface and surfactant-concentration restart data have been stored every $\Delta t = 1$. The simulations have been (re)started on a single core of an Intel Xeon E5620 at times $t_0 = 0$, $t_1 = 1$, $t_2 = 2$, $t_3 = 3$ and the SI and DI algorithms were advanced each by 1000 time steps. Δt_{SI} and Δt_{DI} denote the wall-clock times necessary for SI and DI.

4.2. Evaluation of Marangoni and viscous stress modeling

To verify the sharp-interface model for the viscous and Marangoni stresses, a thermocapillary driven flow in a heated micro channel with two superimposed planar fluids, as proposed by Pendse and Esmaeeli [62], is considered. The geometric setup is shown in Fig. 12. The heights of the fluid layers ξ_1 and ξ_2 are δ_1 and δ_2, respectively. The domain is periodic in horizontal direction, the no-slip boundary condition applies to the upper and lower walls. Uniform temperature $T(x_1, \delta_2) = T_c$ is imposed to the upper wall. At the lower wall, the temperature follows the sinusoidal distribution $T(x_1, -\delta_1) = T_h + \Delta T \cos(\widetilde{x_1})$ (which is higher than that of the upper wall). $T_h > T_c > \Delta T > 0$ and $\omega = \frac{2\pi}{l}$ is a wave number with l being a length scale. The temperature boundary conditions establish a periodic temperature field in the horizontal direction with a period length scale of l. At steady state the temperature field follows [62]:

$$T^{\xi_1} = \frac{\chi\,(T_c - T_h)\,y + \chi\,T_c\delta_1 + T_h\delta_2}{\chi\,\delta_1 + \delta_2} + \Delta T f\left(\widetilde{\delta_2}, \widetilde{\delta_1}, \chi\right)\left[\sinh(\widetilde{\delta_2})\cosh(\widetilde{x_2}) - \chi\sinh(\widetilde{x_2})\cosh(\widetilde{\delta_2})\right]\cos(\widetilde{x_1}), \tag{53a}$$

$$T^{\xi_2} = \frac{(T_c - T_h)\,y + \chi\,T_c\delta_1 + T_h\delta_2}{\chi\,\delta_1 + \delta_2} + \Delta T f\left(\widetilde{\delta_2}, \widetilde{\delta_1}, \chi\right)\sinh(\widetilde{\delta_2} - \widetilde{x_2})\cos(\widetilde{x_1})\,, \tag{53b}$$

where $\widetilde{\bullet} = \bullet\omega$, $f\left(\widetilde{\delta_2}, \widetilde{\delta_1}, \chi\right) = 1.0/\left[\chi\sinh(\widetilde{\delta_1})\cosh(\widetilde{\delta_2}) + \sinh(\widetilde{\delta_2})\cosh(\widetilde{\delta_1})\right]$. Let $T_h = 20$, $T_c = 10$, $\Delta T = 4$, $\mu^{\xi_1} = \mu^{\xi_2} = 0.2$, $(\rho, a, p_0)^{\xi_1} = (\rho, a, p_0)^{\xi_2} = (1.0, 1.0, 0)$, and the ratio of thermal conductivity $\chi = 1.0$, see [63]. We set $\gamma(\mathbf{x}) = T(\mathbf{x})$. σ depends linearly on γ, i.e. Eq. (12) holds, $\zeta E = 1/60$, and $\sigma_0 = 0.03$.

Initially, the fluids are at rest. Due to $\frac{\partial \gamma}{\partial x_1} \neq 0$ along the non-deforming interface the fluids are accelerated. The tangential (viscous and Marangoni) interface interaction establishes a velocity field of

$$u_1^{\xi_1} = U_{max}\{\left[C_1^{\xi_1} + \omega\left(C_2^{\xi_1} + C_3^{\xi_1} y\right)\right]\cosh(\widetilde{x_2}) + \left(C_3^{\xi_1} + C_1^{\xi_1}\widetilde{x_2}\right)\sinh(\widetilde{x_2})\}\sin(\widetilde{x_1}), \tag{54a}$$

$$u_2^{\xi_1} = -\omega U_{max}\left[C_1^{\xi_1} y\cosh(\widetilde{x_2}) + \left(C_2^{\xi_1} + C_3^{\xi_1} y\right)\sinh(\widetilde{x_2})\right]\cos(\widetilde{x_1}) \tag{54b}$$

within Ω^{ξ_1}, and of

$$u_1^{\xi_2} = U_{max}\{\left[C_1^{\xi_2} + \omega\left(C_2^{\xi_2} + C_3^{\xi_2} y\right)\right]\cosh(\widetilde{x_2}) + \left(C_3^{\xi_2} + C_1^{\xi_2}\widetilde{x_2}\right)\sinh(\widetilde{x_2})\}\sin(\widetilde{x_1}), \tag{55a}$$

$$u_2^{\xi_2} = -\omega U_{max}\left[C_1^{\xi_2} y\cosh(\widetilde{x_2}) + \left(C_2^{\xi_2} + C_3^{\xi_2} y\right)\sinh(\widetilde{x_2})\right]\cos(\widetilde{x_1}), \tag{55b}$$

within Ω^{ξ_2}, see [62], for which the system is at equilibrium. The constants in Eqs. (54), (55) are:

$$C_1^{\xi_2} = \frac{\sinh^2(\widetilde{\delta_2})}{\sinh^2(\widetilde{\delta_2}) - \widetilde{\delta_2}^2}\ ,\ C_2^{\xi_2} = \frac{-\delta_2\widetilde{\delta_2}}{\sinh^2(\widetilde{\delta_2}) - \widetilde{\delta_2}^2}\ ,\ C_3^{\xi_2} = \frac{2\widetilde{\delta_2} - \sinh(2\widetilde{\delta_2})}{2\left[\sinh^2(\widetilde{\delta_2}) - \widetilde{\delta_2}^2\right]},$$

$$C_1^{\xi_1} = \frac{\sinh^2(\widetilde{\delta_1})}{\sinh^2(\widetilde{\delta_1}) - \widetilde{\delta_1}^2}\ ,\ C_2^{\xi_1} = \frac{-\delta_1\widetilde{\delta_1}}{\sinh^2(\widetilde{\delta_1}) - \widetilde{\delta_1}^2}\ ,\ C_3^{\xi_1} = \frac{\sinh(2\widetilde{\delta_1}) - 2\widetilde{\delta_1}}{2\left[\sinh^2(\widetilde{\delta_1}) - \widetilde{\delta_1}^2\right]},$$

$$U_{max} = -\frac{\Delta T\sigma_0\zeta E}{\mu^{\xi_1}} g\left(\widetilde{\delta_2}, \widetilde{\delta_1}, \chi\right) h\left(\widetilde{\delta_2}, \widetilde{\delta_1}, \lambda\right)\ ,$$

where

$$g\left(\widetilde{\delta_2}, \widetilde{\delta_1}, \chi\right) = \sinh(\widetilde{\delta_2}) f\left(\widetilde{\delta_2}, \widetilde{\delta_1}, \chi\right)\ ,$$

$$h\left(\widetilde{\delta_2}, \widetilde{\delta_1}, \lambda\right) = \frac{\left[\sinh^2(\widetilde{\delta_2}) - \widetilde{\delta_2}^2\right]\left[\sinh^2(\widetilde{\delta_1}) - \widetilde{\delta_1}^2\right]}{\lambda\left[\sinh^2(\widetilde{\delta_1}) - \widetilde{\delta_1}^2\right]\left[\sinh(2\widetilde{\delta_2}) - 2\widetilde{\delta_2}\right] + \left[\sinh^2(\widetilde{\delta_2}) - \widetilde{\delta_2}^2\right]\left[\sinh(2\widetilde{\delta_1}) - 2\widetilde{\delta_1}\right]}\ .$$

Note that $\lambda = \frac{\mu^{\xi_2}}{\mu^{\xi_1}}$. With $L_{ref} = \delta_1 = 1.0$, $l = 4\delta_1$, $U_{ref} = \frac{\sigma_0\zeta E\Delta T}{l}\frac{\delta_1}{\mu^{\xi_1}} = 2.5 \cdot 10^{-3}$, it follows that $Re = 0.0125 \ll 1$ and $We = 1/4800 \ll 1$. The computed u_1, u_2 velocity fields at a resolution of $\Delta x = 1/80$ agree well with the analytical solutions, Fig. 13. Fig. 14 shows the average errors

$$L_1 = \int_{\Delta V} |\epsilon| dV' \approx \sum_M \{|\epsilon|\Delta V\}_{[i,j]}\ , \tag{58a}$$

$$L_2 = \left(\int_{\Delta V} |\epsilon|^2 dV'\right)^{1/2} \approx \left(\sum_M \{|\epsilon|^2\Delta V\}_{[i,j]}\right)^{1/2}\ , \tag{58b}$$

of u_1 and u_2 between the computed and exact solution at different grid resolutions at steady state. M is the number of cells within Ω. An at least linear convergence rate is observed for the L_1 and L_2 errors with grid refinement. We note that already at a resolution of $\Delta x = 1/40$ the difference to the analytical solution is barely noticeable.

4.3. Evaluation of interface stress modeling

Young et al. [64] have investigated the motion of cylindrical drops under the influence of a linear temperature gradient and gravity experimentally. As temperature gradients alter the local surface tension the implementation of the Marangoni and capillary stresses may be validated by applying an interfacial surfactant concentration field that varies linearly in x_2 direction. E.g. Teigen et al. [28] have consulted a comparable axisymmetric configuration, Herrmann et al. [65] have compared results obtained with different methods for 2D and 3D configurations.

Following Young et al., our setup consists of a two-dimensional, planar channel of width $5r_0$ and height $L = 15r_0$ containing a cylindrical drop of radius r_0. The interfacial surfactant concentration is

$$\frac{\gamma(x_2)}{\gamma_\infty} = \frac{x_2}{L}\ . \tag{59}$$

The surface tension coefficient is obtained from Eq. (12) with $\zeta E = 1$ and $\sigma_0 = 1$. The bulk and the disperse phase are characterized by $(\rho, a, p_0)^{\xi_1} = (0.2, 5.0, 0)$ and $(\rho, a, p_0)^{\xi_2} = (0.2, 40.0, 0)$, $\mu^{\xi_1} = \mu^{\xi_2} = 0.1$, $g = 0$. According to Young et al. [64] the stationary ascent velocity for a cylindrical drop is

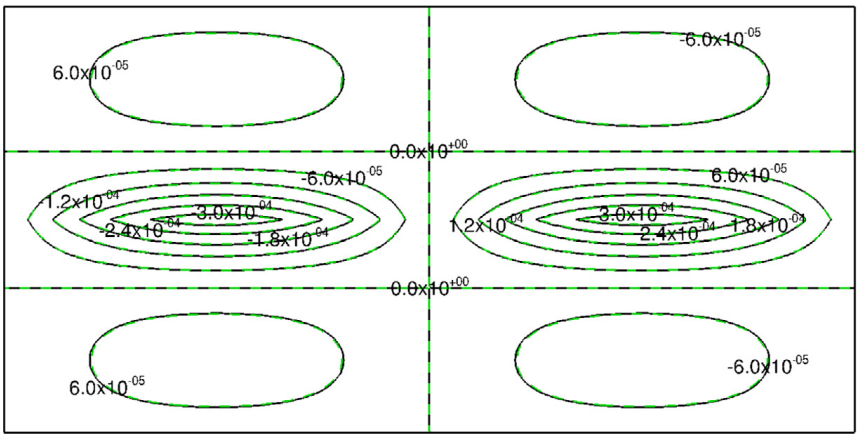

(a) u_1

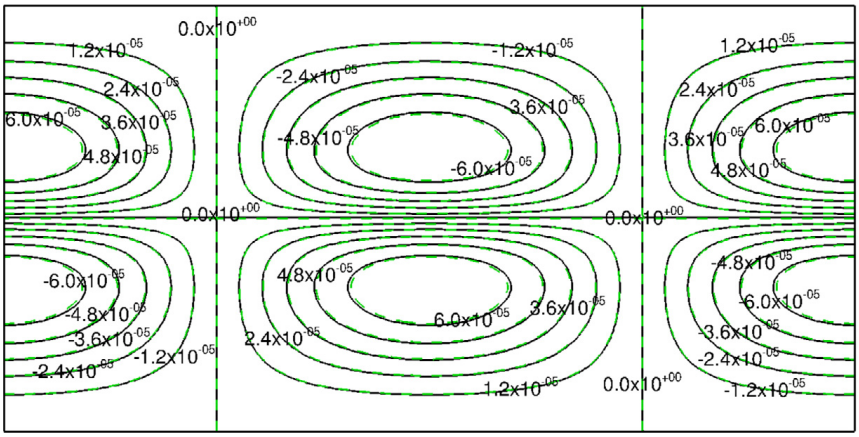

(b) u_2

Fig. 13. u_1 and u_2 contours at steady state (————), $t = 20$ has been chosen, as compared to the analytical results (- - - - - -). Resolution: $\Delta x = 1/80$.

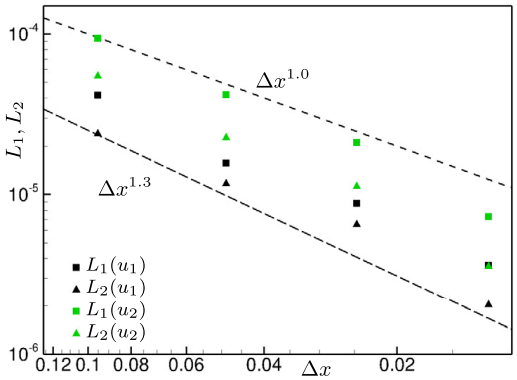

Fig. 14. Errors for velocity fields u_1, u_2 with grid refinement for a thermocapillary flow at steady state, $t = 20$.

$$u_{2,YBG} = \frac{2\left(\zeta E \frac{r_0}{L} - \Delta\rho r_0^2 g \frac{(\mu^{\xi_1} + \mu^{\xi_2})}{\mu^{\xi_1}}\right)}{9\mu^{\xi_1} + 6\mu^{\xi_2}} . \tag{60}$$

With these parameters, (60) gives $u_{2,YBG} \approx 0.088$, hence, $Re \approx 0.088$. This is well within the creeping flow regime for which Eq. (60) is valid. The Ω^2-average ascent velocity is determined from

$$u_2^{\xi_2} = \frac{1}{V}\int_{\Omega^{\xi_2}} u_2(\mathbf{x})\zeta^{\xi_2} dV = \frac{1}{\Delta V^{\xi_2}} \sum_{[i,j,k]\in\Omega^2} \{u_2(\mathbf{x})\zeta^{\xi_2}\}_{[i,j,k]} . \tag{61}$$

AMR is used with resolutions from $5r_0/32$ to $5r_0/512$. The time step is set according to Eq. (45).

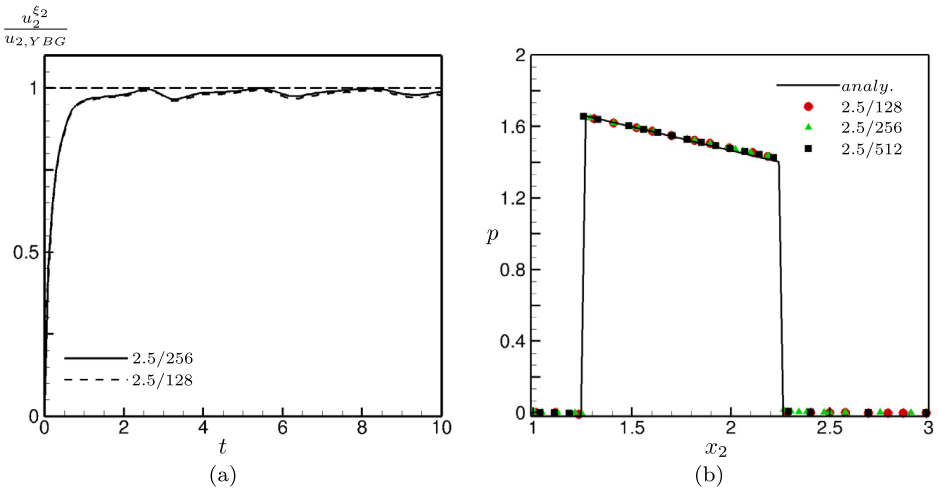

Fig. 15. (a) Normalized ascent velocity over time, and (b) pressure at centerline of the bubble at $t = 10$ as compared to the theoretical expected ones.

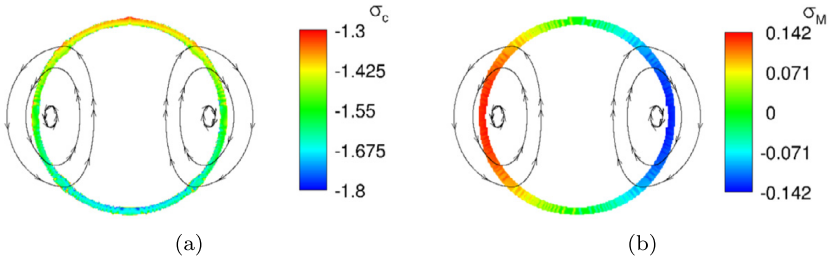

Fig. 16. (a) $\sigma_c(\mathbf{x}, t)$ and (b) $\sigma_M(\mathbf{x}, t)$ at $t = 10$ in a narrow band of five cells around Υ.

The ascent velocity reaches the theoretical value approximately independent of grid refinement, see Fig. 15a, the average $u_2^{\xi_2}/u_{2,YBG}$, for $t \geq 5$ is 98%. Note that results obtained on a grid with $\Delta h_{min,AMR} = 2.5/512$ are not shown, as they agree with the ones with $\Delta h_{min,AMR} = 2.5/256$. Our results for $u_2^{\xi_2}$ are in very good agreement with those depicted in Fig. 1 of [65] and obtained on basis of the conservative level-set/ghost fluid method as well as the volume of fluid method on same grid resolutions. Fig. 15b shows the pressure along the centerline of the drop at $t = 10$ as compared to the analytical pressure $p(x_2) = \frac{\sigma(x_2)}{r_0} = \frac{\left(1-\frac{x_2}{L}\right)}{r_0}$, which is the internal pressure according to Eqs. (12), (22). The agreement is excellent and grid-independent. The capillary and Marangoni stresses within a narrow band around Υ, at $t = 10$, are shown in Fig. 16 along with streamlines indicating the approximate centers of the driving vortices. The normalized ascent velocity of a 3D drop in a linear surfactant gradient, with identical parameters as in 2D is shown in Fig. 17a. It is found that $u_2^{\xi_2}/u_{2,YBG} = 93\%$. The velocity components in the other two spatial directions, with zero surfactant gradient, are on the order of 10^{-10} within the simulation time interval $T = 10$. The pressure along the symmetry axis of the 3D drop at $t = 10$ is compared to the analytical pressure $p(x_2) = \frac{2\sigma(x_2)}{r_0} = \frac{2\left(1-\frac{x_2}{L}\right)}{r_0}$ in Fig. 17b. At the upper side the relative error of p to the theoretically expected is $+4\%$, at the lower side it is -2%.

5. Single drop in linear shear flow

In this section we study the evolution of a drop in shear flow, similar to [66], as a demonstration application of our method. The interest is on the transient deformation behavior. We initialize a circular drop of $r_0 = 1$ and $(\rho, a, p_0)^{\xi_2} = (1.0, 40, 1000)$ at the center of a computational domain, $\Omega = [-4; 4] \times [-4; 4]$, immersed in a bulk fluid of $(\rho, a, p_0)^{\xi_1} = (1.0, 5, 1000)$. If not noted otherwise, $\mu^{\xi_1} = \mu^{\xi_2} = 0.1$, which corresponds to $Re = 10$, also $\gamma(\Upsilon, t = 0) = 1$, and $\sigma_0 = 1$, i.e. $We = 1$ or $Ca = 0.1$, and $Pe_s = 1$. The domain boundaries are periodic in x_1 direction. In x_2, the no-slip boundaries move at constant speed $\mathbf{u} = (x_2; 0)$. At $t = 0$, the flow field is initialized with a shear flow $u' = \frac{\partial u_1}{\partial x_2} = 1$. Based on Sec. 4.1, $\Delta x_1 = \Delta x_2 = 1/32$ is chosen. A grid refinement study, see App. 7.5, shows that results do not further improve with higher resolutions.

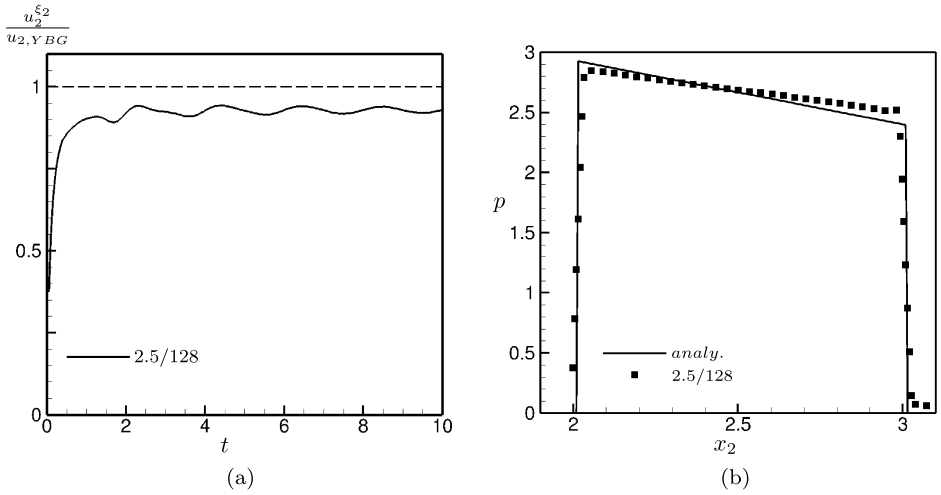

Fig. 17. (a) Normalized ascent velocity over time, and (b) pressure at symmetry axis of the bubble at $t = 10$ as compared to the theoretical expected ones.

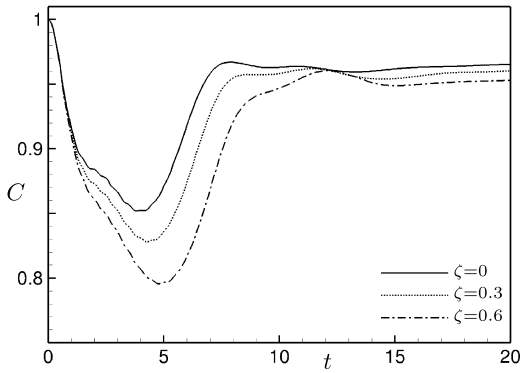

Fig. 18. Degree of circularity over time.

5.1. Effect of surfactant coverage

The qualitative effect of surfactant coverage (ζ) on dynamic and steady drop deformation is studied. At four characteristic stages of drop development, drop morphologies and the interface quantities γ, σ, σ_c, and σ_M are shown in Figs. 19a–19d. The ζ-dependent degree of circularity,

$$C = \frac{P_a}{P_b} = \frac{\pi d_a}{\int_{\Delta\Upsilon} 1 d\Upsilon'} , \tag{62}$$

where P_a denotes the perimeter of a circle with diameter d_a and same area of the drop. For a perfectly circular drop the circularity is equal to unity, due to deformation C decreases. The degree of circularity is shown as a function of time in Fig. 18.

Due to the flow, γ is washed from the flanks towards the drop tips, see first and second row, second column of Figs. 19a–19d. Higher ζ lead to a stronger effect of $\gamma(\mathbf{x})$ onto σ according to Eq. (12), compare third column of Figs. 19a–19d. The early stages of drop development, are characterized by large drop deformations, see Fig. 18. As $|\sigma_c|$ is smaller for higher ζ at early stages, the drop elongates more. Due to the strong elongation around $t \approx 5$, κ and $|\sigma_c|$ diminish at the flanks. For higher ζ, κ is larger at the tips, yet, σ and thus $|\sigma_c|$ are much lower. In conjunction with $|\sigma_M| \neq 0$, due to the large $\nabla_s\gamma$ between the tips and the flanks, the drop recontracts. Recontraction is delayed for larger ζ, as these entail "larger gradients in Marangoni stresses that retard the motion of the drop interface and the drop behaves as though it is more viscous" [67], see therefore the intermediate state Fig. 19c. At steady-state, capillary stresses are higher for lower ζ, lowering circularity, see Fig. 18. Where Marangoni stresses are non-negligible the interface-displacement is identical, see Fig. 19d. The qualitative observations on the effect of surfactant coverage are in full agreement with e.g. Refs. [13,67,68].

5.2. Effect of capillary number

The capillary number relates viscous stresses to capillary stresses. Increasing Ca decreases stabilizing surface tension in favor of viscous stresses, and stretching of the drop. The capillary number is $Ca = \frac{We}{Re}$, demonstrating interaction of viscous, inertial and capillary forces. Hence, the effect of Ca, We, and Re in conjunction with $\sigma = f(\gamma(\mathbf{x}, t)$ is studied.

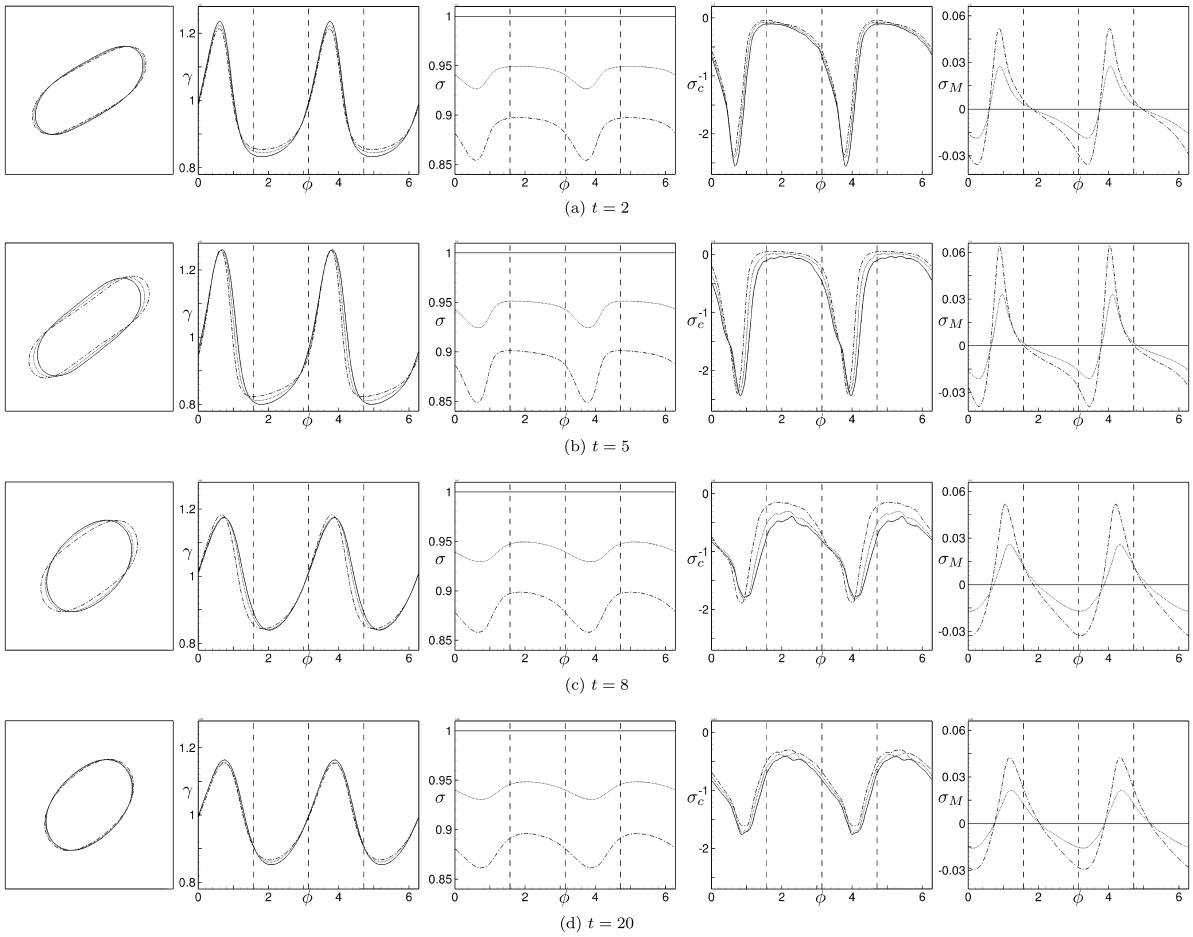

Fig. 19. Drop morphologies, $\zeta = 0$ γ, σ, σ_c, and σ_M over the azimuth as dependent on surfactant coverage, $\zeta = 0$ (————), $\zeta = 0.3$ (- - - - - -), $\zeta = 0.6$ (— · — · — · —).

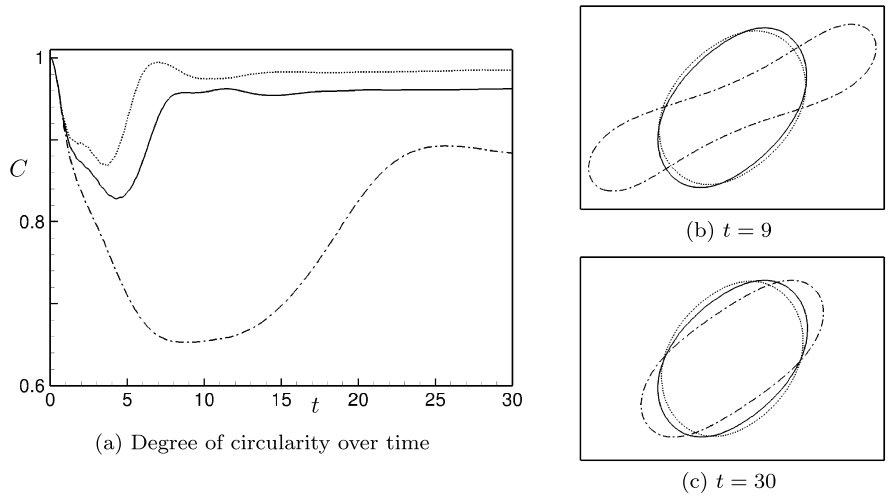

Fig. 20. Temporal evolution of degree of circularity, and drop morphologies at two characteristic times for $Re = 20$ ($Ca = 0.05$) (- - - - - -), $Re = 10$ ($Ca = 0.1$) (————), $Re = 5$ $Ca = 0.2$ (— · — · — · —). $We = 1$, $E = 0.2$, $\zeta = 0.3$.

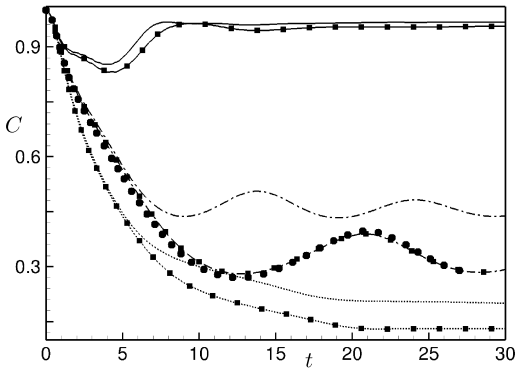

Fig. 21. Evolution of degree of circularity for $We = 1$ ($Ca = 0.1$) (————), $We = 2$ ($Ca = 0.2$) (— · — · —), $We = 4$ ($Ca = 0.4$) (- - - - - -). Square symbols indicate $\zeta = 0.3$, and circles $\zeta = 0.6$. $E = 0.2$, $Re = 10$.

The Reynolds number relates inertial to viscous stresses. To test the effect on drop deformation, $We = 1$, $E = 0.2$, $\zeta = 0.3$, and variable $\mu^{\xi_1} = \mu^{\xi_2}$ is assumed. At lower Re, implicating higher Ca, temporary and steady-state drop deformation is larger, and the time to reach steady-state extends, see Fig. 20.

The We-, and time-dependent circularity for $Re = 10 = const.$ is shown in Fig. 21 for $E = 0.2$, $\zeta = 0.3$ and clean interfaces. For the case of $We = 2$, results for $E = 0.2$, $\zeta = 0.6$ are included. Larger We imply lower σ, hence, larger drop deformation, see also Sec. 5.1. At a critical We_c, the drop shape oscillates harmonically with a distinct frequency instead of returning to an elliptical steady-state. For even higher We, the drop elongates continuously. The observations of e.g. Lai et al. [18], and Lee et al. [69] that increasing Ca at $Re = const.$ implies smaller surface tension, and larger drop deformation is confirmed.

Increasing Re and We, while maintaining $Ca = 0.1$, entails a stronger dynamic and steady-state drop elongation, see Fig. 22. Based on Figs. 22 and 20a, one finds that for small Re, potentially leading to strong initial drop elongation, a low We ensures that an approximately circular drop shape is maintained. At high We, the initial drop deformation is large due to the initial momentum. For high Re, the lack of viscous straining allows the drop to return to a steady-state ellipsoidal shape.

5.3. Effect of Peclet number

Small Pe_s implies small diffusion time scales for γ. Rapid diffusion of γ reduces both, gradients and magnitudes of γ, σ, σ_c, and σ_M, which in turn suppresses drop deformation, see Fig. 23b. At steady-state, independently of ζ (not shown), drop deformation increases slightly with increasing Pe_s. For the steady-state, we thus confirm the observation of Lai et al. [18] that Pe_s has an insignificant effect on drop deformation.

5.4. On the choice of constitutive equation and the effect of E and ζ

Variation of elasticity E and surfactant coverage ζ have the same effect when modeling the dependence of σ on γ with a linear Langmuir constitutive equation (12). For small ζ, Eq. (10) and Eq. (12) lead to the same results. When modeling

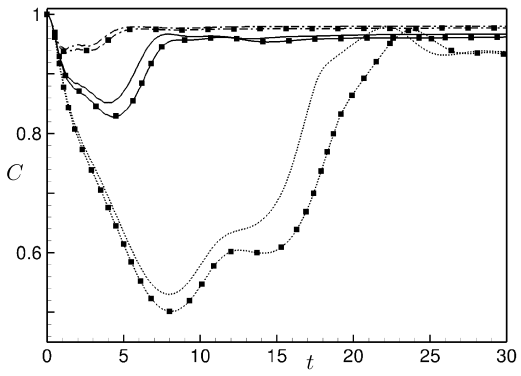

Fig. 22. Evolution of degree of circularity for $We = 0.5$ $(Re = 5)$ $(- \cdot - \cdot - \cdot)$, $We = 1$ $(Re = 10)$ (————), $We = 2$ $(Re = 20)$ (- - - - - -). Symbols indicate $E = 0.2$, $\zeta = 0.3$.

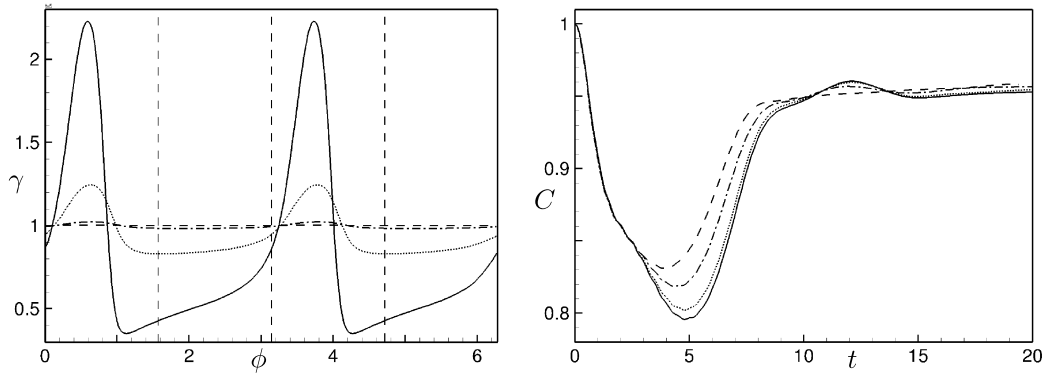

(a) γ along over the azimuth at $t = 5$. (b) Evolution of degree of circularity

Fig. 23. $Pe_s = 10$: (————), $Pe_s = 1$: (- - - - - -), $Pe_s = 0.1$: $(- \cdot - \cdot - \cdot)$, $Pe_s = 0.01$: $(- - - - - -)$. $We = 1$, $Re = 10$, $\zeta = 0.6$.

$\sigma(\gamma)$ non-linearly, reducing E has a similar effect as increasing We, the same holds for linear modeling and reduction of $E\zeta$. For $We = 1$, $Re = 10$, $E = 0.6$ and $\zeta = 0.6$ and employing Eq. (10), a harmonically oscillating drop may be observed, refer to the discussion of Fig. 21.

6. Concluding remarks

In this paper, we have developed and validated a conservative interface-interaction method for viscous flows with surface tension and insoluble surfactant based on an interface-interaction method of Hu et al. [34]. We employ a level-set sharp-interface formulation to include inviscid, viscous, capillary and Marangoni stresses at the interface. Surfactant mass conservation is reproduced even for low resolution and severe interface deformation. Embedding the surfactant-conservation correction algorithm, originally formulated within a diffuse interface framework, into the sharp-interface framework further improves efficiency. Overall we observe a speed-up by a factor of about 2 to 3 compared to a typical diffuse-interface model implemented into the same background code. Moreover, we observe error-decay rates for surfactant concentration with grid refinement of about 1st to 2nd-order. The simulation results of a thermocapillary flow [62] and drops ascending due to a surfactant gradient [64] are in excellent agreement with analytical and experimental data. A single, two-dimensional drop in a shear flow is an application demonstration. Our observations are in agreement with previous numerical and experimental studies. These verification and validation studies demonstrate the robustness and accuracy of the conservative interface-interaction model for Marangoni and shear flows.

7. Appendix

7.1. Constructing sub-cell corrected of the interface curvature

Let the radius of the osculating circle at a point on the interface be r. Its curvature, the reciprocal of its radius, $k(r) = \frac{1}{r}$, equals the principal curvature of the local interface segment. In two-dimensional space the mean curvature is $\kappa_M(r) = k(r)$. By Taylor-series expansion of κ_M, one obtains a first-order accurate approximation to the interface curvature

$$\kappa_\Upsilon = \kappa_M(r) + \frac{d\kappa_M(r)}{dr}\Delta r + \mathcal{O}^2 = \kappa_M(r) - \frac{1}{r^2}\Delta r + \mathcal{O}^2 = \kappa_M(r) - \kappa_M(r)^2\Delta r + \mathcal{O}^2 \,. \tag{63}$$

Considering that $\kappa_M(r)$ may also be negative, Eq. (63) is modified as

$$\kappa_{\Upsilon,2d} = \kappa_M(r+\Delta r) \approx \left(|\kappa_M(r)| - \kappa_M(r)^2 \Delta r \right) S(\kappa_M(r)) \,. \tag{64}$$

In 3D the local mean curvature relates to the radii of the maximal and minimal osculating circles as

$$\kappa_M = \frac{1}{2}(k_1 + k_2) = \frac{1}{2}\left(\frac{1}{r_1} + \frac{1}{r_2} \right). \tag{65}$$

Assuming an osculating sphere of $k_1 = k_2 = k$, Eq. (65) becomes $\kappa_M(r) = k = \frac{1}{r}$, and it can readily be seen that $\kappa_{\Upsilon,3d} = \kappa_{\Upsilon,2d}$. Note that $\phi_{i,j,k} < 0$ corresponds to $\Delta r > 0$ and vice versa. Generally, the local mean curvature $\kappa(\mathbf{x}, t)$ of the interface is obtained from the local level-set according to

$$\begin{aligned} \kappa_{M,2D}(\phi) &= \frac{|\nabla\phi|^2 \, tr\left(H_\phi\right) - (\nabla\phi)^T \cdot H_\phi \cdot (\nabla\phi)}{|\nabla\phi|^3} = \\ &= \frac{\frac{\partial\phi}{\partial x_1}^2 \frac{\partial^2\phi}{\partial x_2^2} + \frac{\partial\phi}{\partial x_2}^2 \frac{\partial^2\phi}{\partial x_1^2} - 2\frac{\partial\phi}{\partial x_1}\frac{\partial\phi}{\partial x_2}\frac{\partial^2\phi}{\partial x_1 \partial x_2}}{\left(\frac{\partial\phi}{\partial x_1}^2 + \frac{\partial\phi}{\partial x_2}^2 \right)^{3/2}} \end{aligned} \tag{66}$$

in 2D and with

$$\begin{aligned} \kappa_{M,3D}(\phi) &= \frac{|\nabla\phi|^2 \, tr\left(H_\phi\right) - (\nabla\phi)^T \cdot H_\phi \cdot (\nabla\phi)}{2\,|\nabla\phi|^3} = \\ &= \frac{\frac{\partial\phi}{\partial x_1}^2 \left(\frac{\partial^2\phi}{\partial x_2^2} + \frac{\partial^2\phi}{\partial x_3^2} \right) + \frac{\partial\phi}{\partial x_2}^2 \left(\frac{\partial^2\phi}{\partial x_1^2} + \frac{\partial^2\phi}{\partial x_3^2} \right) + \frac{\partial\phi}{\partial x_3}^2 \left(\frac{\partial^2\phi}{\partial x_1^2} + \frac{\partial^2\phi}{\partial x_2^2} \right)}{2\left(\frac{\partial\phi}{\partial x_1}^2 + \frac{\partial\phi}{\partial x_2}^2 + \frac{\partial\phi}{\partial x_3}^2 \right)^{3/2}} - \\ &- \frac{2\left(\frac{\partial\phi}{\partial x_1}\frac{\partial\phi}{\partial x_2}\frac{\partial^2\phi}{\partial x_1 \partial x_2} + \frac{\partial\phi}{\partial x_1}\frac{\partial\phi}{\partial x_3}\frac{\partial^2\phi}{\partial x_1 \partial x_3} + \frac{\partial\phi}{\partial x_2}\frac{\partial\phi}{\partial x_3}\frac{\partial^2\phi}{\partial x_1 \partial x_2} \right)}{2\left(\frac{\partial\phi}{\partial x_1}^2 + \frac{\partial\phi}{\partial x_2}^2 + \frac{\partial\phi}{\partial x_3}^2 \right)^{3/2}} \,, \end{aligned} \tag{67}$$

in 3D, where $tr\left(H_\phi\right)$ denotes the trace of the Hessian of ϕ.

7.2. Details of the algorithm on extending surfactant off the interface

Within the sharp-interface framework [34], full cells are not cut by the interface. They are determined once per time step for advancing the fluid phases, hence, it is unnecessary to compute these separately within the off-interface extension algorithm, which, in contrast to using a smoothed sign function as e.g. in [31,70], reduces computational costs. The numerical approximation of the off-interface extension equation $\frac{\partial\gamma}{\partial\tau} + \mathbf{n}_I^{\zeta_i,T} \cdot \nabla\gamma = 0$, $\gamma(\mathbf{x}, \tau = 0) = \gamma_0(\mathbf{x})$ is

$$\gamma_{[i,j,k]}^{m+1} = \gamma_{[i,j,k]}^{m} - \Delta\tau \left[\sum_{\beta=1}^{3} \overline{F}_{x_\beta}[\gamma]_{[i,j,k]}^{m} \right] , \tag{68}$$

where $\overline{F}_{x_\beta}[\gamma]_{[i,j,k]}^{m} = \{ n_{I,\beta}^{i} D_\beta[\gamma] \}_{[i,j,k]}$, with $\beta = 1, 2, 3$. $\Delta\tau = 0.5\Delta x$ is the pseudo-time step size. The differential operator is

$$D_\beta[\gamma] = \begin{cases} D_\beta^-[\gamma]_{[i,j,k]} & \text{if } n_{I,\beta,[i,j,k]}^{\zeta_i} > 0 \\ D_\beta^+[\gamma]_{[i,j,k]} & \text{if } n_{I,\beta,[i,j,k]}^{\zeta_i} < 0 \\ 0 & \text{if } n_{I,\beta,[i,j,k]}^{\zeta_i} = 0 \end{cases} \tag{69}$$

D^- and D^+ are approximated with 1st-order biased differences. Twenty pseudo-time iterations guarantee $\nabla_n\gamma = 0$ in proximity to the interface.

7.3. Discrete surfactant concentration transport equation

Within a narrow band around the interface, $\gamma_{[i,j,k]}$ is advanced in time by

$$\gamma^{n+1}_{[i,j,k]} = \gamma^{n}_{[i,j,k]} + \Delta t \overline{\mathbf{L}}[\gamma]_{[i,j,k]} \,, \tag{70}$$

where

$$\overline{\mathbf{L}}[\gamma]_{[i,j,k]} = \overline{\mathbf{L}}[\gamma]^{adv}_{[i,j,k]} + \overline{\mathbf{L}}[\gamma]^{diff}_{[i,j,k]} + \overline{\mathbf{L}}[\gamma]^{evol}_{[i,j,k]} \tag{71}$$

denotes the numerical flux. The evolution of surfactant due to advection with the interface velocity $\mathbf{u}_I$ is accounted for by

$$\overline{\mathbf{L}}[\gamma]^{adv}_{[i,j,k]} = -\left(\sum_{\beta=1}^{3} F_{x_\beta}[\gamma]_{[i,j,k]} + \gamma \left[D^c[u_{I\alpha}]_\beta \right]_{[i,j,k]} \right) \,, \tag{72}$$

where

$$\overline{F}_{x_\beta}[\gamma]_{[i,j,k]} = \{ u_{I,\beta} D_\beta[\gamma] \}_{[i,j,k]} \,, \beta = 1,2,3 \tag{73}$$

with

$$D_\beta[\gamma] = \begin{cases} D^-_\beta[\gamma] & \text{if } u_{I,\beta} > 0 \,, \\ D^+_\beta[\gamma] & \text{if } u_{I,\beta} < 0 \,, \\ 0 & \text{if } u_{I,\beta} = 0 \,. \end{cases} \tag{74}$$

A 5th-order upwind WENO scheme [71] is employed for $D_\beta[\gamma]$. The surface diffusion flux is

$$\begin{aligned} &\overline{\mathbf{L}}[\gamma]^{diff}_{[i,j,k]} \frac{1}{Pe_s} \{ \nabla_s^2 \gamma \}_{[i,j,k]} = \\ &= \frac{1}{Pe_s} \{ \Delta\gamma(\mathbf{x}) - \left(\mathbf{n}_I^T \cdot \nabla\gamma(\mathbf{x}) \right) \left(\nabla^T \cdot \mathbf{n}_I \right) - \mathbf{n}_I^T \cdot H_\gamma \cdot \mathbf{n}_I \}_{[i,j,k]} = \\ &= \frac{1}{Pe_s} \left[\frac{\partial^2 \gamma}{\partial x_\alpha^2} - \left(n_{I,\alpha} \frac{\partial \gamma}{\partial x_\alpha} \right) \kappa - \left(n_{I,\alpha} \frac{\partial^2 \gamma}{\partial x_\alpha \, \partial x_\beta} n_{I,\beta} \right) \right]_{[i,j,k]} \approx \\ &\approx \frac{1}{Pe_s} \left[D^{2,c}[\gamma]_\alpha - \left(n_{I,\alpha} D^c[\gamma]_\alpha \right) \kappa - \left(n_{I,\alpha} \, D^c[D^c[\gamma]_\alpha]_\beta \, n_{I,\beta} \right) \right]_{[i,j,k]} . \end{aligned} \tag{75}$$

Herein, $\kappa = \frac{|\nabla\phi|^2 tr(H_\phi) - (\nabla\phi)^T \cdot H_\phi \cdot (\nabla\phi)}{|\nabla\phi|^3}$.

The deformation of the interface entails transport of $\gamma_{[i,j,k]}$ in the form of

$$\begin{aligned} \overline{\mathbf{L}}[\gamma]^{evol}_{[i,j,k]} &= \{ \gamma \left((\mathbf{n}_I \otimes \mathbf{n}_I) \cdot \nabla \right) \cdot \mathbf{u} \}_{[i,j,k]} = \\ &= \{ \gamma \left(\mathbf{n}_I^T \cdot (\nabla \mathbf{u}) \cdot \mathbf{n}_I \right) \}_{[i,j,k]} = \\ &= \{ \gamma \, n_{I,\alpha} \frac{\partial u_\alpha}{\partial x_\beta} n_{I,\beta} \}_{[i,j,k]} \approx \\ &\approx \{ \gamma \, n_{I,\alpha} D^c[u_\alpha]_\beta n_{I,\beta} \}_{[i,j,k]} \,, \end{aligned} \tag{76}$$

where $D^c[u_\alpha]_\beta$ denotes the central approximation to the local derivative of the component u_α in direction β, which are approximated by a 2nd-order central scheme.

7.4. The influence of the order of spatial differentiation

Surfactant may be transported due to interface evolution, advection and diffusion. The latter has been identified as the dominant source for discretization errors, see Sec. 4.1. The first and second derivatives in the numerical surfactant surface diffusion flux, i.e. Eq. (75), have been approximated with central finite differences of 2nd-order accuracy. We find that increasing the order of difference approximation decreases all three error norms, see Fig. 24. Moreover, except for the highest resolution, the convergence rates increase with the order of accuracy.

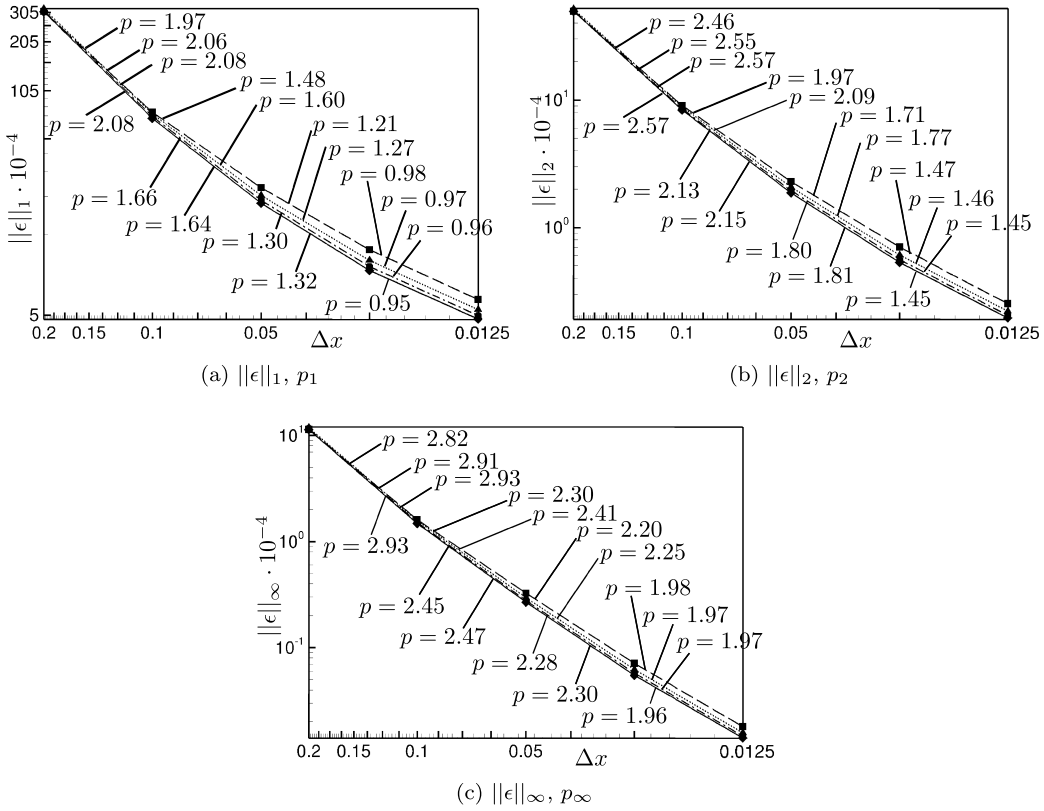

Fig. 24. Errors and convergence rates with grid refinement for diffusion of γ along Υ 2nd-order: (– – – – –), 4th-order: (- - - - - -), 6th-order: (– · – · – ·), 8th-order: (————), $Pe_s = 1$, $t = 2$.

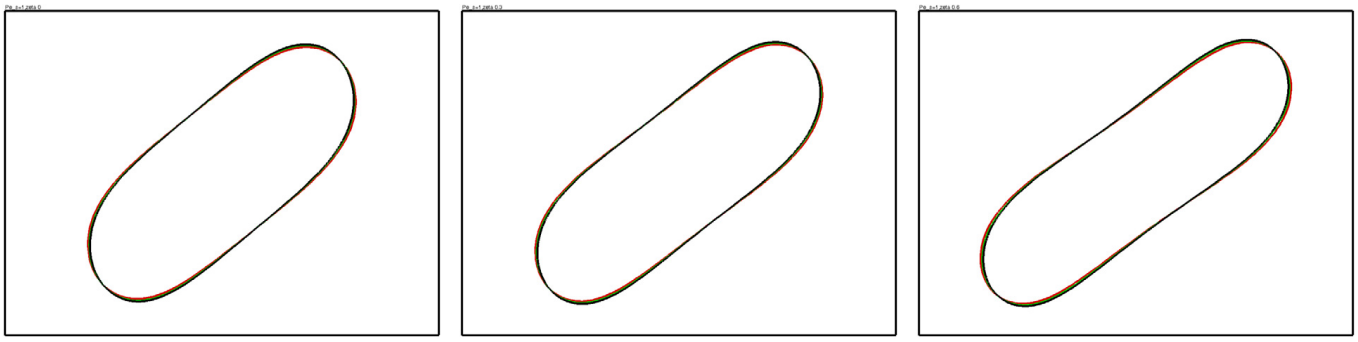

(a) $\zeta = 0$ (b) $\zeta = 0.3$ (c) $\zeta = 0.6$

Fig. 25. Interface at $t = 5$ for grids of $\Delta h = \Delta x_1 = \Delta x_2$ with $\Delta h_1 = 1/32$ (red line), $\Delta h_2 = 1/64$ (green line), $\Delta h_3 = 1/128$ (black line) and three different surfactant coverages. (For interpretation of the references to color in this figure legend, the reader is referred to the web version of this article.)

7.5. The influence of grid-refinement on the interface of a single drop in shear flow

The dependence of our results of the flow-problem of a single drop in shear flow is illustrated by visual inspection of the interface at three resolutions. We chose grids with $\Delta x_1 = \Delta x_2$, that are adaptively refined with a maximum resolution of $\Delta h_1 = 1/32$, $\Delta h_2 = 1/64$, $\Delta h_3 = 1/128$. Deformation is found to be most significant for $t \approx 5$, see e.g. 5.1. To account for the influence of surfactant, ζ is varied; $Pe_s = 1$, and a linear dependence of σ on ζ is chosen. Fig. 25 shows that for Δh_2 and Δh_3 the interfaces are almost perfectly identical, and results for Δh_1 differ only insignificantly. Furthermore, our results are independent of surfactant concentration.

We note that for other Pe_s, surfactant constitutive equations, as well as for other parameters discussed in section 5, grid refinement does not influence the results.

Acknowledgements

We acknowledge the Deutsche Forschungsgemeinschaft (DFG) for funding this work under Grant No. AD 186/7-2. Felix S. Schranner is a member of the TUM Graduate School. The Munich Centre of Advanced Computing (MAC) has provided the computational resources. V. Rozov and D. Azarnykh have contributed by invigorating discussions and proposing tests.

References

[1] J. Magnaudet, I. Eames, The motion of high-Reynolds-number bubbles in inhomogeneous flows, Annu. Rev. Fluid Mech. 32 (1) (2000) 659–708, http://dx.doi.org/10.1146/annurev.fluid.32.1.659.
[2] R. Clift, J. Grace, M.E. Weber, Bubbles, Drops, and Particles, Dover Publications, Inc., Mineola, New York, USA, 2005.
[3] S. Takagi, Y. Matsumoto, Surfactant effects on bubble motion and bubbly flows, Annu. Rev. Fluid Mech. 43 (1) (2011) 615–636, http://dx.doi.org/10.1146/annurev-fluid-122109-160756.
[4] R. Scardovelli, S. Zaleski, Direct numerical simulation of free-surface and interfacial flow, Annu. Rev. Fluid Mech. 31 (1999) 567–603.
[5] J. Sethian, P. Smereka, Level set methods for fluid interfaces, Annu. Rev. Fluid Mech. 35 (2003) 341–372.
[6] A. de Vries, A. Biesheuvel, L. van Wijngaarden, Notes on the path and wake of a gas bubble rising in pure water, Int. J. Multiph. Flow (ISSN 0301-9322) 28 (11) (2002) 1823–1835, http://dx.doi.org/10.1016/S0301-9322(02)00036-8, http://www.sciencedirect.com/science/article/pii/S0301932202000368.
[7] P.C. Duineveld, The rise velocity and shape of bubbles in pure water at high Reynolds number, J. Fluid Mech. (ISSN 1469-7645) 292 (1995) 325–332, http://dx.doi.org/10.1017/S0022112095001546.
[8] O.K. Matar, S.M. Troian, The development of transient fingering patterns during the spreading of surfactant coated films, Phys. Fluids (1994-present) 11 (11) (1999) 3232–3246.
[9] L.G. Leal, Flow induced coalescence of drops in a viscous fluid, Phys. Fluids (1994-present) 16 (6) (2004) 1833–1851.
[10] R.D. Bruijn, Tipstreaming of drops in simple shear flows, Chem. Eng. Sci. (ISSN 0009-2509) 48 (2) (1993) 277–284.
[11] R.B. Fdhila, P. Duineveld, The effect of surfactant on the rise of a spherical bubble at high Reynolds and Peclet numbers, Phys. Fluids 8 (2) (1996) 310–321.
[12] R. Defay, I. Priogine, Surface Tension and Adsorption, Wiley, New York, 1966.
[13] H.A. Stone, L.G. Leal, The effects of surfactants on drop deformation and breakup, J. Fluid Mech. (ISSN 1469-7645) 220 (1990) 161–186.
[14] X. Li, C. Pozrikidis, The effect of surfactants on drop deformation and on the rheology of dilute emulsions in Stokes flow, J. Fluid Mech. (ISSN 1469-7645) 341 (1997) 165–194.
[15] G. Tryggvason, B. Bunner, A. Esmaeeli, D. Juric, N. Al-Rawahi, W. Tauber, J. Han, S. Nas, Y.-J. Jan, A front-tracking method for the computations of multiphase flow, J. Comput. Phys. (ISSN 0021-9991) 169 (2) (2001) 708–759.
[16] Y.-J. Jan, Computational studies of bubble dynamics, Ph.D. thesis, University of Michigan, 1994.
[17] R. Mittal, G. Iaccarino, Immersed boundary methods, Annu. Rev. Fluid Mech. 37 (2005) 239–261.
[18] M.-C. Lai, Y.-H. Tseng, H. Huang, An immersed boundary method for interfacial flows with insoluble surfactant, J. Comput. Phys. (ISSN 0021-9991) 227 (15) (2008) 7279–7293.
[19] Y.-H. Tseng, J.H. Ferziger, A ghost-cell immersed boundary method for flow in complex geometry, J. Comput. Phys. (ISSN 0021-9991) 192 (2) (2003) 593–623.
[20] F. Jin, K.J. Stebe, The effects of a diffusion controlled surfactant on a viscous drop injected into a viscous medium, Phys. Fluids (1994-present) 19 (11) (2007) 112103.
[21] H.D. Ceniceros, The effects of surfactants on the formation and evolution of capillary waves, Phys. Fluids (1994-present) 15 (1) (2003) 245–256.
[22] Y.-C. Liao, E.I. Franses, O.A. Basaran, Deformation and breakup of a stretching liquid bridge covered with an insoluble surfactant monolayer, Phys. Fluids (1994-present) 18 (2) (2006) 022101.
[23] Q. Xu, Y.-C. Liao, O.A. Basaran, Can surfactant be present at pinch-off of a liquid filament?, Phys. Rev. Lett. 98 (2007) 054503.
[24] D. Adalsteinsson, J.A. Sethian, A fast level set method for propagating interfaces, J. Comput. Phys. (ISSN 0021-9991) 118 (2) (1995) 269–277.
[25] A.J. James, J. Lowengrub, A surfactant-conserving volume-of-fluid method for interfacial flows with insoluble surfactant, J. Comput. Phys. (ISSN 0021-9991) 201 (2) (2004) 685–722.
[26] M. Hameed, M. Siegel, Y.-N. Young, J. Li, M.R. Booty, D.T. Papageorgiou, Influence of insoluble surfactant on the deformation and breakup of a bubble or thread in a viscous fluid, J. Fluid Mech. (ISSN 1469-7645) 594 (2008) 307–340.
[27] D. Anderson, G.B. McFadden, A. Wheeler, Diffuse-interface methods in fluid mechanics, Annu. Rev. Fluid Mech. 30 (1) (1998) 139–165.
[28] K.E. Teigen, P. Song, J. Lowengrub, A. Voigt, A diffuse-interface method for two-phase flows with soluble surfactants, J. Comput. Phys. (ISSN 0021-9991) 230 (2) (2011) 375–393, http://dx.doi.org/10.1016/j.jcp.2010.09.020, http://www.sciencedirect.com/science/article/pii/S0021999110005231.
[29] S. Osher, J.A. Sethian, Fronts propagating with curvature-dependent speed: algorithms based on Hamilton–Jacobi formulations, J. Comput. Phys. (ISSN 0021-9991) 79 (1) (1988) 12–49.
[30] D. Adalsteinsson, J. Sethian, Transport and diffusion of material quantities on propagating interfaces via level set methods, J. Comput. Phys. (ISSN 0021-9991) 185 (1) (2003) 271–288.
[31] J.-J. Xu, H.-K. Zhao, An Eulerian formulation for solving partial differential equations along a moving interface, J. Sci. Comput. (ISSN 0885-7474) 19 (1–3) (2003) 573–594.
[32] R.J. LeVeque, Z. Li, The immersed interface method for elliptic equations with discontinuous coefficients and singular sources, SIAM J. Numer. Anal. 31 (4) (1993) 1019–1044.
[33] J.-J. Xu, Z. Li, J. Lowengrub, H. Zhao, A level-set method for interfacial flows with surfactant, J. Comput. Phys. (ISSN 0021-9991) 212 (2) (2006) 590–616.
[34] X. Hu, B. Khoo, N.A. Adams, F. Huang, A conservative interface method for compressible flows, J. Comput. Phys. 219 (2) (2006) 553–578.
[35] L. Han, X. Hu, N. Adams, Adaptive multi-resolution method for compressible multi-phase flows with sharp interface model and pyramid data structure, J. Comput. Phys. (ISSN 0021-9991) 262 (2014) 131–152.
[36] E. Lauer, X.Y. Hu, S. Hickel, N.A. Adams, Numerical investigation of collapsing cavity arrays, Physics of Fluids 24 (5) (2012) 052104.
[37] J. Luo, X. Hu, N. Adams, A conservative sharp interface method for incompressible multiphase flows, J. Comput. Phys. (ISSN 0021-9991) 284 (2015) 547–565.
[38] F.S. Schranner, X. Hu, N.A. Adams, A physically consistent weakly compressible high-resolution approach to underresolved simulations of incompressible flows, Comput. Fluids 86 (2013) 109–124.
[39] F.S. Schranner, X. Hu, N.A. Adams, On the convergence of the weakly compressible sharp-interface method for two-phase flows, J. Comput. Phys. 324 (2016) 94–114.
[40] R.L. Panton, Incompressible Flows, 3rd edn., John Wiley & Sons, Inc., 2005.

[41] L. Foucard, X. Espinet, E. Benet, F.J. Vernerey, The Role of the Cortical Membrane in Cell Mechanics: Model and Simulation, John Wiley & Sons Ltd, ISBN 9781118402955, 2013, pp. 241–265.
[42] G. Miller, P. Colella, A conservative three-dimensional Eulerian method for coupled solid–fluid shock capturing, J. Comput. Phys. 183 (1) (2002) 26–82.
[43] Y. Pawar, K.J. Stebe, Marangoni effects on drop deformation in an extensional flow: the role of surfactant physical chemistry. I. Insoluble surfactants, Phys. Fluids (1994-present) 8 (7) (1996) 1738–1751.
[44] S. Schwarz, J. Fröhlich, Numerical study of single bubble motion in liquid metal exposed to a longitudinal magnetic field, Int. J. Multiph. Flow (ISSN 0301-9322) 62 (2014) 134–151, http://dx.doi.org/10.1016/j.ijmultiphaseflow.2014.02.012, http://www.sciencedirect.com/science/article/pii/S0301932214000470.
[45] J.R. Frisvad, Building an orthonormal basis from a 3D unit vector without normalization, J. Graph. Tools 16 (3) (2012) 151–159.
[46] R.A. Berry, R. Saurel, F. Petitpas, E. Daniel, O.L. Metayer, S. Gavrilyuk, N. Dovetta, Progress in the development of compressible, multiphase flow modeling capability for nuclear reactor flow applications, INIS 40 (13) (2008).
[47] G.L. Leal, Laminar Flow and Convective Transport Processes, Butterworth–Heinemann Series in Chemical Engineering, 1992.
[48] W.M. Deen, Analysis of Transport Phenomena, Oxford University Press, 1998.
[49] D.Q. Shaofan Li (Ed.), Multiscale Simulations and Mechanics of Biological Materials, Wiley, 2013.
[50] R. Saurel, S. Gavrilyuk, F. Renaud, A multiphase model with internal degrees of freedom: application to shock–bubble interaction, J. Fluid Mech. 495 (2003) 283–321.
[51] J.F. Hughes, T. Moller, Building an orthonormal basis from a unit vector, J. Graph. Tools 4 (4) (1999) 33–35, http://dx.doi.org/10.1080/10867651.1999.10487513.
[52] F.S. Schranner, V. Rozov, N.A. Adams, Optimization of an implicit large-eddy simulation method for underresolved incompressible flow simulations, AIAA J. 54 (5) (2016) 1567–1577, http://dx.doi.org/10.2514/1.J054741.
[53] S. Osher, R.P. Fedkiw, Level set methods: an overview and some recent results, J. Comput. Phys. (ISSN 0021-9991) 169 (2) (2001) 463–502.
[54] M. Sussman, P. Smereka, S. Osher, A level set approach for computing solutions to incompressible two-phase flow, J. Comput. Phys. (ISSN 0021-9991) 114 (1) (1994) 146–159.
[55] R.P. Fedkiw, T. Aslam, B. Merriman, S. Osher, A non-oscillatory Eulerian approach to interfaces in multimaterial flows (the ghost fluid method), J. Comput. Phys. (ISSN 0021-9991) 152 (2) (1999) 457–492.
[56] S. Gottlieb, C.-W. Shu, Total variation diminishing Runge–Kutta schemes, Math. Comput. 67 (221) (1998) 73–85, http://dx.doi.org/10.1090/S0025-5718(98)00913-2.
[57] M. Sussman, E.G. Puckett, A coupled level set and volume-of-fluid method for computing 3D and axisymmetric incompressible two-phase flows, J. Comput. Phys. (ISSN 0021-9991) 162 (2) (2000) 301–337.
[58] J. Brackbill, D. Kothe, C. Zemach, A continuum method for modeling surface tension, J. Comput. Phys. (ISSN 0021-9991) 100 (2) (1992) 335–354.
[59] E. Lauer, X.Y. Hu, S. Hickel, N.A. Adams, Numerical modelling and investigation of symmetric and asymmetric cavitation bubble dynamics, Comput. Fluids (ISSN 0045-7930) 69 (0) (2012) 1–19.
[60] A.-K. Tornberg, B. Engquist, Numerical approximations of singular source terms in differential equations, J. Comput. Phys. (ISSN 0021-9991) 200 (2) (2004) 462–488.
[61] S. Khatri, A.-K. Tornberg, An embedded boundary method for soluble surfactants with interface tracking for two-phase flows, J. Comput. Phys. (ISSN 0021-9991) 256 (2014) 768–790.
[62] B. Pendse, A. Esmaeeli, An analytical solution for thermocapillary-driven convection of superimposed fluids at zero Reynolds and Marangoni numbers, Int. J. Therm. Sci. (ISSN 1290-0729) 49 (7) (2010) 1147–1155, http://dx.doi.org/10.1016/j.ijthermalsci.2010.02.003, http://www.sciencedirect.com/science/article/pii/S1290072910000542.
[63] H. Liu, Y. Zhang, A.J. Valocchi, Modeling and simulation of thermocapillary flows using lattice Boltzmann method, J. Comput. Phys. (ISSN 0021-9991) 231 (12) (2012) 4433–4453, http://dx.doi.org/10.1016/j.jcp.2012.02.015, http://www.sciencedirect.com/science/article/pii/S0021999112000940.
[64] N.O. Young, J.S. Goldstein, M.J. Block, The motion of bubbles in a vertical temperature gradient, J. Fluid Mech. (ISSN 1469-7645) 6 (1959) 350–356.
[65] M. Herrmann, J. Lopez, P. Brady, M. Raessi, Thermocapillary motion of deformable drops and bubbles, in: Center for Turbulence Research Proceedings of the Summer Program, 2008, pp. 155–170.
[66] G.I. Taylor, The formation of emulsions in definable fields of flow, in: Proceedings of the Royal Society of London, 1934.
[67] W.J. Milliken, H.A. Stone, L.G. Leal, The effect of surfactant on the transient motion of Newtonian drops, Phys. Fluids A: Fluid Dyn. (1989–1993) 5 (1) (1993) 69–79.
[68] P. Smith, T. van de Ven, Shear-induced deformation and rupture of suspended solid/liquid clusters, Colloids Surf. (ISSN 0166-6622) 15 (1985) 191–210.
[69] J. Lee, C. Pozrikidis, Effect of surfactants on the deformation of drops and bubbles in Navier–Stokes flow, Comput. Fluids (ISSN 0045-7930) 35 (1) (2006) 43–60.
[70] J.-J. Xu, Y. Yang, J. Lowengrub, A level-set continuum method for two-phase flows with insoluble surfactant, J. Comput. Phys. (ISSN 0021-9991) 231 (17) (2012) 5897–5909.
[71] G. Jiang, C.-W. Shu, Efficient implementation of weighted ENO schemes, J. Comput. Phys. 126 (1996) 202–228.

C Copyright Permissions for Adopted and Reproduced Material

AIP PUBLISHING LLC LICENSE TERMS AND CONDITIONS

Oct 12, 2016

This Agreement between Felix S Schranner ("You") and AIP Publishing LLC ("AIP Publishing LLC") consists of your license details and the terms and conditions provided by AIP Publishing LLC and Copyright Clearance Center.

License Number	3898110697197
License date	Jun 29, 2016
Licensed Content Publisher	AIP Publishing LLC
Licensed Content Publication	Physics of Fluids
Licensed Content Title	Numerical investigation of rising bubble wake and shape variations
Licensed Content Author	Daniel Gaudlitz,Nikolaus A. Adams
Licensed Content Date	Dec 3, 2009
Licensed Content Volume Number	21
Licensed Content Issue Number	12
Type of Use	Thesis/Dissertation
Requestor type	Student
Format	Print and electronic
Portion	Figure/Table
Number of figures/tables	2
Title of your thesis / dissertation	Weakly Compressible Models for Complex Flows
Expected completion date	Nov 2016
Estimated size (number of pages)	212
Requestor Location	Felix S Schranner Boltzmannstrasse 15 Garching, 85748 Germany Attn: Felix S Schranner
Billing Type	Invoice
Billing Address	Felix S Schranner Boltzmannstrasse 15 Garching, Germany 85748 Attn: Felix S Schranner
Total	**0.00 EUR**
Terms and Conditions	

AIP Publishing LLC -- Terms and Conditions: Permissions Uses

AIP Publishing hereby grants to you the non-exclusive right and license to use and/or distribute the Material according to the use specified in your order, on a one-time basis, for the specified term, with a maximum distribution equal to the number that you have ordered. Any links or other content accompanying the Material are not the subject of this license.

1. You agree to include the following copyright and permission notice with the reproduction of the Material:"Reprinted from [FULL CITATION], with the permission of AIP Publishing." For an article, the credit line and permission notice must be printed on the first page of the article or book chapter. For photographs, covers, or tables, the notice may appear with the Material, in a footnote, or in the reference list.
2. If you have licensed reuse of a figure, photograph, cover, or table, it is your responsibility to ensure that the material is original to AIP Publishing and does not contain the copyright of another entity, and that the copyright notice of the figure, photograph, cover, or table does not indicate that it was reprinted by AIP Publishing, with permission, from another source. Under no circumstances does AIP Publishing purport or intend to grant permission to reuse material to which it does not hold appropriate rights.
   You may not alter or modify the Material in any manner. You may translate the Material into another language only if you have licensed translation rights. You may not use the Material for promotional purposes.
3. The foregoing license shall not take effect unless and until AIP Publishing or its agent, Copyright Clearance Center, receives the Payment in accordance with Copyright Clearance Center Billing and Payment Terms and Conditions, which are incorporated herein by reference.
4. AIP Publishing or Copyright Clearance Center may, within two business days of granting this license, revoke the license for any reason whatsoever, with a full refund payable to you. Should you violate the terms of this license at any time, AIP Publishing, or Copyright Clearance Center may revoke the license with no refund to you. Notice of such revocation will be made using the contact information provided by you. Failure to receive such notice will not nullify the revocation.
5. AIP Publishing makes no representations or warranties with respect to the Material. You agree to indemnify and hold harmless AIP Publishing, and their officers, directors, employees or agents from and against any and all claims arising out of your use of the Material other than as specifically authorized herein.
6. The permission granted herein is personal to you and is not transferable or assignable without the prior written permission of AIP Publishing. This license may not be amended except in a writing signed by the party to be charged.
7. If purchase orders, acknowledgments or check endorsements are issued on any forms containing terms and conditions which are inconsistent with these provisions, such inconsistent terms and conditions shall be of no force and effect. This document, including the CCC Billing and Payment Terms and Conditions, shall be the entire agreement between the parties relating to the subject matter hereof.

This Agreement shall be governed by and construed in accordance with the laws of the State of New York. Both parties hereby submit to the jurisdiction of the courts of New York County for purposes of resolving any disputes that may arise hereunder.

V1.1

Questions? customercare@copyright.com or +1-855-239-3415 (toll free in the US) or +1-978-646-2777.

AIP PUBLISHING LLC LICENSE TERMS AND CONDITIONS

Oct 12, 2016

This Agreement between Felix S Schranner ("You") and AIP Publishing LLC ("AIP Publishing LLC") consists of your license details and the terms and conditions provided by AIP Publishing LLC and Copyright Clearance Center.

License Number	3898101351664
License date	Jun 29, 2016
Licensed Content Publisher	AIP Publishing LLC
Licensed Content Publication	Physics of Fluids
Licensed Content Title	Bubbles
Licensed Content Author	Andrea Prosperetti
Licensed Content Date	Apr 28, 2004
Licensed Content Volume Number	16
Licensed Content Issue Number	6
Type of Use	Thesis/Dissertation
Requestor type	Student
Format	Print and electronic
Portion	Photograph/Image
Title of your thesis / dissertation	Weakly Compressible Models for Complex Flows
Expected completion date	Nov 2016
Estimated size (number of pages)	212
Requestor Location	Felix S Schranner Boltzmannstrasse 15 Garching, 85748 Germany Attn: Felix S Schranner
Billing Type	Invoice
Billing Address	Felix S Schranner Boltzmannstrasse 15 Garching, Germany 85748 Attn: Felix S Schranner
Total	**0.00 EUR**

Terms and Conditions

AIP Publishing LLC -- Terms and Conditions: Permissions Uses

AIP Publishing hereby grants to you the non-exclusive right and license to use and/or distribute the Material

according to the use specified in your order, on a one-time basis, for the specified term, with a maximum distribution equal to the number that you have ordered. Any links or other content accompanying the Material are not the subject of this license.

1. You agree to include the following copyright and permission notice with the reproduction of the Material:"Reprinted from [FULL CITATION], with the permission of AIP Publishing." For an article, the credit line and permission notice must be printed on the first page of the article or book chapter. For photographs, covers, or tables, the notice may appear with the Material, in a footnote, or in the reference list.
2. If you have licensed reuse of a figure, photograph, cover, or table, it is your responsibility to ensure that the material is original to AIP Publishing and does not contain the copyright of another entity, and that the copyright notice of the figure, photograph, cover, or table does not indicate that it was reprinted by AIP Publishing, with permission, from another source. Under no circumstances does AIP Publishing purport or intend to grant permission to reuse material to which it does not hold appropriate rights.
   You may not alter or modify the Material in any manner. You may translate the Material into another language only if you have licensed translation rights. You may not use the Material for promotional purposes.
3. The foregoing license shall not take effect unless and until AIP Publishing or its agent, Copyright Clearance Center, receives the Payment in accordance with Copyright Clearance Center Billing and Payment Terms and Conditions, which are incorporated herein by reference.
4. AIP Publishing or Copyright Clearance Center may, within two business days of granting this license, revoke the license for any reason whatsoever, with a full refund payable to you. Should you violate the terms of this license at any time, AIP Publishing, or Copyright Clearance Center may revoke the license with no refund to you. Notice of such revocation will be made using the contact information provided by you. Failure to receive such notice will not nullify the revocation.
5. AIP Publishing makes no representations or warranties with respect to the Material. You agree to indemnify and hold harmless AIP Publishing, and their officers, directors, employees or agents from and against any and all claims arising out of your use of the Material other than as specifically authorized herein.
6. The permission granted herein is personal to you and is not transferable or assignable without the prior written permission of AIP Publishing. This license may not be amended except in a writing signed by the party to be charged.
7. If purchase orders, acknowledgments or check endorsements are issued on any forms containing terms and conditions which are inconsistent with these provisions, such inconsistent terms and conditions shall be of no force and effect. This document, including the CCC Billing and Payment Terms and Conditions, shall be the entire agreement between the parties relating to the subject matter hereof.

This Agreement shall be governed by and construed in accordance with the laws of the State of New York. Both parties hereby submit to the jurisdiction of the courts of New York County for purposes of resolving any disputes that may arise hereunder.

V1.1

Questions? customercare@copyright.com or +1-855-239-3415 (toll free in the US) or +1-978-646-2777.

Bibliography

[1] D. Gaudlitz, N. A. Adams, Numerical investigation of rising bubble wake and shape variations, Physics of Fluids 21 (12) 122102.

[2] R. Rzehak, E. Krepper, Bubble-induced turbulence: Comparison of CFD models, Nuclear Engineering and Design 258 (2013) 57 – 65, ISSN 0029-5493.

[3] A. Prosperetti, Bubbles, Physics of Fluids 16 (6) (2004) 1852–1865.

[4] L. da Vinci, C. Pedretti, The Codex Hammer of Leonardo da Vinci, Giunti Barbra, 1987.

[5] L. da Vinci, The Notebooks of Leonardo da Vinci, Konecky & Konecky, 1 edn., 1938.

[6] "L'aria che si sommerse insieme coll'acqua che sopra l'altr'acqua percosse, ritorna alla aria penetrando l'acqua in moto flessuoso, variando il suo corpo in moltissime forme. E questo accade, perché il lieve non po' stare sotto il grieve, anzi al continuo è premuto dalla parte del liquido che sopra se li posa..." by Leonardo da Vinci, in: E. MacCurdy (Ed.), The Notebooks of Leonardo da Vinci, vol. 1, Konecky & Konecky, 112, 1938.

[7] R. Hartunian, W. Sears, On the instability of small gas bubbles moving uniformly in various liquids, Journal of Fluid Mechanics 3 (1957) 27–47, ISSN 1469-7645.

[8] P. Saffman, On the Rise of Small Air Bubbles in Water, Journal of Fluid Mechanics 1 (3) (1956) 249 – 275.

[9] K. Ellingsen, F. Risso, On the rise of an ellipsoidal bubble in water: oscillatory paths and liquid-induced velocity, Journal of Fluid Mechanics 440 (2001) 235–268.

[10] M. Wu, M. Gharib, Experimental studies on the shape and path of small air bubbles rising in clean water, Physics of Fluids 14 (7) (2002) L49–L52.

[11] W. Shew, S. Poncet, J.-F. Pinton, Force measurements on rising bubbles, Journal of Fluid Mechanics 569 (2006) 51–60.

[12] M. A. R. Talaia, Terminal Velocity of a Bubble Rise in a Liquid Column, in: World Academy of Science, Engineering and Technology, vol. 22, 2007.

[13] O. Miyagi, The motion of an air bubble rising in water, Philosophical Magazine Series 6 50 (295) (1925) 112–140.

[14] M. P. O'Brien, J. E. Gosline, Velocity of Large Bubbles in Vertical Tubes, Industrial & Engineering Chemistry 27 (12) (1935) 1436–1440.

[15] R. M. Davies, G. Taylor, The Mechanics of Large Bubbles Rising through Extended Liquids and through Liquids in Tubes, Proceedings of the Royal Society of London. Series A, Mathematical and Physical Sciences 200 (1062) (1950) 375–390, ISSN 00804630.

[16] W. L. Haberman, R. K. Morton, An experimental investigation of the drag and shape of air bubbles rising in various liquids, David W. Taylor Model Basin, Washington, D.C., 1953.

[17] P. C. Duineveld, The rise velocity and shape of bubbles in pure water at high Reynolds number, Journal of Fluid Mechanics 292 (1995) 325–332, ISSN 1469-7645.

[18] N. M. Aybers, A. Tapucu, The motion of gas bubbles rising through stagnant liquid, Wärme - und Stoffübertragung 2 (2) (1969) 118–128, ISSN 1432-1181.

[19] N. O. Young, J. S. Goldstein, M. J. Block, The motion of bubbles in a vertical temperature gradient, Journal of Fluid Mechanics 6 (1959) 350–356, ISSN 1469-7645.

[20] D. Legendre, R. Zenit, J. R. Velez-Cordero, On the deformation of gas bubbles in liquids, Physics of Fluids 24 (4) 043303.

[21] V. Tesa, Shape oscillation of microbubbles, Chemical Engineering Journal 235 (2014) 368 – 378, ISSN 1385-8947.

[22] D. Bhaga, M. E. Weber, Bubbles in viscous liquids: shapes, wakes and velocities, Journal of Fluid Mechanics 105 (1981) 61–85, ISSN 1469-7645.

[23] C. Brücker, Structure and dynamics of the wake of bubbles and its relevance for bubble interaction, Physics of Fluids 11 (7) (1999) 1781–1796.

[24] A. de Vries, A. Biesheuvel, L. van Wijngaarden, Notes on the path and wake of a gas bubble rising in pure water, International Journal of Multiphase Flow 28 (11) (2002) 1823 – 1835, ISSN 0301-9322.

[25] K. Lunde, R. J. Perkins, Shape Oscillations of Rising Bubbles, in: A. Biesheuvel, G. F. van Heijst (Eds.), Fascination of Fluid Dynamics, Springer-Science+Business Media, B.V., 387–408, 1998.

[26] C. Veldhuis, A. Biesheuvel, L. van Wijngaarden, Shape oscillations on bubbles rising in clean and in tap water, Physics of Fluids 20 (4) 040705.

[27] J. R. Landel, C. Cossu, C. P. Caulfield, Spherical cap bubbles with a toroidal bubbly wake, Physics of Fluids 20 (12) 122101.

[28] J. Magnaudet, I. Eames, The Motion of High-Reynolds-Number Bubbles in Inhomogeneous Flows, Annual Review of Fluid Mechanics 32 (1) (2000) 659–708.

[29] R. Clift, J. Grace, M. E. Weber, Bubbles, Drops, and Particles, Dover Publications, Inc., Mineola, New York, USA, 2005.

[30] D. Gaudlitz, Numerische Untersuchung des Aufstiegsverhaltens von Gasblasen in Flüssigkeiten, Ph.D. thesis, Technische Universität München, 2009.

[31] J. B. W. Kok, Dynamics of gas bubbles moving through liquid, Ph.D. thesis, Universiteit Twente, Enschede (Netherlands)., 1989.

[32] R. B. Fdhila, P. Duineveld, The effect of surfactant on the rise of a spherical bubble at high Reynolds and Peclet numbers, Physics of Fluids 8 (2) (1996) 310–321.

[33] C. Bachhuber, C. Sanford, The rise of small bubbles in water, Journal of Applied Physics 45 (6) (1974) 2567–2569.

[34] W. Martin, G. Chandler, The local measurement of the size and velocity of bubbles rising in liquids, Applied Scientific Research 38 (1) (1982) 239–246, ISSN 1573-1987.

[35] A. Brankovic, I. Currie, W. Martin, Laser-Doppler measurements of bubble dynamics, Physics of Fluids 27 (2) (1984) 348–355.

[36] F. Durst, B. Schönung, K. Selanger, M. Winter, Bubble-driven liquid flows, Journal of Fluid Mechanics 170 (1986) 53–82, ISSN 1469-7645.

[37] R. Griffith, The effect of surfactants on the terminal velocity of drops and bubbles, Chemical Engineering Science 17 (12) (1962) 1057 – 1070, ISSN 0009-2509.

[38] C. Ybert, J.-M. di Meglio, Ascending air bubbles in protein solutions, The European Physical Journal B - Condensed Matter and Complex Systems 4 (3) (1998) 313–319, ISSN 1434-6036.

[39] N. Abi Chebel, J. Vejraka, O. Masbernat, F. Risso, Shape oscillations of an oil drop rising in water: effect of surface contamination, Journal of Fluid Mechanics 702 (2012) 533–542, ISSN 1469-7645.

[40] Y. Zhang, J. A. Finch, A note on single bubble motion in surfactant solutions, Journal of Fluid Mechanics 429 (2001) 63–66.

[41] E. Almatroushi, A. Borhan, Surfactant effect on the buoyancy-driven motion of bubbles and drops in a tube, Annals of the New York Academy of Sciences 1027 (2004) 330–341.

[42] T. Sanada, M. Shirota, M. Watanabe, Bubble wake visualization by using photochromic dye, Chemical Engineering Science 62 (24) (2007) 7264 – 7273, ISSN 0009-2509, 8th International Conference on Gas-Liquid and Gas-Liquid-Solid Reactor Engineering.

[43] C. Zhang, S. Eckert, G. Gerbeth, The flow structure of a bubble-driven liquid-metal jet in a horizontal magnetic field, Journal of Fluid Mechanics 575 (2007) 57–82, ISSN 1469-7645.

[44] C. Zhang, S. Eckert, G. Gerbeth, Experimental study of single bubble motion in a liquid metal column exposed to a DC magnetic field, International Journal of Multiphase Flow 31 (7) (2005) 824 – 842, ISSN 0301-9322.

[45] Y. Mori, K. Hijikata, I. Kuriyama, Experimental Study of Bubble Motion in Mercury With and Without a Magnetic Field, ASME 99 (3) (1977) 404–410.

[46] S. Eckert, G. Gerbeth, O. Lielausis, The behaviour of gas bubbles in a turbulent liquid metal magnetohydrodynamic flow: Part II: Magnetic field influence on the slip ratio, International Journal of Multiphase Flow 26 (1) (2000) 67 – 82, ISSN 0301-9322.

[47] S. Eckert, G. Gerbeth, O. Lielausis, The behaviour of gas bubbles in a turbulent liquid metal magnetohydrodynamic flow: Part I: Dispersion in quasi-two-dimensional magnetohydrodynamic turbulence, International Journal of Multiphase Flow 26 (1) (2000) 45 – 66, ISSN 0301-9322.

[48] D. S. Balsara, C.-W. Shu, Monotonicity Preserving Weighted Essentially Non-oscillatory Schemes with Increasingly High Order of Accuracy, Journal of Computational Physics 160 (2) (2000) 405 – 452, ISSN 0021-9991.

[49] S. Hickel, N. Adams, J. Domaradzki, An adaptive local deconvolution method for implicit LES, Journal of Computational Physics 213 (1) (2006) 413–436.

[50] F. S. Schranner, X. Hu, N. A. Adams, A physically consistent weakly compressible high-resolution approach to underresolved simulations of incompressible flows, Computers & Fluids 86 (2013) 109–124.

[51] D. C. Brabston, H. B. Keller, Viscous flows past spherical gas bubbles, Journal of Fluid Mechanics 69 (1975) 179–189, ISSN 1469-7645.

[52] M. Miksis, J.-M. Vanden-Broeck, J. B. Keller, Axisymmetric bubble or drop in a uniform flow, Journal of Fluid Mechanics 108 (1981) 89–100, ISSN 1469-7645.

[53] M. J. Miksis, A bubble in an axially symmetric shear flow, Physics of Fluids 24 (7) (1981) 1229–1231.

[54] M. J. Miksis, J.-M. Vanden-Broeck, J. B. Keller, Rising bubbles, Journal of Fluid Mechanics 123 (1982) 31–41, ISSN 1469-7645.

[55] T. S. Lundgren, N. N. Mansour, Vortex ring bubbles, Journal of Fluid Mechanics 224 (1991) 177–196, ISSN 1469-7645.

[56] G. Ryskin, L. G. Leal, Numerical solution of free-boundary problems in fluid mechanics. Part 1. The finite-difference technique, Journal of Fluid Mechanics 148 (1984) 1–17, ISSN 1469-7645.

[57] G. Ryskin, L. G. Leal, Numerical solution of free-boundary problems in fluid mechanics. Part 2. Buoyancy-driven motion of a gas bubble through a quiescent liquid, Journal of Fluid Mechanics 148 (1984) 19–35, ISSN 1469-7645.

[58] B. Yang, A. Prosperetti, S. Takagi, The transient rise of a bubble subject to shape or volume changes, Physics of Fluids 15 (9) (2003) 2640–2648.

[59] G. Mougin, J. Magnaudet, The generalized Kirchhoff equations and their application to the interaction between a rigid body and an arbitrary time-dependent viscous flow, International Journal of Multiphase Flow 28 (11) (2002) 1837 – 1851, ISSN 0301-9322.

[60] G. Mougin, J. Magnaudet, Path Instability of a Rising Bubble, Phys. Rev. Lett. 88 (2001) 014502.

[61] G. Mougin, J. Magnaudet, Wake-induced forces and torques on a zigzagging/spiralling bubble, Journal of Fluid Mechanics 567 (2006) 185–194, ISSN 1469-7645.

[62] T. Bonometti, J. Magnaudet, An interface-capturing method for incompressible two-phase flows. Validation and application to bubble dynamics, International Journal of Multiphase Flow 33 (2) (2007) 109 – 133, ISSN 0301-9322.

[63] S. Schwarz, J. Fröhlich, Numerical study of single bubble motion in liquid metal exposed to a longitudinal magnetic field, International Journal of Multiphase Flow 62 (2014) 134 – 151, ISSN 0301-9322.

[64] B. Lalanne, S. Tanguy, F. Risso, Effect of rising motion on the damped shape oscillations of drops and bubbles, Physics of Fluids 25 (11) 112107.

[65] J. Magnaudet, G. Mougin, Wake instability of a fixed spheroidal bubble, Journal of Fluid Mechanics 572 (2007) 311–337, ISSN 1469-7645.

[66] J. Tchoufag, J. Magnaudet, D. Fabre, Linear stability and sensitivity of the flow past a fixed oblate spheroidal bubble, Physics of Fluids 25 (5) 054108.

[67] J. Cano-Lozano, P. Bohorquez, C. Martnez-Bazn, Wake instability of a fixed axisymmetric bubble of realistic shape, International Journal of Multiphase Flow 51 (2013) 11 – 21, ISSN 0301-9322.

[68] M. K. Tripathi, K. C. Sahu, R. Govindarajan, Dynamics of an initially spherical bubble rising in quiescent liquid, Nature Communications 6.

[69] B. Cuenot, J. Magnaudet, B. Spennato, The effects of slightly soluble surfactants on the flow around a spherical bubble, Journal of Fluid Mechanics 339 (1997) 25–53, ISSN 1469-7645.

[70] S. Takagi, Y. Matsumoto, Surfactant Effects on Bubble Motion and Bubbly Flows, Annual Review of Fluid Mechanics 43 (1) (2011) 615–636.

[71] F. Takemura, A. Yabe, Rising speed and dissolution rate of a carbon dioxide bubble in slightly contaminated water, Journal of Fluid Mechanics 378 (1999) 319–334, ISSN 1469-7645.

[72] W. Dijkhuizen, I. Roghair, M. V. S. Annaland, J. Kuipers, DNS of gas bubbles behaviour using an improved 3D front tracking modelDrag force on isolated bubbles and comparison with experiments, Chemical Engineering Science 65 (4) (2010) 1415 – 1426, ISSN 0009-2509.

[73] S. Hysing, S. Turek, D. Kuzmin, N. Parolini, E. Burman, S. Ganesan, L. Tobiska, Quantitative benchmark computations of two-dimensional bubble dynamics, International Journal for Numerical Methods in Fluids 60 (11) (2009) 1259–1288, ISSN 1097-0363.

[74] A. Colagrossi, M. Landrini, Numerical simulation of interfacial flows by smoothed particle hydrodynamics, Journal of Computational Physics 191 (2) (2003) 448 – 475, ISSN 0021-9991.

[75] K. So, X. Hu, N. Adams, Anti-diffusion method for interface steepening in two-phase incompressible flow, Journal of Computational Physics 230 (13) (2011) 5155 – 5177, ISSN 0021-9991.

[76] K.Szewc, A. Tanire, J. Pozorski, J.-P. Minier, A Study on Application of Smoothed Particle Hydrodynamics to Multi-Phase Flows, International Journal of Nonlinear Sciences and Numerical Simulation 13 (6).

[77] N. Grenier, M. Antuono, A. Colagrossi, D. L. Touz, B. Alessandrini, An Hamiltonian interface SPH formulation for multi-fluid and free surface flows, Journal of Computational Physics 228 (22) (2009) 8380 – 8393, ISSN 0021-9991.

[78] E. F. Toro, Riemann Solvers and Numerical Methods for Fluid Dynamics, Springer-Verlag, 2nd edn., ISBN 3-540-65966-8, 1999.

[79] G. H. Miller, E. G. Puckett, A high-order Godunov method for multiple condensed phases, Journal of Computational Physics 128 (1) (1996) 134–164.

[80] A. J. Chorin, A Numerical Method for Solving Incompressible Viscous Flow Problems, Journal of Computational Physics 135 (1997) 118 – 125.

[81] R. Temam, Une méthode d'approximation des solutions des équations Navier-Stokes, Bull.Soc.Math 98 (1968) 115 – 152.

[82] F. S. Schranner, N. A. Adams, A conservative interface-interaction model with insoluble surfactant, Journal of Computational Physics 327 (2016) 653 – 677, ISSN 0021-9991.

[83] G. Miller, P. Colella, A conservative three-dimensional Eulerian method for coupled solid–fluid shock capturing, Journal of Computational Physics 183 (1) (2002) 26–82.

[84] R. L. Panton, Incrompressible Flows, John Wiley & Sons, Inc., 3 edn., 2005.

[85] J. F. Hughes, T. Moller, Building an Orthonormal Basis from a Unit Vector, Journal of Graphics Tools 4 (4) (1999) 33–35.

[86] R. A. Berry, R. Saurel, F. Petitpas, E. Daniel, O. L. Metayer, S. Gavrilyuk, N. Dovetta., Progress in the Development of Compressible, Multiphase Flow Modeling Capability for Nuclear Reactor Flow Applications, INIS 40 (13).

[87] G. L. Leal, Laminar Flow and Convective Transport Processes, Butterworth-Heinemann Series in Chemical Engineering, 1992.

[88] W. M. Deen, Analysis of Transport Phenomena, Oxford University Press, 1998.

[89] D. Q. Shaofan Li (Ed.), Multiscale Simulations and Mechanics of Biological Materials, Wiley, 2013.

[90] Y. Pawar, K. J. Stebe, Marangoni effects on drop deformation in an extensional flow: The role of surfactant physical chemistry. I. Insoluble surfactants, Physics of Fluids 8 (7) (1996) 1738–1751.

[91] A. J. James, J. Lowengrub, A surfactant-conserving volume-of-fluid method for interfacial flows with insoluble surfactant, Journal of Computational Physics 201 (2) (2004) 685 – 722, ISSN 0021-9991.

[92] S. K. Godunov, A finite difference method for the computation of discontinuous solutions of the equation of fluid dynamics, Mat. Sb. (47) (1959) 357–393.

[93] C.-W. Shu, Essentially non-oscillatory and weighted essentially non-oscillatory schemes for hyperbolic conservation laws, in: A. Quarteroni (Ed.), Advanced Numerical Approximation of Nonlinear Hyperbolic Equations, vol. 1697 of *Lecture Notes in Mathematics*, Springer Berlin Heidelberg, ISBN 978-3-540-64977-9, 325–432, 1998.

[94] G. Jiang, C.-W. Shu, Efficient implementation of weighted ENO schemes, Journal of Computational Physics 126 (1996) 202–228.

[95] X. Y. Hu, Q. Wang, N. A. Adams, An adaptive central-upwind weighted essentially non-oscillatory scheme, Journal of Computational Physics 229 (2010) 8952–8965.

[96] X. Y. Hu, N. A. Adams, Scale separation for implicit large eddy simulation, Journal of Computational Physics 230 (2011) 7240–7249.

[97] R. Borges, M. Carmona, B. Costa, W. S. Don, An improved weighted essentially non-oscillatory scheme for hyperbolic conservation laws, Journal of Computational Physics 227 (6) (2008) 3191 – 3211, ISSN 0021-9991.

[98] F. S. Schranner, V. Rozov, N. A. Adams, Optimization of an Implicit Large-Eddy Simulation Method for Underresolved Incompressible Flow Simulations, AIAA Journal 54 (5) (2016) 1567–1577.

[99] F. S. Schranner, V. Rozov, N. A. Adams, Optimization of an Implicit LES Method for Underresolved Simulations of Incompressible Flows, in: Proceedings of the 54th AIAA Aerospace Sciences Meeting, AIAA Science and Technology Forum and Exposition, AIAA, 2016.

[100] P. L. Roe, Approximate Riemann Solvers, Parameter Vectors, and Difference Schemes, Journal of Computational Physics 43 (1981) 357–372.

[101] P. L. Roe, J. Pike, Efficient Construction and Utilisation of Approximate Riemann Solutions, in: Proc. Of the Sixth Int'l. Symposium on Computing Methods in Applied Sciences and Engineering, VI, North-Holland Publishing Co., Amsterdam, The Netherlands, The Netherlands, ISBN 0-444-87597-2, 499–518, 1985.

[102] F. S. Schranner, X. Hu, N. A. Adams, On the convergence of the weakly compressible sharp-interface method for two-phase flows, Journal of Computational Physics 324 (2016) 94 – 114, ISSN 0021-9991.

[103] X. Hu, B. Khoo, N. A. Adams, F. Huang, A conservative interface method for compressible flows, Journal of Computational Physics 219 (2) (2006) 553–578.

[104] E. Lauer, X. Y. Hu, S. Hickel, N. A. Adams, Numerical modelling and investigation of symmetric and asymmetric cavitation bubble dynamics, Computers & Fluids 69 (0) (2012) 1 – 19, ISSN 0045-7930.

[105] X. Y. Hu, B. C. Khoo, An interface interaction method for compressible multifluids, Journal of Computational Physics 198 (1) (2004) 35–64.

[106] R. Saurel, S. Gavrilyuk, F. Renaud, A multiphase model with internal degrees of freedom: application to shock–bubble interaction, Journal of Fluid Mechanics 495 (2003) 283–321.

[107] S. Osher, J. A. Sethian, Fronts propagating with curvature-dependent speed: Algorithms based on Hamilton-Jacobi formulations, Journal of Computational Physics 79 (1) (1988) 12 – 49, ISSN 0021-9991.

[108] S. Osher, R. P. Fedkiw, Level Set Methods: An Overview and Some Recent Results, Journal of Computational Physics 169 (2) (2001) 463 – 502, ISSN 0021-9991.

[109] J. Sethian, P. Smereka, Level Set Methods for Fluid Interfaces, Annual Review of Fluid Mechanics (35) (2003) 341–372.

[110] D. Adalsteinsson, J. A. Sethian, A Fast Level Set Method for Propagating Interfaces, Journal of Computational Physics 118 (2) (1995) 269 – 277, ISSN 0021-9991.

[111] M. Sussman, P. Smereka, S. Osher, A Level Set Approach for Computing Solutions to Incompressible Two-Phase Flow, Journal of Computational Physics 114 (1) (1994) 146 – 159, ISSN 0021-9991.

[112] J.-J. Xu, Z. Li, J. Lowengrub, H. Zhao, A level-set method for interfacial flows with surfactant, Journal of Computational Physics 212 (2) (2006) 590 – 616, ISSN 0021-9991.

[113] C.-W. Shu, High-order Finite Difference and Finite Volume WENO Schemes and Discontinuous Galerkin Methods for CFD, International Journal of Computational Fluid Dynamics 17 (2) (2003) 107–118.

[114] F. S. Schranner, J. A. Domaradzki, S. Hickel, N. A. Adams, Assessing the numerical dissipation rate and viscosity in numerical simulations of fluid flows, Computers & Fluids 114 (0) (2015) 84 – 97, ISSN 0045-7930.

[115] F. S. Schranner, X. Hu, N. A. Adams, Long-Time Evolution of the Incompressible Three-Dimensional Taylor-Green Vortex at Very High Reynolds Number, in: Proceedings of the Eighth International Symposium on Turbulence and Shear Flow Phenomena (TSFP-8), 2013.

[116] S. Gottlieb, C.-W. Shu, Total Variation Diminishing Runge-Kutta Schemes, Mathematics of computation 67 (221) (1998) 73–85, ISSN 0025-5718(98)00913-2.

[117] L. Han, X. Hu, N. Adams, Adaptive multi-resolution method for compressible multiphase flows with sharp interface model and pyramid data structure, Journal of Computational Physics 262 (0) (2014) 131 – 152, ISSN 0021-9991.

[118] M. Sussman, E. G. Puckett, A Coupled Level Set and Volume-of-Fluid Method for Computing 3D and Axisymmetric Incompressible Two-Phase Flows, Journal of Computational Physics 162 (2) (2000) 301 – 337, ISSN 0021-9991.

[119] J. Brackbill, D. Kothe, C. Zemach, A continuum method for modeling surface tension, Journal of Computational Physics 100 (2) (1992) 335 – 354, ISSN 0021-9991.

[120] J. A. Domaradzki, S. Radhakrishnan, Effective eddy viscosities in implicit modeling of decaying high Reynolds number turbulence with and without rotation, Fluid Dynamics Research 36 (2005) 385–406.

[121] E. Tadmor, Convergence of Spectral Methods for Nonlinear Conservation Laws, SIAM Journal on Numerical Analysis 26 (1) (1989) 30–44.

[122] C.-W. Shu, W.-S. Don, D. Gottlieb, O. Schilling, L. Jameson, Numerical Convergence Study of Nearly Incompressible, Inviscid Taylor-Green Vortex Flow, Journal of Scientific Computing 24 (2005) 1–27, ISSN 0885-7474.

[123] L. G. Margolin, W. J. Rider, A rationale for implicit turbulence modelling, International Journal for Numerical Methods in Fluids 39 (9) (2002) 821–841, ISSN 1097-0363.

[124] P. Sagaut, E. Garnier, N. Adams, Large Eddy Simulation for Compressible Flows, ISBN: 9048128188, Springer Berlin / Heidelberg, 2009.

[125] N. Adams, S. Hickel, S. Franz, Implicit subgrid-scale modeling by adaptive deconvolution, Journal of Computational Physics 200 (2) (2004) 412–431.

[126] F. Grinstein, L. Margolin, W. Rider, Implicit Large Eddy Simulation: Computing Turbulent Fluid Dynamics., Cambridge Univ Pr, 2007.

[127] G. I. Taylor, A. Green, Mechanism of the Production of Small Eddies from Larger Ones, Proc. R. Soc. Lond. A 158 (1937) 499–521.

[128] A. J. Chorin, The Numerical Solution of the Navier-Stokes Equations for an Incompressible Fluid, Bull. Amer. Math. Soc. 73 (1967) 928 – 931.

[129] A. J. Chorin, Numerical Solution of the Navier-Stokes Equations, Mathematics Of Computation 22 (1968) 745 – 762.

[130] Y. Marx, Evaluation of the Artificial Compressibility Method for the Solution of the Incompressible Navier-Stokes Equations, in: 9th GAMM Conference of Numerical Methods in Fluid Mechanics, Lausanne 1991.

[131] D. Elsworth, E. Toro, Riemann solvers for solving the incompressible Navier-Stokes equations using the artificial compressibility method, Tech. Rep., Cranfield, College of Aeronautics Report No 9208, June 1992.

[132] D. L. Brown, M. L. Minion, Performance of Under-resolved Two-Dimensional Incompressible Flow Simulations, Journal of Computational Physics 122 (1) (1995) 165 – 183, ISSN 0021-9991.

[133] M. L. Minion, D. L. Brown, Performance of Under-resolved Two-Dimensional Incompressible Flow Simulations, II, Journal of Computational Physics 138 (2) (1997) 734 – 765, ISSN 0021-9991.

[134] W. Kramer, H. J. Clercx, G. J. van Heijst, Vorticity dynamics of a dipole colliding with a no-slip wall, Physics of Fluids 19 (126603) (2007) 1–13.

[135] H. Clercx, C.-H. Bruneau, The normal and oblique collision of a dipole with a no-slip boundary, Computers & Fluids 35 (3) (2006) 245 – 279, ISSN 0045-7930.

[136] E. Erturk, Discussions On Driven Cavity Flow, International Journal for Numerical Methods in Fluids 60 (2009) 275–294.

[137] K. Ghia, W. Hankey, Jr., J. Hodge, Study of incompressible Navier-Stokes equations in primitive variables using implicit numerical technique, in: 3rd Computational Fluid Dynamics Conference, 156–167, 1977.

[138] U. Ghia, K. N. Ghia, C. T. Shin, High-Re solutions for incompressible flow using the Navier-Stokes equations and a multigrid method, Journal of Computational Physics 48 (1982) 387–411.

[139] D. C. Wilcox, Turbulence Modeling for CFD, 0-9636051-0-0, DCW Industries, Inc., 2 edn., 1994.

[140] R. Schwarze, CFD-Modellierung: Grundlagen und Anwendungen bei Strömungsprozessen, Springer-Verlag Berlin Heidelberg, 1 edn., 2013.

[141] H. Versteeg, W. Malalasekra, An Introduction to Computational Fluid Dynamics: The Finite Volume Method, 978-0131274983, Pearson Education Limited, Edinburgh Gate, Harlow, Essex CM20 2JE, England, 2 edn., 2007.

[142] J. H. Ferziger, M. Peric, Computational Methods for Fluid Dynamic, Springer Berlin / Heidelberg, 3rd rev. edition edn., 2002.

[143] M. Lesieur, O. Métais, P. Comte, Large-Eddy Simulations of Turbulence, Cambridge University Press, ISBN 9780511755507, cambridge Books Online, 2005.

[144] P. Sagaut, Large Eddy Simulation for Incompressible Flows, Springer-Verlag Berlin Heidelberg, 3 edn., 2006.

[145] P. S. Eric Garnier, N.A. Adams, Large Eddy Simulation for Compressible Flows (Scientific Computation), Springer Berlin / Heidelberg, 2009.

[146] J. A. Domaradzki, Z. Xiao, P. Smolarkiewicz, Effective Eddy Viscosities in Implicit Large Eddy Simulations of Turbulent Flows, Physics Fluids 15 (2003) 3890–3893.

[147] G. Gerolymos, D. Sénéchal, I. Vallet, Very-high-order weno schemes, Journal of Computational Physics 228 (23) (2009) 8481 – 8524, ISSN 0021-9991.

[148] Guide: Guide for the Verification and Validation of Computational Fluid Dynamics Simulations (AIAA G-077-1998(2002)), 2002.

[149] S. Hickel, N. A. Adams, On implicit subgrid-scale modeling in wall-bounded flows, Physics of Fluids 19 (10) (2007) 105106–105113.

[150] R. D. Moser, J. Kim, N. N. Mansour, Direct numerical simulation of turbulent channel flow up to Re= 590, Phys. Fluids 11 (4) (1999) 943–945.

[151] N. N. Mansour, J. Kim, P. Moin, Reynolds-stress and dissipation-rate budgets in a turbulent channel flow, Journal of Fluid Mechanics 194 (1988) 15–44, ISSN 1469-7645.

[152] G. Keetels, U. D'Ortona, W. Kramer, H. Clercx, K. Schneider, G. van Heijst, Fourier spectral and wavelet solvers for the incompressible Navier-Stokes equations with volume-penalization: Convergence of a dipole-wall collision, Journal of Computational Physics 227 (2) (2007) 919 – 945, ISSN 0021-9991.

[153] W. L. Oberkampf, T. G. Trucano, Verification and validation in computational fluid dynamics, Progress in Aerospace Sciences 38 (3) (2002) 209 – 272, ISSN 0376-0421.

[154] J. Martin, W. J. Moyce, An experimental study of the collapse of liquid columns on a rigid horizontal plane, Philosophical Transactions of the Royal Society of London Series A (244) (1952) 312–324.

[155] S. J. Cummins, M. Rudman, An SPH Projection Method, Journal of Computational Physics 152 (2) (1999) 584 – 607, ISSN 0021-9991.

[156] M. Meister, W. Rauch, Simulating Rising Bubble Problems with Smoothed Particle Hydrodynamics, in: IMA Conference on Mathematical Modelling of Fluid Systems, Bristol, 2014.

[157] R. Scardovelli, S. Zaleski, Direct Numerical Simulation of Free-Surface and Interfacial Flow, Annual Review of Fluid Mechanics 31 (1999) 567–603.

[158] D. Anderson, G. B. McFadden, A. Wheeler, Diffuse-interface methods in fluid mechanics, Annual review of fluid mechanics 30 (1) (1998) 139–165.

[159] S. Adami, X. Hu, N. Adams, A conservative SPH method for surfactant dynamics, Journal of Computational Physics 229 (5) (2010) 1909 – 1926, ISSN 0021-9991.

[160] K. Szewc, J. Pozorski, J.-P. Minier, Analysis of the incompressibility constraint in the smoothed particle hydrodynamics method, International Journal for Numerical Methods in Engineering 92 (4) (2012) 343–369, ISSN 1097-0207.

[161] R. P. Fedkiw, T. Aslam, B. Merriman, S. Osher, A Non-oscillatory Eulerian Approach to Interfaces in Multimaterial Flows (the Ghost Fluid Method), Journal of Computational Physics 152 (2) (1999) 457 – 492, ISSN 0021-9991.

[162] J. Luo, X. Hu, N. Adams, A conservative sharp interface method for incompressible multiphase flows, Journal of Computational Physics 284 (0) (2015) 547 – 565, ISSN 0021-9991.

[163] H. A. Stone, L. G. Leal, The effects of surfactants on drop deformation and breakup, Journal of Fluid Mechanics 220 (1990) 161–186, ISSN 1469-7645.

[164] X. Li, C. Pozrikidis, The effect of surfactants on drop deformation and on the rheology of dilute emulsions in Stokes flow, Journal of Fluid Mechanics 341 (1997) 165–194, ISSN 1469-7645.

[165] G. Tryggvason, B. Bunner, A. Esmaeeli, D. Juric, N. Al-Rawahi, W. Tauber, J. Han, S. Nas, Y.-J. Jan, A Front-Tracking Method for the Computations of Multiphase Flow, Journal of Computational Physics 169 (2) (2001) 708 – 759, ISSN 0021-9991.

[166] Y.-J. Jan, Computational studies of bubble dynamics, Ph.D. thesis, University of Michigan, 1994.

[167] R. Mittal, G. Iaccarino, Immersed Boundary Methods, Annual Review of Fluid Mechanics 37 (2005) 239–261.

[168] Y.-H. Tseng, J. H. Ferziger, A ghost-cell immersed boundary method for flow in complex geometry, Journal of Computational Physics 192 (2) (2003) 593 – 623, ISSN 0021-9991.

[169] F. Jin, K. J. Stebe, The effects of a diffusion controlled surfactant on a viscous drop injected into a viscous medium, Physics of Fluids 19 (11) 112103.

[170] H. D. Ceniceros, The effects of surfactants on the formation and evolution of capillary waves, Physics of Fluids 15 (1) (2003) 245–256.

[171] Y.-C. Liao, E. I. Franses, O. A. Basaran, Deformation and breakup of a stretching liquid bridge covered with an insoluble surfactant monolayer, Physics of Fluids 18 (2) 022101.

[172] Q. Xu, Y.-C. Liao, O. A. Basaran, Can Surfactant Be Present at Pinch-Off of a Liquid Filament?, Phys. Rev. Lett. 98 (2007) 054503.

[173] K. E. Teigen, P. Song, J. Lowengrub, A. Voigt, A diffuse-interface method for two-phase flows with soluble surfactants, Journal of Computational Physics 230 (2) (2011) 375 – 393, ISSN 0021-9991.

[174] D. Adalsteinsson, J. Sethian, Transport and diffusion of material quantities on propagating interfaces via level set methods, Journal of Computational Physics 185 (1) (2003) 271 – 288, ISSN 0021-9991.

[175] J.-J. Xu, H.-K. Zhao, An Eulerian Formulation for Solving Partial Differential Equations Along a Moving Interface, Journal of Scientific Computing 19 (1-3) (2003) 573–594, ISSN 0885-7474.

[176] R. J. LeVeque, Z. Li, The Immersed Interface Method for Elliptic Equations with Discontinuous Coefficients and Singular Sources, SIAM Journal on Numerical Analysis 31 (4) (1993) 1019–1044.

[177] E. Lauer, X. Y. Hu, S. Hickel, N. A. Adams, Numerical investigation of collapsing cavity arrays, Physics of Fluids 24 (5) 052104.

[178] L. Foucard, X. Espinet, E. Benet, F. J. Vernerey, The Role of the Cortical Membrane in Cell Mechanics: Model and Simulation, John Wiley & Sons Ltd, ISBN 9781118402955, 241–265, 2013.

[179] B. Pendse, A. Esmaeeli, An analytical solution for thermocapillary-driven convection of superimposed fluids at zero Reynolds and Marangoni numbers, International Journal of Thermal Sciences 49 (7) (2010) 1147 – 1155, ISSN 1290-0729.